ADVANCES IN

CHEMICAL
PROPULSION

SCIENCE TO TECHNOLOGY

Environmental and Energy Engineering Series

Series Editors

Ashwani K. Gupta
Department of Mechanical Engineering, University of Maryland, College Park, Maryland

David G. Lilley
School of Mechanical and Aerospace Engineering, Oklahoma State University, Stillwater, Oklahoma

Published Titles

Enclosure Fire Dynamics
Björn Karlsson and James G. Quintiere
Integrated Product and Process Design and Development
Edward B. Magrab
Advances in Chemical Propulsion: Science to Technology
Gabriel D. Roy

Forthcoming Titles

High Temperature Air Combustion: From Energy Conservation to Pollution Reduction
Ashwani K. Gupta, Hiroshi Tsuji, Masashi Katsuki, Toshiaki Hasegawa, and Mitsunobu Morita

ADVANCES IN
CHEMICAL PROPULSION
SCIENCE TO TECHNOLOGY

EDITED BY
GABRIEL D. ROY
OFFICE OF NAVAL RESEARCH
MECHANICS AND ENERGY CONVERSION DIVISION
ARLINGTON, VIRGINIA

CRC

CRC PRESS

Boca Raton   London   New York   Washington, D.C.

Contents

SECTION THREE
Control of Combustion

CONCLUSION

The Editor

Gabriel D. Roy received his B.S. and M.S. in mechanical engineering, did his graduate study at the University of Tennessee Space Institute (UTSI) and received his Ph.D. degree in engineering science. He served as a faculty member of the Mechanical Engineering department in India and the U.S. and as a major thesis advisor for over a dozen graduate students, besides managing the Heat Engines Laboratory projects. His early research involved hydrodynamic air bearings, crack propagation, and fatigue failure. As a Senior Research Engineer at UTSI, where he developed the diffuser and heat transfer diagnostics, he conducted heat transfer studies on the magnetohydrodynamic (MHD) power train, and also generated pressure recovery performance curves for slagging MHD diffusers. He was responsible, as Project Leader in Heat Transfer, for all heat transfer aspects of the U.S. DoE — sponsored MHD project. Later, he joined the industry (TRW, Inc.), where he received the TRW Roll of Honor Award, and patents on combustor and atomizer. He was responsible for the development of the pulverized and slurry fuel injector and the high-voltage slag isolation and removal system.

Currently, Dr. Roy manages the Energy Conversion–Propulsion Program for the U.S. Navy at the Office of Naval Research (ONR). He also managed the Pulsed Power Program for the Ballistic Missile Defense Organization. In addition to the fundamental combustion program, he also envisioned and monitored focussed multiyear programs such as High-Energy Strained Hydrocarbon Fuels and Air-Emission Control of Navy Marine Engines, and he presently manages research programs on Pulse Detonation Engines for Propulsion and Combustion Control. With more than 35 years of government, industry, and university experience, he is recognized worldwide in magnetohydrodynamics, propulsion and fuels research, and management. His research interests include control of combustion processes, detonation, electromagnetic propulsion, and electrorheology. He has organized several national and international conferences and workshops on innovative aspects of the combustion field such as electrorheological fuels, electromagnetic propulsion, pulse power, and pulse detonation engines.

Dr. Roy is the recipient of the ASME Jean F. Lewis Energy Systems Award. He has edited several books and has over 100 publications and research reports

to his credit. He is listed in the *Marquis' Who's Who in Science and Engineering* and the *Who's Who in the South and Southwest*. He has been a member in various technical committees of the American Institute of Aeronautics and Astronautics (AIAA) and a number of Government Review Panels. He served as an associate editor of the AIAA Journal of Propulsion and Power, and is a Fellow of AIAA. Dr. Roy is also an artist and has received national awards in painting. As a college student, he received the Duthie Memorial Award for 2 years.

Contributors

B. R. Aavula
Department of Chemistry
University of North Texas
Denton, TX 76203

S. Acharya
Mechanical Engineering Department
Louisiana State University
Baton Rouge, LA 70803

P. Aghalayam
Department of Chemical Engineering
University of Massachusetts
at Amherst
Amherst, MA 01003

R. C. Aldredge, III
Mechanical and Aeronautical
Engineering
University of California at Davis
Davis, CA 95616

S. Alihodzic
Department of Chemistry
University of North Texas
Denton, TX 76203

S. L. Anderson
Department of Chemistry
University of Utah
Salt Lake City, UT 84112

D. S. Baer
High Temperature Gasdynamics
Laboratory
Department of Mechanical Engineering
Stanford University
Stanford, CA 94305

V. Ya. Basevich
Department of Kinetics and Catalysis
N. N. Semenov Institute of Chemical
Physics, Russian Academy of Sciences
Moscow 117977, Russia

A. J. Basu
Jawaharlal Nehru Centre
for Advanced Scientific Research
Jakkur, Bangalore 560064, India

A. A. Belyaev
Department of Kinetics and Catalysis
N. N. Semenov Institute of Chemical
Physics, Russian Academy of Sciences
Moscow 117977, Russia

R. Bhidayasiri
Department of Mechanical Engineering
Imperial College of Science,
Technology and Medicine
London SW7 2BX, UK

S. G. Bott
Department of Chemistry
University of North Texas
Denton, TX 76203

P. A. Bui
Department of Chemical
Engineering
University of Massachusetts
at Amherst
Amherst, MA 01003

E. Chang
Laboratory for Computational
Physics and Fluid Dynamics
U.S. Naval Research Laboratory
Washington, DC 20375

S. R. Charangudia
National Institute of Standards
and Technology
Gaithersburg, MD

P. E. DesJardin
Thermal Science and Propulsion
Center
School of Mechanical Engineering
Purdue University
West Lafayette, IN 47907

E. Z. Dong
Department of Chemistry
University of North Texas
Denton, TX 76203

J. P. Foote
ERC, Inc.
Tullahoma, TN 37388

S. H. Frankel
Thermal Science and Propulsion
Center School of Mechanical
Engineering
Purdue University
West Lafayette, IN 47907

S. M. Frolov
Department of Kinetics and Catalysis
N. N. Semenov Institute of Chemical
Physics, Russian Academy of Sciences
Moscow 117977, Russia

P. Givi
Department of Mechanical
and Aerospace Engineering
State University of New York
at Buffalo
Buffalo, NY 14260

J. P. Gore
Maurice J. Zucrow Laboratories
School of Mechanical Engineering
Purdue University
West Lafayette, IN 47907

F. F. Grinstein
Laboratory for Computational Physics
and Fluid Dynamics
U.S. Naval Research Laboratory
Washington, DC 20375

A. K. Gupta
Department of Mechanical Engineering
University of Maryland
College Park, MD 20742

E. J. Gutmark
Department of Aerospace Engineering
and Engineering Mechanics
University of Cincinnati
Cincinnati, OH 45221

R. K. Hanson
High Temperature Gasdynamics
Laboratory
Department of Mechanical Engineering
Stanford University
Stanford, CA 94305

D. M. Hanson-Parr
Research and Technology Group
Naval Air Warfare Center
Weapons Division
China Lake, CA 93555

J. C. Hewson
Center for Energy and Combustion
Research
University of California at San Diego
La Jolla, CA 92093

D. Hofeldt
Department of Mechanical
Engineering
University of Minnesota
Minneapolis, MN 55455

B. S. Hong
Department of Mechanical
Engineering
The Pennsylvania State University
University Park, PA 16802

V. V. Ivanov
Central Aero-Hydrodynamic
Institute (TsAGI)
Zhukovsky, Moscow Region
140160 Russia

F. A. Jaberi
Department of Mechanical
Engineering
Michigan State University
East Lansing, MI 48824

K. Kailasanath
Laboratory for Computational
Physics and Fluid Dynamics
U.S. Naval Research Laboratory
Washington, DC 20375

E. Koc-Alkislar
Fluid Mechanics Research Laboratory
Department of Mechanical Engineering
Florida A&M University and Florida
State University
Tallahassee, FL 32310

Yu. Ph. Korontsvit
Central Aero-Hydrodynamic Institute
(TsAGI)
Zhukovsky, Moscow Region
140160 Russia

A. Krothapalli
Fluid Mechanics Research Laboratory
Department of Mechanical Engineering
Florida A&M University and Florida
State University
Tallahassee, FL 32310

J. C. Legros
Université Libre de Bruxelles
Bruxelles 1050, Belgique

S. B. Lewis
Department of Chemistry
University of North Texas
Denton, TX 76203

J. Li
Mechanical Engineering Department
Louisiana State University
Baton Rouge, LA 70803

Z. Li
Department of Chemistry
University of Utah
Salt Lake City, UT 84112

J. T. Lineberry
LyTec Inc.
Tullahoma, TN 37388

S. Lonnes

Department of Mechanical Engineering
University of Minnesota
Minneapolis, MN 55455

L. Lourenco

Fluid Mechanics Research Laboratory
Department of Mechanical Engineering
Florida A&M University and Florida
State University
Tallahassee, FL 32310

C. K. Madnia

Department of Mechanical
and Aerospace Engineering
State University of New York
at Buffalo
Buffalo, NY 14260

A. P. Marchand

Department of Chemistry
University of North Texas
Denton, TX 76203

F. Mashayek

Department of Mechanical Engineering
University of Illinois at Chicago
Chicago, IL 60607

M. Megerle

Department of Mechanical Engineering
University of Maryland
College Park, MD 20742

R. M. Moriarty

Department of Chemistry
University of Illinois at Chicago
Chicago, IL 60607

I. N. N. Namboothiri

Department of Chemistry
University of North Texas
Denton, TX 76203

R. Narasimha

Jawaharlal Nehru Centre for Advanced
Scientific Research
Jakkur, Bangalore 560064, India

V. F. Nikitin

Department of Mechanics
and Mathematics
Moscow State University
Moscow 119899, Russia

S. Pal

Department of Aerospace Engineering
Mechanics and Engineering Science
University of Florida
Gainesville, FL 32611

T. P. Parr

Research and Technology Group
Naval Air Warfare Center
Weapons Division
China Lake, CA 93555

R. E. Peck

Department of Mechanical Engineering
Arizona State University
Tempe, AZ 85287

S. Pethe

Department of Aerospace Engineering,
Mechanics and Engineering Science
University of Florida
Gainesville, FL 32611

V. S. Posvianskii

Department of Kinetics and Catalysis
N. N. Semenov Institute of Chemical
Physics, Russian Academy of Sciences
Moscow 117977, Russia

C. Presser

National Institute of Standards
and Technology
Gaithersburg, MD

Yu. B. Radvogin
V. M. Keldysh Institute
of Applied Mathematics
Russian Academy of Sciences
Moscow, Russia

K. C. V. Ramanaiah
Department of Chemistry
University of North Texas
Denton, TX 76203

A. Ray
Department of Mechanical
Engineering
The Pennsylvania State
University
University Park, PA 16802

G. D. Roy
Office of Naval Research
Arlington, VA 22217

V. A. Sabel'nikov
Central Aero-Hydrodynamic
Institute (TsAGI)
Zhukovsky, Moscow
Region, 140160 Russia

K. C. Schadow
Research and Technology Group
Naval Air Warfare Center
Weapons Division
China Lake, CA 93555

C. Segal
Department of Aerospace
Engineering
Mechanics and Engineering
Science
University of Florida
Gainesville, FL 32611

W. Shyy
Department of Aerospace Engineering
Mechanics and Engineering Science
University of Florida
Gainesville, FL 32611

S. Singh
SS Energy Environmental
International, Inc.
Rockford, IL 61108

S. Sivasegaram
Department of Mechanical Engineering
Imperial College of Science,
Technology and Medicine
London SW7 2BX, UK

N. N. Smirnov
Department of Mechanics
and Mathematics
Moscow State University
Moscow 119899, Russia

J. Stephens
Mechanical Engineering Department
Louisiana State University
Baton Rouge, LA 70803

P. Strykowski
Department of Mechanical Engineering
University of Minnesota
Minneapolis, MN 55455

D. B. Taulbee
Department of Mechanical
and Aerospace Engineering
State University of New York
at Buffalo
Buffalo, NY 14260

B. R. Thompson
ERC, Inc.
Tullahoma, TN 37388

H. S. Udaykumar

Department of Aerospace Engineering,
Mechanics and Engineering Science
University of Florida
Gainesville, FL 32611

D. G. Vlachos

Department of Chemical Engineering
University of Delaware
Newark, DE 19716

J. H. Whitelaw

Imperial College of Science,
Technology and Medicine
London SW7 2BX, UK

F. A. Williams

Center for Energy and
Combustion Research
University of California at San Diego
La Jolla, CA 92093

K. J. Wilson

Research and Technology Group
Naval Air Warfare Center
Weapons Division
China Lake, CA 93555

V. Yang

Department of Mechanical Engineering
The Pennsylvania State University
University Park, PA 16802

K. H. Yu

Department of Aerospace Engineering
University of Maryland
College Park, MD 20742

S. A. Zosimov

Central Aero-Hydrodynamic Institute
(TsAGI)
Zhukovsky, Moscow Region
140160 Russia

Preface

Propulsion, in one form or another, is one of the oldest technologies known to the human race. This technology has been utilized in various applications from a simple bicycle to a high-speed bullet train, a catamaran to a submarine, and a helicopter to a hypersonic missile. The motivation behind propulsion science and technology has been, from the days of primitive man, to travel, explore, defend, and sometimes to conquer.

Chemical propulsion is a complex science involving several disciplines. In the past several decades, extensive research has been carried out worldwide in order to advance the scientific findings and to utilize them for technology applications. The subject is vast, as evident from the numerous publications of textbooks, monographs, and journal articles. This book is an attempt to provide a source of reference, for a practicing engineer or a graduate student, or as a textbook for a graduate course in Advanced Topics in Combustion, as it covers some of the major issues in propulsion science and technology today in a single volume.

Today's propulsion systems are required to produce larger and more rapid release of energy from smaller and more compact combustors, to cope with the demand for increased speed and range, and a wider operational envelope. Associated with these requirements are higher temperatures, increased heat transfer and thermal load, and frequent off-design operation. For current and future propulsion systems the following three major criteria are important:

(1) increase the speed and range of vehicles: commercial and military transport and weapons

(2) obtain the maximum combustion efficiency and stable operation possible

(3) to comply with environmental constraints

These three items form the primary subject matter for this book.

The editor has had the opportunity to envision, initiate, and monitor research projects in propulsion for more than a decade under the sponsorship of the Office of Naval Research (ONR). The topics covered range from the concept of convective Mach number to counterflow fluidic thrust vectoring; electrorheological fuels to electromagnetic propulsion; and marine propulsion to aircraft and missile propulsion. This publication is essentially an assembly of results from selected research projects that depict the advances in propulsion science made in the past several years in the context and mission of this book, particularly in air-breathing propulsion.

In addition to the Introduction and Conclusion chapters (written by the editor), the book contains chapters under the following sections:

1. Advanced fuel synthesis and characterization

2. Fundamental combustion issues

3. Control of combustion

4. Emissions and plumes

These chapters are written by those who have actually conducted the research, either independently or as part of a team, on projects that were monitored by the editor. They describe the issues, the approach used, the results obtained, and they show how the scientific findings can be extended to practical applications. In his introductory chapter, the editor has tried to guide the reader through the contents of the four sections of the book. In particular, the interrelations among the chapters in each section are illustrated so as to aid the reader to appreciate how the research by various investigators is focussed to obtain the fundamental understanding revelant to propulsion applications.

In Section 1, the synthesis, combustion characterization, and numerical investigation of high-energy-density fuels are described. The synthesis methods of these fuels and their properties and combustion chemistry (both at microscopic and macroscopic levels) are covered. Section 2 deals with some important fundamental issues in combustion that are relevant to propulsion. The solutions provide the understanding needed to design modern and future combustion devices that will be volume and weight limited; be capable to operate at higher temperatures and in more hostile conditions; be designed for improved performance, stealth, and maneuverability; and be able to comply with more stringent constraints at a wide range of loads.

Combustion instability that leads to performance deterioration and excessive mechanical loads, which could result in reduced life and premature failure, is an important issue with modern gas turbine engines and ramjet and scramjet combustors. Various techniques of passive and active control to reduce combustion instabilities and improve performance are addressed. Since extensive, promising research is being carried out to develop sensors and actuators, these techniques can be used in practical combustors in the near future. The topics covered in Section 3 provide the required chemical, kinetic, and fluid dynamic understanding to help the designer who is involved in active feedback control for combustion systems.

Regulations on environmental pollution are becoming increasingly stringent. Analytical, computational, and experimental efforts focus on emissions reduction to below current and proposed limits. From the scientific research, practical approaches, such as partial premixing and utilization of porous inserts have been developed. These are treated in Section 4.

In the concluding chapter, the editor has elucidated the various opportunities in future propulsion research and shown some of the avenues that are currently pursued, and planned for implementation.

As the title of the book implies, *Advances in Chemical Propulsion: Science to Technology*, the topics chosen are areas of scientific research that have a specific goal of application to technology, and are edited to preserve the context of the book. Because of the vastness of the topics, minor details are limited but the broad scope and information needed for application to practical systems are given. Additionally, a large number of references are provided for those who are interested in finding detailed information on a particular issue, method, or solution. Further, the mailing addresses of the authors are provided for future communication, if needed by the reader.

Careful attention has been paid to maintain uniformity of the individual chapters, and the editor has tried to maintain "clarity and flow" for reading, as well as clarity in understanding the figures. Any endeavor of this type takes time, and the editor acknowledges the cooperation of his wife, Vimala, for letting him stay with his computer during late night hours, and offering support to his "extra-work" as she puts it! His daughter, Sitara, and daughters-in-law, Vino and Rita, have always been his sources of inspiration, and their love and encouragement are acknowledged. The editorial assistance given by Ms. Mary Keegan is greatly appreciated.

The contents of this book have been generated exclusively from research programs that were envisioned and monitored by the editor, and sponsored by ONR. The chapters are illustrations of the research conducted by the respective authors, and are not a review of research on the particular topic. The editor takes

this opportunity to thank Dr. Spiro Lekoudis, his department head at ONR, for his unfailing support over the years. Special thanks is due to the authors who made this work possible. He acknowledges his colleagues, Dr. Julian Tishkoff of the Air Force Office of Scientific Research and Dr. David Mann of the Army Research Office, for their cooperation over a decade. The assistance given by Ms. Cindy Carelli and Ms. Michele Berman of CRC Press is appreciated.

It is hoped that this book will provide a single source of information on advances in propulsion for practicing engineers, faculty and graduate students, and those involved in research in propulsion.

Gabriel D. Roy
Office of Naval Research
Arlington, VA
March 2001

INTRODUCTION

Chapter 1

CHEMICAL PROPULSION: RECENT ACCOMPLISHMENTS

G. D. Roy

Chemical propulsion research has not seen a quantum leap during the past several decades in realizing a new engine concept with substantial improvement in performance and reduction in size in spite of the various significant advances and research accomplishments. This is partly due to the fact that driving the combustion process toward faster energy release rates, higher operational temperatures and pressures, and utilization of exotic high-energy fuels will be dependent upon parallel developments in high-temperature materials with adequate heat management characteristics, control of combustion processes, and elimination of pollutants and signature-carrying species. Propulsion Science and Technology (S&T) calls for multidisciplinary programs with inputs from a wide spectrum of basic and applied sciences.

The last two decades have particularly seen significant S&T in the propulsion field. In the U.S., agencies such as the National Science Foundation (NSF), National Aeronautics and Space Administration (NASA), Defense Advanced Research Projects Agency (DARPA), and the Departments of Defense (DoD) and Energy (DoE) have invested substantial funds in sponsoring S&T in the chemical propulsion area. The worldwide propulsion S&T investment has also been significant. Among the DoD S&T sponsoring agencies the Office of Naval Research (ONR) has been a pioneer organization in sponsoring university research in combustion and propulsion. Hundreds of related topics have been investigated, and noteworthy contributions to the combustion science have been made. A few are selected here in this book to show the progress and the scientific accomplishments made, and to indicate their application to propulsion technology.

1.1 ADVANCED FUEL SYNTHESIS AND CHARACTERIZATION

The specific purpose or mission of a system dictates the type of fuel to be used in the propulsion engine. Both volume and weight are physical limitations of today's propulsion systems. Increased specific impulse (I_{sp}), improved thrust, reduced fuel consumption along with stability, long shelf-storage life, and hazard-free combustion with minimum pollutants and signatures are required of new fuels. Propulsion system volume is a major consideration for sea-launched weapon systems, where the space available for weapon housing is minimal. Weight is of more significance in air-launched systems.

A fuel of increased density for a given gravimetric heat of combustion will have an advantage in volume-limited systems. In general, for hydrocarbon fuels, as the density is increased, the gravimetric heat of combustion decreases (lower shaded arrow in Fig. 1.1). To utilize the density increase to its full advantage, the gravimetric heat of combustion should remain at least constant. However, the novel fuels investigated have shown an increase in gravimetric heat of combustion with increase in density (upper shaded arrow in Fig. 1.1). This is partly due to the strain energy in the molecules.

Research Accomplishments

In the pursuit of new high-energy-density fuels, fuels with strained molecules have been developed and their combustion characteristics studied [1]. Fuels such as dihydrobenzvalene (C_6H_8) and methyl cubane ((C_8H_7)CH_3) are strained dur-
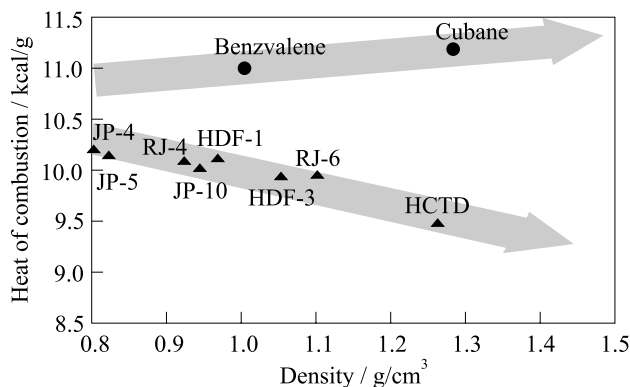
Figure 1.1 Heats of combustion as a function of fuel density

ing synthesis, and this strain energy is released during combustion (Chapter 2). Research by Robert Moriarty at the University of Illinois at Chicago focussed on the synthesis of cubane analogues which contained polyunsaturated side-chains which in turn could be used as starting materials for the production of high-energy derivatives. Other fuels developed by Alan Marchand of North Texas University are new polycarbocyclic "cage" hydrocarbons (Chapter 3), of which one particularly interesting group of compounds includes "PCU alkane dimers." The properties and combustion characteristics of these fuels, including crystal density, thermodynamic properties, and regression rates, were investigated. These fuels can be mixed with JP-10 to provide substantially increased burning rates.

Synthesis of these novel fuels is expensive, and a newly synthesized fuel molecule may not result in an effective fuel. Hence, it is desirable, from testing a very small sample of the fuel (less than a gram), to eliminate those which do not offer promise. In order to accomplish this, a microflow tube reactor has been designed, fabricated, and utilized by Scott Anderson at the University of Utah. The thermal breakdown behavior, and the stability of the fuel as a function of temperature, as well as the product species as a function of temperature, are determined (Chapter 4). The mixture exiting the reactor is analyzed using a mass spectrometer, which is optimized for low-emission energy scattering. The fuels exhibiting thermal instability in the temperature regime of interest are eliminated, avoiding further investment in the production of larger quantities.

The increased density (ρ = 1.2–1.3 g/cm^3), and moderate strain energy of pentacyclic hydrocarbons contribute to increased energy output during combustion. By breaking the molecular symmetry of these fuels with the addition of a methyl group, the melting and boiling points decreased significantly. The boiling point (80 °C) is significantly below the average value of conventional fuels such as JP-10 (280 °C). Corin Segal, at the University of Florida, has shown that mixtures of methylated pentacyclyic undane (PCU) alkane dimer in kerosene lead to the formation of vapors early in the droplet lifetime resulting in effervescent droplet boiling. Increased acceleration in the droplet breakup and vaporization are achieved due to added high-energy release rates (Chapter 5).

Due to the higher carbon-to-hydrogen ratios of these novel heavy hydrocarbon fuels, soot is an issue and elimination of soot is an important aspect of the research. The efficacy of the control of soot was demonstrated using gaseous fuels (including highly sooting benzene) in open and enclosed flames by Ephraim Gutmark, University of Cincinnati, formerly of Naval Air Warfare Center / Weapons Division, China Lake (NAWC/WD) (Chapter 6). Phased circumferential fuel injection into an axisymmetric air vortex was proven capable of reducing soot formation by several orders of magnitude relative to an unforced case, and doubling the flame temperature [2]. When the proper phase angle

of fuel injection was used, soot formation was prevented, and an entirely blue flame was realized. The combustion efficiency reached 99.999% even at overall equivalence ratio of 1.0 with benzene. This methodology shows promise in the soot-free combustion of high-energy-density hydrocarbon fuels, and in enabling complete combustion.

Computational Combustion Dynamics has shown impressive advances during the past decade. The complex flows incurred in multiphase combustion coupled with the large number of chemical reaction steps pose a formidable task to computational scientists. Research by Kazhikathra Kailasanath at the Naval Research Laboratory is focussed on the development of computational models that simulate combustion of high-energy fuels, and on studies of the differential dispersion of fuel droplets in reacting flows (Chapter 7). Although simulations indicate that microexplosions of high-energy fuels can cause flow disruptions and amplifications of pressure fluctuations, phase-coupled fuel injection has been demonstrated as a means to suppress incipient instabilities. It is also shown that even a small amount of energy release can significantly alter the level of pressure oscillations in the combustor. These results in conjunction with the sequential fuel injection scheme elucidated in Chapter 6 will be helpful in devising strategies for utilization of high-energy-density fuels, both from combustion and control points of view. Reduced chemistry formulations [3] will allow the computationists to perform simulations with fewer chemical reactions resulting in a substantial reduction in computer time, without compromising accuracy.

Combustion of aluminum particle as fuel, and oxygen, air, or steam as oxidant provides an attractive propulsion strategy. In addition to hydrocarbon fuel combustion, research is focussed on determining the particle size and distribution and other relevant parameters for effectively combusting aluminum/oxygen and aluminum/steam in a laboratory-scale atmospheric dump combustor by John Foote at Engineering Research and Consulting, Inc. (Chapter 8). A Monte-Carlo numerical scheme was utilized to estimate the radiant heat loss rates from the combustion products, based on the measured radiation intensities and combustion temperatures. These results provide some of the basic information needed for realistic aluminum combustor development for underwater propulsion.

1.2 FUNDAMENTAL COMBUSTION ISSUES

Current and future combustor applications require increased energy release with reduced chamber volume, increased equilibrium temperature, multiphase reacting flows with radiative heat transfer, and sometimes even with electric and magnetic fields. A thorough understanding of the basic physical and chemical

processes involved in combustion becomes a necessity for the design of efficient and reliable combustion systems.

Traditional development of combustion systems, based largely on empirical data and relatively simple design models, will not be adequate if energy utilization is to be maximized. Detailed, near full-scale experiments are extremely expensive. However, recent advances in high-resolution diagnostics with improved spatial and temporal measurement capability, nonintrusive measurement techniques, and fast and reliable (often *in situ*) data reduction algorithms have enabled researchers, in recent years, to limit the number of such expensive experiments. Careful planning of research, together with cooperative research efforts among several investigators, resulted in better understanding of the practical issues and faster transition of the knowledge to the design community.

A rapid advance in supercomputing and massively parallel processing has brought forth computational capabilities hitherto unheard of. Computational combustion dynamics has paved a new route to perform numerical experiments and to guide experimentalists to design more optimal test configurations [4]. Numerical experiments also help in performing detailed parametric studies, enabling the variation of a single parameter at a time. This has been reflected in the large number of papers on computational work presented in technical meetings, and published in journals. This volume is not an exception, and the majority of work described in this section is analytical and computational in nature.

Research Accomplishments

Probability modeling of turbulent combustion, large-eddy simulation (LES) of turbulent reacting flows, and turbulence closures for multiphase flows performed by Peyman Givi's group at the State University of New York at Buffalo have shed greater insight in understanding combustion in propulsion systems (Chapter 9). From the subject described, it is clear that statistical methods seem to be among the most practical means of predicting "engineering turbulent combustion," and probability density function (PDF) schemes remain as the most powerful tool in relevant predictions.

Current combustion systems, due to the increased operational temperature, require inclusion of radiative heat transfer in their design. To this end, a computational study of coupled turbulence, chemistry, and radiation interactions in an idealized sooting and radiating nonpremixed turbulent planar jet has been conducted by Steven Frankel's group at Purdue University using LES (Chapter 10). The effects of radiative cooling on flame structure and the highly intermittent behavior of the soot volume fraction have been captured. The effect of volumetric heating on the distribution of vorticity and the entrainment characteristics of a temporally evolving jet has been studied by Roddam Narasimha and his group at the Jawaharlal Nehru Centre for Advanced Scientific Research in Bangalore

(Chapter 11). The simulations show enhanced vorticity in all three directions with a rich fine structure at later times in the evolution of the jet and an entrainment velocity field qualitatively different from that of around unheated turbulent jets.

Extending flame stability, combustion limits, and blow-off are important considerations in combustion device design. From the fundamental research carried out in this regard, subsequent control strategies have been formulated. The Presumed Probability Density Function (PPDF) method has been developed and implemented to study flame stabilization in subsonic combustors with flame holders by Sergei Frolov's group at the N. N. Semenov Institute in Moscow (Chapter 12). Turbulence–chemistry interaction, multiple thermochemical variables, variable pressure, near-wall effects, etc. are taken into account. This method provides an efficient research tool for studying flame stabilization and blow-off in practical combustors enabling transfer of science to technology.

Combustion involves mixing of fuel and oxidant through large-scale structures and further intimate mixing through small-scale turbulence, and hence mixing in general is of paramount importance for efficient combustion. Nonaxisymmetric nozzles and inlets have been developed during the past decade in order to improve mixing and reduce combustion instability [5]. Experiments with various geometric configurations (triangle, square, rectangle, elliptic, tapered ellipse, etc.) have shown clearly their effectiveness and superior performance. Fernando Grinstein's (Naval Research Laboratory) computational studies of low-aspect ratio rectangular jets were focussed on the characterization of the effects of unsteady vorticity dynamics on jet entrainment and nonpremixed combustion, including the effects of Reynolds and Lewis numbers (Chapter 13). It is also shown, by numerical simulations, that nonaxisymmetric jets provide increased mixing and reduce combustion instability.

In another effort, by Nickolay Smirnov's group at the M. V. Lomonosov Moscow State University, Moscow, a model for theoretical investigation of turbulent mixing and combustion of polydispersed mixtures in confined volumes was developed (Chapter 14). The numerical model and the software created make it possible to determine the combustion and ignition characteristics of polydispersed mixtures. The model has been validated with experiments.

In an experimental effort, measurements of turbulent flame speeds in gaseous reactants in a classic cylindrical Taylor–Couette burner were made by Ralph Aldredge at the University of California at Davis (Chapter 15). The study established sensitivity of the turbulent flame speed to turbulence intensity, and provided some influence of flame front wrinkling on flame propagation.

Effective atomization plays an important role in efficient combustion as well as in influencing the pattern factor. Atomization of kerosene with steam rather than with air as the atomization fluid is presented by Ashwani Gupta, of the University of Maryland, and his colleagues using a commercially available air-assist atomizer. The results suggest that, because of the higher viscosity of

steam compared to that of normal air, steam yields finer liquid atomization and enhanced heat transfer (Chapter 16). This could very well show that atomization of fuel with another appropriate vaporized fuel can be a future approach.

1.3   CONTROL OF COMBUSTION

Though combustion control has been studied and utilized for nearly a century beginning from the use of mechanical governors in steam engines, as the engines become more complex, correspondingly more complex control systems are required to maintain the desired level of performance. Further, each additional component used to control, and the system as a whole, should be as reliable as the least reliable other component in the propulsion unit. Also, the propulsion device should be able to operate without unacceptable performance penalty in case the control fails.

As a result of the extensive research in atomization, vaporization, and mixing of fuel and oxidizer, current engines have decent specific fuel consumption with substantial reductions in fuel cost. However, once the fuel and air (oxidizer) are mixed and ignited, the governing mechanisms take over their natural course. Future engines will need to be controlled throughout the combustion process (before, during, and after) even at off-design conditions to ensure maximum utilization of energy, optimum and stable performance, and environmental compliance.

Combustion control is currently a hot area of research in the U.S. and abroad. In addition to basic research at a number of universities, joint industry–university S&T efforts are also underway to implement the control strategies developed by researchers in industry applications. Though some of the demonstrations have been made using gaseous fuels, the techniques can be extended to liquid fuels as well, and efforts are underway to accomplish this. It is hoped that future engines will perform equally well in off-design conditions, with improved reliability and easier maintenance, and reduced operational costs.

Research Accomplishments

Current research on control of combustion is focussed not only to reduce combustion-induced pressure oscillations and instability but also to improve combustion performance. Attention is being paid to increased flame speed and improved flame lift-off limits. Flame speeds ranging from laminar to 3.5 times laminar values have been examined, using a Countercurrent Swirl Combustor

(CSC), with premixed natural gas as fuel by Paul Strykowski at the University of Minnesota. The CSC's emission characteristics indicate typical range of NO_x concentrations at 10 ppm with 3% O_2. This concept could lead to compact combustor designs with increased residence time and reduced heat losses (Chapter 17).

The countercurrent shear layer control concept is also utilized to increase the blow-off limit of premixed flames (Chapter 18). The basis of this method is the self-excitation of a countercurrent shear layer that is established by the introduction of a reverse flow around the perimeter of an axisymmetric jet through the annular gap between the nozzle and a suction collar [6]. High-resolution Particle Imaging Velocimetry (PIV) enabled Anjaneyulu Krothapalli at Florida State University to measure the near flame structure with sufficient detail and obtain the velocity gradient with good accuracy. It has been shown that the blow-off limit of premixed jet flame can be extended by an order of magnitude by the technique, thus providing a practical means for increasing the range of operation of propulsion devices.

Several techniques have been investigated, with and without swirl, to control the pressure oscillations in combustion that are detrimental to performance, and may even cause failure and breakdown. James Whitelaw and his group at Imperial College of Science, Technology and Medicine, London, actively controlled the pressure oscillations in two models of lean-burn gas turbine combustors through oscillations in the fuel flow (Chapter 19). The flames were stabilized behind an annular ring and a step in one case, and utilizing swirl in the other. However, the active reduction of pressure oscillations did result in a slight increase in NO_x emissions. More sophisticated sensor–actuator combinations, and identification of the "right" region of fuel oscillation, could provide a practical control methodology.

Control of diffusion flames (liquid fuel) by pulsed fuel injection, investigated by Sumanta Acharya's group at Louisiana State University (Chapter 20), utilized three different swirl-stabilized combustor configurations. It is shown that the basic mechanisms of enhanced mixing through increased entrainment into the near-field vortical structures also apply to swirling flows. One of the major experimental findings, among others, is liquid fuel pulsations proved most effective in a forced flame, and injecting fuel in phase with air vortices provided the highest temperatures. In both swirling and nonswirling flames, injecting fuel out of phase with air vortices proved to be the least efficient. Properly timed sequential fuel injection has been a pioneering innovation (Ephraim Gutmark, while at NAWC/WD) in soot reduction (Chapter 6) which has subsequently been applied successfully for instability control and NO_x reduction.

As an extension of the research at NAWC/WC, Ken Yu (presently at the University of Maryland) conducted an experimental study to understand the physical mechanisms associated with active combustion control (ACC) of liquid-fueled systems (Chapter 21). The novel feature of the study involves direct

liquid fuel injection into the combustion zone and the controlled dispersion of fuel droplets using vortex–droplet interaction. Using additional pulsed liquid fuel injections for control, active instability suppression was demonstrated in a partially premixed dump combustor. Although a simple closed-loop controller, which had been well tested in studies with gaseous fuel, was utilized, the study shed new light on the significance of dynamic interaction between flow structures and pulsed sprays in controlling spatial distribution of fuel droplets. Important parameters for scale-up have been identified, and the study paves the foundation for technology application of ACC in future ramjets.

A robust feedback controller for suppressing combustion instabilities with distributed actuators has been investigated by Vigor Yang's group at the Pennsylvania State University (Chapter 22). The control synthesis is based on an improved H_∞ algorithm, which guarantees the stability of all perturbed dynamics within a given uncertainty bound. The model developed appears to be a complete one of its kind and accommodates various unique phenomena commonly observed in practical combustion devices. Important aspects of distributed control processes, such as time delay, plant disturbance, sensor noise, model uncertainty, etc. are treated systematically, with emphasis on the optimization of control robustness and system performance. Successful demonstration of controller operation in a generic dump combustor assures promise for this being scaled-up and implemented on practical combustors.

One of the significant innovations in control of pressure oscillations and supersonic mixing enhancement has been very simple, namely using nonaxisymmetric nozzles. Simple triangular, square, rectangular, and elliptic nozzles have been shown to effectively decrease combustion pressure oscillations, as well as increase supersonic mixing [7].

Studies have been carried out by Vladimir Sabel'nikov's group at Central Aero-Hydrodynamic Institute (TsAGI), Moscow Region to investigate supersonic mixing and combustion enhancement in a scramjet combustor using aerated (hydrogen or air) liquid kerosene jets (effervescent) injected through elliptic nozzles from tube-micropylons and fin-pylons (Chapter 23). It has been shown that elliptic nozzles provided greater mixing and combustion efficiencies in comparison with round nozzles, and indicate promise for utilization in fuel injection in supersonic combustors. Optimization of the aspect ratio, divergence (tapered elliptic nozzles), and placement will assure maximum mixing and combustion efficiencies possible with this passive control.

In order to implement the control methodologies indicated, one needs proper measurements (sensors and diagnostics), controllers, and actuators. Extensive research and development are carried out to realize the most appropriate sensors and actuators for various applications. Diagnostics developed serve dual purpose: to physically measure the various combustion parameters and interpret the results as quickly as possible, preferably *in situ*, so that the mechanisms involved can be understood; and to validate the numerical computer codes so that

the predictive and design capability can be improved in order to improve performance. To achieve this, efforts are made in the development of various diagnostic techniques and the acquisition of state-of-the-art instrumentation related to combustion. One approach taken by Ronald Hanson at Stanford University is to make combustion measurements with the required temporal and spatial resolution utilizing diode-laser sensors (Chapter 24). Diagnostic tools are developed to accurately measure CO, CO_2, and unburned hydrocarbons in high-temperature, high-speed flows that are vital for active feedback and control systems [8].

1.4   EMISSIONS AND PLUMES

It is a logical speculation that the current environmental constraints on propulsion engines will only become stricter in the future, and for the next generation engines. It, therefore, becomes necessary to address the fundamental mechanisms involved in the emission of undesirable species, and to focus research to alleviate the problem. Mixing is of paramount importance in any combustion process, and good mixing and efficient combustion will reduce UHC, CO, and soot. In order to achieve higher combustion efficiency, minimum pressure oscillations and emissions, control measures should be taken before, during, and after combustion and/or with a combination of active and passive techniques.

Present day gas turbines are already pushed to the operational limits in terms of clean emissions and combustion efficiency. Catalytic converters, popular in automobiles, use metals as the catalytic surface that initiates reactions with greatly reduced activation energy for bond breaking. However, in-chamber catalytic combustion takes away combustor space (use of catalytic surfaces), and large particles, eroded off from the catalytic metal surface, deposit and erode downstream components such as turbine blades. These call for innovations in the control of effluents in the engine exhaust. Emissions from weapons, though, may not be as trivial as in platform systems, yet can leave signatures that can lead to the platforms from where they were launched. Then control of emissions and plume signatures becomes a universal issue.

Research Accomplishments

Theoretical, computational, and experimental research has been pursued in the area of contaminant emission. If novel control methodologies are to be developed, a thorough understanding of the mechanisms involved in the generation of these constituents must be known. To this end, asymptotic analysis of flame structure to predict contaminant production has been successfully performed by Forman Williams at the University of California at San Diego (Chapter 25).

In general, analytical methods employing Rate-Ratio Asymptotics (RRA) can help contribute to understanding of mechanisms of NO_x production in diffusion flames, and can provide prediction of emission indices within reasonable accuracy. This method appears to hold promise for calculation of contaminant production in the combustion process, and can be extended to those involving novel high-energy hydrocarbon fuels.

Interactions between the flame and the surrounding wall (in a combustion chamber) could influence the contaminant production. This is examined by Dionisios Vlachos and his group at the University of Delaware (formerly at the University of Massachusetts at Amherst) using numerical bifurcation techniques (Chapter 26). For the first time, oscillatory instabilities have been found and control methodologies have been proposed to reduce flame temperatures and NO_x emissions.

Partial premixing has been proposed as a means of NO_x reduction in gas turbine engines by Jayavant Gore at Purdue University. An experimental and computational study was conducted to observe NO behavior under the circumstances of moderate stretch rate, opposed-flow, partially premixed flames. The results show that the minimum NO emissions at an optimal level of partial premixing result as a consequence of decrease in CH radical concentrations. Partial premixing appears to be a possible practical immediate solution for NO remediation in gas turbines.

Shayam Singh of SS Energy Environmental International, Inc. demonstrated another innovative emission control strategy involving the utilization of porous inserts in the combustion chamber (Chapter 28). Experimental results indicated porous inserts are not only beneficial for NO_x reduction, but also provide a uniform pattern factor, thereby improving combustion performance. Optimization of the size and placement of the inserts, and the porosity can lead to a practical methodology for emissions control and performance enhancement in future engines, as well as retrofit applications of existing engines without elaborate modifications.

Though benign in terms of emissions regulations perspective, species in plumes that cause signatures can be of significant consequence in military platform and weapons. This includes plume afterburning as well. Kenneth Yu at the University of Maryland (formerly at NAWC/WD) examined the response of supersonic afterburning plumes to passive excitation in order to explore the potential of initial mixing control in modifying the afterburning flame characteristics. It seems that the excitation frequency plays an important role in changing the plume afterburning intensity either in positive or negative directions. The directional change was related to the turbulence cascade characteristics of large-scale structures with wavelength similar to that of the preferred mode. Properly and optimally designed mixing characteristics can be an effective tool to control plume afterburning. Current actuator technology will allow this technique to be extended in an active mode.

1.5   CONCLUDING REMARKS

Substantial progress has taken place in combustion research and development in the past couple of decades. This has resulted in several transitions leading the science findings to technology applications, such as, sequential fuel injection for controlling combustion instability in gas turbine engines, and rugged diode-laser sensor for active combustion control. Focussed research addressed the synthesis of a new class of high-energy strained hydrocarbon fuels. These fuels have
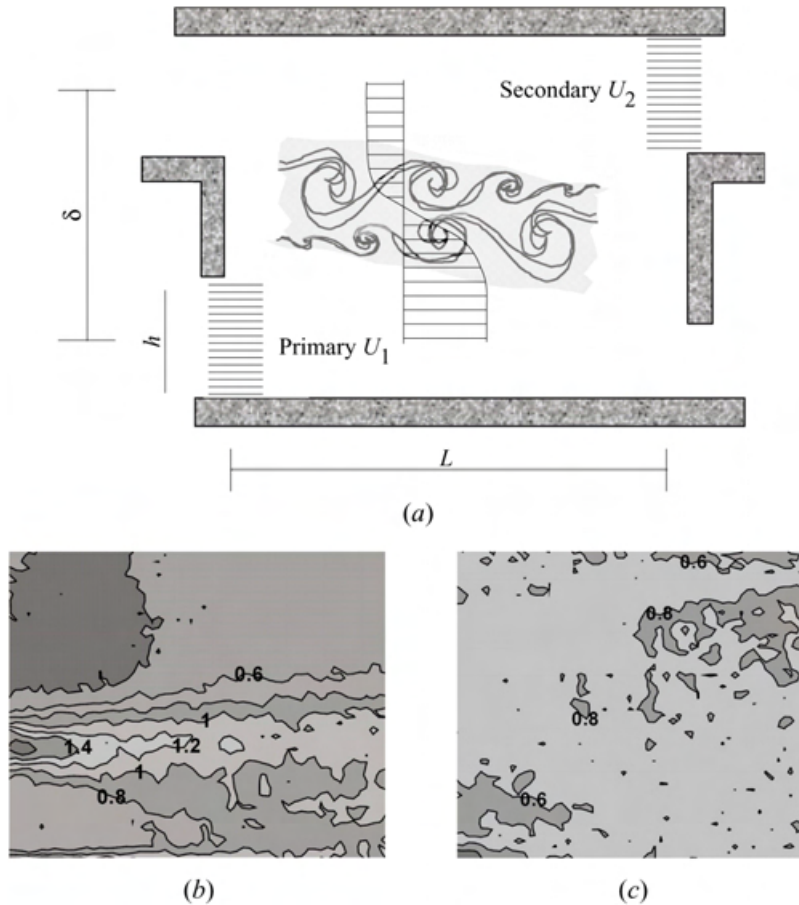
Figure 1.2 Schematic of a compact combustor using countercurrent shear layer (a) and comparison of measured strain rate fields in a single-stream (b) and countercurrent (c) shear layers [9]
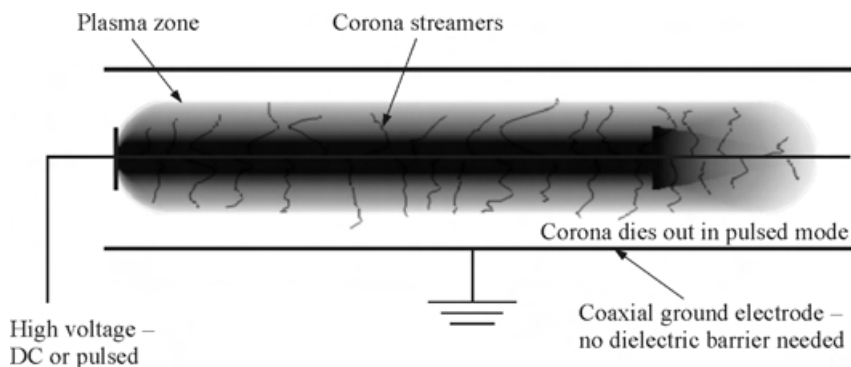
Figure 1.3 Schematic of corona reactor for NO reduction [10]

the capability of increasing the range and speed of propulsion systems. Droplet combustion studies indicate promise in using these fuels. Future research and development should address large-scale production of these fuels, rheology studies, and full-scale engine demonstrations using these fuels.

Reduced kinetics studies of fuels have led to significant simplification in component performance and systems analysis. However, heavier hydrocarbons require further systematic study, and the reaction pathways need to be identified. Though heat release and turbulent reacting flows have been widely studied numerically, more accurate models are evolving, and their validation and utilization as a predictive tool are warranted. Active combustion control has received worldwide attention in the past decade. The focus has been on the improvement of mixing and combustion efficiency and reduction of combustion-generated instability. Several new techniques have emerged, and are being considered for technology demonstration. Supersonic combustion phenomena for future hypersonic vehicles pose the difficult issue on mixing enhancement as efficient high-speed combustion is required in compact combustors with very short residence times. New combustion concepts are emerging (Fig. 1.2); one based on counter-current shear offers promise [9]. A current project addresses the utilization of this concept in a practical combustor.

Exploration of new avenues to reduce emissions to comply with environmental regulations has always been a priority in the past decade. As regulations get more and more stringent, innovative concepts are researched and applied to real engines. Soot control has been an issue with hydrocarbon fuel combustion, both from emission and signature points of view. Certain signatures are of concern for military weapon and platform propulsion. Recently, nonthermal plasma techniques for remediation of emissions have been found to be a vi-

able, reliable, and practical means, with the advantage of operation on demand (Fig. 1.3) [10].

In conclusion, although quantum improvements have not been achieved, there has been phenomenal growth in understanding the various fundamental mechanisms in combustion devices, and applying them scientifically and more effectively for designing practical propulsion systems. Some of the major accomplishments in the various aspects of combustion for propulsion engines have been elucidated. Future opportunities in combustion research call for multidisciplinary programs with a balanced emphasis on analysis, computations, diagnostics, and experimentation. The new paradigm of integrated research, development, and production can lead the evolution from new concepts through real systems, faster and cheaper.

REFERENCES

1. Roy, G. D. 2000. Utilization of high-density strained hydrocarbon fuels for propulsion. *J. Propulsion Power* 16 (4):546-51.

2. Gutmark, E., T. P. Parr, K. J. Wilson, K. H. Yu, R. A. Smith, D. M. Hanson-Parr, and K. C. Schadow. 1996. Compact waste incinerator based on vortex combustion. *Combustion Science Technology* 121:333–49.

3. Williams, F. A. 1989. Reduced kinetic schemes in combustion. In: *Propulsion combustion: Fuels to emissions*. Ed. G. D. Roy. New York: Taylor & Francis. 93–125.

4. Kailasanath, K., and G. D. Roy. 1995. Computational combustion approaches to a complex phenomenon. *Naval Research Reviews* XLVII(2):32–41.

5. Roy, G. D. 1999. Control of thermoacoustic instabilities in ramjets and gas turbine combustors: An overview. *6th International Congress on Sound and Vibration Proceedings*. Copenhagen, Denmark.

6. Strykowski, P. J., A. Krothapalli, and S. Jendoubi. 1996. The effect of counterflow on the development of compressible shear layers. *J. Fluid Mechanics* 308:63–96.

7. Gutmark, E. J., K. S. Schadow, and K. H. Yu. 1997. Mixing enhancement in supersonic free shear flows. *Annual Reviews Fluid Mechanics* 27:375–417.

8. Baer, D. S., M. E. Newfield, N. Gopaul, and R. K. Hanson. 1994. Multiplexed diode laser sensor system for simultaneous H_2O, O_2 and temperature measurements. *Optic Letters* 19(22):1900–2.

9. Strykowski, P. J., and D. J. Forliti. 2000. Flow control applications using countercurrent shear. In: *Recent advances in experimental fluid mechanics*. Eds. E. Rathakrishnan and A. Krothapalli. Kanpur, India: Sahitya Nikkan. 41–56.

10. Liu, J. B., J. Yampolsky, P. Ronney, and M. A. Gundersen. 2000. Plasma-enhanced combustion for reduction of rocket plume soot. *13th ONR Propulsion Meeting Proceedings*. Eds. G. Roy and P. Strykowski. Minneapolis, MN.

SECTION ONE

ADVANCED FUEL SYNTHESIS AND CHARACTERIZATION

Chapter 2

HIGH-ENERGY, HIGH-DENSITY, POLYCYCLIC HYDROCARBONS AND AZIDO DERIVATIVES

R. M. Moriarty

Efforts towards the synthesis of strained polycyclic hydrocarbons have been described. These compounds are of interest as fuels and fuel additives for advancedpropulsion. Chemistry has been devised for the attachment of azido functionality to the strained hydrocarbon nucleus. Highly unsaturated substituted cubanes have been synthesized. Ring-opening metathesis polymerization of basketene and 2,3-diazabicyclo[2.2.1]hept-2-ene has been studied.

2.1   INTRODUCTION

The primary objective of this research was the synthesis of cubane analogs which contained polyunsaturated side-chains, which, in turn, could be used as starting materials for the production of high-energy derivatives [1–5]. Target molecules were 1,4-*bis*-azidomethyl cubane, 1,4-*bis*(1′,2′-diazidomethyl)cubane, 1,4-*bis*(2′,3′-diazidopropyl)cubane, 1,4-*bis*(2′,3′-diazidopentyl)cubane, 1′,4′-*bis*(2′,3′-diazidohexyl)cubane, and 1,4-*bis*(2′,3′-diazidoheptyl)cubane. The rationale for the design of these analogs is centered around the combination of two energetic groups, namely, the azido group and the cubane system within the same molecule. The thermal decomposition of alkyl azides proceeds with loss of molecular dinitrogen and production of an alkyl nitrene:

$$\mathrm{RCH_2\!-\!N_3} \xrightarrow{\Delta} \mathrm{[RCH_2\!-\!N] + N_2}$$

$$\mathrm{RCH\!\!=\!\!NH} \qquad \mathrm{RN\!\!=\!\!CH_2}$$
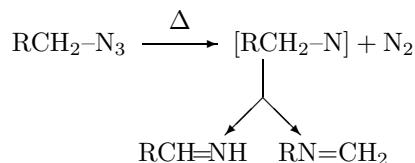
This process has been shown in collaboration with C. K. Law of Princeton University to be extremely useful for the creation of microexplosions for

fuel droplet atomization. Cubane has an extremely high-strain energy around 166 kcal/mole and ring opening releases a substantial amount of this strain energy.

2.2   SYNTHESIS OF CUBYL SYSTEMS

2.2.1   Synthesis of 1,4-*Bis*-Azidomethylcubane

This compound (**4**) was synthesized via the route shown in Fig. 2.1. Compound **4** was prepared in overall 35% yield and the synthesis could be scaled to gram quantities in polyunsaturated cubane considered in the next section.
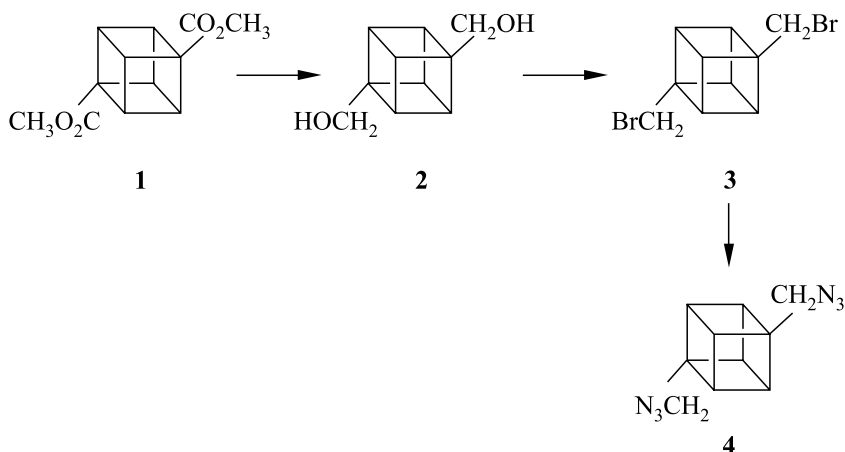
Figure 2.1 Synthesis of 1,4-*bis*-azidomethylcubane (**4**)

2.2.2   Synthesis of Polyunsaturated Cubanes

Next, the attention was turned to addition of azido groups to carbon–carbon double bonds of side-chains attached to the cubyl ring system. In this approach, cubane derivatives with unsaturated side-chains and added azido groups to these side-chains were synthesized using the reaction:

$$\text{R--CH=CH} \xrightarrow[\text{(PhIO)}_n]{\text{NaN}_3} \text{RCH(N}_3)\text{CH}_2\text{N}_3$$
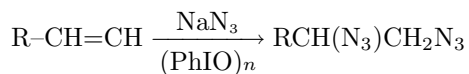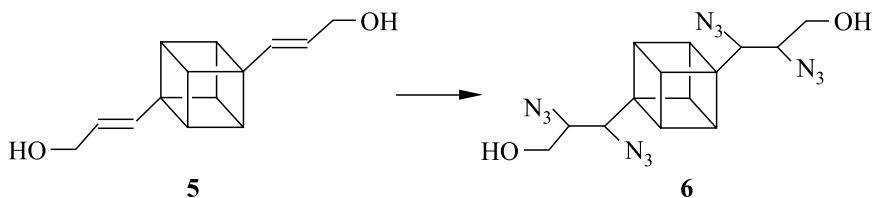
Figure 2.2 Synthesis of tetraazide (**6**)
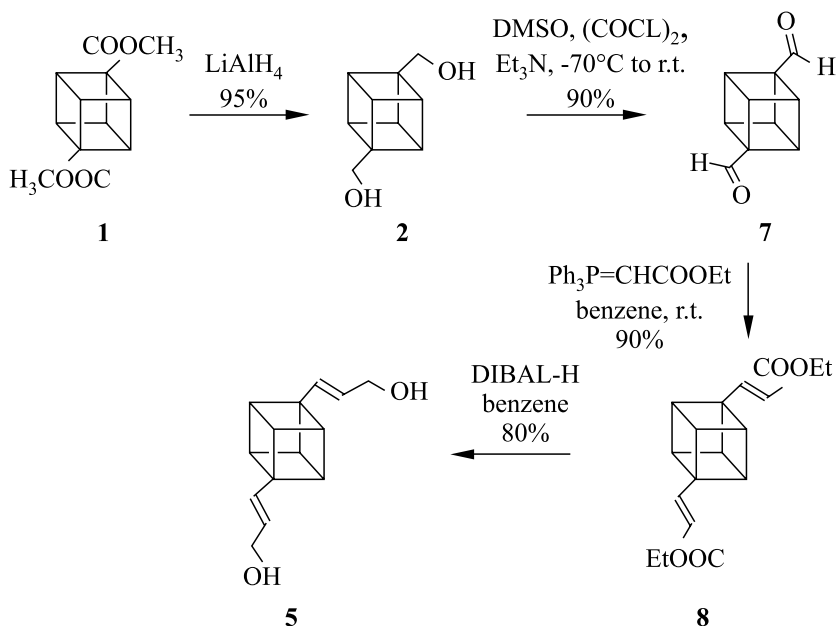
Figure 2.3 Synthesis of compound **5**

In the case of 1,4-disubstituted system, tetraazide **6** was formed proceeding from **5** as shown in Fig. 2.2.

Compound **5** in Fig. 2.2 was synthesized as shown in Fig. 2.3.

Compound **5** was protected as the *bis*-TBDMS ether (**5** ⟶ **2**). Treatment with $NaN_3/(PhIO)n$ yielded **10** as a mixture of diastereomers (Fig. 2.4).

Deprotection of **10** using TBAF led to some decomposition, but sufficient **6** was obtained for characterization. The detailed procedures of obtaining compounds **2**, **7**, **8**, and **5** are described in subsections 2.2.3 to 2.2.6. The procedure of obtaining compound **6** is described in subsection 2.2.7.
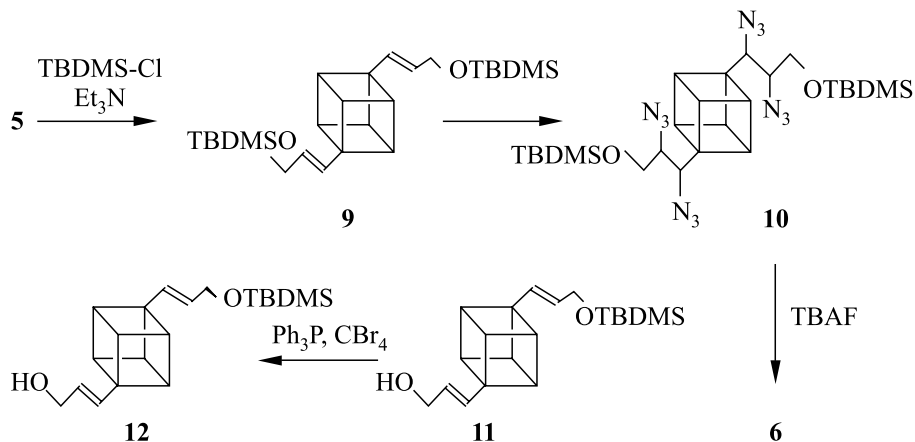
Figure 2.4 Processing of compound **5**

2.2.3 Synthesis of 1,4-*Bis*-Hydroxymethylcubane (2)

Figure 2.5 shows the procedure of synthesizing 1,4-*bis*-hydroxymethylcubane [3].

A solution of 3.0 g (13.6 mmol) of diester in 100 ml of dry THF–ether mixture (1:1) was added dropwise to a stirred suspension of LAH (54 mmol) in 200 ml of dry THF at room temperature. After the addition, the reaction mixture was refluxed for an additional 3 hours. The excess LAH was carefully quenched with a small amount of water. The organic layer was filtered, dried, and evaporated to give 2.1 g (95%) of pure diol. ^{1}H NMR(CD$_3$OD) δ 3.73 (s, 6H), 3.64 (s, 4H). ^{13}C NMR (CD$_3$OD) δ 63.95 (t, 2C), 60.72 (s, 2C), 44.78 (d, 6C).
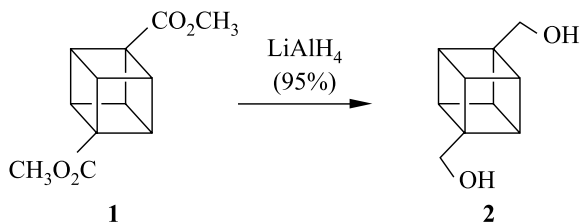
Figure 2.5 Synthesis of 1,4-*bis*-hydroxymethylcubane (**2**)

2.2.4 Synthesis of 1,4-Cubanedicarboxaldehyde (7)

Figure 2.6 shows the procedure of synthesizing 1,4-cubanedicarboxaldehyde.

Oxalyl chloride (4.8 ml of 1.25 M solution in dichloromethane, 6 mmol) was placed in a 3-neck flask equipped with a stirrer and two pressure-equalizing addition funnels protected by drying tubes. One additional funnel contained DMSO
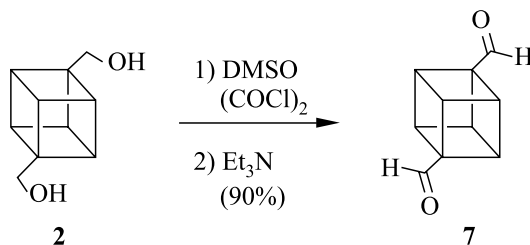
Figure 2.6 Synthesis of 1,4-cubanedicarboxaldehyde (**7**)

(12 mmol) dissolved in dichloromethane (5 ml) and the other diol (3 mmol) dissolved in DMSO–dichloromethane mixture (1:1; 10 ml). The contents of the flask were cooled to −60 °C and the DMSO solution was added dropwise in ca. 5 min. Stirring was continued at −60 °C for 10 min followed by addition of the diol solution in ca. 5 min. The reaction mixture was stirred for 15 min and TEA (or DIPEA: 24 mmol) was added in ca. 5 min with stirring at −60 °C. The cooling bath was removed and water (30 ml) was added at room temperature. The aqueous layer is reextracted with dichloromethane, organic layers are combined, washed with saturated sodium chloride solution (100 ml), and dried with anhydrous magnesium sulfate. The filtered solution is concentrated in a rotary evaporator to 25 ml, washed successively with dilute aqueous hydrochloric acid (1%), dilute sodium hydrogencarbonate (5%), and water and evaporated to dryness to give a slightly colored crude dialdehyde (80%–90%) which was used immediately* in the next step. ^{1}H NMR(CDCl$_3$) δ 9.74 (s, 2H), 4.37 (s, 6H). ^{13}C NMR has not been taken due to limited stability of dialdehyde.

2.2.5 Synthesis of 1,4-Dimethylcubane-*Bis*-Acrylate (8)

Figure 2.7 shows the procedure of synthesizing 1,4-dimethylcubane-*bis*-acrylate [3]. Crude dialdehyde (530 mg, 3.28 mmol) was dissolved in anhydrous benzene (20 ml). (Carbethoxymethylene)triphenylphosphorane (2.86 g,

---

*Dialdehyde decomposes upon standing in CDCl$_3$ solution at room temperature ($t_{1/2} \approx$ 8 hours; based on ^{1}H NMR spectra).
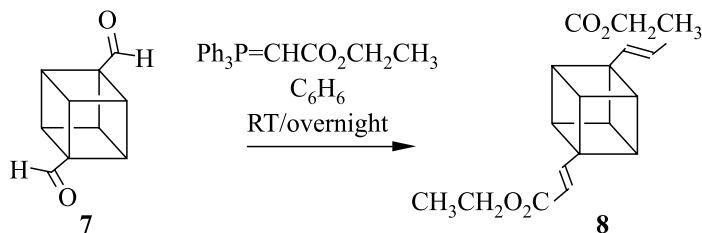
Figure 2.7 Synthesis of 1,4-dimethylcubane-*bis*-acrylate (**8**)

8.19 mmol) was added, and the solution stirred at room temperature* under argon overnight. The solvent was removed under reduced pressure, and purification by column chromatography (silica, 5% ether in hexane) yielded the *trans,trans*-unsaturated diester (890 mg, 90%). ^{1}H NMR (CDCl3) δ 7.13 (*d*, 2H, $J = 16$ Hz), 5.67 (*d*, 2H, $J = 16$ Hz), 4.17 (*q*, 4H, $J = 7$ Hz), 3.96 (*s*, 6H), 1.26 (*t*, 6H, $J = 7$ Hz). ^{13}C NMR (CDCl3) δ 166.64 (*s*, 2C), 146.26 (*d*, 2C), 118.81 (*d*, 2C), 60.15 (*t*, 2C), 59.02 (*s*, 2C), 46.77 (*d*, 6C), 14.19 (*q*, 2C).

2.2.6 Synthesis of 1,4-Propane-1-Ol-Cubane (5)

shows the procedure of synthesizing 1,4-propane-1-ol-cubane [3].

To a magnetically stirred solution of diisobutylaluminum hydride (5.4 ml of 1.5 M solution in toluene) was added a solution of *trans,trans*-diester (600 mg, 2.0 mmol) in 15 ml of anhydrous benzene at a rate sufficient to maintain the
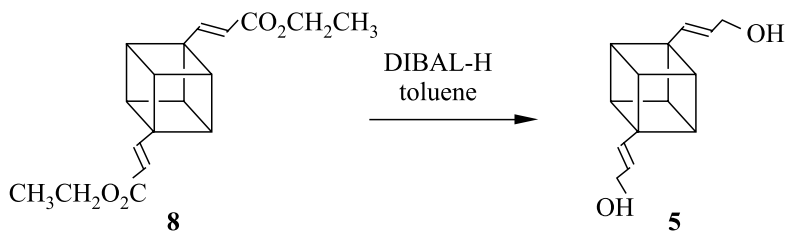
Figure 2.8 Synthesis of 1,4-propane-1-ol-cubane (**5**)

---

*When the reaction was run at reflux for 3 hours, besides diester 10%–20% (based on ^{1}H and ^{13}NMR spectra of crude material) of a "thermal-opening" product was formed, the structure identical with those independently synthesized by Rh(I) promoted rearrangement of cubane diester 4.

temperature at ≤ 5 °C. After addition was complete, the mixture was allowed to stir under nitrogen for an additional 3 hours at 0 °C. After excess diisobutyla-luminum hydride was destroyed by dropwise addition of methanol, the reaction mixture was filtered through a Büchner funnel. The organic layer was washed with saturated sodium hydrogencarbonate, water, and brine. After drying, the solvent was removed *in vacuo* and the residue purified by column chromatography, eluting with a mixture of ether in hexanes (70%) to give 350 mg (80%) of the alcohol as a colorless oil. ^{1}H NMR (CDCl3) δ 6.0–5.8 (*m*, 2H), 5.7–5.3 (*m*, 2H), 4.16–4.12 (AB system, 4H), 3.79 (*s*, 6H), 2.06 (*bs*, 2H), ^{13}C NMR (CDCl3) δ 132.27 (*d*, 2C), 126.93 (*d*, 2C), 63.28 (*t*, 2C), 59.18 (*s*, 2C), 46.11 (*d*, 6C).
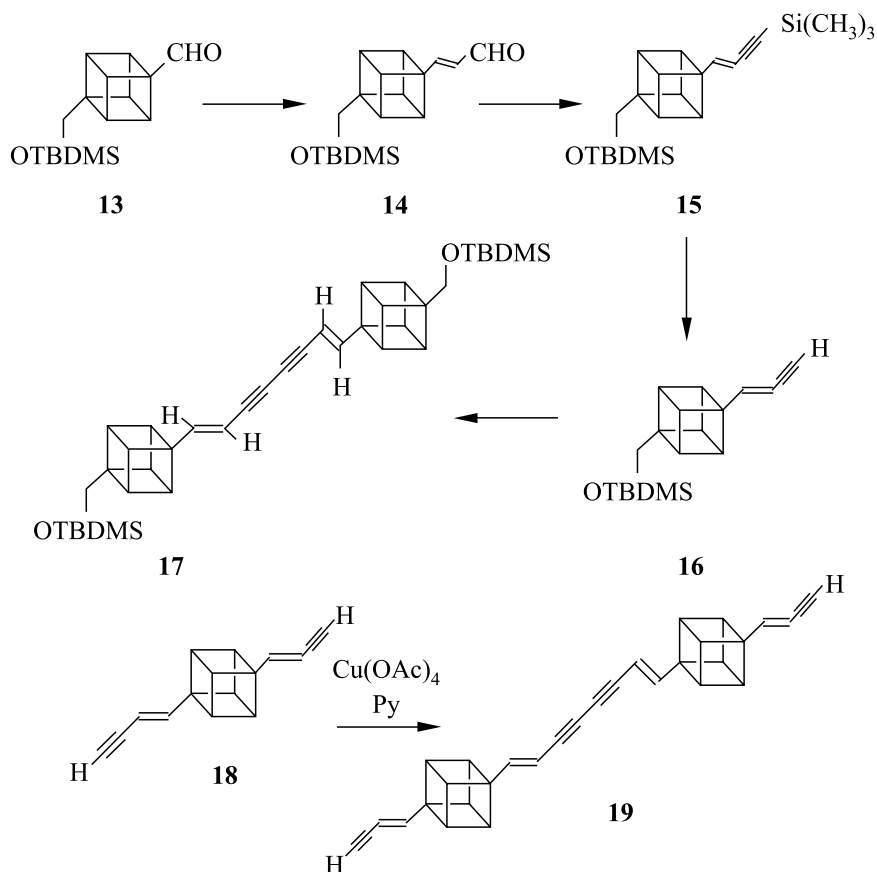
Figure 2.9 Synthesis of cubyl derivatives

Table 2.1 Alkyl azides

R–N$_3$	Method	Physical Properties
n-Butyl	A	nD^{20} 1.4102; 71° (225 mm)
		nD^{22} 1.4193; 65°–69°(220 mm)
n-Amyl	A	nD^{23} 1.4185; 73°–74° (100 mm)
		nD^{20} 1.4266; 63.5° (100 mm)
4-Phenylbutyl	B	nD^{27} 1.5200; 116°–120° (5 mm)
		nD^{27} 1.5188; 114°–116° (4 mm)
4-Heptyl	B	nD^{23} 1.4370; 78°–80° (200 mm)
Cyclohexyl	B	nD^{23} 1.4760; 66°–67° (22 mm)
		nD^{20} 1.4693; 72° (30 mm)
Phenylmethyl	A	106°–108° (42 mm)
Phenyl azide	B	49° (5 mm)
		lit 50° (5 mm)
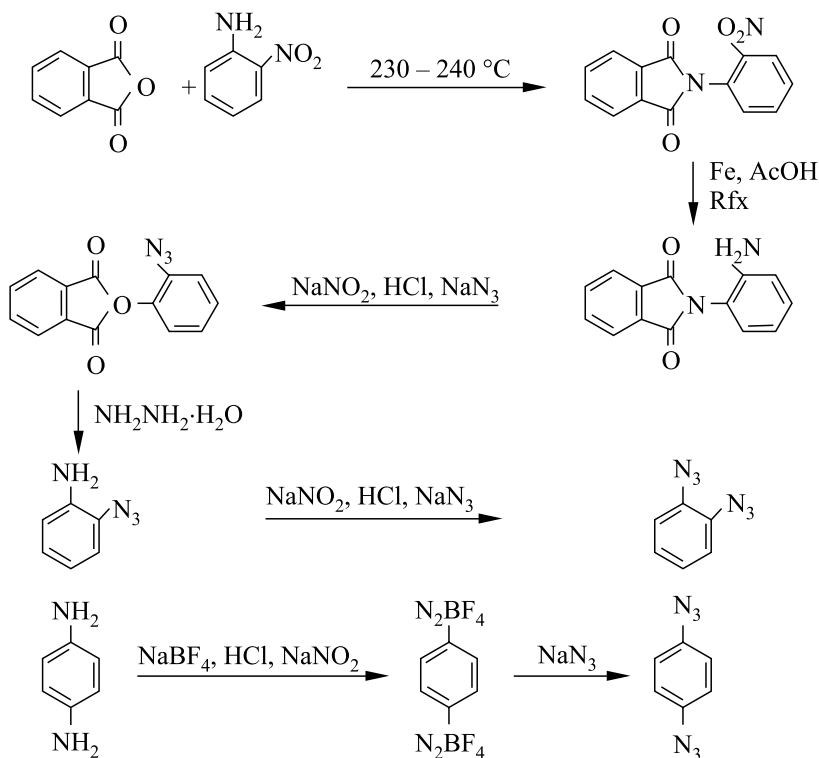
Figure 2.10 Synthesis of 1,2-diazidobenzene and 1,4-diazidobenzene

2.2.7 Azidation of Compound (5)

To a solution of iodosobenzene (2.2 g, 10 mmol) and **5** (1.79 g, 5 mmol) in acetic acid (30 ml) sodium azide (2.3 g, 35 mmol) was added. The mixture was maintained at room temperature for 10 min then kept at 50 °C for 3 hours, then poured into water (200 ml) and extracted with chloroform (4 × 50 ml). The combined extracts were washed with water (2 × 100 ml), dried (mgSO$_4$), and evaporated. The residue was chromatographed on silica gel (60 mesh) elution with benzene-pet.-ether (1:1) **6** (1.27 g, 64%).

Two more extensively conjugated cubyl derivatives were synthesized as shown in Fig. 2.9.

In the case of **16** reaction with NaN$_3$/(PhIO)n gave a mixture of products from which an acetylenic diazide was isolated. Characterization of this material is underway.

Compound **15** has been synthesized in milligram quantities which is an inadequate amount for azidization and the process **13** $\longrightarrow$ **14** $\longrightarrow$ **15** $\longrightarrow$ **16** $\longrightarrow$ **17** will be repeated.

2.3 SYNTHESIS OF ALKYL AZIDES

A number of alkyl azides were synthesized and these are listed in Table 2.1.

The method of preparation and physical properties of the alkyl azides used in the study are also presented in Table 2.1. The alkyl bromide and sodium azide in aq MeOH is denoted as A and aq EtOH and sodium azide is denoted as B. 1,2-Diazidobenzene and 1,4-diazidobenzene were synthesized using the process shown in Fig. 2.10. 1-Azidonorborniane was synthesized according to a modified literature procedure shown in Fig. 2.11.

2.4 SYNTHESIS OF QUADRICYCLANES

Quadricyclane is a strained molecule which is relatively easy to synthesize. The strain energies of related structures are presented in Fig. 2.12.

The aim of this part of the study was to incorporate the azido group into the strained quadricyclane structure. The pathways shown in Fig. 2.13 were pursued.

Reaction **7** $\longrightarrow$ **9** is general for synthesis of bridgehead azides of bridged polycyclic hydrocarbons. Another route which was studied as a general synthesis is shown in Fig. 2.14.
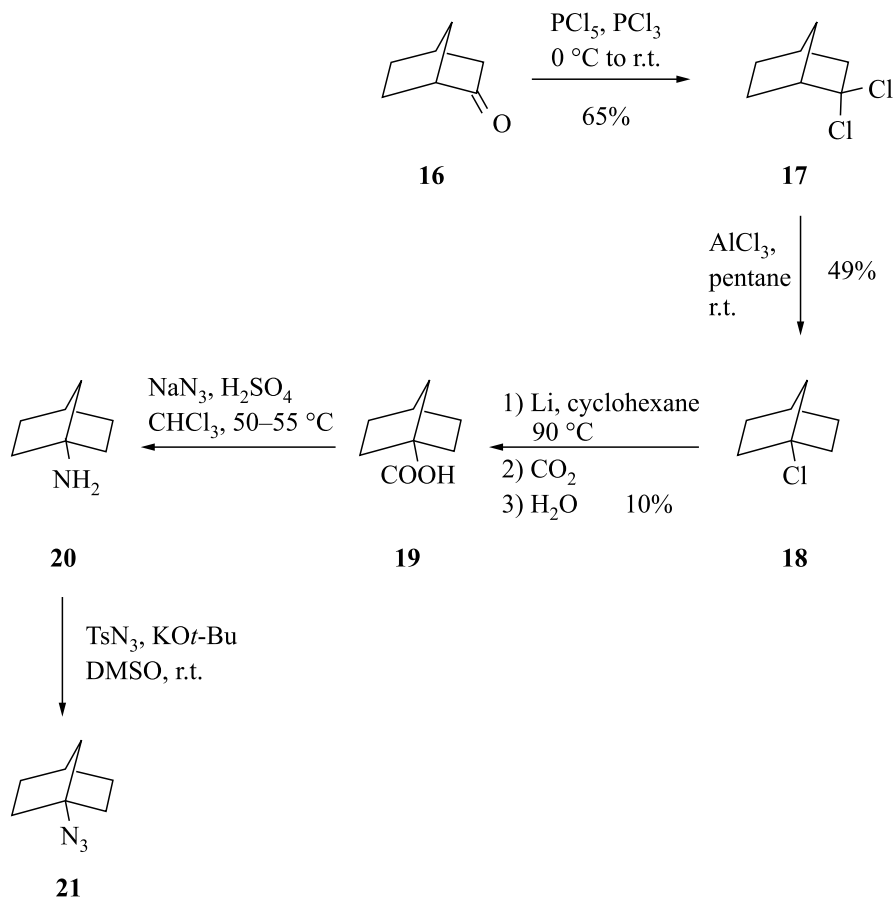
Figure 2.11 Synthesis of 1-azidonorborniane

In a second pathway, the use of hypervalent iodine was studied as shown in Fig. 2.15.

The pathway via the lithio quadricyclane intermediate failed due to an unexpected rearrangement presented in Fig. 2.16.

The oxidative method using $C_6H_5I(OAc)_2$ yielded the desired quadricyclyl azide and the process is being scaled up. In another approach (Fig. 2.17), the hypervalent iodine Hoffmann rearrangement was carried out on quadricyclyl carboxamides.

The reaction shown in Fig. 2.18 was also studied but to date no positive result has been obtained.
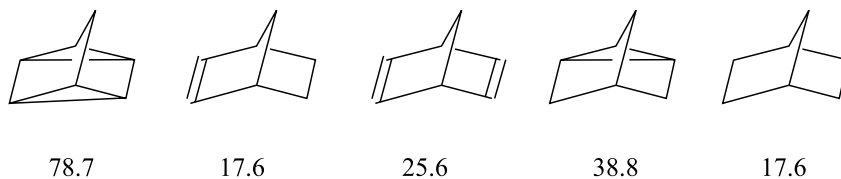
Figure 2.12 Strain energies of quadricyclane structures

78.7   17.6   25.6   38.8   17.6

Dicyclopentadiene $\xrightarrow{\Delta}$ [5] $\xrightarrow{HC\equiv CCOOH}$ [6, COOH]

4   5   6

[6] $\xrightarrow{h\nu}$

[9, N$_3$]   [8, I]   [7, COOH]

9   8   7
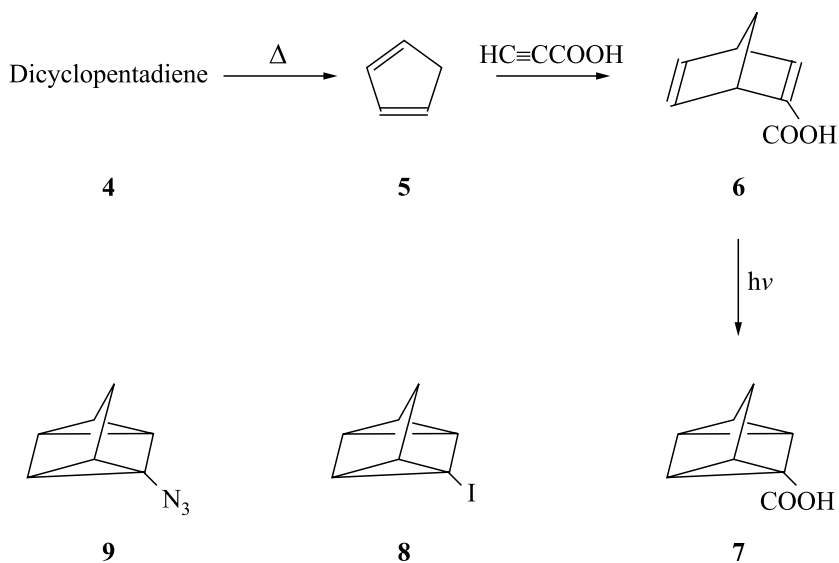
Figure 2.13 Pathways of incorporating the azido group into the strained quadricy-clane structure

8 $\xrightarrow{C_6H_5Li}$ $\left[\text{[Li structure]} \right]$ $\xrightarrow{N_3Ts}$ **9**
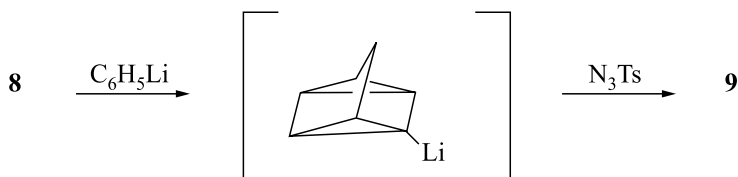
Figure 2.14 Alternative route to synthesize compound **9**
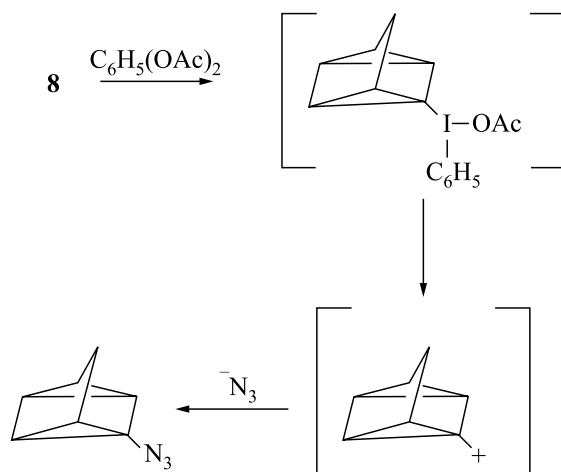
Figure 2.15 The use of hypervalent iodine for synthesizing compound **9**
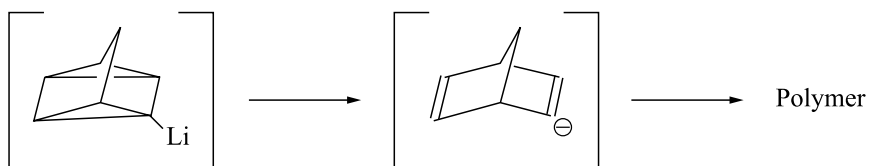
Figure 2.16 Failure of the pathway via the lithio quadricyclane intermediate

Figure 2.17 Alternative approach with Hoffmann rearrangement
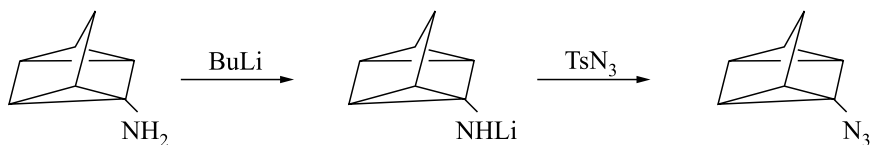
Figure 2.18 Alternative reaction for synthesizing compound **9**

2.5 SYNTHESIS OF SUBSTITUTED CUBANE

Considerable effort has been devoted to the preparation of bridgehead halides from the corresponding acids under decarboxylative halogination conditions [4]. The usual and most commonly used method is of Barton's, which involves the radical decomposition of thiohydroxamic esters in the presence of appropriate halogen donor substituent such as 2,2,2-trifluoroiodoethane. Even though this method is generally used, the 2,2,2-trifluoroiodoethane is quite expensive and it involves the initial preparation of cubane carbonyl chloride which is very sensitive to friction and therefore it is not encouraged in the case of cubanes. Synthesis of bridgehead iodides has also been accomplished by *tert*butyl hypoiodite mediated iodinative decarboxylation or by treating anhydrous silver carboxylates with bromine or iodine (Hundsdiecker–Borodin reaction).

Cubane-1,2-dicarboxylic acid **12** (see Fig. 2.19), a precursor for 1,2-dihalocubanes was prepared from commercially available cubane-1,4-dicarboxylic acid in 65% yield. The other acids **14a** and **14c** were similarly prepared from the cubane-1,4-dicarboxylic acid **14b** according to the literature procedures. ^{1}H NMR spectra of the compound **13a** showed a broad singlet at 4.41 for the clibyl protons, whereas compound **13b** showed two multiplets. Conversion of bridgehead carboxylic acids to the corresponding halides using $Pb(OAc)_4$ and iodine in refluxing benzene under illumination is reported. This is considered to be an alternative to Barton's method, because of its simplicity and ease of preparation, but it involves toxic lead compounds.

Introduction of an iodo group onto the cubyl system is especially desirable. Because iodocubanes can be readily converted to hypervalent iodocubanes which can undergo ligand exchange reactions with acetoxy, trifluoromethanesulfonyloxy, methanesulfonyloxy, *p*-toluenesulfonyloxy, and trifluoroacetoxy groups followed by oxidative deiodination to yield the corresponding substituted cubanes, iodocubanes are used in photosolvolysis study, halogen–metal exchange reactions, and in preparation of chloro- and fluorocubanes.

In view of continuous efforts to develop an alternative procedure for the preparation of bridgehead halides from the corresponding carboxylic acids using hypervalent iodine reagents, a simple, efficient, and inexpensive method has been developed. This improved method involves refluxing a mixture of cubane carboxylic acid and iodine or bromine and (diacetoxy)iodobenzene in dry benzene without irradiation or use of AIBN. This simple method provides various mono- and dihalocubanes (**13a–13b**, **15a–15f**) from the corresponding cubane carboxylic acids (**12**, **14a–14c**) (Table 2.2). The reactions in Fig. 2.19 are illustrative.

Table 2.2 Bridgehead halides

Substrate	Product	Yield (%)
12	**13a**	97
12	**13b**	95
14a	**15a**	85
14a	**15b**	84
14b	**15c**	98
14b	**15d**	97
14c	**15e**	96
14c	**15f**	96

12

13a X=I
13b X=Br

14a R=H
14b R=COOH
14c R=COOCH$_3$

15a R=H; X=I
15b R=H; X=Br
15c R=X=I
15d R=X=Br
15e R=COOCH$_3$; X=I
15f R=COOCH$_3$; X=Br
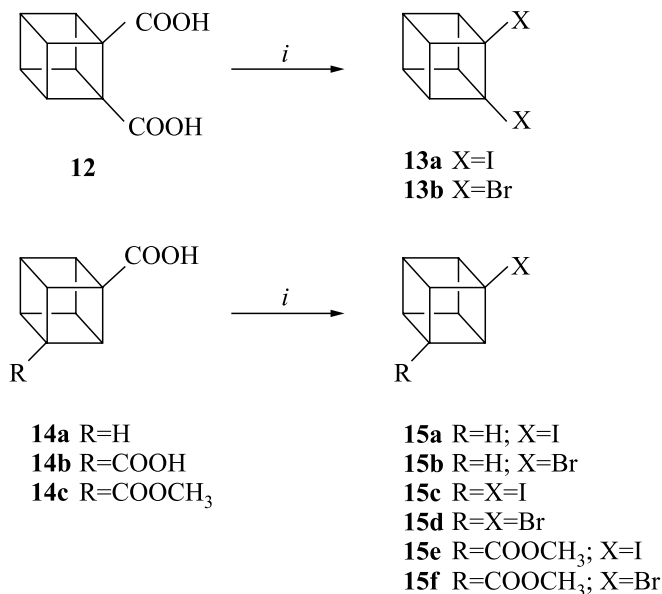
Figure 2.19 Synthesis of substituted cubanes. Reagents: *i*, PhI(OAc)$_2$, I$_2$ or Br$_2$, benzene, reflux

2.6 RING-OPENING METATHESIS POLYMERIZATION

2.6.1 High-Energy Polymers

The following monomers were chosen to be used in polymerization studies that aimed at obtaining polymeric high-energy compounds [3]:

16 — basketene (*bis*-homocubene, pentacyclo[4.2.2.0^{2,5}.0^{3,8}.0^{4,7}]deca-9-ene);

17 — diethyl 2,3-diazabicyclo[2.2.1]hept-5-ene-2,3-dicarboxylate; and

18 — 2,3-diazabicyclo[2.2.1]hept-2-ene.

The polymerization reactions shown in Fig. 2.20 were attempted.

While literature procedures are known for the syntheses of **16**, **17**, and **18**, neither of these three compounds was commercially available. Laboratory syntheses of **16**, **17**, and **18** reproduced the procedures and yields found in the chemical literature.

Attempted polymerization of **16**, **17**, and **18** by ring-opening metathesis polymerization (ROMP) was carried out using two different catalysts:

- Dichloro(3,3-diphenyl-2-propenylidene)-*bis*-(triphenylphosphine)-ruthenium (compound **22**):

22
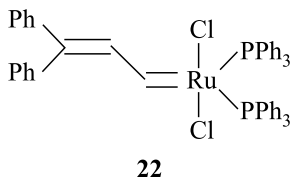
  and

- 2,6-Diisopropylphenylimido-neophylidene-molybdenum-*bis*-(hexafluoro-t-butoxide) (compound **23**):

23
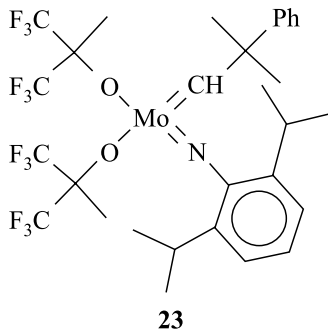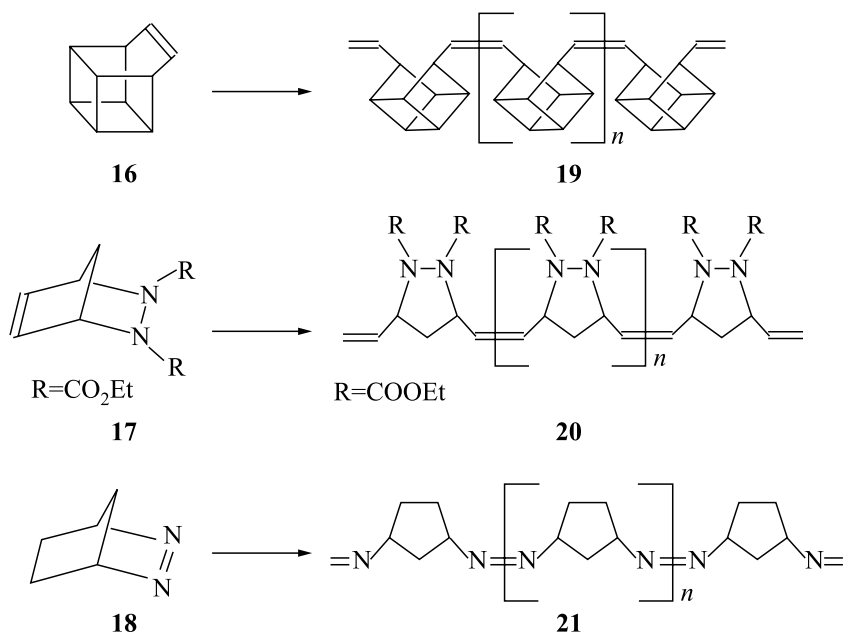
Figure 2.20 Ring-opening metathesis reactions

Compound **22** is a surprisingly stable ROMP catalyst (in both protic and aprotic media). It was made available via the courtesy of Dr. G. L. Gould (U.I.C. — Chemistry).

Compound **23** is the most active of the only two commercially available (Strem Chemicals, Inc.) ROMP catalysts (the other one being the corresponding nonfluorinated product). Its availability prompted the author to test it before similar catalysts that contain tungsten as a core metal and that have been shown to be more stable and more active than the molybdenum ones; molybdenum catalysts seem, nevertheless, to tolerate more functionalities than the tungsten ones.

2.6.2 Polymerization Experiments

(a) Polymerization attempts in the presence of the ruthenium catalyst (compound 22)

Procedure

Reactions were carried out in an NMR tube, at room temperature or with very slight heating, in 0.5 ml of a 1:8 mixture of CD_2Cl_2/C_6D_6. The NMR tubes

were closed under argon. The molar ratio catalyst/monomer was 1:70. The concentration of the catalyst was 0.0045 M (2 mg per batch). The reaction was monitored by ^{1}H NMR spectra.

Results

Under the above conditions, a test reaction using norbormene as monomer proceeded to more than 98% completion in 2 hours (more than 90% completion in 35 min).

Each of the monomers was submitted to the above reaction conditions. After hours, or even days, the ^{1}H NMR spectra showed only completely unreacted starting material, in each case. No reaction occurred even upon heating at 40 °C.

To test for the conversion of catalyst activity with time, norbormene was added to one of the basketene reaction mixtures after 2 days and it was readily polymerized, while the basketene remained intact. Work continues on finding conditions for successful polymerization.

(b) Polymerization attempts in the presence of the molybdenum catalyst (compound 23)

Procedure

Reactions were carried out under argon, in sealed NMR tubes, at room temperature or with mild heating. A stock solution (0.003 M) of catalyst **23** in C_6D_5–CD_3 was prepared. Each reaction was run with 0.5 ml of this solution, to which the appropriate amount of monomer was added, to get the desired molar ratio (50:1 to 100:1) monomer/catalyst. Reagents were mixed, and the NMR tubes were closed in a Vacuum Atmospheres drybox. Reactions were monitored by ^{1}H NMR.

Results

The monomer used in the Mo catalyst attempts was basketene. Reactions were run at room temperature. After 2 hours, the temperature was raised to 70–80 °C. In all cases, the monomer remained unreacted, while the catalyst decomposed. Survey of conditions for successful polymerization continues.

Discussion

Although none of the polymerization attempts of high-energy monomers undertaken so far was successful, these results are considered preliminary and the search for conditions under which high-energy polymers can be obtained through the ROMP technique continues.

There is a very large number of ROMP catalysts described in literature that might work with basketene or diazanorbormene type of monomers. Of a special

interest would be the tungsten ones. While they are not yet available on the market, making and testing a large variety of them in the laboratory is planned. Testing at least one tungsten catalyst, for example one analogous to **23**, on at least the three monomers that appear in this study is absolutely necessary before any conclusion can be drawn.

2.7   CONCLUDING REMARKS

Strained polycyclic hydrocarbons in the form of (1) 1,4-disubstituted cubyl systems with highly unsaturated side-chains, (2) 1,2-disubstituted cubanes, (3) cubylazido derivatives, and (4) high-energy polymers have been synthesized in small quantities sufficient for lab-scale studies of their physical and chemical properties. These compounds are expensive to synthesize, and hence their evaluation as potential candidates for further development in propulsion applications should be carried out. Due to the increasing gravimetric energy density, these fuels appear to be potential candidates for volume-limited applications to achieve increased range. Before realizing these fuels as practically reasonable, combustion experiments should be performed.

ACKNOWLEDGMENTS

REFERENCES

1. Moriarty, R. M., and M. S. Rao. 1993. Strained hydrocarbons. Benzvalene and derivatives. *6th ONR Propulsion Meeting Proceedings*. University of Colorado at Boulder. 1–6.
2. Moriarty, R. M., and M. S. Rao. 1994. Energetic azide compounds. *7th ONR Propulsion Meeting Proceedings*. Eds. G. D. Roy and P. Givi. Buffalo, NY: State University of New York at Buffalo. 75–81.
3. Moriarty, R. M., L. A. Enache, D. Pavlovic, and M. S. Rao. 1995. Synthesis of high-energy compounds. *8th ONR Propulsion Meeting Proceedings*. Eds. G. D. Roy and F. A. Williams. La Jolla, CA: University of California at San Diego. 122–29.
4. Moriarty, R. M., L. A. Enache, D. Pavlovic, D. Huang, and M. S. Rao. 1996. Synthesis of high-energy compounds. *9th ONR Propulsion Meeting Proceedings*. Eds. G. D. Roy and K. Kailasanath. Washington, DC: Naval Research Laboratory. 123–29.
5. Roy, G. D. 1997. Introduction. In: *Propulsion combustion: Fuels to emissions*. Ed. G. D. Roy. Washington, DC: Taylor & Francis. 1–14.

Chapter 3

SYNTHESIS OF NEW HIGH-ENERGY/HIGH-DENSITY HYDROCARBON FUEL SYSTEMS

A. P. Marchand, K. C. V. Ramanaiah, S. Alihodzic,
I. N. N. Namboothiri, E. Z. Dong, B. R. Aavula,
S. B. Lewis, and S. G. Bott

Polycarbocyclic "cage" hydrocarbons comprise a class of new high-energy/high-density fuels that are of interest for volume-limited military applications. Several new candidate fuel systems have been targeted, and syntheses of representative compounds have been devised and executed. One particularly interesting group of compounds includes "PCU alkene dimers," which are prepared via titanium-promoted reductive dimerization of pentacyclo[5.4.0.0^{2,6}.0^{3,10}.0^{5,9}]undecan-8-one ("PCU-8-one") and functionalized PCU-8-ones. Compounds of this type exhibit high crystal densities on the order of 1.2–1.3 g/cm^3 and possess a modicum of steric strain that is released upon combustion. The following studies and syntheses have been undertaken in connection with efforts toward the design and synthesis of new candidate fuel systems: (*i*) PCU-derived vinylidenecarbenes have been generated and trapped *in situ* by alkenes; (*ii*) Oxidative functionalization of unactivated C–H bonds in heptacyclo-[6.6.0.0^{2,6}.0^{3,13}.0^{4,11}.0^{5,9} 0^{10,14}]tetradecane-7-one ("HCTD-7-one") has been performed successfully by using Gif-type oxidants; (*iii*) Two unusual polycyclic alkenes, that contain completely planar C=C double bonds, have been synthesized; and (*iv*) A novel cage diester has been prepared via intramolecular [2 + 2] photocyclization of an isomer of "Thiele's ester," and its structure has been established unequivocally via application of single-crystal *X*-ray crystallographic techniques. Collaborations with other laboratories include: (*i*) new applications of the MOLPAK/WMIN computational method for estimating crystal densities of energetic materials; (*ii*) studies of combustion characteristics of mixtures of PCU alkene dimers as solid fuels in compressible flows; and (*iii*) studies of thermodynamic properties of HCTD and PCU.

3.1   INTRODUCTION

The work descibed herein has been directed toward the synthesis of new poly-carbocyclic hydrocarbon systems that are of interest as a potential new class of high-energy/high-density fuel systems for volume-limited military applications. Compounds of this type generally possess unusually high, positive standard heats of formation and unusually high densities [1, 2]. The objective is to synthesize compounds of this general type in 50–500 g quantities.

An example in this regard is provided by the titanium-promoted reductive dimerization [3–5] pentacyclic monoketones and their monomethylated analogs, as indicated in Scheme 1. We have successfully prepared these compounds in rel-atively large quantities (i.e., several hundred grams). Samples have been sent to other laboratories for evaluation of their fuel properties, selected thermodynamic properties, and combustion characteristics.

In collaboration with Prof. Herman Ammon (University of Maryland), MOLPAK/WMIN computational methods [6–12] have been employed success-fully to predict the crystal densities of (*i*) several isomerically pure monomethy-lated PCU alkene dimers [13] and (*ii*) several polycyclic epoxides [14]. The crys-tal densities calculated from *X*-ray crystal structure data are compared with the corresponding calculated values. Attempts have been made to address discrep-ancies that may exist between computed densities and those derived from *X*-ray data by using advanced theoretical methods.

3.2   RESULTS AND DISCUSSION

3.2.1   Generation and Trapping of PCU-Derived Vinylidenecarbenes

Recently, the successful generation of PCU-8-vinylidenecarbene (**4a**) via reaction of 8-(dibromo-methylene)-PCU (**3**) with *n*-BuLi hs been reported [15]. When this reaction is performed in the presence of an alkene trapping agent (i.e., cyclohexene), a cage-functionalized *exo*-methylenecyclopropane, **5**, is the only product. Compound **5** subsequently was characterized via conversion to the cor-responding substituted dichlorospiro(cyclopentane), **6** (Scheme 2); the structure was established unequivocally via single-crystal *X*-ray structural analysis [15].

In order to further investigate the possibility of cycloalkyne **4b** formed as a transient intermediate in the reaction of **3** with *n*-BuLi, specifically ^{13}C la-beled **3** — ^{13}CBr$_2$ was synthesized and subsequently was reacted with *n*-BuLi. The reactive intermediate(s) thereby generated were trapped *in situ* by cyclo-hexene. Careful integration of the gated-decoupled ^{13}C NMR spectrum of **5** — ^{13}C obtained indicated that no scrambling of the ^{13}C label had occurred in the

Scheme 1

TiCl$_4$, Zn

pyridine, THF
reflux 22 h

R

O

R

2

1a (R=H)	**2a** (R=H)
1b (R=Me)	**2b** (R=Me)
(mixture of isomers)	("PCU alkene dimer," mixture of isomers)

Scheme 2

n-BuLi
THF
− 78 °C to
+ 25 °C

CBr$_2$

3

(?)

C:

4a   **4b**

(trap)

H

H

5

:CCl$_2$

Cl

Cl

H

H

6
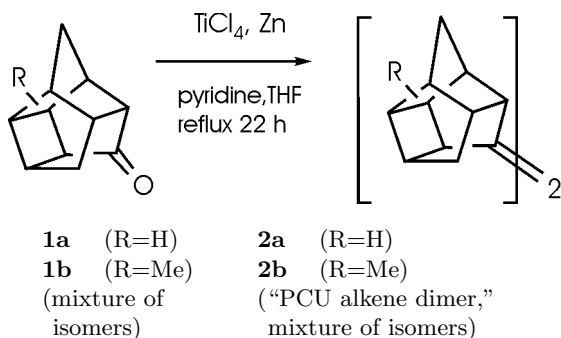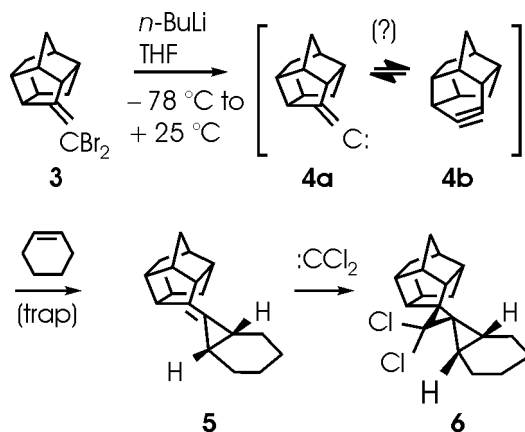
product. This result contradicts the incursion of **4b** as an intermediate in this reaction [16].

More recently, we have investigated the corresponding reaction of 8-(dibromomethylene)-11-methylene PCU (**7**) with *n*-BuLi. Once again, a cage-functionalized *exo*-methylenecyclopropane (i.e., **9**) was obtained as the only product. Compound **9** subsequently was characterized via conversion into **10** (Scheme 3), the structure of which was established unequivocally via single-crystal *X*-ray structural analysis [17].

No experimental evidence was found that products formed as a result of alkene trapping of a putative cycloalkyne intermediate in either of these reac-

Scheme 3
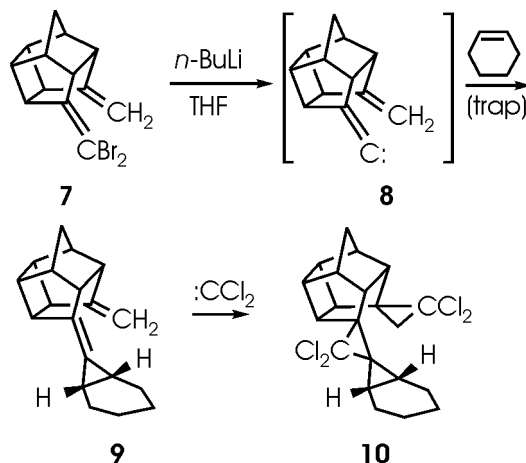
tions. Interestingly, the results of semi-empirical MO calculations (performed by using the AMI and/or PM3 Hamiltonians) indicate that **4b** is only ca. 0.4 kcal/mol less stable than **4a**, but that the energy barrier for rearrangement of **4a** to **4b** is relatively high (> 30 kcal/mol) [15, 16].

3.2.2 Generation and Trapping of a D_3-Trishomocubane-Derived Vinylidenecarbene

The reaction of 4-(dibromomethylene)pentacyclo[6.3.0.0^{2,6}.0^{3,10}.0^{5,9}]undecane (**11**) with n-BuLi resulted in the corresponding vinylidenecarbene, **12a**, which could be trapped *in situ* by cyclohexene to obtain the corresponding cage-functionalized *exo*-methylenecyclopropane (i.e., **13**, Scheme 4). Compound **13** subsequently was characterized via conversion into **14** (Scheme 4), which structure was established unequivocally via single-crystal X-ray structural analysis [18].

In order to further investigate the possibility of cycloalkyne **12b** formed as a transient intermediate in the reaction of **11** with n-BuLi, specifically ^{13}C labeled **11** — ^{13}CBr$_2$ was synthesized and subsequently was reacted with n-BuLi. The reactive intermediate(s) generated were trapped *in situ* by cyclohexene. Careful integration of the gated-decoupled ^{13}C NMR spectrum of **13** — ^{13}C obtained indicated that no scrambling of the ^{13}C label had occurred in the product. This result contradicts the incursion of **12b** as an intermediate in this reaction [18].

Scheme 4
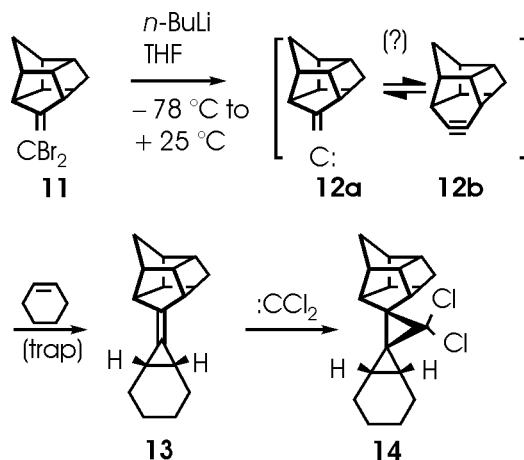
Scheme 5
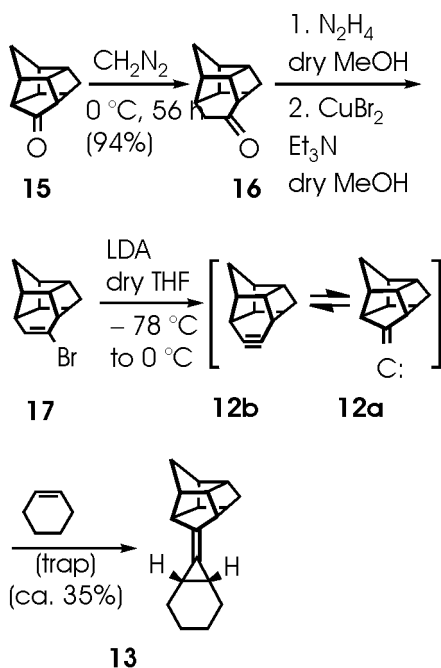
Interestingly, it appeared possible to enter the **12a**–**12b** vinylidenecarbene-cycloalkyne equilibrium from the "cycloalkyne side." This was accomplished by synthesizing the appropriate cage vinyl bromide, **17**; then subsequent reaction of **17** with a base provided indirect access to **12b** (Scheme 5) [18].

3.2.3 Generation and Trapping of an HCTD-Derived Vinylidenecarbene

As an extension of the foregoing studies, the generation and trapping of an HCTD-derived vinylidenecarbene, i.e., **20** (Scheme 6), was investigated. Thus, reaction of heptacyclo[6.6.0.0^{2,6}.0^{3,13}.0^{4,11}.0^{5,9}.−0^{10,14}]tetradecane-7-one (**18**) [19–21] with Ph$_3$P-CBr$_4$ generated the corre-

Scheme 6

18   19   20   21

Scheme 7

Go Agg[III]   **22** (65%) + **23** (6%)

GoAgg[IV]   **22** (61%) + **23** (10%)

22 (56%) + **23** (8%)

GoAgg[V]

18 (1%)   **24** (3.5%)
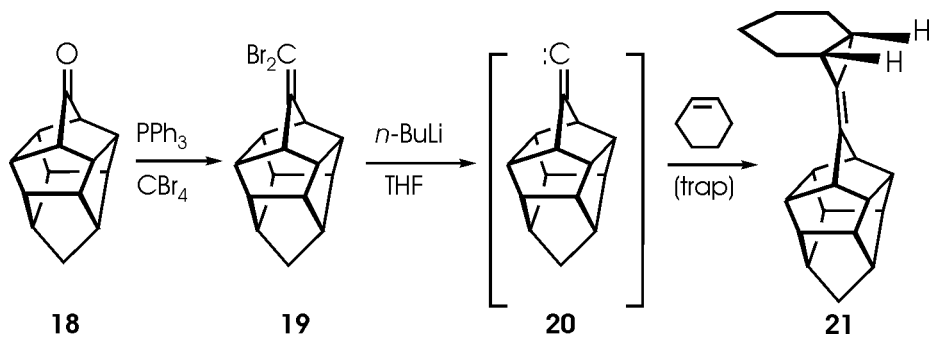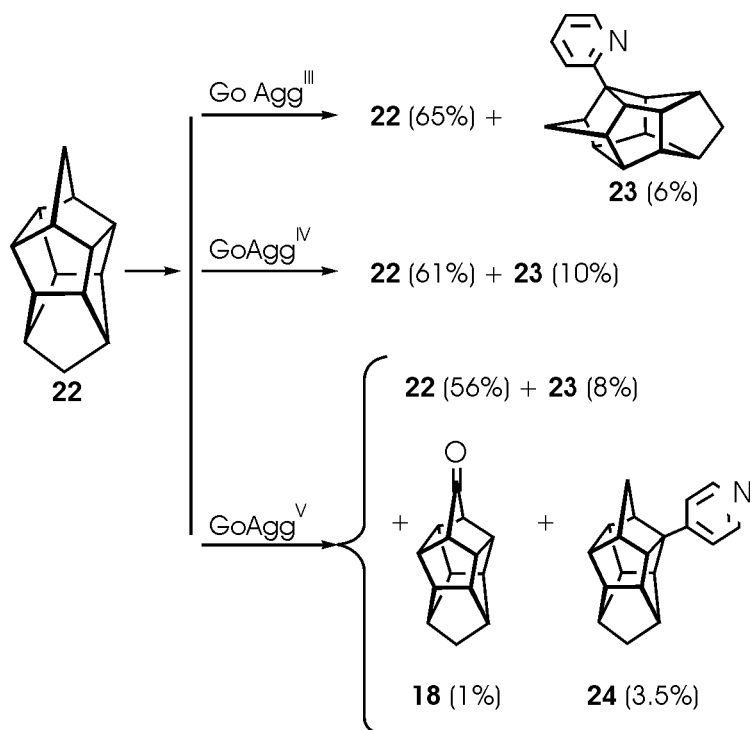
sponding 7-(dibromomethylene)-HCTD (**19**). Subsequent reaction of **19** with
n-BuLi in dry THF produced the corresponding vinylidenecarbene, **20**.

The corresponding cycloadduct, **21**, which structure was established une-
quivocally via single-crystal *X*-ray structural analysis [22], was obtained by trap-
ping **20** *in situ* by cyclohexene.

3.2.4 Oxidative Functionalization of Unactivated Carbon–Hydrogen Bonds in HCTD (22)

Gif-type reactions have been used to perform direct oxidative functionalization of
HCTD (**22**) [19]. Thus, GoAgg^{III}- and GoAgg^{IV}-promoted oxidations of **22** af-
ford 1-(2′-pyridyl)-heptacyclo[6.6.0.0^{2,6}.0^{3,13}.0^{4,11}.0^{5,9}.0^{10,14}]tetradecane [i.e., 1-
(2′-pyndyl)-HCTD, **23**] in 6%–10% isolated yield. In addition to **23**, GoAgg^{V}-
promoted oxidation of **22** produced heptacyclo[6.6.0.0^{2,6}.0^{3,13}.0^{4,11}.0^{5,9}.0^{10,14}]-
tetradecane-7-one (HCTD-7-one, **18**) and 1-(4′-pyridyl)-HCTD (**24**) in low iso-
lated yield (Scheme 7) [19].

Finally, oxidation of **22** performed by using an Fe^{II}-*t*-BuOOH system af-
forded several products, including hexacyclo[6.6.0.0^{2,6}.0^{3,13}.0^{4,11}.0^{5,9}.0^{10,14}]tet-
radecane-10,14-dione (**26**) and 14-hydroxyhexacyclo[6.6.0.0^{2,6}.0^{3,13}.0^{4,11}.0^{5,9}.-
0^{10,14}]tetradecane-10-one (**27**), both of which resulted via oxidative cleavage of
the C(1)–C(2) σ-bond in **22** (see Scheme 8) [19].

3.2.5 Synthesis of a Novel, Polycarbocyclic Alkene which Contains a Strained, Planar C=C Double Bond [22]

The availability of **18** in one synthetic step via direct oxidative functionalization
of HCTD [19–21] allows exploration of this valuable compound's chemistry, for
the first time. Thus, the reaction sequence shown in Scheme 9 has been utilized
to prepare a novel polycyclic alkene, **30**, whose symmetry properties require
that its central, tetrasubstituted C=C double bond be completely planar (in
the isolated molecule). The constraints imposed by the polycarbocyclic cage
framework cause the "CCC bond angles about the central C=C double bond in
30 to deviate significantly from the "preferred" value of 120°, thereby introducing
additional steric strain in this molecule beyond that which is associated with its
framework alone.

The single-crystal *X*-ray structure of **30** was determined at 208 K (see
Fig. 3.1) [22]. The "C–C=C bond angles about the central C=C double bond in
30 were found to lie in the range 113°–115°. In addition, the C=C bond length

Scheme 8

22 (42%) + **23** (7%) +

18 (2–3%) + **24** (5%) +

25
(0.8%)

26
(13–14%)

+

27
(2–3%)

"Fe^{II}-
t-BuOOH

System"

22
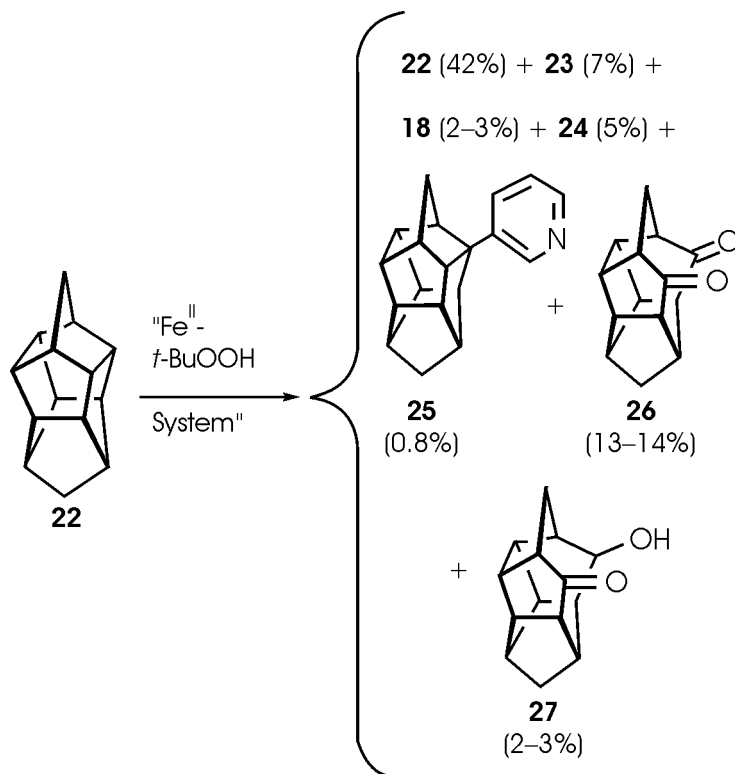
in this compound is unusually short, i.e., 1.334 (7) Å. Importantly, the crystal density of this unusual cage-annulated alkene was found to be 1.36 g/cm^3, thereby rendering **30** one of the most dense cage hydrocarbons that has been prepared [22].

Subsequently, **30** was oxidized by MCPBA at −10 °C to produce the corresponding oxirane, **31**. This compound proved to be unstable to either mild acid or mild base. Thus, work-up of the oxidation reaction product with either dilute aqueous NaHCO$_3$ or via column chromatography on silica gel converted **31** into the corresponding *cis* diol, **32** (Scheme 10). The structure of **32** was established unequivocally via application of X-ray crystallographic methods [22].

In addition, we have prepared a tetracyclic analog of **30**, i.e., **36**. The route shown in Scheme 11 was employed for this purpose.

Scheme 9

18

28 (84%)

1. LAH
THF (90%)

2. CF₃CO₂H
CDCl₃, heat
(84%)

29 (90%)

30
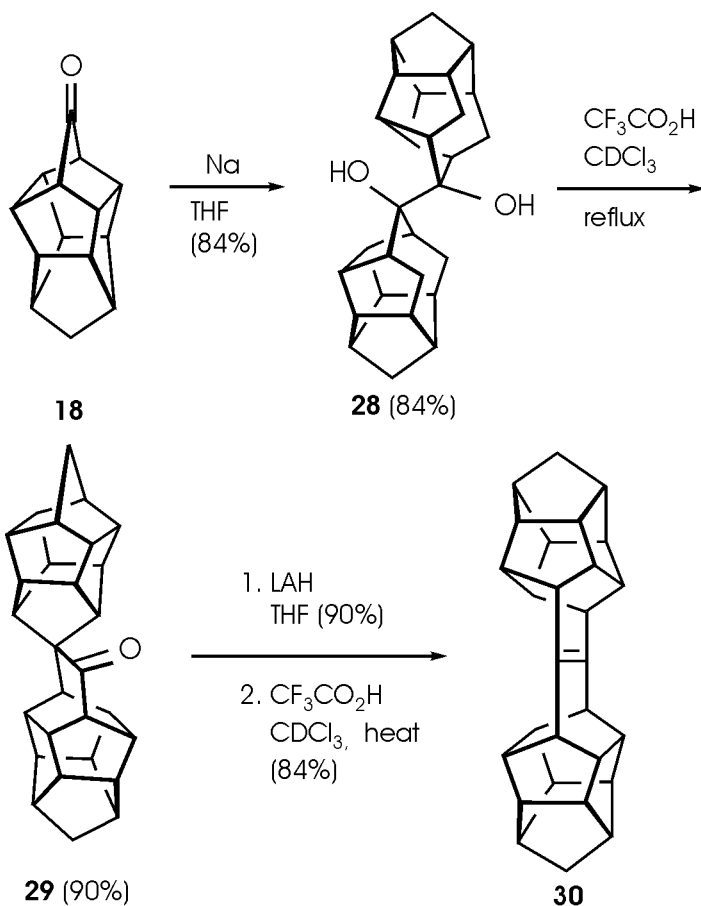
3.2.6 Isolation and Characterization of a Minor Product that Accompanies the Formation of Thiele's Ester via Reaction of Sodium Cyclopentadienide with Ethyl Chloroformate

At the beginning of the 19th century, Thiele [23, 24] reported that carbonation of sodium cyclopentadienide (**37**) affords a cyclopentadienecarboxylic acid dimer whose structure subsequently was firmly established as **38** ("Thiele's Acid," Scheme 12) via chemical [25] and spectroscopic [26] methods.

In 1959, Peters [27] reported the isolation and characterization of a minor product from this reaction. It was determined that this minor product is isomeric
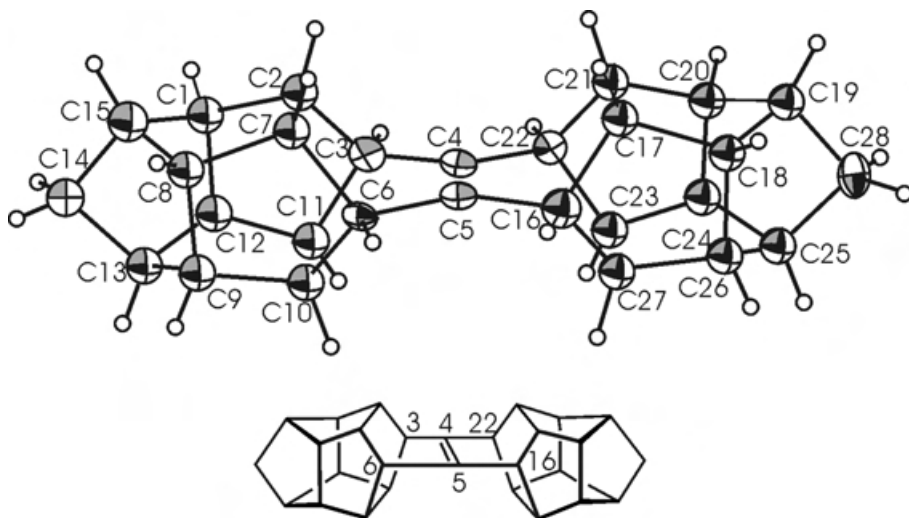
Bond length: C(4)=C(5) = 1.334(7) Å

Bond angles: C(3)–C(4) = C(5) = 113.7(4)°
                C(4)=C(5)–C(6) = 115.1(4)°
                C(4)=C(5)–C(16) = 113.4(4)°
                C(5)=C(4)–C(22) = 115.7(4)°

Figure 3.1 *X*-ray structure of **30a** and selected bond lengths and bond angles in **30b**

Scheme 10
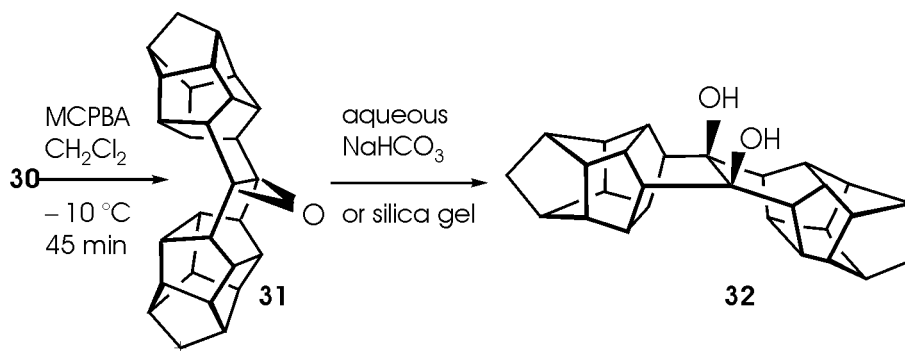
Scheme 11
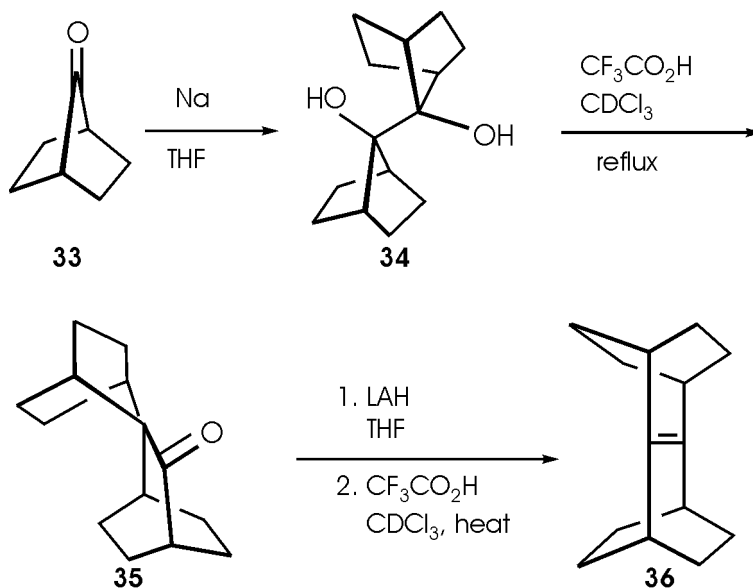
with Thiele's Acid. Analysis of its ultraviolet spectrum suggested that it contains one conjugated and one nonconjugated carboxyl group.

This minor product has been now isolated and converted into the corresponding pentacyclo[5.3.0.0^{2,5}.0^{3,9}.0^{4,8}]decanedicarboxylic acid via intramolecular [2 + 2] photocyclization. The material thereby obtained was converted into the corresponding cage di(p-nitrobenzyl ester) derivative via the method shown in Scheme 12. The structure of the resulting diester was established unequivocally as **40** via application of X-ray crystallographic methods (see Fig. 3.2) [28].

3.3   COLLABORATIONS WITH OTHER LABORATORIES

Collaborations that were initiated during previous contract years have been continued throughout 1996–1997 in an effort to further evaluate the fuel properties of the new high-energy-density materials. A brief description of each of these collaborative efforts follows.

Scheme 12

37 → (CO₂ (dry ice), dry THF) → **38** (64%) + **39** (3.6%)

39 → 1. $h\nu$, acetone Pyrex, 24 h; 2. SOCl₂, pyridine; 3. p-nitrobenzyl alcohol, dry benzene → **40** (3.6%)
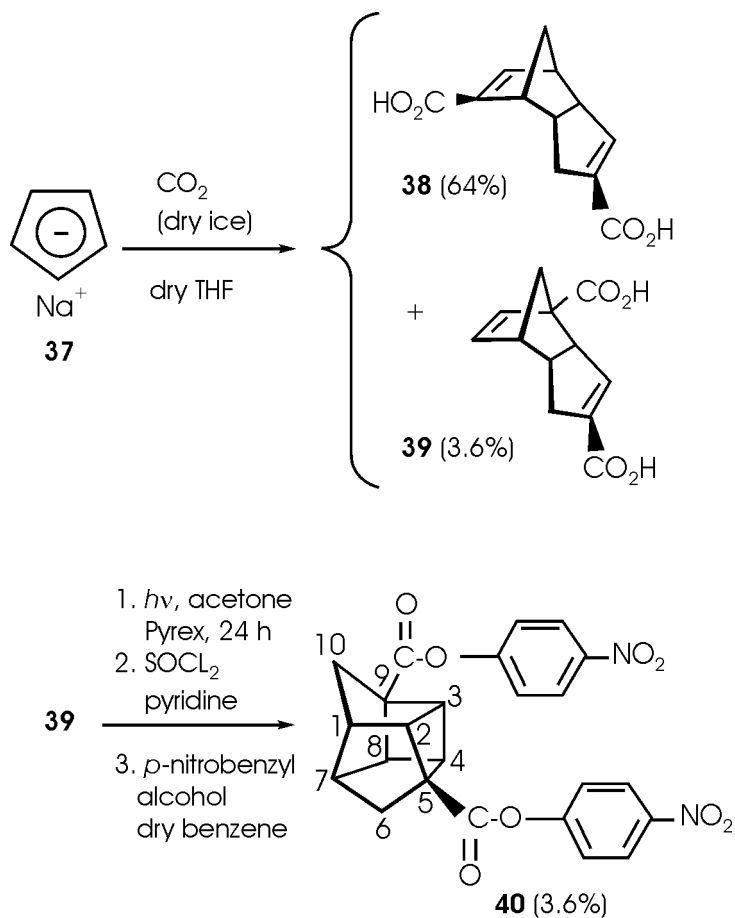
3.3.1 Department of Chemistry, University of Maryland, College Park, MD (Professor Herman L. Ammon)

The importance of high density as a feature of potential fuel systems that seek to maximize net volumetric heat of combustion is well documented. The prediction of the crystal density of an unknown compound typically has been approached through the use of "volume additivity" procedures [29–32]. Here, the crystal-molecular volume (V_{cm}) is calculated by summing appropriate crystal-atomic or group volumes (V_{ca}; $V_{cm} = \sum V_{ca}$) and the corresponding crystal density is ob-
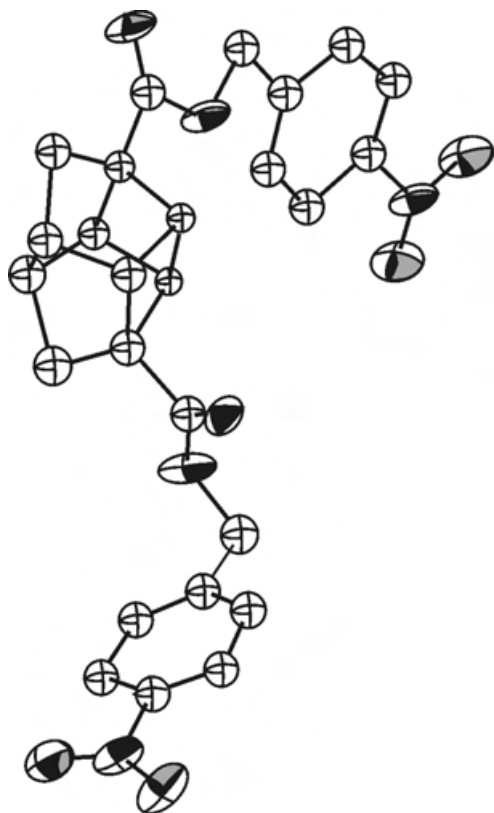
Figure 3.2 *X*-ray structure drawing of **40**

tained by dividing the molecular mass (M) by V_{cm}; thus, $\rho = M/V_{cm}$. V_{ca} values usually are obtained by least-squares procedures which fit V_{cm} values to experimental crystal-molecular volumes (V_{ce}) from X-ray crystal structure data (V_{ce} is the unit cell volume divided by the number of molecules per unit cell).

Volume additivity methods generally do not take into account crystal packing efficiency or molecular conformation effects and thus will afford identical calculated densities for positional and conformational isomers and for compounds that possess different multiples of the same functional group composition. As an example, a volume additivity calculation predicts that 1,3,5-trinitro-1,3,5-triazacyclohexane (RDX), 1,3,5,7-tetranitro-l,3,-5,7-tetraazacyclooctane (α-HMX), and β-HMX all will possess the same crystal density, 1.783 g/cm^3 [32]. In fact, the experimentally observed densities of these three compounds differ markedly (i.e., 1.806 [33], 1.839 [34], and 1.902 [35], respectively).

Recently, Holden, Du, and Ammon [9] reported a procedure for predicting possible crystal structures of C-, H-, N-, O-, and F-containing organic compounds. Their approach involves construction of crude crystal packing arrangements (MOLPAK = MOLecular PAcKing program), which starts with an optimized model (search probe) for the compound of interest, by positioning molecules around a central molecule into predetermined coordination sphere geometries. The best of these arrangements are refined subsequently with a crystal lattice energy minimization (WMIN) [9] program. This procedure takes molecular shape, conformation, and crystal packing efficiency into account.

As part of the study, the authors have collaborated with Prof. Ammon in an effort to perform useful crystal density modeling calculations for four

Scheme 13

41   **42**   **43**   **44**

45   **46**   **47**
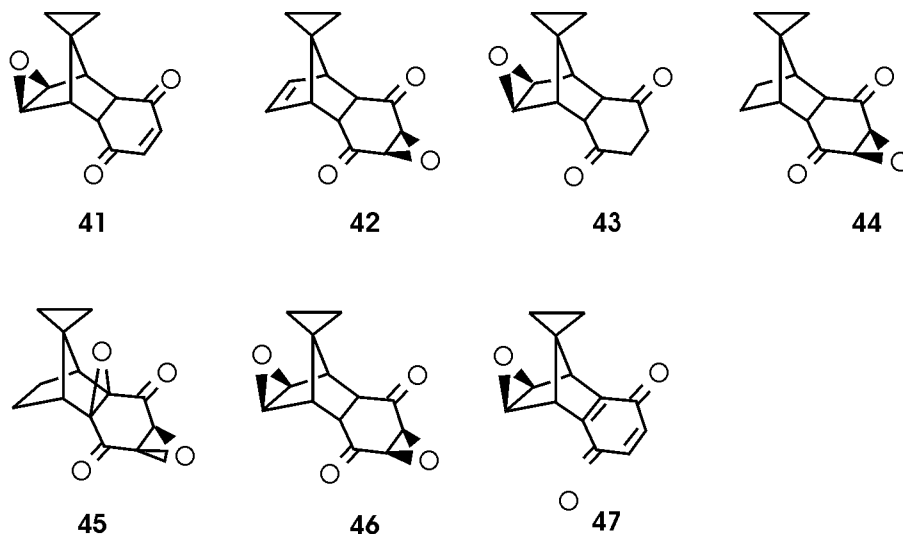
isomeric methylated PCU alkene dimers by using the MOLPAK/WMIN approach [9]. The observed and calculated crystal densities generally agree within 1%–2% [10]. Subsequently, this collaboration with Prof. Ammon was extended to include crystal density modeling calculations for several epoxide-functionalized tetrahydro- and hexahydromethanonaphthalenes [14]. In 1996–1997, this series was extended to include crystal density modeling calculations for spirocyclopropanated, epoxide-functionalized tetrahydro- and hexahydromethanonaphthalenes (see compounds **41**−**47** in Scheme 13). The MOLPAK/WMIN calculated densities thereby obtained have been published [36].

3.3.2 Department of Aerospace Engineering, Mechanics and Engineering Science, University of Florida (Professor Corin Segal)

Initially, Prof. Segal and members of his research group at the University of Florida evaluated the combustion characteristics of mixtures of isomeric PCU alkene dimers (**2a**) as solid fuels in compressible flows. Subsequently, these studies were extended to include evaluation of **2a** as a solid fuel under conditions of high-shear flow. Samples of the mixture of isomeric PCU alkene dimers were cured with a styrene-polybutadiene copolymer (10% w/w) binder on the test

Scheme 14

Compound:	**2a** (R= H)	**48** (mixture of	**49** (mixture of
	2b (R=Me)	isomers)	isomers)
	(mixtures of		
	isomers)		

Quantity:	**2a:** 261 grams	20 grams	2 grams
	2b: 105 grams		
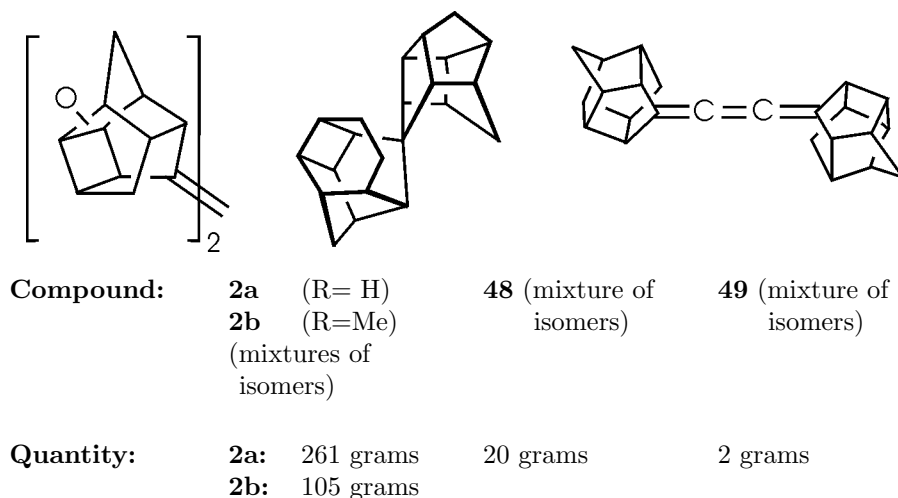
chamber wall and ignited convectively via a gaseous flame in air flow at Mach number 0.12–0.25 at a stagnation temperature and pressure of 300 K and 150–250 kPa, respectively. Ignition times and rates of heat release were measured. The results indicate that, when compared with HTPB fuel under the same thermodynamic conditions and geometrical configuration, **2a** ignition times are an order of magnitude more rapid. The heat released during combustion of **2a** is more than twice as great as that of HTPB fuel under comparable conditions.

The results of this study have been published [37]. Evaluation samples of several candidate energetic hydrocarbon fuel systems have been sent to Prof. Segal for his combustion studies (see Scheme 14). More recently, Prof. Segal and his co-workers have studied rheological properties and burning rates of a mixture of isomeric methylated PCU alkene dimers (**2b**). A stable 18% w/w solution of **2b** in JP-10 was achieved. More concentrated solutions (up to 25% w/w) were unstable and produced sediments after standing for ca. 2 weeks under ambient conditions. An 18% w/w solution of **2b** in JP-10 increased the kinematic viscosity of JP-10 by 1.3 centistokes at 30 °C and by 0.65 centistokes at 70 °C, thereby effectively matching the viscosity of RJ-4.

An 18% w/w solution of **2b** in JP-10 exhibits a burn rate of 1.97 mm^2/s (vs. 0.757 mm^2/s for pure JP-10). The mixture exhibits effervescent boiling that results in increased contact area with the burning surroundings, which results

in a significantly enhanced (i.e., accelerated) burning rate *vis-à-vis* that of pure JP-10.

Finally, the burning rate of "8-(7′-norcaranylidene)-PCU" (i.e., **5**) has been studied. Compound **5** displays a rapid burning rate, i.e., 2.9 mm^2/s. The droplet explodes toward the end of the burn cycle, thereby indicating that a relatively large quantity of heat is released during the burning process.

3.3.3 Belarussian State University, Minsk, Belarus (Professor G. J. Kabo)

Highly purified samples of heptacyclo[6.6.0.0^{2,6}.0^{3,13}.0^{4,11}.0^{5,9}.0^{10,14}]tetrad ecane (HCTD) and pentacyclo[5.4.0.0^{2,6}.0^{3,10}.0^{5,9}]undecane (PCU) were sent to Prof. Kabo for study of their thermodynamic properties. The results of this study have been published in two papers which appeared in [38] and [39].

3.4 CONCLUDING REMARKS

Syntheses of several novel polycarbocyclic "cage" hydrocarbons have been designed and executed successfully as part of an extensive program of research on the development of new high-energy/high-density fuels that are specifically designed for volume-limited military applications. In this connection, relatively large quantities (i.e., several hundred grams) of "PCU alkene dimers" of the type **2a** and **2b** (Scheme 1) have been prepared.

The combustion characteristics of mixtures of PCU alkene dimers as solid fuels in compressible flows have been studied by Prof. Corin Segal and his co-workers at the University of Florida. The results of his combustion studies demonstrate that fuels formed by the addition of mixtures of methylated PCU alkene dimers (18% w/w solutions) to JP-10 have a significant accelerated burning rate relative to that of pure JP-10. In addition, a new candidate hydrocarbon fuel, i.e., compound **5**, was found by Prof. Segal to burn rapidly (i.e., 2.9 mm^2/s) and to release a relatively large quantity of heat during combustion.

New applications of the MOLPAK/WMIN computational method for estimating crystal densities of energetic materials have been investigated in collaboration with Prof. Herman L. Ammon and his co-workers at the University of Maryland. Finally, thermodynamic properties of HCTD and PCU have been determined by Prof. G. J. Kabo and his colleagues at Belarussian State University, Minsk, Belarus.

In the course of this study, several new candidate fuel systems have been synthesized in gram quantities. In the future, it is planned to undertake large-scale syntheses of those new hydrocarbons, like **5**, whose combustion properties suggest that they might excel as energetic fuels or as fuel additives.

It is also planned to continue crystal density modeling studies in collaboration with Prof. Ammon with the expectation that comparison of predicted with experimental (X-ray derived) crystal density values will permit further refinement of the MOLPAK/WMIN computational approach. In this way, the predictive value of this computational method is likely to be enhanced, thereby rendering it of greater value for preliminary screening of proposed new candidate fuel systems as potential synthetic targets.

ACKNOWLEDGMENTS

REFERENCES

1. Marchand, A. P. 1989. High-energy-density solid and liquid hydrocarbon fuels. Technical Report AFWAL-TR-88-2128 (Feb.). Distribution unlimited.

2. Marchand, A. P., Z. Liu, D. Rajagopal, V. D. Sorokin, F. Zaragoza, and A. Zope. 1994. New high-energy/high-density fuel systems: synthesis and characterization. *7th ONR Propulsion Meeting Proceedings*. Eds. G. D. Roy and P. Givi. Buffalo, NY: State University of New York at Buffalo. 82–90.

3. McMurry, J. E., and M. P. Fleming. 1974. A new method for the reductive coupling of carbonyls to olefins: Synthesis of β-carotene. *J. American Chemical Society* 96:4708–9.

4. McMurry, J. E. 1983. Titanium-induced dicarbonyl-coupling reactions. *Accounts Chemical Research* 16:405–11.

5. Lenoir, D. 1989. The application of low-valent titanium reagents in organic synthesis. *Synthesis*. 883–97.

6. Ammon, H. L., Z. Du, and J. R. Holden. 1990. Estimated crystal densities from possible crystal packing arrangements. *9th Annual Working Group Institute on Synthesis of High Energy Density Proceedings*. Kiamesha Lake, NY. 47–61.

7. Ammon, H. L., Z. Du, and J. R. Holden. 1991. Crystal density and packing in [4]peristylanes and *bis*-homopentaprismanes: The effects of basal nitro group sub-

stitution. *10th Annual Working Group Institute on Synthesis of High Energy Density Proceedings*. Kiamesha Lake, NY. 23–33.

8. Ammon, H. L., Z. Du, and J. R. Holden. 1992. Beyond density prediction to *ab initio* crystal structure prediction. *11th Annual Working Group Institute on Synthesis of High Energy Density Proceedings*. Kiamesha Lake, NY. 15–31.

9. Holden, J. R., Z. Du, and H. L. Ammon. 1993. Prediction of possible crystal structures for carbon-, hydrogen-, nitrogen-, oxygen-, and fluorine-containing organic compounds. *J. Computational Chemistry* 14:422–37.

10. Busing, W. R. 1981. WMIN, a computer program to model molecules and crystals in terms of potential energy functions. Report ORNL-5747. Oak Ridge National Laboratory, Oak Ridge, TN.

11. Marchand, A. P., Z. Liu, K. A. Kumar, R. Eckrich, and V. D. Sorokin. 1995. Large-scale synthesis of new high-energy/high-density hydrocarbon fuel systems. *8th ONR Propulsion Meeting Proceedings*. Eds. G. D. Roy and F. A. Williams. La Jolla, CA: University of California at San Diego. 130–41.

12. Marchand, A. P., K. A. Kumar, R. Eckrich, K. C. V. Ramanaiah, G. V. M. Sharma, A. Devasagayaraj, S. Alihodzic, and S. B. Lewis. 1996. Large-scale synthesis of new high-energy–high-density hydrocarbon fuel systems. *9th ONR Propulsion Meeting Proceedings*. Eds. G. D. Roy and K. Kailasanath. Washington, DC: Naval Research Laboratory. 130–38.

13. Marchand, A. P., A. Zope, F. Zaragoza, H. L. Ammon, and Z. Du. 1994. Synthesis, characterization and crystal density modeling of four $C_{24}H_{28}$ cage-functionalized alkenes. *Tetrahedron* 50:1687–98.

14. Marchand, A. P., D. Vidyanand, Z. Liu, K. A. Kumar, F. Zaragoza, L. K. Talafuse, S. G. Bott, W. H. Watson, R. P. Kashyap, and H. L. Ammon. 1996. Synthesis, characterization and crystal density modeling of polycarbocyclic oxiranes. *Tetrahedron* 52:9703–12.

15. Marchand, A. P., K. A. Kumar, D. Rajagopal, R. Eckrich, and S. G. Bott. 1996. Generation and trapping of a caged cyclopentylidenecarbene. *Tetrahedron Letters* 37:467–70.

16. Marchand, A. P., and K. A. Kumar. Unpublished results.

17. Marchand, A. P., Z. Dong, and S. G. Bott. Unpublished results.

18. Marchand, A. P., I. N. N. Namboothiri, B. Ganguly, and S. G. Bott. 1998. Study of a vinylidenecarbene–cycloalkyne equilibrium in the D3-trishomocubyl ring system. *J. American Chemical Society* 120:6871–76.

19. Marchand, A. P., Y. Wang, S. Alihodzic, and D. H. R. Barton. 1997. Oxidative functionalization of unactivated carbon–hydrogen bonds in heptacyclo[6.6.0.0^{2,6}.0^{3,13}.0^{4,11}.0^{5,9}.0^{10,14}]tetradecane (HCTD)8. *Tetrahedron* 53:1257–64.

20. Albert, B., D. Elsasser, H.-D. Martin, B. Mayer, T. J. Chow, A. P. Marchand, C.-T. Ren, and M. N. Paddon-Row. 1991. Cage dimers of norbornadiene with perpendicular arrangement of subchromophores: Orbital interaction in the hep-

tacyclo[6.6.0.-0^{2,6}.0^{3,13}.0^{4,11}.0^{5,9}.0^{10,14}]tetradecane system. *Chemisches Berichte* 124:2871–78.

21. Chow, T. J., J.-J. Feng, H.-J. Shih, T.-K. Wu, L. H. Tseng, C.-Y. Wang, and C. Yu. 1988. The preparation of heptacyclo[6.6.0.-0^{2,6}.0^{3,13}0^{4,11}.0^{5,9}.0^{10,14}]tetradecane derivatives and analysis of their NMR spectra. *J. Chinese Chemical Society* 35: 291–99.

22. Marchand, A. P., S. Alihodzic, and S. G. Bott. Unpublished results.

23. Thiele, J. 1900. On reactions of ketones with cyclopentadiene. *Chemisches Berichte* 34:666–73.

24. Thiele, J. 1901. On derivatives of cyclopentadiene. *Chemisches Berichte* 33:68–71.

25. Dunn, G. L., and J. K. Donohue. 1968. The structure of Thiele's Ester, a dimethyl dicyclopentadienecarboxylate. *Tetrahedron Letters*. 3485–88.

26. Minter, D. E., A. P. Marchand, and S.-P. Lu. 1990. Complete assignment of the ^{1}H and ^{13}C NMR spectra of Thiele's Ester. *Magnetic Resonance Chemistry* 28:623–26.

27. Peters, D. 1959. Cyclopentadienecarboxylic acid. The structure of the monomer and the dimers. *J. Chemical Society*. 1761–65.

28. Marchand, A. P., I. N. N. Namboothiri, S. B. Lewis, and W. H. Watson. Unpublished results.

29. Cady, H. H. 1979. Estimation of the densities of organic explosives from their structural formulas. Report LA-7760-MS. Los Alamos Scientific Laboratory, Los Alamos, NM.

30. Tarver, C. M. 1979. Density estimations for explosives and related compounds using the group additivity approach. *J. Chemical Engineering Data* 24:136–45.

31. Cichra, D. A., J. R. Holden, and C. Dickinson. 1980. Estimation of normal densities of explosive compounds from empirical atomic volumes. Report 79-273. Naval Surface Weapons Center, Silver Spring, MD.

32. Stine, J. R. 1981. Prediction of crystal densities of organic explosives by group additivity. Report LA-8920. Los Alamos National Laboratory, Los Alamos, NM.

33. Choi, C. S., and E. Prince. 1972. The crystal structure of cyclotrimethylenetrinitramine. *Acta Crystallographica, Sect. B* B28:2857–62.

34. Cady, H. H., A. C. Larson, and D. T. Cromer. 1963. The crystal structure of α-HMX and a refinement of the structure of β-HMX. *Acta Crystallographica* 16:617–23.

35. Zhitomirskaya, N. G., N. T. Erernko, N. I. Golovina, and L. O. Atovmyan. 1987. Structural and electronic parameters of some cyclic nitramines. *Bull. Academy Science USSR, Division Chemical Science* 36:525–29.

36. Marchand, A. P., R. Shukla, P. R. J. Davey, H. L. Ammon, Z. Du, and S. G. Bott. 1998. Synthesis, characterization and crystal density modeling of spiropolycyclic oxiranes. *Tetrahedron* 54:4485–92.

37. Segal, C., M. J. Friedauer, H. S. Udaykumar, W. Shyy, and A. P. Marchand. 1997. Ignition characteristics of a new high-energy strained fuel in high-speed flows. *J. Propulsion Power* 13:246–49.

38. Kabo, G. J., A. A. Kozyro, A. P. Marchand, V. V. Diky, V. V. Simirsky, L. S. Ivashkevich, A. P. Krasulin, V. M. Sevruk, and M. L. Frenkel. 1994. Thermodynamic properties of heptacyclotetradecane, $C_{14}H_{16}$. *J. Chem. Thermodynamics* 26: 129–42.

39. Kabo, G. J., A. A. Kozyro, V. V. Diky, V. V. Simirsky, L. S. Ivashkevich, A. P. Krasulin, V. M. Sevruk, A. P. Marchand, and M. L. Frenkel. 1995. Thermodynamic properties of pentacycloundecane, $C_{11}H_{14}$. *J. Chem. Thermodynamics* 27: 707–20.

Chapter 4

DECOMPOSITION CHEMISTRY
OF HIGH-ENERGY-DENSITY FUELS
BY FLOW TUBE MASS SPECTROMETRY

Z. Li and S. L. Anderson

A method is described that allows study of thermal breakdown behavior
of organic high-energy-density fuel molecules. In addition to stability
vs. temperature results, the distribution of product species as a func-
tion of temperature is also determined. The method uses a microflow
tube reactor to allow study of small samples. The mixture exiting the
reactor is analyzed by mass spectrometry. The mass spectrometer is
a unique instrument optimized for low-collision energy scattering, and
this method is used to unambiguously identify product isomer distribu-
tions. Results are presented for four different strained isomer systems,
representing three different families of strained molecules.

4.1 INTRODUCTION

An important strategy for improvement of propulsion system performance is
utilization of fuels and propellants that have significantly enhanced energy den-
sity compared to normal hydrocarbons. For liquid-fueled applications, strained
hydrocarbons are a particularly appealing class of candidate fuel molecules,
because they should work in conventional combustors and fuel systems with
minimal modification. Their high-energy densities result mainly from increased
density compared to normal hydrocarbons; however, they can have up to
$\sim$ 140 kcal/mole of strain energy built into the molecular framework in the
form of distorted bond angles. While this does not greatly increase the heat of
combustion, the strain energy changes the pyrolysis behavior of the molecules
substantially, which should make it possible to tune the ignition/combustion

(a)

(c)

C_2H_5

N

(b)

(d)
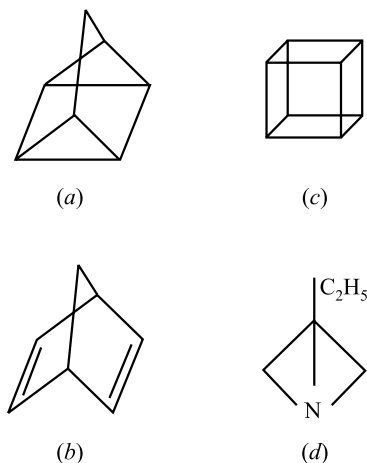
Figure 4.1 Strained hydrocarbon molecules discussed in the paper: (*a*) quadricyclane, (*b*) norbornadiene, (*c*) cubane, (*d*) 1-azo-3-ethylbicyclo[1.1.0]butane

properties. In particular, ignition behavior might be substantially improved by generation of reactive species early in the combustion process or by micro-explosions in fuel droplets. A few simple strained molecules are shown in Fig. 4.1.

There have been a number of successful approaches to synthesizing strained molecules with the idea of developing new fuel systems [1–12]. A number of molecular families have been proposed as candidates, including the benzvalenes, cubanes, and larger cage systems such as the pentacycloundecane (PCU) oligamers. Smaller molecules, such as cyclopropanes or bicyclobutanes, are also candidates for the strained molecule framework. Since the hydrocarbon frameworks can be functionalized, derivatives can be synthesized to tailor the molecular properties to the task at hand. For example, adding a methyl group to cubane converts it from a solid to a free-flowing liquid at room temperature. Functionalization should allow control of vapor pressure, viscosity, melting point, sensitivity, and stability. It should also be possible to add nitro, nitramine, or azide functionality to further increase the energy density [9, 11].

Though this approach has great potential, one problem is that these molecules are nontrivial to synthesize and purify. Only very small samples are often available for new candidate molecules, making it difficult to study their chemistry by conventional methods. One goal of our experiments is to provide a method of characterizing the thermal chemistry of synthetic fuel molecules using samples from small-scale synthesis (20–30 mg). The expectation is that these results will provide feedback to the synthetic chemists, allowing them to focus their efforts on the most promising candidates.

4.2   EXPERIMENTAL DESIGN

For this experiment, an instrument was needed that could perform a full analysis of thermal breakdown *with product identification* using less than 50 mg of sample. On-line, direct sampling of the mixture exiting the reactor was desirable to avoid further reaction/decomposition during the analysis process. The analysis method
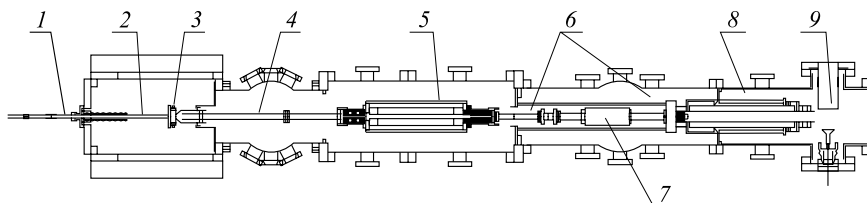
Figure 4.2 The micro-Flow Tube Reactor/Mass Spectrometer instrument. *1* — heated gas inlet/vacuum feedthrough, *2* — hot zone of flow tube, *3* — multiion source block, *4* — ion guide, *5* — quadrupole mass spectrometer, *6* — ion guides, *7* — reaction cell, *8* — quadrupole mass spectrometer, *9* — daly detector

had to be isomer sensitive, even for metastable isomers. The time scale of the kinetic measurements should be appropriate to propulsion applications. Finally, it is desired to maintain the potential for studying bimolecular reactions as larger samples become available. The micro-Flow Tube Reactor/Mass Spectrometer (micro-FTRMS) instrument designed for this purpose is shown in Fig. 4.2. There are three distinct sections of the instrument, discussed below.

4.2.1 The Microflow Tube Reactor

The molecular sample of interest was pre-mixed with an inert buffer gas (argon or helium) at 1%–7% concentration, then passed at constant mass flow rate through the microflow tube reactor. The flow tube was simply a 30-centimeter long quartz tube with 1.9 mm inner diameter. The final 10 cm of the tube was encased in a heater that could raise the temperature to 1000 K. Temperature was measured by a thermocouple embedded in the ceramic heater jacket, and was stable to ± 2 K. The Reynolds number of the flow ranged from ~ 3.5 to ~ 1.5, over the temperature range from 298 to 1000 K, i.e., fully developed laminar flow was established well upstream of the hot zone. Table 4.1 gives the pressure, density, mass-flow-weighted velocity, and mass-flow-weighted residence

Table 4.1 Characteristic behavior of flow tube reactor

Temperature K	Pressure Torr	Density mol/m^3	Residence time ms	Flow velocity m/s
298	1.24	0.065	4.4	16.2
998	2.13	0.033	2.0	31.7

time calculated for the mid-point of the hot zone (i.e., 5 cm from the exit). The ranges given show how the flow properties vary as the temperature is raised from 298 and 998 K.

The advantage of the microflow tube is that sample consumption is very small. For the work discussed below, the consumption rate varied between ~ 5 and ~ 25 μg/s, allowing several hours of experiment time for 20–40 mg of sample. For these flow conditions the diffusion length, i.e., the average distance that the molecules diffuse during the residence time in the hot zone, was about five times the tube diameter. The molecules diffused back and forth across the tube bore several times during their passage through the hot zone. On one hand, this effectively averages out the radial dependence of the residence time, allowing us to treat the flow as pseudo plug flow. On the other hand, the disadvantage is that a combination of homogeneous and heterogeneous kinetics is measured; thus only phenomenological rate constants can be estimated. Purely homogeneous kinetics could be measured with a larger diameter flow tube, and the authors plan to implement this approach as the search for fuel candidates narrows and larger samples become available.

4.2.2 The Ion Source

One of the key requirements for this experiment is the ability to distinguish strained reactant molecules from their more stable isomers, since isomerization is a likely decomposition process. Strained molecules are challenging to distinguish mass spectrometrically, because they tend to isomerize during the ionization process required for mass analysis. A novel combination of two techniques was developed resulting in a mass spectrometric method capable of identifying isomers of these compounds. One facet of the method is to ionize the molecules as gently as possible, i.e., producing ions with little excess internal energy. This is accomplished by a variety of chemical ionization (CI) processes, including proton-transfer and charge-transfer from various molecular ions.

For this purpose, the flow tube emptied directly into a high-pressure ion source. This source was essentially a sealed box with a gas inlet for the CI reagent gas, a 0.58 mm hole to allow injection of a magnetically collimated electron beam, and a 0.99 mm hole to allow ions to exit into the mass spectrometer. The flow tube was coupled to the source using a 0.1 mm annular gap that thermally isolates the source from the flow tube, but allows little of the gas flow to escape. Even at a flow tube temperature of 1000 K, the source temperature increased no more than ~ 50 K. To avoid any variations in source conditions with flow tube temperature, the source was thermostated to a constant temperature of 100 K.

4.2.3 The Guided-Ion-Beam Tandem Mass Spectrometer

The other facet of the isomer identification scheme, and one truly unique feature of the experiment, is the use of low-energy ion beam scattering for isomer identification [13, 14]. The measurements were made possible by the guided-ion beam (GIB) technique [15], in which multipole radio-frequency (rf) fields are used to collimate and guide the ion beam, and to collect daughter ions for analysis. To the best of the authors' knowledge, this represents the first use of low-energy beam scattering for isomer analysis.

The ions from the source are injected into an octapole ion guide that guides them through a differential pumping wall and up to the first mass filter. This is a homemade quadrupole mass filter that has been optimized to mass select without perturbing the kinetic energy distribution of the transmitted ions [16]. This mass filter can either be used to select a particular ion mass for low-energy scattering analysis, or can simply transmit the entire ion mass distribution. For scattering analysis, the selected ions are guided by a second octapole through a cell that can be filled with a low pressure of a target gas where the ions can fragment or react in collisions with the target atoms or molecules. The octapole collects product ions, along with unreacted primary ions, and guides them to the final quadrupole mass analyzer, where a mass spectrum is recorded.

4.2.4 Typical Experimental Results

Several types of experiments were performed for each system. All experiments were repeated at least once and the relative uncertainties were approximately $\pm 5\%$, largely due to the variation of ion source conditions over time, as a result of surface contamination. The most straightforward experiment is to measure a mass spectrum of ions produced by chemical ionization in the source. This provides one with a "primary fingerprint" to identify the reactant and product species that exit the flow tube. Measuring the variations in this primary spectrum as a function of flow tube temperature allows one to follow the decay of reactant molecule signal and growth of products. An example of a variable-temperature CI mass spectra is given in Fig. 4.3 for quadricyclane (C_7H_8), with methane used as the CI reagent. The full data set [17] includes spectra taken at temperature intervals ranging from 50 to 100 K. Here, just three representative spectra are plotted.

The bottom spectrum shows the result for room temperature, i.e., for pure quadricyclane. There are prominent peaks for the molecular ion (M^+: $m/q = 92$) and for the molecular ion plus and minus one atomic mass unit (($M+1$)$^+$: $m/q = 93$; ($M-1$)$^+$: $m/q = 91$). This is typical of methane CI spectra. Electron impact
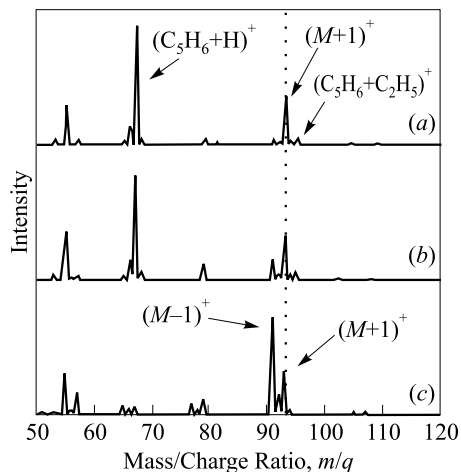
Figure 4.3 Representative CI mass spectra of quadricyclane showing changes with flow tube temperature: (*a*) 973 K; (*b*) 573 K; and (*c*) 298 K
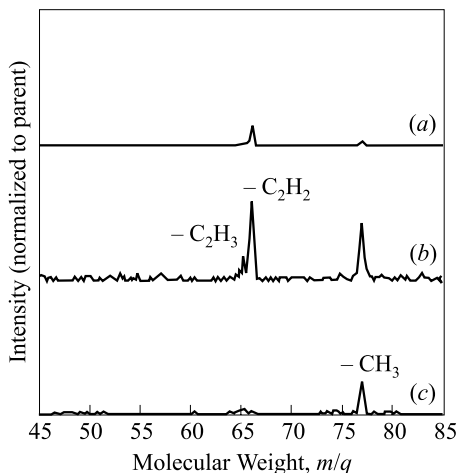
Figure 4.4 Low-energy collision-induced dissociation patterns for C_7H_8 isomers, showing clear differences: (*a*) quadricyclane; (*b*) norbornadiene; and (*c*) toluene

on the methane-generated CH_4^+, as well as a large number of small hydrocarbon ions $C_nH_m^+$, mostly with masses less than 50 amu. $(M + 1)^+$ was produced by proton transfer from these hydrocarbon ions to the molecule. M^+ was produced by charge-transfer ionization, e.g., $CH_4^+ + C_7H_8 \rightarrow C_7H_8^+ + CH_4$. $(M - 1)^+$ was mostly produced by H_2 loss from $(M + 1)^+$, as a consequence of the high internal energy (strain) in the quadricyclane. For a stable C_7H_8 isomer such as toluene, no $(M - 1)^+$ was observed.

There is little change in the CI spectra as the flow tube temperature was increased to 523 K, but decomposition sets in above that temperature. The middle spectrum shows the result for quadricyclane after ~ 3 ms in the flow tube at 573 K. At this temperature, the quadricyclane is about half decomposed, as shown by the decrease in the intensities of ions attributable to quadricyclane ($m/q = 93, 92, 91, 77, 57$), and the increase in the peak at $m/q = 67$. This peak results from proton-transfer ionization of C_5H_6, giving $(C_5H_6 + H)^+$. A small peak at $m/q = 95$ also appeared, and this originates from $(C_5H_6 + C_2H_5)^+$, i.e. formation of an adduct between C_5H_6 and one of the more abundant hydrocarbon ions in the CI source. The growth of C_5H_6 indicates that one of the decomposition channels is acetylene loss, by a retro-Diels–Alder reaction: $C_7H_8 \rightarrow C_5H_6 + C_2H_2$. In addition, it is clear that the $(M - 1)^+$: $(M + 1)^+$

peak ratio changed, and this indicates that one decomposition channel is isomerization to a more stable C_7H_8 structure.

Above ~ 800 K, the CI spectrum again became temperature independent, indicating that the final pyrolysis product distribution had been reached. The upper spectrum in Fig. 4.3 shows the result for 973 K. Note that virtually no $(M-1)^+$ was left, and the spectrum was dominated by $(M+1)^+$ and $(C_5H_6 + H)^+$. These results show that the pyrolysis product distribution is dominated by $C_2H_2 + C_5H_6$ and by isomerization to a more stable C_7H_8 isomer.

The CI spectrum gives a convenient method to monitor decomposition, but it is not always sufficient to provide positive identification of the isomeric structure of the molecules. For this, the low-energy scattering analysis was used. An example is shown in Fig. 4.4, which gives fragmentation patterns for the M^+ ions generated from three different C_7H_8 isomers. Note that the three isomers give distinct fragmentation patterns, allowing positive identification. These low-energy CID experiments are done as a function of flow tube temperature, and allow one to identify product isomers unambiguously.

The experiments were done at a collision energy of 2.9 eV, and it was found that the ability to distinguish quadricyclane from norbornadiene is lost for energies above ~ 5 eV, where conventional tandem mass spectrometers operate. As expected from this result, previous mass spectral studies of C_7H_8 have been unable to distinguish quadricyclane and norbornadiene [18–22].

4.2.5   Extraction of Breakdown Curves

The data just described provide considerable insight into the thermal breakdown behavior of the strained molecules of interest, yielding both product species distributions and stability information. Much of the insight is obvious from examination of raw results such as those presented in Fig. 4.3. To put the results on a more quantitative footing several additional steps were taken. Variable-temperature CI and low-energy scattering experiments were performed for all obtainable isomers of the strained molecule. For example, full data sets were taken for three C_7H_8 isomers: quadricyclane, norbornadiene, and toluene. These data are important in verifying the purity of the strained molecule sample, which may decompose in storage, and also provides both primary and secondary mass spectral "fingerprints" for the likely isomerization products. In addition, where possible, we ran variable-temperature CI spectra of likely product species in order to obtain accurate spectra for aid in identifying and fitting the spectra resulting from strained molecule pyrolysis. In the C_7H_8 system, the only product channel, besides isomerization, was formation of $C_5H_6 + C_2H_2$. The nature of the reaction producing C_5H_6 suggests that the product is probably cyclopentadiene.

To extract the decomposition vs. temperature curves discussed below ("breakdown curves"), curve fit of the variable-temperature CI data was made using two different methods. In both methods, the set of variable-temperature mass spectra was fit by a linear combination of basis spectra (i.e., spectra for individual molecular components), where each basis spectrum was assumed to be temperature independent. In the factor analysis method [23, 24], eigenvectors capable of describing the data were extracted directly, and no assumptions are required regarding the nature or number of components contributing to the signal. The problem is that the eigenvectors must then be manipulated to yield reasonable (i.e., nonnegative) basis spectra that describe the contribution, of each molecular component, to the mixture exiting the flow tube reactor. This is straightforward for data sets where only a few molecules contribute to the signal; however, the factor analysis method proved unusable for more complex systems.

This prompted development of an iterative fitting approach that makes use of the fact that it is possible to identify the molecules contributing to the variable-temperature CI spectra. Then, the CI spectra measured for pure samples of each of these molecules were used as the basis spectra for fitting the total spectrum at each temperature. Excellent fits are obtained by either fitting method, and for the cases where factor analysis was done, the two methods give essentially identical results [17]. This is not surprising, but it confirms the qualitative understanding used to generate the component spectra.

The major assumption in the fitting procedure was that the basis spectra (i.e., spectra for individual molecular components) are independent of flow tube temperature. This approximation was tested by running mass spectra of stable molecules such as toluene and styrene over the full range of flow tube temperatures, and the peak ratios in these spectra change by no more than 1%–2%. Based on this result and the signal–noise ratio in the experiments, the fitting uncertainty was estimated at about 5%.

4.3   STRAINED MOLECULE SYSTEMS

4.3.1   Quadricyclane/Norbornadiene

Both quadricyclane and norbornadiene are high-energy isomers of C_7H_8, and it is interesting to compare their thermal behavior. Figures 4.5 and 4.6 show the pyrolysis breakdown behavior for norbornadiene and quadricyclane, respectively, extracted as described above. As shown, norbornadiene (NBD) is stable on the available time scale for temperatures up to 600 K. (The small apparent decrease in NBD contribution in the 400–600 K range is within the uncertainty of the fitting process — no product species are observed.) Above 600 K decomposition
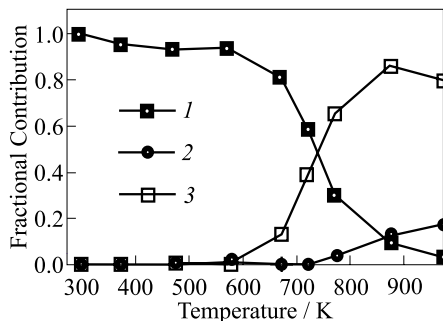
Figure 4.5 Pyrolysis breakdown behavior for norbornadiene: *1* — NBD; *2* — TOL; and *3* — C_5H_6
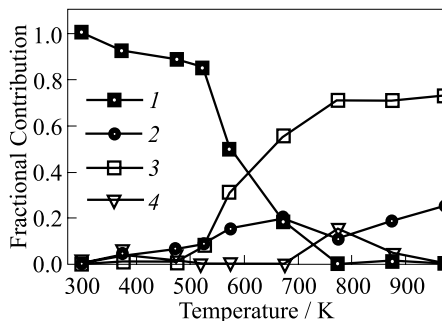
Figure 4.6 Pyrolysis breakdown behavior for quadricyclane: *1* — QC; *2* — C_5H_6; *3* — TOL; and *4* — NBD

sets in, and products begin to appear. By 900 K the NBD signal is almost gone. The pyrolysis reaction with the lowest activation energy, as judged by its appearance temperature, is:

$$C_7H_8(NBD) \longrightarrow C_5H_6 + C_2H_2$$
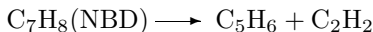
where C_5H_6 is cyclopentadiene (CPD). Above 750 K one also begins to see the isomerization reaction: norbornadiene → toluene (TOL). Note that it is possible that the TOL signal may include some contribution from the cycloheptatriene (CHT) isomer as well. These two isomers gave very similar CI mass spectra, although the peak ratios observed are better matched to toluene. Note that the product branching for the isomerization reaction increases at the highest temperatures, while the acetylene-loss channel decreases slightly. This suggests that while the acetylene-loss channel is lower in energy, isomerization is kinetically favored in the high-temperature limit. Note that over the residence time and temperature range studied, toluene itself is stable; thus we do not expect that the TOL product will undergo any additional decomposition.

The results for quadricyclane (QC) shown in Fig. 4.6 are qualitatively similar to those for norbornadiene, except that the onset of decomposition for quadricyclane is about 100 K lower. QC is stable on the available time scale at temperatures up to 523 K, above which decomposition sets in rapidly. The QC is completely decomposed within $\sim$ 2 ms (Table 4.1) by about 750 K. As with norbornadiene, the dominant low-temperature decomposition channel is fragmentation to $C_5H_6 + C_2H_2$, while isomerization to more stable isomers (TOL) becomes increasingly important at higher temperatures. There is some evidence for production of norbornadiene in the 700–800 K temperature range, but at higher

Table 4.2 Decomposition lifetimes from the microflow tube reactor

Temperature K	τ_{NBD} ms	τ_{QC} ms	τ_{cubane} ms	τ_{AEBCB} ms
373	> 50	> 50	> 50	> 50
473	> 50	26	> 50	> 50
573	> 40	4.2	45	> 30
673	12	1.5	18	14
773	1.9	< 0.5	1.2	3.7
873	0.6	< 0.5	0.8	1.3
973	< 0.5	< 0.5	< 0.5	< 0.5
998	< 0.5	< 0.5	< 0.5	< 0.5

temperatures any nascent norbornadiene would be unstable with respect to further decomposition. As with norbornadiene, one cannot eliminate the possibility that cycloheptatriene contributes to the TOL signal.

Table 4.2 gives decomposition lifetimes extracted from the flow tube data. Keep in mind that these kinetic data are for conditions in which a combination molecule–buffer gas, molecule–molecule, and molecule–wall collisions occur. The wall surface in the flow tube was quartz, and the slight discoloration observed indicates that there was initially some decomposition on the walls. Note, however, that there was no build-up of material on the walls beyond the initial transparently thin carbonaceous coating, and no products (e.g., polymer fragments) were observed that might be expected from reaction on the walls, or from bimolecular reactions. It appears that the decomposition is dominated by true unimolecular reactions; however, collisions with the walls are undoubtedly important in energizing the molecules for dissociation.

In using the obtained low-pressure results to predict what will happen in a higher pressure environment, the decomposition lifetime vs. temperature results should be directly applicable. It is not unlikely, however, that the product distribution might be different. The reason for the difference is that one likely mechanism for production of $C_5H_6 + C_2H_2$ is sequential isomerization, followed by C_2H_2 elimination:

$$C_7H_8 \text{ (QC)} \longrightarrow C_7H_8{}^{\ddagger} \text{ (isomer)} \longrightarrow C_5H_6 + C_2H_2 \qquad \text{pathway 1}$$
$$\searrow C_7H_8 \text{ (isomer)} \qquad \text{pathway 2}$$
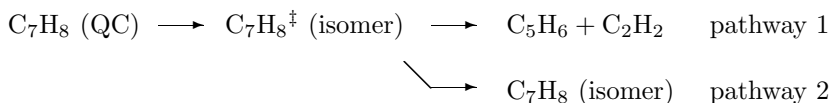
The $C_7H_8{}^{\ddagger}$ produced by the isomerization process is initially highly excited, because the strain energy in the quadricyclane is converted to internal energy of the $C_7H_8{}^{\ddagger}$ isomer. In pathway 1, the excited $C_7H_8{}^{\ddagger}$ undergoes further decomposition

to $C_5H_6 + C_2H_2$. In competition is pathway 2: collisional stabilization of the excited $C_7H_8^{\ddagger}$. In the low-pressure experiment, the rate of collisions with buffer gas or other molecules is relatively low, and most of the $C_7H_8^{\ddagger}$ undergoes decomposition to $C_5H_6 + C_2H_2$. At higher pressures, pathway 2 will become more important, and the branching to C_7H_8 (isomer) should increase. Of course, there may be direct pathways to $C_5H_6 + C_2H_2$ that do not involve a $C_7H_8^{\ddagger}$ intermediate, and these will be unaffected by pressure.

4.3.2 Cubane

For cubane, the least stable isomer of the C_8H_8 system, the pyrolysis behavior of cubane itself, and of the more stable cyclooctatetraene (COT) and styrene isomers were studied. Both COT and styrene were stable over the range of experimental conditions examined. Cubane is a highly unstable isomer, and even with the most gentle CI conditions, no molecular ion (M^+) was observed. The dominant peaks in the cubane CI mass spectrum are $(M-1)^+$ at $m/q = 103$, and peaks at $m/q = 91(M - CH)^+$, and $m/q = 79$ $(C_6H_7^+)$. The $(M - 1)^+$ peak is quite diagnostic for cubane since neither of the more stable $C_8H_8^+$ isomers gives a peak at this mass. Styrene and COT both give CI mass spectra dominated by the $(M + 1)^+$ peak at $m/q = 105$; however, they have quite distinct patterns of other peaks, and are easily distinguished mass spectrometrically.

The pyrolysis breakdown behavior for cubane is plotted in Fig. 4.7. Cubane is found to be stable on the millisecond time scale for temperatures up to ~ 500 K. Minor decomposition was found between 500 and 700 K, and above that point decomposition is faster than the flow tube residence time. By 800 K there is essentially no remaining cubane. The dominant product channel is loss of C_2H_2, yielding benzene. Some rearrangement to COT was observed above ~ 650 K, and a small amount of styrene was found at high temperatures. The decomposition lifetimes corresponding to these breakdown curves are given in Table 4.2. As with the C_7H_8 system, it is not unlikely that the branching to isomerization products would be greater in higher pressure environments.
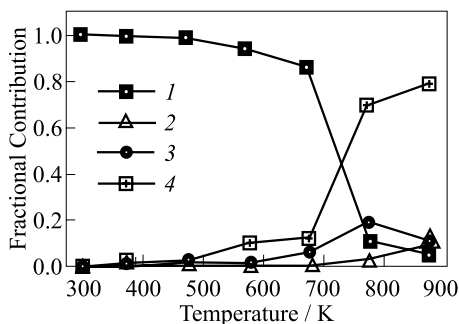
Figure 4.7 Pyrolysis breakdown behavior for cubane: *1* — cubane; *2* — styrene; *3* — COT; and *4* — $C_6H_6 + C_2H_2$

Variable-temperature collision-induced dissociation (CID) experiments were performed for the $(M-1)^+$ and $(M+1)^+$ peaks produced from the three isomers. While these reveal some interesting chemistry, the important result for the purposes of the cubane pyrolysis is that when we studied fragmentation of the $(M+1)^+$ ions resulting from CI of cubane isomerized at high temperatures:

$$C_8H_8 \text{ (cubane)} \xrightarrow{\text{heat}} C_8H_8 \text{ (isomer)} \xrightarrow{\text{CI}} (M+1)^+ \xrightarrow{\text{CID}} \text{fragments}$$

considerably more fragmentation was observed than for $(M+1)^+$ ions produced by CI of styrene or COT at the same temperature. This may reflect the large amount of strain energy released in cubane isomerization (giving very hot COT or styrene), but it may also indicate that the C_8H_8 product isomer distribution contains some more energetic isomers than COT or styrene. Unfortunately, samples of these higher energy isomers are not available; thus one cannot study their ionization/fragmentation behavior for comparison with the cubane pyrolysis results.

4.3.3 1-Aza-3-ethylbicyclo[1.1.0]butane (C_5H_9N)

The bicyclobutane family is interesting because it is one of the simplest and smallest strained ring systems (cyclopropane itself being the smallest). The 1-aza-3-ethylbicyclo[1.1.0]butane (AEBCB) molecule studied here (Fig. 4.1) is particularly interesting in that it also has a nitrogen atom, and presumably this adds to the energy release available from combustion. For this system, variable-temperature CI mass spectra and low-energy CID fragmentation patterns for AEBCB and three unstrained isomers, tetrahydropyridine (THP), methylpyrroline (MPL), and butylisocyanide (BIC), were measured.

In all the other systems reported here, isomerization to a more stable isomeric structure, without fragmentation, is observed to be a significant thermal decomposition reaction. For AEBCB, there was no simple isomerization channel observed in the flow tube mass spectra. At room temperature, the CI mass spectrum is dominated by peaks at $m/q = 84$, 82, and 55. The first two correspond to the protonated parent molecule $(M+1)^+$ and the $(M-1)^+$ ion, probably generated by H_2 loss from $(M+1)^+$. The $m/q = 55$ peak corresponds to $(M-28)^+$, and is probably best thought of as loss of the ethyl (C_2H_5) group from the $(M+1)^+$ ion, initially generated in the CI source. As the flow tube reactor temperature is raised, all three peaks characteristic of the parent molecule disappear and are replaced by a large peak at $m/q = 56$, and a smaller peak at $m/q = 54$. This result clearly indicates that the only significant thermal decomposition reaction for AEBCB is loss of ethene (C_2H_4):

$$C_5H_9N(\text{AEBCB}) \xrightarrow{\text{heat}} C_2H_4 + C_3H_5N \xrightarrow{\text{CI}} C_3H_6N^+ \ (m/q = 56)$$
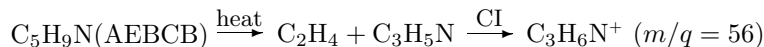
The origin of the small $m/q = 54$ peak could either be loss of H_2 from the $C_3H_6N^+$ ($m/q = 56$) ion, or possibly loss of ethane from the parent molecule, followed by protonation to give $C_3H_4N^+$.

The fact that no isomerization products were observed for AEBCB may reflect the smaller size of the molecule. When AEBCB undergoes isomerization to a more stable structure, the resulting molecule has fewer degrees of freedom over which to distribute the released strain energy, compared to C_7H_8 or C_8H_8. This results in much faster rates of fragmentation compared to larger molecules. By analogy to the discussion for quadricyclane, pathway 1 dominates over pathway 2 because the fragmentation rate is fast compared to the quenching rate. Again, it is possible that in higher pressure environments, some isomerization product might be stabilized.

An important mechanistic question is the structure of the C_3H_5N product generated in the C_2H_4 elimination reaction. One possibility would be to simply lose C_2H_4, which would retain the aza-bicyclobutane skeletal structure. This is rather unlikely, since this simple aza-bicyclobutane molecule is substantially less stable [25] than the ethyl derivative studied.

The C_2H_4 loss involves some rearrangement that was expected to trigger isomerization to a more stable C_3H_5N structure. Several candidates were possible. To help identify the product, comparison of the variable-temperature CID fragmentation pattern of the $C_3H_6N^+$ ion produced by CI of the AEBCB pyrolysis mixture was made, with those for $C_3H_6N^+$ generated by CI of two stable C_3H_5N compounds: propargylamine ($HCCCH_2NH_2$) and propionitrile (CH_3CH_2CN). The $C_3H_6N^+$ ion originating from AEBCB was found to fragment by loss of C_2H_3, with a smaller propensity to lose C_2H_4. This pattern exactly matches that for $C_3H_6N^+$ originating from propionitrile, suggesting that this is the identity of the pyrolysis product.

Figure 4.8 presents the pyrolysis breakdown curves for AEBCB. Slow decomposition sets in at about 500 K and the decomposition lifetime (Table 4.2) decreases with increasing temperature. The available residence time (Table 4.1) decreases and the decomposition fraction increases rapidly for temperatures greater than 800 K, and all the AEBCB is converted to propionitrile + ethene by about 950 K.
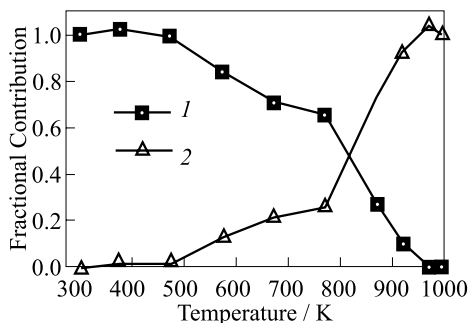
Figure 4.8 Pyrolysis breakdown behavior for 1-Aza-3-ethylbicyclo[1.1.0]butane (AEBCB): *1* — AEBCB; *2* — C_3H_5N + C_2H_4

4.4 CONCLUDING REMARKS

A technique that allows rapid evaluation of molecular stability using small (20–30 mg) samples has been demonstrated and applied to three different families of strained molecules. All of the molecules studied are stable at room temperature, though most must be stored in nonmetallic containers to avoid catalytic decomposition. Of the four molecules shown in Fig. 4.1, the least thermally stable was quadricyclane, for which decomposition lifetimes drop below 10 ms at about 500 K. The other three molecules had similar stabilities, with lifetimes dropping below 10 ms above 700 K. For all systems studied, decomposition by loss of small hydrocarbon fragments (acetylene or ethene) was an important decomposition mechanism in the gas phase. For all but AEBCB, isomerization was also a significant decomposition mechanism. At high pressures, one would expect more isomerization because the very rapid collision rate should allow collisional stabilization of the isomerization products.

There are several interesting future directions for this work. To date, low-energy collision-induced dissociation has been sufficient for unambiguous isomer identification in all the systems studied. There will be systems where this is not adequate, and the authors would like to explore the use of low-energy chemical reactions as a structure-sensitive analysis tool. One example might be in distinguishing stereo-isomers of organic compounds using a chiral scattering gas. This is not particularly relevant to strained fuels, but is a long-standing problem in mass spectrometry.

It is also possible to extend the methodology to measuring rates of bimolecular reactions by going to a larger bore flow tube to allow a movable injector for the second reagent. This will require larger samples, but would be a logical step once a candidate fuel system has been identified, since larger samples will become available at that point. By using a sheathed-flow in a larger tube one should also be able to measure true homogeneous reactions, which could be used to generate quantitative kinetics for input into combustion models.

ACKNOWLEDGMENTS

REFERENCES

1. Marchand, A. P. 1988. Synthesis and chemistry of novel polynitropolycyclic cage molecules. *Tetrahedron* 44:2377–95.
2. Marchand, A. P. 1989. The chemistry of pentacyclo[5.4.0.02,6.03,10.05,9] undecane (PCUD) and related systems. *Advances Theory Interesting Molecules* 1:357–99.
3. Marchand, A. P. 1989. Synthesis and chemistry of homocubanes, bishomocubanes, and trishomocubanes. *Chem. Rev.* 89(5):1011–33.
4. Marchand, A. P., Z. Liu, D. Rajagopal, V. D. Sorokin, F. Zaragoza, and A. Zope. 1994. New high-energy/high-density fuel systems: Synthesis and characterization. *7th ONR Propulsion Meeting Proceedings*. Eds. G. Roy and P. Givi. Buffalo, NY: State University of New York at Buffalo. 82–90.
5. Christi, M., and G. Bruentrup. 1974. Diimine reduction and ozonolysis of benzvalene. *Chemische Berichte* 107:3908–14.
6. Christi, M., B. Mattauch, H. Irngartinger, and A. Goldmann. 1986. Additionen von Benzvalene und Nitriloxide. Eine Synthese fur Benzvalen-3-Carbonitril. *Chemische Berichte* 119:950.
7. Christl, M., and C. Herzog. 1987. 3-(Phenylsulfonyl)tricyclo[4.1.0.02,7]hept-4-en-3-yllithium. *Tetrahedron Letters* 28:187–90.
8. Moriarty, R. M., J. S. Khosrowshahi, R. S. Miller, J. Flippen-Andersen, and R. Gilardi. 1989. Free-radical arylation of cubane using cubyl lead acylates. *J. American Chemical Society* 111:8943–44.
9. Moriarty, R. M., and M. Rao. 1994. Energetic azide compounds. *7th ONR Propulsion Meeting Proceedings*. Eds. G. Roy and P. Givi. Buffalo, NY: State University of New York at Buffalo. 75–81.
10. Eaton, P. E. 1992. Cubanes: Starting materials for the chemistry of the 1990s and the next century. *Angewandte Chemie* 104(11):1447–62.
11. Eaton, P. E. 1994. An itroduction to cubane and its chemistry. *7th ONR Propulsion Meeting Proceedings*. Eds. G. Roy and P. Givi. Buffalo, NY: State University of New York at Buffalo. 117–29.
12. Eaton, P. E., and M. X. Zhang. 1996. A new and more practical approach to the synthesis of methylcubane. *9th ONR Propulsion Meeting Proceedings*. Eds. G. D. Roy and K. Kailasanath. Washington, DC: Naval Research Laboratory. 111–22.
13. Li, Z., D. Peiris, J. Eckwert, and S. L. Anderson. 1996. Flow tube mass spectrometry of strained hydrocarbon fuel molecules. *9th ONR Propulsion Meeting Proceedings*. Eds. G. D. Roy and K. Kailasanath. Washington, DC: Naval Research Laboratory. 145–52.
14. Li, Z., J. Eckwert, A. Lapicki, and S. L. Anderson. 1997. Low-energy high-resolution scattering mass spectrometry of strained molecules and their isomers. *Int. J. Mass Spectrometry Ion Processes* 167/168:269–79.
15. Gerlich, D. 1992. Inhomogeneous RF fields: A versatile tool for the study of processes with slow ions. *Adv. Chem. Phys.* 82:1–176.
16. Smolanoff, J., A. Lapicki, and S. L. Anderson. 1995. Use of a quadrupole mass filter for high-energy resolution ion beam production. *Review Scientific Instruments* 66:3706–8.

17. Li, Z., and S. L. Anderson. 1998. Pyrolysis and isomerization of quadricyclane, norbornadiene, and toluene. *J. Phys. Chem* A 102:9202–12.

18. Kuck, D. 1990. Mass spectrometry of alkylbenzenes and related compounds. Part 1. Gas-phase ion chemistry of alkylbenzene radical cations. *Mass Spectrometry Review* 9:187–233.

19. Field, F. H. 1967. Chemical ionization mass spectrometry. VI. C_7H_8 isomers. Toluene, cycloheptatriene, and norbomadiene. *J. American Chemical Society* 89:5328–34.

20. Cooks, R. G., J. H. Beynon, and M. Bertrand. 1973. Ion structural studies by ion kinetic energy spectrometry: $[C_7H_7]^+$, $[C_7H_8]^+$, $C_7H_7OCH_3]^+$. *Organic Mass Spectrometry* 7:1303–12.

21. Burgers, P. C., J. K. Terlouw, and K. Levsen. 1982. Gaseous $[C_7H_8]^+$ ions: [Methylenecyclohexadiene]$^+$, a stable species in the gas phase. *Organic Mass Spectrometry* 17:295–98.

22. Rabrenovic, M., A. G. Brenton, and T. Ast. 1983. A study of $C_7H_8{}^+$ and $C_7H_8{}^{2+}$ ions formed from different precursor molecules. *Organic Mass Spectrometry* 18: 587–95.

23. Fister, J. C., III, and J. M. Harris. 1996. Factor analysis of transient Raman scattering data to resolve spectra of ground- and excited-state species. In: *Computer assisted analytical spectroscopy*. Ed. S. D. Brown. New York: Wiley.

24. Malinowski, E. R. 1991. *Factor analysis in chemistry*. 2nd ed. New York: Wiley.

25. Marchand, A. P. 1997. Private communications.

Chapter 5

COMBUSTION CHARACTERISTICS OF HIGH-ENERGY-DENSITY FUELS AND SOLID–GAS INTERFACE ANALYSES

C. Segal, S. Pal, S. Pethe, H. S. Udaykumar,
and W. Shyy

Recently developed high-energy-density (HED) pentacyclic hydrocarbons exhibit attractive features including high density (ρ = 1.2–1.3 g/cm^3) and a moderate amount of strain energy, which contributes to the energy output during combustion. To assess their application to air-breathing propulsive devices, investigations were focused in two areas: (a) evaluation of combustion characteristics of solid, low-temperature-melting and liquid-HED formulations, and (b) modeling of solid–gas interface of HED fuels in a turbulent reacting flow. Through direct measurements, basic information related to melting and boiling points, specific heats, latent heats of fusion, and ignition activation energies was determined. Droplet combustion experiments with binary solutions of solid high-energy fuels in liquid formulations, such as JP-10, indicated increased effervescence and higher heat output, doubling the JP-10 burning rate. Evaluations of liquid high-energy-density formulations as single compounds exhibited microexplosive combustion behavior. A theoretical model of solid–gas interface was developed to include moving boundary simulation in response to a two-way solid–liquid interaction. The shape, location, and movement of the solid–gas interface was treated explicitly. A Lagrangian moving grid technique in conjunction with an established body-fitted grid flow solution technique has been developed. Consistent with the experimental observation, the thermal characteristics near the solid–gas interface vary in space and in time, and result in nonuniform regression between the front and the rear ends. The present computational capability can advance the understanding of phase change, thermal decomposition, and subsequent mixing and burning dynamics of energetic fuels.

5.1 INTRODUCTION

In order to improve the performance of air-breathing propulsion systems attention has been focused on means of increasing the energy-density of existing fuels by including energetic metallic/nonmetallic additives, such as aluminum, boron, or other synthetic formulations. New hydrocarbon fuels, with high-energy-density content, have been synthesized and their combustion characteristics assessed under a variety of thermodynamic airflow conditions. These fuels have the potential to contribute to high-thrust, high-temperature, and reduced-size combustor technology. Marchand [1], Segal and Shyy [2], and Yang and Zarko [3] have reviewed various aspects of these research activities. Since the newly synthesized hydrocarbon fuels owe their high-energy content either to strained molecular bonds or to densely packed molecular structures, many of these formulations are solids at normal conditions. It had been found that among these materials certain solid formulations that dissolve in stable solutions exist in liquid fuel systems in substantial concentrations [4]. Due to the compact volumes and large heat release rates exhibited, these materials can possibly be used as additives in existing liquid fuel systems. While their stability is an asset from the point of view of handling logistics, these fuels exhibited a high-activation energy for ignition and, due to the large carbon-to-hydrogen ratio, these fuels have a propensity to soot.

5.1.1 Description of Fuels

Four hydrocarbon fuels were investigated in the experimental part of this study:

1. PCU Alkene Dimer — $C_{22}H_{24}$, is a mixture of isomers with a large heat of formation (+408 kJ/mol), high density (ρ = 1.2–1.3 g/cm^3), and a melting point (m.p.) of 178–179 °C. The calculated heat of combustion is 11,900 kJ/mol. Combustion experiments were performed using this solid fuel under convective heating at high-heat fluxes [4].

2. Methylated PCU Alkene Dimer — $C_{24}H_{28}$, is a low-melting point (about 55 °C) mixture of up to 64 isomers. In contrast to the base PCU alkene dimer, the methylated PCU alkene dimer dissolved in a large proportion in JP-10, which was the selected fuel system used in this study, and stable solutions in proportion of up to 18% have been obtained. The addition of methylated PCU alkene dimers to JP-10 induced droplet boiling and increased the fuel heat output. These mixtures have been studied by means of suspended droplet combustion and spectrometric analyses.

3. Spirocyclic Alkene Dimer — $C_{22}H_{26}$, is a mixture of two isomers. This material is a powder under normal conditions. It was analyzed as a solid sample by the same procedure as the PCU alkene dimers.

4. PCU Functionalized Exo-Methylenecyclopropane — $C_{18}H_{22}$, has a methylenecyclopropane ring attached to the base pentacyclic cage. Two isomers are present with the methylenecyclopropane ring rotated at 90° relative to the cage, forming, in general, a viscous oil. This oil can range from a clear liquid or a cloudy liquid or a semi-solid at room temperature, depending on the relative proportions of the two isomers that are present in a given sample.

All these fuels belong to a group of high-energy-density fuels with compact molecular structure rendered by the presence of pentacyclic cages. They are stable and nonvolatile at room temperature and pressure. Three formulations are solid and the fourth is a viscous liquid. Their synthesis and molecular structure analysis that uses X-ray crystallographic methods have been described by Marchand [5, 6]. Their molecular structure and physical properties are presented briefly below. Measured thermophysical and thermochemical properties follow.

5.1.2   Basic Research Issues

Previous studies of combustion characteristics of these compounds have been undertaken ([7] and [8], for example) with minimal data available regarding the properties of these compounds. However, in order to take advantage of the benefits of HED fuels and to analyze and model these materials, it is necessary to know some of their physical and thermochemical properties that are relevant for combustion. Extensive evaluations of such properties of organic azides were undertaken by Lee *et al.* [9, 10], who investigated the vaporization, combustion, and microexplosion of free-falling droplets of organic azides, and calculated or measured relevant thermophysical properties of these materials. It was found that the organic azides gasify and explode earlier in the droplet lifetime than conventional fuels. It was estimated that this behavior resulted from a higher rate of heat release from the organic azide vapors. These observations are consistent with the results of the present work for a different class of HED hydrocarbons.

It had been shown that acceleration of the vaporization rate of liquid droplets can be achieved only in a small proportion by increasing the droplet heating rate or by enriching the fuel with oxidants [10]. It is possible, however, to induce an early droplet breakup by incorporating additives that promote droplet explosion in the existing fuel, such as organic azides [9] or, as shown in a following section, some of the hydrocarbon compounds studied in this work. Some of the HED

fuels analyzed herein provide such additive capabilities due mainly to three factors: low boiling point, high degree of solubility in existing fuels, and significant exothermicity of their decomposition. Heterogeneous nucleation within the conventional liquid formulation caused by internal gasification of the added HED material promote the desired fast droplet disruption. Evidence of this behavior was obtained in the experiments described below for various concentrations of HED fuels in kerosene. This type of accelerated droplet breakup is quite different from the combustion of slurry hydrocarbons with carbon or metallic additives. For example, in the latter case, the combustion of the solid phase occurs, in general, in a multiple step process that includes heating of the particulate, formation of an oxide shell around a molten core, followed by evaporation of the core and energetic combustion of the gases, and concludes with the combustion of the oxide itself [11–14].

For the present and many other solid energetic materials, key physical processes, including melting/evaporation, pyrolysis, and mixing and combustion, can have different time scales, causing concerns regarding ignition and efficiency of the combustion process. Fundamentally, phase change characteristics are dictated by the rate and distribution of the excess heat flux into the condensed fuel from the high-temperature environment in order to fulfill the latent heat requirement. Accordingly, for sustained burning, the shape and the rate of the movement of the phase boundary change in time and need to be determined as a part of the solutions to the fluid dynamics and combustion processes. Computationally, the existence of the moving phase boundary creates a major difficulty since the locations and physical parameters governing motion of the phase boundary, such as heat flux, species concentration, and interface velocity, vary from location to location, and are not known *a priori* [15]. Much literature exists in treating the multiphase flow phenomena; for summary and references to computational modeling issues, see [15] and [16].

The pyrolysis process, including thermal decomposition and chemical reaction to form intermediate species prior to combustion, closely interacts with the phase change process. In particular, the unsteadiness of the phase change process and mixing between the evaporated energetic fuel and surrounding gas stream are of major importance to effective combustion. In many models, the phase change and pyrolysis processes are not only lumped together, but also treated as a surface phenomenon. With the lumped surface treatment, the condensed phase reaction layer and the gas phase region are often considered capable of responding instantaneously to changes in external conditions, such as the combusting gas stream allows a quasi-steady model to be employed. Furthermore, for both energy and species transport aspects, the effects of chemical reaction appear only through boundary conditions between the nonreacting condensed phase and the gas phase, (e.g., [17]). While this type of model substantially reduces the computational complexities, it has been found inadequate in capturing the physical mechanisms involved [18]. A less restrictive model can be derived

based on distributed condensed phase reaction [18, 19], where both energy and species transport equations need to be solved. In these models, however, the aforementioned phase change process is often drastically simplified or neglected.

In addition to phase change and pyrolysis, mixing between fuel and oxidizer by turbulent motion and molecular diffusion is required to sustain continuous combustion. Turbulence and chemistry interaction is a key issue in virtually all practical combustion processes. The modeling and computational issues involved in these aspects have been covered well in the literature [15, 20–22]. An important factor in the selection of sub-models is "computational tractability," which means that the differential or other equations needed to describe a sub-model should not be so computationally intensive as to preclude their practical application in three-dimensional Navier-Stokes calculations. In virtually all practical flow field calculations, engineering approximations are required to make the computation tractable.

5.1.3 Present Study

In the following sections a description of the HED used in these studies, a list of their measured properties, and preliminary results of droplet experiments for solutions of solid HED formulations in JP-10 and liquid HED compounds are given. These data are needed to evaluate the combustion characteristics of these new fuels as individual compounds or as additives to existing fuel systems and to provide a basis for the development of the predictive capability of solid–gas interface tracking in a turbulent reacting flow.

5.2 THERMOPHYSICAL AND THERMOCHEMICAL PROPERTIES OF HED FUELS

5.2.1 Specific Heats

Specific heats of the fuels described above have been obtained using a TA Instruments, Inc. DSC 2910 Differential Scanning Calorimeter (DSC) in a helium atmosphere at a heating rate of 2 °C/min [23]. While the PCU and Spirocyclic alkene dimers indicate a well-defined melting region, the methylated PCU alkene dimer's melting region is broadened due to the presence of a large number of isomers. The distribution of melting over a temperature range was observed on a High Resolution TGA 2950 Thermogravimetric Analyzer. The first crystals began to melt at 55 °C and the sample became entirely liquid at about 65 °C. The first indication of substantial evaporation appeared at 80 °C. The rates of

Table 5.1 Properties of high-energy fuels (source included in refs.)

Fuel	ρ g/cm^3	Formula	m.p. °C	b.p. °C	c_p J/g/°C (at t °C)	l_f J/g	h_f kJ/mol	E_a kJ/mol	Temp. range °C	Method of determination of E_a
PCU alkene dimer	1.2–1.3	$C_{22}H_{24}$	178		2.168 (127 °C)	72.7	+408	263	700–1300	Flow Reactor
Methylated PCU alkene dimer [4]	1.2–1.3	$C_{22}H_{22}(CH_3)_2$	55	80	1.594 (27 °C)					
Spirocyclic alkene dimer [4]	1.2–1.3	$C_{22}H_{26}$	159		3.875 (107 °C)	29				
Cubane [24]	1.29	C_8H_8	130	133			+602			
Methyl cubane [24]		$C_8H_7(CH_3)$	34	37						
AP [25]	1.55	NH_4ClO_4	450		1.2 (102 °C)		−0.29	54 [26]	420–650	Radiative Heating
RDX [25]	1.82	$C_3H_6N_3(NO_2)_3$	304		1.24 (102 °C)		+0.0614	259 [27]	250–265	Isothermal DTA
								275 [28]	232–241	
HMX [25]	1.9	$C_3H_8N_4(NO_2)_4$	279		1.24 (102 °C)		+0.0179	258 [29]	264–276	TG-DTG
								67.4 [30]	240–260	Mass Spectrography of Decomposition Products
								75.6 [31]	328–420	TGA
								115 [32]	350–400	TGA
								192 [31]	436–470	TGA
HTPB	0.92	$(CH_2)–(OH)_2$			1.63			100 [4]	700–1300	Flow Reactor
								89.9–130 [33]		TGA

evaporation were measured with a TA Thermogravimetric Analyzer (TGA) at a rate of 10 °C/min and indicate a rapid decomposition of these fuels:

- PCU alkene dimer: 11.2 mg in 10 min. between 150–250 °C.

- Spirocyclic alkene dimer: 6.62 mg in 10 min. between 150–250 °C.

- Methylated alkene dimer: 28.15 mg in 20 min. between 75–275 °C.

Table 5.1 shows a comparison of various physical and thermochemical properties of the solid formulations described here and a comparison with other existing HED fuels, cubane, and the nitramine compounds RDX and HMX. The activation energies for ignition are included, along with the methods and the temperature ranges used to obtain this information. The references from which these data have been extracted are indicated in the table. Although hydroxy-terminated polybutadiene, HTPB, is not a HED fuel, it has been studied rather extensively and its data have been included in the table for comparison. It can be seen in the table that although the densities of the HED hydrocarbon formulations (those included in this study and cubane) are lower than those of AP, RDX, and HMX, their heats of formation are remarkably large, positive numbers. It should be noted that cubane owes this large heat of formation to significant molecular bond-strain, whereas, in the case of the pentacyclic compounds, only a small amount of strain is present. It can be seen in the table that the pentacyclic formulations described here have significantly lower m.p. and boiling points (b.p.) than AP, RDX, and HMX. Further, it is interesting to note that the methylated formulations of both PCU alkene dimer and cubane exhibit significantly lower m.p. and b.p. (caused in part by the presence of multiple isomers in the mixture). This characteristic is important for the potential of these materials to be used directly or as additives to existing fuel systems. The HED fuels, including the hydrocarbon compounds in this study and the nitramine formulations (i.e., RDX and HMX), have a higher activation energy than HTPB. It should be noted that there is considerable scatter in the data for HTPB depending on the size of the polymer under study and the various methods used to obtain the data.

5.2.2 Mass Spectrometric Analysis of Methylated PCU Alkene Dimer

For combustion applications and for accurate modeling of the processes involving melting, decomposition, and subsequent oxidation, it is necessary to determine whether or not the fuel undergoes chemical decomposition when it is liquefied and, subsequently, converted to the vapor state. Mass spectral analyses were performed to provide information about the substances in the vapor phase as the fuel is heated.
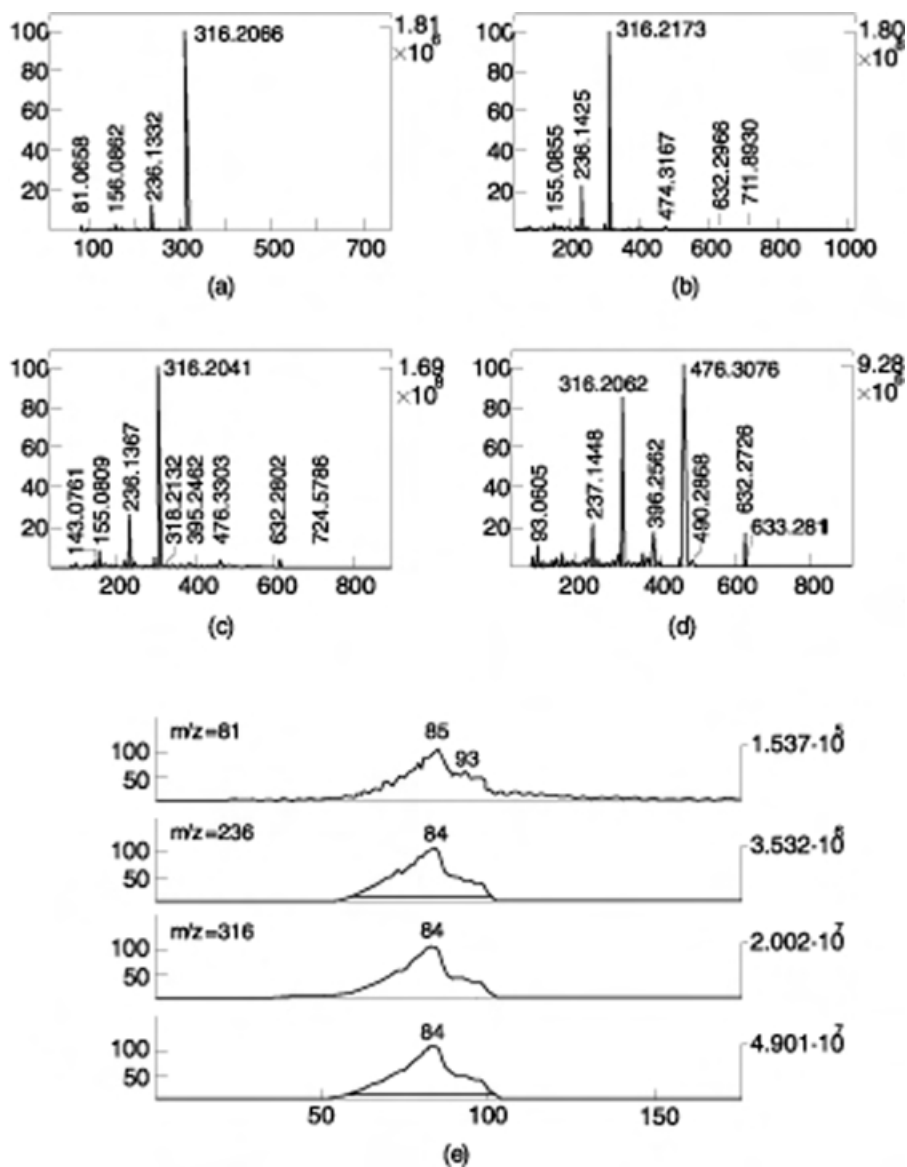
Figure 5.1 Mass spectral results: Summation spectral results at temperatures: (*a*) 30 °C; (*b*) 90–120; (*c*) 210–330; (*d*) 330–780 °C — indicating the most prominent peak corresponding to the PCU alkane dimer and the presence of the $m/z = 476$ at the higher temperature setting; and (*e*) the abundances of the peaks at $m/z = 81, 236,$ and 316 as a function of the scan number

A sample of the PCU alkene dimer was dissolved in a small volume of methylene chloride. Several 10 :L aliquots of the solution were deposited onto the rhenium wire tip of the mass spectral direct insertion probe, and the solvent rapidly evaporated at room temperature. The coated probe was inserted into the ion source of a Finnigan MAT95Q hybrid sector mass spectrometer (Finnigan MAT, San Jose, CA). The ion source was filled with a methane plasma (ca. 1 mTorr). Collisions of the sample molecules with the plasma ions resulted in electron transfer from the sample to the plasma, probably via transfer of H^+ from the $CH_5{}^+$ to the molecule, followed by loss of a hydrogen atom. This "soft" ionization method resulted in formation of the molecular ion without adding excessive energy. The probe was held at ca. 30 °C for one minute, then was heated at a rate of 300 °C per minute. Mass spectral scans ($m/z = 60$ to 1000) were obtained every 1.2 s throughout the isothermal and heating periods.

The mass spectral results are shown in Fig. 5.1. Figures 5.1a to 5.1d are summations spectra obtained at temperatures of 30 °C (a), 90–210 °C (b), 210–330 °C (c), and 330–780 °C (d). Clearly, the most prominent peak in the first three temperature ranges corresponds to the PCU alkene dimer (molecular weight 316), with small contributions from species of smaller mass. Figure 5.1d shows a large peak at $m/z = 476$. It is probably present in the original sample, but it is less volatile and not observed in spectra obtained at lower temperature ranges. Figure 5.1e shows the abundances of the peaks at $m/z = 81$, 236, and 316 as a function of scan number. The profiles track almost exactly, indicating that the smaller peaks result from fragmentation of the 316 ion in the mass spectrometer. (The two lower masses add to 317, the m/z of the (Parent + H) peak initially formed). These peaks are also present in the spectra obtained at 30 °C (Fig. 5.1a), another indication that they do not result from thermal decomposition. Although it is not possible to state definitively that the PCU alkene dimer is thermally stable, all spectra show that there is a significant amount of the parent compound present. Possible decomposition products seem to result from fragmentation of the parent ion, rather than from thermal effects.

5.3 DROPLET COMBUSTION CHARACTERISTICS OF HED FUELS

5.3.1 Solutions of Solid Fuels in Liquid Hydrocarbons — Methylated PCU Alkene Dimers

The methylated PCU alkene dimer was dissolved in JP-10 and stable solutions to 18% have been obtained. Higher concentrations have been achieved, but it
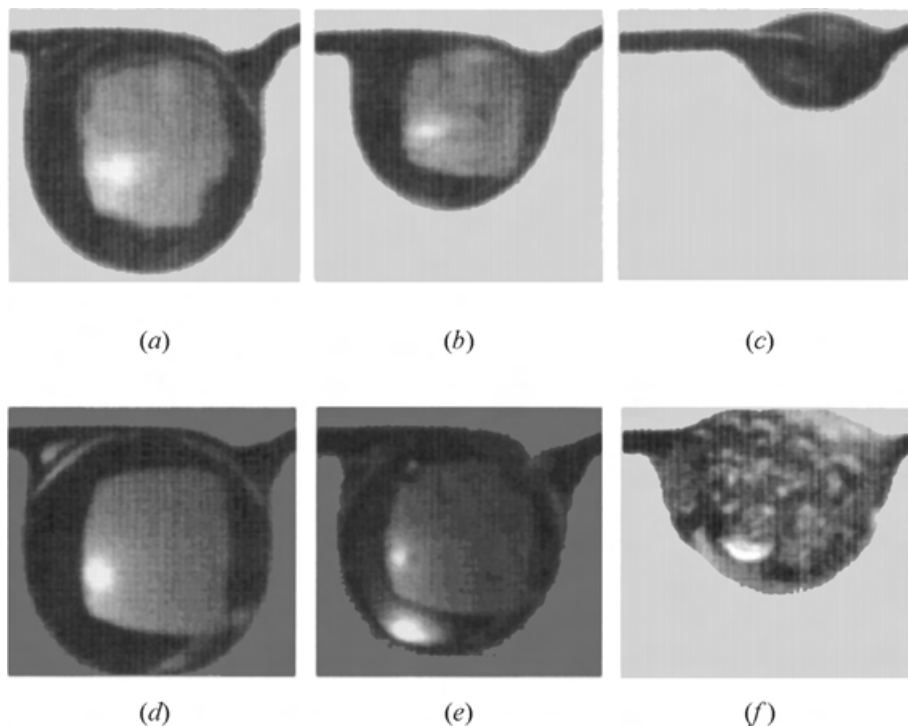
Figure 5.2 Images of burning droplets: (*a*) initial (*t* = 0) JP-10 droplet size; (*b*) JP-10 droplet at *t* = 0.997 s; (*c*) JP-10 droplet close to complete combustion at *t* = 1.673 s shows no indication of internal vaporization; (*d*) initial droplet of a 18% mixture of JP-10 and methylated PCU alkene dimer; (*e*) initial formation of internal vapors in the 18% mixture at *t* = 0.713 s; (*f*) strong effervescence in the 18% mixture at *t* = 1.230 s

was observed that after separation in the centrifuge for a number of hours, the methylated PCU alkene dimer separated from the solution and sedimented on the bottom of the container. Since unstable solutions are impractical for application to most combustion systems further analyses were limited to stable solutions. Subsequently, 1-millimeter diameter droplets of the mixture were suspended on a glass wire, 50 μm in diameter, and ignited with an external source. Images of the burning droplets were collected with a CCD camera at 7.5 ms intervals between consecutive frames. A filter with cutoff at 550 nm was used to eliminate the flame emission and the droplet contour became visible in the image. The droplets maintained an almost spherical form during the evaporation and combustion
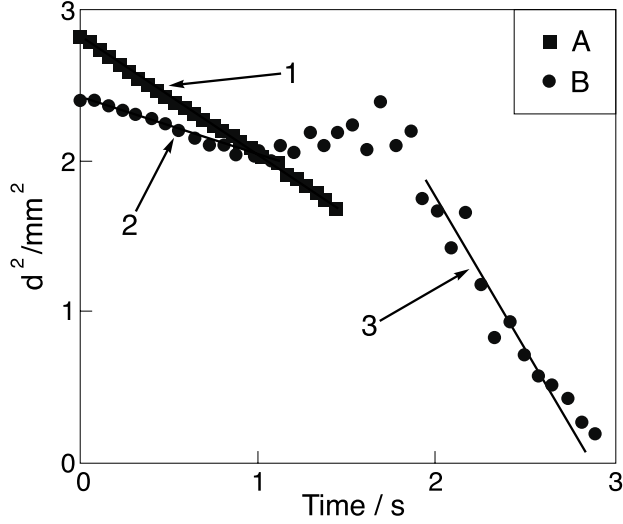
Figure 5.3 Burning rates of pure JP-10 (A) and solution of JP-10 with 18% MPCU (B). The burning rate for the pure fuel is 0.757 mm^2/s (1). The solution vaporization rate is 0.409 mm^2/s (2), and combustion proceeds with a rate of 1.971 mm^2/s (3)

processes and the images were used to determine the burning rate constant K according to the d^2-law [34]:

$$K = \frac{d(d^2)}{dt}$$

where d is the droplet diameter.

Images of pure JP-10 and the mixtures are shown in Figs. 5.2a to 5.2f. As shown in Figs. 5.2a to 5.2c, recorded at $t = 0$, 0.997, and 1.673 s, respectively, the kerosene droplet did not indicate internal vaporization until close to complete combustion. The situation changed when mixtures of kerosene with methylated PCU alkene dimer were used, as shown in Figs. 5.2d to 5.2f for a 18% mixture. For the 18% mixture the first internal vapors appeared at $t = 0.713$ s (Fig. 5.2e) and indication of strong effervescence appeared at $t = 1.23$ s (Fig. 5.2f).

Burning rates of mixtures of PCU alkene dimers in JP-10 are shown in Fig. 5.3. The burning rate for the pure fuel is 0.757 mm^2/s. The solution vaporization rate is 0.409 mm^2/s and combustion proceeds with a rate of 1.971 mm^2/s, significantly higher than the base JP-10.

5.3.2 Liquid HED — PCU Functionalized Exo-Methylenecyclopropane

Suspended droplets of PCU functionalized *exo*-methylenecyclopropane have been ignited as described above and they exhibited an explosive combustion behavior. The total burning time before large surface bubbles appeared was below 0.600 s (cf., times to droplet disruption for solutions of solid fuels in Fig. 5.2). A single large bubble appears in the PCU functionalized *exo*-methylenecyclopropane droplet at $t = 0.180$ s in the droplet lifetime. This bubble increases and at $t = 0.923$ s produces the droplet disruption. Prior to the appearance of the first bubble, the measured vaporization rate was $K = 3$ mm^2/s, which was quite fast in comparison with JP-10 ($K = 0.757$ mm^2/s) or azidohexane ($K = 1.2$ mm^2/s) and diazidononane ($K = 2.13$ mm^2/s) and comparable to $K = 4.05$ mm^2/s for diazidopentane. The last three compounds are energetic fuels that exhibit microexplosive droplet burning and have been analyzed in some detail by Lee *et al.* [9]. The PCU functionalized methylenecyclopropane droplets burned with significant soot production as indicated by the strong yellow emission from the burning region and the heavy depositions of carbon. Towards the end of the droplet lifetime microexplosions were present. These explosions were due to the high exothermicity of the reactions.

5.4 HED FUELS PHASE CHANGE IN TURBULENT REACTING FLOWS

Both numerical and computational studies have been made to investigate the phase-change characteristics of HED fuels in turbulent reacting flows. The computational approach taken here attempts to strike a reasonable balance between two competing aspects of the modeling work, namely, the complicated physical and chemical interactions in the flow field, and the requirements in resolving the multidimensional geometrical constraints of the flow field. The key elements of the numerical algorithm and turbulent combustion models embodied in the present effort are: (*i*) the conserved scalar (with assumed PDF to account for variance effect) and fast chemistry approach for turbulence–chemistry interaction [20], [22], (*ii*) the k–ε, two-equation model with wall function treatment for turbulence effects [35], (*iii*) the semi-implicit iterative algorithm solving strong conservation form of transport equations (mass, momentum, and scalar fields) in general nonorthogonal curvilinear coordinates [15], (*iv*) second-order finite difference operators for all terms including convection, pressure, and diffusion effects [15], [22], (*v*) multistep predictor–corrector method for the pressure correction equation [15], and (*vi*) a Lagrangian method explicitly tracking the interface movement [16].
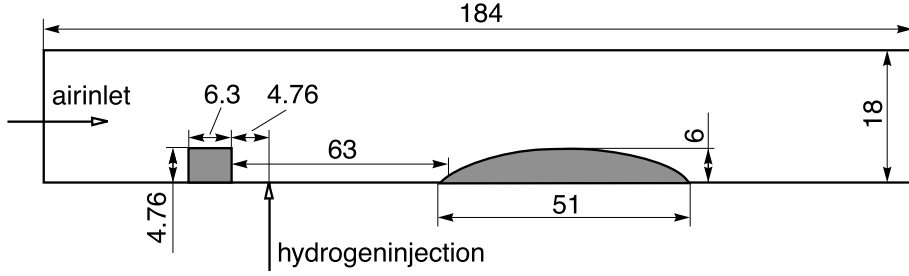
Figure 5.4 Schematic of the geometrical configuration for hydrogen–air flame and solid fuel. The geometry corresponds to the experimental setup. The initial shape of the HED fuel was a circular arc segment as shown above. The relevant material properties: air density = 1.91 kg/m^3, hydrogen density = 0.0898 kg/m^3. For the turbulent quantities: at the inlet $k = (0.03U_{\text{inlet}})^2 = 9.59$ (m/s)^2, $\varepsilon = C_\mu{}^{3/4}k^{3/2}/(0.03L_{\text{inlet}}) = 6360$ m^2/s^3, $\mu_t = C_\mu{}^{3/4}\rho k^2/\varepsilon = 0.00248$ kg/ms. For the fuel sample, m.p. is 450 K, latent heat of fusion is 72.7 J/g. Dimensions in mm. Air inlet velocity 103.3 m/s, hydrogen injection velocity 800 m/s

The combustion characteristics of the solid fuel are studied by placing it in a rectangular duct; the side view of the initial configuration is illustrated in Fig. 5.4. Due to the difficulty in igniting the high-density fuel, a hydrogen–air flame is employed to provide a pilot flame for ignition of the fuel which is placed downstream as shown in Fig. 5.4. In the present configuration, inlet velocity of air at left of the chamber was given to be 103 m/s. Hydrogen was injected through the injection orifice at 800 m/s. Both gases are initially at a temperature of 300 K. The computation is handled by assuming instantaneous establishment of the reacting gas flow field, followed by the phase change simulation. Details can be found in [36]. At the end of each time increment, a new solid–gas interface is established, the geometry is redefined, and a body-fitted grid is regenerated. Based on the new grid, the field equations of mass continuity, momentum, and combustion and turbulence closure models are solved, and a new solution is obtained. In the present effort, the fluid flow is handled as a quasi-steady problem with incrementally updated boundary shape and location.

In Fig. 5.5, the flow configuration and velocity and temperature distributions at the time instant of 12.5 s are depicted. Even though the flow is subsonic, due to the high Reynolds number, the flow structure in the region upstream of the solid propellant is minimally affected by the time-dependent boundary shape due to phase change. However, the thermal characteristics near the propellant interface show clear signs of time dependency, indicating that the mass flux of
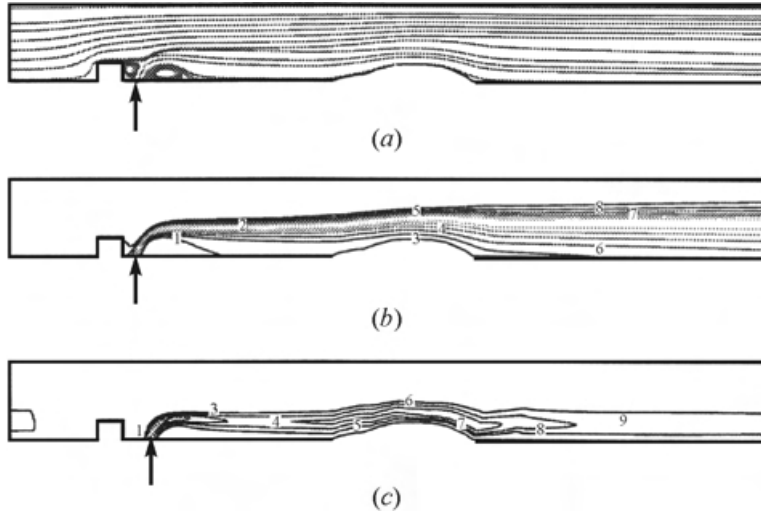
Figure 5.5 The flow characteristics at $t = 12.5$ s. The hydrogen injection location is indicated by the arrow. The regressed shape of the solid is shown clearly at this instant. (*a*) Streamlines at the initial stage. (*b*) Isotherms showing the location of the hydrogen–air flame. The values corresponding to the numbered contours are as follows: *1* — 990, *2* — 1830, *3* — 720, *4* — 2150, *5* — 1550, *6* — 1150, *7* — 1160, and *8* — 1620 K. The isotherms are shown to be lifted from the solid–gas interface. (*c*) Eddy thermal conductivity contours: *1* — 1.5, *2* — 9.0, *3* — 1.8, *4* — 6.1, *5* — 1.9, *6* — 3.2, *7* — 7.3, *8* — 4.1, and *9* — 2.3 W/m·K

the energetic fuel into the hot gas stream varies in time and in space. The eddy thermal conductivity in the region above the solid propellant also exhibits noticeable nonuniformity in magnitude. The combination of the eddy thermal conductivity and temperature distribution dictates the movement of the solid–gas interface. Consequently, the gas temperature inside the combustor will also vary in time.

Figures 5.6*a* and 5.6*b* present the calculated and measured shape and location of the solid–gas interface at selected time instants. Due to the uneven heat flux distribution along the surface, the interface shape changes in time. For example, the rear portion of the solid is consumed faster than the front portion. There are also nonsmooth spots developed at various time instants, reflecting a locally concentrated heat flux.

Experimentally, average burning rates have been measured using thin wire thermocouples imbedded in the sample at the mid-point and at the three-quarter
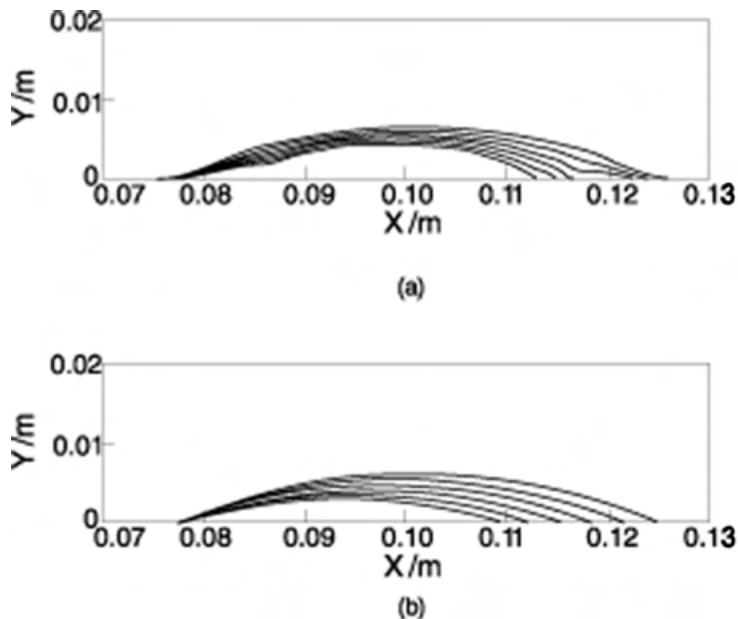
Figure 5.6 Computed (*a*) and experimentally estimated (*b*) shape of the solid–gas interface at selected time instants. Curves from top to bottom correspond to $t = 0.0$, 2.5, 5.0, 7.5, 10.0, and 12.5 s

point from the leading edge of the solid fuel. At each location, the thermocouples are placed at the half thickness of the sample. Due to the low-thermal conductivity of the fuel, the sample temperature remains nearly constant during combustion, until the fuel burns away at the location of the probes and the rapid temperature increase indicates the surface regression to the known depth. For PCU alkene dimers, at the flow condition investigated here, experimental information indicates that the burning rates at these two locations are 0.336 mm/s and 0.505 mm/s, respectively. Figure 5.6*b* shows the experimentally derived surface regression approximated by data at three points: the leading edge of the sample, which remains unburned until the final stages of the sample consumption, and the average burning rates measured at the mid-point and at the three-quarter point. Because only three data points are available, a second-order polynomial is chosen to describe the interface shape, which results in a smoother appearance than actually observed. In contrast, the computational results show substantially more noticeable interface distortion due to uneven heat flux distributions. The surfaces are shown for the same time steps selected in the computation, i.e., from the initial application of the external heat source in 2.5 s intervals.

Both computational and experimental results show that the consumption of the sample propagates upstream from the recirculation region formed at the trailing edge. Obviously, due to the increased residence time and turbulent mixing in this region, the heat transfer from the burning region to the sample is more intense on the backface of the solid fuel, resulting in an accelerated surface regression in this area. In comparison, the leading edge of the sample remains practically unaffected until the final stages of the sample consumption. It can be seen from the comparison with the calculated data that the experimental results indicate a faster consumption of the fuel sample. This is due to the heat contributed by the fuel itself which is unaccounted for in the present computation. This contribution is quite substantial, especially toward the later stage of the computation because of the accumulation of the PCU alkene dimer in the gas phase. As a result, during the experiment the surface of the sample becomes increasingly distorted towards the trailing edge. Nevertheless, the qualitative agreement between the computational and experimental information offers insight into the predictive capabilities of the present computational model.

5.5   CONCLUDING REMARKS

A new class of pentacyclic HED fuels was analyzed and some thermophysical and thermochemical properties have been measured. The main findings were as follows:

– When the molecular symmetry was disrupted by addition of a methyl group, the melting and boiling points of these compounds decreased significantly, from about 180° to 55 °C. The presence of a large number of isomers could contribute, as well, to the lowering of the melting point of the mixture. The boiling point, 80 °C, is significantly below the average values of existing liquid fuel systems, 280 °C for JP-10, for example. As a result, mixtures of methylated PCU alkene dimer in kerosene lead to formation of internal vapors early in the droplet lifetime and effervescent droplet boiling. Coupled with the high rates of energy release from the combustion of the HED component, a substantial acceleration in the droplet breakup and vaporization is achieved.

– Stable mixtures to 18% of methylated PCU alkene dimers in JP-10 have been obtained. This concentration is sufficiently large to increase the density of the fuel to a significant degree and also to augment the exothermicity of the droplet combustion.

– The time to achieve effervescent droplet combustion is reduced as the concentration of the HED component in the mixture increases. However, this

appears to approach a limit at the higher concentrations (close to saturation).

– The liquid HED fuel tested, PCU functionalized *exo*-methylenecyclopropane, exhibits large vaporization rates in comparison with existing liquid fuels and some azido-organic compounds. The droplet's combustion had a microexplosive nature due to the large rates of heat released during combustion.

– In the present study, numerical techniques capable of explicitly tracking the receding solid propellant boundary in turbulent reacting flows are developed. With this capability, nonuniform and time dependent heat fluxes along the propellant interface can be predicted, and a two-way coupling between gas-phase and solid-phase is established. A number of areas requiring further efforts can be identified.

– Although heat deposition from the high-energy compound has been neglected in the present calculation the qualitative agreement with the experiment indicates the predictive capability of the present model.

ACKNOWLEDGMENTS

REFERENCES

1. Marchand, A. P. 1995. Polycyclic cage compounds: Reagents, substrates and materials for the 21st century. *Aldrichchimica Acta* 28(4):95–104.
2. Segal, C., and W. Shyy. 1996. Energetic fuels for combustion applications. *Transactions of ASME — J. Energy Resources Technology* 118:180–86.
3. Yang, V., and V. E. Zarko. 1995. *Special Issue J. Propulsion Power* 11(4).
4. Segal, C., M. J. Friedauer, H. S. Udaykumar, and W. Shyy. 1996. Combustion of high-energy-density hydrocarbons. *9th ONR Propulsion Meeting Proceedings*. Eds. G. D. Roy and K. Kailasanath. Washington, DC: Naval Research Laboratory. 163–72.

5. Marchand, A. P., A. Zope, F. Zaragoza, S. G. Bott, H. L. Ammon, and Z. Du. 1994. Synthesis, characterization and crystal density modeling of four $C_{22}H_{24}$ cage-functionalized alkenes. *Tetrahedron* 50:1687–98.

6. Marchand, A. P., K. A. Kumar, D. Rajagopal, R. Eckrich, and S. G. Bott. 1996. Trapping of a caged cyclopentylidenecarbene. *Tetrahedron Letters* 37:467–70.

7. Law, C. K. 1995. Vaporization and combustion of high-energy-density liquid propellants. *35th Israel Annual Conference on Aerospace Science Proceedings*. Israel.

8. Law, C. K, C. J. Sung, H. Wang, and D. L. Zhu. 1995. Combustion studies of energetic liquid materials. *8th ONR Propulsion Meeting Proceedings*. Eds. G. D. Roy and F. A. Williams. La Jolla, CA: University of California at San Diego. 185–91.

9. Lee, A., C. K. Law, and A. L. Randolph. 1988. Aerothermochemical studies of energetic liquid materials: 2. Combustion and microexplosion of droplets of organic azides. *Combustion Flame* 71:123–36.

10. Lee, A., C. K. Law, and A. Makino. 1989. Aerothermochemical studies of energetic liquid materials: 3. Approximate determination of some thermophysical and thermochemical properties of organic azides. *Combustion Flame* 78: 263–74.

11. Foote, J. P., Y. C. L. Lineberry, S. Wu, and B. C. Winkleman. 1995. Investigation of aluminum particle combustion for application to underwater propulsion. *8th ONR Propulsion Meeting Proceedings*. Eds. G. Roy and F. A. Williams. La Jolla, CA: University of California at San Diego. 95–104.

12. Olsen, S. E., and M. W. Beckstead. 1995. Burn time measurements of single aluminum particle in stream and carbon dioxide mixtures. AIAA Paper No. 95-2715.

13. Turns, S. R., and S. C. Wong. 1987. Combustion of aluminum-based aglomerates. *Combustion Science Technology* 54:299–318.

14. Takahashi, F., I. J. Heilweil, and F. L. Dryer. 1989. Disruptive burning mechanism of free slurry droplets. *Combustion Science Technology* 65:151–65.

15. Shyy, W. 1994. *Computational modeling for fluid flow and interfacial transport*. New York: Elsevier.

16. Shyy, W., H. S. Udaykumar, M. M. Rao, and R. W. Smith. 1996. *Computational fluid dynamics with moving boundaries*. Washington, DC: Taylor & Francis.

17. Zhou, N., and A. Krishnan. 1996. A numerical model for endothermic fuel flows with heterogeneous catalysis. AIAA Paper No. 96-0650.

18. Brewster M. Q., M. A. Zebrowski, T. B. Schroeder, and S. F. Son. 1995. Unsteady combustion modeling of energetic fuels. AIAA Paper No. 95-2859.

19. Liau, Y.-C., and V. Yang. 1995. Analysis of RDX monopropellant combustion with two-phase surface reactions. *J. Propulsion Power* 11:729–39.

20. Libby, P. A., and F. A. Williams., eds. 1994. *Turbulent reacting flows*. San Diego, CA: Academic Press.

21. Oran, E. S., and J. P. Boris. 1987. *Numerical simulation of reactive flow*. New York: Elsevier.

22. Correa S. M., and W. Shyy. 1987. Computational models and methods for continuous gaseous turbulent combustion. *Progress Energy Combustion Science* 13: 249–92.

23. Pethe, S., T. Livingston, C. Segal, K. R. Williams, and D. H. Powell. 1998. Physicochemical properties and combustion characteristics of new high-energy-density caged hydrocarbon compounds. CST 98-03-04. *Combustion Science Technology* 132:1–6.

24. Eaton, P. E., and Mao-Xi-Zhang. 1996. A new and more practical approach to the synthesis of methylcubane. *9th ONR Propulsion Meeting Proceedings*. Eds. G. D. Roy and K. Kailasanath. Washington, DC: Naval Research Laboratory. 111–22.

25. Shoemaker, R. L., J. A. Stark, and R. E. Taylor. 1985. Thermophysical properties of propellants. High temperatures – high pressures. *9th ETPC Proceedings* 17: 429–35.

26. Gindhar, H. L., and A. J. Arora. 1977. Ignition delay of composite solid propellants. *Combustion Flame* 28:109–11.

27. Maycock, J. N., and V. R. Pai Verneker. 1969. Thermal decomposition of δ-HMX (cyclotetramethylene tetranitramine). *Explosivstoffe* 17(1):5–8.

28. Hondee, W. 1971. MS Thesis. U.S. Naval Postgraduate School (AD 729582).

29. Kimura, J., and N. Kubota. 1980. Thermal decomposition process of HMX. *Propellants Expolsives* 5:1–8.

30. Marchand, A. P. 1995. Plato's solid, Eaton's cage: The cubane saga. In: *The Chemical Intelligencer*. October:8–17.

31. Chen, J. K., and T. B. Brill. 1991. *Combustion Flame* 87:217–32.

32. Du, T. 1989. *Thermochimica Acta* 138:189–97.

33. Ninan, K. N., and K. Krishnan. 1982. *J. Spacecraft Rock.* 19:92–94.

34. Glassman, I. 1987. *Combustion*. 2nd ed. San Diego, CA: Academic Press.

35. Launder, B. E., and D. B. Spalding. 1974. The numerical computation of turbulent flow. *Computer Methods Applied Mechanics Engineering* 3:269–89.

36. Segal, C., M. J. Friedauer, H. S. Udaykumar, W. Shyy, and A. P. Marchand. 1997. Ignition characteristics of a high-energy-density fuel in high-speed flows. *J. Propulsion Power* 13(2):246–49.

37. Eaton, P. E. 1994. An introduction to cubane and its chemistry. *7th ONR Propulsion Meeting Proceedings*. Eds. G. Roy and P. Givi. Buffalo, NY: State University of New York at Buffalo.

38. Goshgarian, B. B. 1978. The thermal decomposition of RDX and HMX. AFRPL-TR-78-76.

39. Law, C. K. 1993. Combustion studies of energetic liquid materials. *6th ONR Propulsion Meeting Proceedings*. University of Colorado at Boulder. 25–29.

40. Lupoglazoff, N., and E. Vuillot. 1996. Parietal vortex shedding as a cause of insta-bility for long solid propellant motors — numerical simulations and comparisons with firing tests. AIAA Paper No. 96-0761.

41. Sirignano, W. A. 1983. Fuel droplet vaporization and spray combustion theory. *Progress Energy Combustion Science* 9:291–322.

Chapter 6

SOOT FORMATION IN COMBUSTION OF HIGH-ENERGY FUELS

E. J. Gutmark, E. P. Parr, and D. M. Hanson-Parr

An active control system designed to reduce soot formation and increase energy release was demonstrated in open and enclosed flames. The control is based on synchronized periodic injection of gaseous fuel (propane, ethylene, and benzene) into air vortices at a timing, which ensures energizing of the vortices and homogeneous mixing. It was shown that phased circumferential fuel injection into an axisymmetric air vortex can reduce soot formation by several orders of magnitude relative to an unforced flame and can also double the flame temperature. Laser diagnostics was utilized to obtain planar simultaneous visualizations of the mixing process between the fuel and air flows as well as the combustion zone, indicated by OH, soot production regions indicated by Laser Induced Incandescence (LII), as well as PAH formation regions imaged via PLIF. It was shown that a proper timing of fuel injection results in homogeneous fuel–air mixing within the vortices, while injection, which is out of phase, results in interference with the vortex formation as well as creates islands of unmixed fuel, leading to poor combustion, PAH formation early in the evolution, and soot formation further downstream. The interaction of the flame with the external air was studied using Particle Imaging Velocimetry (PIV). It was determined that the entrained air is crucial to maintain control authority on the flame. Blockage of the entrained external air resulted in the loss of control. A method for substitution for the external air by direct injection of air into the flame base was developed. Its efficacy was demonstrated in open and enclosed systems. The latter is especially significant due to the lack of air-rich flow in the ambient of such systems. The secondary air injection doubled the flame temperature near the flame holder of an enclosed flame. The control system was also tested with highly sooting fuels including benzene. When the proper phase angle of fuel injection was used soot formation could be prevented, and an entirely blue flame

realized, even when gaseous benzene constituted 66% of the combustible content. The combustion efficiency of benzene was beyond 99.999% even at an overall equivalence ratio of 1.0. The controlled flame was found to be largely unaffected by moderate swirl although the stability was slightly reduced. Heavy swirl leads to a further reduction in stability and intermittent formation of soot. The unforced swirling flame was not nearly as efficient in reducing soot formation as the controlled (forced) flame without swirl.

6.1   INTRODUCTION

The interaction between fluid dynamics and chemical reaction during the combustion process determines its efficiency and stability [1, 2]. In reacting jets, the mixing between the reactants participating in the combustion is a crucial part of the process [3]. The mixing occurs in two stages; the initial stage of bringing relatively large amounts of the reactants together (large-scale mixing) is dominated by vortex dynamics, and the second in which molecular contact between the reactants is promoted by small-scale turbulent mixing [4]. The large-scale mixing is associated with the entrainment process through vortex dynamics [5–7]. The small-scale mixing is related to other flow instabilities, energy transfer between scales, and the interaction between vortices [5, 8–10]. Minimizing locations of unmixedness is important to enhance the reaction process and reduce soot formation due to localized high fuel-to-air ratios.

In premixed flames the vortex dynamics and turbulence govern phenomena such as local flame extinction due to excessive stretching, combustion zone thickness, and temperature distribution in open-air combustion. In both cases combustion efficiency, soot formation, and various other phenomena associated with combustion instabilities, such as flame lift-off or blow-out, are determined by local details of the mixing process, the stoichiometry, and the Damköhler number for finite-rate chemistry [11–13]. In order to understand these interwoven complex processes, it is necessary to measure various properties in a spatially and temporally resolved way. Laser diagnostics was used to obtain 2D and 3D measurements of multiparameters in reacting flows with high-spatial and temporal resolution [14]. The understanding of the combustion and soot formation mechanism can be used to develop passive and active control methods to improve these processes. In previous experiments, the regions of soot, which were observed in both diffusion and premixed flames, were related to vortices in the flow field [15]. This phenomenon was most pronounced in nozzles of noncircular geometry used in passive control, where inappropriate fuel injection was used. When active control was applied to enhance energy release in combustors, the soot formation was concurrently minimized [16]. Reference 15 shows that increased CH formation in the combustion, induced by excitation of large-scale

vortices, was accompanied by reduced soot which was observed to be out of phase relative to the energy release.

The soot formation and its control was studied in an annular diffusion flame using laser diagnostics and hot wire anemometry [17, 18]. Air and fuel were independently acoustically forced. The forcing altered the mean and turbulent flow field and introduced coherent vortices into the flow. This allowed complete control of fuel injection into the incipient vortex shedding process. The experiments showed that soot formation in the flame was controlled by changing the timing of fuel injection relative to air vortex roll-up. When fuel was injected into a fully developed vortex, islands of unmixed fuel inside the air-vortex core led to high-soot formation. When fuel was injected into the incipient vortex prior to roll-up initiation, a homogeneous mixture of air and fuel eliminated soot formation. The proper phasing of the fuel injection decreased soot formation in the flame to levels far below that under laminar (no vortex conditions) or that present with air forcing only.

6.2   EXPERIMENTAL

Figure 6.1 shows the apparatus diagram. The diffusion flame burner consisted of an air plenum with an exit diameter of 22 mm, forced at a Strouhal number of 0.73 (100 Hz) by a single acoustic driver, and a coaxial fuel injection ring of diameter 24 mm, fed by a plenum forced by two acoustic drivers at either 100 Hz (single-phase injection) or 200 Hz (dual-phase injection). The fuel was injected circumferentially directly into the shear layer and roll-up region for the air vortices. In addition, this fuel injection was sandwiched between the central air flow and the external air entrainment. Thus the fuel injection was a thin cylindrical flow acted upon from both sides by air flow.

The fuel-to-air ratio was varied from 0.8 to 1.4 to simulate differing soot formation conditions. The fuels used were propane, ethylene, or ethylene with gaseous benzene (the fuel was bubbled through liquid room-temperature benzene to provide up to 20% of the combustible content or the entrainment air flow was bubbled through benzene to provide up to 66%). The centerline velocity at the nozzle exit was 3 m/s, the unforced (natural) RMS was 4.5%, and the forced RMS was 30%. The Reynolds number based on the exit diameter was 3700.

Using a single laser to excite multiple species or phenomena allows multiple parameters to be imaged simultaneously with multiple cameras. A Nd–YAG pumped dye laser with nonlinear crystal doubling was tuned either on or close to (but off) the (1,0) A–X transition of OH radicals located near 283 nm and two cameras simultaneously monitored selected combinations of two of five scalars: OH via PLIF, PAH (via PLIF), soot (via LII), fuel, and air (both via acetone
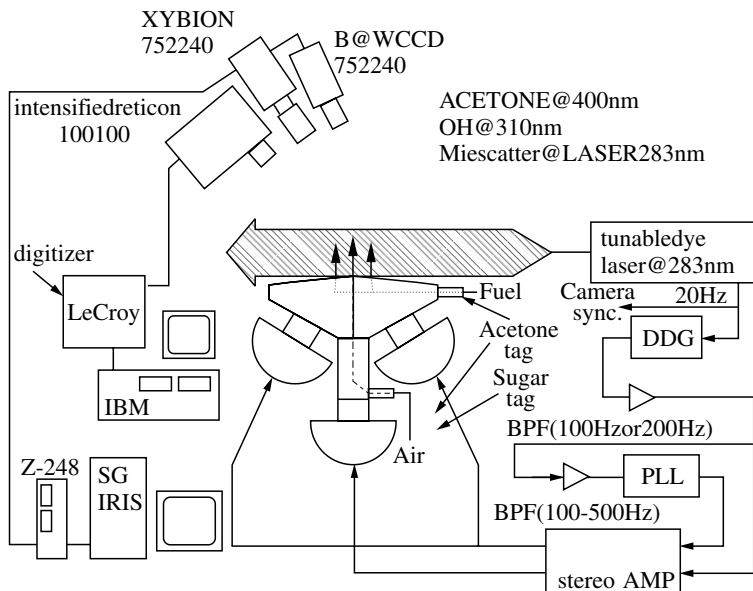
Figure 6.1 Apparatus diagram

PLIF or Mie scatter on seeded particles). The pairs of scalar images were combined by making use of phase locked imaging. By changing the phase angle of the laser with respect to the vortex roll up cycle the time evolution of the mixing and combustion could be measured.

The two cameras used were a $Xybion^{TM}$ ISG240 gated image intensified 752×480 CCD and a gated intensified $Reticon^{TM}$ 100×100 diode array. Both cameras were gated for about 50 ns to encompass the laser pulse but reject flame chemiluminescence. The flows were tagged with either fine sugar particles, monitored with Mie scatter using an 283 nm interference filter, or with acetone, monitored via LII [19]. Acetone has a broad absorption peak centered at 275 nm; when pumped at 283 nm it produces a broad induced fluorescence peak centered at 400 nm and extending from 320 nm to about 600 nm. Acetone PLIF was monitored with a 400-nanometer interference filter having a 65-nanometer FWHM. OH was imaged via fluorescence from the (1,1) A–X band selected using a 311 nm 10 nm FWHM interference filter, and soot was monitored using Mie scatter at 283 nm or LII [20, 21] using a broad band filter (WG335 + UV filter passing 220 nm to 400 nm) that blocked the laser line. PAHs were monitored via LIF using the same filter. The soot LII was distinguished from the PAH LIF by delaying the camera gate: no delay led to PAH LIF + soot LII while adding a delay of tens of nanoseconds removed the PAH PLIF (due to rapid quenching)

Table 6.1 Permutations of scalar measurements

Camera 1 ($Reticon^{TM}$)	Camera 2 ($Xybion^{TM}$)	OH resonance	Flame
OH (LIF)	Fuel (acetone)	on	on
Soot (Mie)	Fuel (acetone)	off	on
Fuel (Mie)	Air (acetone)	off	off
OH (LIF)	Air (acetone)	on	on
Air (Mie)	Fuel (acetone)	off	off
Air (Mie)	Fuel (acetone)	off	on
OH (LIF)	Soot (Mie)	on	on

and showed only soot LII. These measurements were not done simultaneously with any seed acetone PLIF as there would be no way to separate acetone LIF interference from the PAH LIF. Images from the two gated cameras were acquired using two computers, a transient digitizer, and frame grabber.

Table 6.1 shows the permutations of scalar measurements.

The combustion efficiency of benzene was monitored with an on-line real time mass spectrometer ($Ametek^{®}$ model $Dycor^{TM}$ 1000) tracking the parent mass peak for benzene. (Mass scans showed that as the parent peak was removed no peak above $m/e = 40$ appeared so the benzene was not just being cracked into a smaller unsaturated hydrocarbon but was being consumed.)

Flame emission was monitored using fiber optic probes and either a photodiode detector for yellow emission from hot soot or a photo multiplier tube for violet emission from CH radicals (430 nm bandpass filter).

Cold flow mean velocity and turbulence profiles were measured with a calibrated hot wire. Instantaneous phase-sampled velocity vector fields were measured in cold flow using a very simple and inexpensive PIV setup. PIV measures the local flow velocities by following the movement of seed particles with time (usually using two images taken at a given time separation). Instead of a pulsed laser, the light source in these experiments was an unmodulated fiberoptic microscope illuminator (tungsten incandescent bulb). Timing was controlled by gating the $Xybion^{TM}$ camera. The output of the fiberoptic illuminator was loosely focused into a relatively wide (5 mm) light sheet using a cylindrical lens.

The flow associated with this flame is highly complex due to the strong vorticity and, it turns out, strong entrainment, leading to regions of reversal. Therefore the PIV technique had to allow resolution of the direction ambiguity. A simple double exposure PIV image contains a 180° ambiguity in velocity direction as it is impossible to tell which particle image corresponded to the first. There are many ways to remove this ambiguity, such as using different color lasers for the two pulses [22, 23], or by using a moving mirror to shift

the images [24, 25], in effect adding a constant bias velocity analogous to LDV frequency shifting techniques. In this work, a very simple technique was used: instead of gating the camera with two equal pulses, it was gated with a dash-dot pattern. Thus the particle track images consist of lines followed by dots making direction analysis unambiguous. This technique is more akin to PTV (Particle Tracking Velocimetry) than pure PIV and it produces immediate images that, if the particle seeding level is correct and uniform, are already essentially velocity vector plots. Theoretically, each track of these images could be analyzed for acceleration, turbulence, and vorticity since each has three distinct (x, y, t) space/time tuples allowing $\partial^2 x/\partial t^2$ and similar partial derivatives to be evaluated numerically. Practically, however, the images do not have enough resolution to support double derivatives.

6.3   RESULTS AND DISCUSSION

The soot formation and its control was studied in an annular diffusion flame using laser diagnostics and hot wire anemometry [17, 18]. Air and fuel were independently acoustically forced. The forcing altered the mean and turbulent flow field and introduced coherent vortices into the flow. This allowed complete control of fuel injection into the incipient vortex shedding process. The experiments showed that soot formation in the flame was controlled by changing the timing of fuel injection relative to air vortex roll-up. When fuel was injected into a fully developed vortex, islands of unmixed fuel inside the air-vortex core led to
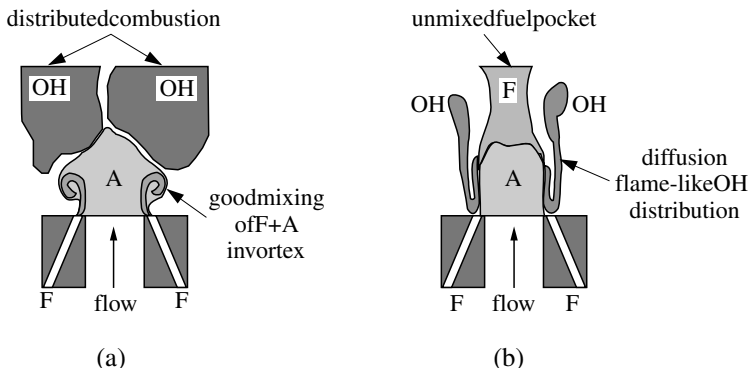
Figure 6.2 Schematic of mixing with relative phase of fuel injection proper (a) and improper (b) with respect to soot formation (traced from PLIF results): (a) low-soot case; (b) high-soot case

high-soot formation (Fig. 6.2b). When fuel was injected into the incipient vortex prior to roll-up initiation, a homogeneous mixture of air and fuel eliminated soot formation (Fig. 6.2a). The proper phasing of the fuel injection decreased soot formation in the flame to levels far below that under laminar (no vortex) conditions or that present with air forcing only.

Measurements showed that the amount of soot produced by the flame was affected by the mixing process between the air jet vortices, the fuel jets, and naturally entrained external air. PIV and smoke flow visualization showed that the air vortices induced strong external air entrainment into the main jet flow very close to the exit plane when the phase angle between the fuel jets and air jet were at the value for minimized soot production. When the wrong phase angle was used, i.e., that which leads to soot formation, the air vorticity coherence was reduced, the vortices appeared to develop further downstream, and the air entrainment at the flame base was significantly reduced.

6.3.1 Soot Reduction

Experiments with propane and ethylene flames were performed to study the effect of the soot control methodology in low and highly sooting flames. A quantitative measure of the effect of soot emission control was obtained by integrating the overall soot black body emission of the flame using a photodiode (Fig. 6.3). The ethylene flame is depicted by the dashed lines and the propane flame by the solid lines. The variation of the soot emission is given as a function of the fuel forcing level. Comparison is made between the fuel injection phase shift corresponding to the maximum soot level and that corresponding to a minimum soot level. The differences between the two conditions are more pronounced for the ethylene flame.

Figure 6.3 Comparison of uncontrolled and controlled soot emissions for different fuel forcing levels between propane (1 — minimum and 2 — maximum soot level) and ethylene (3 — minimum and 4 — maximum soot level)

The initial-unforced emission level is nearly five times larger for the ethylene flame. The drop in soot emission occurred at a certain threshold level of the fuel forcing level. This level is lower in the propane flame relative to the ethylene flame. Following this rapid drop, the slope of all the curves is similar. The

reduction of the soot emission level in the ethylene flame is over two orders of magnitude, and nearly one order of magnitude for the propane flame.

6.3.2   Flow Field

The mixing process between the air jet vortices and the fuel jets affects the amount of soot produced by the flame. A portion of the soot reduction effect seen in the experiments was caused by the strong entrainment of surrounding air into the main jet, induced by air vortices with subsequent reduction in the fuel-to-air ratio. Figure 6.4a shows the PIV measured (cold flow) velocity vector field map under the low-soot case of dual injection. The vortices are clearly evident. Also evident is a very strong entrainment of surrounding air at the base of the flame under the first vortex. The average centerline velocity is about 3 m/s yet the net average entrainment velocity near the exit is more than 1 m/s. The entrainment under the second vortex is much weaker due to a stagnation region from centerline flow moving outward between the vortices. Using PIV it was found that the special combination of air and fuel forcing caused this high-entrainment rate.

   The velocity vector field map of the cold flow corresponding to the high-soot case is shown in Fig. 6.4b. The change in the vortex roll-up location results in reduced external air entrainment at the flame base as alluded to previously.

(a)   (b)
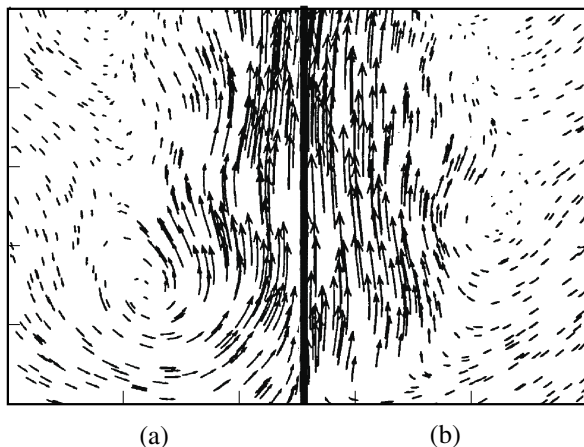
Figure 6.4 Velocity vector field map of (a) low-soot case with dual injection and (b) high-soot case with dual injection, measured in a cold flow using PIV

The air entrainment velocity at the flame base was measured using a hot-wire anemometer at a distance of $0.14D$ above the surface. The radial velocity variation with radial distance from the flame edge is depicted in Fig. 6.5. The entrainment velocity was measured at four different forcing conditions: unforced, forcing of the air flow only, forcing of fuel and air at a phase shift which produces low soot, and at a phase shift producing high soot. The highest entrainment velocity was measured for the low-sooting flame. In fact, the entrainment velocity exceeds 30% of the centerline main jet velocity. It was nearly double the level of that of the high-sooting flame or the flame with only air forcing. The entrainment of the natural flame was all but negligible.

Subsequent tests proved the importance of the external air entrainment to the controllability of soot formation in the flame. When the entrainment into the flame base was blocked in the region between the base and $0.14D$ above it, the soot formation could not be controlled at any phase of fuel injection. The blockage shifted the vortex away from the flame base and reduced the smoke entrainment into the flame in this region.

The timing of the three processes, the vortex formation, fuel jet injection, and external air entrainment, is important to obtain mixing control for soot reduction. Three hot wires were placed on the main jet centerline, at the fuel jet centerline, and near the jet edge to monitor entrainment. The three measurements were performed at the flame base. The time traces of the three hot-wires are shown in Fig. 6.6 for low- and high-soot conditions. Measurements [17, 18] showed that the low-soot formation occurs when the fuel is injected initially into the incipient air vortex and the subsequent fuel injection reaches the hot reacting zone. In the flame with high-soot formation, the fuel injection interferes with the air vortex formation and the fuel is injected into a fully developed vortex. These observations are confirmed by the time traces which show that in the low-soot flame the first fuel injection is completed just as the air flow is being accelerated to initiate the vortex formation. In the sooty flame, the first fuel acceleration occurs together with the air jet and interferes with the vortex formation by pro-
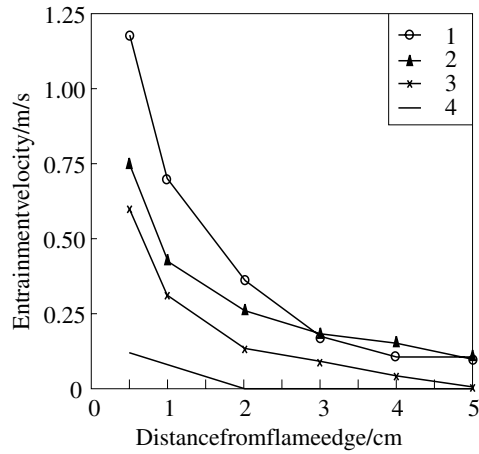
Figure 6.5 Radial entrainment velocity measured at a distance of $0.14D$ above the flame base plate for different flame forcing conditions: *1* — proper fuel injection; *2* — wrong fuel injection; *3* — air forcing only; and *4* — natural flame
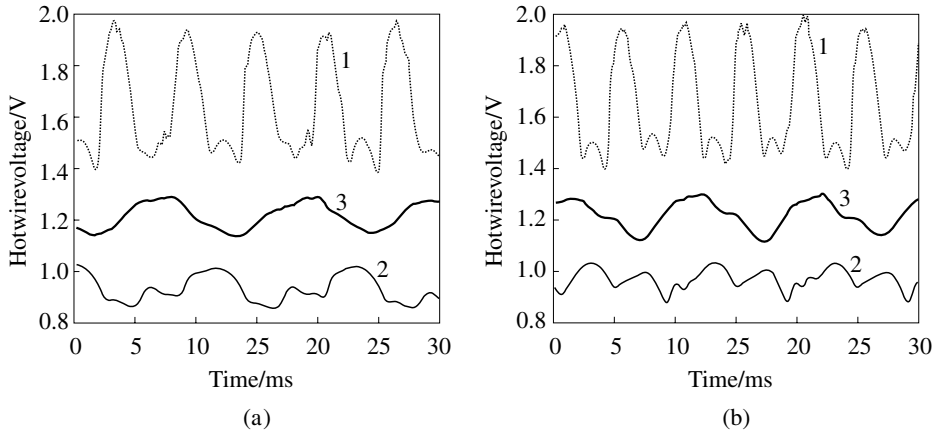
Figure 6.6 Velocity–time traces of the main air jet at the centerline (*1*), fuel jet (*2*), and external air entrainment (*3*), measured at the jet exit plane, for low-soot forcing (*a*) and high-soot forcing (*b*)

ducing opposite vorticity. The fuel jets block the external air entrainment when the air vortex is developing and thus it reaches its peak level between air vortices and fuel injection and does not participate in the combustion. The external entrainment in the low-soot flame coincides with the developing air vortex and the fuel injection leading to proper fuel-to-air mixture ratios which improve the combustion properties.

6.3.3   Heat Release

The external air entrainment affects not only the formation but also the energy release. The temperature along the flame centerline, measured with thermocouple, is shown in Fig. 6.7. The energy release of the low-sooting flame is closer to this flame holder relative to the uncontrolled flame, and its temperature was twice as high. The sooting flame temperature is close to that of the unforced flame and the heat release is distributed further downstream. When the external entrainment of the low-sooting flame was blocked, the temperature dropped to the level of the sooting flame, even though the control parameters remained unaltered.

External air was substituted by injecting additional air radially through the ring which was blocking the entrainment. The control authority was regained with an addition of 30% air relative to the mean central jet flow, the soot level de-
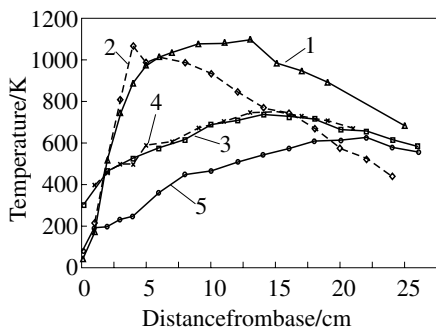
Figure 6.7 Temperature distribution along an open-flame centerline for different control conditions: *1* — proper fuel injection; *2* — air added through ring; *3* — wrong fuel injection; *4* — proper injection with blocked entrainment; and *5* — natural flame
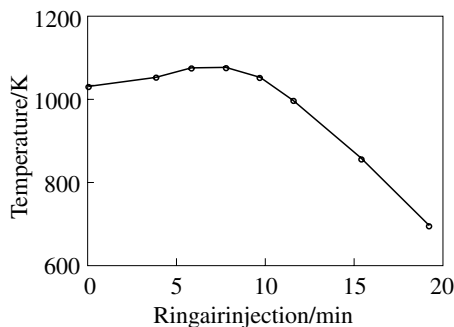
Figure 6.8 Effect of the flow rate of external air injected through a ring around the flame base on the temperature on the centerline at $x/D = 9.1$. The air injection replaces the natural air entrainment which is blocked by the ring
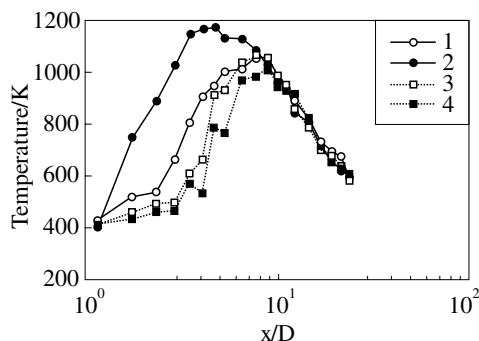
Figure 6.9 Temperature distribution along an enclosed flame centerline for different control conditions: *1* — low soot, no secondary air; *2* — low soot, with secondary air injection; *3* — high soot, no secondary air; and *4* — high soot, with secondary air injection

creased to the level of the controlled low-sooting flame, without entrainment obstruction, and the maximum temperature was recovered (Fig. 6.7). Figure 6.8 demonstrates the sensitivity of the flame temperature to the injection flow rate. The temperature measured at a distance of $9.1D$ from the exit with a flow rate of 8 l/min, approaches the temperature measured with free air entrainment under proper phase forcing. It is lower above and below that level.

The loss of control due to interference with the external air entrainment process, resulting in an increased soot production as well as reduction in energy release, is significant especially in enclosed systems. In enclosed combustors, external air is not readily available at the flame base and the gases entrained at this region are typically burned, air-depleted reaction products. The possibility to recover the control authority by the secondary air injection at the flame base is important for

such an enclosed system. Figure 6.9 shows that this method is indeed applicable to enclosed systems. In an enclosed system the differences between the heat release of the low- and high-sooting flames are not large. However, injection of secondary air at the flame base increases the temperature significantly. At the high-soot conditions, the additional air has a slight adverse effect on the flame temperature.

6.3.4 Mixing Process and Combustion

Laser diagnostics was employed to develop understanding of the mixing mechanism causing the large change in the sooting and energy release characteristics of the flame. A series of two simultaneous and instantaneous planar images of the flame were taken at a time. The fuel injection and air vortical flow were visualized during combustion and in cold flow tests by seeding acetone and mist into the individual flows. Fuel injection was visualized simultaneously with OH to determine the combustion location relative to fuel. The fuel injection was also imaged concurrently with Mie scattering from soot. All images were taken for a full sequence of the air and fuel vortices cycle for both the high- and low-soot conditions.

The planar laser images of the air, fuel, and OH are shown in Fig. 6.10 for the low- and high-soot conditions. The fuel, in this case, was injected once in every air vortex formation cycle. The air and fuel images were acquired simultaneously while the OH image was acquired separately but at the same phase relative to the vortex formation. The images show that for the low-soot fuel phase angle the fuel is injected into the incipient vortex roll-up and homogeneously mixed with the air vortex yielding intense reaction downstream as shown by the OH region above the vortex area (Fig. 6.10a). The homogeneous mixture is emphasized by the gray color of the air–fuel mixture. A dynamic sequence (computer-generated movie) which was produced by displaying the full cycle of events during the vortex roll-up and fuel injection showed that the injection of fuel into the incipient air vortex results in this homogeneous mixing. The air–fuel forcing induces coherent periodic entrainment flow and this flow mixes well with the fuel jets. The resulting flame is lifted (notice the OH stand-off from the exit plane), periodic, and distributed like a premixed turbulent flame.

The images corresponding to the high-soot flame (Fig. 6.10b) and the corresponding movie show that when the fuel is injected out of phase with the air vortex cycle, the air vortex formation is partially inhibited, and the fuel remains unmixed in pockets between air vortices resulting in alternating regions of high and low stoichiometry. The entrainment rate is reduced and not as coherently modulated. This leads to poor combustion and high-soot production. The re-
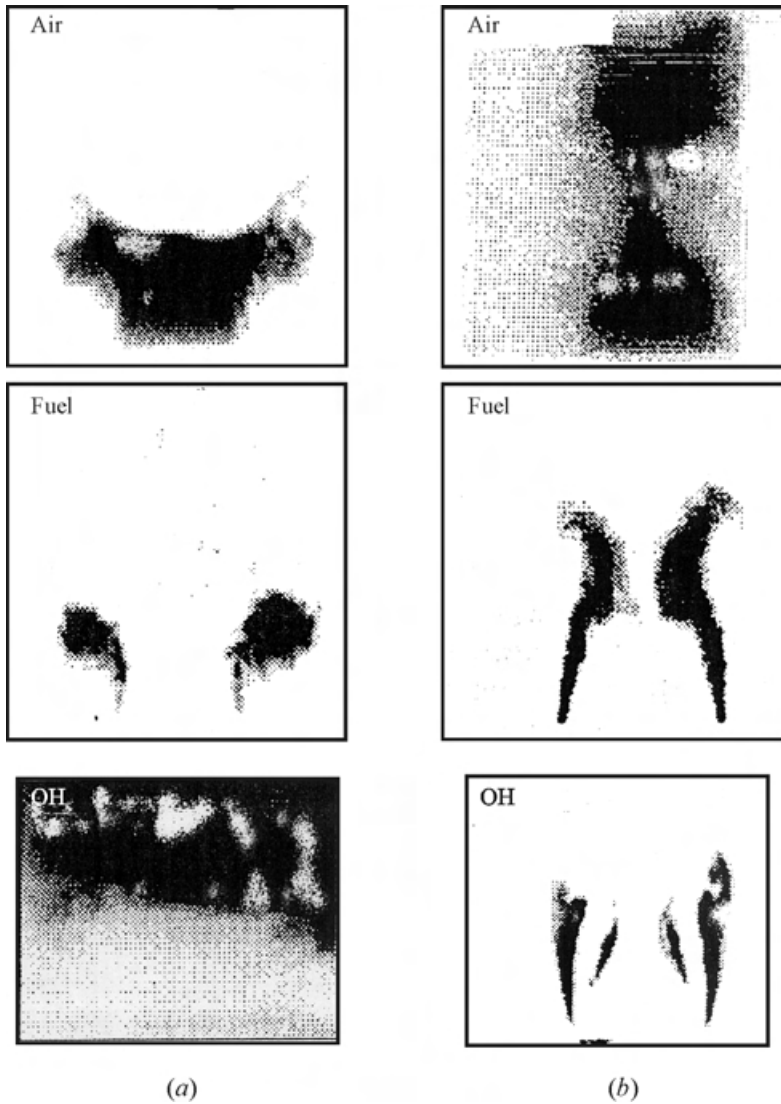
Figure 6.10 Planar images of the air and fuel mixing pattern and reaction zone imaged by OH fluorescence of the ethylene flame at single-fuel injection: low (*a*) and high (*b*) soot conditions

action region as indicated by the OH is primarily at the external shear layer of the jet where the fuel is mixed with the external air, and the OH has a typical narrow "diffusion flame"-like appearance. This flame has a very high-sooting level, which was not visualized in this figure, as the soot was concentrated above the field of view of these images.
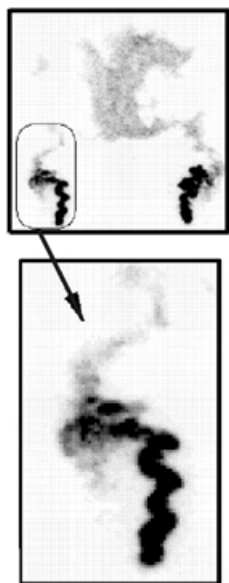
Figure 6.11 Close-up of gaseous fuel jet showing instability

Another interesting fluid mechanics phenomenon in this flame was the interaction of the fuel jets with the air jet and its effect on the jet stability. Figure 6.11 shows that the fuel jets have, under close examination, clearly amplifying instability modes. It may be that the combination of this fine spatial-scale turbulence, in combination with the larger scale folding of the air vortex, leads to good mixing over many length-scales and therefore the good low-soot combustion. If this is true, then one can investigate the use of corrugated nozzles or other means to increase the fine-scale turbulence that is lost when the fuel is liquid instead of a gaseous jet.

Significant improvement of the combustion energy release was obtained by introducing a dual-fuel injection scheme. Fuel is injected twice per air vortex shedding. Figure 6.12a, low-soot case, shows that the first fuel injection, which is synchronized with the formation of the incipient vortex, mixes homogeneously and initiates intense combustion in the vortex as it was convected downstream. The second injection (Fig. 6.12b) penetrates the jet and brings the fuel into the lean combustion products of the prior vortex. The process therefore emulated staged combustion without mechanical stages. This configuration leads to high-soot reduction as well as an increase in energy release rate close to the flame holder (Fig. 6.7). The higher temperatures near the flameholder were also measured off-axis. The more efficient soot-free combustion results also in a higher energy release near the flame holder.

The injection sequence, which results in a highly sooting flame (Fig. 6.13), occurs out of phase with the air vortex formation. The first fuel injection misses the air vortex and stays unmixed while also partially suppressing the roll-up of this air vortex. The second-fuel injection enters the void between the air vortices and stays separated from the air. The rich mixture results in the formation of soot at this point as shown by the white spots. Temperature profiles also show the energy release rate to be lower in this case.
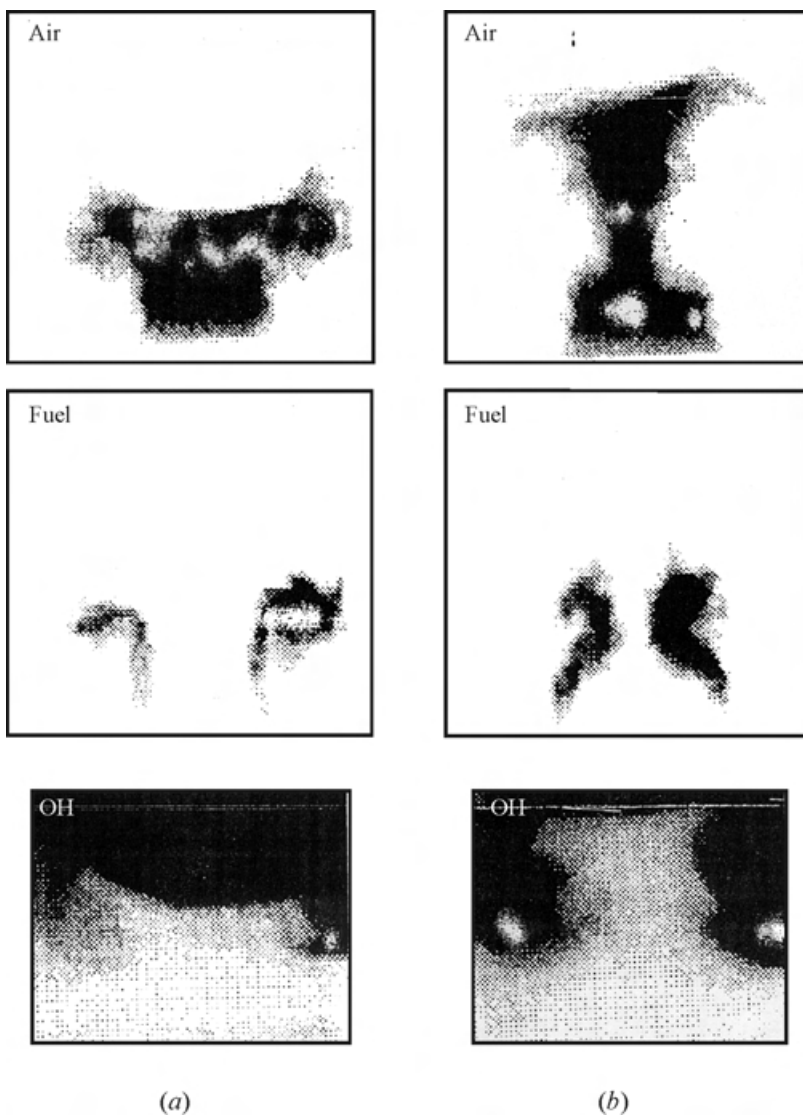
Figure 6.12 Planar images of the air and fuel mixing pattern and reaction zone imaged by OH fluorescence of the ethylene flame at low-soot conditions and dual-fuel injection at the first (*a*) and second (*b*) injection time
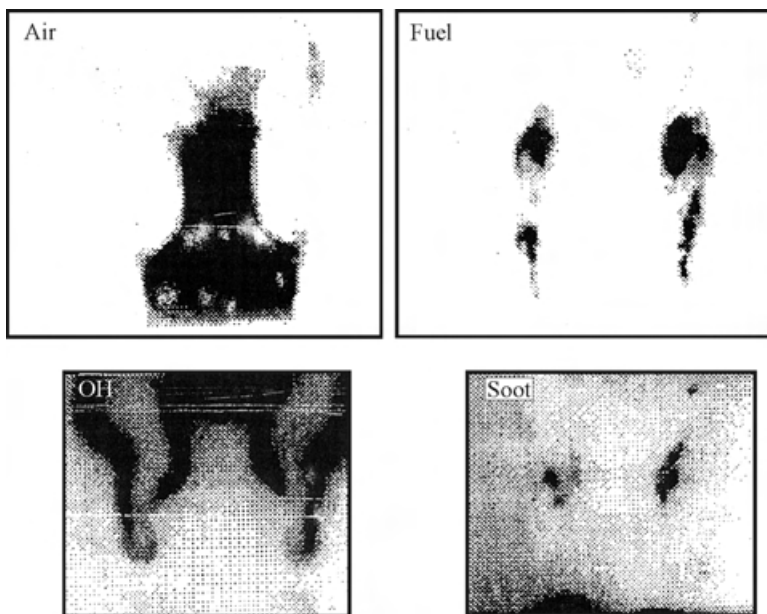
Figure 6.13 Planar images of the air and fuel mixing pattern and reaction zone imaged by OH fluorescence of the ethylene flame and Mie scattering of soot, at the high-soot phase and dual-fuel injection

6.3.5 Other Parameters

PAH: In the low-soot phase case no PAH PLIF was seen, nor was there any soot LII. In contrast, the high-soot case clearly showed regions of PAH and soot production. Figure 6.14 shows a PAH PLIF/soot LII image (frame *a*) along with the corresponding OH (*b*), central air (*c*), and fuel (*d*) images. In frame (*a*) the PAH PLIF and soot LII are distinguished by arrows and this was determined using the camera gate delay as mentioned in the experimental section. The PAHs are formed early in the cycle close to the exit plane and these lead to formation of soot further downstream (in the second vortex in frame *a*). Note that the PAHs form in a fuel-rich region of diffusion-controlled combustion.

Aromatic fuel: The prior results were obtained using propane (not very sooty) and ethylene (considerably more sooty) as fuels. The results were extended to a very sooty aromatic fuel by choosing benzene, as it had a sufficient vapor pressure to be entrained into the fuel flow.

The efficacy of this control system was demonstrated in both open and enclosed systems with benzene introduced both into the ethylene fuel (as 20% of
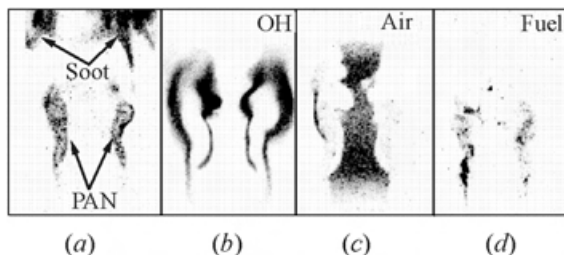
Figure 6.14 Single phase in vortex evolution showing (*a*) PAH PLIF and soot LII, (*b*) OH PLIF, (*c*) central air, and (*d*) fuel (seeded acetone PLIF). Flow is bottom to top in this set of images

the combustible content) as well as into the entrained airflow (as 66% of the combustible content). When the proper phase angle of fuel injection was used, soot formation could be entirely prevented, and a *completely blue flame* realized, even when gaseous benzene constituted 66% of the combustible content.

The combustion efficiency of the benzene was beyond 99.999% even at an overall equivalence ratio of 1.0 (including the entrainment air which was 30% of the total air flow). With the controller off, the flame was *extremely sooty* and, in fact, *sooting*, as the quartz tube would be blackened and the mass spectrometer sampling probe clogged in a matter of seconds, and soot was sucked into the scrubber system. This comparison between "controller off" and "controller on" conditions with benzene fuel is extremely dramatic and shows the efficacy of active combustion control in vortices to eliminating soot from diffusion flames.

Swirl: Since swirl is present in many propulsion burners, studies were undertaken to test the robustness of the control system by imposing swirl in the central air flow. Another objective of these studies was to see if added swirl could improve the operation of the controller. The swirl was introduced by letting the airflow into the central tube from two off-axis 90-degree inlets. The "percent swirl" quoted here is the percent of the total central air flow that entered from these swirl inlets as opposed to the nonswirling inlets. The average axial velocity radial profile showed a strong minimum on the centerline, and at higher levels of swirl the flame could actually be sucked back into the airflow.

The controlled flame was found to be largely unaffected by moderate swirl (levels up to 40%) although the stability was slightly reduced. Heavy swirl (beyond 75%) led to a further reduction in stability and intermittent formation of soot. The unforced swirling flame was not nearly as efficient in reducing soot formation as the controlled (forced) flame without swirl. The flame was unstable, quite yellow, and spread out to impinge upon the dump diameter

(quartz tube of 130-millimeter internal diameter). At 80% swirl without the controller on, the flame was very yellow and unstable and intermittently lifted off. In addition, there was extremely strong naturally excited high-frequency instability at 240 Hz. High-speed imaging showed the instability was associated with coherent spanwise axisymmetric vortices being shed at 240 Hz at the dump. Even with this naturally occurring vorticity the system was not particularly stable and did not reduce soot nearly as much as the controlled system. In summary, the actively controlled flame, with *or* without swirl, was much better at preventing soot formation than the swirl flame without control.

6.4   CONCLUDING REMARKS

The efficacy of the active control system for soot reduction was demonstrated in both open and enclosed combustion systems using gaseous fuels.

Two-fuel injection schemes were tested. In one the fuel was injected once per air vortex formation cycle. In the other, the fuel was injected twice in each cycle. Laser diagnostics was used to measure the mixing and combustion processes. The air, entrainment air, fuel, OH, PAH, and soot were visualized in the center-line plane. Analysis of the simultaneous images showed that in a single-injection system, low-soot and high energy release could be realized when the fuel was injected into the incipient vortices. For such timing, the fuel jet energized the air vortex and also was homogeneously mixed with the air. At an injection phase 180° off the optimized conditions, the fuel jet interfered with the formation of the air vortex partially inhibiting its roll-up. The fuel remained unmixed in pockets between the air vortex resulting in poor combustion, PAH formation, and, subsequently downstream, soot formation. In the dual fuel injection scheme, the first injection occurred at a phase similar to the single injection. The second injection brought the fuel into the region of hot lean combustion products, intensifying the reaction. The dual-injection scheme remained inefficient for the 180° phase shift; the fuel remained unmixed and vortex formation was reduced.

The control system was also demonstrated in open and enclosed systems with highly sooting fuels including benzene. When the proper phase angle of fuel injection was used, soot formation could be prevented, and an entirely blue flame realized, even when gaseous benzene constituted 66% of the combustible content. The combustion efficiency of the benzene was beyond 99.999% even at an overall equivalence ratio of 1.0.

The controlled flame was found to be largely unaffected by moderate swirl although the stability was slightly reduced. Heavy swirl led to further reduction in stability and intermittent formation of soot. The unforced swirling flame was not nearly as efficient in reducing soot formation as the controlled (forced) flame without swirl.

Flow visualization, hot-wire measurements, and PIV showed that the external entrained air plays an important role in the controlled combustion process. In the low-sooting flame, a strong vortex was formed close to the flame base, entraining a large amount of external air into the flame very close to its base. Blockage of this entrained air resulted in the loss of the control authority. This fact was especially significant in an enclosed system in which the amount of entrained air was limited by the geometry of the system.

It was shown that the naturally entrained air could be substituted by adequate injection of air at the base of the flame. This injection had to be at the proper angle, speed, flow rate, and location to be effective. By using this method, it was possible to regain control in an open system in which the entrainment was blocked, and in enclosed systems. The amount of entrained air needed to regain control is 30% of the main flow.

ACKNOWLEDGMENTS

REFERENCES

1. Broadwell, J. E., and R. E. Breidenthal. 1982. A simple model of mixing and chemical reaction in a turbulent shear layer. *J. Fluid Mechanics* 125:397–410.
2. Chen, T. H., and L. P. Goss. 1989. Flame lifting and flame/flow interactions of jet diffusion flames. AIAA Paper No. 89-0156.
3. Yule, A. J. Chigier, S. Ralph, R. Boulderstone, and J. Ventura. 1981. Combustion–transition interaction in a jet flame. *AIAA J.* 19:752–60.
4. Gutmark, E., T. P. Parr, D. M. Hanson-Parr, and K. C. Schadow. 1988. Evolution of vortical structures in flames. *22nd Symposium (International) on Combustion Proceedings.* Pittsburgh, PA: The Combustion Institute. 523–29.
5. Ho, M., and P. Huerre. 1984. Perturbed free shear layers. *Annual Reviews Fluid Mechanics* 16:365.
6. Strawa, W., and B. I. Cantwell. 1985. Investigation of an excited jet diffusion flame at elevated pressure. *J. Physics Fluids* 28:2319–20.
7. Chen, L. D., J. P. Seaba, W. M. Roquemore, and L. P. Goss. 1988. Buoyant diffusion flames. *22nd Symposium (International) on Combustion Proceedings.* Pittsburgh, PA: The Combustion Institute. 677–84.

8. Brown, L., and A. Roshko. 1974. On density effects and large structure in turbulent mixing layers. *J. Fluid Mechanics* 64:775–816.

9. Crow, S. C., and F. H. Champagne. 1971. Orderly structure in jet turbulence. *J. Fluid Mechanics* 48:547–91.

10. Winant, D., and F. K. Browand. 1974. Vortex pairing, the mechanism of turbulent mixing-layer growth at moderate Reynolds number. *J. Fluid Mechanics* 63:237–55.

11. Glassman, I. 1987. *Combustion.* 2nd ed. San Diego, CA: Academic Press.

12. Peters, N., and F. A. Williams. 1983. Liftoff characteristics of turbulent jet diffusion flames. *AIAA J.* 21:423–29.

13. Vandsburger, V., G. Lewis, M. Seitzman, M. G. Allen, C. T. Bowman, and R. K. Hanson. 1986. Flame-flow structure in an acoustically driven jet flame. *Western States Section Proceedings.* Paper No. 86-19. Pittsburgh, PA: The Combustion Institute.

14. Gutmark, E., T. P. Parr, D. M. Hanson-Parr, and K. C. Schadow. 1988. Three-dimensional structure of an axisymmetric reacting jet. AIAA Paper No. 88-0148.

15. Gutmark, E., T. P. Parr, D. M. Hanson-Parr, and K. C. Schadow. 1990. Use of chemiluminescence and neural networks in active combustion control. *23rd Symposium (International) on Combustion Proceedings.* Pittsburgh, PA: The Combustion Institute. 1101–6.

16. McManus, K. R., V. Vandsburga, and C. T. Bowman. 1990. Combustor performance enhancement through direct shear layer excitation. *Combustion Flame* 82:75–92.

17. Gutmark, E., T. P. Parr, D. M. Hanson-Parr, and K. C. Schadow. 1994. Control of sooty high-energy fuel combustion. *Spring Meetings of the Western States Section Proceedings.* Pittsburgh, PA: The Combustion Institute.

18. Gutmark, E., T. P. Parr, and D. M. Hanson-Parr. 1995. Synchronized acoustic excitation of fuel and oxidizer for efficient combustion. *16th CEAS/AIAA Aeroacoustics Conference Proceedings.* Munich, Germany.

19. Lozano, A., B. Yip, and R. K. Hanson. 1992. Acetone: A tracer for concentration measurements in gaseous flows by planar laser-induced fluorescence. *Experiments Fluids* 13:369–76.

20. Ni, T., J. A. Pinson, S. B. Gupta, and R. J. Santoro. 1995. 2-Dimensional imaging of soot volume fraction using laser induced incandescence. *Applied Optics* 34:7083–91.

21. Ni, T., S. B. Gupta, and R. J. Santoro. 1994. *25th Symposium (International) on Combustion Proceedings.* Pittsburgh, PA: The Combustion Institute. 585–92.

22. Goss, L. P., *et al.* 1991. Two-color particle velocimetry. *J. Laser Appl.* 3:36.

23. Post, M. E., and L. P. Goss. 1993. Two-color particle-imaging velocimetry in vortex structures. *31st Aerospace Sciences Meeting Proceedings.* AIAA Paper No. 93-0412.

24. Adrian, R. J. 1986. Image shifting technique to resolve directional ambiguity in double pulsed velocimetry. *Applied Optics* 25:3855.

25. Lourenco, L., and A. Krothapalli. 1994. Application of PIV in high-speed wind tunnel testing. *32nd Aerospace Sciences Meeting Proceedings.* AIAA Paper No. 94-0084.

Chapter 7

COMBUSTION OF HIGH-ENERGY FUELS
IN AN AXISYMMETRIC RAMJET

K. Kailasanath and E. Chang

Understanding the combustion of high-energy fuels could lead to a major breakthrough in the quest to attain increased range and speed for missiles and other Navy propulsion systems. Numerical simulations can play a major role in developing this understanding. With this objective, a new computational model has been developed for simulating the combustion of these high-energy fuels. The fuel droplets are considered to be multicomponent, consisting of a solid cubane core surrounded by a liquid phase carrier. The fuel droplets' position in the flow field is computed by solving the Lagrangian equations of motion for the droplets taking into account the inertial drag force that depends on the droplet size and density. Simulations using this newly developed model have been used to study the differential dispersion of fuel droplets of various sizes, soot control strategies such as timed fuel injection, and the effects of microexplosion. These simulations indicate that microexplosions of high-energy fuels can cause significant flow disruption and amplification or attenuation of pressure fluctuations. When there is a strong coupling between the energy released and the low-frequency pressure fluctuations in the system, there is a tendency towards combustion instability. Phase-coupled fuel injection has been demonstrated as a means to suppress incipient combustion instabilities.

7.1   INTRODUCTION

A new class of high-energy fuels based on strained hydrocarbons is being developed. Thorough understanding of the combustion of these fuels is needed in order to achieve a major breakthrough in the quest to attain increased range and speed for missiles and other Navy propulsion systems. The properties of high-energy fuels responsible for their excellent performance characteristics also

imply challenging combustor development problems. For example, some of these fuels tend to microexplode and rapidly release their energy and this introduces a new concern because microexploding fuels have not been tested and evaluated in closed combustion systems such as those relevant to the Navy. Another basic characteristic of most of the proposed fuels is their propensity to soot. Therefore, techniques such as vortical control and timed fuel injection are investigated to control the formation and destruction of soot. Some of these fuels are also not in liquid form at standard operating temperatures. If they are diluted in some other liquid fuel, one has to burn it as a slurry or if the base fuel quickly vaporizes, as a gaseous fuel with distributed condensed particles of high-energy fuels. The mixing and combustion characteristics of such a multiphase mixture need to be understood.

There have been numerous studies on droplet motion and vaporization in a flow. Early studies focused on the vaporization and combustion of single droplets with little emphasis on the fluid flow (e.g., [1, 2]). Detailed description and discussion of these models and other early work can be found in several excellent review articles [3–6]. More recent studies have considered the detailed dynamics of jets, but have focussed on particles with constant diameter [7–11]. Studies in which various vaporization models have been included in the simulation of droplet-laden jet flows and sprays [12–16] are of more interest to us. However, for flows seeded with strained hydrocarbon based high-energy fuels, knowledge is limited because they have not yet been available in large quantities to conduct extensive experiments. Therefore, numerical simulations provide an ideal means to gain a better understanding of the mixing and combustion characteristics of these high-energy fuels. These numerical simulations require input concerning the physical and chemical characteristics of the fuels and these can be obtained from limited experiments using small quantities of the fuels. However, even if these input data were available when this study was initiated, there were no numerical models readily available that could be used to simulate the dynamic interaction between large-scale vortex structures and vaporizing and microexploding droplets of high-energy fuels. The significant accomplishment reported in this paper is the development of such a capability and the performance of relevant time-dependent numerical simulations that address several basic issues in the combustion of high-energy fuels.

Although several different system configurations have been simulated, the focus of this paper will be on the unsteady, compressible, multiphase flow in an axisymmetric ramjet combustor. After a brief discussion of the details of the geometry and the numerical model in the next section, a series of numerical simulations in which the physical complexity of the problem solved has been systematically increased are presented. For each case, the significance of the results for the combustion of high-energy fuels is elucidated. Finally, the overall accomplishments and the potential impact of the research for the simulation of other advanced chemical propulsion systems are discussed.

7.2   THE NUMERICAL MODEL

The geometry of the ramjet system simulated is shown in Fig. 7.1, which consists of a cylindrical inlet connected to a central dump combustor that has an exhaust nozzle. This specific geometry was chosen because extensive studies have been made in the past of the interaction between acoustics, vorticity dynamics, and chemical energy release in this system [17–20]. These earlier gas-phase flow studies are very helpful in interpreting the current multiphase flow simulations.

The flow into the central dump combustor is computed by solving the compressible, time-dependent, conservation equations for mass, momentum, and energy using the Flux-Corrected Transport (FCT) algorithm [21], a conservative, monotonic algorithm with fourth-order phase accuracy. No explicit term representing physical viscosity is included in the model.

No artificial viscosity is needed to stabilize the algorithm due to the residual numerical diffusion present, which effectively behaves like a viscosity term for short wavelength modes on the order of the zone size. This damping of the short wavelengths is nonlinear and the effects of the residual viscosity diminish very quickly for long wavelength modes resulting in a very high effective Reynolds number.

This approach called MILES (monotonically integrated large-eddy simulation) is described in detail elsewhere [22]. This is the same approach used in previous simulations of ramjet combustor flows [17–20].

The particles' position in the flow field is computed by solving the Lagrangian equations of motion for the particles with the inertial drag force, dependent on the density and size of the particles taken into account.

Details of the model as well as more comprehensive discussion of the various cases simulated have been published elsewhere [23–26] and only the highlights and the overall significance of the work are presented here.
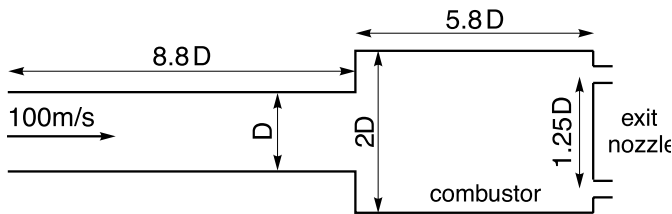
Figure 7.1 Geometry of the idealized axisymmetric combustor used for the numerical simulations. $D = 6.35$ cm

7.3 RESULTS AND DISCUSSION

For a typical case, an axisymmetric jet with a mean velocity of 100 m/s flows through the cylindrical inlet of diameter D into a cylindrical combustion chamber of twice the diameter. An annular or central exit at the end of the combustion chamber is modeled to produce choked flow. Particles are injected from the inlet–combustor junction with a streamwise velocity of 50 m/s and zero radial velocity. If the number of particles is small (that is, for low-mass loadings), the effect of the particles on the flow can be neglected. Still the flow has an effect on the particles that depends on parameters such as the size and density of the particles. Such systems are called one-way coupled systems and are discussed next.

7.3.1 One-Way Coupled Systems

In Fig. 7.2, vorticity contours and particle positions within the combustor for particles of different sizes are shown at a particular time, 20,000 timesteps ($\sim$ 7.5 ms) from the start of the simulations. Since the system is axisymmetric, only the upper half of the flow field is shown. The vorticity contours (Fig. 7.2a) clearly show the presence of large-scale vortical structures that merge or pair as they convect downstream. The other three frames in the figure highlight the distinctly different interactions between the large-scale vortical structures and particles of different sizes. Very small particles such as the 1 μm particles (Fig. 7.2b) closely track the vortical structures and are a good marker for the flow field itself. Very large particles such as the 30 μm particles are not strongly affected by the structures while the intermediate size particles show a strong interaction in the sense that they appear to form distinct sheets as they are entrained along the outer regions of the vortical structures and are then flung out. These observations support the different mechanisms for particle dispersion postulated in the earlier study of particle dispersion in axisymmetric jets [2]. The significance of these results is twofold. First, for applications such as laser diagnostics, it indicates that the size of the seeding particles must be small enough for tracking the flow and be useful as a flow visualization indicator. The specific size to be used depends on the flow velocity and other flow field dynamics, as discussed below. The second significant implication of these results is that intermediate sized particles are dispersed more than the very small particles that track the flow. Similar results have been observed before in mixing layers and free jets, but it is interesting that it carries over to confined systems where the acoustics of the system also interacts with the flow field.

To generalize the above results, it is convenient to invoke the nondimensional Stokes number (St) which is a ratio of the particle response time to a characteris-
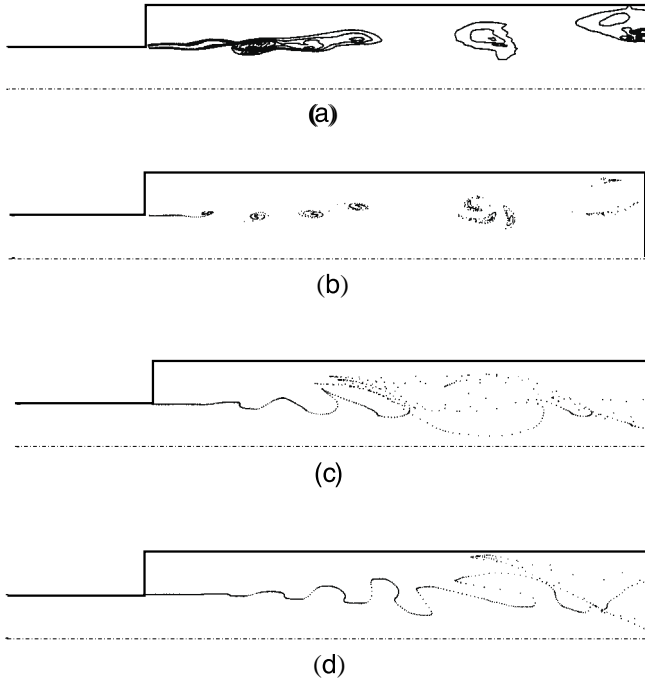
Figure 7.2 Instantaneous visualization of vorticity contours (a), and locations of 1 μm (b), 15 μm (c), and 30 μm (d) diameter particles

tic flow time. Quantitative studies of the dispersion of the particles show that the dispersion is maximized at Stokes numbers on the order of unity when the particles that have been deposited on the walls are neglected. The dominant role of vortex shedding was further confirmed when the Fourier analysis of the particle dispersion at various locations in the combustor showed that the vortex-shedding frequency characterizes the dispersion, even at locations where the merging frequency governs the local fluid flow. This property is observed for all particle sizes studied except for cases at very low-Stokes numbers, where traces of the merging frequency, as well as the harmonic associated with combining the merging and shedding frequencies, were observed. A correlation between particle size and flow vorticity has also been obtained and shows that high concentrations of particles can be associated with high vorticity for small particles while the opposite is true for moderate to large sized particles. With the insight from these simulations on the mechanisms responsible for the enhanced dispersion, additional studies were performed to enhance or suppress the dispersion as both may be desired in specific situations.

7.3.2 Effects of Acoustic Forcing

Based on the initial studies of unforced flows described above, inflow was selectively perturbed to investigate if the amount of particle dispersion and the location of enhanced dispersion within the combustor can be shifted as desired. Calculations were performed in which an acoustic perturbation was imposed from the back wall of the combustor with an amplitude of 0.5% of the initial chamber pressure and a frequency of 1380 Hz, 690 Hz, or 145 Hz, the characteristic frequencies of the system under study. The vortex-shedding frequency was 1380 Hz, the first-merging frequency was 690 Hz, and 145 Hz was the quarter-wave mode of the inlet. In addition, simulations were also performed with forcing at a frequency unrelated to the system, 1000 Hz. The particle size chosen for these simulations was 15 μm in diameter (St = 0.97), since this size particles were found to be optimally dispersed in the unforced flow case. All other parameters remain unchanged from the unforced case discussed above.

Forcing at the shedding frequency has the greatest initial effect on dispersion. In the front region of the combustor this is the characteristic frequency in the shear layer and governs the dispersion. The forcing enhances development of the flow structures (vortex shedding) and increases lateral dispersion via larger centrifugal effects. As particles travel farther downstream, the characteristic flow frequency changes from the shedding to the merging frequency. Therefore forcing at the merging frequency has some effect at locations away from the step in the combustor. Similarly, forcing at the inlet mode (145 Hz), which exists at a low level throughout the combustor, has only a small effect. Finally, forcing at 1000 Hz did not lead to enhancement of any flow structures and no significant gains in dispersion were achieved.

7.3.3 Timed Fuel Injection

To further control the particle dispersion, the particle (which simulates the fuel) injection was timed in or out of phase with the forcing at the shedding frequency of 1380 Hz. The injection rate is increased to one every 5 time-steps, but occurs only when the pressure perturbation is either positive (in phase) or negative (out of phase). Thus the average injection rate remains the same as in the previous cases. Figure 7.3 shows the dispersion for injecting in and out of phase with the forcing frequency. Dispersion is increased when injection is in phase with the forcing, because the particles travel downstream with the flow structures. Similarly, decreased dispersion is observed when injecting out of phase. Here, particles are injected "in between" flow structures and centrifugal effects are minimized.
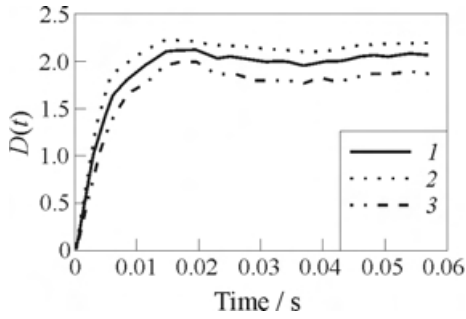
Figure 7.3 Time history of dispersion for 15 μm particles injected in and out of phase with the forcing at 1380 Hz: *1* — 1380 Hz, *2* — 1380 Hz in phase, and *3* — 1380 Hz out of phase
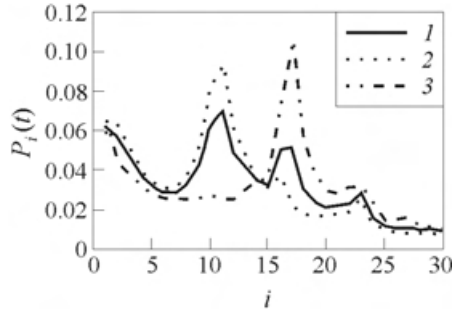
Figure 7.4 Time averaged axial distribution of 15 μm particles when injected continuously and in and out of phase with the forcing frequency of 1380 Hz. *1* — continuous, *2* — in phase, and *3* — out of phase

The time averaged axial particle distribution is shown in Fig. 7.4. Injection in phase with the extended forcing increases dispersion, and a higher percentage of particles do not travel as far downstream. Axial distribution is weighted to the front of the combustor. Conversely, injecting out of phase allows particles to travel much further downstream. This demonstrates that by suitably choosing the forcing frequency and timing the fuel injection, enhanced dispersion of particles can be achieved at different locations in the combustor as desired for particular applications. For example, in compact ramjet systems we would like the fuel to be dispersed and mixed and burnt quickly, and hence in-phase timed injection of fuel will be beneficial.

7.3.4 Two-Way Coupled Systems

In many practical applications, the amount of particles or droplets would be large enough that the effects on the flow are not negligible. That is, two-way coupling needs to be considered. In order to take the effect of the particles on the gas-phase flow into account, the particle momentum and energy are calculated for each particle location and a linear weighting scheme based on cell volume is used to find the corresponding source terms for the gas-phase calculation at the surrounding grid locations. Two different techniques are employed in order to achieve significant particle mass loadings (particle mass flux in / gas-phase mass flux in). In both, 1024 equally distributed azimuthal locations are assumed. In the first technique, which is referred to as the direct simulation method, 16 radial

injection locations are used per azimuthal position. The first radial injection location is at the combustor step and each subsequent location is 194.4 μm from the previous location, inwards toward the combustor center. This guarantees at least a 10 particle radius separation upon injection for the largest sized particles used (32.4 μm diameter). As the surface generated vorticity associated with each particle decays at a minimum rate (Stokes flow) of $1/r^2$, where r is the distance from the particle, this spacing should be adequate for neglecting the presence of neighboring particles. For higher particle Reynolds numbers, this decay would be even faster. With this method, it was possible to obtain "real" mass loadings of up to 20% using 32.4 μm diameter particles.

The second technique involves the use of "ghost" or "virtual" particles. This is a method commonly used to obtain higher mass or volume loading without the necessary computational expense of tracking every particle in the system (e.g., as in [15]). Instead, each particle in the simulation acts as a marker for a group of virtual particles with a center of mass located at the simulation particle's position. It is assumed that each of the virtual particles has the same size and mass of the simulation particle but its velocity and location are not explicitly calculated as it is assumed to move with its associated marker particle's velocity and position. However, the momentum and energy from the virtual particles are included in the coupling feedback source terms and are assumed to be located at the same position as the marker particle. Thus, similar mass loadings as in the direct simulation method can be achieved at a fraction of the computational cost. In the simulations, 15 virtual particles were used for each simulation particle and were injected either at the step corner (equivalent to the outer edge of the particle stream used in the direct simulation method), at $r = 3.01$ cm (equivalent to the center of the particle stream used in the direct simulation method), or at $r = 2.88$ cm (equivalent to the inner edge of the particle stream used in the direct simulation method). For the direct simulation method, particle diameters of 1.5, 15, and 32.4 μm corresponding to 0.001%, 1%, and 10% mass loading were used while for the virtual particle method only 32.4 μm diameter particles were used. Flow modulation effects, due to the increased mass loading and the differences observed between the two methods, are addressed below.

7.3.5   Direct Simulation Method

The effects of higher mass loading on the flow structure and composition using the direct simulation method can be seen in Fig. 7.5, where the time averaged RMS fluctuating velocity in the shear layer (at $r = 3.175$ cm) is shown as a function of downstream axial distance. The amplitude of the fluctuations decreases significantly as the particle size, and therefore the mass loading, are increased. This attenuation is also observed in the magnitude of the vortex-shedding fre-
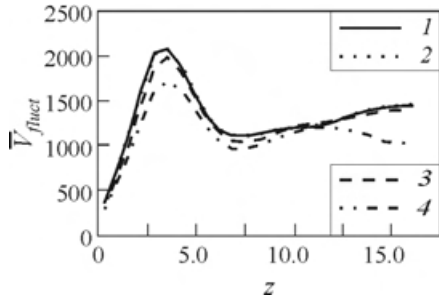
Figure 7.5 Axial variation of the time averaged RMS fluctuating velocity in the shear layer. *1* — no particles, *2* — 0.001% mass loading, *3* — 1% mass loading, and *4* — 10% mass loading
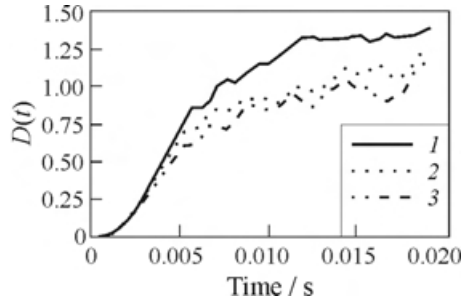
Figure 7.6 Effect of injection location on the time history of dispersion when using the virtual particle technique. *1* — $r_{inj} = 3.175$ cm; *2* — 3.01 cm; and *3* — 2.84 cm

quency. The frequency itself remains at 1380 Hz. Although the amplitude of the shedding frequency remains essentially unchanged for 0.001% mass loading, it decreases substantially at higher loadings, indicating significant attenuation of the intensity of the shed vortices.

7.3.6 Virtual Particle Simulation Method

Figure 7.6 shows the dispersion for the three different injection locations used for the virtual particle simulations. As expected, dispersion is highest when injecting at the center of the shear layer ($r = 3.175$ cm) and decreases as the injection location is moved inward towards the axis of symmetry and away from the shear layer center. When using the virtual particle technique, a small shift in the vortex shedding and merging frequencies, not seen in the previous direct simulations, can be observed even though the mass loading remains the same. For example, a decrease in the flow fluctuation frequency is seen when injecting at a radius less than that of the combustor step. Because the gas-phase flow velocity increases with decreasing radius, particles that are injected closer to the center of the combustor extract more momentum. This leads to a decrease in the relative gas-phase flow velocity difference between the inner (above the step), higher speed and outer (below the step), lower speed regions of the combustor and a consequent thickening of the shear layer. A thicker shear layer results in a reduction in the vortex-shedding frequency. Noticeable differences in the fluctuating velocities in the shear layer are also observed with the virtual particle

simulation method. Therefore, this method must be used with some caution even though it saves significant computer time.

7.3.7   Effects of Droplet Vaporization

So far the discussion has focused on gas–particle flows. However, the combustion of high-energy and other fuels used in propulsion usually involves liquid droplets that vaporize and burn as they are convected by the flow. The general treatment of gas–particle flows presented above is still valid for this case, because most of these models assume that information at the droplet level is included as a sub-model. These sub-models are usually derived primarily from studies of single-droplet vaporization and combustion. Some of the common droplet models in use are those based on the d^2-law and the infinite conductivity model for heat transfer. These have been included and studies have been carried out to ascertain the effect of vaporization on the droplet dispersion in the axisymmetric combustor considered here. The primary conclusion from these studies is that the initial trajectories of the particles or droplets are the same and depend on the initial size chosen. For example, starting with droplets (particles) of size 50 μm, the initial trajectories of the droplets or particles are not affected by the flow due to the inertia of the large droplets. However, in the case of the vaporizing droplet, the size reduces and soon there is stronger interaction with the flow structures, and by the time the droplets reach a third of the combustor they have been flung out of the vortical flow. These results indicate that one must be careful in generalizing observations based on constant-size particles for application to flows involving vaporizing droplets.

7.3.8   Effects of Microexplosions

The fact that the combustion of high-energy fuels is more complex than those of conventional liquid fuels has been shown by the experiments of Law [27] on the burning of monodisperse droplet streams of high-energy fuels (such as cubane 1,4-dimethyl ester) diluted in a carrier liquid, benzene. Those experiments showed that the benzene gasifies first, leaving behind a droplet rich with cubane which then microexplodes rapidly, releasing the stored energy.

To represent the above phenomena, the present simulations consider the fuel droplets to be multicomponent, consisting of a solid high-energy fuel core surrounded by a liquid carrier. For example, cubane has been used as the core material embedded in n-heptane. n-Heptane was chosen because of the availability of experimental data, but in principle any other carrier liquid could be used in the model. An infinite conductivity model is used to account for droplet
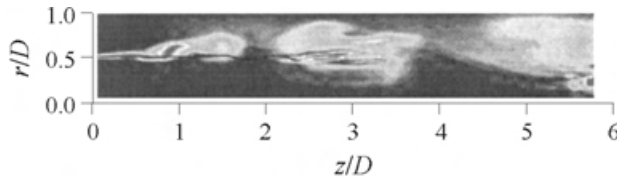
Figure 7.7 Vorticity distribution and droplet positions in combustor with microexploding droplets

heating and vaporization. The energy released during the microexplosion has been obtained from thermodynamic considerations such as those discussed by Davis [28].

In the simulations, the droplets are assumed to have a lifetime shorter than that for the entire surrounding liquid to evaporate. This appears to be a good approximation based on experiments [27] which show that the change in droplet size can be approximated by that of the theoretical regression rate of a droplet composed only of the surrounding fluid. In the simulations, each droplet is assumed to have a lifetime based on the fractional value of the droplet size at a given time compared to its original size. When this threshold is reached the droplet is allowed to microexplode. This microexplosion is modeled as an extra source of energy added to the flow based on the mass of the cubane core.

The effects of the rapid energy release from the droplet microexplosions on the flow field can be seen in Fig. 7.7. Initially, vortex structures in the immediate area of the microexplosions are disrupted. An examination of the pressure field shows that an area of high pressure is formed in the vicinity of the microexplosions. This high-pressure region alters the path of vortex structures and the large vortices are seen to migrate radially outward, toward the combustor wall, as they travel downstream past the microexploding droplets. The pressure waves also travel back towards the inlet (and forward to the nozzle) and are partially reflected. With time, the smaller, tightly grouped, vortex structures in the front region of the combustor disappear, indicating vortex shedding at a different frequency.

Figure 7.8 shows the changes in the Fourier composition of the radial gas-

Figure 7.8 Fourier spectrum of radial velocity fluctuations in the shear layer for unseeded flow and fully developed flow with microexploding droplets: *1* — no particles; *2* — particles

phase flow velocity in the shear layer due to the microexplosions. The characteristic shedding frequency (1360 Hz) as well as the acoustic quarter wave inlet mode at 320 Hz are evident in the unseeded case. However, for the microexploding case the flow has coupled to the acoustic mode creating large-scale flow structures at the lower frequency. In addition, the inlet mode has shifted to a slightly higher frequency, in this case to 340 Hz. This is due to an increase in the combustion chamber pressure (and sound speed) caused by the energy release. Further effects of microexplosions on the flow field are discussed next.

7.3.9   Effects of the Size of the Microexploding Droplet

A key parameter in multiphase combustion is the droplet size. By varying the droplet size, the lifetime of the droplet can be changed. The change in the lifetime will change the location of microexplosion and hence the location of energy release. The coupling between the energy release and the pressure fluctuations may change when the location of the energy release is changed and this could result in significant changes in the flow field and the tendency of the system towards combustion instabilities.

The effects of microexplosions of droplets of two different initial diameters (but same core size) are shown in Fig. 7.9. The flow fields are significantly different in the two cases. In the first case (Fig. 7.9a), there is some local effect on the flow field but the overall flow is quite similar to the nonmicroexploding case. When the initial droplet diameter is 50 μm, the droplet lifetimes

(a)

(b)
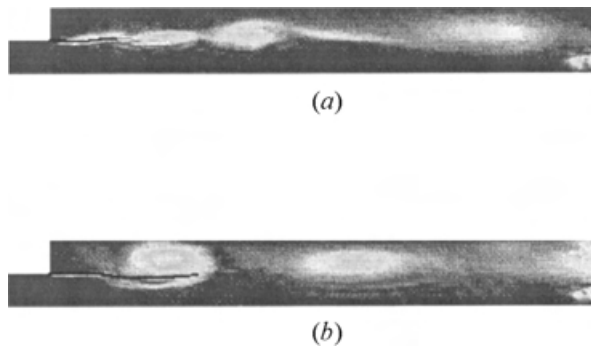
Figure 7.9 Vorticity distribution and droplet locations for microexploding droplets of initial diameter 35 μm (a) and 50 μm (b).

are longer and they microexplode further downstream. In this case (Fig. 7.9b), the flow field is drastically altered and is now composed of fewer and larger vortical structures. Detailed analysis of these simulations [26] shows that in this case, the low-frequency quarter-wave mode of the inlet has been excited and the shear layer at the inlet–combustor junction is essentially forced at this frequency. Further energy release in these larger structures sustains this low-frequency oscillation.

7.3.10   Effects of Core Size

In another series of simulations, the overall droplet size was kept constant at 50 μm while the core size was varied from 1 μm to 25 μm. By varying the core size, the amount of energy released was varied. The location of energy release is essentially the same since it depends primarily on the overall droplet size. Some variation in the location is to be expected since the droplet lifetimes also depend on the temperature field which could change based on the amount of energy released. However, this is only a secondary effect since the amount of droplets in the flow field is small. Results from this series of simulations showed that even a small amount of energy release, such as from the 1-micron core case, could significantly amplify the pressure fluctuations at the low frequency. For the smaller core sizes (1, 5, and 10 μm), the amplification of the low-frequency oscillation was prominent only for locations near the step in the combustor while for larger core sizes (20 and 25 μm) the low-frequency mode was noticeably amplified also at a location further downstream in the combustor.

7.3.11   Phase-Coupled Fuel Injection

As discussed earlier, the particle/droplet dynamics can be significantly modified by timing the fuel injection to be in- or out-of-phase with the large-scale vortex structures. To explore if timed fuel injection could alter the stability characteristics, the flow was forced at the quarter-wave mode of the inlet and droplet injection was timed to be in- or out-of-phase with the forcing. Results from these simulations show that the pressure fluctuations at the quarter-wave mode of the inlet can indeed be amplified or attenuated depending on the phasing of the droplet injection.

This result along with the studies on the effect of core size, which show that a small amount of energy release can make a significant change in the amplitude of pressure fluctuations, suggests that high-energy fuels may be a good candidate for use as a secondary fuel-injection source to suppress combustion instabilities in systems operating primarily with a different fuel source. This

idea has been explored further and demonstrated in simulations that use a small amount of high-energy fuels in a system burning premixed propane–air mixtures.

7.4 CONCLUDING REMARKS

In summary, a computational model has been developed for the simulation of the combustion of high-energy fuels. The unsteady gas-phase flow in the combustor is computed by solving the conservation equations for mass, momentum, and energy using the Flux-Corrected Transport (FCT) algorithm. The fuel droplets' position in the flow field is computed by solving the Lagrangian equations of motion for the droplets taking into account the inertial drag force that depends on the droplet size and density. The fuel droplets are considered to be multicomponent, consisting of a solid cubane core surrounded by a liquid phase carrier.

Using this newly developed model, simulations have been carried out to address several basic issues in the combustion of high-energy fuels. The time and location where the droplets microexplode have been varied by changing the size of the droplets. The amount of energy released has been varied by changing the core size. These simulations indicate that even a small amount of energy release can significantly alter the level of pressure fluctuations in the combustor. In general, microexplosions of high-energy fuels can cause significant flow disruption and amplification or attenuation of pressure fluctuations. When there is a strong coupling between the energy released and the low-frequency pressure fluctuations in the system, there is a tendency towards combustion instability. Phase-coupled fuel injection has been explored as a means to suppress incipient combustion instabilities. The simulations have also been used to study the differential dispersion of fuel droplets of various sizes and soot control strategies such as timed fuel injection. Another general use of the developed capability is to investigate a variety of other problems involving multiphase flow and combustion in chemical propulsion systems.

ACKNOWLEDGMENTS

REFERENCES

1. Law, C. K., and F. A. Williams. 1972. Kinetics and convection in the combustion of alkane droplets. *Combustion Flame* 19:393–405.

2. Aggarwal, S. K., A. Y. Tong, and W. A. Sirignano. 1984. A comparison of vaporization models in spray calculations. *AIAA J.* 22:1448–57.

3. Williams, F. A. 1973. Combustion of droplets of liquid fuels: A review. *Combustion Flame* 21:1–31.

4. Faeth, F. M. 1977. Current status of droplet and liquid combustion. *Progress Energy Combustion Science* 3:191–224.

5. Law, C. K. 1982. Recent advances in droplet vaporization and combustion. *Progress Energy Combustion Science* 8:171–201.

6. Sirignano, W. A. 1983. Fuel droplet vaporization and spray combustion theory. *Progress Energy Combustion Science* 9:291–322.

7. Chung, J. N., and T. R. Trout. 1988. Simulation of particle dispersion in an axisymmetric jet. *J. Fluid Mechanics* 186:199–222.

8. Longmire, E. K., and J. K. Eaton. 1992. Structure of a particle-laden round jet. *J. Fluid Mechanics* 236:217–57.

9. Uthuppan, J., S. K. Aggarwal, F. F. Grinstein, and K. Kailasanath. 1994. Particle dispersion in a transitional axisymmetric jet: A numerical simulation. *AIAA J.* 32:2040–48.

10. Chang, E. J., and K. Kailasanath. 1995. Heavy particles in a confined high-speed shear flow. In: *Gas–solid flows*. ASME-FED 228:3–8.

11. Yu, K., K. J. Wilson, T. P. Parr, R. A. Smith, and K. C. Schadow. 1996. Characterization of pulsating spray droplets and their interaction with vortical structure. AIAA Paper No. 96-0083.

12. Faeth, G. M. 1983. Evaporation and combustion of sprays. *Progress Energy Combustion Science* 9:1–77.

13. Chiarig, C. H., M. S. Raju, and W. A. Sirignano. 1989. Numerical analysis of convecting, vaporizing fuel droplet with variable properties. AIAA Paper No. 89-0834.

14. Continello, G., and W. A. Sirignano. 1990. Counterflow spray combustion modeling. *Combustion Flame* 81:325–40.

15. Raju, M. S., and W. A. Sirignano. 1990. Multicomponent spray computations in a modified centerbody combustor. *J. Propulsion Power* 6:97–105.

16. Aggarwal, S. K., and S. Chitre. 1991. Computations of turbulent evaporating sprays. *J. Propulsion Power* 7:213–20.

17. Kailasanath, K., J. H. Gardner, J. P. Boris, and E. S. Oran. 1987. Numerical simulations of acoustic–vortex interactions in a central-dump ramjet combustor. *J. Propulsion Power* 3:525–33.

18. Kailasanath, K., J. H. Gardner, E. S. Oran, and J. P. Boris. 1988. Numerical simulations of high-speed flows in an axisymmetric ramjet. AIAA Paper No. 88-0339.

19. Kailasanath, K., J. H. Gardner, J. P. Boris, and E. S. Oran. 1989. Acoustic–vortex interactions and low-frequency oscillations in axisymmetric combustors. *J. Propulsion Power* 5:165–71.

20. Kailasanath, K., J. H. Gardner, E. S. Oran, and J. P. Boris. 1991. Numerical simulations of unsteady reactive flows in a combustion chamber. *Combustion Flame* 86:115–34.

21. Boris, J. P., and D. L. Book. 1976. *Methods of computational physics*. Ch. 11. NY: Academic Press 16:85–129.

22. Boris, J. P., F. F. Grinstein, E. S. Oran, and R. L. Kolbe. 1992. New insights into large eddy simulation. *Fluid Dynamics Research* 10:199–228.

23. Chang, E. J., and K. Kailasanath. 1996. Simulations of particle dynamics in a confined shear flow. *AIAA J.* 34:1160–66.

24. Chang, E. J., and K. Kailasanath. 1996. Behavior of heavy particles in an acoustically forced confined shear flow. *AIAA J.* 34:2429–31.

25. Chang, E. J., K. Kailasanath, and S. K. Aggarwal. 1995. Compressible flows of gas–particle systems in an axisymmetric ramjet combustor. AIAA Paper No. 95-2561.

26. Chang, E. J. and Kailasanath, K. 1997. Dynamics and microexplosion of high-energy fuels injected into a combustor. AIAA Paper No. 97-0126.

27. Law, C. K. 1994. Combustion studies of energetic liquid materials. *7th ONR Propulsion Meeting Proceedings*. Eds. G. Roy and P. Givi. Buffalo, NY: State University of New York at Buffalo. 100–116.

28. Davis, S. R., P. L. Tan, W. E. Owens, and W. T. Webb. 1994. Reaction pathways and energetics for combustion of high-energy fuels. *7th ONR Propulsion Meeting Proceedings*. Eds. G. Roy and P. Givi. Buffalo, NY: State University of New York at Buffalo. 91–103.

Chapter 8

COMBUSTION OF ALUMINUM WITH STEAM FOR UNDERWATER PROPULSION

J. P. Foote, B. R. Thompson, and J. T. Lineberry

Results of an experimental program in which aluminum particles were burned with steam and mixtures of oxygen and argon in small-scale atmospheric dump combustor are presented. Measurements of combustion temperature, radiation intensity in the wavelength interval from 400 to 800 nm, and combustion products particle size distribution and composition were made. A combustion temperature of about 2900 K was measured for combustion of aluminum particles with a mixture of 20%(wt.) O_2 and 80%(wt.) Ar, while a combustion temperature of about 2500 K was measured for combustion of aluminum particles with steam. Combustion efficiency for aluminum particles with a mean size of 17 μm burned in steam with $(O/F) / (O/F)_{st} \approx 1.10$ and with residence time after ignition estimated at 22 ms was about 95%. A Monte Carlo numerical method was used to estimate the radiant heat loss rates from the combustion products, based on the measured radiation intensities and combustion temperatures. A peak heat loss rate of 9.5 W/cm^3 was calculated for the O_2/Ar oxidizer case, while a peak heat loss rate of 4.8 W/cm^3 was calculated for the H_2O oxidizer case.

8.1 INTRODUCTION

Combustion of powdered aluminum with steam is a potentially attractive propulsion system for torpedoes, because of the very high-energy density (energy per unit volume) that can be achieved. Since the oxidizer can be taken from the environment, on-board storage is required only for the aluminum propellant. A study of potential torpedo propellant/oxidizer combinations including Al, Zr, Mg, and Li metals, hydrocarbon fuels, and typical solid rocket propellants, and

oxidizers including H_2O, H_2O_2, and $LiClO_4$ found that the Al/H_2O combination had the highest theoretical performance of any combination considered [1]. Additional calculations by the authors showed that B/H_2O and Be/H_2O combinations have higher specific energy than Al/H_2O; however, boron and beryllium are much less desirable fuels than aluminum in terms of cost and toxicity.

The concept of using aluminum combustion with seawater as a torpedo propulsion system has existed at least since the early 1940s, and research on this concept was conducted during the 1940s and continued through the early 1960s [1–5]. However, little past technical literature on the practical requirements for such a system has been discovered by the authors. Of particular interest are ignition requirements, combustor heat transfer, and residence time requirements for the combustion of powdered aluminum with steam. It is assumed that steam can be generated by using water as a combustor coolant, thus eliminating the need for vaporizing water in the combustor.

The goal of the present study is to provide the information needed for design of a practical underwater propulsion system utilizing powdered aluminum burned with steam. Experiments are being conducted in atmospheric pressure dump combustors using argon/oxygen mixtures and steam as oxidizers. Spectrometer measurements have been made to estimate combustion temperatures and radiant heat transfer rates, and samples of combustion products have been collected to determine the composition and particle size distribution of the products.

8.2 BACKGROUND

The combustion equation for aluminum and oxygen is

$$2Al(s) + 3/2 O_2(g) \rightarrow Al_2O_3(s) - 404.08 \text{ kcal/g-mole} \quad (298 \text{ K, 1 atm})$$
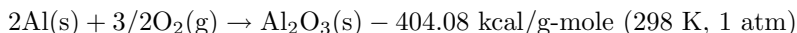
The heat of combustion amounts to 7483 cal/g of aluminum fuel and the adiabatic flame temperature calculated by the NASA chemical equilibrium program [6] is 4005 K. The combustion equation for aluminum and steam is

$$2Al(s) + 3H_2O(g) \rightarrow Al_2O_3(s) + 3H_2(g) - 230.69 \text{ kcal/g-mole} \quad (298 \text{ K, 1 atm})$$
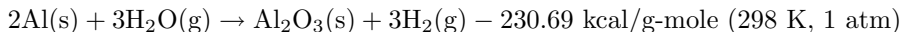
The heat of combustion amounts to 4272 cal/g of aluminum fuel and the adiabatic flame temperature calculated by the chemical equilibrium program is 3036 K. Thus, the heat released when aluminum is burned with steam is about 57% of the amount released when aluminum is burned with O_2. Many experimental investigations have been carried out on the combustion of aluminum in atmospheres where the primary oxidizer was O_2 [7–16], and also in atmospheres where the primary oxidizer was H_2O and/or CO_2 [16–19]. There is general

agreement in the literature that single aluminum particles burn with a detached spherical flame surrounding a liquid aluminum drop, with the combustion rate being limited by the rate at which heat and oxidizer can diffuse to the drop surface. In recent work, the radial profiles of AlO and Al_2O_3 concentrations and temperature have been measured around a single burning particle, confirming this basic view of how single aluminum particles burn [15].

The consensus concerning combustion of dense clouds of aluminum particles is not clear, owing to the difficulty in making measurements in these conditions. In general, as the concentration of aluminum particles increases the ignition time becomes less than that for a single particle at the same gas temperature, due to the additional supply of heat from particles already burning. Conversely, the burning time increases due to the depletion of oxidizer in the gas stream. According to [19], at a gas temperature of 2400 K and 50 atm pressure, the ignition time for 70 μm particles decreased from 5 ms to less than 1 ms when the aluminum concentration was increased from 0%(wt.) to 10%(wt.), while the burning time increased by a factor of 5–8.

Most sources agree that in order for an aluminum particle to ignite in an oxygen atmosphere, its temperature must be raised above the Al_2O_3 melting point $(2327 \pm 6$ K), since vaporization of the aluminum within is impeded by an oxide coating formed on the particle surface. Previous research indicates that the ignition temperature for aluminum particles in an H_2O atmosphere may be as low as 1600–1700 K [16, 18]. It has been suggested that the reduced ignition temperature in H_2O atmospheres may be due to formation of a less protective hydroxide or hydrated oxide layer on the particle surface.

8.3   EXPERIMENTAL PROCEDURE

Experiments were performed in refractory lined atmospheric pressure dump combustors. The inner diameter of the combustion chambers was 4 in., with a two- or three-inch thick high-alumina heavy castable refractory lining. The nominal aluminum powder flow rate was 5 g/s, for a nominal combustor heat release rate of 155 kW when using O_2 as oxidizer. *Reynolds* S–592 aluminum powder, with a volume average particle size of 17.3 μm, was used as fuel. Initial tests were performed using mixtures of 80%(wt.) Ar and 20%(wt.) O_2 as oxidizer and later tests were performed using superheated steam as oxidizer. Aluminum powder was supplied from a fluidized bed and was pumped into the combustor using an annular ejector. Part of the oxidizer (either argon or steam) was used as the ejector motive gas. The remaining oxidizer was added in the ejector tailpipe; so the aluminum/oxidizer stream entering the combustion chamber was premixed. Injection velocities of about 400 ft/s and 100 ft/s were used for the O_2/Ar and H_2O oxidizer tests, respectively.
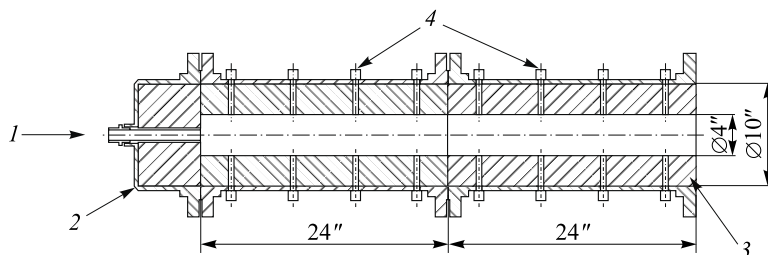
Figure 8.1 Experimental aluminum combustor. *1* — injector, *2* — removable head section, *3* — refractory lining, and *4* — optical ports

The O_2/Ar oxidizer tests and initial steam oxidizer tests were carried out in a 24-inch long combustion chamber. It was found that the 24-inch long combustion chamber did not provide enough residence time to complete combustion, so a 48-inch long combustion chamber was constructed. The 48-inch long combustor is shown in Fig. 8.1. The combustor was constructed from 10-inch carbon steel pipe with a 3-inch thick refractory lining. Eight sets of ports are provided at 6-inch spacing along the combustor axis for optical measurements and extraction of combustion product samples. The combustor has a removable head section to simplify cleanout of deposits between test runs. The premixed aluminum/steam mixture enters through a stainless steel tube 0.745-inch in inner diameter. About 10% of the steam is not premixed with the aluminum, but is introduced through an annulus surrounding the injection tube. This arrangement reduces melting of the fuel and buildup of recirculated combustion products at the injector exit. The combustor is cooled by water running over an external wick.

Argon and oxygen for O_2/Ar oxidizer tests were supplied from high-pressure gas bottles. Steam for H_2O oxidizer tests was supplied by a 150 psig electric steam boiler and was superheated to 600 °F using electric heaters. To start a H_2O oxidizer test run, the steam flow was first set to the required rate for the test condition. An amount of oxygen sufficient to complete combustion of the aluminum was then mixed with the steam, and a flow of propane into the combustor was initiated.

The combustor was ignited on propane. After a short period of operation on propane, aluminum flow was started and the propane flow was turned off. Once aluminum combustion was established, the oxygen flow was gradually decreased until only operation on H_2O could be sustained. Typically, one to two minutes of aluminum firing on an O_2/H_2O mixture was required before the combustor was warmed up enough to make H_2O only operation possible. Total duration of test runs was usually about 10 min. Preheating was not required for test runs using an O_2/Ar oxidizer.

8.4   RESULTS

8.4.1   Temperature and Radiation Intensity Measurements

Measurements of thermal radiation intensity were made in the wavelength range from 400 to 800 nm using a scanning spectrometer. The measured intensity distributions were then fitted to a gray-body intensity distribution using the Levenberg–Marquardt method to provide an estimate of combustion temperature. The temperature thus estimated is an average radiating temperature with contributions from Al_2O_3 particles, aluminum metal particles, gas emission, and the combustor walls. Radiation from the Al_2O_3 particles is expected to dominate, due to their high-temperature and surface area.

   A typical intensity distribution measured during a test run using an O_2/Ar oxidizer is shown in Fig. 8.2. The best fit to a gray-body intensity distribution is also shown. Spectra measured during combustion of aluminum with an O_2/Ar oxidizer typically had a considerable amount of structure at wavelengths shorter than about 600 nm, which is attributed to gas emission from partial oxidation products [20]. Due to the gas emission at the short wavelengths, the temperature fitting procedure was applied only in the region between 600 and 760 nm for O_2/Ar runs. Spectra measured during runs using an H_2O oxidizer did not include the short wavelength gas emission noted in the O_2/Ar runs. A typical intensity distribution measurement obtained during combustion of aluminum with an H_2O
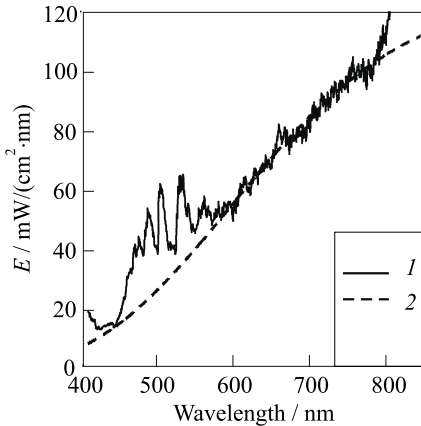
Figure 8.2 Typical measured hemispherical emissive power distribution for the O_2/Ar oxidizer test. *1* — Port 7 Data, *2* — Fit: $T = 2887$ K, EM = 0.46
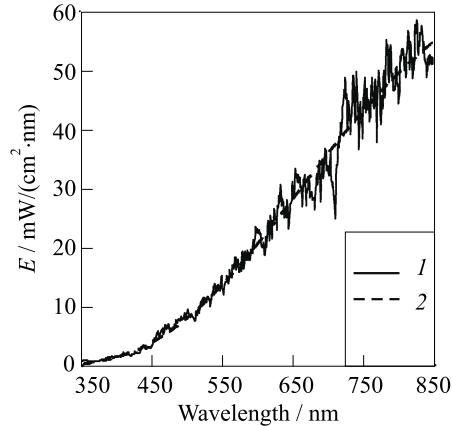
Figure 8.3 Typical measured hemispherical emissive power distribution for the H_2O oxidizer test. *1* — Port 7 Data, *2* — Fit: $T = 2609$ K, EM = 0.42
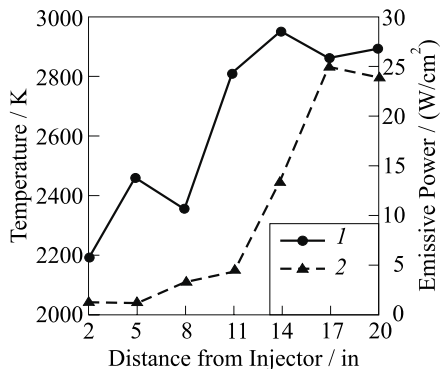
Figure 8.4 Measured temperature and radiation intensity distributions for the O_2/Ar oxidizer test in 24-inch long combustor. *1* — temperature, *2* — power, 425–800 nm
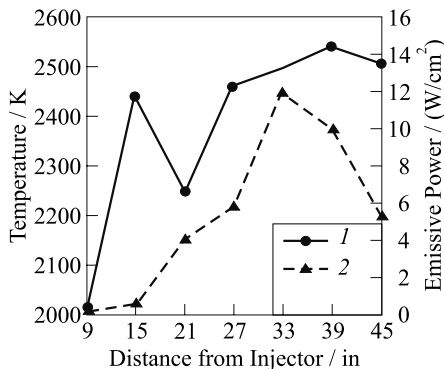
Figure 8.5 Measured temperature and radiation intensity distributions for the H_2O oxidizer test in 48-inch long combustor. *1* — temperature, *2* — power, 400–800 nm

oxidizer is shown in Fig. 8.3. For H_2O oxidizer runs, the temperature fitting procedure was applied in the region between 450 and 760 nm.

Temperatures estimated from the measured intensity distributions at each port location during an O_2/Ar oxidizer run in the 24-inch long combustor are plotted in Fig. 8.4, along with the measured hemispherical emissive power in the wavelength range from 425 to 800 nm. (The hemispherical emissive power, E, is related to the radiant intensity, I, by $E = \pi I$. Radiant intensity is also referred to as radiance.) The stoichiometry, $(O/F)/(O/F)_{st}$, for this run was about 1.10. The measured combustion temperature was about 2900 K, as compared to an adiabatic flame temperature of about 3650 K. The intensity measurements indicate that ignition occurs about 12 in. downstream from the injector. The intensity is near its peak at the most downstream port location, which indicates that combustion is still underway at that location.

Temperatures estimated from the measured intensity distributions at each port location during an H_2O oxidizer run in the 48-inch long combustor are plotted in Fig. 8.5, along with the measured hemispherical emissive power in the wavelength range from 400 to 800 nm. The stoichiometry for the H_2O oxidizer run was also about 1.10, based on the combustion reaction $2Al + 3H_2O \rightarrow Al_2O_3 + 3H_2$. The measured combustion temperature was about 2500 K, as compared to an adiabatic flame temperature of about 3050 K. The intensity measurements indicate that ignition occurs about 18 in. downstream from the injector. The intensity is highest in the region 33 to 39 in. downstream from the injector, and is significantly lower at the most downstream port location, indicating that combustion is mostly complete at that point.

The measurements indicate that the 24-inch long combustor does not provide enough residence time to complete combustion using the O_2/Ar oxidizer mixture. On the other hand, the residence time in the 48-inch long combustor appears to be adequate. Residence times were estimated by simultaneously measuring the radiation intensities at two-port locations using photodiodes and recording the signals at 10 kHz. The two signals were then cross-correlated to estimate the time of flight between the two ports. For the O_2/Ar oxidizer case in the 24-inch long combustor, intensities were measured at locations 14 and 20 in. from the injector. The maximum cross-correlation occurred at a delay time of 6.5 ms, which corresponds to a velocity of about 77 ft/s. An estimated combustor length, from the ignition point to the exit, of 12 in., yields a residence time of about 13 ms. For the H_2O oxidizer case, intensities were measured at 33 and 39 in. from the injector. The maximum cross-correlation occurred at a delay time of 5.6 ms, which corresponds to a velocity of about 89 ft/s. An estimate of combustor length, from the ignition point to the exit, is 24 in., corresponding to a residence time of about 22 ms.

8.4.2 Combustion Products Particle Size and Composition

Samples of combustion products have been collected and analyzed for composition and particle size distribution for both O_2/Ar and H_2O oxidizer runs. During tests using O_2/Ar oxidizer, which were all conducted in the 24-inch long combustor, particle samples were collected from the exhaust plume outside the combustor. A sample was analyzed by X-ray diffraction and determined to be $> 80\%$ δ-Al_2O_3 with no matches to any other phase including Al metal. It was later recognized that unburned aluminum exiting the combustor was afterburning with atmospheric O_2; during testing of the 48-inch long combustor, samples have been collected either through the ports or through a water cooled probe so there is no mixing with atmospheric O_2. No O_2/Ar runs have been made in the 48-inch combustor to date; so no particle samples without afterburning have been collected for O_2/Ar runs.

The first method used for sampling the combustion products in the 48-inch long combustor was simultaneous extraction of samples through ports at seven locations along the combustor axis. Samples were extracted by using a vacuum source to draw gas through each port and across a filter. A sample collected by this method at the most downstream location during an H_2O oxidizer run was analyzed by X-ray diffraction and found to contain significant amounts of α-, δ-, and θ-Al_2O_3 along with aluminum metal. No phases containing hydrogen were detected. It was determined that samples extracted through the ports contained more Al_2O_3 particles and less unburned Al particles than the bulk flow, probably because the much larger size of the unburned particles makes it

more difficult to divert them into the port. In order to overcome this problem, a water-cooled sampling probe was constructed to allow extraction of samples at the combustor centerline. The probe had an inner diameter of 5/16 in. and an outside diameter of 7/8 in. First the probe was inserted from the downstream end of the combustor and an argon purge was used to keep particles from entering the probe until it was inserted to the desired depth. Then the purge was turned off and the downstream end of the probe was opened to atmosphere so a stream of the particle-laden combustion gas was directed through the probe. After the test, the sample is recovered from the inside of the probe using a bottle brush. We believe that this sampling method provides samples that are representative of the bulk flow at the point where they are collected.

Samples were analyzed for unburned aluminum using the eudiometer method [21]. In this method, the sample is mixed with a potassium hydroxide (KOH) solution. KOH reacts with aluminum to form potassium aluminate according to the reaction

$$2Al + 2KOH + 2H_2O \rightarrow 2KAlO_2 + 3H_2$$
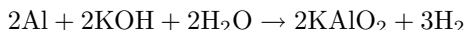
By measuring the volume of hydrogen gas evolved, the weight of aluminum metal in the sample can be calculated. The eudiometer analysis provides a lower limit estimate of the amount of unburned aluminum in the sample, since some unburned aluminum could be coated with a layer of Al_2O_3 that would keep it from reacting. For a sample collected using the water-cooled probe at a location 45 in. from the injector (3 in. from the exit) during an H_2O oxidizer run with stoichiometry of about 1.10, the eudiometer analysis indicated that the sample was about 3%(wt.) unburned aluminum. Assuming that the remaining sample is all Al_2O_3, this corresponds to a combustion efficiency (aluminum burned / total aluminum in sample) of about 95%.

Samples were analyzed for particle size distribution using a *Horiba* LA-900 laser light scattering instrument, with the particles suspended in a liquid water medium. The measured particle size distribution of a typical sample collected through a downstream port during a H_2O oxidizer run is shown in Fig. 8.6. The size distribution is bimodal, with the large diameter fraction consisting of unburned fuel and the small diameter fraction consisting of Al_2O_3. The small diameter fraction contains about 65% of the particle volume. Using standard values for the density of Al metal and Al_2O_3, and assuming that all of the larger diameter fraction is Al and all of the smaller size fraction is Al_2O_3, the estimated weight fraction of unburned aluminum in this sample is 43%. The particle size distribution for a sample of combustion products collected from the exhaust plume outside the combustor during an O_2/Ar oxidizer run is shown in Fig. 8.7. Also shown in Fig. 8.7 is the distribution for the small diameter fraction of the H_2O oxidizer sample shown in Fig. 8.6. The mean particle size of the H_2O combustion products is about twice the mean size of the O_2/Ar products, 0.30 μm vs.
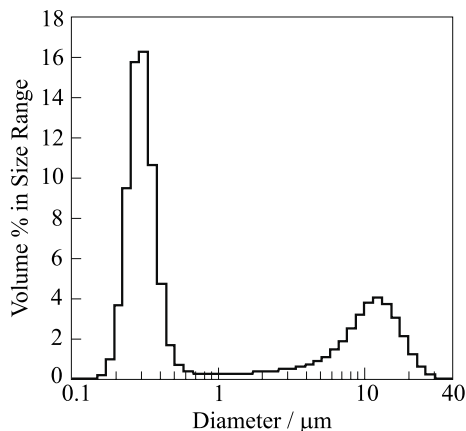
Figure 8.6 Particle size distribution for combustion products collected during H_2O oxidizer test
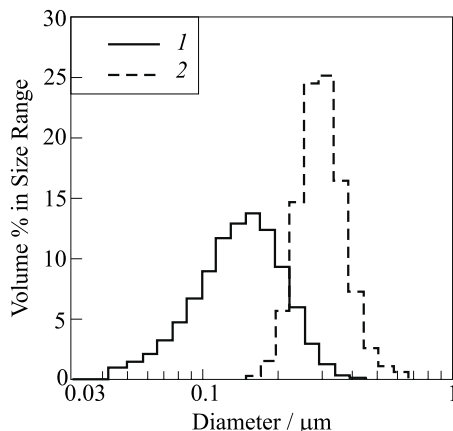
Figure 8.7 Combustion products particle size distributions for O_2 oxidizer tests: *1* — O_2/Ar, *2* — H_2O
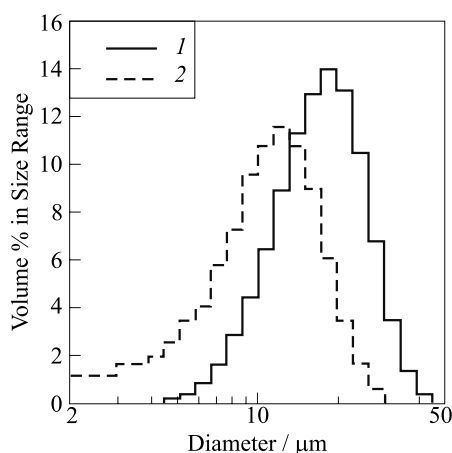
Figure 8.8 Particle size distribution of fuel and unburned fraction in products from H_2O oxidizer test: *1* — fuel, *2* — products

0.14 μm. The distribution around the mean is considerably narrower for the H_2O combustion products.

The size distribution for the large diameter fraction of the H_2O oxidizer combustion products is shown in Fig. 8.8, along with the size distribution of the aluminum powder fuel. The mean particle size of the unburned fuel fraction in the combustion products is about 10.7 μm, while the mean size of the fuel particles is 17.4 μm. Most sources report that burning aluminum particles follow a rate law of the form $d^n = d_0{}^n - \beta t$, where β is a constant and the exponent n is between 1.5 and 2.0. In that case, the size distribution of the unburned fraction of the combustion products would be expected to be larger than that of the fuel. A size distribution of unburned aluminum smaller than that of the parent fuel is more consistent with particles that never ignited, since the larger particles would probably be undersampled. On the other hand, it seems unlikely that any particle could

remain in the high-temperature gas stream for several milliseconds without igniting. Thus, the explanation for the observed size distribution is not clear.

8.4.3 General Observations on Combustor Operation

It was found that when using an O_2/Ar oxidizer stable combustion could be maintained with cold combustor walls, while a warmup period of approximately two minutes assisted with O_2 was required when using the H_2O oxidizer before H_2O-only operation was possible. Apparently, with the lower heat release using the H_2O oxidizer, the recirculated combustion products do not stay hot enough to ignite the incoming fuel when the combustor walls are cold.

Buildup of combustion products inside the combustor is a potential problem for long-term combustor operation, although probably less so on a larger scale. After about one hour of total test time in the 24-inch long combustion chamber using the O_2/Ar oxidizer, deposit buildup in the area upstream from the jet attachment point (about the first 12 in.) had reduced the inner diameter from the original 4 in. down to about 3 in. At the same time, in the area downstream from the attachment point, the diameter increased to about 4.9 in. at the largest point due to melting of the lining. After a few minutes of operation, a stream of liquid Al_2O_3 would typically begin to drip from the open end of the combustor.

In contrast, during operation of the 48-inch long combustor on the H_2O oxidizer, a fairly uniform coating of ash deposited along the entire length of the combustor during each run. Deposits were removed between runs; so it was not determined if the deposit would eventually reach a stable thickness. Typically, about 25% of the total ash generated during a run remained inside the combustor. The combustor lining remained below its melting point through the entire length of the combustor. Melting of deposits was noted only in the downstream end where the outer surface of a thick deposit layer would sometimes begin to melt.

Plugging the injection port was a problem during operation of the 24-inch long combustor. Through a combination of melting of the incoming fuel stream and/or buildup of recirculated combustion products around the injection port, the injector would often plug after a few minutes of operation. The plugging problem was effectively eliminated in the design of the 48-inch long combustor by introducing about 10% of the oxidizer through an annulus surrounding the main premixed fuel/oxidizer stream. The annular flow keeps the recirculated combustion products from coming in contact with the fuel stream at the injector exit; however, the annular flow does not completely eliminate melting of the incoming fuel stream, as liquid aluminum is sometimes observed dripping from the injector at the conclusion of tests.

8.4.4 Analysis of Test Data

Measurements of combustion temperatures, radiation intensity distributions in the range from 400 to 800 nm, and particle size distributions of combustion products have been made for the reaction of aluminum powder with both O_2/Ar and H_2O oxidizers in atmospheric dump combustors. The fraction of unburned aluminum in the combustion products was also determined for the H_2O oxidizer case. An analytical study was performed to determine if the measurements are consistent with each other and with theory, and also to estimate the rate of heat loss from the combustion products. A Monte Carlo technique was used to determine the expected spectral energy distribution that would be emitted from a viewport located in the side of a combustion chamber containing products of aluminum combustion.

The combustion chamber was modeled as a 4-inch diameter and 12-inch long cylinder with diffuse-gray walls at the Al_2O_3 melting temperature of 2300 K and with a uniform emissivity of 0.60. The viewport location was assumed to be at the center of the cylindrical wall, i.e., 6 in. from either end. The combustion chamber was filled with a uniform mixture of particles and combustion gas at temperature T_c. Using the measured particle size distribution of the combustion products and the known aluminum and oxidizer flow rates, the particle size distribution and number density in the combustor can be estimated. The values of the complex index of refraction, $n - ik$, for liquid Al_2O_3 in the temperature range from 2320 to 3000 K have been estimated from experimental measurements and are tabulated in [22]. Mie scattering calculations were performed using the assumed particle size distribution and optical constants, using algorithms presented in [23]. Mie scattering theory gives the spectral extinction and scattering efficiencies for a single particle, from which the extinction and absorption coefficients for the medium can be calculated. These coefficients can be used along with Planck's spectral energy distribution to determine the emissive power of the medium. The particles were assumed to scatter isotropically. Emission and absorption by the gas and by unburned aluminum particles were not considered.

For both the O_2/Ar and H_2O oxidizer cases, the value of T_c assumed in the calculations was varied and an effective radiating temperature, T_{fit}, was determined by fitting the radiation intensity distribution calculated by the computer program to a gray-body distribution, using the same fitting procedure that was employed for the test data. The value of T_c was varied parametrically until the value of T_{fit} was reasonably close to the experimental value. Another parameter in the calculations was the reactedness, R, the fraction of the aluminum fuel converted to Al_2O_3. For example, if $R = 0.6$ the particle loading is 60% of the value for a completely burned mixture. Results of the calculations are shown in Table 8.1.

The close agreement between the experimental values for ε_{fit}, which is the emissivity of a surface emitting the same radiation as that exiting the port,

Table 8.1 Comparison of Monte Carlo Radiation Calculations with Test Data

O_2/Ar Oxidizer, (O/F) / $(O/F)_{st} \approx 1.10$	
Data for Port 6 (17″ downstream from injector):	$T_{fit} = 2860$ K, $\varepsilon_{fit} = 0.51$
Monte Carlo results, assuming $T_c = 3050$ K and $R = 0.6$:	$T_{fit} = 2842$ K, $\varepsilon_{fit} = 0.49$
Calculated rate of heat loss from gas/particle mixture:	$Q = 9.5$ W/cm^3
H_2O Oxidizer, $(O/F)/(O/F)_{st} \approx 1.10$	
Data for Port 5 (33" downstream from injector):	$T_{fit} = 2494$ K, $\varepsilon_{fit} = 0.84$
Monte Carlo results, assuming $T_c = 2575$ K and $R = 1.0$:	$T_{fit} = 2476$ K, $\varepsilon_{fit} = 0.82$
Calculated rate of heat loss from gas/particle mixture:	$Q = 4.8$ W/cm^3

and the calculated values for ε_{fit} for both the O_2/Ar oxidizer and H_2O oxidizer cases is an indication that the values adopted for the Al_2O_3 optical constants, particle size distribution, and particle loading are close to the actual values. The calculations indicate that the particle temperature is approximately 200 K higher than the measured effective radiating temperature for the O_2/Ar oxidizer case and approximately 100 K higher for the H_2O oxidizer case. The calculated radiant heat loss rates are for a uniform mixture at T_c and correspond to the area of the combustor where the radiation intensity is highest.

Based on the measured distribution of radiation intensity along the combustor length, the average radiant heat loss rate for the entire combustor volume for the O_2/Ar case is estimated at about 4.0 W/cm^3, corresponding to a total radiant heat loss of about 20 kW or 160 cal/g of combustion products. Heat loss of 160 cal/g, together with an estimated combustion products temperature of 3050 K, implies that the reactedness of the mixture is on the order of 60% to 70%. The lower estimate of reactedness corresponds to a case in which the unburned aluminum never ignited. The higher estimate of reactedness corresponds to a case where the unburned aluminum is at the same temperature as the rest of the mixture, which implies that it is in vapor phase. The actual reactedness should fall between these two extremes.

For the H_2O oxidizer case, the average radiant heat loss rate for the entire combustor volume is estimated at about 1.9 W/cm^3, corresponding to a total radiant heat loss of about 19 kW, or 420 cal/g of combustion products. A heat loss of 420 cal/g, together with an estimated combustion products temperature of 2575 K, implies that the reactedness of the mixture is on the order of 85% to 95%, depending on whether we assume that the unburned aluminum never ignited or that the unburned aluminum is at the same temperature as the rest of the mixture.

The calculations indicate that the experimental measurements are generally consistent with each other and with theory. A more detailed analysis would be required to model the variation in the radiation intensity and combustion tem-

perature along the length of the combustor, since these parameters are influenced by the combustor flow pattern, aluminum ignition and burning times, and both convective and radiant heat transfer rates.

8.5 CONCLUDING REMARKS

In this study, measurements of the combustion temperature, radiation intensity, combustion products particle size distribution, and combustion efficiency have been made for combustion of aluminum particles with steam in a small-scale atmospheric dump combustor. This data will be useful for designers of combustion chambers for burning of aluminum powder with steam.

To date, data have been obtained for only a very limited number of cases. Additional measurements at a variety of conditions are needed to investigate the effects of firing rate, stoichiometry, aluminum particle size, and chamber pressure on combustion performance. A detailed theoretical combustion model of the process including the combustor fluid dynamics, a particle ignition and burning model, and heat transfer is needed to relate the measured combustion performance to fundamental properties such as the particle ignition and burning times and the radiation properties of the combustion products, which can then be used for design of full-scale combustors.

ACKNOWLEDGMENTS

REFERENCES

1. Greiner, L. 1960. Selection of high-performance propellants for torpedoes. *ARS J.* 30 (Dec):1161–63.
2. U.S. Naval Ordinance Test Station. 1940. China Lake, CA.
3. Texaco Experiment Inc. 1955. Study coordinated by the Bureau of Naval Weapons, Project 61-5.
4. Rasor, O. 1942. U.S. Patent 2, 289, 682. (July). (Patent for use of powdered metal as fuel for propulsion of submarines.)
5. Greiner, L., ed. 1962. *Underwater missile propulsion.* Compas Publications Inc.
6. Gordon, S., and B. J. McBride. 1971. Computer program for calculation of complex chemical equilibrium compositions, rocket performance, incident and reflected shocks, and Chapman–Jouguet detonations. NASA SP-273. NASA Lewis Research Center.

7. Friedman, R., and A. Macek. 1962. Ignition and combustion of aluminum particles in hot ambient gases. *Combustion Flame*. 6.

8. Friedman, R., and A. Macek. 1962. Combustion studies of single aluminum particles. *9th Symposium (International) on Combustion Proceedings*. Pittsburgh, PA: The Combustion Institute. 703.

9. Keshavan, R., and T. A. Brzustowski. 1972. Ignition of aluminum particle streams. *Combustion Science Technology* 6:203–9.

10. Wilson, R. P., Jr. 1970. Combustion of aluminum particles in O_2/Ar. Doctoral Dissertation. San Diego: University of California.

11. Grosse, A. V., and J. B. Conway. 1958. Combustion of metals in oxygen. *Ind. Engineering Chemistry* 50:663–72.

12. Egorov, A. G., *et al.* 1989. Experimental study of ignition and stabilization of powder aluminum flame in combustion chamber with sudden expansion. *Izvestiya VUZ, Aviatsionnaya Tekhnika* 32(2):85–86.

13. Marion, M., *et al.* 1995. Studies on the ignition and burning of aluminum particles. Paper No. 95S-060, Joint Technical Meeting of Central and Western States Sections and Mexican National Section of The Combustion Institute and American Flame Research Committee, San Antonio, TX. April 23–26.

14. Brzustowski, T. A., and I. Glassman. 1964. Vapor-phase diffusion flames in the combustion of magnesium and aluminum: II. Experimental observations in oxygen atmospheres. In: *Heterogeneous combustion*. AIAA progress in astronautics and aeronautics ser. 15:117–58.

15. Bucher, P., *et al.* 1996. Observations on aluminum particles burning in various oxidizers. 33rd JANNAF Combustion Subcommittee Meeting.

16. Kuehl, D. K. 1965. Ignition and combustion of aluminum and beryllium. *AIAA J.* 3:12.

17. Mellor, A. M., and I. Glassman. 1964. Vapor-phase diffusion flames in the combustion of magnesium and aluminum: III. Experimental observations in carbon dioxide atmospheres. In: *Heterogeneous combustion*. AIAA progress in astronautics and aeronautics ser. 15:159–76.

18. Belyaev, A. F., *et al.* 1968. Combustion and ignition of particles of finely dispersed aluminum. *Fizika Goreniya Vzryva* 4(3):323–29.

19. Belyaev, A. F., *et al.* 1969. Combustion characteristics of powdered aluminum. *Fizika Goreniya Vzryva* 5(2):207–17.

20. Oblath, S. B., and J. L. Gole. 1980. On the continuum emissions observed upon oxidation of aluminum and its compounds. *Combustion Flame* 37:293–312.

21. Furman, N. H., ed. 1962. *Standard methods of chemical analysis*. 6th ed. R. E. Krieger Publishing Co. 53–55.

22. Parry, D. L., and M. Q. Brewster. 1991. Optical constants of Al_2O_3 smoke in propellant flames. *AIAA J. Thermophysics* 5(2):142–49.

23. Bohren, C. F., and D. R. Huffman. 1983. *Absorption and scattering of light by small particles*. Wiley-Interscience.

SECTION TWO

FUNDAMENTAL
COMBUSTION ISSUES

Chapter 9

ADVANCES IN ANALYTICAL DESCRIPTION OF TURBULENT REACTING FLOWS

F. A. Jaberi, F. Mashayek, C. K. Madnia,
D. B. Taulbee, and P. Givi

An overview of the major accomplishments in analytical description of turbulent combustion is presented. This deals with mathematical modeling and large-scale numerical simulation of chemically reacting turbulent flows, with a particular emphasis on capturing physical phenomena. A presentation of the primary findings in probability modeling of turbulent combustion, large-eddy simulation of turbulent reactive flows, and the development of turbulence closures for multiphase flows is made. The role of direct numerical simulation in aiding the modeling activities is also highlighted. Due to the nature of this overview, the procedural details are not discussed but a reasonably updated bibliography is furnished.

9.1 INTRODUCTION

Turbulent combustion remains as a very difficult, and perhaps the most important, problem in chemical propulsion [1, 2]. The challenges in establishing a thorough understanding of this phenomenon have been well recognized [3]. Despite being the subject of widespread research, there are many physical issues in enhancing our understanding of turbulent combustion that are yet to be resolved. These issues are not only associated with turbulence, but also include other phenomena such as chemistry of combustion, multiphase transport, scalar mixing, thermal radiation, compressibility, etc. [4]. All of these have been subjects of research on their own merits; they are substantially more difficult when considered in conjunction with turbulent transport.

The authors' efforts have been primarily involved in analytical description of turbulent reacting flows. This involves both modeling and simulation. These

terminologies are now standard in turbulence literature. The first is primarily based on statistical and/or stochastic descriptions and is the traditional means of dealing with turbulence [5]. The second approach is along the lines of what Givi [6] refers to as model-free simulation, but is also known as direct numerical simulation (DNS), full turbulence simulation, detailed numerical simulation, etc. [7–10]. All of these refer to numerical simulations in which turbulence is fully captured without resorting to statistical and stochastic modeling. Simulation is not mathematically rigorous as there are certain elements of one approach in the other. Also, there are other approaches which involve both methodologies [11].

Due to its nature, this review is solely devoted to authors' achievements, rather than the procedural details or review of other contributions. Consequently, the discussions and the references are strongly biased towards authors' work. Also, due to space limitations it is not possible to discuss all of the problems considered in the work; the discussions are limited to three problems which constitute the basic theme of authors' activities:

 (i) probability density function (PDF) modeling in turbulent combustion,

 (ii) large-eddy simulation of turbulent reacting flows, and

(iii) statistical modeling of two-phase turbulent flows.

These are discussed in the next three sections, followed by some concluding remarks.

9.2   PROBABILITY MODELING IN TURBULENT COMBUSTION

Modeling of scalar fluctuations in "Reynolds averaged" equations of turbulent reacting flows has been the subject of broad investigations since the early work of Toor [12]. An approach which has proven particularly useful in such modeling is based on the probability density function (PDF) or the joint PDF of scalar quantities [13–16]. The systematic approach for determining the PDF is by means of solving the transport equation governing its evolution. In this equation, the effects of chemical reaction appear in a closed form, constituting the primary advantage of the PDF schemes over other statistical procedures. However, modeling is needed to account for the PDF transport in the composition domain, and there are extra dimensions associated with this domain which must be considered. An alternative approach in PDF modeling is based on a field-parameterization method in which the form of the PDF is "assumed" in terms of its (finite) lower order moments. Obviously, this approach is *ad hoc* but is justified in cases where there is strong evidence that the PDF adopts a particular distribution [17].

Both of these modeling strategies have been considered in this research. The first approach is preferred if an appropriate closure is available to account for the molecular action. Traditionally the family of models based on the coalescence/dispersion (C/D) closures [18–20] or linear mean square estimation (LMSE) methods [13] also known as the IEM [21] (interaction by exchange with the mean) closure have been employed. Although these closures are convenient from the computational standpoint and can be effectively simulated via Monte Carlo numerical methods [14], there are several drawbacks associated with these closures [18]. Some of these drawbacks are overcome by the Amplitude Mapping Closure (AMC) [22, 23], as shown in a number of validation assessments of the AMC by comparison with extensive data obtained by direct numerical simulation (DNS) [24–27], and laboratory experiments [28]. However, the authors have also experienced that the following issues associated with the AMC require further investigations:

(i) the single-point nature of the closure,

(ii) its numerical implementation especially in multivariate statistical analyses,

(iii) its ability to account for migration of scalar "bounds" as mixing proceeds.

The first problem is shared with C/D models and reflects the deficiency of the approach in accounting for variations of turbulent length and time scales. The other issues are exclusive to the AMC. Despite these problems, it has been found that the AMC is very convenient for predicting the "limiting" rate of reactant conversion in homogeneous reacting flows with initially segregated reactants. In several laboratory experiments in such flows (such as plug flow reactors) [29] it has been observed that the PDF of the mixture fraction evolves from a double-delta distribution (indicating the initially nonpremixed reactants) to an asymptotic Gaussian distribution. The AMC predicts this evolution reasonably well (albeit not exactly), and the authors have been able to provide an analytical relation for the limiting rate of the mean reactant conversion via this model, the results of which compare well with both laboratory and DNS data [26, 28, 30]. However, the AMC is constructed in such a way that the asymptotic PDF of the mixture fraction becomes approximately Gaussian. It has been shown that this behavior is not universal [31]; it is possible to establish other mixing scenarios with an asymptotic behavior other than Gaussian [27, 32]. Nevertheless, the closed form relation obtained for the limiting rate of reactant conversion via AMC works reasonably well even for cases in which the PDF does not relax to a Gaussian state.

For engineering predictions, it has been argued that assumed PDF methods are more practical than the PDF transport equation approach. This is not to suggest the superiority of assumed methods. Rather, it is to encourage further research on the first scheme before it can be implemented routinely. Therefore,

a part of the research has been devoted to investigating the properties of some of the assumed PDF methods [26, 30, 33]. The general conclusion drawn from these studies is that in cases where the AMC has proven useful, other approaches based on parameterized PDFs are also effective. For example, in homogeneous turbulence the family of PDFs based on the "Johnson Edgeworth Translation" (JET) [34, 35] can also be used. In fact, the solution generated by the AMC [23] for the problem of binary scalar mixing can be categorized as a member of the JET family. Furthermore, due to established similarities of the JET with simpler distributions belonging to the Pearson Family (PF) of PDFs [36], it can be argued that the PF can also be considered as a viable alternative. This is somewhat pleasing as there is a long history of the application of PDFs via PF in turbulent combustion [37–40]. In most applications to date, this family has been used in the form of Type I and Type II distributions. This is due to the flexibility of this density in portraying bimodal distributions.

The authors have studied the properties of this density in detail [24, 33] and have observed some similarities between the PF and the AMC as well as some differences. Both these methods are utilized in the context of a single-point closure. Therefore, in both cases the magnitudes of moments up to second order must be provided externally. Also, neither method accounts for migration of the scalar's bounds as mixing proceeds. This is portrayed by the evolution of the conditional statistics of the scalar; namely, the conditional expected dissipation and the conditional expected diffusion [41, 42].

For equilibrium homogeneous flows, both closures are satisfactory regardless of the magnitude of the equivalence ratio [24, 26]. However, the actual implementation of the AMC appears difficult in inhomogeneous flows [23]. In these cases, the application of the PF is much more straightforward but obviously cannot be justified rigorously. The corresponding multivariate form of this PDF for multiscalar mixing is the Dirichlet frequency [43, 44]. This frequency, also referred to as a joint Beta density, has been used in several applications [45–47]. The general conclusion is that the Dirichlet frequency parameterized by the scalar-energy can be recommended, but with caution! This density yields a Beta frequency for the marginal PDF of each of the reactants. This univariate frequency is applicable for statistical treatment of both frozen and equilibrium flows. But the model does not yield a consistent limiting condition for equilibrium flows. Moreover, the Dirichlet distribution for the two reactants does not yield Damköhler invariant statistics for the mixture fraction. This is due to the inability of the distribution to include all of the first- and the second-order moments in its parameterization. This problem is well recognized in statistics and biometric literature [48].

It is possible to construct a modified multivariate density which overcomes this problem. However, the parameters of the model may not be algebraically related to input moments (because the PDF may not be analytically integrated); thus the model cannot be recommended for practical applications [49]. The other

known multivariate frequencies such as the joint Gaussian (and distributions generated by other schemes [44]) do not share this problem; rather they do not possess some of the required physical properties.

9.3 LARGE-EDDY SIMULATION OF TURBULENT REACTING FLOWS

Since the early work of Smagorinsky [50], significant efforts have been devoted to large-eddy simulation (LES) of turbulent flows [7, 51–56]. The most prominent model has been the Smagorinsky-eddy viscosity closure which relates the unknown subgrid-scale (SGS) Reynolds stresses to the local large-scale rate of flow strain [57]. This viscosity is aimed at mimicking the dissipative behavior of the unresolved small scales. The extensions to "dynamic" models [58–59] have shown some improvements. This is particularly so in transitional flow simulations where the dynamic evolutions of the empirical model "constant" result in (somewhat) better predictions of the large-scale flow features.

It appears that Schumann [60] was one of the first to conduct LES of a reacting flow. However, the assumption made in this work to neglect the contribution of the SGS scalar fluctuations to the filtered reaction rate needs to be justified for general applications. As indicated in section 9.2, the importance of such fluctuations is well recognized in Reynolds averaged procedures. Therefore, it is natural to believe that these fluctuations are also important in LES. This issue has been the subject of broad investigation [61–76].

In authors' research, the efforts were concentrated on the use of PDF methods for LES of turbulent combustion. This approach was suggested by Givi [6] and its first application is due to Madnia and Givi [77]. In this work, the PF distributions are assumed to characterize PDF of SGS scalars in homogeneous turbulence under chemical equilibrium. This procedure was also used by Cook and Riley [65]. The extension of assumed PDF methods for LES of nonequilibrium reacting shear flows is reported by Frankel *et al.* [78]. While the generated results are encouraging, they do reveal the need for more systematic schemes in which the transport of the PDF of SGS scalar quantities are considered. Pope [79] introduced the concept of "filtered density function" (FDF) which is essentially the PDF of SGS scalar variables. With the formal definition of the FDF, Pope [79] demonstrates that the effects of chemical reaction appear in a closed form in the FDF transport, thus making it a viable candidate for LES of chemically reacting flows. Gao and O'Brien [64] develop a transport equation for the FDF and offer several suggestions for modeling the unclosed terms in this equation.

Colucci *et al.* [80] demonstrate that the FDF does indeed provide a very powerful means of conducting reliable LES of turbulent combustion. In this work,

a modeled transport equation is developed for the FDF in which the unclosed terms are modeled in a fashion similar to that in PDF methods [14, 16]. In particular the LMSE closure is employed for modeling the SGS mixing and the gradient diffusion approximation is used for SGS convection of the FDF. It is also shown that the Lagrangian Monte Carlo scheme [14] provides the most convenient means of solving the FDF transport equation numerically. The scheme is applied for LES of two- and three-dimensional flows under both nonreacting and reacting conditions. The simulated results are compared with those based on a "conventional" LES in which the effects of subgrid scalar fluctuations are ignored (LES–FD), and those via DNS of flows with identical values of the physical parameters. The convergence of the Monte Carlo generated results and the consistency of the FDF formulation are demonstrated by comparisons with the LES–FD results of nonreacting flows. The superiority of the FDF over LES–FD is demonstrated by detailed comparative assessments with DNS results of reacting flows. It is shown that the SGS scalar fluctuations impose a very significant influence on the filtered reaction rate; the neglect of these fluctuations results in overpredictions of the filtered reactant conversion rate. Thus the LES via FDF is superior to LES–FD. The extension of the methodology for LES of variable density turbulent reacting flows is also completed [81]. In doing so, the concept of the "filtered mass density function" (FMDF) is introduced which is essentially the density weighted FDF. An excellent agreement is observed between FMDF and data obtained by DNS and laboratory experiments. The latest contributions via FDF include LES of a turbulent round jet [82], and a methane/air planar jet flame [83]. Currently, the FDF methodology is extended to also account for the SGS of the velocity field [84].

The computational requirement for LES via FDF (or FMDF) is as expected, more than that for conventional LES (LES–FD), but is significantly less than that for DNS. The range of flow parameters (such as the Reynolds and the Damköhler numbers) that can be considered by FDF is significantly larger than can be treated by DNS, and the results are more accurate than those by LES–FD. These comparisons could be made only in flows for which DNS was possible, i.e., low Damköhler and Reynolds number values. At higher values of these parameters, the computational cost of DNS would be exceedingly higher than that of FDF. Thus for practical flows for which DNS is currently impossible, FDF would be a good alternative.

9.4 TURBULENCE MODELING IN TWO-PHASE FLOWS

Another important, but very complicated, issue in the theoretical description of turbulent combustion is the phenomenon of "dispersion" of discrete particles

(liquid or solid) [85]. With the presence of such a dispersed phase in a turbulent flow of a gas or liquid (the "carrier phase"), the physical complexities, due to multiphase transport including the couplings between the various phases, make the mathematical description of the problem very complex. Due to its inherent physics, dispersion is best understood when analyzed in the Lagrangian context [86]. This alone would make investigations via laboratory experiments very challenging.

A variety of statistical models are available for predictions of multiphase turbulent flows [85]. A large number of the "application oriented" investigations are based on the Eulerian description utilizing turbulence closures for both the dispersed and the carrier phases. The closure schemes for the carrier phase are mostly limited to "Boussinesq" type approximations in conjunction with modified forms of the conventional k–ϵ model [87]. The models for the dispersed phase are typically via the "Hinze–Tchen" algebraic relation [88] which relates the eddy viscosity of the dispersed phase to that of the carrier phase. While the simplicity of this model has promoted its use, its nonuniversality has been widely recognized [88].

Authors' efforts in this part of the work have been concentrated on developing turbulence closures for the statistical description of two-phase turbulent flows. The primary emphasis is on development of models which are more rigorous, but can be more easily employed. The main subjects of the modeling are the Reynolds stresses (in both phases), the cross-correlation between the velocities of the two phases, and the turbulent fluxes of the void fraction. Transport of an incompressible fluid (the carrier gas) laden with monosize particles (the dispersed phase) is considered. The Stokes drag relation is used for phase interactions and there is no mass transfer between the two phases. The particle–particle interactions are neglected; the dispersed phase viscosity and pressure do not appear in the particle momentum equation.

The models are of second order and are expressed via both: (I) differential equations, and (II) explicit algebraic equations. In (I), the operational procedure requires the construction of transport equations for the second-order moments, and modeling of various terms in these transport equations. In (II), the additional steps involve simplification of the transport differential equations to implicit "algebraic equations," and solution of the algebraic equations to generate "explicit" algebraic models. The mathematical derivations in each of these steps are rather involved but are detailed in [89, 90]. Here a brief outline is provided of this procedure. The differential equations are obtained by standard averaging of the governing equations of the dilute two-phase flow. Models are required for the pressure–strain correlation, pressure–void fraction gradient correlation, and pressure–dispersed phase velocity gradient correlation. To close these equations the starting point in deriving a model for the fluid pressure–strain correlation is the "Poisson's equation" [91] which, for the two-phase flow, is obtained from the carrier phase momentum equation. With imposition of the physical restrictions

(continuity, symmetry, and normalization [91]) a linear relation is obtained for each of these correlations. The final model involves some additional empirical constants, but the model reduces identically to those in [92, 93] in the limit of single-phase flows. The authors could not find sufficient experimental data for determination of the empirical constants appearing in the final second-order moment transport equations. Therefore, an extensive DNS of particle laden flows was conducted in both isotropic and homogeneous shear flows [89, 94–101]. With use of the data generated in these simulations, the values of the constants were specified. The final model was further assessed by comparison with experimental data [102] and encouraging agreements were observed.

Despite the excellent performance of the second-order differential closures, their application for "routine" predictions of complex flows is not straightforward. Therefore, some time was devoted to development of "algebraic models." The procedure for deriving algebraic equations from the differential equations is similar to that in single-phase flows [92, 93]. The primary assumption is that the flow is in "equilibrium" state. With this assumption, the acceleration terms in the normalized Reynolds stress equations vanish, yielding a set of coupled algebraic equations for the second-order moments. The resulting algebraic equations can be used directly in conjunction with the mean equations. However, the "implicit" form of these equations makes them inconvenient for actual computations. This has been the primary factor in motivating the development of explicit algebraic closures in single-phase flows [103]. To present the solution in the explicit form, a rather liberal use of the "Cayley–Hamilton Theorem" (CHT) was used [104]. The procedure is analogous to, but significantly more complex than those in single-phase turbulent flows [71, 72, 79]. The complexity is due to the fact that the Reynolds stress tensor is a function of "three tensors" (mean strain, mean vorticity, and the fluid–particle velocity covariance) in contrast to the case of a single-phase flow where the Reynolds stresses are dependent on only two tensors (mean strain and mean vorticity). With the additional parameter, new integrity basis and irreducible matrix polynomials must be specified. For two-dimensional mean flows with three-dimensional turbulence, it has been possible to identify the integrity basis and the corresponding matrix polynomials. By doing so, it has been possible to express the Reynolds stresses via a "finite" set of polynomials in which the expansion coefficients are expressed explicitly. While the mathematical derivation leading to the final equations is somewhat involved, the final form of the model is easy to implement. The results predicted by the model are observed to be very close to those via the differential equation model and compare well with DNS and laboratory experiments.

The authors' latest work on turbulence modeling of multiphase flow is via PDF methods based on the recent kinetic equation model of Pozorski and Minier [106]. This model is being applied for PDF modeling of evaporating droplets, the results of which will be appraised via comparative assessments against the DNS data bank [96–101] and laboratory data.

9.5 CONCLUDING REMARKS

There is clearly a strong need for further developments of analytical schemes for description of turbulent reacting flows. Based on the authors' work, as summarized in this chapter and also recent contributions by others, there are some suggestions for future work. These suggestions are outlined briefly in this section together with a projection of achievements within the foreseeable future.

The authors feel that statistical methods are the most practical means of predicting engineering turbulent reacting flows; PDF schemes remain the most powerful tool in such predictions. The use of assumed PDF methods can be justified in some cases, but the emphasis must be placed upon the PDF transport equation. For that, improved closures are needed for the subcomponents of the PDF model, together with inclusion of heterogeneous effects, complex geometry (e.g., wall effects), thermal radiation, and development of improved schemes for numerical solution of the PDF. Amongst these, modeling of molecular action effects in scalar mixing requires special attention [107–109] as these effects are present in simplest flows with absence of other physical complexities.

The encouraging results obtained by FDF (or FMDF) warrant further improvements and implementations of this methodology for a wider class of reacting flows. Future works should be concentrated on improvements of the closures of various terms in the FDF transport equation, consideration of the velocity–scalars, improvements of the numerical procedure for solving the FMDF transport equations, and simulations of flames in complex geometries. With such developments, it is conceivable that LES of reactive flows with realistic chemical kinetics may be conducted for engineering applications in the near future, if the computational overhead associated with the FDF can be tolerated. In this regard the scalar FDF methodology is attractive in that the present Monte Carlo solver can be used directly in commercially available CFD codes. Similar to PDF methods, the closure problems associated with the FDF are the correlations involving the velocity field (such as SGS stresses and mass fluxes). This may be overcome by considering the joint velocity–scalar FDF similar to that in PDF [110]. Several means of reducing the FDF's computational requirements are possible; e.g., see [111]. In general, the FDF methodology will benefit from ongoing and future improvements in PDF schemes from both modeling and computational standpoints [112].

Further development of statistical closures, especially in the algebraic form, is strongly recommended for description of two-phase flows. Of interest is inclusion of evaporation in the modeling strategies. It is expected that optimum closures will remain at the level of single-point, one-time, second-order moment. Consideration of differential transport equations for such moments appears to be computationally excessive; so algebraic closures are expected to be more widely utilized. These closures portray the simplicity of zero-order schemes, yet preserve (some of) the capabilities of second-order closures. In more complicated flows, it

is not clear if these closures can be expressed explicitly. The degree of complexity depends on the extent of polydispersity, flow compressibility, exothermicity, and dimensionality amongst other factors. With optimal manipulation of CHT (possibly augmented by an efficient use of symbolic computation procedures), it may be possible to furnish an explicit solution to a model algebraic equation. The "usefulness" of such a solution, however, must be established before it can be recommended for routine predictions [113]. In some cases it might be better to leave the closure, or a portion of it, in an implicit form if it does not cause numerical stability problems.

Direct numerical simulation is expected to play a more dominant role for analytical treatment of turbulent flames. In addition to capturing physical phenomena, the authors feel that a very powerful role of DNS is its capability for model validations. In fact, in most of our modeling activities, DNS has been the primary means of verifying "specific" assumptions and/or approximations. This is partially due to difficulties in laboratory measurements of some of the correlations and also in setting configurations suitable for model assessments. Of course, the overall evaluation of the "final" form of the model requires the use of laboratory data for flows in which all of the complexities are present.

ACKNOWLEDGMENTS

REFERENCES

1. Roy, G. D., ed. 1998. *Propulsion combustion: Fuels to emissions*. Washington, DC: Taylor & Francis.
2. Roy, G. D., S. M. Frolov, and P. Givi, eds. 1997. *Advanced computation and analysis of combustion*. Moscow, Russia: ENAS Publ.

3. Libby, P. A., and F. A. Williams, eds. 1980. *Turbulent reacting flows. Topics in applied physics*. Vol. 44. Chemical engineering communications. Rational and mechanics. Heidelberg: Springer-Verlag.

4. Libby, P. A., and F. A. Williams, eds. 1994. *Turbulent reacting flows*. London, UK: Academic Press.

5. Panchev, S. 1970. *Random functions and turbulence*. Oxford, UK: Pergamon Press.

6. Givi, P. 1989. Model free simulations of turbulent reactive flows. *Progress Energy Combustion Science* 15:1–107.

7. Rogallo, R. S., and P. Moin. 1984. Numerical simulation of turbulent flow. *Annual Reviews Fluid Mechanics* 16:99–137.

8. Oran, E. S., and J. P. Boris. 1987. *Numerical simulations of reactive flows*. Washington, DC: Elsevier Publ. Comp.

9. Jou, W.-H., and J. J. Riley. 1989. Progress in direct numerical simulations of turbulent reacting flows. *AIAA J.* 27(11):1543–56.

10. Lumley, J. L., ed. 1990. Whither turbulence? Turbulence at the crossroads. *Lecture notes in physics*. Vol. 357. New York, NY: Springer-Verlag.

11. Givi, P. 1994. Spectral and random vortex methods in turbulent reacting flows. In: *Turbulent reacting flows*. Eds. P. A. Libby and F. A. Williams. London, UK: Academic Press. 475–572.

12. Toor, H. L. 1962. Mass transfer in dilute turbulent and nonturbulent systems with rapid irreversible reactions and equal diffusivities. *AIChE J.* 8:70–78.

13. O'Brien, E. E. 1980. The probability density function (PDF) approach to reacting turbulent flows. In: *Turbulent reacting flows, Topics in applied physics*. Eds. P. A. Libby and F. A. Williams. Heidelberg: Springer-Verlag. 185–218.

14. Pope, S. B. 1985. PDF methods for turbulent reactive flows. *Progress Energy Combustion Science* 11:119–92.

15. Dopazo, C. 1994. Recent developments in PDF methods. In: *Turbulent reacting flows*. Eds. P. A. Libby and F. A. Williams. London, UK: Academic Press. 375–474.

16. Pope, S. B. 2000. *Turbulent flows*. Cambridge, UK: Cambridge University Press.

17. Pope, S. B. 1994. Lagrangian PDF methods for turbulent flows. *Annual Reviews Fluid Mechanics* 26:23–63.

18. Pope, S. B. 1982. An improved turbulent mixing model. *Combustion Science Technology* 28:131–45.

19. Kosály, G. 1986. Theoretical remarks on a phenomenological model of turbulent mixing. *Combustion Science Technology* 49:227–34.

20. Kosály, G., and P. Givi. 1987. Modeling of turbulent molecular mixing. *Combustion Flame* 70:101–18.

21. Borghi, R. 1988. Turbulent combustion modeling. *Progress Energy Combustion Science* 14:245–92.

22. Chen, H., S. Chen, and R. H. Kraichnan. 1989. Probability distribution of a stochastically advected scalar field. *Physical Review Letters* 63(24):2657–60.

23. Pope, S. B. 1991. Mapping closures for turbulent mixing and reaction. *Theoretical Computational Fluid Dynamics* 2:255–70.

24. Madnia, C. K., S. H. Frankel, and P. Givi. 1992. Reactant conversion in homogeneous turbulence: Mathematical modeling, computational validations and practical applications. *Theoretical Computational Fluid Dynamics* 4:79–93.

25. Jiang, T.-L., F. Gao, and P. Givi. 1992. Binary and trinary scalar mixing by Fickian diffusion — some mapping closure results. *J. Physics Fluids A* 4(5):1028–35.

26. Frankel, S. H., C. K. Madnia, and P. Givi. 1993. Comparative assessment of closures for turbulent reacting flows. *AIChE J.* 39(5):899–903.

27. Jaberi, F. A., and P. Givi. 1995. Inter-layer diffusion model of scalar mixing in homogeneous turbulence. *Combustion Science Technology* 104(4–6):249–72.

28. Frankel, S. H., T.-L. Jiang, and P. Givi. 1992. Modeling of isotropic reacting turbulence by a hybrid mapping-EDQNM closure. *AIChE J.* 38(4):535–43.

29. Brodkey, R. S., ed. 1975. *Turbulence in mixing operation.* New York, NY: Academic Press.

30. Frankel, S. H., C. K. Madnia, P. A. McMurtry, and P. Givi. 1993. Binary scalar mixing and reaction in homogeneous turbulence: Some linear eddy model results. *Energy Fuels* 7(6):827–34.

31. Jaberi, F. A., R. S. Miller, C. K. Madnia, and P. Givi. 1996. Non-Gaussian scalar statistics in homogeneous turbulence. *J. Fluid Mechanics* 313:241–82.

32. Livescu, D., F. A. Jaberi, and C. K. Madnia. 2000. Passive-scalar wake behind a line source in grid turbulence. *J. Fluid Mechanics* 416:117–49.

33. Miller, R. S., S. H. Frankel, C. K. Madnia, and P. Givi. 1993. Johnson–Edgeworth translation for probability modeling of binary scalar mixing in turbulent flows. *Combustion Science Technology* 91(1–3):21–52.

34. Johnson, N. L. 1949. Systems of frequency curves generated by methods of translation. *Biometrika* 36:149–76.

35. Edgeworth, F. Y. 1907. On the representation of statistical frequency by a series. *J. Royal Statistical Society, Series A.* 70:102–6.

36. Pearson, K. 1895. Contributions to the mathematical theory of evolution: II. Skew variations in homogeneous material. *Philos. Trans. Royal Society London, Series A.* 186:343–414.

37. Rhodes, P. R. 1975. A probability distribution function for turbulent flows. In: *Turbulent mixing in nonreactive and reactive mixing.* Ed. S. N. B. Murthy. New York, NY: Plenum Press. 235–41.

38. Lockwood, F. C., and H. A. Moneib. 1980. Fluctuating temperature measurement in a heated round free jet. *Combustion Science Technology* 22:63–81.

39. Priddin, C. H. 1991. Turbulent combustion modeling — a review. In: *Advances in turbulence 3.* Eds. A. V. Johansson and P. H. Alfredsson. Berlin: Springer-Verlag. 279–99.

40. Gaffney, R. L., J. A. White, S. S. Girimaji, and J. P. Drummond. 1994. Modeling of temperature and species fluctuations in turbulent, reacting row. *Computing Systems Engineering* 5(2):117–33.

41. Girimaji, S. S. 1992. On the modeling of scalar diffusion in isotropic turbulence. *J. Physics Fluids A* 4(11):2529–37.

42. Jaberi, F. A., R. S. Miller, and P. Givi. 1996. Conditional statistics in turbulent scalar mixing and reaction. *AIChE J.* 42(4):1149–52.

43. Narumi, S. 1923. On the general form of bivariate frequency distributions which are mathematically possible when regression and variation are subjected to limiting conditions, I. *Biometrika* 15:77–88.

44. Wilks, S. S. 1962. *Mathematical statistics*. 2nd ed. New York, NY: Wiley.

45. Girimaji, S. S. 1991. Assumed β-PDF model for turbulent mixing: Validation and extension to multiple scalar mixing. *Combustion Science Technology* 78:177–96.

46. Narayan, J. R., and S. S. Girimaji. 1992. Turbulent reacting flow computations including turbulent–chemistry interactions. AIAA Paper No. 92-0342.

47. Sabini, G. J., G. S. Shieh, and P. Givi. 1996. Modeling of the fluctuations and the frequency-spectra of reactants in turbulent scalar mixing layers. *Chemical Engineering Communications* 154:147–81.

48. Johnson, N. L. 1949. Bivariate distributions based on simple translation systems. *Biometrika* 36:297–304.

49. Baurie, R. A., G. A. Alexopoulos, H. A. Hassan, and J. P. Drummond. 1992. An assumed joint-beta PDF approach for supersonic turbulent combustion. AIAA Paper No. 92-3844.

50. Smagorinsky, J. 1963. General circulation experiments with the primitive equations. I. The basic experiment. *Monthly Weather Review* 91(3):99–164.

51. Ferziger, J. H. 1981. Higher level simulations of turbulent flows. Stanford University Report TF-16. Stanford, CA: Department of Mechanical Engineering, Stanford University.

52. Voke, P. R., and M. W. Collins. 1983. Large eddy simulation: Retrospect and prospects. *Physico-Chemical Hydrodynamics* 4(2):119–61.

53. Oran, E. S., and J. P. Boris, eds. 1991. *Numerical approaches to combustion modeling*. Progress in astronautics and aeronautics ser. New York, NY: AIAA Publ. Co. 135.

54. Metais, O., and M. Lesieur. 1992. Special large-eddy simulations of isotropic and stably stratified turbulence. *J. Fluid Mechanics* 239:157–94.

55. Galperin, B., and S. A. Orszag, eds. 1993. *Large eddy simulations of complex engineering and geophysical flows*. Cambridge, UK: Cambridge University Press.

56. Meneveau, C., and J. Katz. 2000. Scale-invariance and turbulence models for large-eddy simulations. *Annual Reviews Fluid Mechanics*. 1–32.

57. Lilly, D. K. 1967. The representation of small-scale turbulence in numerical simulation experiments. *IBM Scientific Computing Symposium Environmental Sciences Proceedings*. IBM Form No. 320-1951:195–210.

58. Germano, M., U. Piomelli, P. Moin, and W. H. Gabot. 1991. A dynamic subgrid-scale eddy viscosity model. *J. Physics Fluids A* 3(7):1760–65.

59. Germano, M. 1992. Turbulence: The filtering approach. *J. Fluid Mechanics* 238:325–36.

60. Schumann, U. 1989. Large eddy simulation of turbulent diffusion with chemical reactions in the convective boundary layer. *Atmospheric Environment* 23(8): 1713–26.

61. McMurtry, P. A., S. Menon, and A. R. Kerstein. 1992. A linear eddy sub-grid model for turbulent reacting flows: Application to hydrogen–air combustion. *24th Symposium (International) on Combustion Proceedings*. Pittsburgh, PA: The Combustion Institute. 271–78.

62. Boris, J. P., F. F. Grinstein, E. S. Oran, and R. L. Kolbe. 1992. New insights into large eddy simulations. NRL Report NRL/MR/4400-92-6979. Washington, DC: Naval Research Laboratory.

63. Menon, S., P. A. McMurty, and A. K. Kerstein. 1993. A linear eddy subgrid model of turbulent combustion. In: *Large-eddy simulations of complex engineering and geophysical flows*. Eds. B. Galperin and S. A. Orszag. Cambridge, UK: Cambridge University Press. 287–314.

64. Gao, F., and E. E. O'Brien. 1993. A large-eddy simulation scheme for turbulent reacting flow. *J. Physics Fluids A* 5(6):1282–84.

65. Cook, A. W., and J. J. Riley. 1994. A subgrid model for equilibrium chemistry in turbulent flows. *J. Physics Fluids* 6(8):2868–70.

66. Fureby, C., and C. Lofstrom. 1994. Large-eddy simulations of bluff body stabilized flames. *25th Symposium (International) on Combustion Proceedings*. Pittsburgh, PA: The Combustion Institute. 1257–64.

67. Möller, S. I., E. Lundgren, and C. Fureby. 1996. Large eddy simulations of unsteady combustion. *26th Symposium (International) on Combustion Proceedings*. Pittsburgh, PA: The Combustion Institute. 241.

68. Branley, N., and W. P. Jones. 1997. Large-eddy simulation of a turbulent nonpremixed flame. *11th Symposium (International) on Turbulent Shear Flow Proceedings*. Grenoble, France. 21.1–21.6.

69. Cook. A. W., J. J. Riley, and S. M. deBruynKops. 1997. A sub-grid model for nonpremixed turbulent combustion. *11th Symposium (International) on Turbulent Shear Flow Proceedings*. Grenoble, France. 16.13–16.18.

70. Cook, A. W., J. J. Riley, and G. Kosály. 1997. A laminar flamelet approach to subgrid-scale chemistry in turbulent flows. *Combustion Flame* 109:332–41.

71. Jiménez, J., A. Liñán, M. M. Rogers, and F. J. Higuera. 1997. *A priori* testing of subgrid models for chemically reacting nonpremixed turbulent flow. *J. Fluid Mechanics* 349:149–71.

72. Mathey, F., and J. P. Chollet. 1997. Large-eddy simulation of turbulent reactive flows. *11th Symposium on Turbulent Shear Flows Proceedings*. Grenoble, France. 16.19–24.

73. DesJardin, P. E., and S. H. Frankel. 1998. Large-eddy simulation of a turbulent nonpremixed reacting jet: Application and assessment of subgrid-scale combustion models. *J. Physics Fluids* 10(9):2298–314.

74. Jaberi, F. A., and S. A. James. 1998. A dynamic similarity model for large eddy simulation of turbulent combustion. *J. Physics Fluids* 10(7):1775–77.

75. Réveillon, J., and L. Vervisch. 1998. Subgrid-scale turbulent micromixing: Dynamic approach. *AIAA J.* 36(3):336–41.

76. Pitsch, H., and H. Steiner. 2000. Large-eddy simulation of a turbulent piloted methane/air diffusion flame (Sandia flame D). *J. Physics Fluids* 12(10):2541–54.

77. Madnia, C. K., and P. Givi. 1993. Direct numerical simulation and large eddy simulation of reacting homogeneous turbulence. In: *Large-eddy simulations of complex engineering and geophysical flows*. Eds. B. Galperin and S. A. Orszag. Cambridge, UK: Cambridge University Press. 315–46.

78. Frankel, S. H., V. Adumitroaie, C. K. Madnia, and P. Givi. 1993. Large eddy simulations of turbulent reacting flows by assumed PDF methods. In: *Engineering applications of large eddy simulations*. Eds. S. A. Ragab and U. Piomelli. New York, NY: ASME, FED. 162:81–101.

79. Pope, S. B. 1990. Computations of turbulent combustion: Progress and challenges. *23rd Symposium (International) on Combustion Proceedings*. Pittsburgh, PA: The Combustion Institute. 591–612.

80. Colucci, P. J., F. A. Jaberi, P. Givi, and S. B. Pope. 1998. Filtered density function for large eddy simulation of turbulent reacting flows. *J. Physics Fluids* 10(2):499–515.

81. Jaberi, F. A., P. J. Colucci, S. James, P. Givi, and S. B. Pope. 1999. Filtered mass density function for large eddy simulation of turbulent reacting flows. *J. Fluid Mechanics* 401:85–121.

82. Garrick, S. C., F. A. Jaberi, and P. Givi. 1999. Large-eddy simulation of scalar transport in a turbulent jet flow. In: *Recent advances in DNS and LES, fluid mechanics and its applications*. Eds. D. Knight and L. Sakkel. The Netherlands: Kluwer Academic Publ. 54:155–66.

83. James, S., and F. A. Jaberi. 2000. Large-scale simulations of two-dimensional non-premixed methane jet flames. *Combustion Flame* 123:465–87.

84. Gicquel, L. Y. M., P. Givi, F. A. Gaberi, and S. B. Pope. 1989. Velocity filtered density function for large eddy simulation of turbulent flows. *Bull. American Phys. Society* 45(9):129.

85. Faeth, G. M. 1987. Mixing, transport and combustion in sprays. *Progress Energy Combustion Science* 13:293–345.

86. Corrsin, S. 1961. Turbulent flow. *American Scientist* 49:300–24.

87. Launder, B. E., and D. B. Spalding. 1972. *Lectures in mathematical modeling of turbulence*. London, UK: Academic Press.

88. Zhou, L. 1993. *Theory and numerical modeling of turbulent gas–particle flows and combustion*. Boca Raton, FL: CRC Press.

89. Taulbee, D. B., F. Mashayek, and C. Barré. 1999. Simulation and Reynolds stress modeling of particle-laden turbulent shear flows. *Int. J. Heat Fluid Flow* 20(4): 368–73.

90. Mashayek, R., D. B. Taulbee, and P. Givi. 1998. Modeling and simulation of two-phase turbulent flow. In: *Propulsion combustion: Fuels to emissions*. Ed. G. D. Roy. Washington, DC: Taylor & Francis. 241–80.

91. Lumley, J. L. 1978. Computational modeling of turbulent flows. *Adv. Appl. Mech.* 18:123–76.

92. Taulbee, D. B. 1992. An improved algebraic Reynolds stress model and corresponding nonlinear stress model. *J. Physics Fluids A* 4(11):2555–61.

93. Gatski, T. B., and C. G. Speziale. 1993. On explicit algebraic stress models for complex turbulent flows. *J. Fluid Mechanics* 254:59–78.

94. Mashayek, F., F. A. Jaberi, R. S. Miller, and P. Givi. 1997. Dispersion and poly-dispersity of droplets in stationary isotropic turbulence. *Int. J. Multiphase Flow* 23(2):337–55.

95. Mashayek, F., and F. A. Jaberi. 1999. Particle dispersion in forced isotropic low-Mach-number turbulence. *Int. J. Heat Mass Transfer* 42:2823–36.

96. Mashayek, F. 1998. Droplet–turbulence interactions in low-Mach-number homogeneous shear two-phase flows. *J. Fluid Mechanics* 376:163–203.

97. Mashayek, F. 1998. Direct numerical simulations of evaporating droplet dispersion in forced low-Mach-number turbulence. *Int. J. Heat Mass Transfer* 41(17):2601–17.

98. Mashayek, F. 1999. Simulations of reacting droplets dispersed in isotropic turbulence. *AIAA J.* 37(11):1420–25.

99. Mashayek, F. 2000. Numerical investigation of reacting droplets in homogeneous shear turbulence. *J. Fluid Mechanics* 405:1–36.

100. Mashayek, F., and G. B. Jacobs. 2001. Temperature-dependent reaction in droplet-laden homogeneous turbulence. *Numerical Heat Transfer B* 39:101–21.

101. Mashayek, F. 2001. Velocity and temperature statistics in reacting droplet-laden homogeneous shear turbulence. *J. Propulsion Power* 77(1).

102. Shuen, J.-S., A. S. P. Solomon, Q.-F. Zhang, and G. M. Faeth. 1985. Structure of particle-laden jets: Measurements and predictions. *AIAA J.* 23(23):396–404.

103. Pope, S. B. 1975. A more general effective-viscosity hypothesis. *J. Fluid Mechanics* 72:331–40.

104. Spencer, A. J. M. 1971. Theory of invariants. In: *Continuum Physics*. Ed. A. C. Eringen. New York, NY: Academic Press. 1:240–352.

105. Adumitroaie, V., D. B. Taulbee, and P. Givi. 1997. Algebraic scalar flux models for turbulent reacting flows. *AIChE J.* 43(8):1935–46.

106. Pozorski, J., and J. P. Minier. 1999. Probability density function modeling of dispersed two-phase turbulent flow. *Phys. Rev. E* 59:855–63.

107. Fox, R. O. 1996. Computational methods for turbulent reacting rows in chemical process industry. *Revue De L'Institut Francois Du Petrole* 51(2):215–46.

108. Subramaniam, S., and S. B. Pope. 1998. A mixing model for turbulent reactive flows based on Euclidean minimum spanning trees. *Combustion Flame* 115:487–514.

109. Subramaniam, S., and S. B. Pope. 1999. Comparison of mixing model performance for nonpremixed turbulent reactive flow. *Combustion Flame* 117:732–54.

110. Pope, S. B. 1994. On the relation between stochastic Lagrangian models of turbulence and second-moment closures. *J. Physics Fluids* 6(2):973–85.

111. Pope, S. B. 1997. Computationally efficient implementation of combustion chemistry using *in situ* adaptive tabulation. *Combustion Theory Modeling* 1:41.

112. Pope, S. B. 1997. Turbulence combustion modeling: Fluctuations and chemistry. In: *Advanced computation and analysis of combustion*. Eds. G. D. Roy, S. M. Frolov, and P. Givi. Moscow, Russia: ENAS Publ. 310–20.

113. Taulbee, D. B. 1989. Engineering turbulence models. In: *Advances in turbulence*. Eds. W. K. George and R. Arndt. New York, NY: Hemisphere Publ. Co. 75–125.

Chapter 10

COUPLED TURBULENCE, RADIATION, AND SOOT KINETICS EFFECTS IN STRONGLY RADIATING NONPREMIXED FLAMES

P. E. DesJardin and S. H. Frankel

A computational study of coupled turbulence, chemistry, and radiation interactions in an idealized strongly sooting and radiating nonpremixed turbulent planar jet flame has been conducted. The two-dimensional, density-weighted, spatially filtered compressible Navier–Stokes, energy and species equations were numerically integrated using a second-order time, fourth-order space accurate compact finite-difference scheme in the context of the Large-Eddy Simulation (LES) technique. The subgrid-scale (SGS) stress tensor, scalar flux vectors, and related subgrid correlations were closed using the dynamic Smagorinsky turbulence model. An idealized single-step, irreversible exothermic chemical reaction of the type $F + rO \rightarrow (1 + r)P$ with Arrhenius kinetics was employed. The filtered chemical source terms were closed using a scale-similarity filtered reaction rate SGS combustion model. An extension of the laminar flamelet concept to soot in the form of a presumed soot volume fraction state relationship was employed. The radiative transfer equation was integrated using an S_4 level discrete ordinates method and the gray gas assumption. The results show that the LES model was able to capture several unique features of strongly radiating turbulent flames consistent with previous experimental and numerical observations, including the effects of radiative cooling on flame structure and the highly intermittent behavior of the soot volume fraction.

10.1   NOMENCLATURE

A_f Chemical kinetics rate constant

c Speed of sound

C_v Specific heat at constant volume

C_p Specific heat at constant pressure

C_0 Fuel-dependent soot constant

C_2 Blackbody radiation constant

D Slot width

E Nondimensional radiative emission

E_a Activation energy

$h^{\circ}{}_{f_i}$ Enthalpy of formation (chemical energy) for the ith species

I Nondimensional radiative intensity

MW_i Molecular weight of the ith species

n Total number of species

O Oxidizer species

P Product species

r Stoichiometric ratio of oxidizer to fuel

R Gas constant (R_e/MW_{mix})

R_e Universal gas constant

Q_{rad} Radiation source term

$\widehat{s}_i$ Unit vector

T Nondimensional temperature

w_i Weighting factor for DOM

Z Mixture fraction

Greek Symbols

κ_P Nondimensional Planck mean absorption coefficient

ρ Nondimensional density

ΔU Difference between the core and co-flow velocities

$\xi_i,\ \eta_i,\ \mu_i$ Directional cosines for the ith direction discrete ordinate

10.2 INTRODUCTION

Future combustion devices may burn alternative fuels with higher carbon-to-hydrogen ratios and operate at higher pressures. The combustion of such fuels under these conditions will result in more intense turbulence, higher levels of soot formation, and the associated increase in radiative heat loss compared to more traditional fuels burned at lower pressures. Depending upon the design objectives, it may be desirable to control soot levels using predictive capabilities.

In numerical modeling of soot emissions in strongly radiating turbulent flames, it is important to accurately account for the coupling between turbulent mixing, finite-rate combustion and soot chemistry, and radiation effects due to the highly nonlinear behavior of these phenomena [1]. Traditional modeling approaches based on moment methods have difficulties because of a lack of detailed, e.g., temporally and spatially resolved, information or accurate models to account for turbulence–chemistry–radiation interactions [2]. Several recent efforts have begun to address some of these coupling effects (see citations in [3]), but transient simulations are still needed.

In Large-Eddy Simulation (LES), the conservation equations are spatially filtered to remove small scales and therefore they only describe the space and time dependence of the large or resolved scales. As a result of this filtering operation, nonlinear terms generate unknown SGS correlations which require closure models. One of the major obstacles to applying LES to turbulent combustion is related to closure of the filtered reaction rate term, which appears in the filtered species mass fractions and energy conservation equations [4]. The flame thickness is typically smaller than the smallest resolved scales, making this problem even more difficult. There have been several recent efforts reported in the literature directed at this subgrid closure problem. These have included assumed probability density function (PDF) methods [5, 6], eddy breakup models [7, 8], linear eddy modeling [9, 10], laminar flamelet models [11, 12], and PDF transport methods [13]. Each method has its advantages and disadvantages, but there is a considerable need for improvement.

Recently, both scale-similarity and dynamic modeling ideas have dominated the nonreacting LES literature (see [14] for recent review). Scale-similarity assumes that the largest of the unresolved scales, which contain most of the SGS energy, have a similar structure to the smallest of the resolved scales. A model for the SGS stress tensor could then be constructed from the stress computed from the resolved field. The dynamic modeling approach involves filtering the grid-scale field with a larger filter width and relating SGS stresses at the two levels via Germano's identity to allow direct evaluation of SGS model constants. The scale-similarity and dynamic modeling ideas have been very useful in SGS modeling for nonreacting flows and need to be exploited in LES of reacting flows.

The focus of the present study is to develop and apply the LES technique to strongly radiating turbulent jet flames in order to address issues related to turbulence–chemistry–radiation interactions. The present study is restricted to planar, two-dimensional jets in the near-field region. The assumption of two-dimensional flow precludes the vortex stretching mechanism and three-dimensional structure, but does allow for enhanced mixing, coherent structures, and unpredictability, which are important features of turbulent flows [15]. It also makes the LES calculations more affordable, allowing for comparison to direct numerical simulations in simple cases, and is generally considered to be a logical first step in the simulation of turbulent flows [16]. In addition, near-field tran-

sitional mixing in turbulent jets is thought to be dominated by two-dimensional, large-scale coherent structures, which are captured in the simulations.

The rest of the paper is organized as follows. In the next three sections, details of the LES models, the soot and radiation models, and the computational details are presented. The key results of the study follow. The conclusions of the study are then summarized.

10.3   LES MODELS

The physics of the problem under study is assumed to be governed by the compressible form of the Favre-filtered Navier–Stokes energy and species equations for an ideal gas mixture with constant specific heats, temperature-dependent transport properties, and equal diffusion coefficients. The molecular Schmidt, Prandtl, and Lewis numbers are set equal to 1.0, 0.7, and 1.43, respectively [17].

The SGS turbulence model employed is the compressible form of the dynamic Smagorinsky model [17, 18]. The SGS combustion model involves a direct closure of the filtered reaction rate using the scale-similarity filtered reaction rate model. Derivation of the model starts with the reaction rate for the ith species, $\dot{\omega}_i'''$, which represents the volumetric rate of formation or consumption of a species due to chemical reaction and appears as a source term on the right hand side of the species conservation equations:

$$\dot{\omega}_i''' = \dot{\omega}_i'''(\rho, T, Y_1, Y_2, \dots, Y_n) \tag{10.1}$$

where ρ, T, and Y_i are the density, temperature, and ith species mass fraction, respectively, and n is the total number of species in the mixture. In LES, the spatially filtered species conservation equations involve evaluation of the filtered (indicated by overbar) reaction rate:

$$\overline{\dot{\omega}_i'''} = \overline{\dot{\omega}_i'''(\rho, T, Y_1, Y_2, \dots, Y_n)} \tag{10.2}$$

This term is decomposed as:

$$
\begin{aligned}
\overline{\dot{\omega}_i'''} = {} & \overline{\dot{\omega}_i'''\left(\overline{\rho}, \widetilde{T}, \widetilde{Y}_1, \widetilde{Y}_2, \dots, \widetilde{Y}_n\right)} \\
& + \underbrace{\overline{\dot{\omega}_i'''(\rho, T, Y_1, Y_2, \dots, Y_n)} - \overline{\dot{\omega}_i'''\left(\overline{\rho}, \widetilde{T}, \widetilde{Y}_1, \widetilde{Y}_2, \dots, \widetilde{Y}_n\right)}}_{\omega_{\mathrm{SGS}}}
\end{aligned} \tag{10.3}
$$

where $\tilde{\phi}$ is a Favre-filtered variable defined as $\overline{\rho\phi}/\overline{\rho}$. This decomposition breaks the filtered reaction rate into a filtered large-scale and SGS contribution. The underbraced term, ω_{SGS}, represents the contribution of SGS fluctuations and

requires a model. To develop a closure for this term, the above expression is filtered again at the same filter level resulting in:

$$\overline{\overline{\dot{\omega}_i{'''}}} = \overline{\overline{\dot{\omega}_i{'''}\left(\overline{\rho},\, \widetilde{T},\, \widetilde{Y_1},\, \widetilde{Y_2},\, \dots,\, \widetilde{Y_n}\right)}} + \overline{\omega}_{\text{SGS}} \tag{10.4}$$

and then expressed in terms of large-scale and SGS contributions to the twice-filtered reaction rate, using the same decomposition strategy as in Eq. (10.3):

$$\overline{\overline{\dot{\omega}_i{'''}}} = \overline{\overline{\dot{\omega}_i{'''}\left(\overline{\overline{\rho}},\, \widetilde{\widetilde{T}},\, \widetilde{\widetilde{Y_1}},\, \widetilde{\widetilde{Y_2}},\, \dots,\, \widetilde{\widetilde{Y_n}}\right)}}$$
$$+ \underbrace{\overline{\overline{\dot{\omega}_i{'''}\left(\overline{\rho},\, \widetilde{T},\, \widetilde{Y_1},\, \widetilde{Y_2},\, \dots,\, \widetilde{Y_n}\right)}} - \overline{\dot{\omega}_i{'''}\left(\overline{\overline{\rho}},\, \widetilde{\widetilde{T}},\, \widetilde{\widetilde{Y_1}},\, \widetilde{\widetilde{Y_2}},\, \dots,\, \widetilde{\widetilde{Y_n}}\right)}}_{\mathcal{L}_\omega} + \overline{\omega}_{\text{SGS}} \tag{10.5}$$

where $\widetilde{\widetilde{\phi}}$ is computed as $\overline{\overline{\rho\widetilde{\phi}}}/\,\overline{\overline{\rho}}$ and the underbraced term represents the contribution of the resolved fluctuations to the twice-filtered reaction rate and is denoted as $\mathcal{L}_\omega$. Invoking scale-similarity one can assume that:

$$\omega_{\text{SGS}} = K\mathcal{L}_w \tag{10.6}$$

where K is a model coefficient chosen equal to 1 [17]. The final form for the filtered reaction rate is:

$$\overline{\dot{\omega}_i{'''}} = \overline{\dot{\omega}_i{'''}\left(\overline{\rho},\, \widetilde{T},\, \widetilde{Y_1},\, \widetilde{Y_2},\, \dots,\, \widetilde{Y_n}\right)}$$
$$+ K\left(\overline{\overline{\dot{\omega}_i{'''}\left(\overline{\rho},\, \widetilde{T},\, \widetilde{Y_1},\, \widetilde{Y_2},\, \dots,\, \widetilde{Y_n}\right)}} - \overline{\dot{\omega}_i{'''}\left(\overline{\overline{\rho}},\, \widetilde{\widetilde{T}},\, \widetilde{\widetilde{Y_1}},\, \widetilde{\widetilde{Y_2}},\, \dots,\, \widetilde{\widetilde{Y_n}}\right)}\right) \tag{10.7}$$

Physically, this closure attempts to model the effect of SGS fluctuations on the filtered reaction rate by assuming that the largest of the SGS are dynamically similar to the smallest of the resolved scales. The influence of the smallest eddies, in particular Kolmogorov eddies, on the filtered reaction rate is assumed negligible because the large viscosity in the flame tends to rapidly dissipate these scales [19]. Further discussion and assessment of this model with comparisons to other SGS combustion closures and DNS results can be found in [17].

10.4 SOOT AND RADIATION MODELS

Soot formation is a complicated process involving nucleation, surface growth, particle coagulation, and oxidation [20]. These processes pose a great challenge
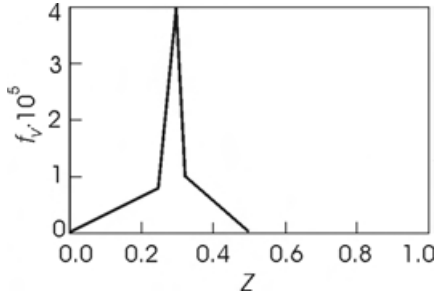
Figure 10.1 Soot volume fraction state relationship used in LES

to the development of simplified chemical reaction kinetics mechanisms. In this study, the soot model involves a direct extension of the laminar flamelet concept through the use of a soot volume fraction state relationship, e.g., $f_v(Z)$ (f_v denotes the soot volume fraction and Z is the gas-phase mixture fraction in a locally homogeneous flow approximation [21]). The form of the soot volume fraction state relationship used in this study is presented in Fig. 10.1, which represents a fit to the type of scatter observed in soot measurements in laminar flames [2, 22]. Previous work has shown this model to be effective in the over-fire region of turbulent flames [2, 23] and was in qualitative agreement with results obtained using a soot transport and finite-rate kinetics model [3]. In this study, the location of the peak value of the soot volume fraction in mixture fraction space, $Z = 0.3$, is exaggerated towards the rich side of stoichiometric, $Z_{st} = 0.07$. This is done to increase soot levels for the mixing environment produced in the present jet simulations. The filtered by convoluting the state relationship with a presumed SGS filtered density function for mixture fraction. Here, a Dirac delta function is used which does not account for SGS mixture fraction fluctuations.

Luminous thermal radiation from soot is treated by solving the filtered radiative transfer equation (FRTE) for a nonscattering, gray gas using an S_4 level discrete ordinates method (DOM) with open-boundary conditions [24]. The gray gas assumption for the absorption and the S_4 approximation allows for more efficient computations and is consistent with previous studies [25]. The discrete radiative transfer equation is nondimensionalized by the quantity, σT_0^4, where σ ($= 5.67 \cdot 10^{-8}$ W/(m^{2}K^4)) is the Stefan–Boltzmann constant. This equation is then spatially filtered resulting in the following nondimensional form of the FRTE:

$$\xi_i \frac{\partial \overline{I}_i}{\partial x} + \eta_i \frac{\partial \overline{I}_i}{\partial y} + \mu_i \frac{\partial \overline{I}_i}{\partial z} = \overline{\kappa_P \left(\frac{T^4}{\pi} - I_i \right)} \tag{10.8}$$

where κ_P is the Planck mean absorption coefficient and $\overline{I}_i$ is the discrete version of the local filtered radiation intensity for the ith discrete ordinate direction [24]. Here, $\kappa_P = K f_v T$, where $K = 3.83 D T_0 C_0 / C_2 = 1863 D T_0$ is a nondimensional parameter chosen as 10000, consistent with the conditions of typical turbulent flames. The constants C_0 ($= 7$) and C_2 ($= 0.014388$ m·K) are the

fuel dependent soot constant and the second Planck-mean coefficient [24], respectively. The Boltzmann number, $\mathrm{Bo} = \rho_0 C_{p_0} \Delta U / (\sigma T_0{}^3)$, which is the ratio of the convective-to-radiative heat fluxes, is chosen as 2000. The nondimensional discrete version of the radiation source term that appears in the energy conservation equation is:

$$\overline{Q}_{rad} = \frac{1}{\mathrm{Bo}\,(\gamma-1)\,\mathrm{M}^2} \left[-4\overline{\kappa_P T^4} + \sum_{i=1}^{m} w_i \overline{\kappa_P I_i\,(\widehat{s}_i)} \right] \qquad (10.9)$$

where w_i are the quadrature weights associated with the m directions of $\widehat{s}_i$ [24]. The parameters M $(= \Delta U / c_0)$ and $\gamma\ (= C_p / C_v)$ are the reference Mach number and specific heat ratio, which are set at 0.3 and 1.4, respectively.

As a first step, SGS turbulence–radiation interactions associated with the nonlinear correlations in Eqs. (10.8) and (10.9) are neglected, thus:

$$\xi_i \frac{\partial \overline{I}_i}{\partial x} + \eta_i \frac{\partial \overline{I}_i}{\partial y} + \mu_i \frac{\partial \overline{I}_i}{\partial z} \simeq \overline{\kappa}_P \left(\frac{\widetilde{T}^4}{\pi} - \overline{I}_i \right)$$

$$\overline{Q}_{rad} \simeq \frac{\overline{\kappa}_P}{\mathrm{Bo}\,(\gamma-1)\,\mathrm{M}^2} \left[-4\widetilde{T}^4 + \sum_{i=1}^{m} w_i \overline{I}_i\,(\widehat{s}_i) \right] \qquad (10.10)$$

$$\overline{\kappa}_P = \overline{K f_v T} \simeq K \overline{f}_v \widetilde{T}$$

10.5 COMPUTATIONAL DETAILS

The flow involves fuel, F, issuing from a central slot of width D with an oxidizer, O, co-flow with both streams at the reference temperature, T_0. A global single-step, irreversible, exothermic chemical reaction of the type $F + rO \rightarrow (1+r)P$ with an Arrhenius reaction rate coefficient is assumed. A hot layer of combustion products, P, at the inlet serves to separate the fuel and oxidizer streams and acts as an ignition source. The inlet conditions for the velocity, temperature, and composition are shown in Fig. 10.2. The ratio of the inlet velocities of the fuel to oxidizer streams is chosen as 4. Inlet velocity forcing is used to induce early roll-up and pairing of the jet shear layer vortices.

The governing equations are nondimensionalized using the fuel slot width, D, the difference between the inlet fuel and oxidizer velocities, ΔU, and T_0. The jet Reynolds number, $\mathrm{Re} = D \Delta U \rho_0 / \mu_0$, where ρ_0 and μ_0 are the reference density and viscosity, respectively, is chosen as 5000. The nondimensional Damköhler $(\mathrm{Da} = D \rho_0 A_f / (\Delta U M W_O))$, Zel'dovich $(\mathrm{Ze} = E_a / (RT)_0)$, and heat
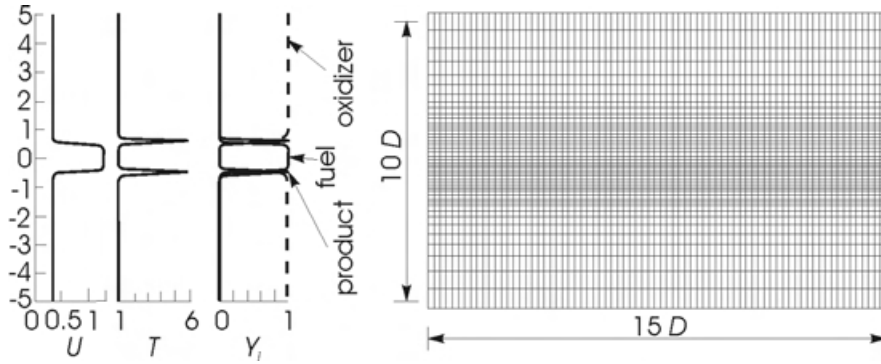
Figure 10.2 Inlet conditions, computational domain, and mesh used in the LES

release parameter $(\mathrm{Ce} = -h^{\circ}{}_{fP}(C_pT)_0^{-1} = (T_{\mathrm{ad}} - T_0)/T_0)$ are chosen as 10, 5, and 5, respectively, where T_{ad} is the adiabatic flame temperature. The stoichiometric oxidizer-to-fuel mass ratio, r, is chosen as 13.2 to mimic acetylene–air combustion.

The LES equations are numerically integrated using an explicit second-order time, fourth-order space accurate compact finite-difference scheme [26]. The computational domain extends 15 slot widths in the axial direction and 10 slot widths in the transverse direction and is discretized with a 101×75 LES nonuniform grid, as shown in Fig. 10.2. Box filtering is employed with grid-filter width twice the grid size and test-filter width four times the grid size. No attempt has been made to explicitly account for the commutation errors associated with the filtering and differentiation operators. Navier–Stokes low-reflection characteristic boundary conditions for multicomponent reacting flow are employed on all sides of the computational domain [27].

In the next section, LES results are presented and discussed for cases both with and without the effects of radiation. Qualitative comparisons to laboratory data are made when possible.

10.6   RESULTS AND DISCUSSION

An instantaneous snapshot of the jet showing soot volume fraction contours and radiation heat flux vectors is shown in Fig. 10.3. The soot forms immediately downstream of the jet exit as a result of the mixing controlled soot formation model. The soot appears in thin streaks in physical space which is consistent with previous experimental observations [2]. The radiation heat flux vectors are seen
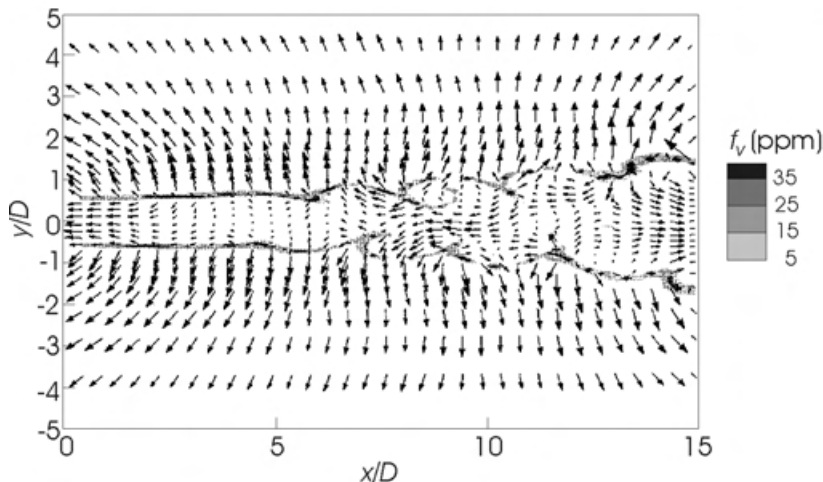
Figure 10.3 Instantaneous soot volume fraction contour plot with radiation heat flux vectors

to be emanating from the soot layer and are minimum in the central region of the fuel jet. In Figs. 10.4a and 10.4b, the mean $\langle T \rangle$ and RMS temperature σ_T profiles at several different downstream locations are shown, both with and without the effects of radiation. Radiative cooling lowers the mean flame temperatures. This lowers the molecular viscosity and increases large-scale mixing in the jet, which would tend to increase temperature RMS levels near the flame zones. Also notice that the transverse location of the peak mean temperature corresponds to the minimum in the temperature RMS due to the laminarization effect of heat release. In addition, radiative cooling selectively attenuates high temperatures, which tends to decrease temperature RMS levels outside the flame zones. The enhanced mixing with radiative cooling can be seen in Fig. 10.5, which shows an increase in the vorticity thickness δ_ω with radiation.

To examine the effects of radiative cooling on the flame structure, instantaneous scatter plots of temperature and reaction rate are plotted in Figs. 10.6 and 10.7, respectively, without and with radiation. These plots are constructed by collecting numerical data at several locations in the jet flame over a period of time. Figures 10.6a and 10.7a demonstrate turbulence–chemistry interactions without radiation effects. Figures 10.6b and 10.7b show effects of radiative cooling causing a depression in the temperature scatter in regions where the soot levels are high, showing how soot acts as an enthalpy sink. These regions radiate energy received from the flame via diffusion. This results in a unique flame structure for strongly radiating flames, first reported and discussed in [22]. As a result of the decrease in flame temperature due
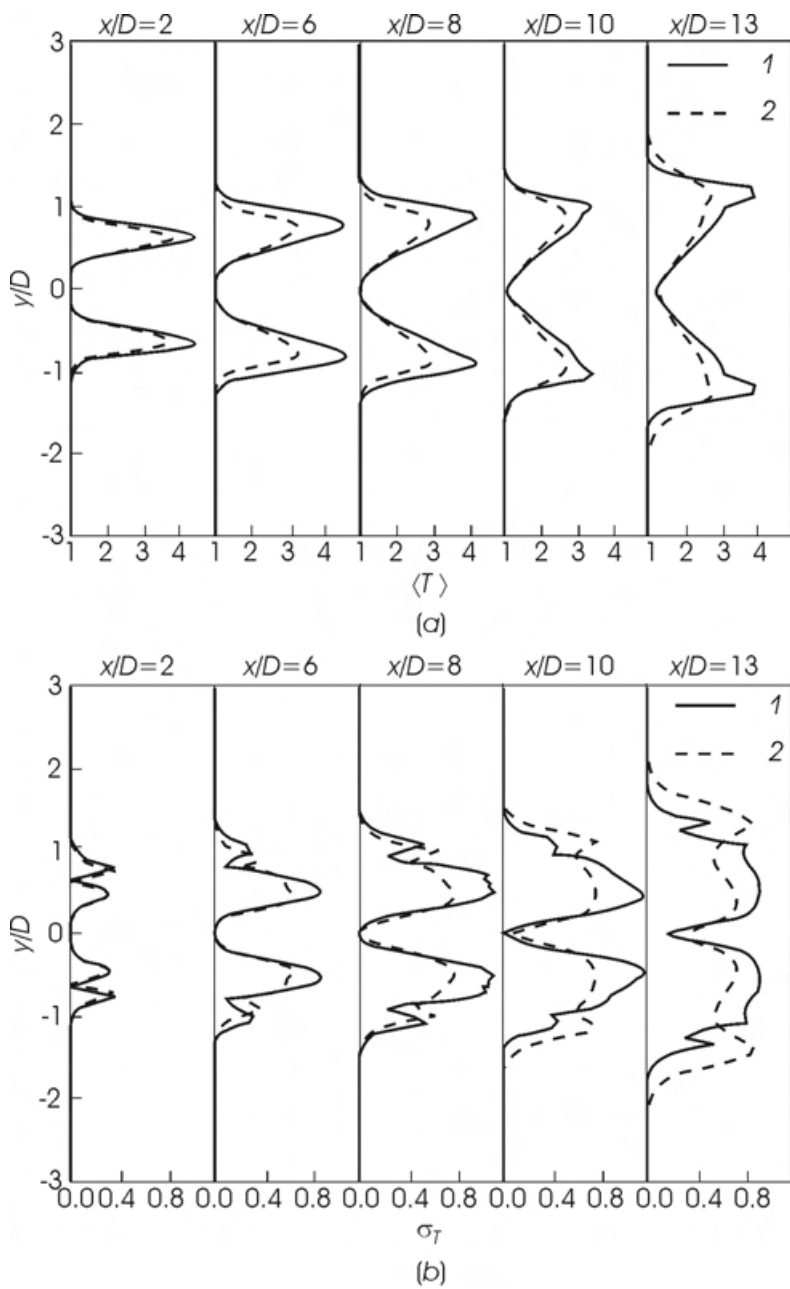
Figure 10.4 Transverse profiles of (*a*) mean and (*b*) RMS nondimensional temperature at five axial locations without (*1*) and with (*2*) radiation

to radiative cooling, the chemical re-action rate is partly suppressed, as shown in Fig. 10.7. The observed increase in reaction rates with radiation is due to an increase in density and large-scale mixing. Consequently, product formation is diminished with radiation due to the lower reaction rates, but is also enhanced due to the increase in reaction rates. The net effect of these trends can be observed in the product thickness δ_p plot shown in Fig. 10.8, which highlights the importance of chemistry–radiation interactions in this strongly radiating flame.
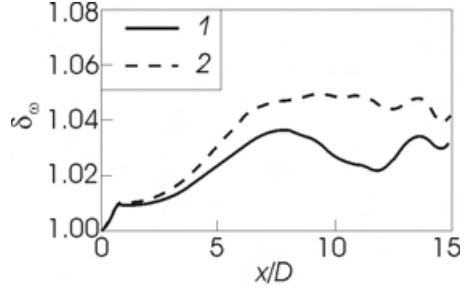
Figure 10.5 Inlet-normalized vorticity thickness vs. streamwise distance without (1) and with (2) radiation

The transverse profiles of the mean and RMS of the soot volume fraction are shown at the same axial locations in Fig. 10.9. The figure shows that soot fluctuations are larger or on the same order as the mean. These behaviors are in qualitative agreement with several previous experimental and numerical studies of strongly radiating turbulent flames [3, 28–30]. This highly intermittent behavior is suggestive of long-tailed PDFs, high kurtosis, short integral scales, and a flat power spectrum [29]. Similar behavior for soot volume fraction statistics has been observed in homogeneous turbulence simulations of strongly radiating nonpremixed flames using finite-rate soot chemistry and therefore is not an artifact of the soot volume fraction state relationship used here [3].
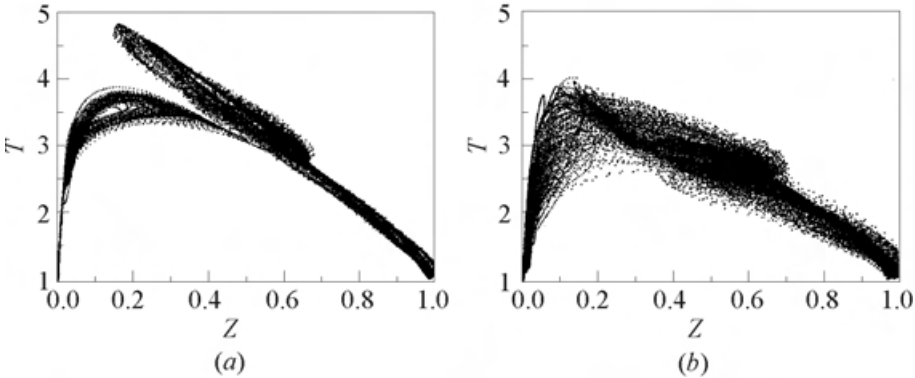
Figure 10.6 Instantaneous scatter plot of nondimensional temperature vs. mixture fraction: (a) without radiation; (b) with radiation
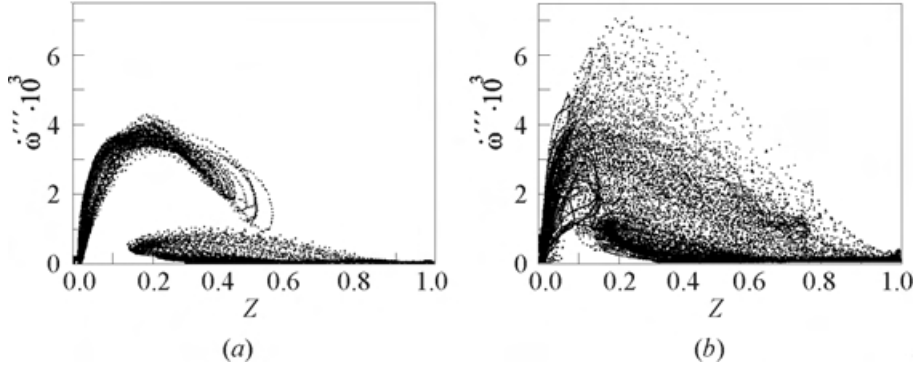
Figure 10.7 Instantaneous scatter plot of nondimensional reaction rate vs. mixture fraction: (*a*) without radiation; (*b*) with radiation
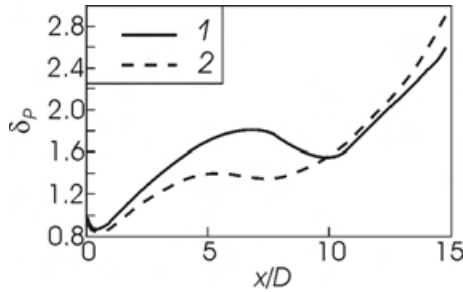
Figure 10.8 Inlet-normalized product thickness vs. streamwise distance without (*1*) and with (*2*) radiation

In order to examine the effects of large-scale turbulence–radiation interactions, transverse profiles of the time-averaged radiative emission and the radiative emission expressed in terms of the time-averaged temperature and Planck mean soot absorption coefficient at several axial locations are shown in Fig. 10.10. The absolute value of the nondimensional radiative emission term is defined as $E = 4\kappa_P T^4/(\mathrm{Bo}(\gamma - 1)\mathrm{M}^2)$. From this figure, neglecting large-scale turbulence–radiation interactions results in a severe underprediction of the mean radiative emission term, suggesting that they need to be accounted for in strongly radiating flame computations. This is due to the nonlinear dependence of the radiation source/sink term on the soot volume fraction and temperature.

10.7 CONCLUDING REMARKS

The interaction between turbulence, chemistry, and radiation from soot in a two-dimensional, planar jet diffusion flame was investigated using LES. A dynamic
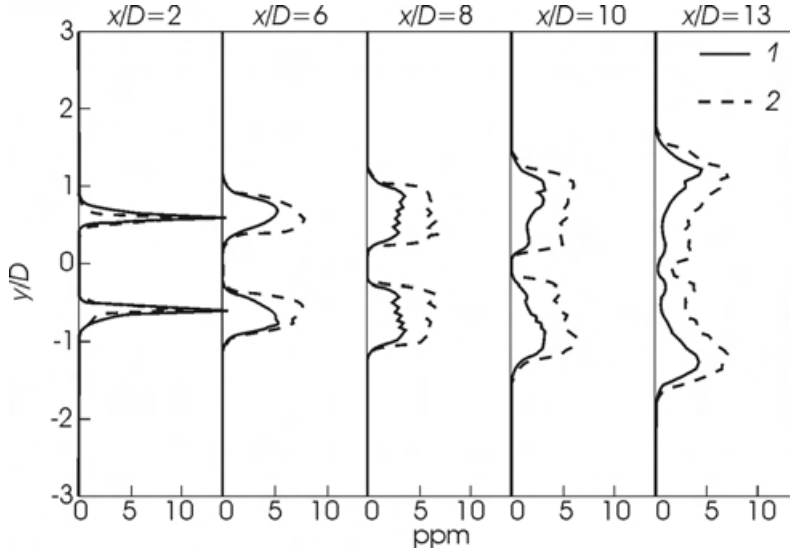
Figure 10.9 Profiles of mean $\langle f_v \rangle$ (*1*) and RMS σ_{f_v} (*2*) soot volume fraction
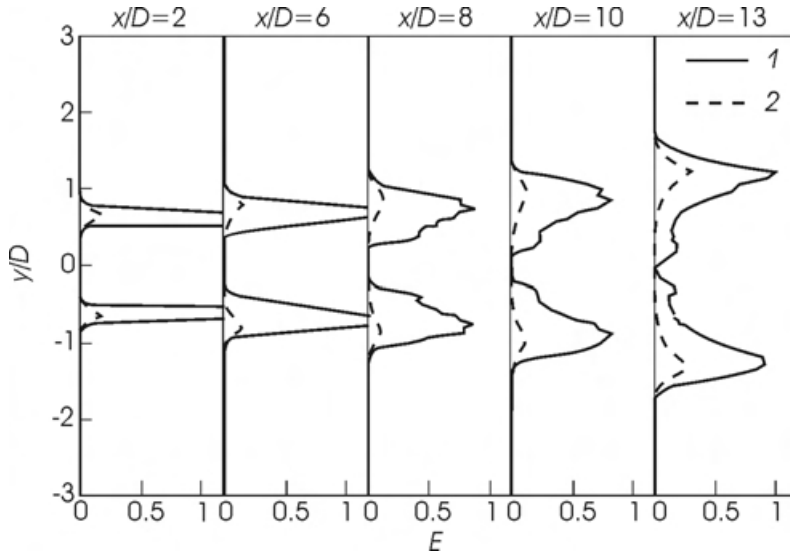
Figure 10.10 Profiles of nondimensional emission source term with large-scale turbulence–radiation interactions accounted for (*1*) $\langle E \rangle$ and without them (*2*) $E(\langle \widetilde{T} \rangle, \langle \overline{\kappa}_P \rangle)$

SGS turbulence model and a scale-similarity filtered reaction rate SGS combustion model were employed to close the governing equations. The calculations involved a soot volume fraction state relationship model and a discrete ordinates method solution of the radiative transfer equation for a gray gas. The effects of radiative cooling on flame structure and soot statistics were studied. Comparisons were made to the case without radiation. The results showed that radiative cooling lowered mean flame temperatures. Radiative cooling increased RMS temperature levels in certain regions of the flame due to lower viscosity and more large-scale mixing, and decreased RMS temperature levels in other regions of the flame due to selective attenuation of high temperatures. A unique flame structure, showing an inflection point in the temperature vs. mixture fraction scatter plot, previously discussed by [22], due to radiative cooling in high-soot regions, was observed. The effect of radiation on reaction rates and product formation observed herein was twofold. First, radiative cooling lowered reaction rates due to lower temperatures, which decreased product formation for $x/D < 10$. Second, radiative cooling tended to increase the reaction rate due to higher density and enhanced large-scale mixing, which increased product formation for $x/D > 10$. The soot volume fraction exhibited a highly intermittent behavior, showing RMS levels greater than the mean. Finally, significant underprediction in the calculation of the mean radiative emission term was observed when large-scale turbulence–radiation interactions were neglected. Future work should involve simulation of more realistic turbulent flames, include the effects of soot transport and finite-rate soot chemistry, and address subgrid-scale modeling of turbulence–soot–radiation interactions such as begun in the companion study in [3].

ACKNOWLEDGMENTS

REFERENCES

1. Faeth, G. M., J. P. Gore, S. G. Chuech, and S. M. Jeng. 1989. Radiation turbulent diffusion flames. *Annual Reviews Numerical Fluid Mechanics. Heat Trans.* 2:1–38.
2. Gore, J. P., and G. M. Faeth. 1988. Structure and radiation properties of luminous turbulent acetylene/air diffusion flames. *J. Heat Transfer* 110:173–81.
3. Zimberg, M. J., S. H. Frankel, J. P. Gore, and Y. R. Sivathanu. 1998. A study of coupled turbulence, soot chemistry and radiation effects using the linear eddy model. *Combustion Flame* 113:454–69.

4. Bray, K. N. C. 1996. The challenge of turbulent combustion. *26th Symposium (International) on Combustion Proceedings*. Pittsburgh, PA: The Combustion Institute. 1–26.

5. Frankel, S. H., V. Adumitroaie, C. K. Madnia, and P. Givi. 1993. Large eddy simulation of turbulent reacting flow by assumed PDF methods. *Fluids Engineering Conference on Engineering Applications of Large Eddy Simulations Proceedings*. FED 162: 81–101.

6. Cook, A. W., and J. J. Riley. 1994. A subgrid model for equilibrium chemistry in turbulent flows. *J. Physics Fluids* 6(8):2868–70.

7. Garrick, S. C. 1995. Large eddy simulations of a turbulent reacting mixing layer. AIAA Paper No. 95-0010.

8. Fureby, C., and C. Lofstrom. 1994. Large eddy simulations of bluff body stabilized flames. *25th Symposium (International) on Combustion Proceedings*. Pittsburgh, PA: The Combustion Institute. 1257–64.

9. Calhoon, W., and S. Menon. 1996. Subgrid modeling for reacting large eddy simulations. AIAA Paper No. 96-0516.

10. Calhoon, W. H., and S. Menon. 1997. Linear-eddy subgrid model for reacting large eddy simulations: Heat release effects. AIAA Paper No. 97-0368.

11. Cook, A. W., J. J. Riley, and G. Kosaly. 1997. A laminar flamelet approach to subgrid-scale chemistry in turbulent flows. *Combustion Flame* 109(3):332–41.

12. DesJardin, P. E., M. J. Zimberg, and S. H. Frankel. 1997. Towards large eddy simulation of strongly radiating turbulent diffusion flames. In: *Advanced computation and analysis of combustion*. Ed. G. D. Roy, S. M. Frolov, and P. Givi. Moscow, Russia: ENAS Publ. 503–19.

13. Colucci, P. J., F. A. Jaberi, P. Givi, and S. B. Pope. 1998. Filtered density function for large eddy simulation of turbulent reacting flows. *J. Physics Fluids* 10:499–515.

14. Moin, P. 1997. Progress in large eddy simulations of turbulent flows. AIAA Paper No. 97-0749.

15. Lesieur, M. 1990. *Turbulence in fluids*. 2nd rev. ed. Boston, MA: Kluwer Academic Publ.

16. Givi, P. 1989. Model-free simulations of turbulent reactive flows. *Progress Energy Combustion Science* 15:1–107.

17. DesJardin, P. E. 1998. Large eddy simulation of strongly radiating nonpremixed turbulent jet flames. Ph.D. Thesis. School of Mechanical Engineering, Purdue University, West Lafayette, IN.

18. Moin, P., K. Squires, W. Cabot, and S. Lee. 1991. A dynamic subgrid-scale model for compressible turbulence and scalar transport. *J. Physics Fluids* 3(11):2746–57.

19. Poinsot, T. 1996. Using direct numerical simulations to understand premixed turbulent combustion. *26th Symposium (International) on Combustion Proceedings*. Pittsburgh, PA: The Combustion Institute. 219–32.

20. Glassman, I. 1988. Soot formation in combustion processes. *22nd Symposium (International) on Combustion Proceedings*. Pittsburgh, PA: The Combustion Institute. 295–311.

21. Faeth, G. M. 1987. Mixing, transport and combustion in sprays. *Progress Energy Combustion Science* 13:293–345.

22. Gore, J. P., and J. H. Jang. 1992. Transient radiation properties of a subgrid eddy. *J. Heat Transfer* 114:234–42.

23. Sivathanu, Y., and G. M. Faeth. 1990. Soot volume fractions in the overfire region of turbulent diffusion flames. *Combustion Flame* 81:133–49.

24. Modest, M. F. 1993. *Radiative heat transfer*. New York: McGraw-Hill.

25. Kaplan, C. R., S. W. Back, E. S. Oran, and J. L. Ellzey. 1994. Dynamics of strongly radiating unsteady ethylene jet diffusion flame. *Combustion Flame* 96:1–22.

26. Kennedy, C. A., and M. H. Carpenter. 1994. Several new numerical methods for compressible shear-layer simulations. *Applied Numerical Methods* 14:397–433.

27. Baum, M., T. Poinsot, and D. Thevenin. 1994. Accurate boundary conditions for multicomponent reactive flows. *J. Comput. Phys.* 116:247–61.

28. Sivathanu, Y. R., J. P. Gore, and J. Dolinar. 1991. Transient scalar properties of strongly radiated jet flames. *Combustion Science Technology* 76:45–66.

29. Magnussen, B. F., and B. H. Hiertager. 1976. On mathematical modeling of turbulent combustion with special emphasis on soot formation and combustion. *16th Symposium (International) on Combustion Proceedings.* Pittsburgh, PA: The Combustion Institute. 719–29.

30. Coppalle, A., and D. Joyeux. 1994. Temperature and soot volume fraction in turbulent diffusion flames: Measurements of mean and fluctuating values. *Combustion Flame* 96:275–85.

Chapter 11

VORTICITY AND ENTRAINMENT IN A JET SUBJECTED TO OFF-SOURCE VOLUMETRIC HEATING

A. J. Basu and R. Narasimha

The effect of volumetric heating on the distribution of vorticity and the entrainment characteristics of a temporally evolving jet has been investigated. The data from a set of 128^3 simulations have been used for this purpose. The simulations show very good qualitative similarity with experiments on a jet subjected to volumetric heat injection between two chosen diametral stations. In addition, it is shown that the baroclinic torque resulting from heating enhances the vorticity dramatically in all three directions, with a preferential amplification at the higher wavenumbers that results in a rich fine structure at later times in the evolution of the jet. Large expulsive motions are seen in the ambient fluid near the heated flow; this results in an entraining velocity field that is qualitatively different from that around unheated turbulent jets.

11.1 INTRODUCTION

Entrainment and mixing are problems of major concern when one attempts to understand, control, or model combustion flows in air-breathing propulsion systems, as well as in such geophysical problems as the evolution of clouds. A variety of experimental studies carried out in recent years have illuminated the connections between the coherent structures found in turbulent shear flows and entrainment, chemical reaction, and combustion [1–3]. It is important to realize that in experiments on reacting flows, the heat released is a *result* of chemical reactions, and that the rate of such reactions is determined by the amount of *mixing* (in the sense of molecule-to-molecule interaction) that takes place. The mixing itself depends on — and in turn affects, through the chemical reaction — the structure of turbulence in the flow. Turbulence, mixing, and reaction therefore form a tightly coupled system. To understand the mutual influences in

such a complex problem, there is need for considering a flow situation in which this cyclical connection between mixing, combustion, and heat release can be broken, and one may focus on the specific effect *on* turbulence of substantial amounts of heat release. With this objective in view, a series of simulations have been performed here using a pseudospectral method to compute the evolution of a jet-like flow with volumetric heat injection.

This disassociation of the heat release from chemical reaction enables the investigation of the effect of heating on mixing, the two together accounting for the dynamics of turbulence in reacting flows. Such a separation permits the use of the Boussinesq approximation, which is not directly applicable to most combustion problems, but describes what may be an important ingredient of mutual influences. Interestingly, the Boussinesq approximation happens to be quite realistic in many geophysical applications (see, e.g., [4]). Furthermore, recent experimental work on such flows ([5] and [6]) can provide a basis for mutual validation and enhanced understanding. The studies by Bhat and Narasimha [6], which are of great relevance here, have been performed over a Reynolds number range (based on initial jet diameter and velocity) of 1360 to 3200, which are low enough to be computed using the Direct Numerical Simulation (DNS) technique. The jets studied in [6] are, however, spatially evolving, and so direct quantitative comparisons with those experiments cannot be made. It is gratifying, however, that strong qualitative similarities with the experiments have been observed in the present simulations.

The experimental studies show that heating accelerates the flow and arrests jet growth; absolute values of turbulence intensity increase but not as rapidly as the mean velocities. So, normalized turbulence intensities are lower. The effects of the amount of heating and its distribution on the evolution of the computed jet have been previously reported in [7]. These results show all the qualitative features that have been found in the experiments. In this paper, the findings of the study related to the effects of heat release on the vortical structure and entrainment characteristics of the jet are described.

11.2 NUMERICAL METHOD

The *temporal* development of a cylindrical mixing layer under local volumetric heating is investigated. It is assumed that the Boussinesq approximation is valid in the given situation — that is, density changes in the flow (because of heating) introduce a buoyancy term in the momentum equation, and the changes in the inertial terms or the values of the transport parameters are negligible (see [4] for a critical discussion of this approximation). The heat deposited into the flow appears as a source term in the energy equation. The governing equations for the problem are therefore

$$\nabla \cdot \mathbf{V} = 0 \tag{11.1}$$

$$\frac{\partial \mathbf{V}}{\partial t} + (\mathbf{V} \cdot \nabla)\mathbf{V} = -\frac{1}{\rho}\nabla p + \nu \nabla^2 \mathbf{V} - \mathbf{g}\alpha T \tag{11.2}$$

$$\frac{\partial T}{\partial t} + (\mathbf{V} \cdot \nabla)T = \kappa \nabla^2 T + \frac{J}{\rho c_p} \tag{11.3}$$

where ρ is the density of the fluid, ν the kinematic viscosity, p the pressure, $\mathbf{V}$ the velocity vector, $\mathbf{g}$ the acceleration due to gravity, α the coefficient of thermal expansion, κ the thermal diffusivity, J the *rate* of heat addition per unit volume, c_p the specific heat at constant pressure, and T is the *change* in temperature above ambient.

Equations (11.1)–(11.3) respectively express conservation of mass, momentum, and energy. To nondimensionalize these equations, the initial diameter d_0, the initial centreline velocity U_0, and a characteristic temperature difference T_0 are used as scales. If the heat is deposited *uniformly* over a unit volume at a constant rate J, for a total time t_h into the flow, T_0 may be defined as the resultant net temperature change that would result if this heat was deposited: $T_0 \equiv Jt_h/\rho c_p$.

Nondimensionalizing the energy equation based on the above characteristic quantities (using * for nondimensional variables), one obtains:

$$\frac{\partial T^*}{\partial t^*} + (\mathbf{V}^* \cdot \nabla)T^* = \frac{1}{\text{Re}\,\text{Pr}}\nabla^2 T^* + \frac{d_0}{U_0 t_h}g(r) \tag{11.4}$$

where $\text{Re} = U_0 d_0/\nu$ is the Reynolds number, $\text{Pr} = \nu/\kappa$ is the Prandtl number, and $g(r)$ is a prescribed radial distribution function.

Similarly, nondimensionalizing the momentum equations, one obtains:

$$\frac{\partial \mathbf{V}^*}{\partial t^*} + (\mathbf{V}^* \cdot \nabla)\mathbf{V}^* = -\nabla p^* + \frac{1}{\text{Re}}\nabla^2 \mathbf{V}^* + GC_h T^* \tag{11.5}$$

where

$$G = \frac{g\alpha d_h{}^2}{\rho c_p}\,\frac{J}{U_h{}^3} \tag{11.6}$$

and d_h, U_h are respectively the relevant length and velocity scales in the heating region. Now G is a heating parameter that is analogous to the nondimensional heat release number introduced by Bhat and Narasimha [6], except that Eq. (11.6) incorporates a modification to take account of the fact that in the present simulation the heat release occurs over a finite duration t_h in time, and not over a finite region in space as in [6]. Either version of G is a measure of the ratio of buoyancy to inertia forces, like the Richardson number. The other nondimensional parameter in Eq. (11.5) is

$$C_h = \frac{U_h t_h}{d_h}\frac{d_0}{d_h}\left(\frac{U_h}{U_0}\right)^2$$

whose value will remain constant during the present study. (This corresponds to fixing the spatial region over which heat is added in a real jet.)

Since G and C_h appear only as a product, $G^* = GC_h$ is used as the relevant nondimensional parameter governing heat release in the present studies. The other governing parameters for this flow are Re and Pr, along with the precise strength and distribution of the source term in the energy equation.

Equations (11.4) and (11.5) are solved, along with the continuity equation (which does not change upon nondimensionalization), in a *Cartesian* coordinate system using the Fourier–Galerkin (spectral) technique under periodic boundary conditions in all three space dimensions. The scheme is similar to that used by Orszag [8] for direct solution of the incompressible Navier–Stokes equations. More details can be found in [9] and [7], and the scheme may be considered to be "pseudospectral."

Small errors in computation that may result in pockets of small negative temperature T^* can have disastrous effects here since temperature is an *active* scalar, and influences the flow directly (unlike passive scalars like dye concentration). To maintain positivity of temperature, a simple procedure used by Riley *et al.* [10] is followed, which merely involves setting any small negative temperature that may arise to zero at every time step. It has been shown [10] that one is still able to get superalgebraic convergence using this simple filter.

The initial conditions for the velocity components are set up so that there is a tubular shear layer aligned along the z-direction at time $t = 0$. The w-velocity has a top-hat profile with a tan-hyperbolic shear layer. Streamwise and azimuthal perturbations are introduced to expedite roll-up and the development of the Widnall instability. The details can be found in [7]. The initial velocity field is made divergence-free using the Helmholtz decomposition. The size of the computational domain (one periodic cubical box) is $4d_0$ on each side.

11.3   EFFECT OF HEATING ON VORTICITY

In order to examine in detail the effect of heating on vorticity, two simulations based on the 128^3 grid are considered specifically. The first case is an unheated jet whose evolution has been computed up to nondimensional time $t = 40$; in the other case, heat is applied between the times $t = 25$ and $t = 32$ and the flow evolution is computed up to $t = 35$. The relevant parameters for the computations are Re = 1600, Pr = 7, $G^* = 0.04$. The time step used for computing the evolution of the unheated jet is $\Delta t = 0.0025$, whereas for the heated jet it has been reduced to $\Delta t = 0.00125$.

The vorticity transport equation can be obtained by taking the curl of Eq. (11.2):

$$\frac{\partial \boldsymbol{\omega}}{\partial t} + (\mathbf{u}\cdot\nabla)\boldsymbol{\omega} - (\boldsymbol{\omega}\cdot\nabla)\mathbf{u} - \nu\nabla^2\boldsymbol{\omega} = \alpha\mathbf{g} \times \nabla T \qquad (11.7)$$

where the terms on the left are familiar from classical, incompressible flow theory. The term on the right is a source of vorticity; it arises from the baroclinic torque $\nabla p \times \nabla \rho$ when the pressure gradient ∇p is replaced by its value in the hydrostatic approximation, and the density gradient $\nabla \rho$ by the temperature gradient, to which it is proportional in the approximation used.

By decomposing the vorticity into a mean $\overline{\boldsymbol{\omega}}$ and a fluctuation $\boldsymbol{\omega}'$, the mean baroclinic generation terms are

$$\frac{\alpha g}{r}\frac{\partial \overline{T}}{\partial \theta}, \qquad -\alpha g\frac{\partial \overline{T}}{\partial r}, \qquad 0 \qquad (11.8)$$

for $\overline{\omega}_r$, $\overline{\omega}_\theta$, and $\overline{\omega}_z$, respectively.

11.3.1 Vorticity Components

The effect of heating on the azimuthal and streamwise components of the vorticity field is shown in Fig. 11.1; the effect on the radial component is comparable to that on the azimuthal component, and is therefore not separately shown. The vorticity distributions at the same nondimensional time $t = 35$ are plotted side by side for the unheated and heated case for each component. The positive and negative values of vorticity are shown by solid and dotted lines, respectively.

The dramatic effect of heating on the vortical structures is quite evident from Fig. 11.1. There is a large overall increase in vorticity strength in the flow, along with the emergence of intense small-scale structures. In general, the vorticity field with heating reveals much less organization than the unheated case.

11.3.2 Enstrophy

To quantify the vorticity increases due to heating, the total enstrophy and also the enstrophies corresponding to the azimuthal, streamwise, and radial components of vorticity are examined. Computed values are shown using a linear-log scale in Fig. 11.2. In the absence of heating, the total as well as the component enstrophies all fall beyond time $t = 25$, as would be expected in a fully developed turbulent jet. When heat is applied, there is a virtually exponential rise of the enstrophies after some time. At $t = 35$, the enstrophies are one order of magnitude higher with heating than without.

It is interesting to note that the streamwise enstrophy is almost as large as the other two components, although the generation term for mean streamwise
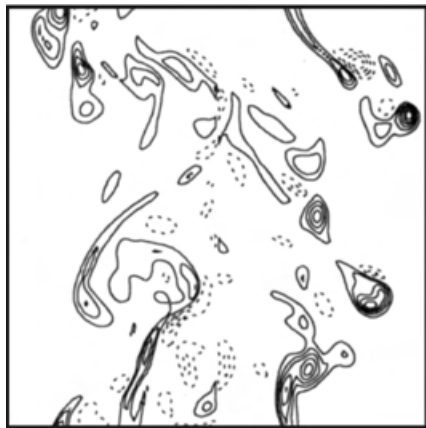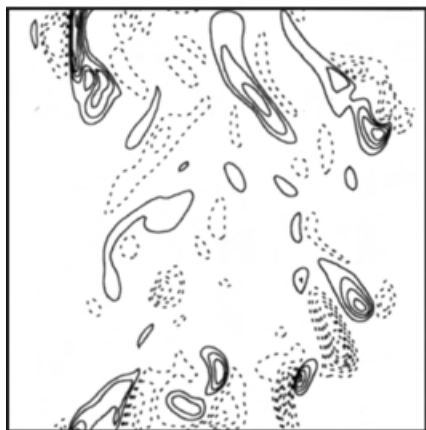
Figure 11.1 Streamwise sections (in the yz-plane passing through the axis of the jet) of different components of vorticity in the unheated (a), (c) and heated (b), (d) jets at time $t = 35$; (a), (b) — azimuthal vorticity, (c), (d) — streamwise vorticity. Negative contours are shown using dotted lines in steps of -0.5 starting from -0.5, while positive contours are in solid lines in steps of 0.5 starting from 0.5
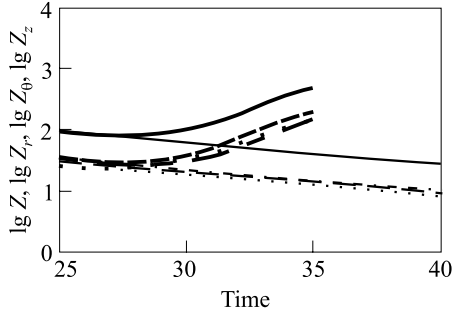
Figure 11.2 Comparison of evolution of enstrophy in the heated (thick lines) and unheated (thin lines) jet. The enstrophy components are: total (solid line), azimuthal (dashed), radial (dotted), and streamwise (long-dashed). Note logarithmic scale on y-axis
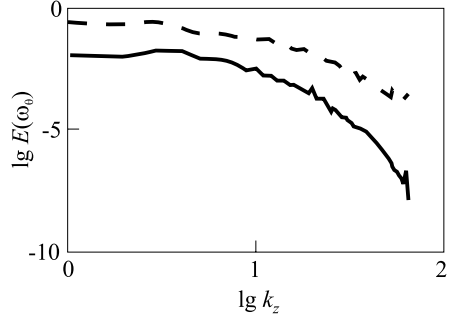
Figure 11.3 Comparison of computed spectra for the azimuthal component of vorticity for the heated (dashed curve) and unheated (solid curve) jets. The spectra are plotted on log–log scales

vorticity is zero, from Eq. (11.8). It is concluded that intercomponent transfer, from nonlinear interactions, must therefore be substantial.

11.3.3 Spectra

The computed spectra of the three vorticity components at time $t = 35$ for both the unheated and heated jets are shown in Fig. 11.3. The heated jet has higher energy in all modes, but there appears to be a preferential amplification at higher wavenumbers. Thus, while the increase in enstrophy is about dozen times at low wavenumbers, it is 3–4 dozens at the highest wavenumbers. As vorticity generation depends on the temperature *gradient*, there is an additional weighting at higher wavenumbers due to the derivative in the source term in Eq. (11.7).

11.3.4 Vorticity Fluctuations

Figure 11.4 shows the radial profile of the RMS vorticity fluctuations at $t = 25$, 30, and 35, representing conditions before, during, and immediately after heat deposition. The large increases in vorticity fluctuations on heating are evident. It is interesting that the azimuthal fluctuation $\hat{\omega}'_\theta$ shows a rather flat maximum around $r \simeq 0.6$ (so does $\hat{\omega}'_r$, although it is not included in the figure), whereas the
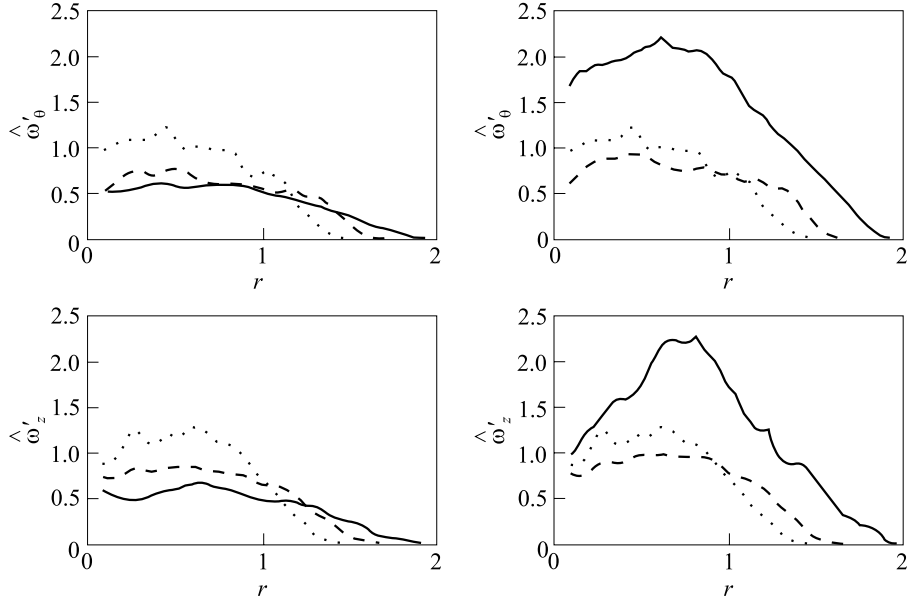
Figure 11.4 Radial distributions of the RMS of the fluctuating vorticity components at different times for the unheated (left column) and heated (right column) jet. The times are: $t = 25$ (dotted curve), $t = 30$ (dashed curve), and $t = 35$ (solid curve)

streamwise fluctuation $\hat{\omega}'_z$ shows a sharp peak at $r \simeq 0.8$. It is presumably this peak that is responsible for the strong expulsive motions seen in the entraining velocity field discussed in the next section.

11.4   EFFECT OF HEATING ON ENTRAINMENT

A major question concerning the development of jet flow subjected to heating is the effect on entrainment. Now because of the periodic boundary conditions imposed on the computational domain in the present simulation, the net entrainment over the domain has to vanish. Nevertheless, as shown below, considerable insight into the problem can be obtained by examining the "entraining velocity field," which displays velocity vectors in the ambient fluid in the immediate neighbourhood surrounding the jet.

Figure 11.5 shows the computed entraining velocity fields at the widest transverse cross-sections at $t = 35$ in the heated and unheated jets. (This corresponds to looking at the flow in the plane of the cross-section of the spatially developing jet.) The figure shows velocity vectors in the ambient fluid, and contours of streamwise vorticity within the jet.
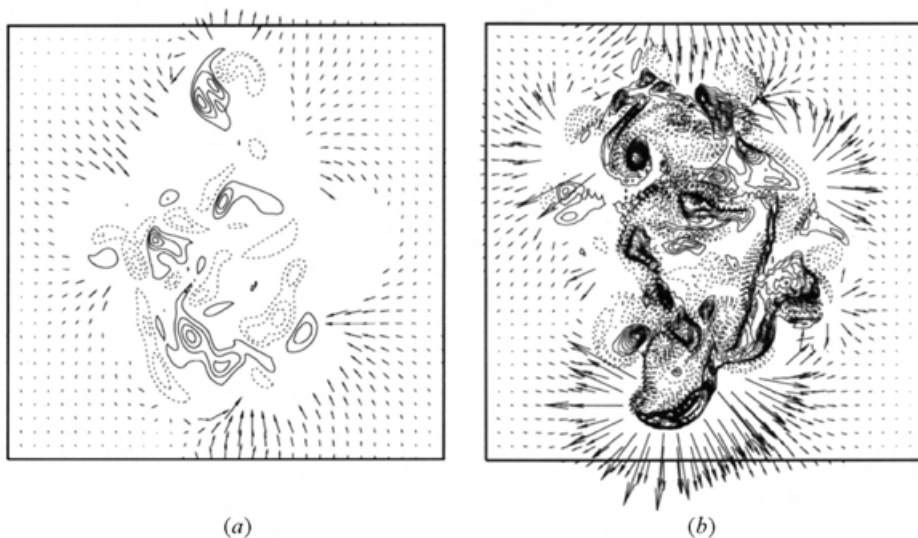
Figure 11.5 Comparison of computed entraining velocity fields at the widest transverse sections of the (a) unheated and (b) heated jet at time $t = 35$. The contours of streamwise vorticity, at intervals of 0.5, are shown using solid lines for positive values, and dotted lines for negative values. Contour for level 0 is not shown

The enormous increase in vorticity due to heating is once again displayed, but it will be noted that there are striking differences in the entraining velocity field in the two cases. In the unheated case, the dominant motion is inward, and may be attributed to velocities induced in the ambient fluid by the toroidal component of the coherent vorticity. As already suggested, this toroidal component appears structurally disrupted by the heat addition. Now the induced velocities in the heated flow are actually much higher, but the chief difference is that the dominant motion (at least in the transverse section shown) appears to be *outward*: there is a considerable *expulsion* of fluid from the vortical core of the flow. These expulsions are highly localized, and are clearly due to vorticity on a scale between a fifth and a tenth of the total width of the flow. The strength and direction of the motion in the horizontal plane suggests that it is due to streamwise vortex pairs. Although much more detailed analysis is required in order to be sure, it can be speculated that the enhancement of streamwise vorticity, due to vortex-stretching and transfer from other components generated by the baroclinic torque, results in intense small-scale vortex dipoles that tend to expel core fluid into the ambient. The present simulations therefore suggest a plausible physical explanation for the lower entrainment observed in the experiments when heat is deposited:

namely, that it is the consequence of two reinforcing factors, the enhancement of local streamwise vorticity and a disruption of organized azimuthal vorticity.

11.5   CONCLUDING REMARKS

The present temporal simulations have shown qualitative similarity with previously published experimental results on a jet subjected to local volumetric heating. In addition, they have shown that heating leads to dramatic increases in the different components of vorticity in the flow, and to striking differences in the flow characteristics. It is found that, due in part to vortex stretching induced by the acceleration of the flow due to buoyancy, the streamwise vortices become intense, leading to large expulsive motions in the ambient neighbourhood. Together with a disruption of the coherent structures in the flow, this causes dramatic changes in the entraining velocity field. In the future, it is planned to investigate how selective heating can be used to control turbulence.

ACKNOWLEDGMENTS

REFERENCES

1. Roshko, A. 1993. In: *Theoretical and applied mechanics*. Eds. S. R. Bodner, J. Singer, A. Solan, and Z. Hashin. New York: Elsevier.
2. Dimotakis, P. E. 1991. Turbulent free shear layer mixing and combustion. *Prog. Astro. Aero.* 137:265–340.
3. Broadwell, J. E., and M. G. Mungal. 1991. *J. Physics Fluids* A3:1193–206.
4. Turner, J. S. 1973. *Buoyancy effects in fluids*. Cambridge, UK: Cambridge University Press.
5. Elavarasan, R., G. S. Bhat, R. Narasimha, and A. Prabhu. 1995. An experimental study of a jet with local buoyancy enhancement. *Fluid Dyn. Res.* 16(4):189–202.
6. Bhat, G. S., and R. Narasimha. 1996. A volumetrically heated jet: Large-eddy structure and entrainment characteristics. *J. Fluid Mechanics* 325:303–30.
7. Narasimha, R., and A. J. Basu. 1996. Local volumetric heating of a turbulent jet: Effect of amount and distribution of heating. *9th ONR Propulsion Meeting Proceedings*. Eds. G. D. Roy and K. Kailasanath. Washington, DC: Naval Research Laboratory.
8. Orszag, S. A. 1971. *Stud. Appl. Maths.* 50:293–327.
9. Basu, A. J., R. Narasimha, and U. N. Sinha. 1992. *Curr. Sci.* 63:734–40.
10. Riley, J. J., R. W. Metcalfe, and S. A. Orszag. 1986. *J. Physics Fluids* 29:406–22.

Chapter 12

MODELING OF CONFINED FLAME STABILIZATION BY BLUFF BODIES

S. M. Frolov, V. Ya. Basevich, A. A. Belyaev,
V. S. Posvianskii, and Yu. B. Radvogin

New computational approaches are developed to explore flame stabilization techniques in subsonic ramjets. The primary focus is statistical modeling of turbulent combustion and derivation of the adequate boundary conditions at open boundaries. The mechanism of flame stabilization and blow-off in ramjet burners is discussed. The criterion of flame stability based on the clearly defined characteristic residence and reaction times is suggested and validated by numerical simulations.

12.1 INTRODUCTION

One of the widely applied means for flame anchoring in high-speed flows is flame stabilization by bluff bodies. The wake of a bluff body placed into the flow can maintain continuous ignition of the reactive mixture by recirculating hot combustion products. The flame originating in the wake can spread throughout the whole combustor cross-section, resulting in significant acceleration of burned gases in the direction of the flow.

The technique of flame stabilization by bluff bodies has been used for a long time; however, the mechanism by which the fresh gases are ignited, the flame spreads and blows off, is not well defined. Even for the simplest case of premixed flame stabilization there are still a number of uncertainties that are reflected in inconsistencies as indicated in available literature. As for the flames of fuel sprays, a topic of significant practical importance, the understanding of relevant phenomena is far from satisfactory.

Available experimental studies of premixed flame stabilization focus on the effect of the bluff-body (stabilizer) configuration, combustion chamber geometry

and operating conditions on the flame spreading process, flame stability limits, combustion efficiency, and pressure loss associated with the flame-holding devices.

The most important aspect for ramjet combustion is the fuel–air ratio range during operation. Many investigators studied this factor in detail (e.g., [1–12]). It has been found that larger flame holders, higher pressures, higher inlet temperatures, and lower velocities give wider stability limits in unconfined flows. Several other variables influence the stability limits in terms of the mixture equivalence ratio, namely, fuel type, flame-holder temperature, turbulence of the entering stream, stabilizer type, blockage ratio, channel wall properties, and channel length. Choosing among various combinations of quantitative parameters relevant to these variables can result in an optimum design of the ramjet burner, which accounts for multiple compromises between combustion requirements and vehicle design requirements.

Bluff-body flame stabilization in nonpremixed and partially premixed gaseous systems is complicated by the mixing of fuel and oxidizer. In addition to the aspects considered above, it is necessary to control the fuel distribution in the burner.

Theoretical studies are primarily concentrated on the treatment of flame blow-off phenomenon and the prediction of flame spreading rates. Dunskii [12] is apparently the first to put forward the phenomenological theory of flame stabilization. The theory is based on the characteristic residence and combustion times in adjoining elementary volumes of fresh mixture and combustion products in the recirculation zone. It was shown in [13] that the criteria of [1, 2, 5] reduce to Dunskii's criterion. Longwell *et al.* [14] suggested the theory of bluff-body stabilized flames assuming that the recirculation zone in the wake of the baffle is so intensely mixed that it becomes homogeneous. The combustion is described by a second-order rate equation for the reaction of fuel and air.

The available criteria of flame blow-off do not provide complete understanding of the phenomenon. There is no evidence of the effect of multiple variables on flame stability mentioned above.

Early theoretical treatments of bluff-body stabilized flame spreading have been based, in general, on the assumption that the flame is a discontinuous surface separating gas streams of different densities and temperatures [1, 15–17]. These theories neglect the finite thickness of turbulent flame zone and predict the increase of the spreading rate both with the density ratio across the flame, and with the increase in the laminar flame velocity of fuel–air mixture. This does not correspond to experimental observations (e.g., [8, 10]).

The effect of the finite thickness of the turbulent flame was introduced in theories [18, 19]. In [18], the set of governing gas dynamic equations is supplemented by the empirical dependency of flame thickness on the distance to the ignition source, obtained by means of statistical processing of the instantaneous position of a thin wrinkled flame front in model experiments. Semi-empirical the-

ories [18, 19] provided satisfactory predictions and were used for designing simple ramjet burners. A number of theoretical models are based on mixing-controlled combustion in the flame spreading from the bluff-body stabilizer [20–22]. The basic drawback of the theory is that it does not predict the effect of chemical kinetic factors on flame spread and stability.

Currently, computing the structure of bluff-body stabilized flames has become a subject of intense activity. The general objective of numerical studies is to describe the phenomenon by solving the fundamental differential equations coupled with turbulence and combustion closures. Since there are many possible approaches, more or less substantiated, the reported results are often contradictory. Apparently, this is caused by the lack of basic understanding of the physico-chemical phenomena accompanying flame stabilization and spreading.

Thus, theoretical modeling of bluff-body flame stabilization cannot yet compete with the experimental approaches. Partially, it is due to the fundamental problems relevant to the turbulent combustion theory. The underestimation of the role of theory is also due to the lack of systematic studies based on existing models.

The present study is to elaborate on the computational approaches to explore flame stabilization techniques in subsonic ramjets, and to control combustion both passively and actively. The primary focus is on statistical models of turbulent combustion, in particular, the Presumed Probability Density Function (PPDF) method and the Pressure-Coupled Joint Velocity–Scalar Probability Density Function (PC JVS PDF) method [23, 24].

The results of numerical simulation of bluff-body stabilized premixed flames by the PPDF method are presented in section 12.2. This method was developed to conduct parametric studies before applying a more sophisticated and CPU time consuming PC JVS PDF method. The adequate boundary conditions (ABC) at open boundaries derived in section 12.3 play an essential role in the analysis. Section 12.4 deals with testing and validating the computational method and discussing the mechanism of flame stabilization and blow-off.

12.2 PRESUMED PDF METHOD FOR MODELING TURBULENT COMBUSTION

The PC JVS PDF method [23, 24] requires remarkable computational power for attaining reasonable accuracy of results. Hence an alternate mathematical method is needed to determine interrelations between various governing parameters. This method should have acceptable accuracy to obtain necessary estimates relatively fast and to test the efficiency of various approaches to passive and active combustion control. The corresponding estimates obtained would be used for more detailed studies by the PC JVS PDF method.

Such a method has been additionally developed. The method uses the mean values of temperature and species concentrations and applies a presumed PDF, to obtain the mean reaction rate. The PDF takes into account the effect of fluctuating temperature on the mean reaction rate.

Mathematically, the PPDF method is based on the Finite Volume Method of solving full Favre averaged Navier–Stokes equations with the k–ϵ model as a closure for the Reynolds stresses and a presumed PDF closure for the mean reaction rate.

The mean rate of energy release S and the rate of consumption/production of species j, r_j, are calculated on the basis of the detailed or reduced reaction mechanism of fuel oxidation in air and a single-point bimodal normalized PDF of temperature $P(T, \overline{T})$ in the turbulent flame brush:

$$
\begin{aligned}
S &= \sum_j \int_{T_0}^{T_c} \mathcal{D}_j W_j(T) P(T, \overline{T}) \, dT \\[2mm]
\dot{r}_j &= \sum_j \int_{T_0}^{T_c} [W_{1j}(T) - W_{2j}(T) Y_j] P(T, \overline{T}) \, dT
\end{aligned}
\tag{12.1}
$$

where T is the local instantaneous temperature, $\overline{T}$ is the local mean temperature, T_0 and T_c are the initial and combustion temperatures, respectively, $\mathcal{D}_j$ is the heat of decomposition of jth species to atoms [25], $W_j = \sum_i W_{ij}$ is the rate of change in the jth species concentration in all reactions, i is the reaction number, and W_{1j} and W_{2j} are the rates of production and consuption of the jth species in all reactions.

The rates W_j, W_{1j}, and W_{2j} in a turbulent flame are assumed to be similar to those in a laminar flame. Thus, prior turbulent flame calculations, W_j, W_{1j}, and W_{2j}, are tabulated in the form of look-up tables.

In general, the PDF $P(T, \overline{T})$ should be obtained from the solution of a PDF transport equation, or taken from experimental or DNS studies. In this study, a simple bimodal PDF of temperature was applied, which qualitatively corresponds to experimental findings [26–28].

The PDF is constructed as follows. For any mean temperature $T_0 \leq \overline{T} \leq T_c$ the PDF is defined as:

$$
\widetilde{P}(T, \overline{T}) =
\begin{cases}
\dfrac{T_c - \overline{T}}{T_c - T_0} & \text{at} \quad T = T_0 \\[4mm]
\dfrac{\overline{T} - T_0}{T_c - T_0} & \text{at} \quad T = T_c \\[4mm]
P_T(T, \overline{T}) & \text{at} \quad (T_0 + \Delta) < T < (T_c - \Delta)
\end{cases}
\tag{12.2}
$$

For intermediate temperatures $(T_0 + \Delta) < T < (T_c - \Delta)$, a preset constant value $P_T(T, \overline{T})$, similar for all T and $\overline{T}$, is used. The "thickness" of PDF, Δ, is also the parameter of the model. The PDF is normalized as

$$P(T, \overline{T}) = \widetilde{P}(T, \overline{T}) \Big/ \int\limits_{T_0}^{T_c} \widetilde{P}(T, \overline{T}) \, dT$$

to satisfy the condition

$$\int\limits_{T_0}^{T_c} P(T, \overline{T}) \, dT = 1 \tag{12.3}$$

Clearly, such a definition of $P(T, \overline{T})$ implies a finite width of the turbulent flame.

The other definition of the PDF was also applied, effectively accounting for flame quenching under high-turbulence intensities:

$$\widetilde{P}(T, \overline{T}) = \begin{cases} 1 & \text{at} \quad T = T_0 \\[2mm] \dfrac{\overline{T} - T_0}{T_c - T_0} & \text{at} \quad T = T_c \\[2mm] P_T(T, \overline{T}) & \text{at} \quad (T_0 + \Delta) < T < (T_c - \Delta) \end{cases} \tag{12.4}$$

The parameters $P_T(T, \overline{T})$ and Δ are used to construct the PDF in such a way that the model predictions for well-defined conditions correspond to experimental measurements. For constructing a proper temperature PDF, the PPDF method was applied to the problem of planar turbulent flame propagation.

12.3 ADEQUATE INLET–OUTLET BOUNDARY CONDITIONS

One of the basic elements of the computational algorithm is the determination of dependent variables at the inlet/outlet boundaries of a computational domain representing a finite length combustor. The essence of the problem lies in the fact that the nonstationary flow field has to be considered throughout a whole (unbounded) physical space, and only in this case the problem is mathematically well-posed. When solving a specific problem numerically, one has to consider a computational domain of a finite size, in which boundary conditions at artificial boundaries are to be imposed.

12.3.1 Adequate Outlet Boundary Conditions

Assume that to the left of the combustor outlet boundary, $x = 0$, there exists a stationary solution of the Euler equations: $p = p_0$, $\rho = \rho_0$, $u = u_0$, where p_0, ρ_0, and u_0 are the constant pressure, density, and velocity. Flow velocity has a single nonzero component, u_0, along the x axis. The flow is assumed subsonic, i.e., $M = u_0/c_0 < 1$, where c_0 is the speed of sound. We consider the solution of the nonstationary Euler equations and linearize the problem in the vicinity of the stationary solution by assuming that

$$p = p_0 + p', \qquad \rho = \rho_0 + \rho', \qquad u = u_0 + u'$$

where p', ρ', and u' are the variations of the corresponding parameters in the sound wave ($p' << p_0$, $\rho' << \rho_0$, $u' << u_0$). Standard transformation of the Euler equations results in the following equation for p' ("prime" is removed for convenience):

$$p_{tt} + 2u_0 p_{tx} + u_0{}^2 p_{xx} = c_0{}^2 \Delta p \qquad (12.5)$$

At $u_0 = 0$, Eq. (12.5) reduces to the standard wave equation. In the 2D Cartesian coordinate system, the Laplace operator Δ is given by

$$\Delta p = p_{xx} + p_{yy} \qquad (12.6)$$

The boundary condition at impermeable walls and symmetry planes at $y = 0$ and $y = a$ (a being the width of the combustor exit) is $\partial p/\partial y = 0$.

Assume that the geometry of the channel allows for separation of variables in Eq. (12.5). In Cartesian coordinates, this can be expressed in the form

$$p = Y(x,t)f(y) \qquad (12.7)$$

In this case, the ABC can be derived analytically. In a case of arbitrary geometry, the separation of variables is hardly possible.

Substitution of Eq. (12.7) into Eq. (12.5) results in the following equation for the nth mode of solution $Y^{(n)}$:

$$Y_{tt}{}^{(n)} + 2u_0 Y_{tx}{}^{(n)} - (c_0{}^2 - u_0{}^2)Y_{xx}{}^{(n)} + c_0{}^2 k^2 Y^{(n)} = 0 \qquad (12.8)$$

where $k = \pi n/a$ and n is the arbitrary integer.

ABC at $x = 0$ for function $Y^{(n)}(x, t)$ which satisfies Eq. (12.8) at $x \leq 0$ is now constructed.

Equation (12.8) has two families of characteristics (see Fig. 12.1). For an arbitrary point P at $x \geq 0$, one can plot characteristics BP and AP to some points A and B at $x = 0$, such that

$$\text{on } BP: \qquad \frac{dx}{dt} = -(c_0 - u_0) = -c_0(1 - M)$$

$$\text{on } AP: \qquad \frac{dx}{dt} = (c_0 + u_0) = c_0(1 + M)$$

Since for an arbitrary function, $dF = (\partial F/\partial x)dx + (\partial F/\partial t)dt$, then

$$\text{on } BP: \qquad dF = \left[\frac{\partial F}{\partial x} - \frac{1}{c_0(1-\text{M})} \frac{\partial F}{\partial t} \right] dx$$

$$\text{on } AP: \qquad dF = \left[\frac{\partial F}{\partial x} + \frac{1}{c_0(1+\text{M})} \frac{\partial F}{\partial t} \right] dx \qquad (12.9)$$
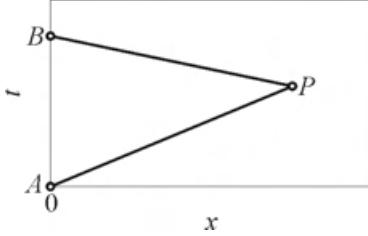
Figure 12.1 Flow characteristics at the outlet boundary

Let at $t = 0$ and $x \geq 0$ $Y(x,0) = 0$, and $Y_x(0,0) = 0$. Clearly, in this case $Y|_{AP} = 0$, and in particular $Y(P) = 0$. Equation (12.8) can be treated as the equation with initial conditions specified on section AB, and the solution to be found at $x \geq 0$. Since the solution is zero at P, the Cauchy values of Y and $\partial Y/\partial x$ for Eq. (12.8) are not arbitrary, and there exists a certain relationship between these functions. This relationship is nothing other than the ABC.

For solving the problem, the Riemann method is applied. Riemann function $V(x, t, \theta)$ for the problem under solution is the function which satisfies Eq. (12.8) for variables x and t under the boundary condition $V|_{BP} = 1$ (point B corresponds to time $t = \theta$).

Define the operator L as

$$L = \frac{\partial^2}{\partial t^2} + 2u_0 \frac{\partial^2}{\partial x \partial t} - (c_0{}^2 - u_0{}^2)\frac{\partial^2}{\partial x^2} + c_0{}^2 k^2$$

The standard procedure then gives:

$$LY = 0, \qquad LV = 0, \qquad VLY - YLV = 0,$$

$$VLY - YLV = (VY_t - YV_t)_t$$
$$+ u_0[(VY_t - YV_t)_x + (VY_x - YV_x)_t] - (c_0{}^2 - u_0{}^2)(VY_x - YV)_x$$
$$(12.10)$$

It follows from Eqs. (12.10) that

$$[(VY_t - YV_t) + u_0(VY_x - YV_x)]_t$$
$$- [(c_0{}^2 - u_0{}^2)(VY_x - YV_x) - u_0(VY_t - YV_t)]_x = 0 \qquad (12.11)$$

Integrating Eq. (12.11) in triangle APB in a counterclockwise direction, and applying Green's formula and Eqs. (12.9), one arrives at the required boundary condition

$$c_0 Y(B) + \int_A^B [(c_0{}^2 - u_0{}^2)(VY_x - YV_x) - u_0(VY_t - YV_t)]\,dt = 0 \qquad (12.12)$$

Note, that function V is defined with the accuracy of an arbitrary (allowed) boundary condition at AB. In particular, one can require that $V\big|_{AB} = 1$. Then, Eq. (12.12) is transformed to a simpler form

$$Y(B) = c_0(1 + \mathrm{M}) \int_A^B (YV_x - Y_x)\, dt \qquad (12.13)$$

Condition (12.13) can be replaced by condition

$$Y_t + c_0(1 + \mathrm{M})Y_x = -c_0(1 + \mathrm{M}) \int_A^B (YV_{xt})\, dt \qquad (12.14)$$

obtained by differentiating Eq. (12.13) with respect to t. Applying Laplace transformation and the standard technique of taking contour integrals, the analytical form for function V_{xt} is obtained:

$$V_{xt} = \frac{\alpha^2}{1 + \mathrm{M}} \frac{J_1[c_0(1 - \mathrm{M})(\theta - t)\alpha]}{(\theta - t)\alpha} \qquad (12.15)$$

where $\alpha^2 = k^2(1 + \mathrm{M})/(1 - \mathrm{M})$ and J_1 is the Bessel function of the first order. Finally, for either nth mode, the function $Y^{(n)}(x, t)$ takes the form

$$Y_t^{(n)} + c_0(1 + \mathrm{M})Y_x^{(n)} = -c_0\alpha \int_0^t Y^{(n)}(0, \tau) \frac{J_1[c_0(1 - \mathrm{M})(t - \tau)\alpha]}{t - \tau}\, d\tau \qquad (12.16)$$

For the initial function $p(x, t)$, Eq. (12.16) can be rewritten in the final form

$$p_t + c_0(1 + \mathrm{M})p_x =$$

$$- c_0\sqrt{\frac{1 + \mathrm{M}}{1 - \mathrm{M}}} \sum_n \int_0^t Y^{(n)}(0, \tau) \frac{J_1[c_0(1 - \mathrm{M})(t - \tau)\alpha]}{t - \tau} \cos(ky)\, d\tau \qquad (12.17)$$

Equation (12.17) represents the required boundary condition. It should be emphasized that it is essentially nonlocal both in space and time. In general, the numerical implementation of the operator in the right hand side of Eq. (12.17) is a nontrivial task.

The boundary condition of Eq. (12.17) can be simplified. Note that at $\xi < 0.5$ the function $J_1(\xi)/\xi$ under the integral in the right hand side of Eq. (12.17) is

$$\frac{J_1(\xi)}{\xi} \approx 0.5$$

By using this asymptotics, Eq. (12.17) can be rewritten as

$$p_t + c_0(1 + \mathrm{M})p_x = -\frac{c_0(1 + \mathrm{M})}{2} \sum_n n k^2 \int_0^t Y^{(n)}(0, \tau) \cos(ky)\, d\tau \qquad (12.18)$$

which is equivalent to

$$p_t + c_0(1 + \mathrm{M})p_x = \frac{c_0{}^2(1 + \mathrm{M})}{2} \int\limits_0^t p_{yy}(0, \tau)\, d\tau \qquad (12.19)$$

If the flow is described by first N harmonics, then the applicability condition of Eq. (12.19) is

$$t^* < \frac{a}{2c_0\pi N\sqrt{1 - \mathrm{M}^2}} \qquad (12.20)$$

Thus, ABC approximated in the form of Eq. (12.19) can be efficiently applied for ensuring nonreflecting outlet boundaries for two-dimensional disturbances. Such disturbances leave the computational domain for a limited time interval Δt. Clearly, at $\Delta t < t^*$, the approximation of Eq. (12.19) is satisfactory.

If the flow at the outlet boundary is quasi-one-dimensional, then p_{yy} becomes small, the right hand side of Eq. (12.17) vanishes, and one gets the local boundary condition

$$p_t + c_0(1 + \mathrm{M})p_x = 0 \qquad (12.21)$$

which is often applied as an approximation of ABC [29].

Figure 12.2 (left part) shows the example of applying the ABC of Eq. (12.19) when solving full 2D Navier–Stokes equations coupled with the standard k–ϵ turbulence model. The problem considered is the propagation of pressure disturbance in a 2D duct with the flow of nonreacting stoichiometric methane–air mixture. The flow enters the duct through the left boundary (inlet) at 40 m/s and leaves the computational domain through the right boundary (outlet). The upper boundary is the rigid wall and the lower is the symmetry plane. Initially, a provision for the small region with pressure differential $\Delta p/p_0 = 0.5$ was made in the flow nearby the outlet. The solution with standard von Neumann conditions at the outlet boundary is shown in Fig. 12.2 (right part) for comparison. Contrary to the von Neumann (and Dirichlet) conditions, the ABC of Eq. (12.19) provide the transparency of the outlet to the pressure wave.

12.3.2 Adequate Inlet Boundary Conditions

Similar considerations can be used for deriving the Adequate Boundary Conditions at combustor inlet. The analogs of Eqs. (12.17) and (12.19) at the inlet will take the form
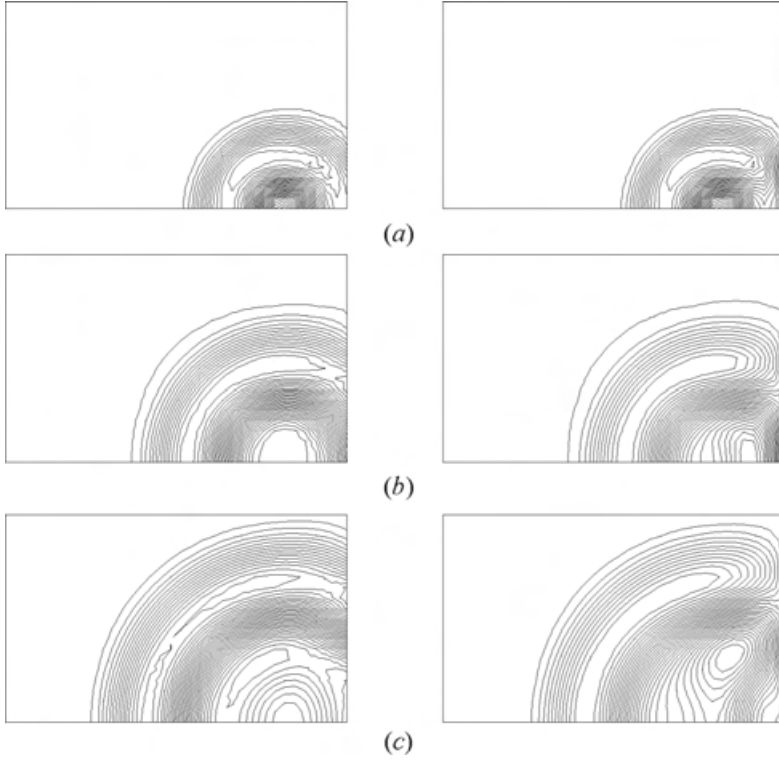
Figure 12.2 Application of the nonreflecting boundary conditions (left part) and standard von Neumann boundary conditions (right part) in the problem on pressure disturbance propagation in a flow reactor with open left and right boundaries. Time instants: (a) 10 μs, (b) 20 μs, (c) 30 μs. Flow velocity at the inlet 40 m/s, $p_0 = 0.1$ MPa, $T_0 = 300$ K, $k_0 = 9$ J/kg, $l_0 = 2$ mm. Initial pressure differential $\Delta p / p_0 = 0.5$. The size of the computational domain is 3.3×2 cm

$$p_t - c_0(1 - \mathrm{M})p_x =$$

$$- c_0 \sqrt{\frac{1 + \mathrm{M}}{1 - \mathrm{M}}} \sum_n k \int_0^t Y^{(n)}(0, \tau) \frac{J_1[c_0(1 + \mathrm{M})(t - \tau)\alpha]}{t - \tau} \cos(ky) \, d\tau \quad (12.22)$$

$$p_t - c_0(1 - \mathrm{M})p_x = \frac{c_0{}^2(1 - \mathrm{M})}{2} \int_0^t p_{yy}(0, \tau) \, d\tau \quad (12.23)$$

In the 1D case, the precise ABC at the combustor inlet are obtained by omitting the right hand sides of Eqs. (12.22) and (12.23), i.e.,

$$p_t - c_0(1 - \mathrm{M})p_x = 0 \quad (12.24)$$

In addition, the entropy-based boundary condition should be specified for the energy equation at the inlet. This latter condition can be written in the form

$$c_p \ln \frac{p^{1/\gamma}}{\rho} = c_{p_0} \ln \frac{p_0^{1/\gamma_0}}{\rho_0} \qquad (12.25)$$

where γ and γ_0 are the specific heat ratios at inlet and at infinity upstream of the flow; c_p and c_{p_0} are the corresponding specific heats at constant pressure.

12.4 CONFINED TURBULENT FLAMES STABILIZED ON BLUFF BODIES

The behavior of confined flames differs considerably from that of unconfined flames. Acceleration of the gases, caused by confinement, results in the generation of shear stresses and turbulent motions, which decrease the influence of approach stream turbulence and the effect of chemical kinetic factors. How the implementation of the ABC and the PPDF method helps to obtain the experimentally observed flow patterns and to understand the mechanism of flame stabilization and blow-off is demonstrated in this section.

12.4.1 Flow Patterns

Numerical tests show that the boundary conditions of Eqs. (12.19), (12.23), and (12.25) provide well-defined short- and long-time solutions of full 2D Navier–Stokes equations coupled with the k–ϵ model of turbulence and with the PPDF model of turbulent combustion. The conditions avoid considerable numerical reflections of pressure waves at open boundaries, which are characteristic to standard Dirichlet and von Neumann conditions.

Figure 12.3 shows some computational examples of nonreactive and reactive turbulent flows in a combustor with the bluff-body flame holder. The size of the combustor in Fig. 12.3 is 35×8 cm. The characteristic height and length of the bluff body is $H = 2$ cm. The left boundary is set as inlet, right boundary as outlet, and the upper and lower boundaries as rigid walls.

Figure 12.3a shows the absolute mean velocity distribution in a nonreactive flow at time 98 ms, which is considered to be a long-time asymptotics.

For initial conditions in Fig. 12.3a, uniform flow of stoichiometric methane–air mixture with $u_x = 30$ m/s, $u_y = 0.0$, $k_0 = 0.54$ J/kg, $l_0 = 4$ mm, $p_0 = 0.1$ MPa, $T_0 = 293$ K is assumed throughout the whole combustor, with x-axis directed along the mean flow.

Boundary conditions at the inlet are the conditions provided by Eqs. (12.23), (12.25). In addition, constant turbulent parameters and constant mixture com-
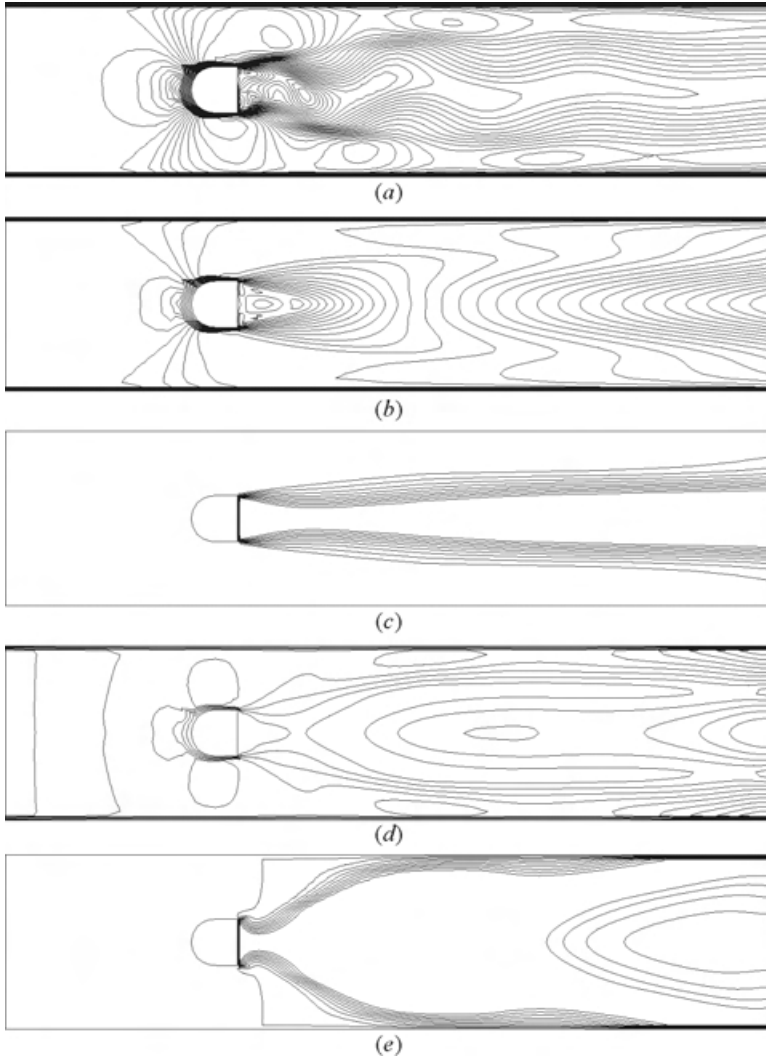
Figure 12.3 Predicted flow patterns in a combustor with semi-cylindroid flame holder. Premixed stoichiometric methane–air mixture. (a) Absolute mean velocity distribution in a nonreactive flow at $t = 98$ ms; (b) absolute mean velocity; and (c) temperature fields at $t = 22.1$ ms in a reactive flow after symmetrical ignition behind a bluff body. The isoterms divide the entire temperature interval from T_0 to T_c into 10 uniform parts. Boundary condition at outlet is ABC of Eq. (12.19). (d) absolute mean velocity and (e) temperature fields at $t = 22.1$ ms at standard von Neumann boundary conditions at the outlet. Mean velocity at inlet 30 m/s (a) and 10 m/s (b, c, d, e). Other conditions: (a) $p_0 = 0.1$ MPa, $T_0 = 293$ K, $k_0 = 0.54$ J/kg, $l_0 = 4$ mm; (b, c, d, e) $p_0 = 0.1$ MPa, $T_0 = 293$ K, $k_0 = 0.06$ J/kg, $l_0 = 4$ mm

position are specified. Outlet boundary conditions are the conditions provided by Eq. (12.19). At the rigid wall, no slip and constant temperature conditions are specified. Clearly, the flow in Fig. 12.3a exhibits vortex shedding with the frequency about 300 Hz. This frequency corresponds to the Roshko correlation [30] for cylindrical bluff bodies at high-Reynolds numbers.

Figures 12.3b and 12.3c show mean velocity (Fig. 12.3b) and mean temperature (Fig. 12.3c) fields under bluff-body stabilized combustion of stoichiometric methane–air mixture at inlet velocity 10 m/s, and ABC of Eq. (12.19) at the combustor outlet. Functions W_j, W_{1j}, and W_{2j} in Eq. (12.1) were obtained by solving the problem of laminar flame propagation with the detailed reaction mechanism [31] of C_1–C_2-hydrocarbon oxidation (35 species, 280 reactions) including CH_4 oxidation chemistry. The PDF of Eq. (12.4) was used in this calculation.

Ignition is triggered by making a provision for a hot region of combustion products enveloping the bluff body. Preliminary studies have indicated that such an arrangement of mixture ignition avoids vigorous pressure disturbances at initial stages of flow development. This decreases considerably the CPU time required for attaining a stabilized flow pattern.

Application of ABC of Eqs. (12.19), (12.23), and (12.25), on the one side, and standard Dirichlet or von Neumann boundary conditions at open boundaries, on the other side, reveals the drastic effect of outlet boundary conditions on the flow pattern.

In the case of nonreflecting boundaries (Figs. 12.3b and 12.3c), the flow is smooth, symmetrical, and no vortex shedding is detected. It is to be noted that the symmetrical flame is developed irrespective of the ignition arrangements. Qualitatively, the pictures correspond to numerous experimental observations with symmetrical flames (e.g., [2, 10]). Similar to [2, 10], the stabilized flame (see Fig. 12.3c) first diminishes in size and reaches its smallest width approximately 1.7 baffle diameters downstream of the baffle. Then, the flame width increases almost linearly with the distance from the baffle, showing a small spreading angle (about 3° to 5°). In the case of von Neumann or Dirichlet (reflecting) boundary conditions, the flow is irregular and exhibits strong longitudinal pressure oscillations, resulting in vortex shedding. Flame behavior is unusual, and does not correspond to experimental observations (see Figs. 12.3d and 12.3e).

12.4.2 Flame Spread

Analyzing Fig. 12.3, it is noticed that the flame width in the bluff-body stabilized flame increases almost linearly with the distance from the baffle with the spreading angle of about 3° to 5°. Since the flame spreading angle directly affects the ramjet combustion efficiency, it is important to check the performance of the ABC by applying it to combustors with different tailpipes.
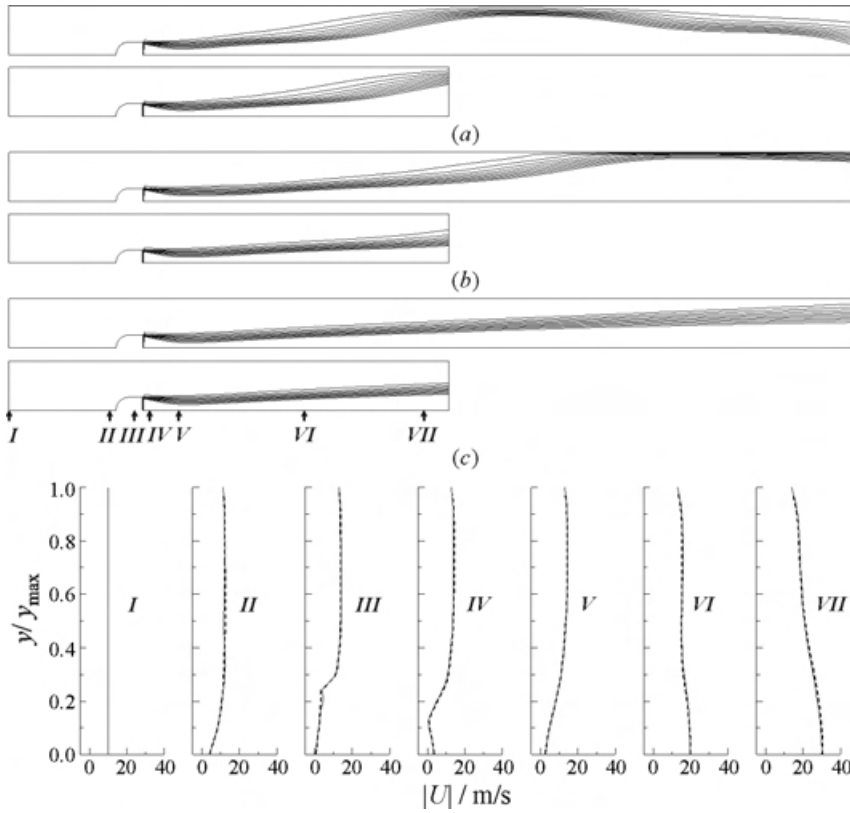
Figure 12.4 The comparison of predicted mean temperature fields in long and short combustors at $t = 14.9$ ms (a), 22.1 (b), and 58.1 ms (c) after ignition behind a bluff body. Boundary condition at outlets is ABC of Eq. (12.19). Mean velocity at the inlet $u_{in} = 10$ m/s. Other conditions are: $p_0 = 0.1$ MPa, $T_0 = 293$ K, $k_0 = 0.06$ J/kg, $l_0 = 4$ mm. A set of graphs below compares mean absolute velocity distributions in the different cross-sections (I to VII) of both combustors (from left to right: $x = 0$, 80, 100, 112, 135, 235, and 330 mm). Solid line — short combustor, dashed line — long combustor, y_{max} is the height of the corresponding cross-section of the combustor

Figure 12.4 provides the direct comparison of temperature fields in long and short combustors, other conditions being similar to those relevant to Figs. 12.3b and 12.3c. Because of the symmetry of the flow pattern discussed in subsection 12.4.1, only a half of the combustor was modeled. The lower boundary of the computational domain is taken as the symmetry plane. Clearly, the flame spreading angle at the outlet of the shorter combustor is the same as the flame angle in the corresponding cross-section of the longer combustor. The flame cone
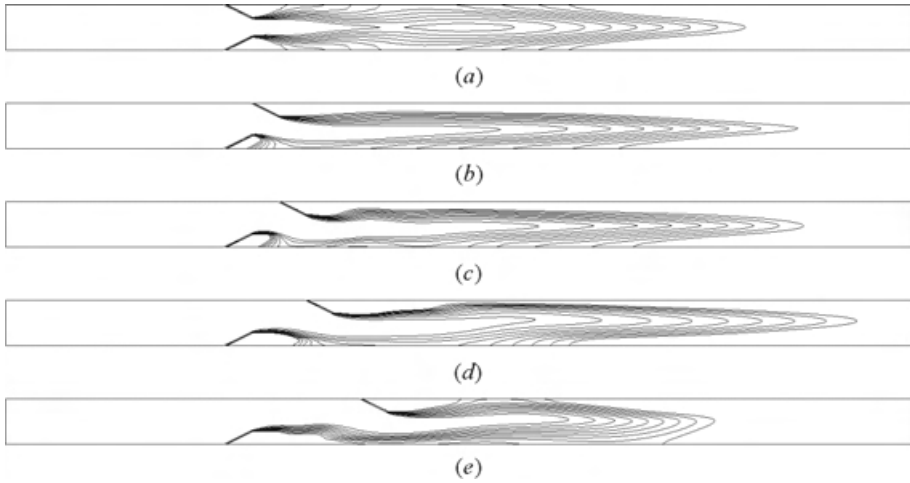
Figure 12.5 Calculated mean temperature fields in combustors with a set of similar open-edge V-gutter flame holders of height $H = 3$ cm and apex angle of 60°. The isoterms divide the entire temperature interval from the initial temperature T_0 to combustion temperature T_c into 10 uniform parts and correspond to $t = 27.5$ ms. The combustor is 1 m long and the distance between the planes of flame holders is 0.05 m. Flame holders are shifted in longitudinal direction by $0H$ (no shift) (a), $1H$ (b), $2H$ (c), $3H$ (d), and $5H$ (e). Combustion of stoichiometric methane–air mixture at the mean inlet velocity $u_{in} = 20$ m/s, $p_0 = 0.1$ MPa, $T_0 = 293$ K, $k_0 = 0.24$ J/kg, $l_0 = 4$ mm. The lower and upper boundaries of the computational domain are the symmetry planes

angle slightly decreases with the distance from the flame holder, being about 3° at $x = 10H$ and falling down to 1.5° at $x = 25H$. This corresponds both qualitatively and quantitatively to the experimental observations [10]. In general, the flow fields in the shorter combustor reproduce quite precisely those computed for the longer combustor. This is substantiated by graphs below the flow patterns, which compare mean absolute velocity distributions in the different cross-sections of both combustors.

For attaining higher combustion efficiencies with shorter tailpipes, a provision should be made for several flame holders in the combustion chamber. The optimum arrangement of the flame holders in the combustor in terms of the combustion efficiency, flame stability, and pressure loss should be found. The methodology suggested in sections 12.2 and 12.3 helps to solve this problem.

Figure 12.5 shows the calculated temperature fields in the combustors with a set of similar 3-centimeter wide open-edge V-gutter flame holders with the apex angle of 60°. The combustor is 1 m long and the distance between the planes of flame holders is 0.05 m. Depending on the location of the flame holders relative to each other, five combustor configurations were considered. Figure 12.5a cor-

responds to the zero longitudinal shift, $0H$ in the location of the flame holders. Figures 12.5b to 12.5e correspond to the cases when the flame holders are shifted in longitudinal direction by $1H$ (b), $2H$ (c), $3H$ (d), and $5H$ (e).

The analysis of Fig. 12.5 shows that all the configurations provide the combustion efficiency of about 96% at the combustor outlet located 0.76 m downstream of the tip of the lower flame holder. The deficit of 4% is explained by the presence of CO and other products of incomplete combustion at the combustor outlet. When the tailpipe of the combustor is shortened to 0.5 m, the combustor configurations in Fig. 12.5 are graded in terms of the descending combustion efficiency as follows: $0H$, $5H$, $1H$, $2H$, and $3H$. Note that the flames in Figs. 12.5a and 12.5e are unstable and blow off at later stages. Flames in Figs. 12.5b–12.5d are stable only on the upper flame holders. Thus, the highest stable combustion efficiency is attained for the case with $1H$ shift. An increase in the inlet velocity from 20 m/s to 30 m/s, other conditions being equal, results in the following grading of the combustor configuration in terms of the combustion efficiency: $0H$, $2H$, $1H$, $5H$, and $3H$. Note that at the inlet velocity of 30 m/s, only the configuration with $3H$ shift provided stable combustion on the upper flame holder in the long run. The efficiency of the configurations in terms of pressure loss was not analyzed.

12.4.3   Mechanism of Flame Stabilization and Blow-Off

So far, the flow patterns around bluff bodies in combustible flows are not understood completely. However, a recirculation zone in the immediate wake of the stabilizer which takes the form of a pair of eddies, similar to isothermal flows, is known to exist. The length L_{RZ} of the recirculation zone differs for 2D and axisymmetric bluff bodies. For 2D bodies (V-gutters, rods, prisms), the measured values of L_{RZ}/H range from 3 to 6 depending on the operating conditions of combustor [11], which is considerably larger than for isothermal flows, where $L_{\mathrm{RZ}}/H \approx 2$ [11]. For axisymmetric bluff bodies (discs, cones, cylinders), at low-blockage ratio $L_{\mathrm{RZ}}/H \approx 2$ [32], which is similar to isothermal flows [32, 33], or $L_{\mathrm{RZ}}/H \approx 2.5$–4 [34], or even $L_{\mathrm{RZ}}/H \approx 10$–11 [35].

As mentioned in section 12.1, Dunskii [12] was the first who put forward the phenomenological theory of flame stabilization. The theory is based on the characteristic residence time, t_r, and combustion time, t_c, in adjoining elementary volumes of fresh mixture and combustion products in the recirculation zone behind the bluff body. Dunskii's condition for flame blow-off is $t_r/t_c = \mathrm{Mi}$, where Mi is the Mikhelson number close to unity (for example, for cone flame holder the measurements give $\mathrm{Mi} = 0.45$ [36]). Residence time t_r is taken proportional to the flame holder size, H, and inversely proportional to the approach flow velocity, U, i.e., $t_r = H/U$. Combustion time is estimated as $t_c = a_t/S_L{}^2$, where

a_t is the temperature diffusivity coefficient and S_L is the laminar flame velocity. Thus, at the blow-off limit

$$\frac{t_r}{t_c} = \frac{H S_L{}^2}{U a_t} = \text{Mi} \approx const \qquad (12.26)$$

or when taking into account that $S_L{}^2/a_t$ is the function of fuel–air ratio, Φ, it reads as

$$\Phi = f\left(\frac{U}{H}\right) \qquad (12.27)$$

Williams *et al.* [1] and Longwell [2, 5] arrived at the same criterion.

Apparently, the criterion (12.27) does not provide the complete understanding of the phenomenon. There is no evidence of the effect of multiple variables on flame stability mentioned in section 12.1. Moreover, the physical grounds for estimating the characteristic times t_r and t_c entering the Dunskii's criterion remain unclear. Therefore the interpretation of t_r and t_c in the relevant literature is quite ambiguous.

The application of the PPDF method of section 12.2 and ABC of section 12.3 sheds light on some important peculiarities of the phenomenon. Figures 12.6 and 12.7 show the set of calculated flow patterns for the bluff-body stabilized stoichiometric methane–air flames in terms of temperature isolines. The combustor under study is a plane channel 1 m long and 0.2 m wide. The bluff bodies are the open-edge V-gutters with the apex angle 60° and height 10 cm (Fig. 12.6) and 5 cm (Fig. 12.7), introducing a considerably different blockage to the flow.

In Fig. 12.6, frames a to e show the transformation of the flow pattern with increase in the combustor inlet velocity from 40 m/s (a) to 50 (b), 60 (c), 70 (d), and 80 m/s (e). Similarly, in Fig. 12.7 frames a to e correspond to the inlet velocity of 30 m/s (a), 40 (b), 50 (c), 60 (d), and 70 m/s (e). All the flow patterns are plotted for time $t = 50$ ms. The patterns in Figs. 12.6a and 12.6b and Figs. 12.7a–12.7c are steady-state, while the residual flames in Figs. 12.6c–12.6e and Figs. 12.7d–12.7e blow out with time.

To understand the reason of the abrupt change in the flame behavior when the inlet velocity approaches a certain limiting value, it is imperative to follow the trajectories of fluid particles in the steady-state flowfield. Figure 12.8 shows five such trajectories for the flow pattern presented in Fig. 12.6b. The recirculation zone behind the bluff body is clearly seen in Fig. 12.8. Three of the five trajectories have the turning points where the flow changes to the opposite direction. There exists the limiting trajectory (marked by the arrow) which separates the nonturning and turning trajectories in the flow. The present analysis of numerous computations of bluff-body stabilized flames revealed that the turning point of the limiting trajectory is of significant importance to flame stability.

When following the mean temperature evolution along the limiting trajectory, it was observed that a flame is definitely stable if the temperature attains
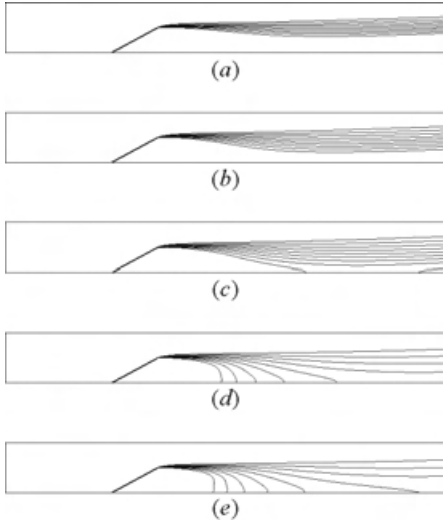
Figure 12.6 Calculated mean temperature fields in the combustor with an open-edge V-gutter flame holder of height $H = 10$ cm and apex angle of $60°$. The isoterms divide the entire temperature interval from T_0 to T_c into 10 uniform parts and correspond to $t = 50$ ms. The combustor is 1 m long and 0.2 m wide. Combustion of stoichiometric methane–air mixture at the mean inlet velocity $u_{in} = 40$ (a), 50 (b), 60 (c), 70 (d), and 80 m/s (e). Other conditions: $p_0 = 0.1$ MPa, $T_0 = 293$ K, turbulence intensity 2%, $l_0 = 4$ mm. The lower boundary of the computational domain is the symmetry plane
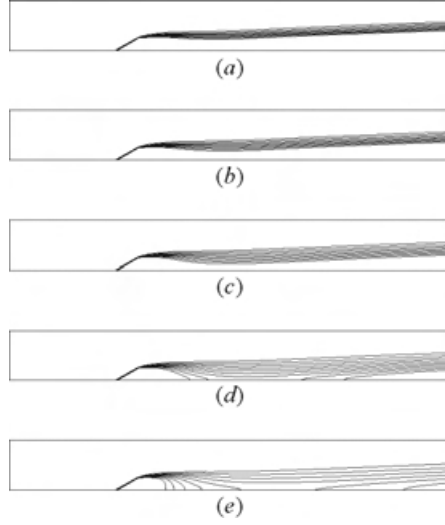
Figure 12.7 Calculated mean temperature fields in the combustor with an open-edge V-gutter flame holder of height $H = 5$ cm and apex angle of $60°$. The isoterms divide the entire temperature interval from T_0 to T_c into 10 uniform parts and correspond to $t = 50$ ms. The combustor is 1 m long and 0.2 m wide. Combustion of stoichiometric methane–air mixture at the mean inlet velocity $u_{in} = 30$ (a), 40 (b), 50 (c), 60 (d), and 70 m/s (e). Other conditions: $p_0 = 0.1$ MPa, $T_0 = 293$ K, turbulence intensity 2%, $l_0 = 4$ mm. The lower boundary of the computational domain is the symmetry plane

the value T_* close to T_c (eventually, $T_* \approx 0.95 T_c$) before reaching the turning point. If this temperature $T = T_*$ is attained after passing the turning point at the limiting trajectory, the flame is definitely unstable. In the latter case, even if T_* is attained very close to but after the turning point, the flame inevitably blows off, though, exhibiting a few violent longitudinal oscillations.

Quantitatively, these observations can be treated in terms of the characteristic residence time t_r and the characteristic reaction time t_c, introduced by
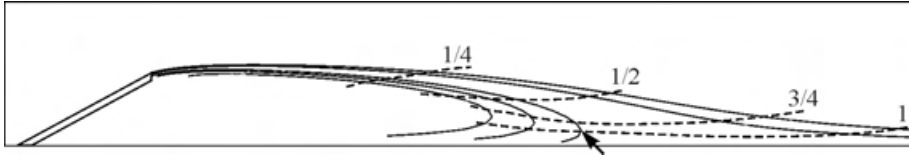
Figure 12.8 Calculated trajectories of fluid particles in the combustor with flame holder (solid lines) and the curves of constant dimensionless residence time t/t_r (dashed curves). The residence time t_r is defined as the time taken for the fluid particle to reach the turning point at the limiting trajectory (marked by the arrow). Conditions are similar to Fig. 12.6*b*

Dunskii. Defining the residence time as the time taken for the imaginary fluid particle to reach the turning point at the limiting trajectory, the calculated curves $t/t_r = const$ (dashed curves) to illustrate the flow field behind the bluff body are shown in Fig. 12.8. Clearly, the fluid particles entering the wake of the bluff-body lag considerably behind the particles moving in the free stream. The reaction time is defined as the time taken for the fluid particle to attain temperature $T_* \approx 0.95T_c$. Then, the flame stability criterion will read as

$$\frac{t_r}{t_c} = \text{Mi} \geq 1 \tag{12.28}$$

Table 12.1 summarizes the calculated data for t_r, t_c, and Mi for various flow patterns including those shown in Figs. 12.6 and 12.7 calculated on the basis of mean velocity fields at $t = 50$ ms irrespective of combustion stability. In addition to the inlet velocity u_{in}, the calculated values of maximum flow velocity in the narrowest cross-section of the combustor, u_m, are also presented in Table 12.1. In confined flows, flame stability is determined by the values of u_m rather than u_{in}, in spite of the fact that they are closely connected to each other. As follows from Table 12.1, the Mikhelson number of unity, defined by Eq. (12.28), separates the solutions with stabilized and unstable flames. The limiting inlet velocity can be estimated as the intersection of $t_r(u_{in})$ and $t_c(u_{in})$ curves as shown in Fig. 12.9. It follows from Fig. 12.9 that the limiting inlet velocity for the 5-centimeter V-gutter is higher than for the 10-centimeter V-gutter. This is caused by a considerable increase in the maximum velocity u_m in the latter case and agrees with experimental observations [36]. Quantitatively, the limiting values of the maximum flow velocity $u_m = 40$–100 m/s are in a reasonable agreement with experimental findings for the stoichiometric methane–air flame stabilization (50–60 m/s for the 2-centimeter cylindrical bluff body at blockage ratio 0.3 [37]). Note that the calculations under discussion were performed

Table 12.1 Calculated characteristic reaction time t_c, residence time t_r, and the Mikhelson number Mi for the combustion of the stoichiometric methane–air mixture in a combustor with the open-edge V-gutter flame holder of height H and apex angle $60°$ at the mean inlet velocity u_{in}. Also presented is the maximum approach-stream velocity u_m. Signs "+" and "−" correspond to stabilized flame and unstable flame, respectively

H cm	u_{in} m/s	u_m m/s	t_c ms	t_r ms	Mi	Stability
	40	85	4.4	8.4	1.9	+
10.0	50	106	6.4	7.6	1.2	+
	60	130	8.0	6.4	0.8	−
	20	28	3.5	11.2	3.2	+
	40	57	4.4	8.8	2.0	+
5.0	50	72	5.6	7.2	1.3	+
	60	87	7.6	6.0	0.8	−
	20	23	4.4	8.8	2.0	+
2.0	30	35	4.6	5.6	1.2	+
	40	47	6.4	4.8	0.75	−
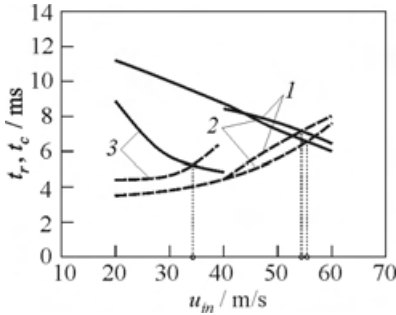
Figure 12.9 To the determination of the limiting inlet velocity u_{in} for the stabilized combustion of the stoichiometric methane–air mixture in the combustor with open-edge V-gutter flame holders. Solid curves correspond to the calculated residence time t_r. Dashed curves correspond to the calculated reaction time t_c. Flame holders with $H = 10$ cm (*1*), 5 cm (*2*), and 2 cm (*3*). Conditions are similar to those in Figs. 12.6 and 12.7

with the PDF of Eq. (12.4). The use of the PDF of Eq. (12.2) allows increasing the limiting maximum flow velocity u_m to 60 m/s for the 2-centimeter V-gutter.

The typical evolution of the flow pattern at Mi slightly less than 1.0 is shown in Fig. 12.10 in terms of temperature fields for the 3-centimeter V-gutter of the same apex angle ($60°$). The time interval between frames is 2 ms. After ignition, the combustion zone is divided into two parts, the wake flame and the trail flame. The former tends periodically to "catch" the latter, resulting in energetic jumps of the flame tongue downstream of the recirculation zone. However, due to expansions of the recirculation zone, an enhanced flow of unburned mixture repeatedly cuts the flame tongue, resulting in splitting the flames. In the long run, the flame blows-off.
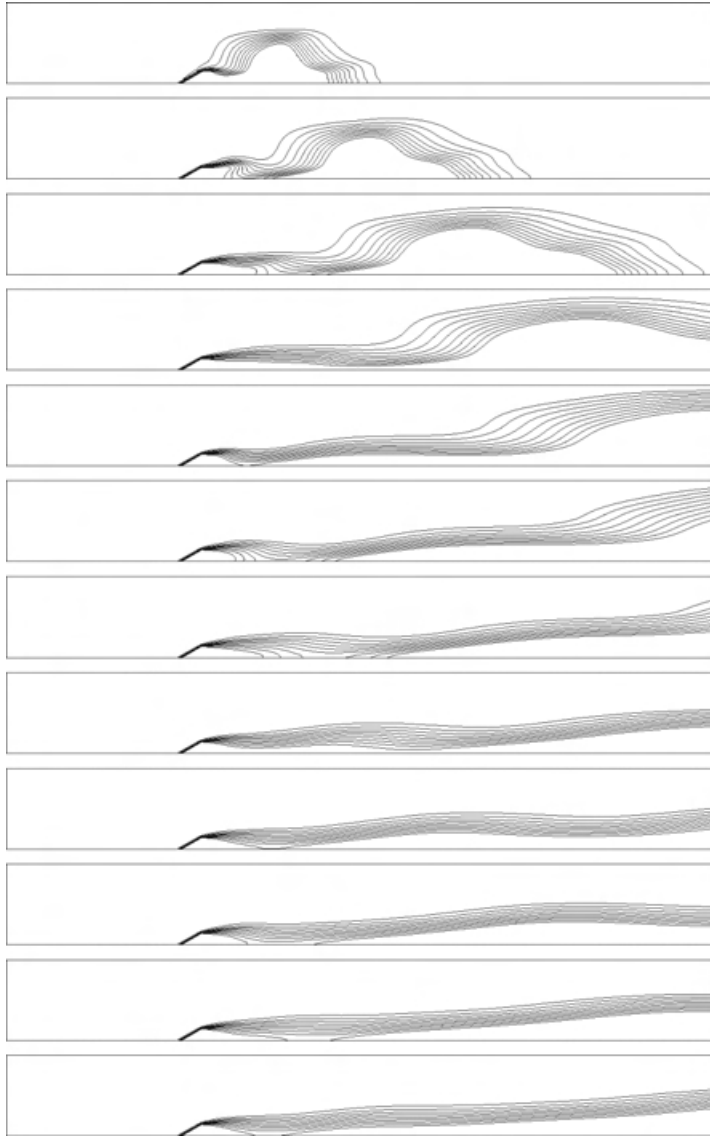
Figure 12.10 Typical evolution of the mean temperature field under combustion of stoichiometric methane–air mixture at the Mikhelson number Mi slightly less than 1.0. Time interval between frames is 2 ms. The isoterms divide the entire temperature interval from T_0 to T_c into 10 uniform parts. Flame holder is the open-edge V-gutter of height $H = 3$ cm and apex angle $60°$. The combustor is 1 m long and 0.2 m wide. Combustion at $u_{in} = 50$ m/s, $p_0 = 0.1$ MPa, $T_0 = 293$ K, turbulence intensity 2%, $l_0 = 4$ mm. The lower boundary of the computational domain is the symmetry plane

12.5   CONCLUDING REMARKS

The Presumed Probability Density Function method is developed and implemented to study turbulent flame stabilization and combustion control in subsonic combustors with flame holders. The method considers turbulence–chemistry interaction, multiple thermo-chemical variables, variable pressure, near-wall effects, and provides the efficient research tool for studying flame stabilization and blow-off in practical ramjet burners. Nonreflecting multidimensional boundary conditions at open boundaries are derived, and implemented into the current research. The boundary conditions provide transparency to acoustic waves generated in bluff-body stabilized combustion zones, thus avoiding numerically induced oscillations and instabilities. It is shown that predicted flow patterns in a combustor are essentially affected by the boundary conditions. The derived nonreflecting boundary conditions provide the solutions corresponding to experimental findings.

Numerical studies of combustion control in simple combustors with flame holders have been made. The criterion of flame stabilization, based on the unambiguously defined characteristic residence and reaction times, is suggested and validated against numerous computational examples. The results of calculations were compared with available experimental findings. A good qualitative and reasonable quantitative agreement between the predictions and observations were attained. Futher studies are planned to include mixing between fuel jets with oxidizer and to extend the analysis to transonic and supersonic flow conditions.

ACKNOWLEDGMENTS

REFERENCES

1. Williams, G. C., H. C. Hottel, and A. C. Scurlock. 1949. Flame stabilization and propagation in high-velocity gas streams. *3rd Symposium on Combustion, Flame and Explosion Phenomena Proceedings.* Baltimore: The Williams and Wilkins Co. 21–40.
2. Longwell, J. P., J. E. Chenevey, W. W. Clark, and E. E. Frost. 1949. Flame stabilization by baffles in a high-velocity gas stream. *3rd Symposium on Combustion, Flame and Explosion Phenomena Proceedings.* Baltimore: The Williams and Wilkins Co. 40–44.
3. Nicholson, H. M., and J. P. Field. 1949. Some experimental techniques for the investigation of the mechanism of flame stabilization in the wakes of bluff bodies. *3rd Symposium on Combustion, Flame and Explosion Phenomena Proceedings.* Baltimore: The Williams and Wilkins Co. 44–68.

4. DeZubay, E. A. 1950. Characteristics of disk-controlled flame. *Aero Digest* 61(1):54–56.

5. Longwell, J. P. 1953. Flame stabilization by bluff bodies and turbulent flames in ducts. *4th Symposium (International) on Combustion, Combustion and Detonation Waves Proceedings*. Baltimore: The Williams and Wilkins Co. 90.

6. Williams, G. C., and C. W. Shipman. 1953. Some properties of rod-stabilized flames of homogeneous gas mixtures. *4th Symposium (International) on Combustion, Combustion and Detonation Waves Proceedings*. Baltimore: The Williams and Wilkins Co. 733–42.

7. Zukoski, E. E., and I. E. Marble. 1955. The role of wake transition in the process of flame stabilization on bluff bodies. In: *AGARD combustion research and reviews*. London: Butterworths.

8. Solntsev, V. P. 1961. Influence of turbulence parameters on the combustion process of homogeneous gasoline–air mixture behind a stabilizer under conditions of confined flow. In: *Flame stabilization and the development of combustion in turbulent flow*. Ed. G. N. Gorbunov. Moscow: Oborongiz. 75.

9. Filippi, F., and L. Fabbrovich-Mazza. 1962. Control of bluff-body flameholder stability limits. *8th Symposium (International) on Combustion Proceedings*. Baltimore: The Williams and Wilkins Co. 256.

10. Wright, F. H., and E. E. Zukoski. 1962. Flame holding: Selected engine combustion problems. *8th Symposium (International) on Combustion Proceedings*. Baltimore: The Williams and Wilkins Co. 933.

11. Solokhin, E. L. 1961. Study of flame propagation and stabilization behind a V-gutter stabilizer. In: *Flame stabilization and the development of combustion in turbulent flow*. Ed. G. N. Gorbunov. Moscow: Oborongiz. 48.

12. Dunskii, V. F. 1949. A study of the mechanism of flame stabilization behind a bluff body. Dissertation. Moscow.

13. Iliashenko, S. M., and A. V. Talantov. 1964. *Theory and design of ramjets*. Moscow: Mashinostroenie.

14. Longwell, J. P., E. E. Frost, and M. A. Weiss. 1953. Flame stability in bluff-body recirculation zones. *Ind. Eng. Chem.* 45(8):1629–33.

15. Zel'dovich, Ya. B. 1944. Remarks on combustion of a high-speed flow in a duct. *Sov. J. Technical Physics* XIV(3):162.

16. Tsien, H. S. 1951. *J. Applied Mechanics*. 188.

17. Iida, H. 1956. Combustion in turbulent gas streams. *6th Symposium (International) on Combustion Proceedings*. Baltimore: The Williams and Wilkins Co. 341–56.

18. Talantov, A. V. 1958. Fundamentals for evaluating the simplest ramjet combustor. *Izv. Vuzov USSR, Ser. aviation techn.* 2.

19. Vlasov, K. P. 1961. To the evaluation of the simplest combustor of a ramjet type. In: *Flame stabilization and the development of combustion in turbulent flow*. Ed. G. M. Gorbunov. Moscow: Oborongiz. 128.

20. Spalding, D. B. 1959. Theory of rate of spread of confined turbulent premixed flames. *7th Symposium (International) on Combustion Proceedings*. Baltimore: The Williams and Wilkins Co. 595–603.

21. Spalding, D. B. 1967. The spread of turbulent flames confined in ducts. *11th Symposium (International) on Combustion Proceedings*. Pittsburgh, PA: The Combustion Institute. 807–15.

22. Spalding, D. B. 1971. Mixing and chemical reaction in steady confined turbulent flames. *13th Symposium (International) on Combustion Proceedings*. Pittsburgh, PA: The Combustion Institute. 649–57.

23. Pope, S. B. 1985. PDF methods for turbulent reactive flows. *Progress Energy Combustion Science* 11:119.

24. Frolov, S. M., V. Ya. Basevich, M. G. Neuhaus, and R. Tatschl. 1997. A joint velocity-scalar PDF method for modeling premixed and nonpremixed combustion. In: *Advanced computation and analysis of combustion*. Eds. G. D. Roy, S. M. Frolov, and P. Givi. Moscow: ENAS Publ. 537.

25. Gurvich, L. V., I. V. Veiz, V. A. Medvedev, *et al.* 1978. *Thermodynamic data of individual substances*. Moscow: USSR Academy Science Publ.

26. Kokushkin, N. V. 1958. A study of combustion of a homogeneous mixture in a turbulent flow by means of recording temperature oscillations. *Izv. Academy Science USSR, Technical science ser.* 3.

27. Shepherd, G., and J. B. Moss. 1983. *Combustion Science Technology* 33:231.

28. Basevich, V. Ya., and S. M. Kogarko. 1975. On characteristics of the burning surface of a turbulent flame. *Archivum Termodyn. Spalan.* 6(1):95.

29. Grinstein, F. 1994. Open boundary conditions in the simulation of subsonic turbulent shear flows. *J. Compt. Physics* 115(1):43.

30. Roshko, A. 1953. On the development of turbulent wakes from vertex streets. NACA TN 2913, March.

31. Basevich, V. Ya. 1990. Chemical kinetics in the combustion processes. In: *Handbook of heat and mass transfer*. Ed. N. Cheremisinoff. Houston: Gulf Publ. 4:769.

32. Dudkin, V. T., and V. A. Kosterin. 1978. Effect of a trout device on the performance of a ramjet combustor. In: *Combustion in flow*. Ed. A. V. Talantov. Kazan: Kazan Aviation Inst. Publ. 2:14.

33. Davies, T. W., and J. M. Beer. 1971. Flow in the wake of bluff-body flame stabilizers. *13th Symposium (International) on Combustion Proceedings*. Pittsburgh, PA: The Combustion Institute. 631–38.

34. Winterfeld, G. 1965. On process of turbulent exchange behind flame holder. *10th Symposium (International) on Combustion Proceedings*. Pittsburgh, PA: The Combustion Institute. 1265–75.

35. Shepherd, I. G., J. R. Hertzberg, and L. Talbot. 1992. Flame holding in unconfined turbulent premixed flames. In: *Major research topics in combustion*. Eds. M. Y. Hussaini, A. Kumar, and R. G. Voigt. ILAE/NASA LaRC ser. New York: Springer-Verlag. 253–70.

36. Raushenbakh, B. V., S. A. Belyi, I. B. Bespalov, V. Ya. Borodachev, M. S. Volynskii, and A. G. Prudnikov. 1964. *Physical fundamentals of the operation process in the combustion chambers of ramjets*. Moscow: Mashinostroenie.

37. Basevich, V. Ya., and S. M. Kogarko. 1972. Comparison of limiting flame blow-off velocities for different types of stabilizers. *Sov. J. Combustion, Explosion, Shock Waves* 8(4):582.

38. Frolov, S. M., V. Ya. Basevich, and A. A. Belyaev. 1999. Flame stabilization in a ramjet burner. *12th ONR Propulsion Meeting Proceedings*. Eds. G. D. Roy and S. L. Anderson. University of Utah, Salt Lake City, UT. 76–81.

Chapter 13

VORTEX DYNAMICS, ENTRAINMENT, AND NONPREMIXED COMBUSTION IN RECTANGULAR JETS

F. F. Grinstein

An overview of recent investigations of low-aspect-ratio (AR) rectangular jets based on numerical simulations is presented. The main focus of this work was to characterize the effects of the unsteady vorticity dynamics on jet entrainment and nonpremixed combustion, including effects of Reynolds and Lewis numbers. The understanding of the effects of initial conditions on axis-switching phenomena is discussed, with special focus on the underlying dynamics and topology of coherent vortical structures. Qualitatively different vorticity topologies characterizing the near-flow field of low-AR rectangular jets involve (*i*) self-deforming and bifurcating vortex rings, including interacting ring and rib (braid) vortices, (*ii*) single ribs aligned with corner regions (AR $\geq$ 2), and (*iii*) rib pairs (hairpins) aligned with the corners (AR = 1), and (*iv*) smaller scale elongated "worm" vortices in the turbulent jet regime. The near-field entrainment and nonpremixed combustion properties of low-AR rectangular jets are largely determined by the characteristic jet vortex dynamics and topology.

13.1   INTRODUCTION

Improved mixing of a jet with its surroundings is of considerable interest in practical applications that demand enhanced combustion between injected fuel and background oxidizer. In this context, there is a crucial interest in recognizing and understanding the local nature of jet instabilities and their global nonlinear development in space and time. The vorticity dynamics and mixing processes determine the overall heat release pattern within the flame. Regions with enhanced mixing and proper air-to-fuel ratio, where the combustion process is

intense, and localized combustion-inactive regions are included. By understanding these combined processes it is possible to select optimal jet initial conditions and fuel injection features to improve jet combustion.

Mixing between a turbulent jet and its surroundings occurs in two stages: an initial stage of bringing relatively large amounts of the fluids together (large-scale stirring), and a second stage promoted by the small-scale velocity fluctuations which accelerate mixing at the molecular level. The entrainment rate of the jet is especially important as it measures the rate at which fluid elements from the jet and from its surroundings become entangled, or mixed, as they join at the mixing layers. The entrainment-controlling large-scale vortices tend to be coherent and easily recognizable features, hence their name *coherent structures* (CS) (e.g., [1]). Control of the jet development is strongly dependent on understanding the dynamics and topology of CS. In particular, it is important to know how the jet properties can be affected through control of the formation, interaction, merging, and breakdown of CS.

Extensive studies have been devoted to the investigation of passive shear-flow control methods to enhance the three-dimensionality of the flow and hence entrainment and mixing [2]. Passive mixing-control strategies are based on geometrical modifications of the jet nozzle, which can directly alter the flow development downstream relative to using a conventional circular nozzle. Jet studies using nonaxisymmetric nozzles show that as the jet spreads, its cross-section can evolve through shapes similar to that at the jet exit, but with the axis successively rotated at angles characteristic of the jet geometry, which is denoted as the axis-switching phenomenon. Axis switching is the main mechanism underlying the enhanced entrainment properties of noncircular jets relative to those of comparable circular jets (Fig. 13.1), and results from self-induced Biot–Savart deformation of vortex rings with nonuniform azimuthal curvature, and interaction between azimuthal and streamwise vorticity.

Rectangular jet configurations are of particular interest because they offer passively improved mixing at both ends: enhanced large-scale entrainment due to axis switching, and enhanced small-scale mixing near corner regions and farther downstream — due to faster breakdown of vortex-ring coherence and hence faster transition to turbulence. In addition, jet entrainment can be affected further by streamwise vorticity production through suitable vortex generators placed at the jet nozzle exit (e.g., [3]). Theoretical studies gave insights on mechanisms by which jet initial conditions can promote the azimuthally nonuniform growth characteristic of rectangular jets (e.g., [4, 5]). Laboratory experiments (e.g., [6–8]) demonstrated complex vortex evolution and interaction related to self-induction and interaction between azimuthal and axial vortices leading to axis switching; however, the laboratory experiments can typically show only the end outcome of the physical processes, exhibiting complex three-dimensional (3D) flame structure with many unexplained features such as the distribution and evolution of the geometry of the reaction zones.
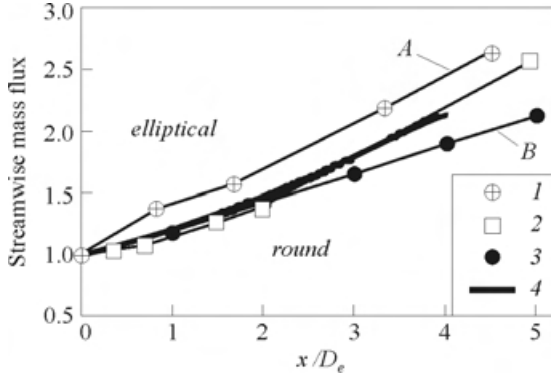
Figure 13.1 Near-field entrainment measurements in noncircular jets based on experimental and computational studies [16]. Subsonic regimes. Experiments: *1* — elliptic [37]; *2* — square [16]; *3* — round [38]. Simulations: *4* — square [16]. *A*: $(D_e/Q_0)(dQ/dx) \sim 0.36$; *B*: ~ 0.24

In this paper, an overview of recent jet investigations is presented describing the details and clarifying the mechanisms of the vorticity dynamics and chemical-reaction exothermicity effects on the behavior of rectangular (low-AR) transitional diffusion flames. First, the main features of the numerical jet model are outlined that were used to study the compressible (subsonic) moderately high-Re jet regimes investigated. Next, the understanding gained on the dynamics and topology of CS underlying axis-switching phenomena is discussed, with special focus on the role of initial conditions, self-induced vortex deformation, braid vortices, and AR effects. The database of low-AR rectangular jet investigations is used to relate unsteady entrainment and fluid dynamics, and to address the significance of basic vorticity topological features and AR effects in the context of nonpremixed jet combustion.

13.2   NUMERICAL JET MODEL

The time-dependent simulations of free jets discussed here focus on the vortex dynamics and transition to turbulence downstream of the jet exit. For the sake of computational efficiency, the author concentrates on the study of jet flow initialized with laminar conditions with a thin rectangular vortex sheet having slightly rounded-off corner regions and uniform initial momentum thickness [9]. Initial conditions for the simulated jets involve top-hat initial velocity profiles

and nonpremixed conditions modeled in terms of appropriate top-hat and step profiles for the reacting species concentrations.

The numerical jet model [9–11] is based on the numerical solution of the time-dependent, compressible flow conservation equations for total mass, energy, momentum, and chemical species' number densities, with appropriate inflow/outflow open-boundary conditions and an ideal gas equation of state. In the reactive simulations, multispecies temperature-dependent diffusion and thermal conduction processes [11, 12] are calculated explicitly using central difference approximations and coupled to chemical kinetics and convection using timestep-splitting techniques [13]. Global models for hydrogen [14] and propane chemistry [15] have been used in the 3D, time-dependent reactive jet simulations. Extensive comparisons with laboratory experiments have been reported for nonreactive jets [9, 16]; validation of the reactive/diffusive models is discussed in [14].

The nonreactive jet systems investigated consist of spatially developing low-AR (AR = 1–4) rectangular air jets emerging into ambient air background. The jets emerge at uniform temperature T_0 and $P_0 = 1$ atm into quiescent background (also at the same uniform T_0 and P_0), with Mach number M $\sim$ 0.3–0.6, and ratio $D_e/\theta_0 = 50$–75, where D_e is the circular-equivalent jet diameter and θ_0 is the initial shear layer momentum thickness. The reactive jets are made of propane (hydrogen) diluted in nitrogen, and the background consists of oxygen also diluted in nitrogen, with reactant molar concentrations chosen to be the same and equal to 0.4, so that the jet-to-background mass density ratio is $s = \rho_j/\rho_b = 1.16$ (0.6). A temperature $T = 1400$ K was used for the reactive cases to ensure autoignition for the chosen initial conditions. For the reactive cases, the heat release parameter Ce $= T_{\text{peak}}/T_0$ (Ce $\sim$ 2.5–2.8) gives a characteristic measure of chemical exothermicity, and peak Damköhler numbers Da $\sim 1\,000$ are typically involved [10]. Lewis numbers (Le) are based on appropriate free-stream gas-mixture thermal conductivities, mass densities, and diffusion coefficients for the jet and background; for the hydrogen–nitrogen jet studies, the ratio of jet-to-background Le varied between $\text{Le}_j/\text{Le}_b = 0.3/1.1$ and $\text{Le}_j/\text{Le}_b = 1.1/1.1$ (reference case used to assess Le effects) [11]; for the propane–nitrogen jet studies a ratio closer to unity, $\text{Le}_j/\text{Le}_b = 0.94/0.80$, was involved [12]. For the nonreactive cases, more generic jets with $s = 1$ and Le $= 1$ were considered, with $T_0 = 298$ K, and both jet and background made of air. Typical values of Re for the jets studied here with the monotonically integrated LES (MILES) approach [17, 18] involve Re $= U_j D_e/\nu > 78\,000$ (Re$_T > 90$) — based on upper bounds for the effective numerical viscosity of the Flux-Corrected Transport (FCT) algorithm [19] (or comparisons with DNS turbulence data [18]); the direct numerical simulations involve Re $= 3200$–4450 (Re$_T \cong 20$), based on the mean free-stream gas-mixture kinematic viscosity. Discussion of subgrid-scale (SGS) modeling issues, and comparative studies using MILES and various other typical LES approaches for compressible nonreactive [18, 20] and reactive [21] shear flows, have been recently reported.

13.3   NONREACTIVE JET DYNAMICS

13.3.1   Axis Switching and Jet Initial Conditions

The occurrence of axis switching for a given noncircular nozzle geometry depends on initial conditions, such as azimuthal distribution of momentum thickness θ, ratio D_e/θ, turbulence level, and jet forcing [16], and on the presence of streamwise vorticity at the jet exit due to secondary flows within the nozzle [2] or due to vortex generators placed at the rim of the nozzle [3]. Even if effectively absent at the jet exit, the streamwise vorticity has an increasingly more important role on the jet development further downstream. In contrast with the plane free mixing layer — where primary 2D spanwise vortex rollers are continuously supported downstream by the imposed constant shear — the jet velocity decreases downstream towards the end of the jet potential core, thus attenuating the shear supporting the vortex rings in the jet. Sufficiently far downstream, three-dimensionality is the inherent feature of jets with moderate-to-high Re and high M. The streamwise vorticity has the crucial role in entraining fluid from the surroundings [28], and large-scale vortices other than vortex rings dominate the jet dynamics as one moves downstream. The discussion that follows focuses on the vorticity dynamics underlying axis switching when the initial conditions at the jet exit are such that (azimuthal) nonuniformities of the momentum thickness and presence of streamwise vorticity are negligible.

13.3.2   Axis Switching and Vortex Dynamics

In the early views of axis switching (e.g., [4, 8, 22]), the dynamics of vortex rings was presumed to dominate the jet development, axis switchings of the jet cross-section were directly associated with successive self-induced axis rotations of vortex rings, and the important role of jet initial conditions and braid vortices was not recognized. In noncircular jets, vortex-ring deformation can take place without the aid of azimuthal forcing, as a result of Biot–Savart self-induction [23] associated with azimuthal nonuniform shear layer curvature. Such self-induced deformation is clearly distinct from vortex-ring distortion due to azimuthal instabilities [24], which also affects the noncircular ring dynamics. Simulations of the development in space and time of isolated low-AR pseudo-elliptic [25] and rectangular [26] vortex rings showed that such rings undergo quite regular self-induced nonplanar deformations for AR < 4, approximately recovering shape and flatness with axis rotated with respect to its initial configuration, and with axis rotation periods exhibiting nearly linear dependence on AR. Vortex-ring splitting was observed for $4 \leq$ AR ≤ 12; vortex bridging and threading were demonstrated to be the main mechanisms underlying the circulation-
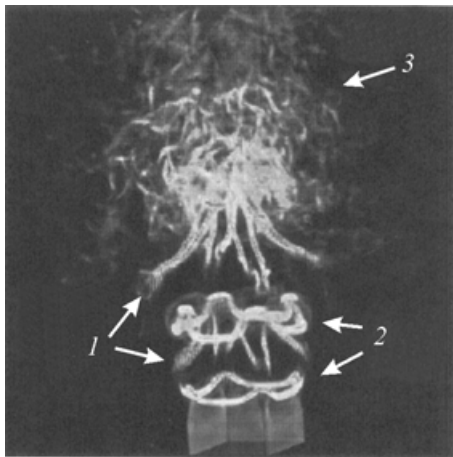
Figure 13.2 Instantaneous volume visualizations of the vorticity magnitude for the M = 0.6 square jet [9]: *1* — hairpin (braid) vortices, *2* — vortex rings, and *3* — "worm" vortices

redistributing vortex "fission" process [26] — roles that had been conjectured [22], but not captured by the previous flow visualizations of these phenomena [8, 22, 25].

The dynamics of *nonisolated* vortex rings in developed jets can be significantly different from that of isolated rings. Further downstream away from the jet exit, strong interactions with other large-scale vortices are to be considered. The free square jet development is illustrated in Fig. 13.2 (from [9]); it is controlled by the dynamics of interacting vortices including (*i*) deformation of virtually flat (square) initial vortex rings due to Biot–Savart self-induction, (*ii*) hairpin (braid) vortices aligned with the corner regions that form in the initial jet shear layer due to vorticity redistribution and stretching induced by the self-deformation of the vortex rings, and (*iii*) strong coupling of these vortices into ring–hairpin bundles. Vortex interactions and azimuthal instabilities lead to more contorted vortices; stretching, kinking, and reconnection of vortices lead to their breakdown, and to a more disorganized flow regime farther downstream, where the jet flow is characterized by slender, tube-like "worm" vortices [9, 18] — as observed in fully developed turbulent flows [29, 30]. The important role of streamwise braid vortices on the jet dynamics was recognized only recently [9]. Braid (rib) vortices were identified in studies of square [31], elliptic [32], and rectangular [33, 34] jets; these vortices appear as a result of redistribution and stretching of the streamwise vorticity in the high-strain-rate braid regions between vortex rings into vortices aligned with fixed azimuthal locations (e.g., corner regions) characteristic of the geometry at the jet exit. In addition to enhancing fluid entrainment from the jet surroundings, braid vortices induce further vortex-ring deformation and triggering of azimuthal instabilities, and thus have a direct role in affecting axis switching and the transition to turbulence.

Depending on the particular jet initial conditions, several or no axis rotations can occur in the first few diameters of jet development (e.g., [3, 16]). Results of experiments, stability analysis, and simulations support the concept that the basic mechanism for the first axis rotation of the jet cross-section is the self-deformation of the vortex rings due to nonuniform azimuthal curvature at the

Figure 13.3 Instantaneous isosurfaces of the vorticity magnitude for the square jet [9] at two times t_1 (*a*) and t_2 (*b*). *1* — hairpin rib pairs, *2* — vortex rings, *3* — vortex lines, *4* — flow ejection, and *5* — vortex-ring flattening

initial jet shear layer. However, subsequent axis rotations of the jet cross-section are not linked to successive vortex-ring axis rotations. Strong interactions with braid vortices and other rings can inhibit axis rotations of nonisolated rings — which do not recover shape and flatness after the initial self-deformation. In the square jet case [9], for example, the faster jet spreading in the corner-region directions necessary to have a second axis rotation of the jet cross-section is directly related to the strength of the hairpin vortices, inducing flow ejection at corner regions and flattening on the upstream portions of the undulating vortex rings (Fig. 13.3).

Laboratory investigations of elliptic [37] and rectangular [6] jets with AR ≥ 2 indicate that the spreading of the jet in the direction of the flow is accompanied by deformation of its transverse section, with the minor-axis side increasing while the major-axis side decreases, the jet cross-section approaching an approximately rhomboidal shape, and then, with subsequent development, the minor and major axis directions being interchanged, thus undergoing a 90° axis rotation.
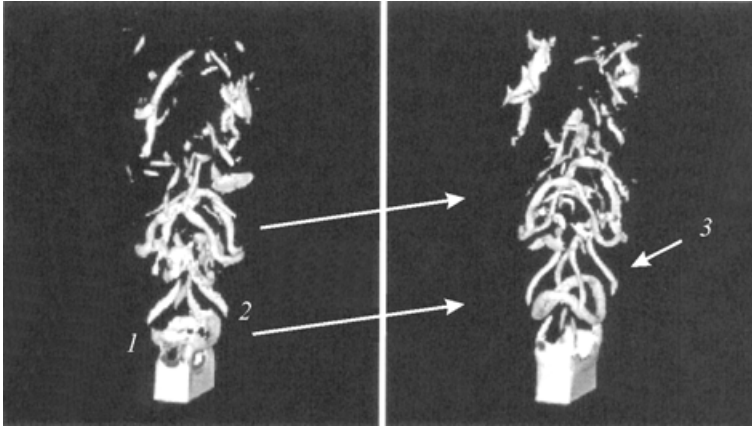
Figure 13.4 Instantaneous isosurfaces of the vorticity magnitude for the AR = 3 rectangular jet [34]. *1* — single ribs aligned with corners, *2* — vortex rings, and *3* — braid (rib) vortices

The unsteady jet vorticity dynamics for AR = 3 is illustrated in Fig. 13.4. In the first phase of the rectangular ring deformation, its corner regions move ahead faster due to the self-induced velocity; the higher-curvature portions left behind (at major-axis locations) then move quickly ahead, and further self-induced deformation of the ring follows, where the minor sides of the ring stretch and effectively move faster downstream, while the centers of the longer sides tend to stay behind and move away from the jet centerline. However, rather than an approximate recovery of its flatness and shape, as in the isolated ring case [26], the ring is a nonplanar vortex ring with a transverse cross-section and formally switched characteristic axes (compared to those at the jet exit).

As noted above, the dynamical mechanisms underlying axis switchings subsequent to the first cannot be attributed to just vortex-ring self-deformation. As one moves downstream, the jet development is controlled by strong interactions between ring and braid vortices, which combined with azimuthal instabilities will eventually lead to their breakdown and to the turbulent flow regime downstream. Rectangular jets with AR $\geq$ 2 are characterized by single ribs aligned with corner regions [34] — in contrast with pairs of counterrotating ribs aligned with the corners for square jets (cf. Fig. 13.3 and Fig. 13.4).

Further distinct topological features of the jet vorticity dynamics are expected for larger AR (e.g., for AR $\geq$ 4), for which vortex-ring bifurcation has been observed [8, 22, 25, 26].
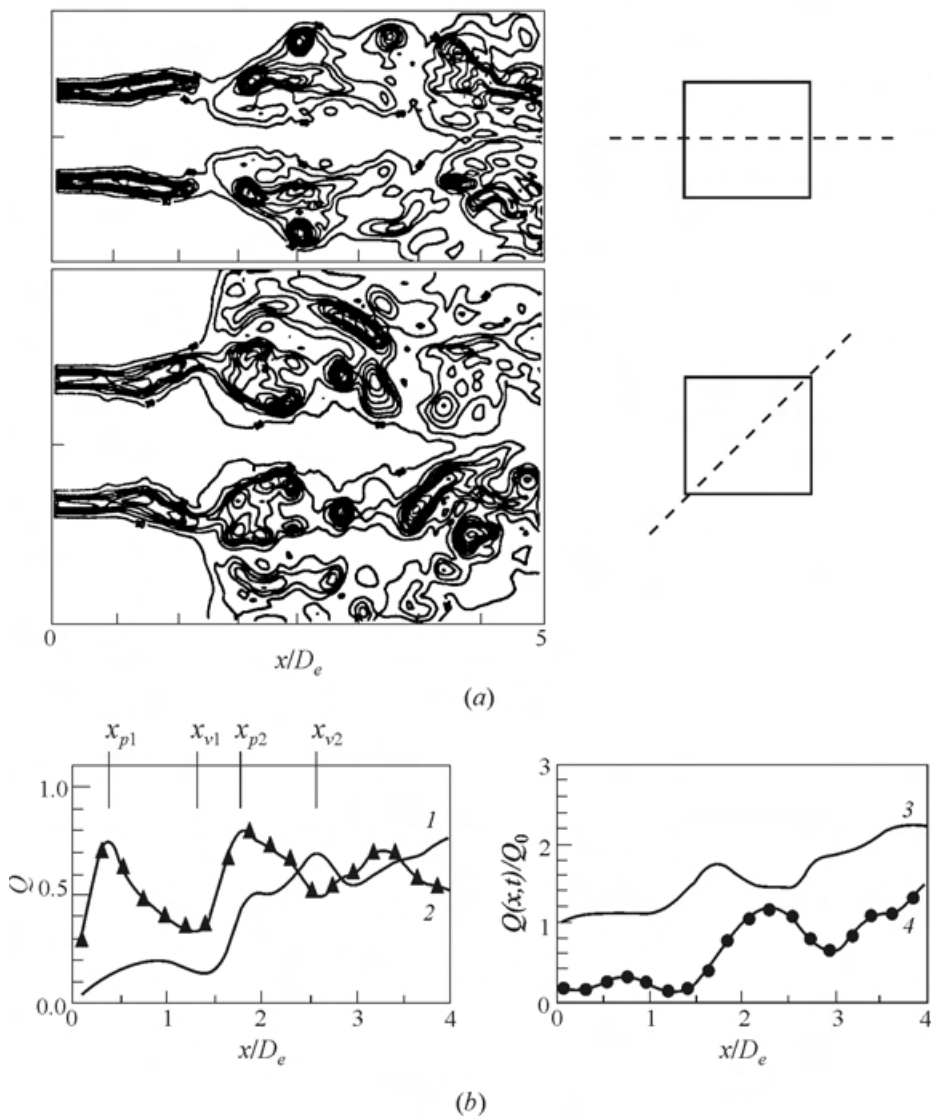
13.4 NONPREMIXED COMBUSTION DYNAMICS

13.4.1 Square Jets

The database of the jet simulations has also been used to obtain insights on the close relationship between unsteady fluid and nonpremixed-combustion jet dynamics [10–12, 35]. The combustion of propane–nitrogen (hydrogen–nitrogen) square jets emerging into a quiescent gaseous background of oxygen–nitrogen was investigated [10–12], with focus on: (1) regimes with a moderately high Reynolds number, for which chemical exothermicity affects the jet development mainly through inviscid volumetric expansion and baroclinic vorticity production mechanisms; (2) regimes with sufficiently low Re, for which local temperature changes in the flow due to chemical energy release and compressibility combined with temperature-dependent viscous effects play a major role controlling the flow dynamics. Investigation of the effects of density differences, exothermicity, relaminarization, and preferential diffusion on the jet dynamics produced the first detailed documentation of temperature and mixedness distributions in reactive square jets, and the relation between combustion and underlying fluid dynamics.

The instantaneous product formation rates were shown [10] to be closely correlated with entrainment rates $(D_e/Q_0)dQ/dx$ — found to be first significant in the regions of roll-up and initial self-deformation of vortex rings, and then farther downstream, where fluid and momentum transport between jet and surroundings are considerably enhanced by the presence of braid vortices (Fig. 13.5). The role of Re and nonunity-Le effects was also addressed [11]: associated with lower Re and jet Le less than unity, the reactive simulations generally predicted a significantly reduced jet entrainment (Fig. 13.6a), as well as higher jet temperatures (Fig. 13.6b) and fuel burning rates (Fig. 13.6c). In contrast with the only slight stabilizing effect of reducing Re for the nonreactive cases, considerable viscous damping effects are found for the reactive jets (Figs. 13.6a) because of exothermicity and the monotonically increasing dependence of viscosity with temperature [11, 12]. Viscous damping has the effect of smoothing the flow, reducing its small-scale content and characteristic vortex strengths, which reflects on reduced jet spread, lower temperatures, and reduced entrainment and combustion.

Chemical exothermicity influences the jet development by effectively modifying the jet shear layer initial conditions [10, 14, 35] and by directly affecting the vorticity dynamics through expansion and baroclinic torque effects (e.g., as in [36]). Specific combustion features of the observed reactive jet development include: (1) distinct high-temperature regions associated with local chemical exothermicity and the convective concentration of burnt gas governed by the dynamics of vortex rings and hairpin vortices; (2) instantaneous fuel burning occurring mainly at the outer sides of the jet shear layer, at the interfaces between

Figure 13.5 Unsteady nonpremixed combustion and fluid dynamics: (a) contours of the vorticity magnitude Ω in planes indicated to the right; (b) cross-sectional averaged measures of instantaneous chemical product and product formation (left frame), instantaneous unconstrained and vorticity-bearing ($\Omega > 5\%$ peak-value) streamwise mass flux Q (right frame). 1 — product, 2 — instantaneous production, 3 — $\Omega_0 = 0$, and 4 — $\Omega_0/\Omega_{\text{peak}} = 0.05$.
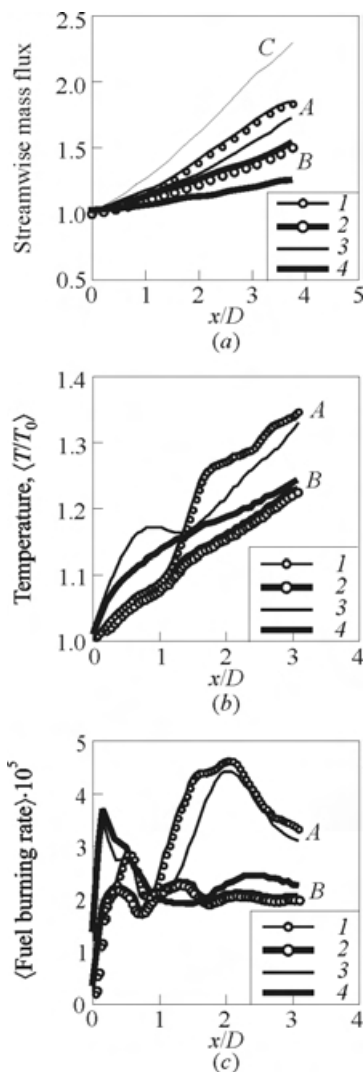
Figure 13.6 Preferential diffusion and Reynolds number effects in the combustion of a hydrogen–nitrogen square jet with oxygen–nitrogen background [11]. *1* — Re > 85 000, Le = 1.1/1.1; *2* — Re = 2 600, Le = 1.1/1.1; *3* — Re > 85 000, Le = 0.3/1.1; *4* — Re = 2 600, Le = 0.3/1.1. *A* — high Re, *B* — low Re, *C* — nonreactive

reactants, where most of the mixing takes place in thin laminar diffusion layers; (3) high-strain regions (spatially uncorrelated with high-rate fuel-burning regions) in the jet outer-edge regions aligned with the corners — due to the strong interaction between advanced vortex-ring corners and hairpin tips, and in inner flame edges between vortex rings [12]. As a result of vortex-ring self-deformation and presence of braid vortices, there is enhanced near-jet mixing and combustion in regions aligned with the nozzle flat-side centers.

13.4.2 Aspect Ratio Effects

The database of jet simulations can also be used to obtain insights on the potential impact of AR on non-premixed rectangular-jet combustion.

By design, the jets with AR = 1 and AR = 2 compared in Fig. 13.7 (from [34]) only differ on the actual shape of the initial jet cross-section but have otherwise identical initial conditions, e.g., including the same cross-sectional jet outlet areas. The near-jet entrainment and nonpremixed combustion properties are largely determined by the characteristic braid-vortex topology and vortex-ring axis rotation times. Because of the initial enhanced entrainment associated with rib pairs aligned with the corner regions, the square jet nonpremixed combustion turns out to be more effective immediately downstream of the nozzle; on the other hand, the jet with AR = 2 exhibits better combustion farther away from the jet exit, reflecting
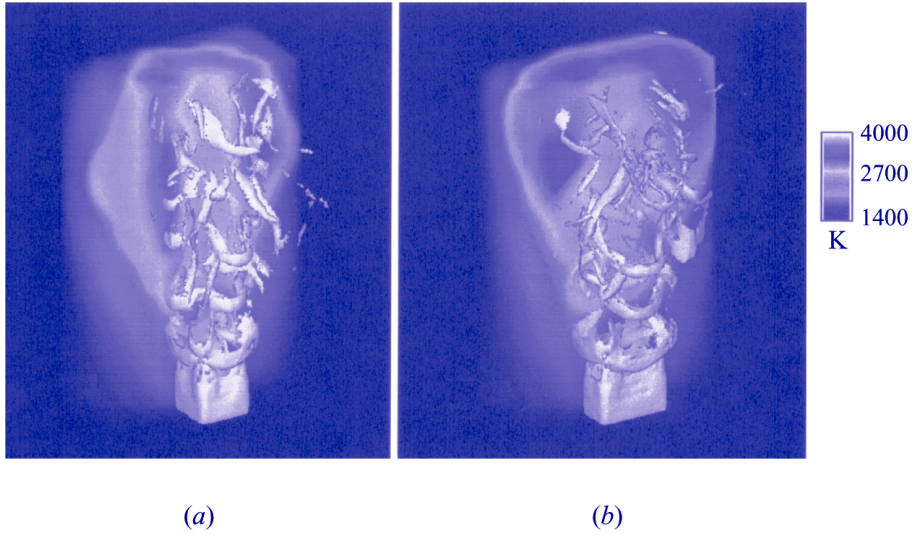
Figure 13.7 Aspect ratio effects on the combustion of a propane–nitrogen jet with oxygen–nitrogen surroundings. Instantaneous visualizations; temperature distributions superimposed on vorticity isosurfaces [34]: (*a*) AR = 1; (*b*) AR = 2

better entrainment there due to the azimuthally more stable vortex rings and on the axis-switching process being completed farther downstream — since vortex-ring axis-rotation times increase with AR [25, 26].

Axis-rotation times are typically twice as large for AR = 2, compared with AR = 1; because of this difference in timescales, axis switchings occur closer to the jet exit and can be more frequent in the near jet for AR = 1, e.g., first axis switching occurring at $x \cong D_e$ for AR = 1, compared with its occurrence at $x \cong 3D_e$ for AR = 2, for the jet initial conditions considered.

An important open question relates to whether an optimal AR exists with regard to entrainment enhancement. Laboratory jet experiments with pseudo-elliptical geometries [27] suggest that an optimal AR with regard to nozzle-geometry-enhanced entrainment might be at a value AR = 3. However, the experiments are not conclusive since they involved AR up to 3.5 and nonuniform momentum-thickness distributions, which are known to also affect the entrainment process [5]. Moreover, the possible effects on jet entrainment of other more complicated interactions such as vortex-ring bifurcation still need to be established.

13.5 CONCLUDING REMARKS

The goal of this work has been to characterize the effects of the unsteady vorticity dynamics on jet entrainment and nonpremixed combustion. The main focus of the numerical simulations of rectangular jets has been on the vorticity dynamics underlying axis switching when the initial conditions at the jet exit involve laminar conditions, negligible streamwise vorticity, and negligible azimuthal nonuniformities of the momentum thickness.

Simulations of compressible (subsonic) jet regimes with AR = 1–4 and moderately high Reynolds numbers were discussed. Qualitatively different vorticity topologies characterizing the near-flow field of low-AR rectangular jets were demonstrated, involving (*i*) self-deforming and bifurcating (AR = 4) vortex rings, interacting ring and rib (braid) vortices — including (*ii*) single ribs aligned with corner regions (AR ≥ 2), (*iii*) rib pairs (hairpins) aligned with the corners (AR = 1), and (*iv*) elongated "worm" vortices in the turbulent jet regime. Even if effectively absent at the jet exit, the streamwise vorticity has an increasingly important role in affecting the axis-switching dynamics as one moves downstream, by inducing motions directly affecting the transverse jet cross-section.

The reactive jet simulations reviewed included hydrogen–air and propane–air jet systems, and cases with nonunity AR. The jet development is controlled by the dynamics of interacting vortex rings and braid vortices. The reactive jet shows distinct high-temperature regions associated with local chemical exothermicity and the convective concentration of burnt gas, and instantaneous chemical production occurring mainly at the outer edges of the fuel jet. Most of the mixing scalar dissipation is found to be concentrated in thin laminar diffusion layers. The instantaneous product formation rates are closely correlated with the local entrainment rates controlled by the vorticity bearing fluid.

The reactive simulations generally predict higher jet temperatures and significantly reduced jet entrainment associated with lower Re and jet Le less than unity. The near-jet entrainment and nonpremixed combustion properties of low-AR rectangular jets are largely determined by the characteristic braid-vortex topology and vortex-ring axis-rotation times. The vorticity dynamics and ensuring mixing processes determine the regions of combustion within the flame and thus the overall heat release pattern. By understanding these combined processes it is possible to select optimal fuel injection features to improve jet combustion.

ACKNOWLEDGMENTS

REFERENCES

1. Hussain, A. K. M. F. 1986. Coherent structures and turbulence. *J. Fluid Mechanics* 173:303.

2. Gutmark, E. J., and F. F. Grinstein. 1999. Flow control with noncircular jets. *Annual Reviews Fluid Mechanics* 31:239–72.

3. Zaman, K. B. M. Q. 1996. Axis switching and spreading of an asymmetric jet: The role of coherent structure dynamics. *J. Fluid Mechanics* 316:1–27.

4. Abramovich, G. N. 1983. Deformation of the transverse section of a rectangular turbulent jet. *Izv. Akad. Nauk SSSR. Mekh. Zhidk. Gaza* 1:54–63.

5. Koshigoe, S., E. Gutmark, and K. Schadow. 1989. Initial development of noncircular jets leading to axis switching. *AIAA J.* 27:411.

6. Tsuchiya, Y., C. Horikoshi, and T. Sato. 1986. On the spread of rectangular jets. *Experiments Fluids* 4:197–204.

7. Gutmark, E., K. C. Schadow, T. P. Parr, D. M. Hanson-Parr, and K. J. Wilson. 1989. Noncircular jets in combustion systems. *Experiments Fluids* 7:248.

8. Toyoda, K., and F. Hussain. 1989. Vortical structures of noncircular jets. *4th Asian Congress of Fluid Mechanics Proceedings*. Hong Kong. A117–27.

9. Grinstein, F. F., and C. R. DeVore. 1996. Dynamics of coherent structures and transition to turbulence in free square jets. *J. Physics Fluids* 8:1237–51.

10. Grinstein, F. F., and K. Kailasanath. 1995. Three-dimensional numerical simulations of unsteady reactive square jets. *Combustion Flame* 100:2; 101:192.

11. Grinstein, F. F., and K. Kailasanath. 1996. Exothermicity and relaminarization effects in reactive square jets. *Combustion Science Technology* 113–114:291.

12. Grinstein, F. F., and K. Kailasanath. 1996. Exothermicity and three-dimensional effects in unsteady propane square jets. *26th Symposium (International) on Combustion Proceedings*. Pittsburgh, PA: The Combustion Institute. 91–96.

13. Oran, E. S., and J. P. Boris. 1987. *Numerical simulation of reactive flow*. New York: Elsevier.

14. Grinstein, F. F., and K. Kailasanath. 1992. Chemical energy release and dynamics of transitional reactive, free shear flows. *J. Physics Fluids A* 4:2207.

15. Westbrook, C. K., and F. L. Dryer. 1981. *Combustion Science Technology* 27:31–43.

16. Grinstein, F. F., E. Gutmark, and T. P. Parr. 1995. Near-field dynamics of subsonic, free square jets. A computational and experimental study. *J. Physics Fluids* 1:1483–97.

17. Boris, J. P., F. F. Grinstein, E. S. Oran, and R. J. Kolbe. 1992. New insights into large eddy simulation. *Fluid Dyn. Res.* 10:199–228.

18. Grinstein, F. F., and C. Fureby. 1998. Monotonically integrated large eddy simulation of free shear flows. AIAA Paper No. 98-0537.

19. Grinstein, F. F., and R. H. Guirguis. 1992. Effective viscosity in the simulation of spatially evolving shear flows with monotonic FCT models. *J. Comput. Phys.* 101:165–75.

20. Fureby, C. 1996. On subgrid scale modeling in large eddy simulations of compressible fluid flow. *J. Physics Fluids* 8:1301–11.

21. Möller, S. I., E. Lundgren, and C. Fureby. 1996. Large eddy simulations of unsteady combustion. *26th Symposium (International) on Combustion Proceedings.* Pittsburgh, PA: The Combustion Institute. 241.

22. Hussain, F., and H. S. Husain. 1989. Elliptic jets. Part 1. Characteristics of unexcited and excited jets. *J. Fluid Mechanics* 208:257–320.

23. Batchelor, J. K. 1967. *An introduction to fluid dynamics.* London, UK: Cambridge University Press. 510.

24. Widnall, S. E., and J. P. Sullivan. 1973. On the stability of vortex rings. *Proc. Royal Society A (London)* 332:335–53.

25. Kiya, M., K. Toyoda, H. Ishii, M. Kitamura, and T. Ohe. 1992. Numerical simulation and flow visualization experiment on deformation of pseudo-elliptic vortex rings. *Fluid Dyn. Res.* 10:117–31.

26. Grinstein, F. F. 1995. Self-induced vortex ring dynamics in subsonic rectangular jets. *J. Physics Fluids* 7:2519–21.

27. Schadow, K., K. Wilson, M. Lee, and E. Gutmark. 1987. Enhancement of mixing in reacting fuel-rich plumes issued from elliptical jets. *J. Propulsion Power* 3:145.

28. Liepmann, D., and M. Gharib. 1992. The role of streamwise vorticity in the near-field entrainment of round jets. *J. Fluid Mechanics* 245:643–68.

29. Jimenez, J., A. Wray, P. Saffman, and R. Rogallo. 1993. The structure of intense vorticity in isotropic turbulence. *J. Fluid Mechanics* 255:65–90.

30. Porter, D. H., A. Pouquet, and P. R. Woodward. 1994. Kolmogorov-like spectra in decaying three-dimensional supersonic flows. *J. Physics Fluids* 6:2133–42.

31. Grinstein, F. F., and C. R. DeVore. 1992. Coherent structure dynamics in spatially-developing square jets. AIAA Paper No. 92-3441.

32. Husain, H. S., and F. Hussain. 1993. Elliptic jets. Part 3. Dynamics of preferred mode coherent structure. *J. Fluid Mechanics* 248:315–61.

33. Grinstein, F. F. 1993. Vorticity dynamics in spatially-developing rectangular jets. AIAA Paper No. 93-3286.

34. Grinstein, F. F. 1997. Entrainment, axis-switching, and aspect-ratio effects in rectangular jets. AIAA Paper No. 97-1875.

35. Grinstein, F. F., E. G. Gutmark, T. P. Parr, D. M. Hanson-Parr, and U. Obeysekare. 1996. Streamwise and spanwise vortex interaction in an axisymmetric jet. A computational and experimental study. *J. Physics Fluids* 8:1515–24.

36. McMurtry, P. A., J. J. Riley, and R. W. Metcalfe. 1989. *J. Fluid Mechanics* 199:297–332.

37. Ho, C. M., and E. Gutmark. 1987. Vortex induction and mass entrainment in a small-aspect ratio elliptic jet. *J. Fluid Mechanics* 179:383.

38. Zaman, K. B. M. Q. 1986. Flow field and near and far sound field of a subsonic jet. *J. Sound Vibration* 106:1–16.

Chapter 14

TURBULENT COMBUSTION
OF POLYDISPERSED MIXTURES

N. N. Smirnov, V. F. Nikitin, and J. C. Legros

A model for theoretical investigation of turbulent mixing and combustion
of polydispersed mixtures in confined volumes is developed. The nu-
merical model and the created software make it possible to determine
the characteristics of polydispersed mixtures turbulent combustion and
ignition. The model is validated against with experiments on dust com-
bustion in confined volumes under different initial turbulization of the
mixture.

14.1   INTRODUCTION

The problems of polydispersed mixtures ignition and combustion modeling are
very acute for the description of processes taking place in motor chambers and
burners of different types as well as for making forecasts of accidental explo-
sions.

The problem of dust particle evolution in turbulent stratified flows near the
sources of accidental heat release is of great practical importance for description
of dust explosions and large fires.

The aim of the present investigation is to create adequate semi-empirical
physical and mathematical models that describe dynamics of turbulent com-
bustion in heterogeneous mixtures of gas with polydispersed suspended particles.

Long-term investigations of the processes of turbulent combustion in dust
explosions have contributed to great progress achieved in this branch of sci-
ence [1].

The existing theoretical models, accounting for the influence of turbulence on
the transport processes and the chemical reaction rates, use, as a rule, two differ-
ent types of approaches to the phenomenon. One is to apply Reynolds average

equations for modeling the mean values of parameters introducing different models for turbulent fluxes to close the system of equations [2]. The method works rather effectively for determining mean characteristics for gaseous mixtures but becomes complicated for heterogeneous systems with polydispersed phases. The complication is due to an enormous number of additional terms arising in averaging that can hardly be modeled to close the system of equations. Different definitions need to be introduced for average values of various parameters to maintain consistency of the approach. The other approach is based on the assumption that instability plays a predominant role in the nature of turbulent flows. The model presents direct numerical modeling of unstable flows and drift of vortices (the modeling for "infinite Reynolds numbers" [3]), thus obtaining results that are not microscopically reproducible, but that correspond with the nature of the phenomenon.

The present investigation applies deterministic methods of continuous mechanics of multiphase flows to determine the mean values of parameters of the gaseous phase. It also applies stochastic methods to describe the evolution of polydispersed particles and fluctuations of parameters [4]. Thus the influence of chaotic pulsations on the rate of energy release and mean values of flow parameters can be estimated. The transport of kinetic energy of turbulent pulsations obeys the deterministic laws.

Theoretical investigations of the problem were carried out on the base of the mathematical model, combining both deterministic and stochastic approaches to turbulent combustion of organic dust–air mixtures modeling. To simulate the gas-phase flow, the k–ε model is used with account of mass, momentum, and energy fluxes from the particles' phase. The equations of motion for particles take into account random turbulent pulsations in the gas flow. The mean characteristics of those pulsations and the probability distribution functions are determined with the help of solutions obtained within the frame of the k–ε model.

The model for phase transitions and chemical reactions takes into account thermal destruction of dust particles, vent of volatiles, chemical reactions in the gas phase, and heterogeneous oxidation of particles influenced by both diffusive and kinetic characteristics.

The ignition process was modeled as an energy release in a relatively small volume inside the vessel with the power as a given function of time.

14.2   PRINCIPLES OF MODELING

The system of equations for gas phase was obtained by Favre averaging the system of multicomponent multiphase medium. The modified k–ε model is used to describe the behavior of the gas phase. The generalization of this model will

take into account the influence of the other phases as well as the combustion and heat and mass transfer in the gas phase.

14.2.1 Balance Equations in the Gas Phase

Using the Favre averaging procedure [2, 5] one obtains the following set of equations for the gas phase in a multiphase flow [6] (the averaging bars are removed for simplicity):

$$\partial_t(\alpha\rho) + \nabla\cdot(\alpha\rho\vec{u}) = \dot{M} \tag{14.1}$$

$$\partial_t(\alpha\rho Y_k) + \nabla\cdot(\alpha\rho\vec{u}Y_k) = -\nabla\cdot\vec{I}_k + \dot{M}_k + \dot{\omega}_k \tag{14.2}$$

$$\partial_t(\alpha\rho\vec{u}) + \nabla\cdot(\alpha\rho\vec{u}\otimes\vec{u}) = \alpha\rho\vec{g} - \alpha\nabla p + \nabla\cdot\tau + \dot{\vec{K}} \tag{14.3}$$

$$\partial_t(\alpha\rho E) + \nabla\cdot(\alpha\rho\vec{u}E) = \alpha\rho\vec{u}\vec{g} - \nabla\cdot p\vec{u} - \nabla\vec{I}_q + \nabla\cdot(\tau\vec{u}) + \dot{E} \tag{14.4}$$

where α is the volume fraction of the gas phase, ρ is fluid density, $\vec{u}$ is the fluid velocity vector, $\dot{M}$ is the specific mass flux to the gas phase, Y_k is the mass fraction of the kth gas species, $\vec{I}_k$ is the turbulent diffusive flux to the kth gas species, $\dot{M}_k$ and $\dot{\omega}_k$ are, respectively, mass fluxes to the kth gaseous species due to mass exchange with particles and due to chemical reactions, $\vec{a}\otimes\vec{b}$ is the tensor with components $a_i b_i$, $\vec{g}$ is the acceleration of gravity vector, p is the pressure, τ is the turbulent viscosity tensor, $\vec{K}$ is the specific momentum flux to gas phase, E is the specific energy of fluid, $\vec{I}_q$ is the turbulent energy flux, and $\dot{E}$ is the specific energy flux to gas phase. Equations (14.1)–(14.4) include mass balance in the gas phase, mass balance of the kth component, momentum balance, and energy balance, respectively. The following relations hold between the terms in Eqs. (14.1) and (14.2):

$$\sum_k Y_k = 1, \quad \sum_k \dot{M}_k = \dot{M}, \quad \sum_k \vec{I}_k = 0, \quad \sum_k \dot{\omega}_k = 0$$

The state equations for gaseous mixture are the following:

$$p = R_g\rho T\sum_k Y_k W_k, \quad E = \sum_k Y_k(c_{vk}T + h_{0k}) + \vec{u}^2 + k \tag{14.5}$$

where R_g is the universal gas constant, T is the temperature, W_k is the molar mass of the kth species, c_{vk} and h_{0k} are, respectively, the specific heat at constant volume and the specific internal energy of the kth species, and k is the turbulent kinematic energy.

Two chemical reactions in the gas phase were considered: generalized volatiles component L oxidizing (unidirectional) and carbon monoxide CO oxidizing

(reversible). The kth component mass origination $\dot{\omega}_k$ was calculated using the Arrhenius law for the reaction rate; averaged magnitudes for mass fractions, temperature, and density were used in the law as the first approximation. The turbulent heat flux was split into two terms:

$$\vec{I}_q = \vec{J}_q + \sum k(c_{pk}T + h_{0k})\vec{I}_k \qquad (14.6)$$

where $\vec{J}_q$ could be interpreted as the turbulent conductive heat flux.

The eddy kinematic viscosity ν' is expressed according to the k–ε model as $\nu' = C_\mu K^2/\varepsilon$, where C_μ is the k–ε model constant.

Using the standard k–ε model for compressible flows [5], the turbulent fluxes are modeled in the following way:

$$\tau = \alpha(\mu + \rho\nu')\left(\nabla\vec{u} + \nabla\vec{u}^T - \frac{2}{3}(\nabla\cdot\vec{u})U\right) - \frac{2}{3}\alpha\rho k U \qquad (14.7)$$

$$\vec{I}_k = -\alpha\rho\left(D + \frac{\nu'}{\sigma_d}\right)\nabla\cdot Y_k \qquad (14.8)$$

$$\vec{J}_q = -\alpha\left(\lambda + \sum k c_{pk}\rho\frac{\nu'}{\sigma_t}\right)\nabla\cdot T \qquad (14.9)$$

where μ is the effective laminar viscosity, U is the unit tensor of the 2nd range, D is the overall laminar-diffusive coefficient, σ_t and σ_d are the model constants, and λ is the effective laminar termoconductivity.

The model is closed then by two equations for k and ε:

$$\partial_t(\alpha\rho k) + \nabla\cdot(\alpha\rho\vec{u}k) = \nabla\cdot(\alpha\left(\mu + \rho\frac{\nu'}{\sigma_k}\right)\nabla k) + \tau' : \nabla\vec{u} - \alpha\rho\varepsilon \quad (14.10)$$

$$\partial_t(\alpha\rho\varepsilon) + \nabla\cdot(\alpha\rho\vec{u}\varepsilon) =$$
$$\nabla\cdot\left(\alpha\left(\mu + \rho\frac{\nu'}{\sigma_\varepsilon}\right)\nabla\varepsilon\right) + \frac{\varepsilon}{k}(C_{1\varepsilon}\tau' : \nabla\vec{u} - C_{2\varepsilon}\alpha\rho\varepsilon) \qquad (14.11)$$

where σ_k, σ_ε, $C_{1\varepsilon}$, and $C_{2\varepsilon}$ are the other model constants. The constants take the following standard values [2, 5]:

$$C_\mu = 0.09, \quad C_{1\varepsilon} = 1.45, \quad C_{2\varepsilon} = 1.92$$

$$\sigma_d = 1, \quad \sigma_t = 0.9, \quad \sigma_k = 1, \quad \sigma_\varepsilon = 1.13$$

To close the model, one needs the expressions for mass, momentum, and energy fluxes from the other phases.

14.2.2 Particulate Phase Modeling

The motion of polydispersed particulate phase is modeled making use of a stochastic approach. A group of representative model particles is distinguished. Motion of these particles is simulated directly taking into account the influence of the mean stream of gas and pulsations of parameters in gas phase. Properties of the gas flow — the mean kinetic energy and the rate of pulsations decay — make it possible to simulate the stochastic motion of the particles under the assumption of the Poisson flow of events.

A great amount of real particles (for instance, liquid droplets) is modeled by an ensemble of model particles (their number is of the order of thousands). Each model particle is characterized by a vector of values, representing its location, velocity, mass, and other properties. The following vector, determined for each model particle, is introduced:

$$\{N,\, m,\, m_s,\, \vec{r},\, \vec{v},\, \vec{w},\, \omega,\, T_s\}_i\,, \quad i = 1, \dots, N_p \tag{14.12}$$

where N is the number of real particles represented by the model particle, m is the mass of the model particle, m_s is the mass of carbon in the model particle, $\vec{r}$ and $\vec{v}$ are, respectively, the radius-vector and velocity vector of the model particle, $\vec{w}$ is the random term in the velocity of fluid in the neighborhood of the model particle, ω and T_s are, respectively, the volume and temperature of the model particle, and N_p is the total number of model particles. The values of N_i are initialized to satisfy the equality $\Sigma_i N_i m_i = M_p$, and are not changed in the process of calculations. When a particle is burnt out, its mass m_i is set to zero, and the particle is excluded from calculations.

Modeling the particles phase, therefore, is split into two stages. The first stage is to evaluate the vector (14.12) for each model particle. The second stage is to evaluate the particle's phase volumetric share, $\alpha_2 = 1 - \alpha$, and fluxes $\dot{M}_k$, $\dot{M}$, $\dot{\vec{K}}$, $\dot{E}$ that are used in equations describing the gas phase behavior.

To model the motion of particles, the approach described in detail in [6, 7] is used. The laws of ith particle motion are

$$m_i \frac{d\vec{v}_i}{dt} = m_i \vec{g} - \frac{m_i}{\rho} \nabla p + \vec{f}_d\,, \qquad \frac{d\vec{r}_i}{dt} = \vec{v}_i \tag{14.13}$$

where the force affecting the particle consists of gravity and Archimedus forces, drag force, and Langevin force (with $\vec{f}_d$ denoting the resultant force). The Langevin force that models turbulent pulsations is evaluated together with the drag force for each model particle using the random vector, $\vec{w}_i$. The details of this force evaluation are shown in [7].

The decay of mass from a particle is evaluated by

$$\frac{dm_i}{dt} = -\dot{m}_i \tag{14.14}$$

The decay of volume was determined by the decay of mass of carbon component rather than by the total mass decay. Thus, the extraction of volatiles causes the decay of mean density of the particle.

The internal energy of the particle, $e_i = c_i T_i + h_i{}^0$, changes because of heat exchange with the surrounding gas and phase transitions or, if any, chemical reactions on the surface

$$m_i \frac{de_e}{dt} = q_i + Q_{si} \qquad (14.15)$$

where Q_{si} is the heat release on the surface of the ith model particle, and q_i is a heat flux between the gas and a particle:

$$q_i = \pi d \lambda \text{Nu}_i (T - T_{si}) \qquad (14.16)$$

Here d is the model particle diameter; Nu is the Nusselt number. The Nusselt number for the ith particle is determined as

$$\text{Nu}_i = 2 + 0.16\text{Re}_i{}^{2/3}\text{Pr}^{2/3}$$

where Pr is the Prandtl number and the Reynolds number Re_i is determined by the influence of turbulent pulsations of velocity which induce oscillations in the heat flux between gas and particles.

The internal energy for the case of multicomponent particles is determined by the formula

$$e_i = \sum_{j=1}^{L} (c_{ij} T_{si} + h_{ij}{}^0) Y_{ij}$$

where c_{ij} is the heat capacity of the jth component within the ith particle and $h_{ij}{}^0$ are the terms representing energy release in gas-phase reactions and L is the number of components in the particulate phase. The heat release or absorption on the surface of the particle due to chemistry or phase transitions can be determined by the formula

$$Q_{si} = \sum_{j=1}^{L} \dot{m}_{ij} h_{ij}$$

where m_{ij} is the mass rate of consumption (or extraction) of the jth component from the ith particle; h_{ij} is the enthalpy of surface chemical reactions or phase transformations.

14.2.3 Fluxes from Model Particles

The mass exchange processes between a particle and the gaseous phase can take place because of phase transitions (evaporation or condensation on the surface

of liquid droplets), devolatilization of dust particles, chemical transformations on the interface, etc. A mixture of gas with organic dust particles is considered with due account for a possibility of volatiles extraction and chemical reactions. Two overall reactions are assumed to take place on a particle surface together with volatiles extraction. The reactions are

$$C + 0.5O_2 \rightarrow CO, \qquad C + CO_2 \rightarrow 2CO$$

Thus, three species from the gas phase, O_2, CO, and CO_2, take part in the reaction, and the generalized volatiles component, L, is extracted. The following formulae for the volatiles extraction and carbon decay rates from the ith model particle are used:

$$\dot{m}_{Li} = (m_i - m_{si})A_L(T_{si}) \tag{14.17}$$

$$\dot{m}^1{}_{Ci} = K_1 \lg\left(1 + \frac{Y_{O_2,i}W_C}{y_1 W_{O_2}}\right)^{y_1}, \quad \dot{m}^2{}_{Ci} = K_2 \lg\left(1 + \frac{Y_{CO_2,i}W_C}{y_2 W_{CO_2}}\right)^{y_2} \tag{14.18}$$

where

$$K_1 = \pi d^2 \left(\frac{0.5 W_{O_2}}{W_C A_{C1}(T_{si})} + \frac{d_i}{\rho D \mathrm{Nu}_i}\right)^{-1}$$

$$K_2 = \pi d^2 \left(\frac{0.5 W_{O_2}}{W_C A_{C2}(T_{si})} + \frac{d_i}{\rho D \mathrm{Nu}_i}\right)^{-1}$$

$$y_k = \frac{\dot{m}_{Ck}}{\dot{m}}; \quad k = 1, 2$$

Here sub/superscripts 1 and 2 denote carbon oxidation by oxygen and by carbon dioxide, respectively; $A_L(T_{si})$, $A_{C1}(T_{si})$, $A_{C2}(T_{si})$ are the Arrhenius functions for heterogeneous kinetics depending on the surface temperature T_{si}.

Equations (14.18) are the generalization of the solutions obtained in [8] for quasisteady heterogeneous diffusive combustion of the spherical particles. Under the condition $Y_{k,i}W_C \ll y_k W_k$, for at least one of the species ($k = 1$ or $k = 2$), the respective formula (14.18) could be essentially simplified:

$$\dot{m}_{Ci}{}^k = K_k \log\left(1 + \frac{Y_{k,i}W_C}{W_k}\right)$$

The rate of particle mass decrease and rates of gaseous species CO, CO_2, and O_2 release from a particle are calculated (subscript i omitted for simplicity):

$$\begin{aligned}
\dot{m} &= \dot{m}^1{}_C + \dot{m}^2{}_C, & \dot{m}_{O_2} &= 0.5\dot{m}^1{}_C \frac{W_{O_2}}{W_C} \\
\dot{m}_{CO_2} &= 0.5\dot{m}^2{}_C \frac{W_{CO_2}}{W_C} & \dot{m}_{CO} &= (\dot{m}^1{}_C + \dot{m}_C{}^2)\frac{W_{CO_2}}{W_C}
\end{aligned}$$

Momentum and energy fluxes are calculated as follows:

$$\vec{k}_i = \dot{m}\vec{v}_i - \vec{f}_{ri}\,, \quad \dot{e}_i = q_i + \dot{m}(e_i + 0.5|\vec{v}_i|^2) - (\vec{v}_i \cdot \vec{R}_i)$$

where F_{ri} is the drag force.

Fluxes $\dot{M}_k$, $\dot{M}$, $\dot{\vec{K}}$, to gas phase as well as the volumetric share of particles phase α_2, are obtained evaluating corresponding fluxes from model particles and volume of model particles. The procedure of recalculating (see [6, 7]) is the following.

For each grid node n with the volume Ω_n attached to it, one evaluates at the first stage:

$$F_n{}^1 = \frac{1}{|\Omega_n|} \sum_{i:(x_i, r) \in \Omega_n} f_i$$

where F is an element of the set defined on the grid: $F \in \{\alpha_2,\ \dot{M},\ \dot{M}_k,\ \dot{K}_x,\ \dot{K}_r,\ \dot{E}\}$, and f is an element of the corresponding set defined on model particles via the values from the particle vector (14.12) and fluxes evaluated from it: $f \in \{\omega,\ \dot{m},\ \dot{m}_k,\ \dot{k}_x,\ \sqrt{\dot{k}_y + \dot{k}_z},\ \dot{e}\}$.

Then, one applies the procedure smoothing the fields of F^1 in order to ensure stability of calculations. The detailed description of the algorithm can be found elsewhere [6, 7].

14.2.4   Overall Method of Computation

Calculations were performed in the cylindrical geometry with the uniform grid 61×41 and 5000 model particles. Each time step contained the calculations of model particles motion, determining fluxes from particles to the gas phase and recalculating them to the grid. Then, two half-steps to calculate gas dynamics parameters were taken, accounting for fluxes from the particulate phase. Used at each half-step was the space splitting in x and r coordinates as well as the splitting in three physical processes: chemistry and turbulent energy production, convection (hyperbolic part of the equations), and diffusion (parabolic part of the equations). The hyperbolic part was solved using the explicit FCT technique [9]; the parabolic part was solved implicitly. The time step was calculated using the CFL criterion. The gas dynamic part of the scheme was found to be validated after comparing it with standard solutions. The present set of calculations was made for combustion in a closed cylindrical vessel filled with an air and dextrin dust suspension. The volatiles composition and model chemistry for the dextrin dust was described in [6] and [7].

The dust–air mixture was ignited in the center of the site by the energy release in a ball-shape volume.

14.3 RESULTS AND DISCUSSIONS

14.3.1 Flame Zone Evolution in a Closed Vessel

Results of the flow parameters calculation for the stage of ignition of the air–dust mixtures are shown in [6]. Here, the results are presented for the volatiles oxidizing intensity $\dot{M}_L/\rho$ for the following stages of the process: the formation of a flame ball at time $t = 10$ ms just after switching off the igniter (Fig. 14.1a); the formation of the turbulent flame at time $t = 40$ ms after the ignition (Fig. 14.1b); the developed flame at $t = 66$ ms (Fig. 14.1c); and further evolution of the flame at $t = 91.6$ ms when the flame forefront nearly reaches the walls (Fig. 14.1d).
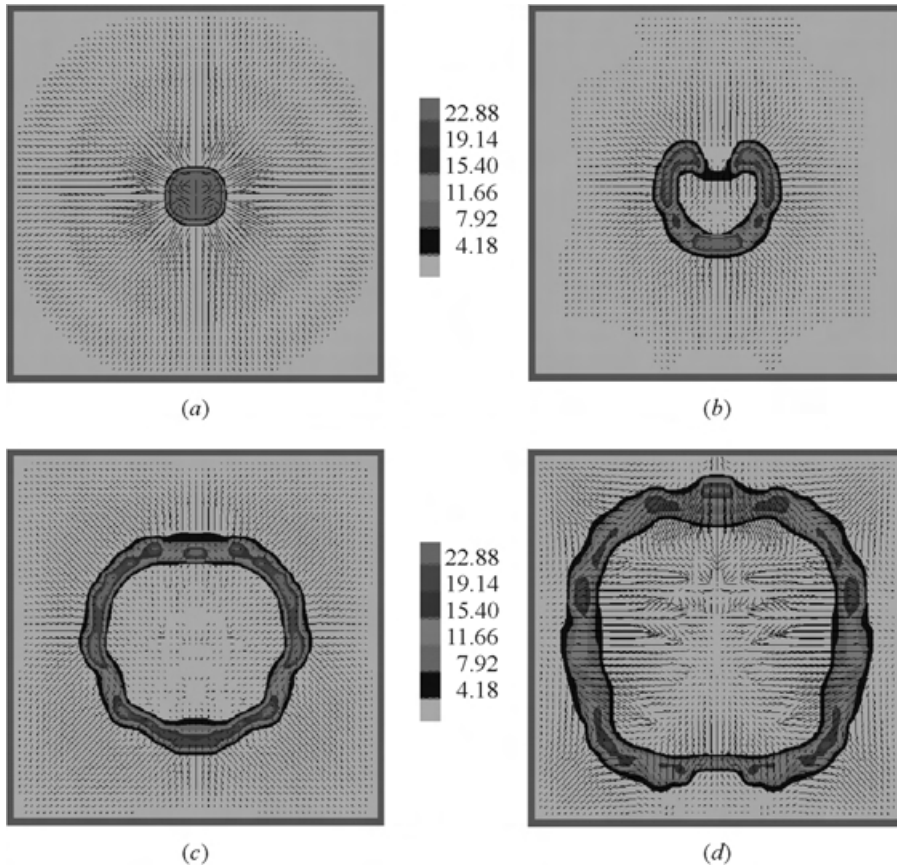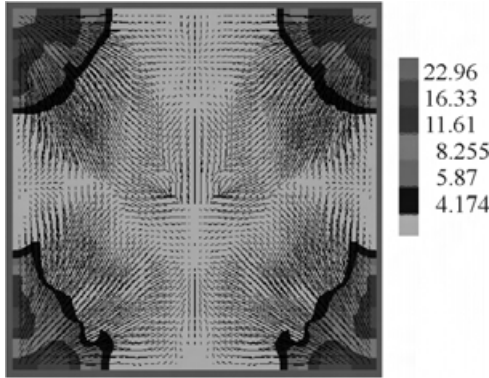

Figure 14.1 Flame intensity after ignition of a polydispersed particle suspension in air at (a) $t = 10$ ms; (b) 40; (c) 66.3; and (d) 91.6 ms

It is seen from Fig. 14.1*a* that there is a hot spot in the center of the volume where the ignition took place. The rate of volatiles oxidation is high there because many particles within the ignition zone were devolatilized completely and the concentrated volatiles cluster had just begun to burn. The short line segments reflect the propagation of a weak compression wave in the gas caused by the ignition energy input. The wave is being overtaken by the other one formed in expansion of the ignited gas–volatiles mixture in the zone of ignition. The reaction rate decreases in the center and the reaction zone forms a rather thick expanding spherical layer.

The results from Fig. 14.1*b* show the developing turbulent flame zone. The nonsymmetries of the reaction rate field are due to inhomogeneity of the polydispersed mixture, i.e., nonsymmetrical distribution of model particles and their velocities. The reaction front is under formation: oxygen and partially the volatiles in the center are burnt out, but the reaction front is not sphere-shaped yet. The nonuniformity of the model particles distribution was induced initially due to the stochastic modeling of the particulate phase.

Figure 14.1*c* illustrates the reaction rate in the well-developed flame at $t = 66$ ms. The reaction front is nearly ball-shaped. Some nonsymmetries due to initial nonsymmetry of particles distribution are still present and some hot spots are evident within the reaction zone. The hot spots are very unstable; they appear and die within the reaction zone arbitrarily.

Figure 14.1*d* illustrates the state of the process when the flame front is about to reach the walls. The flame front deviates from a sphere not only by nonsymmetries of the particles distribution but also by its proximity to the walls.

After the flame reaches the walls it propagates toward the corners (Fig. 14.2) causing the intensive gas flow out of the corners and towards the center.

Figure 14.2 Flame intensity in a polydispersed particle suspension in air at $t = 114.5$ ms after ignition

The results were obtained for the polydispersed mixtures possessing the following characteristic properties of particle size distribution function (Figs. 14.1–14.2):

$$d_{\min} = 10^{-5} \text{ m}, \quad d_{\mathrm{med}} = 5 \cdot 10^{-5} \text{ m}, \quad d_{\max} = 7 \cdot 10^{-5} \text{ m}$$

The second set of numerical simulations was performed for the polydispersed mixture characterized by the presence of larger particles:

$$d_{\min} = 10^{-5} \text{ m}, \quad d_{\text{med}} = 5 \cdot 10^{-5} \text{ m}, \quad d_{\max} = 10^{-4} \text{ m}$$

and the increased initial concentration of oxygen. The list of problem parameters is given in Table 14.1.

The dynamics of the reaction zone (volatiles oxidizing intensity) and the particles' temperatures are shown in Figs. 14.3–14.4. It is clearly seen that the width of the reaction zone is larger, for the present case, and irregularities in the reaction zone are stronger. That is mostly because the larger particles have a longer induction time for ignition and longer combustion time. Large particles due to the large content of volatiles cause nonuniformities in the volatiles concentration field, promoting the formation of hot spots in the reaction zone (Fig. 14.3). An increase in the initial content of oxygen widens the reaction

Table 14.1 Problem parameters list for Figs. 14.1–14.2

Parameter Description	Value	Unit
Grid points along OX	61	
Grid points along OR	41	
Number of model particles	5000	
Vessel dimension along the axis	1.18	m
Vessel radius	0.59	m
Initial pressure	$1.013 \cdot 10^5$	Pa
Initial temperature	300	K
Initial turbulent energy	50	J/kg
Initial turbulent rate of decay	100	J/(kg·s)
Mass concentration of O_2 in volatiles	0	
Mass concentration of H_2O in volatiles	0	
Mass concentration of CO_2 in volatiles	0.081	
Mass concentration of CO in volatiles	0.256	
Mass concentration of N_2 in volatiles	0.128	
Mass concentration of CH_4 in volatiles	0.438	
Mass concentration of H_2 in volatiles	0.097	
Mass concentration of NH_3 in volatiles	0	
Specific heat of condensed volatile component	1000	J/(kg·K)
Initial volume concentration of O_2	0.22	
Initial volume concentration of volatiles	0	
Initial volume concentration of H_2O	0	
Initial volume concentration of CO_2	0	
Initial volume concentration of CO	0	
Initial volume concentration of N_2	0.78	
Initial density of dust	0.22	kg/m^3
Initial density of each particle	1800	kg/m^3
Initial porosity (volumetric share of voids)	0.1	
Initial volumetric share of carbon in a particle	0.1	
Minimum diameter of particles	10^{-5}	m

Table 14.1 Problem parameters list for Figs. 1–2 (Continued)

| Parameter Description	Value	Unit
Medium diameter of particles	$5 \cdot 10^{-5}$	m
Maximum diameter of particles	$7 \cdot 10^{-5}$	m
Initial particles temperature	300	K
Volatiles oxidizing heat	$1.881 - 10^7$	J/kg
CO oxidizing heat	$2.23 \cdot 10^5$	J/mol
C oxidizing to CO heat	$1.105 \cdot 10^5$	J/mol
Volatiles extraction heat	$5 \cdot 10^5$	J/kg
Volatiles oxidizing rate: Arrhenius coefficient	$2 \cdot 10^5$	s^{-1}
Volatiles oxidizing rate: activation energy	$2 \cdot 10^4$	J/mol
Volatiles oxidizing rate: minimum temperature	400	K
$C + O \rightarrow CO_2$ forward rate: Arrhenius coefficient	$5.89 \cdot 10^6$	s^{-1}
$CO + O_2 \rightarrow CO_2$ forward rate: activation energy	$1.72 \cdot 10^4$	J/mol
$CO + O_2 \rightarrow CO_2$ forward rate: minimum temperature	400	K
$CO + O_2 \rightarrow CO_2$ reverse rate: Arrhenius coefficient	$2.75 \cdot 10^6$	s^{-1}
$CO + O_2 \rightarrow CO_2$ reverse rate: activation energy	$1.83 \cdot 10^5$	J/mol
$CO + O_2 \rightarrow CO_2$ reverse rate: minimum temperature	700	K
$C + O_2 \rightarrow CO$ rate: Arrhenius coefficient	10^{10}	$s^{-1}m^{-2}$
$C + O_2 \rightarrow CO_2$ rate: activation energy	$1.0775 \cdot 10^5$	J/mol
$C + O_2 \rightarrow CO$ rate: minimum temperature	500	K
$C + CO_2 \rightarrow CO$ rate: Arrhenius coefficient	10^{10}	$s^{-1}m^{-2}$
$C + CO_2 \rightarrow CO$ rate: activation energy	$1.9113 \cdot 10^5$	J/mol
$C + CO_2 \rightarrow CO$ rate: minimum temperature	500	K
Volatiles extraction rate: Arrhenius coefficient	$1.5 \cdot 10^4$	s^{-1}
Volatiles extraction rate: activation energy	$4.4 \cdot 10^4$	J/mol
Volatiles extraction rate: minimum temperature	380	K
Total ignition energy	3000	J
Ignition time	10^{-2}	s
Vertical position of the ignition point	0.59	m
Ignition spark inner radius	10^{-3}	m
Ignition spark outer radius	10^{-2}	m
Energy consumption factor for particles	0.8	

zone because heterogeneous combustion of particles continues after the gas-phase reaction has terminated.

The results show that the dynamics of the reaction zone in a turbulent flame can be traced by the evolution of the volatiles oxidation intensity field. Ignited in the ball-shaped volume, the turbulent flame expands as a relatively wide spherical layer containing strong nonuniformities of the reaction rate. Similar nonuniformities were also detected in the experiments by means of direct optical registration of the flame-ball dynamics [10]. Thus, the numerical results qualitatively reflect the influence of dust concentration nonuniformities that existed
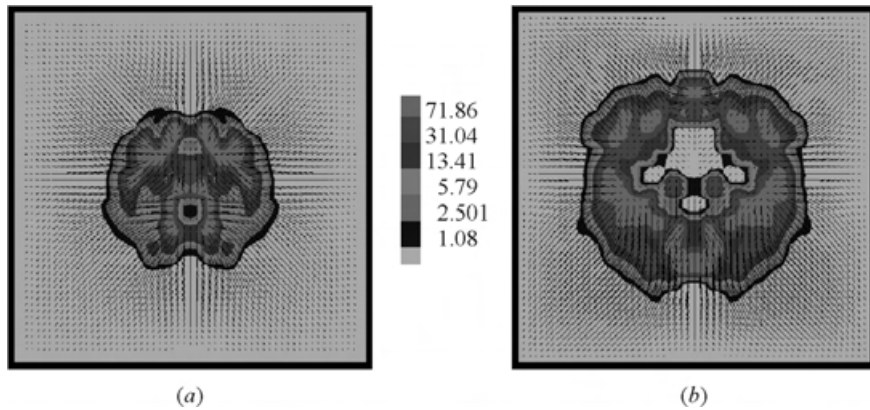
Figure 14.3 Flame intensity in a polydispersed particle suspension in oxygen: (*a*) $t = 34.8$ ms and (*b*) 41.8 ms
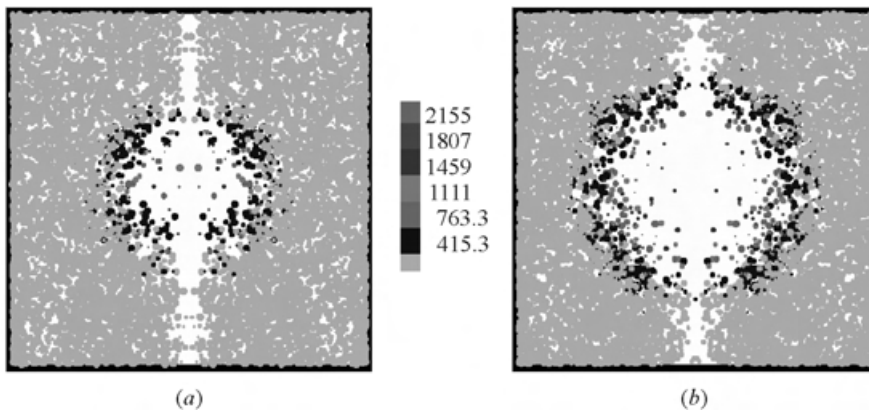
Figure 14.4 Particulate phase temperature in polydispersed particle suspension in oxygen: (*a*) $t = 34.8$ ms and (*b*) 41.8 ms

in the experiment. The width of the reaction zone increases with time and is thicker than that in combustion of homogeneous mixtures.

14.3.2 Numerical Model Validation

The model was validated by comparing the numerical results with experimental data for macroscopic characteristics: flame zone dynamics and pressure growth
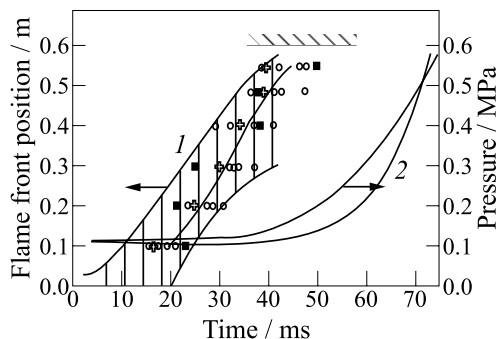
Figure 14.5 Comparison between experimental and theoretical results for turbulent flame front position and pressure–time line. Cornstarch with air at $\rho_{av} = 0.22$ kg/m^3

in a closed vessel. The validation was based on a set of experiments on ignition and combustion of dextrin–air mixtures [10] in a cylindrical 1.25 m^3 vessel.

The mean flame trajectory being a result of averaging is shown in Fig. 14.5 for a high initial level of turbulence (RMS = 9.7 m/s). The right axis of Fig. 14.5 reflects the pressure increase inside the vessel detected by a pressure gauge located on the wall. Arrows on the curves point the axis relating to the curve. Different symbols reflect the dynamics of flame forefront position for different directions from the center and different experiments. Those results reflect irregularity of the flame zone behavior. The solid curve presents the averaged trajectory of flame front expansion from the center.

The dashed zone in Fig. 14.5 presents the results of the numerical modeling of turbulent flame propagation for the same value of initial turbulence. The flame boundaries were detected along five central rays (in horizontal, vertical directions and 45° to the horizon) as points of maximum gradient of oxidizer on each ray. The dashed zone in Fig. 14.5 presents the flame trace being the result of averaging in those five directions. The dashed curves 1 bounding the dashed zone were obtained by estimating the position of the forefront and the rear front of the flame. The dashed curve 2 in Fig. 14.5 shows the growth of the mean wall pressure obtained as a result of averaging the ratio of pressure integral to the wall surface area.

Experimental results show the increase of the mean flame propagation velocity and the rate of pressure growth with the increase of the initial turbulization of the flow. The pressure growth is rather slow in the beginning when the flame occupies a relatively small central zone of the vessel but then it increases with the increase of the radius of the flame-ball. The increase of pressure continues after the leading flame front reaches the walls due to continuation of combustion and devolatilization of particles in a thick combustion zone. Theoretical results agree well with the experimental data. The theoretical curve 2 has a slight shift in time in comparison with the experimental one at $t < 65$ ms. It can be explained by different initiation conditions. The energy of ignition was probably released more rapidly in the experiments than it was assumed in numerical modeling. After $t > 60$ ms the theoretical curve grows faster than the experimental one, and

this could be due to the fact that the heat loss in the chamber was not accounted for in the calculations. Since the walls were assumed adiabatic in the numerical investigations, the resulting temperature in the chamber was higher than that obtained in the experiments. This led to higher values of pressure when the combustion process has developed within a significant portion of the chamber.

14.3.3 Influence of Governing Parameters on Flame Propagation and Ignition Dynamics

The numerical investigations of flame propagation in the initially turbulized mixture of air with dextrin particles were performed in [11] and compared with the available experimental data.

The initial conditions for all the experiments were nearly the same but for the initial turbulence and initial density of the particulate phase. It was shown that for the larger RMS values the combustion zone was wider and the flame propagated faster. Thus the increase of the initial level of the flow turbulization promotes the flame propagation in polydispersed mixtures due to the increase of the turbulent transport processes.

Now, let us consider the influence of the initial flow turbulization on the mixture ignition. The ignition energy was $E_0 = 3 \cdot 10^3$ J, the ignition time $t_0 = 10^{-2}$ s. The data on flame propagation velocities for different RMS values and particulate phase averaged density are given in Table 14.2. Table 14.2 shows that the increase of dust share and initial turbulization of the flow promotes the flame propagation. But near the ignition limits the increase of the turbulence inhibits the ignition.

To understand the mechanisms leading to such a phenomenon one needs to investigate in detail the radiative ignition dynamics. The peculiarity of the radiative ignition of the air–dust mixtures is the following. At the first stage, the ignition energy is mostly consumed by the particles; chemical reaction starts on their surface and then gas is gradually heated and gas chemistry proceeds, switching on the convective-conductive flame propagation mechanisms. If the initiation energy is sufficient, the propagating flame zone originates as shown in Figs. 14.1–14.3. Near the limit conditions, a long delay time is necessary for the ignited particles to burn out and heat the gas and then the flame starts its propagation. Below the limit conditions, the particles ignited by the igniter burn out but do not initiate essential combustion in the gas phase due to rapid diffusion of energy. Thus, high temperature and the surface chemistry are maintained for some time in the ignition zone after switching off the igniter, and then the reaction extinguishes.

For high levels of turbulence, the heat delivered to the gas phase from the ignited particles diffuses very rapidly due to high rates of turbulent transport in

Table 14.2 Predicted flame propagation velocities at different RMS velocities and particulate phase-averaged densities

RMS m/s	ρ_{av} kg/m^3	Flame propagation velocity, m/s
	0.35	8.5
10	0.22	6.5
	0.13	No ignition
	0.35	5.7
1.4	0.22	5.0
	0.13	3.5

the gas. The necessary heating of gas sufficient to launch the gas chemistry does not occur and combustion extinguishes some time after switching off the igniter.

To investigate the influence of the ignition conditions (the energy E_0 and duration t_0) a set of numerical calculations for the case of low-limit dust concentrations was performed. All the parameters of the air–dust mixtures were maintained constant. The variable parameters were E_0, t_0, and the RMS value. The ignition was assumed to take place if the flame propagated in self-sustaining mode after switching off the igniter. The results are shown in Table 14.3. The dust content was assumed to be $\rho_{av} = 0.13$ kg/m^3 for all the calculations.

The results show that the increase of the ignition energy and the decrease of the duration promote the ignition.

The increase of the initial turbulence creates less favorable conditions for the ignition for all the values of the ignition energy and time (E_0 and t_0).

The domain of parameters wherein the ignition takes place and the domain wherein the ignition does not occur are separated by the zone of parameters corresponding to "slow ignition." The introduced notation "slow ignition" denotes the process wherein the combustion does not start simultaneously on ignition but there exists a relatively long period after switching off the igniter when the flame zone does not propagate and the mean temperature in the ignited zone is $T \approx 1000$ K. The chemical reactions proceed relatively slow. Then temperature increases very quickly up to $T \approx 2000$ K and self-sustaining flame propagation starts.

The results shown in Table 14.3 explain the situation with the absence of ignition in one of the cases regarded in Table 14.2. Under ignition conditions No. 3 (Table 14.3) the mixture was not ignited. But this result does not mean that the mixture could not be ignited. Under ignition conditions No. 1, the same

Table 14.3 Predicted ignition performance of the air–dust mixture with the dust content $\rho_{av} = 0.13$ kg/m^3

No.	1	2	3	4
E_0 (kJ)	10	3	3	1
t_0 (ms)	1	1	10	10
RMS = 1.4 m/s	Yes	Yes	Slow ignition	No
RMS = 10 m/s	Yes	Slow ignition	No	No

Table 14.4 Predicted ignition performance of the oxygen–dust mixtures

E_0 (kJ)	3	2	1.6	1.5	1.45	1.25	1
Ignition	Yes	Yes	Slow ignition	No	No	No	No

mixture is ignited and comes to a self-sustaining flame propagation with the characteristic velocity of 4.8 m/s.

The next series of numerical experiments was performed for the oxygen–dust mixtures with the values of governing parameters taken from Table 14.1. The dust concentration, initial turbulization, and the ignition duration were maintained constant: $\rho_{av} = 0.21$ kg/m^3, RMS = 1.4 m/s, $t_0 = 10^{-2}$ s. The results are shown in Table 14.4*. It is seen that the increase of oxygen fraction in the oxidizer promotes the ignition and reduces the necessary ignition energy.

14.4   CONCLUDING REMARKS

Physical and numerical models are created describing the dynamics of turbulent combustion in heterogeneous mixtures of gas with polydispersed particles. The models take into account the thermal destruction of particles, chemistry in the gas phase, and heterogeneous oxidation on the surface influenced by both diffusive and kinetic factors. The models are validated against independent experiments and enable the determination of peculiarities of turbulent combustion of polydispersed mixtures.

The developed mathematical model is used for numerical investigation of the sensitivity of the polydispersed mixture initiation limits to the variations of the governing parameters. The combustion zone in heterogeneous mixtures is shown to be very wide having an irregular structure with a number of hot spots. Its propagation velocity strongly depends on initial turbulence, particles size distribution, and concentration of oxygen in gas. The increase of particles size and oxygen concentration brings an increase of the reaction zone width and irregularity. The increase of the initial level of turbulence promotes the flame propagation but inhibits ignition near the limits. The decrease of the mean concentration of the dispersed phase lowers the flame propagation velocity and creates less favorable ignition conditions near the limits.

The preliminary results obtained show that the initiation limits for polydispersed mixtures and stability of flame propagation strongly depend on inhomogeneity of particles (droplets) concentration distribution typical for the majority of practical cases wherein the ignition and combustion of polydispersed mixtures take place. Thus to ensure stable ignition and combustion characteristics

---

*Reported values of ignition energies seem to be too overestimated (*Editor's remark*).

in technical propulsion systems, further development of modeling and experimentation is necessary, especially for polydispersed mixtures with nonuniform condensed-phase distribution.

ACKNOWLEDGMENTS

REFERENCES

1. Eckoff, R. K. 1994. Prevention and mitigation of dust explosions in process industries — a survey of recent research and development. *6th Colloquium (International) on Dust Explosions Proceedings*. Shenyang. 5–34.
2. Launder, B. E., and D. B. Spalding. 1972. *Mathematical models of turbulence*. New York: Academic Press.
3. Kuhl, A. L., R. E. Ferguson, K. Y. Chien, J. P. Collins, and A. K. Oppenheim. 1995. Gasdynamic model of turbulent combustion in an explosion. *Combustion, Detonation, Shock Waves. Zel'dovich Memorial Proceedings*. Eds. A. G. Merzhanov and S. M. Frolov. Moscow: ENAS Publ. 1:181–89.
4. Nikitin, V. F., N. N. Smirnov, V. R. Dushin, and N. I. Zverev. 1994. Numerical simulation of particle's evolution in turbulent stratified flows. *6th Colloquium (International) on Dust Explosions Proceedings*. Shenyang. 61–70.
5. Pironneau, O., and B. Mohammadi. 1994. *Analysis of the k–ε turbulence model*. Paris: Mason Editeur.
6. Smirnov, N. N., V. F. Nikitin, J. Klammer, R. Klemens, P. Wolanski, and J. C. Legros. 1996. Dust–air mixtures evolution and combustion in confined and turbulent flows. *7th Colloquium (International) on Dust Explosions Proceedings*. Bergen, Norway. 552–66.
7. Smirnov, N. N., V. F. Nikitin, and J. C. Legros. 1997. Turbulent combustion of multiphase gas–particles mixtures. In: *Advanced computation & analysis of combustion*. Eds. G. D. Roy, S. M. Frolov, and P. Givi. Moscow: ENAS Publ. 136–60.
8. Smirnov, N. N., and N. I. Zverev. 1992. *Heterogeneous combustion*. Moscow: Moscow University Publ.
9. Oran, E. S., and J. P. Boris. 1987. *Numerical simulation of reactive flow*. New York: Elsevier.
10. Gieras, M., R. Klemens, and P. Wolanski. 1996. Evaluation of turbulent burning velocity for dust mixtures. *7th Colloquium (International) on Dust Explosions Proceedings*. Bergen, Norway. 535–51.
11. Smirnov, N. N., V. F. Nikitin, J. Klammer, R. Klemens, P. Wolanski, and J. C. Legros. 1997. Turbulent combustion of air-dispersed mixtures: Experimental and theoretical modeling. *Experimental Heat Transfer, Fluid Mechanics Thermodynamics* 4:2517–24.

Chapter 15

TURBULENT COMBUSTION REGIME CHARACTERISTIC OF A TAYLOR–COUETTE BURNER

R. C. Aldredge, III

The first experimental measurements of turbulent flame speeds in gaseous reactants using a cylindrical Taylor–Couette burner have been made. A decreasing sensitivity of the turbulent flame speed to increases in turbulence intensity is found to occur beyond turbulence intensities of approximately 2.5 times the laminar flame speed. It is determined using dimensional analysis that this observed behavior is a result of a transition to a nonflamelet combustion regime where flame propagation is influenced by both small-scale flame-structure modification and large-scale flame-front wrinkling. It is also found that chemical heat release enhances turbulent combustion, giving rise to increased flame propagation rates. Results are compared both with those obtained by earlier investigators using other experimental apparatuses and theoretical predictions.

15.1 NOMENCLATURE

D_k Damköhler number characterizing Kolmogorov-scale fluctuations
D_l Damköhler number characterizing large-scale fluctuations
I integral length scale
Pe   Peclet number
Pr   Prandtl number
R_l turbulence Reynolds number
u' turbulence intensity
U_L laminar flame speed

Greek Symbols
α thermal diffusivity of the reactive mixture at 298° and 1 atm
δ laminar flame thickness
ϵ ratio of laminar flame thickness to turbulence integral scale
ϕ equivalence ratio

Subscripts
T turbulence

15.2 INTRODUCTION

A variety of combustion configurations have been employed by previous investigators in studies of turbulent burning velocities of premixed flames. These include (1) rod-stabilized v-flames; (2) tube-stabilized conical flames; (3) stagnation-flow stabilized flames [1]; (4) weak-swirl stabilized flames [2]; and (5) fan-stirred chambers [3]. All of these configurations suffer to varying degrees from turbulence that is inhomogeneous, unsteady, or subject to significant mean flow velocity or mean strain.

In contrast, most models of turbulent flame speeds assume homogeneous isotropic turbulence with no mean flow or strain. This leads to substantial differences between model predictions and experimental observations [4].

For example, in configuration (1), the vertex of a v-shaped flame is attached to a round rod positioned at the exit of a nozzle. Although the flame brush on either side of the rod is relatively planar, the turbulence length scales and turbulent flame structure both vary with the distance away from the rod. In configuration (2), the turbulent flame can be stabilized over a wide range of turbulence intensities with the use of a pilot flame, and if the tube diameter is large enough (e.g., 50 mm) a uniform profile of turbulence intensity may be achieved; however, a disadvantage is that the structure of the turbulent flame is not uniform along the length of the flame brush.

Although a nearly planar premixed turbulent flame is maintained in the stagnation-flow burning configuration (3), the divergence of flow-field streamlines results in mean strain rates which also modify the turbulent flame structure and burning rates.

In configuration (4) a turbulent premixed flame is stabilized at the exit of a tube by a pressure gradient along the direction of mean flame propagation, induced by transverse swirl, but again the turbulence is inhomogeneous and there is appreciable mean flow.

The constant-volume fan-stirred combustion chamber used by Abdel-Gayed *et al.* [3], configuration (5), offers an advantage of high-turbulence intensities while having negligible mean flow velocities. The disadvantage is that in the early stages of propagation the flame kernel is small compared to the turbulence

integral length scale and therefore develops unsteadily, whereas later in the latter stages thermal expansion in the constant-volume chamber leads to unsteady and nonuniform mean reactant temperature and pressure.

Recently Ronney *et al.* [5] employed turbulent Taylor–Couette (TC) flow to study freely propagating nearly isothermal aqueous chemical fronts. As discussed by Ronney *et al.* [5] and Aldredge [6], the TC flow offers several key advantages over burning configurations (1–5) discussed above, including: (*a*) turbulence characteristics that are statistically steady upstream of the flame and uniform over most of the flame surface area; (*b*) turbulence intensities that are independent of the mean flow speed along the direction of flame propagation; (*c*) the mean strain rate, which is known to affect burning velocities and extinction conditions of turbulent flames [7], is zero over most of the annulus width; (*d*) capability to generate either large-scale, low-intensity, or small-scale high-intensity turbulence, depending on the Reynolds numbers of the inner and outer cylinders; and (*e*) independent control of heat loss and buoyancy influences on flame propagation by appropriate selection of the cylinder Reynolds numbers and the annulus gap width.

The focus of the present work is the extension of the isothermal-front experiments of Ronney *et al.* [5] to measurements of turbulent flame speeds in exothermic hydrocarbon–air mixtures, as originally proposed by Aldredge [6]. Of course, a number of differences are expected. In particular, the presence of thermal expansion in the gaseous flames may lead to wrinkling induced by flame instabilities not present in the aqueous systems [8]. Also, some differences will occur because, as discussed by Ronney [4], the aqueous systems are nearly isothermal and not influenced by heat losses, whereas it is well known that gaseous flames are strongly influenced by these losses. Furthermore, since the laminar "burning velocities" of the autocatalytic reactions are smaller than those of hydrocarbon–air mixtures by a factor of 10^{-4} to 10^{-5}, much higher turbulence intensities are required in the gaseous combustion system to achieve moderate-to-high turbulence intensities relative to the laminar front speed (although the Reynolds numbers in the two systems will be comparable). Even though turbulence intensities up to 500 times the local laminar front propagation speed were achievable in the constant-density TC experiments of Ronney *et al.* [5], lower turbulence intensities, below 20 times the local front speed, were precluded by viscous dissipation. The present study provides new data for this lower range of moderate-to-high intensities for turbulent flame propagation with heat release.

In an earlier phase of this work [9] the intensities of axial and circumferential components of velocity fluctuation were measured in the TC annulus, using Laser Doppler Velocimetry (LDV), for a wide range of cylinder rotation speeds. On average, the intensities of axial velocity fluctuations were found to be within 25% of the intensities of circumferential velocity fluctuations [9]. As in Ronney *et al.* [5], turbulence intensities were found to be nearly homogeneous along the axial direction and over most of the annulus width, and to be linearly proportional

to the average cylinder speed. The integral scale of turbulence l was found to be essentially equal to half the cylinder gap, i.e., $l = d/2$. Moreover, the mean circumferential flow velocity and the mean strain rates were shown to be nearly zero across the entire cylinder gap except very near the walls, where no-slip conditions must apply. In this sense the TC flow in the Reynolds-number regimes studied here can be thought of as high-Reynolds-number channel flow with zero mean flow and the two walls moving in opposite directions.

15.3   EXPERIMENTAL APPROACH
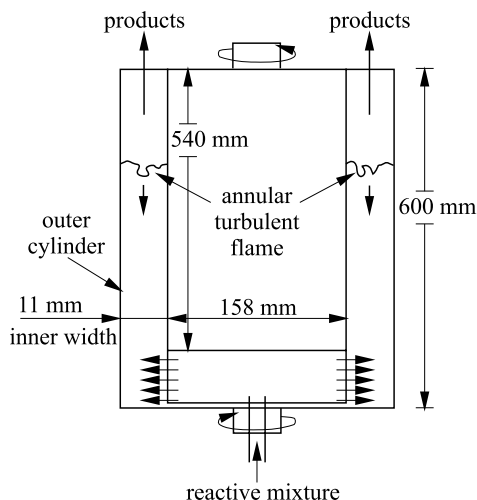
Figure   15.1   Schematic diagram of the Taylor–Couette apparatus used for studies of turbulent flame propagation

A schematic of the TC apparatus employed with rounded numerical dimensions is shown in Fig. 15.1. It consists of two concentric cylinders which can be rotated independently in either direction at up to 3450 revolutions per minute. The inner cylinder is made of aluminum and has an outer-surface radius of 79 mm, while the outer cylinder is of Pyrex construction to allow optical access into the TC annulus and has an inner-surface radius of 90 mm. Each cylinder has a length of 600 mm, giving an aspect ratio (of cylinder length to annulus width) of 55, consistent with that attained in earlier investigations [5, 10] and large enough to minimize cylinder-end effects. The annulus of width 11 mm is sealed at the bottom of the apparatus and open to the atmosphere at the top. A more detailed description of the experimental facility, including the LDV configuration, is given in Vaezi *et al.* [9].

The methane–air mixtures were introduced into the annulus through 900 holes at the bottom of the inner cylinder, each 2 mm in diameter. After allowing at least 2.5 annulus volumes of gas to pass through the apparatus, the mixtures were then ignited at the top of the annulus causing a flame to propagate downward until all of the reactants were consumed. Since the hole diameter is smaller than the quenching distance, the flame does not propagate into the supply line. By igniting the mixture at the open end of the tube, the effects of thermal ex-

pansion are minimized because the flame front is not being pushed ahead by an expanding slab of hot products as it would if the flame were propagating from the closed end of the tube towards the open end. For the same reason, studies of flammability limits in tubes [11] employ the same strategy. A video camera is used to record the downward progression of the flame at 30 frames per second. The turbulent flame speed is calculated from this video record; the turbulent flame speed (the speed of the flame brush relative to the upstream reactant flow) is obtained by adding the mean upward speed of the reactants, maintained at 5 cm/s in all cases, to the downward rate of flame propagation measured in the laboratory frame of reference. This upward reactant speed of 5 cm/s is small compared to the turbulence intensities and flame propagation speeds characteristic of the experiments and therefore is considered to have a negligible effect on the results. Higher values than this make calculation of the reactant equivalence ratio less accurate as a result of a pressure increase in the rotometers, while lower values make the establishment of a completely annular flame ring more difficult when the cylinders are not rotating. It should be noted also that the Reynolds number based on the annulus gap and the axial mean flow velocity is only 37 and is much lower than that based on the cylinder wall velocities.

Reynolds numbers Re_i and Re_o are defined for the inner and outer cylinders, respectively, and are based on the annulus width d and on the tangential velocity of the inner and outer cylinders. Hence, $\mathrm{Re}_i \equiv \Omega_i r_i d/\nu$, and $\mathrm{Re}_o \equiv \Omega_o r_o d/\nu$, where Ω_i and Ω_o are the angular rotation rates and r_i and r_o are the radii of the inner and outer cylinders, respectively; ν is the kinematic viscosity of the reactive mixture. The onset of fully developed turbulence in the TC apparatus occurs when $\mathrm{Re}_i > 50,000$ if the outer cylinder is fixed [12]. However, if the outer cylinder is rotated in the direction opposite to that of the inner cylinder, a significantly lower minimum Reynolds number of approximately 1000 defines the fully developed turbulence regime [10]. In this case, Re_o and Re_i must be of the same order of magnitude, with the magnitude of the ratio $\mathrm{Re}_o/\mathrm{Re}_i$ being larger than unity. If the magnitude of this ratio is too small then steady Taylor vortices are present, while if it is too large then steady laminar Couette flow exists [13]. As in Ronney *et al.* [5], for all of the present experiments $\mathrm{Re}_o/\mathrm{Re}_i = -1.4$ was maintained, as this value accesses the *featureless turbulence* regime of the TC flow identified by Andereck *et al.* [10].

15.4 RESULTS

In Fig. 15.2 the average relative flame position in the TC apparatus, measured from the top of the TC annulus, is plotted vs. time (measured from the time of ignition) for the equivalence ratio $\phi = 1.1$ and average Reynolds number $\mathrm{Re}_{ave} = 7500$. The square (diamond) symbols represent the location of the left (right) side of the annular flame, relative to the fixed location of the observer,
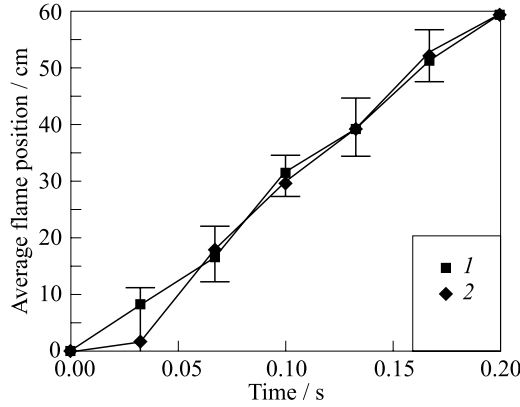
Figure 15.2 The ensemble-averaged absolute flame position in the TC apparatus, measured from the top of the TC annulus, plotted vs. absolute time (measured from the time of ignition) for $\phi = 1.1$ and $\text{Re}_{ave} = 7500$: *1* — left; *2* — right

and close proximity of these two symbols to each other at a given time indicates a statistically planar annular flame. The average flame position is based on a minimum of six measurements of the flame position under identical parametric conditions at each of the fixed time intervals indicated in the figure. A short time after ignition the flame becomes statistically planar and propagates downward at a steady rate. This is the case for the other values of ϕ and Re_{ave} considered ($0.8 \leq \phi \leq 1.5$ and $0 \leq \text{Re}_{ave} \leq 10{,}500$) as well.

The turbulent flame speed U_T is calculated by determining the rate of increase of the average relative flame position with respect to time (obtained, for example, from Fig. 15.2), over the range of time where a statistically steady flame exists, and then adding the upward mean reactant speed of 5 cm/s. In Fig. 15.3, U_T is plotted vs. the turbulence intensity u', the square root of the ensemble-averaged total turbulence kinetic energy of axial and circumferential velocity fluctuations. The turbulent flame speed generally increases with increasing u' (for fixed values of ϕ), as expected, with the highest turbulent flame speeds obtained for stoichiometric and slightly rich mixtures ($1 \leq \phi \leq 1.3$).

In Fig. 15.4, the measured turbulent flame speeds, normalized with mixture-specific laminar flame velocities obtained recently by Vagelopoulos *et al.* [14], are compared with experimental and theoretical results obtained in earlier studies. Also shown in the figure are the measurements made by Abdel–Gayed *et al.* [3] for methane–air mixtures with $\phi = 0.9$ and $\phi = 1$; a correlation of measured turbulent flame speeds with intensity obtained by Cheng and Shepherd [1] for rod-stabilized v-flames, tube-stabilized conical flames, and stagnation-flow stabilized flames, $U_T/U_L = 1 + 3.2(u'/U_L)$; a correlation of measured turbulent flame
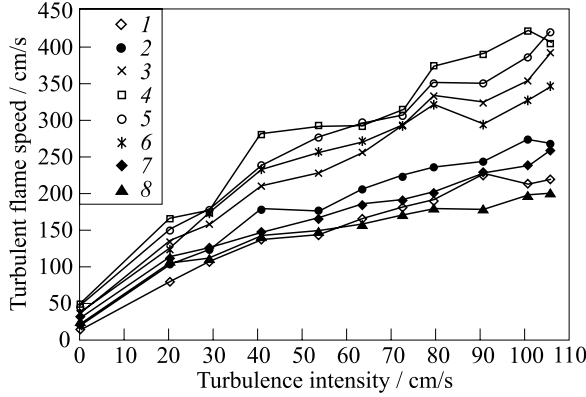
Figure 15.3 Measured turbulent flame speeds plotted vs. measured turbulence intensities for fixed equivalence ratios from 0.8 to 1.5: *1 — $\phi = 0.8$, 2 — 0.9, 3 — 1.0, 4 — 1.1, 5 — 1.2, 6 — 1.3, 7 — 1.4, and 8 — 1.5*

speeds with intensity obtained by Bedat and Cheng [2] for weak-swirl stabilized flames, $U_T/U_L = 1 + 2.5(u'/U_L)$; theoretical PDF-based predictions by Anand and Pope [15]; and a prediction by Yakhot [16] obtained using renormalization group theory.

Many models of the relationship between U_T/U_L and u'/U_L appear in the literature; some recent ones are summarized by Ronney [4]. Of those models which include the effects of thermal expansion, the one that most nearly matches the present experimental data is the PDF-based prediction of Anand and Pope [15]. This model has been heuristically modified in Fig. 15.4 to read $U_T/U_L = 1 + c(u'/U_L)$ to obtain the proper behavior $U_T/U_L \rightarrow 1$ in the limit $4u'/U_L \rightarrow 0$. The parameter c increases from a value of 1.5, for flames with large heat release (where the ratio of burnt- and unburnt-gas temperatures is at least 4), to a value of 2.1 for flames with no heat release. Ronney *et al.* [5], who studied the propagation rates of constant-density aqueous chemical fronts in the same type of TC flow as employed in this work, found that the relation $U_T/U_L = \exp((u'/U_T)^2)$ obtained by Yakhot [16] for constant-density flow using renormalization group theory agreed well with their results obtained for u'/U_L above 20. Other constant-density experiments by Ronney *et al.* [5] in high-intensity capillary-wave turbulence and by Shy *et al.* [17] in vibrating-grid turbulence also agreed with Yakhot's result. However, Yakhot's prediction is seen in Fig. 15.4 to lie well below the predictions of Anand and Pope [15]. While Anand and Pope's model predicts U_T/U_L to decrease with increasing heat release, for fixed u'/U_L, the opposite is suggested by both the agreement between Yakhot's constant-density model and earlier constant-density experiments, and
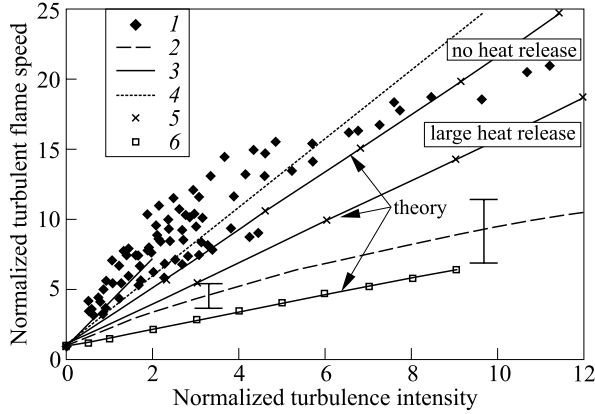
Figure 15.4 A comparison of turbulent flame speeds measured in the TC apparatus with theoretical predictions and measurements by earlier investigators using other types of burners: *1* — TC results, *2* — Abdel-Gayed *et al.* [3], *3* — Chang and Shepherd [1], *4* — Bedat and Cheng [2], *5* — Anand and Pope [15], and *6* — Yakhot [16]

a comparison of Yakhot's prediction with the present TC results for flame propagation with heat release. Theoretical models by Bray [18] and Cambray and Joulin [19], on the other hand, do predict enhancement of the normalized turbulent flame speed with increasing heat release. Thus, to our knowledge, there is still no model of premixed turbulent combustion which can accurately model experimental flame propagation rates in both the zero and large thermal-expansion limits, even for a relatively simple turbulent flow field such as that which the TC apparatus provides.

Figure 15.4 shows good agreement of the present normalized turbulent flame speeds with those of Cheng and Shepherd [1] over the low range of u'/U_L for which their correlation is valid. There is also good qualitative agreement between the present results and those of Bedat and Cheng [2] for u'/U_L up to about 4, beyond which the *bending effect* exhibited in the present data becomes significant. The normalized turbulent flame speeds obtained by Abdel-Gayed *et al.* [3] are significantly lower than those measured in the authors' TC apparatus. This might be expected, because in the constant-volume chamber they used the unsteady increases in reactant temperature and pressure during flame propagation which may result in substantial damping of turbulent velocity fluctuations and an increase in the speed of the laminar flame and its ability to resist turbulent wrinkling. In fact, values of U_L measured in their apparatus, which they used for normalizing U_T, were 42 cm/s for $\phi = 0.9$ and 51 cm/s for $\phi = 1$, considerably higher than the more recent laminar flame speed measurements of Vagelopou-

los *et al.* [14] at the same equivalence ratios, of approximately 32 and 38 cm/s, respectively.

15.5   COMBUSTION REGIMES

In order to identify the regimes of turbulent combustion characterizing flame propagation in the TC apparatus the Damköhler number D_l, characterizing the largest turbulence time scales relative to the characteristic chemical reaction time of the methane–air mixture, is plotted vs. the turbulence Reynolds number R_l in Fig. 15.5, following Liñán and Williams [20]. With $D_l \equiv (l/u')/(\delta/U_L)$ and R_l defined above, it can be shown that $D_l = (Pe^2/4Pr)R_l^{-1}$, where $Pr \equiv \nu/\alpha$ is the Prandtl number, $Pe \equiv U_L/d/\alpha$ is the Peclet number, and δ is the flame thickness, estimated as α/U_L. In the logarithmic coordinates of Fig. 15.5 the relation between D_l and R_l is represented by a straight line having a slope equal to -1 and bounded by $70 \le R_l \le 375$ (the range of turbulence Reynolds numbers considered in the present experiments). The height of this straight line increases with increasing Pe which ranges from 50 to about 200 for the laminar flame speeds obtained by Vagelopoulos *et al.* [14] plotted in Fig. 15.3. Values of the turbulent combustion parameters characterizing the present experiments therefore lie within the trapezoid shown in Fig. 15.5, the boundaries of which are determined by the ranges $70 \le R_l \le 375$ and $50 \le Pe \le 200$ which were considered and the assumption $Pr = 0.7$.
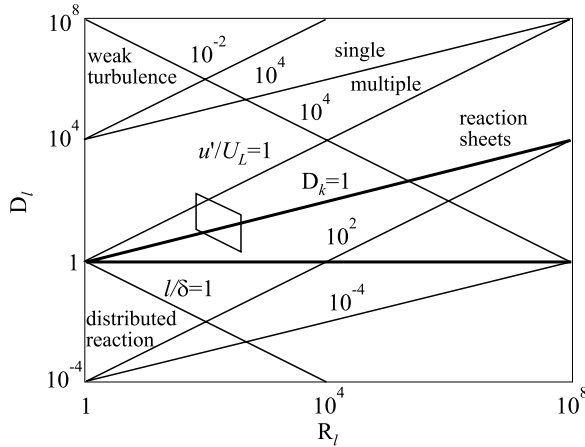
Figure 15.5 A Damköhler–Reynolds number plot revealing the turbulent combustion regimes characterizing flame propagation in the TC apparatus, identified by the region enclosed by the parallelogram

Also plotted in Fig. 15.5 are the ratios l/δ and u'/U_L, and the Damköhler number D_k based on the smallest turbulence time scale, associated with fluctuations on the Kolmogorov length scale, obtained from the relation $D_k = (Pe^2/4Pr)R_l^{-3/2}$. Parameter values in regions above (below) the line $D_k = 1$ ($D_l = 1$) in Fig. 15.5 characterize a flow having turbulence length and time scales which are all larger (smaller) than the laminar flame thickness and chemical reaction time, respectively. For turbulent combustion parameters in regions between the two lines $D_k = 1$ and $D_l = 1$ the largest (smallest) turbulence length and time scales are larger (smaller) than the laminar flame thickness and chemical reaction time, respectively. This assertion is consistent with theoretical work by Ronney and Yakhot [21] which predicted that at sufficiently low D_k (which is inversely proportional to the Karlovitz number they employed) flame-structure modification by small-scale turbulence causes U_T/U_L to decrease below the Huygens propagation speed (i.e., the value of U_T/U_L in the limit $D_k \to \infty$), for fixed values of u'/U_L. It can be shown that $u'/U_L = (Pr \cdot Pe/2)^{1/3}$ when $D'_k = 1$. Since the smallest value of Pe is 50 (based on velocities plotted in Fig. 15.3), this means that turbulent flame propagation in the TC apparatus is likely influenced to some extent by small-scale flame-structure modification when u'/U_L is above about 2.5. Indeed, examination of Fig. 15.4 reveals that the *bending effect* observed in the present data begins at u'/U_L approximately equal to 2.5.

When Pe is less than about 46, heat loss effects on $U_{L,TC}$ may be appreciable. If an analogy is made with turbulent flames using a turbulence Peclet number defined by $Pe_T \equiv U_T d/\alpha_T$, where $\alpha_T \approx 0.058 Re_i \nu$ [21, 22], it is readily shown that Pe_T is substantially above 46 for all of the present turbulent flame experiments. The influence of heat loss is therefore not likely a contributor to the *bending effect* exhibited in Fig. 15.4.

15.6 CONCLUDING REMARKS

The first measurements of flame speeds in turbulent, exothermic TC flow have been obtained and comparisons of these measurements with experimental and theoretical results from earlier studies have been made. Good agreement of present results with those of Cheng and Shepherd [1] and Bedat and Cheng [2] is found for u'/U_L up to about 4, beyond which the *bending effect* exhibited in the data becomes significant.

Direct comparison with earlier measurements by Ronney *et al.* [5] of turbulent front propagation in constant-density TC flow was not possible because the lowest normalized turbulence intensities they considered are twice as large as the highest values achieved in the present study. However, good agreement of their results for constant-density front propagation in high-intensity turbulence with the constant-density theoretical model of Yakhot [16], and a comparison

of present results for flame propagation with heat release with Yakhot's model, in Fig. 15.4, suggest that heat release enhances turbulent flame propagation. This conclusion, corroborated by theoretical models by Cambray and Joulin [19] and Bray [18], however, is inconsistent with the model of Anand and Pope [15] which predicts U_T/U_L to decrease with increasing heat release, for fixed values of u'/U_L. There is therefore still no model of premixed turbulent combustion to our knowledge which can accurately model experimental flame propagation speeds in both the zero and large thermal-expansion limits, even for a relatively simple turbulent flow field such as that which the TC apparatus provides.

In a log–log plot of turbulent combustion parameters using Damköhler and Reynolds coordinates (Fig. 15.5), following Liñán and Williams [20], regimes characterizing the present turbulent combustion experiments were identified. For the lower turbulence intensities considered, flame propagation is governed by large-scale flame front wrinkling by eddies having long lifetimes relative to the laminar flame thickness and chemical reaction time, respectively. For values of u'/U_L above about 2.5, however, dimensional analysis predicts that turbulent flame propagation in the TC apparatus is likely influenced, to some extent, by small-scale flame-structure modification. Graphical examination of the present results in Fig. 15.4 corroborates this prediction, revealing that the *bending effect* observed in the data begins when u'/U_L is about 2.5. This assertion is consistent with theoretical work by Ronney and Yakhot [21] which predicted that at sufficiently low D_k flame structure modification by small-scale turbulence causes U_T/U_L to decrease below the Huygens propagation speed for fixed values of u'/U_L.

ACKNOWLEDGMENTS

REFERENCES

1. Cheng, R. K., and I. C. Shepherd. 1991. The influence of burner geometry on premixed turbulent flame propagation. *Combustion Flame* 85:7–26.
2. Bedat, B., and R. K. Cheng. 1995. Experimental study of premixed flames in intense isotropic turbulence. *Combustion Flame* 100:485–94.
3. Abdel-Gayed, R. G., K. J. AI-Khishali, D. Bradley, and M. Laws. 1984. Turbulent burning velocities and flame straining in explosions. *Proc. Royal Society London A* 391:393–414.

4. Ronney, P. D. 1995. Some open issues in premixed turbulent combustion. In: *Modeling in combustion science*. Eds. J. D. Buckmaster and T. Takeno. Lecture Notes in Physics. Berlin: Springer-Verlag 449:3–22.

5. Ronney, P. D., B. D. Haslam, and N. O. Rhys. 1995. Front propagation rates in randomly stirred media. *Phys. Rev. Letters* 74:3804.

6. Aldredge, R. G. 1996. A novel flow reactor for the study of heat-loss effects on turbulent flame propagation. *International Communications Heat Mass Transfer* 22:1173–79.

7. Kostiuk, L. W., K. N. C. Bray, and T. C. Chew. 1989. Premixed turbulent combustion in counterflowing streams. *Combustion Science Technology* 64:233–41.

8. Aldredge, R. C., and F. A. Williams. 1991. Influence of wrinkled premixed-flame dynamics on large-scale, low-intensity turbulent flow. *J. Fluid Mechanics* 228:487–511.

9. Vaezi, V., E. S. Oh, and R. C. Aldredge. 1997. High-intensity turbulence measurements in a Taylor–Couette flow reactor. *J. Experimental Thermal Fluid Science* 15:424–31.

10. Andereck, C. D., S. S. Liu, and H. L. Swinney. 1986. Flow regimes in a circular Couette system with independently rotating cylinders. *J. Fluid Mechanics* 164:155–83.

11. Coward, H. F., and G. W. Jones. 1953. Limits of flammability of gases and vapors. U.S. Bur. Mines Bull. No. 503.

12. Smith, G. P., and A. A. Townsend. 1982. Turbulent Couette flow between concentric cylinders at large Taylor numbers. *J. Fluid Mechanics* 123:187–217.

13. Golub, J. P., and H. L. Swinney. 1975. Onset of turbulence in a rotating fluid. *Physical Review Letters* 35:927.

14. Vagelopoulos, C. M., F. N. Egolfopoulos, and C. K. Law. 1994. Further considerations on the determination of laminar flame speeds with the counterflow twin-flame technique. *25th Symposium (International) on Combustion Proceedings*. Pittsburgh, PA: The Combustion Institute. 1341–47.

15. Anand, M. S., and S. B. Pope. 1987. Calculations of premixed turbulent flames by PDF methods. *Combustion Flame* 67:127–42.

16. Yakhot, V. 1988. Propagation velocity of premixed turbulent flames. *Combustion Science Technology* 60:191–214.

17. Shy, S. S., R. H. Jang, and P. D. Ronney. 1996. Laboratory simulation of flamelet and distributed models for premixed turbulent combustion using aqueous autocatalytic reactions. *Combustion Science Technology* 113:329–50.

18. Bray, K. N. C. 1990. Studies of the turbulent burning velocity. *Proc. Royal Society London A* 431:315–35.

19. Cambray, P., and G. Joulin. 1992. On moderately-forced premixed flames. *24th Symposium (International) on Combustion Proceedings*. Pittsburgh, PA: The Combustion Institute. 61–67.

20. Liñán, A., and F. A. Williams. 1993. *Fundamental aspects of combustion*. New York: Oxford University Press.

21. Ronney, P. D., and V. Yakhot. 1992. Flame broadening effects on premixed turbulent flame speed. *Combustion Science Technology* 86:31–43.

22. Yakhot, V., and S. A. Orzag. 1986. *Physical Review Letters* 57:1722.

Chapter 16

SPRAY FLAME CHARACTERISTICS WITH STEAM-ASSISTED ATOMIZATION

A. K. Gupta, M. Megerle, S. R. Charangudia,
and C. Presser

Atomization of kerosene with steam as the atomization fluid is shown to be finer than with air, using a commercially available air-assist atomizer. Data on droplet size, and velocity, were obtained using a phase Doppler interferometer. The higher viscosity of steam, as compared to air, results in finer atomization of fuel. Enhanced vaporization of liquid fuel from the enthalpy of the steam in gas-assisted spray flames, as well as the decrease of fuel viscosity by heating-up the fuel nozzle, is believed to result in smaller droplet sizes as compared to the same atomizer operated with air. The effect of steam enthalpy is simulated by preheating the atomization air to higher temperatures. Near the nozzle exit, enhanced vaporization of the fuel with preheated air is found to be similar to that of steam. Steam is miscible with kerosene so that the droplets contain two liquids with widely different boiling points. It is conjectured that the presence of these widely different boiling-point liquids within the droplet may assist in the further breakup of the droplet. However, due to the presence of negligible oxidant near the nozzle exit on the centerline of the spray, the process of combustion is somewhat retarded. The droplet size, vaporization, and trajectory are different with steam than air as the atomization fluid. Furthermore, the flame plume size is different for steam and air. The combination of steam with air or oxygen enables one to control the droplet size and fuel vapor distribution in sprays and flames. The flame stability limits were not found to be affected significantly by steam under the examined conditions. Steam also influences the flame radiative heat transfer. The results suggest that the use of steam yields finer liquid atomization and enhanced heat transfer. The results also suggest that a suitable combination of steam, preheated air, or oxygen-enriched air may enhance the performance of twin-fluid atomizers.

16.1   INTRODUCTION

Most previous studies have used air as the atomizing fluid in air-assist or air-blast sprays [1–5]. Our current level of understanding is only based on atomization using air as the fluid. Previous studies have also shown that physical and chemical properties of the gas have a significant influence on atomization quality [1, 2]. The atomization gases examined were argon, carbon dioxide, nitrogen, and air. These gases were used to study the effect of gas density and heat capacity on the atomization quality. The effect was examined by maintaining the mass or momentum flux of atomization gas fixed to the fuel nozzle. The results showed that maintaining a constant-momentum flux with the different gases yields the same size distribution. Enrichment of atomization air with oxygen was also found to have a significant effect on the flame dynamics and flame radiation characteristics [3].

The purpose of this study is to investigate the effect of using steam for the atomization of kerosene fuel in a twin-fluid atomizer on spray flame characteristics. The use of steam in place of air will not significantly alter the thermal loading (much less than one percent) so that the power output of the system remains essentially unchanged. The energy associated with the fuel is of the order of 45 MJ/kg while that for steam is only about 2 MJ/kg. The amount of steam used per kg of fuel is typically about 10% so that less than 0.5% of the energy is associated with the steam. By preheating the atomization air so that the total energy contained in steam and preheated atomization air is the same, the effects of the thermal energy in the air are obtained. Characteristic properties of steam, preheated air, and normal air are given in Table 16.1.

Table 16.1 Characteristics of the atomization gases

Atomization gas	Density kg/m^3	Kinematic viscosity (m^2/s) $\times 10^5$
Steam	0.71	12.4
Preheated Air	0.78	3.44
Normal Air	1.16	1.57

16.2   EXPERIMENTAL APPARATUS

Experiments were carried out in a spray combustion facility that can simulate the combustion behavior of many practical combustion systems. The facility

consists of a swirl burner in which 12 swirl vanes rotate simultaneously to impart swirl (both co-flow or counter-flow) to the combustion air that surrounds the centrally located fuel nozzle. The fuel nozzle is a commercially available twin-fluid nozzle having a solid-cone spray with a nominal 75° spray cone angle. Further details on the experimental facility are given in [3].

Results are presented for swirling spray flames with steam, normal air, and preheated air as the atomization gas. The use of preheated atomization air simulated the enthalpy associated with steam, while the normal atomization air isolated the chemical effects on atomization. The swirl vane angle in the burner was fixed at 32°; this corresponded to a geometric swirl number of about 0.29. This swirl number provided stable flames at all operating conditions. The swirl number needed to stabilize the flame is dependent on several parameters including fuel nozzle type, burner geometry, atomization gas, and burner operating parameters. The momentum of the atomization steam and air, measured in the gas delivery passage at entrance to the fuel nozzle, was maintained constant at $3.94 \cdot 10^4$ kg·m/h^2 between the three gases. This momentum corresponds to a steam atomization mass flow rate of 0.57 kg/h. Total combustion air and kerosene fuel flow rates were 210 and 4.1 kg/h, respectively. The combustion air was therefore almost two orders of magnitude greater than the atomization gas. The combustion air swirl and fuel flow rate was maintained constant for all data reported here. This provided an inlet equivalence ratio of approximately 0.28. The burner was mounted on a stepper-motor-controlled, three-dimensional traversing mechanism that permitted measurement of different spatial profiles.

A two-component phase Doppler interferometer (PDI) was used to determine droplet size, velocity, and number density in spray flames. The data rates were determined according to the procedure discussed in [5]. Statistical properties of the spray at every measurement point were determined from 10,000 validated samples. In regions of the spray where the droplet number density was too small, a sampling time of several minutes was used to determine the spray statistical characteristics. Results were repeatable to within a 5% margin for mean droplet size and velocity. Measurements were carried out with the PDI from the spray centerline to the edge of the spray, in increments of 1.27 mm at an axial position (z) of 10 mm downstream from the nozzle, and increments of 2.54 mm at $z =$ 15 mm, 20, 25, 30, 35, 40, 50, and 60 mm using steam, normal-temperature air, and preheated air as the atomization gas.

Global feature of the spray and spray flames were observed using planar Mie scattering. A CW Argon-ion laser sheet was used to illuminate vertical cross-sections of the spray. A 35-millimeter camera placed nearly normal to the illuminated spray cross-section was used to record the results using a narrow depth of field and short exposure times ($\approx 1/125$ s). This also provided the flame stand-off distance, which is defined as the distance between the fuel nozzle exit and mean upstream position of the flame.

16.3 RESULTS AND DISCUSSION

### 16.3.1 Global Features of the Spray and Spray Flames

The global structure of the spray and spray flames was observed to be influenced significantly by the atomization gas. Photographs of the flame, obtained with steam, preheated air, and normal air as the atomization fluids, are shown in Fig. 16.1. The stand-off distance of the flame from the nozzle exit was largest (about 25 mm) with steam as the atomization fluid (see Fig. 16.1a), as compared to the two air cases. For the case of preheated air, the flame was stabilized closest to the nozzle exit. This increase in stand-off distance with steam is attributed to the decreased availability of oxygen immediately downstream of the nozzle exit. The variation in flame stand-off distance for the three flames, although small (≈ 1 to 2 mm), provided the same relative trends between the three gases. Preheating the atomization air developed the highest flame luminosity; see Fig. 16.1b. Lowest flame luminosity was found with the normal (unheated) air; see Fig. 16.1c. The flame was shorter and wider (and also appeared hotter) with preheated atomization air. A comparison of steam with normal air revealed a lack of initial oxygen for the steam case that resulted in a wider flame plume; compare Fig. 16.1a with Fig. 16.1c. The lack of oxygen availability immediately downstream of the nozzle exit is observed from the increase in flame stand-off distance. The flame radiative heat transfer from the steam case was in between the two air cases, i.e., highest for preheated air and lowest for normal air. Quantitative data on heat flux from flames formed with different operational conditions will be reported in a future publication.

Photographs of the spray under nonburning conditions with steam, preheated air, and normal unheated air as the atomization fluids are shown in Fig. 16.2. The addition of enthalpy to the fuel for the steam and preheated-air cases enhanced initial droplet vaporization under nonburning conditions, as compared to the normal-air case (compare the spray pattern shown in Figs. 16.2a and 16.2b with Fig. 16.2c near to the nozzle exit). Further downstream, the general spray features for the two air cases are essentially the same except for the significantly reduced number of droplets in the preheated-air case. Droplets appear to be smaller for steam than for the two air cases, with few larger size droplets. The presence of a mist of droplets for the steam case, Fig. 16.2a, is attributed to the finer droplet atomization. Fuel viscosity is reduced as a result of enthalpy transfer from the steam to the fuel, and viscosity of the steam increases relative to the normal or preheated air.
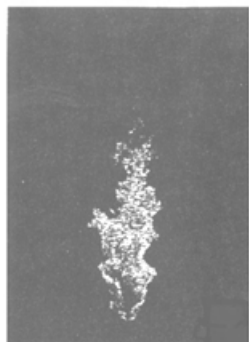
These results show that droplet vaporization must be different between the three flames. Droplet and fuel vapor transport must be significantly different for these flames and must affect combustion efficiency. The solid-cone nature of the spray flame was found to be preserved irrespective of the atomization gas.
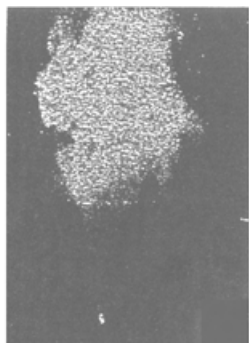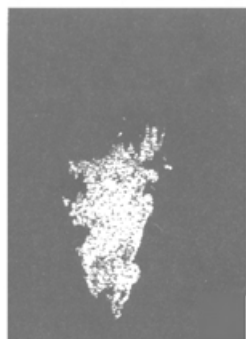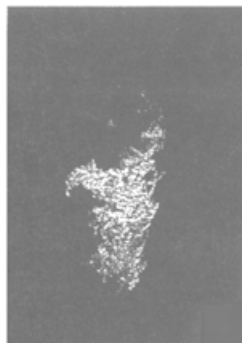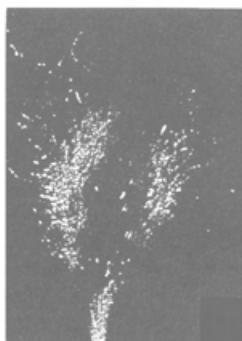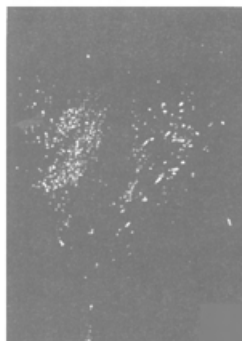
Figure 16.1 Observed features of spray flames with three different atomization gases, (a) steam at 195 °C, (b) preheated air at 185 °C, and (c) normal air at 25 °C

Figure 16.2 Observed features of the spray with three different atomization gases, (a) steam at 195 °C, (b) preheated air at 185 °C, and (c) normal air at 25 °C

Chemical composition and reactivity of the atomization air, therefore, affects droplet vaporization and transport in spray flames. In order to determine quantitatively the extent of this variation, information was obtained on the spatial distribution of droplet size and velocity, as well as their temporal distributions at various spatial positions in the spray flames.

16.3.2 Droplet Size and Velocity Measurements

The observed flame features indicated that changing the atomization gas (normal or preheated air) to steam has a dramatic effect on the entire spray characteristics, including the near-nozzle exit region. Results were obtained for the droplet Sauter mean diameter (D_{32}), number density, and velocity as a function of the radial position (from the burner centerline) with steam as the atomization fluid, under burning conditions, and are shown in Figs. 16.3 and 16.4, respectively, at axial positions of $z = 10$ mm, 20, 30, 40, 50, and 60 mm downstream of the nozzle exit. Results are also included for preheated and normal air at $z = 10$ and 50 mm to determine the effect of enthalpy associated with the preheated air on fuel atomization in near and far regions of the nozzle exit. Smaller droplet sizes were obtained with steam than with both air cases, near to the nozzle exit at all radial positions; see Fig. 16.3. Droplet mean size with steam at $z = 10$ mm on the central axis of the spray was found to be about 58 μm as compared to 81 μm with preheated air and 96 μm with normal unheated air. Near the spray boundary the mean droplet sizes were 42, 53, and 73 μm for steam, preheated air, and normal air, respectively. The enthalpy associated with preheated air, therefore, provides smaller droplet sizes as compared to the normal (unheated) air case near the nozzle exit. Smallest droplet mean size (with steam) is attributed to decreased viscosity of the fuel and increased viscosity of the gas.

An increase in droplet size with axial position is observed for all three gases. However, the relative trend of smallest droplet mean size with steam and largest with normal (unheated) air remains unchanged. As an example, at 50 mm downstream from the nozzle exit at $r = 0$, droplet mean size for steam, preheated air, and normal air were found to be 69, 86, and 107 μm, respectively; see Fig 16.3. The droplet size with steam is also significantly smaller than air at all radial positions; see Fig. 16.3. The droplet size with preheated air is somewhat smaller than normal air due to the decreased effect of preheated air at this location and increased effect of combustion. Early ignition of the mixture with preheated air (see Fig. 16.1) must provide a longer droplet residence time which results in a smaller droplet size. In addition, the increased flame radiation with preheated air increased droplet vaporization at greater distances downstream from the nozzle exit. Indeed, the results indicate that the measured droplet sizes with preheated atomization air are smaller than normal air in the center
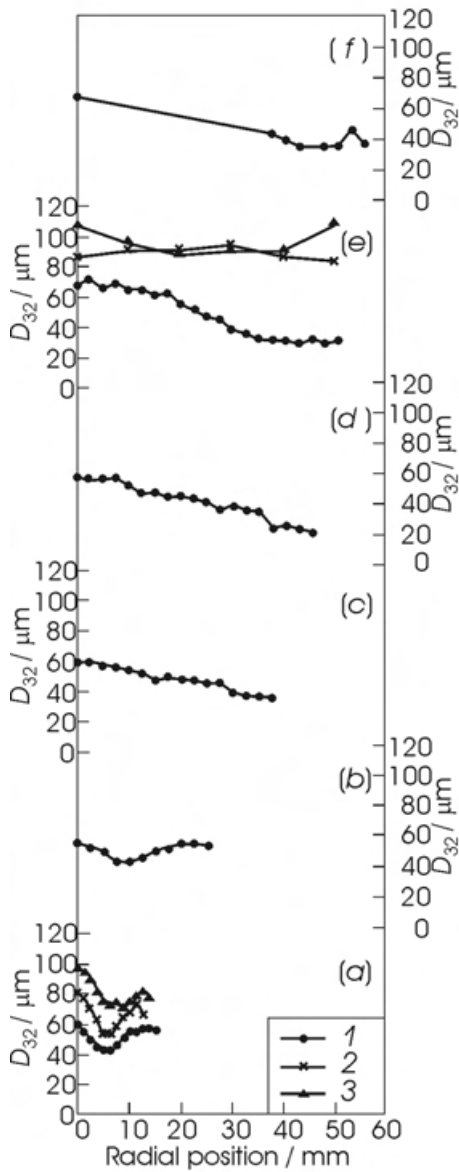
Figure 16.3 Variation of Sauter mean diameter (D_{32}) with radial and axial positions for different atomization gases: *1* — steam; *2* — preheated air; *3* — normal air. (*a*) $z = 10$ mm, (*b*) 20, (*c*) 30, (*d*) 40, (*e*) 50, and (*f*) 60 mm
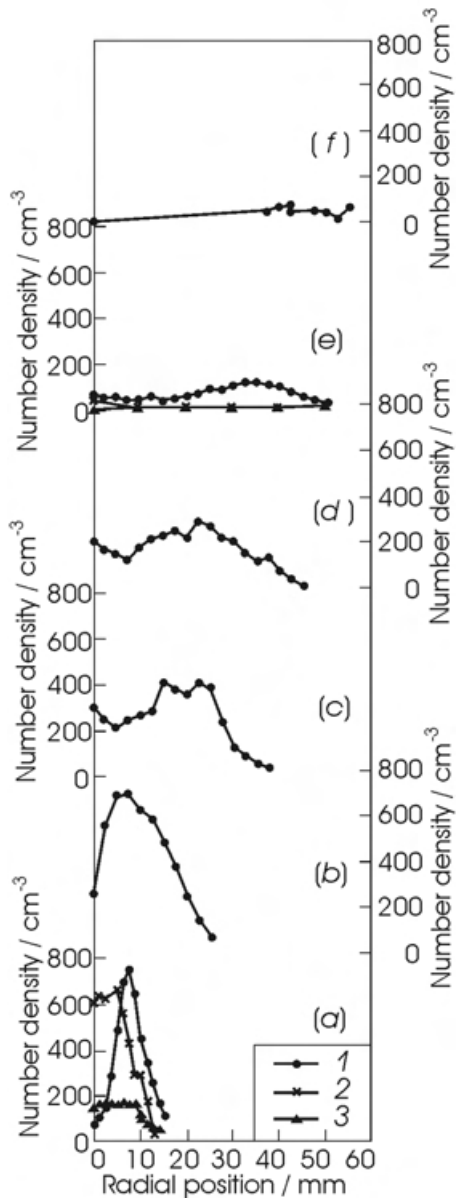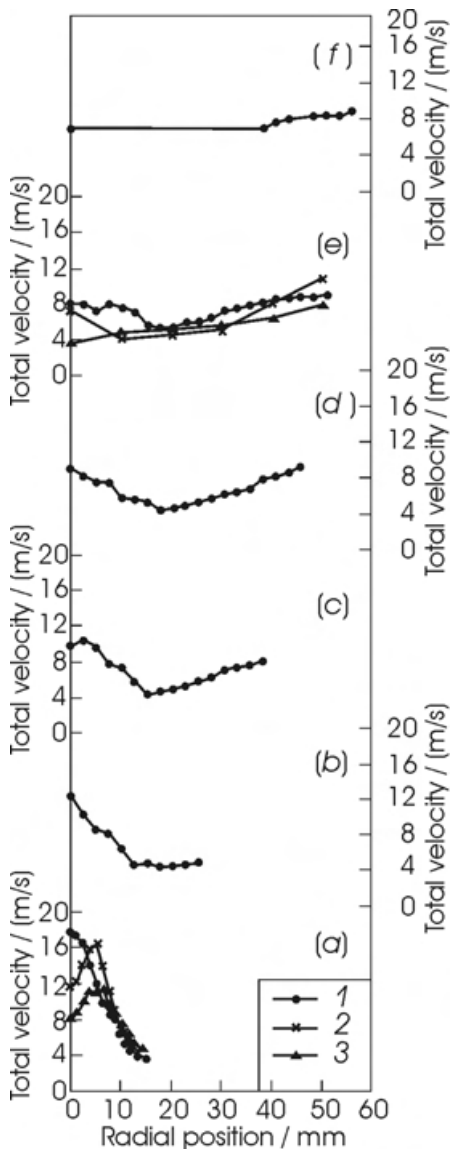
Figure 16.4 Variation of droplet number density with radial and axial positions for different atomization gases: *1* — steam; *2* — preheated air; *3* — normal air. (*a*) $z = 10$ mm, (*b*) 20, (*c*) 30, (*d*) 40, (*e*) 50, and (*f*) 60 mm

of the spray and at positions located radially outwards. At $z = 60$ mm the data arrival rate in the center of the spray flame was too low to obtain any meaningful statistics for the two air cases.

These results indicate that the enthalpy associated with air (and also steam) has an effect on the resulting droplet size. A larger droplet size with preheated air than steam reveals that there must be effects other than just the enthalpy associated with steam. Some of the possible factors include viscosity and density differences between the gases, and that water contained in steam may become miscible under these conditions. In this case, the large differences in the boiling points between the two fluids (water and kerosene) may lead to disruptive breakup of the liquid fuel, even at 10 mm, via rapid heat transfer from the flame.

At $z = 10$ mm, the results indicate two maxima in the value for droplet size, one occurring near to the center of the spray and the other near to the spray boundary for all three atomization gases. The peak near to the spray centerline decays rapidly as one progressively moves radially outwards towards the edge of the spray cone and surrounding combustion air; see Fig. 16.3. The size distribution obtained near to the nozzle exit is quite different with the three atomization gases. Therefore the enthalpy associated with steam (and also heated atomization air) must have a significant effect on the initial breakup of the liquid fuel. Farther downstream (at $z > 30$ mm) only the central peak remains. This is due to the presence of a flame cone envelope and combustion air swirl on the spray cone boundary which assists to transport larger size droplets from the spray boundary to the center (colder) regions of the spray [3]. Near to the outer flame cone the temperatures are expected to be higher than those in the inner regions of the spray. This will then enhance droplet vaporization in the outer regions as compared to the inner regions of the spray. This effect would therefore diminish the outer peak more than the inner peak as one moves progressively downstream of the nozzle exit. It is also to be noted that a solid-cone spray was used in this study.

The droplet number density presented in Fig. 16.4 indicates the solid-cone nature of the spray except in the immediate vicinity downstream of the nozzle exit. On the spray centerline at $z = 10$ mm, steam provides a lower number density as compared to the two air cases. This is due to the expansion of the spray jet at a relatively lower Reynolds number with steam and rapid vaporization of smaller sized droplets. At increased radial positions and $z = 10$ mm, a peak in the number density corresponds to the spray cone boundary. This peak shifts radially outwards with an increase in axial distance due to the expansion of the spray cone. Similar phenomena are observed for the normal and preheated air cases except that droplet number density for the preheated air case is much higher on the spray central axis (at $r = 0$). This is attributed to the effect of preheated air on atomization (i.e., larger mean droplet size and smaller number density with normal air as compared to that for heated atomization

Figure 16.5 Variation of droplet total velocity with radial and axial positions for different atomization gases: 1 — steam; 2 — preheated air; 3 — normal air. (a) $z = 10$ mm, (b) 20, (c) 30, (d) 40, (e) 50, and (f) 60 mm

air; see Figs. 16.3 and 16.4). A relatively low number density and smaller mean droplet size with steam, as compared to the heated air case, reveal that steam must provide some additional effect other than the enthalpy. Possible reasons include the chemical effect of water in the steam as discussed earlier. Further downstream of the nozzle exit, at $z = 50$ mm, the droplet number density with steam is higher than that for the normal or preheated air cases. This is due to the delayed ignition and lower temperature flame with steam than the two air cases. Note that the droplet number density for the two air cases is relatively low across the entire cross-section of the spray; see Fig. 16.4.

Droplet total velocity for the three gases was determined from the droplet axial and radial velocity and the results are presented in Fig. 16.5. Near the spray centerline, droplet velocity for steam is higher than the normal air case. Note that, at this location, droplet size and number density for steam was the smallest. Higher total velocity and smaller droplet size and number density suggest that the fuel may have gone through some disruptive behavior due to the presence of a distinct two-phase mixture with steam. The droplets maintain their higher total velocity with steam than for the two air cases even at the downstream location of $z = 50$ mm; see Fig. 16.5. At this location the droplets associated with all three gases have experienced significant deceleration. The droplets near the spray centerline experience deceleration while the droplets near to the spray boundary
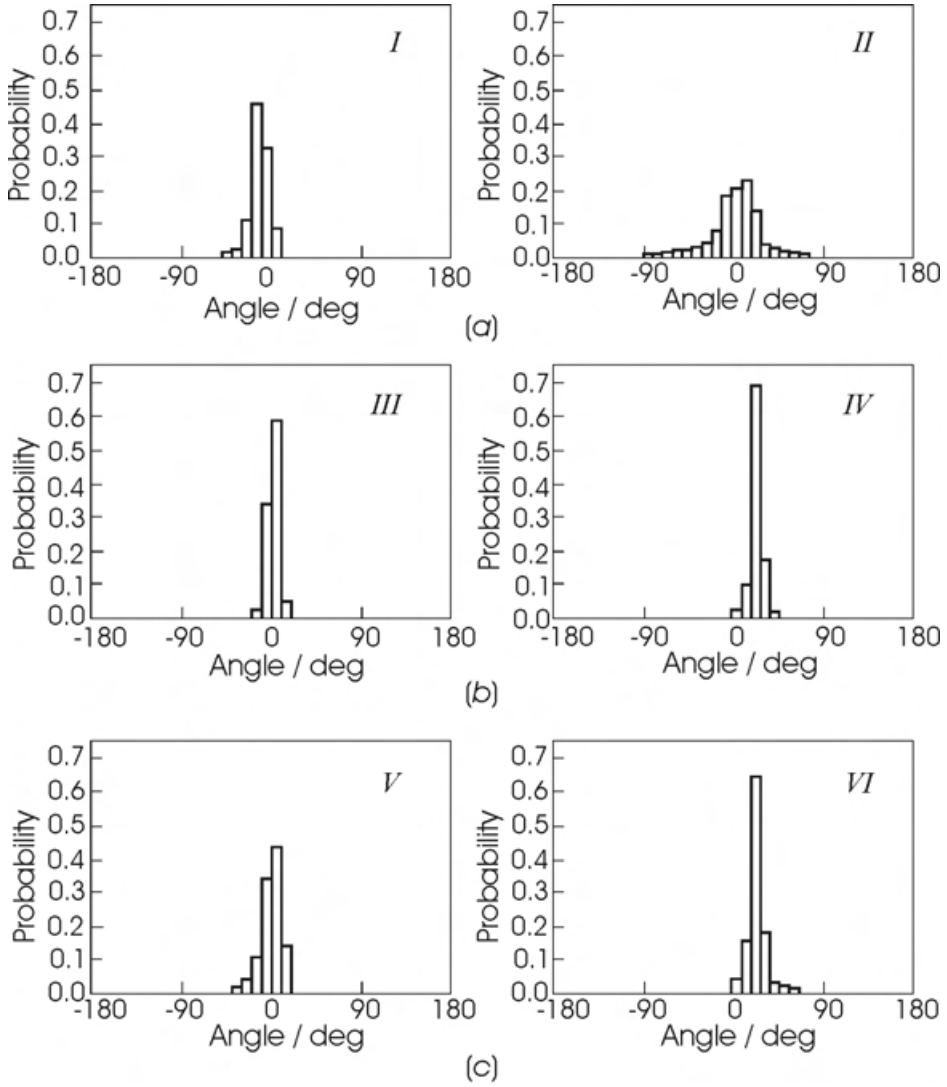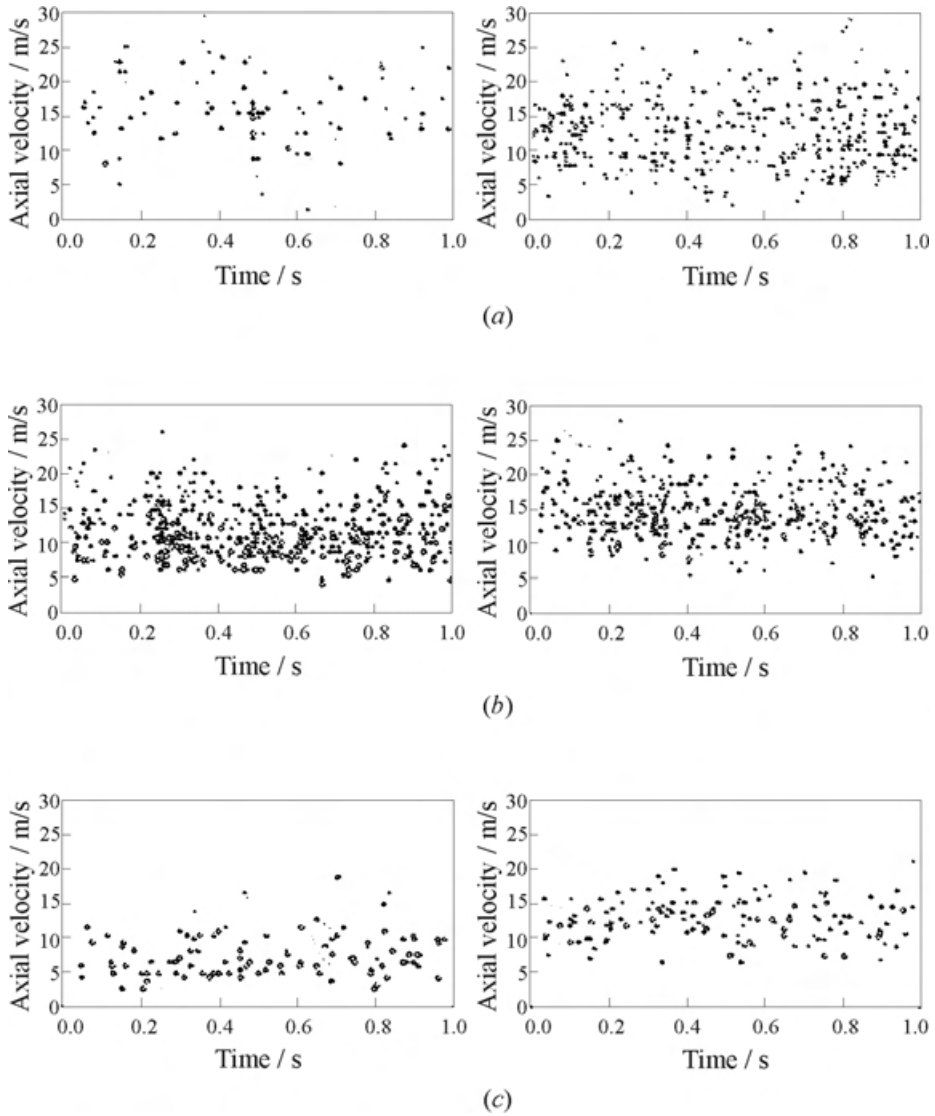
Figure 16.6 Probability distributions for droplet trajectory angles at $z = 10$ mm at the spray centerline (left column) and spray boundary at $r = 6.4$ mm (right column) for (*a*) steam, (*b*) preheated air, and (*c*) normal air. *I* — $D_{32} = 57.8$ μm, $u = 17.383$ m/s, $v = -3.449$ m/s, $\theta = -11.22°$; *II* — $D_{32} = 42.2$ μm, $u = 9.800$ m/s, $v = 1.192$ m/s, $\theta = 6.93°$; *III* — $D_{32} = 81.0$ μm, $u = 11.569$ m/s, $v = 0.372$ m/s, $\theta = 1.84°$; *IV* — $D_{32} = 53.3$ μm, $u = 12.354$ m/s, $v = 6.141$ m/s, $\theta = 26.43°$; *V* — $D_{32} = 96.4$ μm, $u = 7.956$ m/s, $v = -0.077$ m/s, $\theta = -0.55°$; and *VI* — $D_{32} = 72.7$ μm, $u = 9.941$ m/s, $v = 5.010$ m/s, $\theta = 26.75°$

experience an acceleration due to combustion. The solid-cone nature of the spray is also apparent from Fig. 16.5.

Further details on the droplet transport with the three gases is determined by examining the droplet trajectory angle associated with the total velocity vector. The results obtained at $z = 10$ mm and $r = 6.4$ mm are given in Fig. 16.6 for steam, preheated air, and normal air. The effect of steam is predominant at this location, $z = 10$ mm, both on the spray axis and boundary; compare the angles in Fig. 16.6a with Figs. 16.6b and 16.6c. The total velocity angle for preheated and normal air on the spray axis is near zero and the width of the distribution is narrow (i.e., droplets are travelling essentially downstream in the axial direction) as compared to the steam case which has a wider distribution of flow angles with a mean about $-20°$. This suggests larger turbulence levels for the steam case which helps to break up the liquid sheet emerging from the nozzle. This is in agreement with the quantitative droplet size data presented in Fig. 16.3 and the qualitative photographic data presented in Fig. 16.2. A larger flow angle distribution associated with the droplets near to the spray centerline and spray boundary, compared to the two air cases, reveals large turbulence motion to the entire spray. It is also possible that the smaller droplets produced with steam are affected significantly by the local aerodynamics from the little swirl created inside the fuel nozzle. Note the swirler is in the atomization air passage. Further downstream, the relative differences in flow angle distribution between steam, normal air, and preheated air were negligible. It is interesting to note that even though some of the smaller droplets possess negative flow angle in the steam case at $z = 10$ mm, the flame is not stabilized at this location due to the lack of oxygen in this region.

16.3.3   Droplet Size/Velocity Distributions and Arrival Times

Data on droplet size and velocity distributions, and the time of arrival of droplets into the measurement volume of the phase Doppler system, were obtained at different axial positions (10 and 50 mm) and two radial positions (spray centerline and boundary) for the three gases; see Fig. 16.7. The size coded symbols on the axial velocity distributions for $z = 10$ mm are presented in Fig. 16.7a (at $r = 0$ mm) and in Fig. 16.7b near the spray boundary (at $r = 6.4$ mm). For all three gases, higher velocities are found at the spray boundary than the center of the spray; compare Figs. 16.7a and 16.7b. At any location, droplet axial velocity is lower with normal air than with steam or preheated air. At both the spray centerline and boundary, a larger velocity range is found with steam than with normal air. Droplet size and velocity at the centerline with normal air are large as compared to the steam. Also note from these time-of-arrival histograms

Figure 16.7 Droplet time of arrival sequence for droplet axial velocity at $z = 10$ mm at the spray centerline (left column) and spray boundary at $r = 6.4$ mm (right column) for (a) steam, (b) preheated air, and (c) normal air. 1 — $d < 10$ μm, 2 — $d = 10$–30 μm, 3 — $d = 30$–70 μm, and 4 — $d > 70$ μm

that at $z = 10$ mm the size and velocity are uncorrelated, i.e., large droplets do not travel at higher velocity as compared to the smaller size droplets. A larger droplet population at the spray boundary than near the spray centerline is as expected. More droplet clustering occurs with the preheated air as compared to the steam. Smaller droplet sizes with steam are attributed to the enhanced droplet vaporization and possibly disruptive droplet breakup as described earlier. Note that with steam many droplets were found to travel at velocity twice that of the normal air case (maximum droplet velocity with normal air is around 15 m/s while that with steam is found to reach near 30 m/s). In both cases, the momentum of the gas jet as well as the mass flow rate of fuel flow was constant.

16.4 CONCLUDING REMARKS

Droplet size and velocity measurements were carried out using a commercially available air-assist atomizer with steam, preheated air, and normal (unheated) air. Direct flame photography in conjunction with a laser sheet beam was used to record the features of the kerosene spray and spray flames. Droplet size and velocity distributions were obtained using a two-component phase Doppler interferometer. The higher viscosity of steam, as compared to normal air, assists in disintegrating the liquid sheet and provides finer atomization. The effect of enthalpy that is associated with steam was simulated by preheating the atomization air to higher temperatures. The steam is miscible with the kerosene so that the mixture yields a wide range of boiling points. It is conjectured that the presence of water in kerosene may assist to break up the droplets. However, due to the presence of negligible oxidant near to the nozzle exit on the centerline of the spray with steam the process of combustion is somewhat retarded. Spray characteristics are clearly different with steam than air as the atomization fluids. The results indicate that steam-assisted atomization provides smaller droplet sizes than with normal or preheated air-assisted atomization. Near to the nozzle exit, enhanced vaporization of fuel with preheated air is similar to that of steam. The flame luminosity is highest with the preheated air and lowest with normal unheated atomization air. Enhanced flame radiation with preheated atomization air is attributed to hotter ignition of the fuel. Droplet size, velocity, and number density were found to change significantly with the gas used in the atomizer. The results presented in this study indicate the potential benefits of using steam for finer atomization of fuel and enhanced heat transfer. These results also suggest strategies to enhance the performance of twin-fluid atomizers via a suitable combination of steam and preheated air.

ACKNOWLEDGMENTS

REFERENCES

1. Aftel, R., A. K. Gupta, C. Cook, and C. Presser. 1997. Gas property effects on droplet atomization and combustion in an air-assist atomizer. *26th Symposium (International) on Combustion Proceedings.* Pittsburgh, PA: The Combustion Institute. 1645–51.
2. Presser, C., A. K. Gupta, and H. G. Semerjian. 1988. Dynamics of pressure-jet and air-assist nozzle sprays: Aerodynamic effects. AIAA Paper No. 88-3139.
3. Gupta, A. K., T. Damm, and C. Presser. 1997. Effect of oxygen-enriched atomization air on the characteristics of spray flames. AIAA 35th Aerospace Sciences Meeting, Paper No. 97-0268, Reno, NV.
4. Presser, C., A. K. Gupta, and H. G. Semerjian. 1993. Aerodynamic characteristics of swirling spray–pressure jet atomizer. *Combustion Flame* 92:25–44.
5. Gupta, A. K., C. Presser, J. T. Hodges, and C. T. Avedisian. 1996. Role of combustion on droplet transport in pressure-atomized spray flames. *J. Propulsion Power* 12(3):543–53.
6. Presser, C., A. K. Gupta, H. G. Semerjian, and C. T. Avedisian. 1994. Droplet transport in a swirl-stabilized spray flame. *J. Propulsion Power* 10(5):631–38.

SECTION THREE

CONTROL
OF COMBUSTION

Chapter 17

FLAME SPEED CONTROL USING
A COUNTERCURRENT SWIRL COMBUSTOR

S. Lonnes, D. Hofeldt, and P. Strykowski

The Countercurrent Swirl Combustor (CSC) is a modified cyclone design that utilizes fluid dynamic mechanisms as a means to control flame speed and thus turn down. The CSC geometry consists of two axial counter-flowing but tangentially co-swirling reactant ring jets, at different radii, contained within a cylindrical vessel. An exhaust port is located on the axis of the cylinder at one end. A self-stabilized, constant-diameter cylindrical flame sheet resides inside of the shear layer, with the low-density products confined along the axis by the swirl field. The turbulence levels in the near field of the flame are controlled by manipulating the vorticity in the shear layer through axial shear, tangential shear, and radial ring jet separation. The present experimental study has observed flame speeds ranging from laminar to 3.5 times laminar values using premixed natural gas as a fuel. Emission characteristics of the CSC indicate typical NO_x concentrations in the range of 10 ppm at 3% O_2.

17.1 INTRODUCTION

Legislative restrictions on pollutant emissions have motivated the combustion community to seek new low-emission combustion techniques that are practical industrial energy sources. However, to meet the needs in most industrial applications, a combustion source needs to be able to maintain low-emission output over a range of heat release rates, occupy minimal volume, and have low operating costs per unit energy produced. One would like to maximize the turn-down ratio, volumetric heat release, and overall thermal efficiency while minimizing NO_x, CO, and hydrocarbon emission levels. The ultra-low NO_x emission performance of the CSC has been previously documented by the authors and its

merits regarding overall thermal efficiency associated with low-air-pumping requirements have been discussed [1]. This paper focuses on turbulent flame speed control to achieve reasonable turn-down ratios and volumetric heat release rates while maintaining low NO_x output.

The CSC is a modified cyclone combustor design. Cyclone combustors have been studied in various forms since the 1960's using fuels ranging from coal to natural gas. The reactants enter tangentially at one end, flow in a helical path toward the opposite end of the chamber, reverse directions axially, and exhaust out of a centerline port on the same end as the inlet. Most NO_x investigations of cyclone combustors focused on generating subthermal NO_x operating temperatures by stabilizing a flame at low-equivalence ratios [2, 3], or by heat removal from the flame zone [4]. The methods proved to be effective at the expense of energy diverted to cooling water or additional pumping work for excess combustion air.
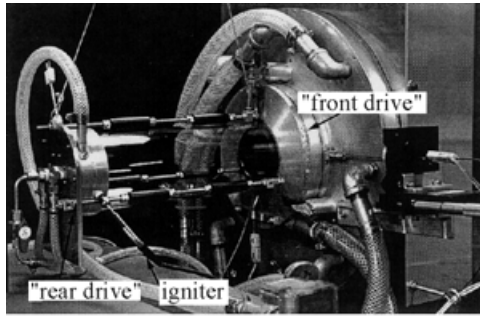
Four different flame configurations, or modes, were experimentally observed and documented in a cyclone combustor examined by Najim *et al.* [3], which was fueled with premixed natural gas and air. In this work, the transition between modes was controlled by varying fuel–air equivalence ratios and reactant flow rates through the system. In the first two modes, the flame was stabilized near the inlet annulus of the cyclone, where flow velocities were relatively high, and hence required high-equivalence ratios to produce the elevated flame speeds needed to stabilize a flame. Consequently, flame temperatures were relatively high, and, coupled with long residence times of post-flame fluid elements, led to undesirable NO_x levels. An ultra-low NO_x mode was achieved by reducing the equivalence ratio and flow rates such that a flame was stabilized close to the chamber walls and extended axially over the entire combustor length. Flame speeds in this case were low enough that very lean equivalence ratios could be used such that thermal NO_x temperatures were never produced; thus the elevated residence times did not produce excessive NO_x levels. However, the turn-down ratio of this mode was limited due to bounds on the flow rates and equivalence ratios needed to stabilize the flame at this position. A fourth mode was identified in which an annular flame was again stabilized along the entire length of the combustor, but this time at a diameter on the order of the exit port. This mode is referred to as being dynamically contained due to the fluid mechanics involved in the system. Najim *et al.* [3] only observed this mode for very lean operating conditions — equivalence ratios less than 0.55 — and hence low flame speeds, but judged it to be of no practical significance because of "inefficient" combustion (i.e., high hydrocarbon emission).

Based on the authors' work, it is believed that the majority of the hydrocarbons emissions associated with the dynamically contained mode can be traced to unburned reactants exiting the burner in a thin zone separating the product gases from the exhaust nozzle. Although these reactants are not consumed within the burner, many possible techniques exist for consuming or eliminating
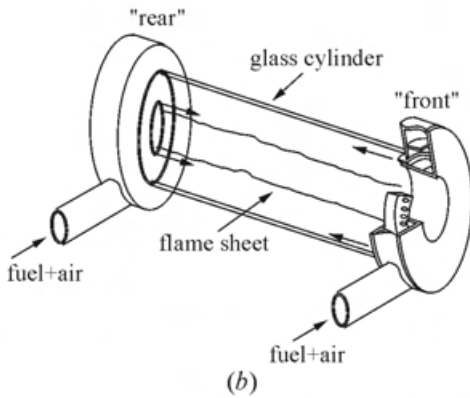
the reactant flux without significantly altering the operation of the rest of the burner. In the authors' system, they simply impact on a hot surface of the exhaust duct, and are either burned off there or during subsequent mixing with product gases. The authors have not attempted to optimize this aspect of the burner, although the efficiencies over 90% (i.e., the percent of hydrocarbons consumed within the burner) have been achieved. As long as complete combustion can be achieved, this mode of operation offers several key advantages. First, significantly higher equivalence ratios can be used without adversely impacting NO_x emissions. The small-diameter flame increases axial velocities and significantly reduces post-flame residence times such that NO_x levels within the burner remain low. Second, the high-velocity swirling exhaust jet promotes rapid entrainment and mixing of air downstream of the burner and thus NO_x kinetics can be rapidly frozen. Finally, and probably most importantly for practical utilization, the flame is stabilized in relative proximity to a countercurrent shear layer which must exist between the inflowing reactants and the outflowing products. Such shear layers can generate nonconvecting but temporally unstable modes with increased spatial amplification rates [5, 6], and are thus well suited for turbulence generation in a compact geometry. With proper control of the fluid velocity profiles and mixture equivalence ratios, turbulent structures can be generated in a reactant stream shear layer and convected to the flame. Manipulation of the shear layer vorticity then allows turbulent flame speed control. The potential exists for a low-emission combustor which has a reasonable volumetric heat release at the upper end of its operating range and a good turn-down ratio achieved through turbulent flame speed control. This provides the motivation for the present study.
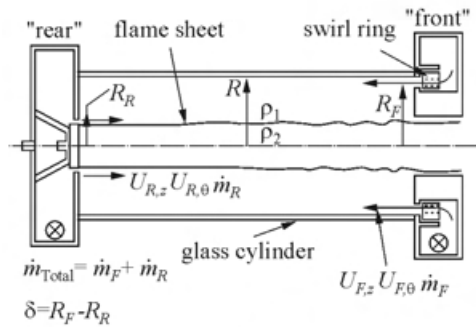
17.2   COUNTERCURRENT SWIRL COMBUSTOR

The burner is a modified cyclone combustor, with several features, including the addition of a rear jet, designed to facilitate shear layer control. The combustor consisted of a 10.2-centimeter diameter glass cylinder, either 30.5 or 15.3 cm in length, with "front" and "rear" swirl chambers on either end for introduction of reactants, and a 5.1-centimeter diameter coaxial exhaust port at the front as shown in Fig. 17.1. Mass flows of air and natural gas were controlled and monitored by adjusting flows through a venturi and a rotameter, respectively, and then premixed prior to being introduced into the combustor. A flame was initiated by inserting a spark igniter into the rear portion of the CSC as seen in Fig. 17.1a. After ignition, the igniter was withdrawn to prevent flame and/or flow field interactions; the flame remained self-stabilized near the rear face of the burner. The glass cylinder allowed observations of the flame along the entire axis of the chamber.
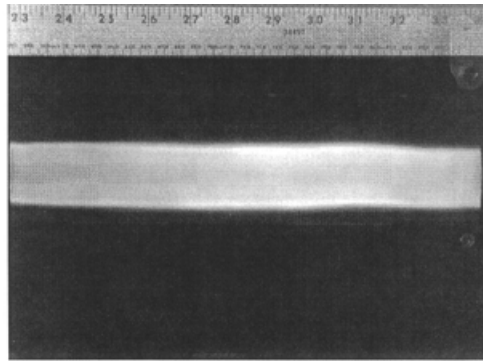
The front and rear drive swirl chambers create axially counterflowing but tangentially co-swirling annular reactant jets at different radii as indicated by the perspective and side views of Figs. 17.1b, 17.1c. The drives are designed to allow parametric variation of the inlet jet conditions for experimental study, but most likely would not appear this way in a practical system. At the front, a swirl ring consisting of thirty 6.4-millimeter diameter holes drilled at an angle to the CSC axis were used to vary the angular momentum of the reactants, while various collars controlled the width of the annular gap and hence the axial momentum. These pieces were discretely variable, but the jet always issued along the wall of the cylinder at a radius of R_F, as shown in Fig. 17.1c. The rear section incorporated several plates (not shown) which permitted discrete variability of the annular radius R_R, but no provision was made for independent adjustment of either the gap width or angular momentum in this study. Therefore, the rear angular momentum was fixed by the radial offset and size of the rear inlet port for a given rear mass flow rate.

In this study, parameters were varied over the following ranges: chamber lengths of 30.5 cm and 15.3 cm, radial ring jet separation of $\delta = 3.4$ mm to 35.1 mm (see Fig. 17.1c), total mass flows of 0.015 to 0.060 kg/s, front inlet swirl angles of 31°, 41°, and 68°,

Figure 17.1 (a) Countercurrent Swirl Combustor experimental facility; (b) isometric view of the burner; and (c) cross-sectional view of the burner indicating relevant parameters

rear inlet swirl angles of 0° and 80°, rear mass flows of 0% to 60% of the total mass flow, and equivalence ratios between 0.68 and 0.85. Heat release rates thus spanned 30–150 kW, where the upper end was limited by system flow capabilities, not flame stability.

17.3   HEURISTIC MODEL OF COMBUSTOR OPERATION

As previously stated, the burner is opperated in a mode where the flame extends over the entire length of the burner, but is confined to a radial size on the order of the exit port diameter. A typical time-averaged picture of the flame sheet is shown in Fig. 17.2. Under most of the operating conditions, the flame is observed to have a nominally constant diameter along the entire length of the cylinder. The following description of the internal mechanics supporting such operation is based upon observations of the flame be-

Figure 17.2 Twenty frame composite image of the flame within the Countercurrent Swirl Combustor (exhaust port is on the right)

havior and various measurements of the exhaust flow, but to date, no local velocity measurements have been made within the chamber.

The front jet produces a countercurrent shear environment which entrains reactants and pumps them radially inward toward the flame as depicted in the sketch of Fig. 17.3a. Since the reactants are premixed, the flame sheet must reside at a position where the flame speed (determined by the reactant equivalence ratio and the local turbulence intensity) matches the radial inward velocity of reactants. Since the radial velocity must be zero at the cylinder axis and wall, a maximum must exist (as indicated in Fig. 17.3b). As long as the flow rates are maintained at high enough rates, this maximum is greater than the local flame speed and the flame remains confined. If the flame speed exceeds the maximum radial velocity anywhere along the axis of the cylinder, the flame changes modes and flashes out to the cylinder wall.

As the reactant elements pass through the shear layer, they pick up and convect turbulent fluctuations to the flame. There is no constraint that the flame speed and radial velocity be uniform along the axis; however, since the flame
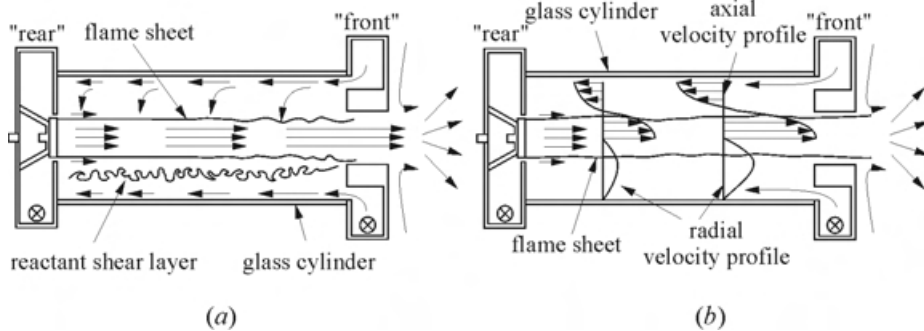
Figure 17.3 (*a*) Cross-sectional view of the Countercurrent Swirl Combustor; (*b*) anticipated velocity profiles within the combustor

remains at a nominally fixed diameter, one can infer that they must balance at approximately the same radial position everywhere. Designing the burner with rear jet access will provide control of the shear and vorticity characteristics within the burner, and thereby the axial turbulence distribution, and the turbulence levels reaching the flame.

However, the nature of turbulence is that, some instant, the balance will not be exact at some location along the cylinder axis. One would thus expect the flame to either move in or out (i.e., wrinkle). Since countercurrent shear layers are known to be particularly violent, one might worry about the stability of such a system. Nevertheless, the flame is observed to remain remarkably stable over a wide range of operating conditions. This is attributed to the influence of the radial pressure gradient set up by the swirling flow, and the density difference between the reactants and the products. If a structure, convected from the shear layer, radially perturbs an element of the flame sheet, the density difference between the reactants and products causes the element to be restored to its initial position. The argument is really an extension of the Rayleigh circulation criteria to include a density discontinuity [7, 8].

To simplify the discussion, let us reconsider the velocity profiles shown in Fig. 17.3*b* for the basic cyclone configuration where little or no rear drive flow is present. As reactants are entrained out of the front jet, conservation of mass and momentum requires that the axial velocity of the outer jet decrease with increasing distance from the front drive. But, as the reactants are converted to products when they cross the flame sheet, mass is added at fixed area to the product flow. This causes the axial velocity of the products to accelerate toward the exhaust nozzle as in classic constant-area heat addition. Thus, one expects
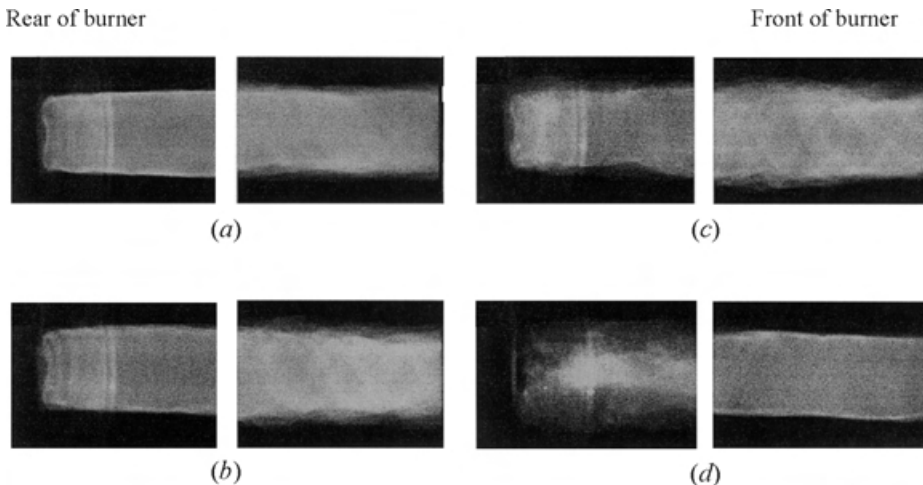
Figure 17.4 Images of the CSC flame at the "rear" (left side of figure) and "front" (right side of figure) with rear mass fractions of 10% (a), 20% (b), 30% (c), and 40% (d) of the total mass flow delivered to the burner. Each image extends 7.5 cm axially

axial velocities to be highest at the front and lowest at the rear, with the radial gradient of axial velocity increasing as one moves from rear to front (left to right in the figures). Assuming that to first order the turbulence intensity scales with U_z/r, this should result in a nonuniform turbulence intensity distribution, and hence local flame speed variation along the axis of the CSC. Figures 17.4a and 17.4b show images of the flame luminosity taken with 2-millisecond exposure times. The flame appears almost laminar at the rear drive assembly and becomes increasingly turbulent toward the exhaust nozzle, but a nominally constant flame diameter is maintained. (The vertical striations at the left of the rear images are an artifact of reflections off the rear drive and should be ignored.) Because the density gradient between reactants and products effectively scales the velocity profiles, the mean convective speed of structures in the shear layer also increases with distance from the rear drive. Both the structure velocity and the turbulence intensity affect the radial manifolding of reactants into the flame, so the inward radial velocity also increases with distance from the rear drive. This allows a balance to be set up between the radial pumping and the flame speed everywhere along the cylinder axis.

A close examination of the cylindrical flame as it exits the exhaust nozzle will reveal that there is a thin annular flow of unburned reactants near the front of the burner which never passes through the flame. The authors know this

to be the case because the temperature and hydrocarbon level of the flow have been measured. Even though the gap between the exhaust port and the flame is generally small under the present operating conditions, both the radius of the annular gap and the axial velocity component are high at this point. So, the flow of unburned reactants leaving the burner cannot simply be neglected. This is mentioned here not because of any particular importance to flame stability or burner operation, but because it can be an important source of hydrocarbon emission as it has been already noted, and because it has to be measured in order to determine the average flame speed inside the burner, as will be discussed later in this paper. Although these unburned reactants are undesirable from an emissions standpoint, the burner was not designed to optimize efficiency since the research to date has focused on understanding the shear-layer/swirl-field interactions to control flame speeds within the burner. Since the source of the flow is known, any number of options from boundary-layer tripping to recirculation into the burner to ignition of the layer could be used to reduce its impact. In all the cases described here as well as those reported earlier in ONR contractor's reports, the reactants are consumed as they mix with hot products and overfire air in a recirculation region, which exists immediately downstream of the exhaust port, resulting in extremely low emissions of NO_x and hydrocarbons.

When flow is introduced through the rear drive, the local shearing increases both the radial manifolding of reactants as well as the turbulence transmitted to the flame. The local increase in turbulence transmitted to the flame is observed in the image sequence from Figs. 17.4a–17.4d, as the fraction of mass delivered to the rear drive of the burner is increased (total mass flow rate is constant). The local radial inflow must also be increasing because the flame diameter remains essentially constant even though the local turbulence intensity, and hence the local flame speed, has increased. The premise was that, by adjusting the overall vorticity associated with the front and rear jets, one could control the turbulence intensity levels inside the burner and, hence, adjust the overall flame speed. However since, as it has been just demonstrated, the turbulence intensity levels vary locally throughout the chamber, the key is to obtain the desired turndown range without approaching any locally unstable flame conditions. Here, the suppressing effect of the swirl coupled with the density difference between products and reactants is critical.

The trend observed in Fig. 17.5 illustrates the importance of swirl. The image sequence corresponds to data points using front swirl angles of 31°, 41°, and 68° with all other parameters fixed ($\phi = 0.68$, RMS = 0.1, $L = 12$ in. (30.48 cm), total mass flow rate of 0.03 kg/s, and rear swirl angle of 85°). The chamber averaged swirl is defined as the sum of the front and rear drive angular momentum divided by the chamber radius and total mass flow. This provides a measure of the swirl experienced by the combustion chamber confined flow and allows comparison between different test conditions. The flame speed ratio
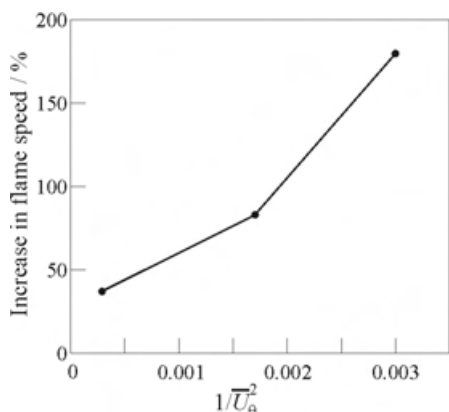
Figure 17.5 Percent increase in flame speed versus the inverse of a squared average chamber (global) swirl number
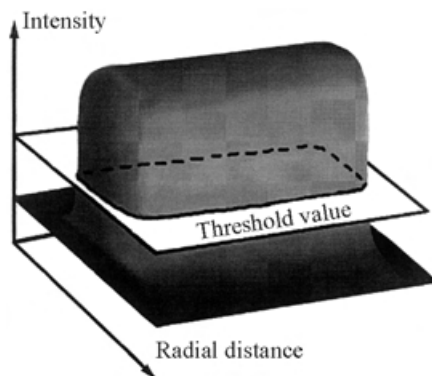

Figure 17.6 Representation of a flame image with the gray scale value plotted on the vertical axis

was plotted against the inverse of the squared chamber averaged swirl velocity to demonstrate the dependence on centrifugal acceleration. The data reinforce the radial pressure gradient (centrifugal acceleration) mechanism described earlier. Decreased chamber average swirl results in an increase in turbulent flame speed. The anticipated near linear behavior with centrifugal acceleration is observed.

17.4 FLAME SPEED MEASUREMENT TECHNIQUE

An average flame speed, defined as the mass flow of reactants consumed within the CSC divided by the flame area and reactant density, was used to document flame speed controllability. Hence, measurements of reactant mass flow consumed within the burner, reactant density, and average flame area were required. An average flame area was determined by analyzing composite images obtained from a sequence of twenty 2-millisecond exposures of the flame luminosity. The acquired images had a resolution of 640×480 pixels and an 8-bit dynamic range. Thus, regions of high turbulence result in more gradual intensity gradients in the radial direction, whereas laminar interfaces appear with sharp intensity jumps from black background to intense flame. A thresholding approach was used to define the "edge" of the flame from which a representative flame area could be calculated.
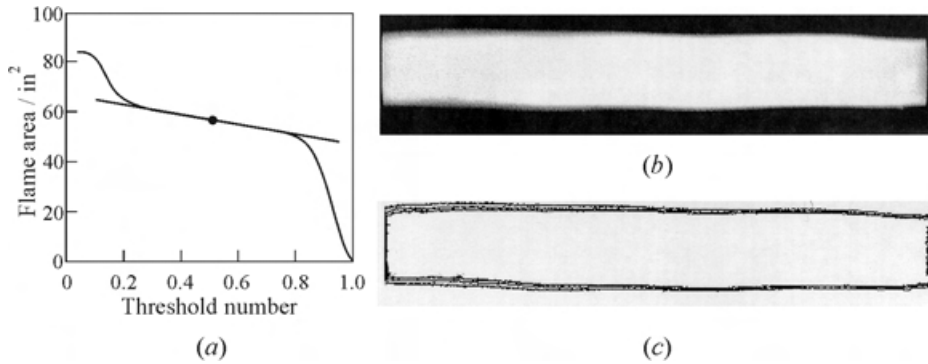
Figure 17.7 (*a*) Cylindrical flame sheet area as a function of gray scale threshold; (*b*) corresponding flame image; and (*c*) image contours at threshold values of 0.34, 0.54, and 0.69

Figure 17.6 shows the results for a typical composite image of the entire flame in which the image intensity, or gray scale value, is plotted on the vertical axis against radial and axial distance coordinates. To find the flame area, a threshold intensity is first picked and a binary image is created with all pixels with intensities above the threshold set to 1 (white) and the rest set to 0 (black). The number of white pixels is then proportional to the surface area of the flame at that intensity contour. This process is then repeated to build up a plot of flame area versus a normalized threshold number (intensity value/256) such as that shown in Fig. 17.7*a*.

The area corresponding to threshold numbers between 0 and 0.2 is relatively large because it contains essentially all of the black background and the flame. The values between 0.2 and 0.8 correspond to flame areas from the inner core out to the outer fringe of the turbulent brush — the wider the range of flame areas covered by these intensities, the more turbulent fluctuations must have washed out the average image. Thus, the slope of the region from 0.2 to 0.8 is related to the globally averaged turbulence intensity, and the line between 0.2 and 0.8 on Fig. 17.7*a* would appear more horizontal for a sharp laminar interface. A line is fit to the linear portion of the plot and the center threshold value defined as a representative flame area. Contours of intensity thresholds derived in this way (Fig. 17.7*c*) were laid on top of the original image (Fig. 17.7*b*) along with neighboring intensity thresholds, and the central value identified in this fashion always fell in the area of the flame brush. The radial separation between contour lines such as that shown in Fig. 17.7*c* also provides an indication of the axial distribution of turbulence.
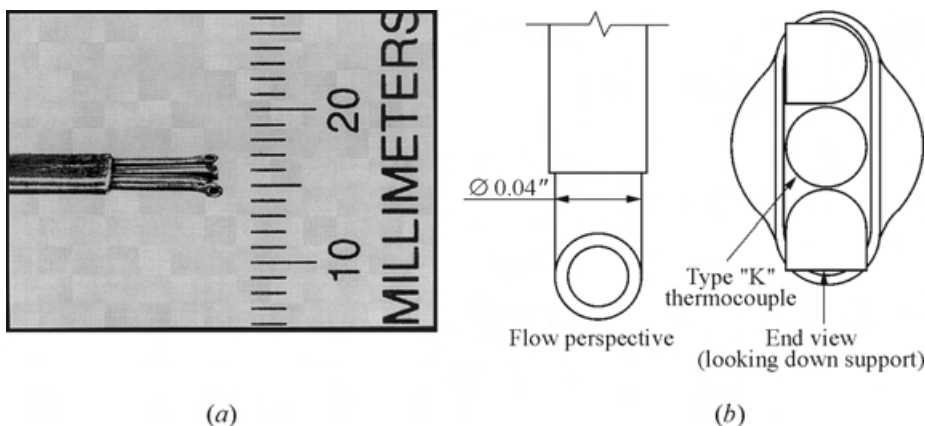
Figure 17.8 Magnified views of the Low-Profile Vectoring Velocity–Temperature probe used to capture the mass flow rate of reactants leaving the CSC

In addition to the flame area, the mass flow of reactants consumed by the flame must be measured to determine the flame speed. As previously mentioned, there is a flow of unburned reactants which takes a short circuit path from the front drive out the exhaust port, and it must be subtracted from the overall mass flow entering the CSC in order to obtain the mass flow rate of reactants consumed inside the burner. The measurement challenge arises in attempting to integrate the axial component of a swirling, variable density reactant stream over a radial distance of less than 5 mm (the gap thickness). A novel, low-profile vectoring velocity probe complete with a built-in thermocouple was designed for monitoring temperatures to measure the mass flow associated with this flow. The probe was miniaturized to allow nominal point measurements of two velocity components and temperature in a 2D flow field.

Figure 17.8 shows the probe, which consists of a 1-millimeter diameter type "K" thermocouple centered between two 1-millimeter diameter pressure taps. Each of the pressure tubes was bent 90° and sheared at the bend. To obtain a measurement, the tube is rotated until the pressure difference between the two taps is maximized. This is the position at which one tube is directed into the oncoming flow and the other is parallel to it. The approach flow thus observes an approximately 1-millimeter thick planar obstruction. The pressure difference and temperature are then recorded. The pressure difference is related to the approach velocity, and the angle determines the tangential and axial velocity components in this case. The local mass flux is then determined from the axial velocity component and the temperature (necessary to compute the flow density), and

the results are integrated as the probe is scanned across the gap extending from the wall to the flame. The probe was calibrated over a velocity range from 10 to 75 m/s using a well-conditioned free jet. Unusual assets of the probe design are the invariant nature of the calibration coefficient with respect to velocity (above 18 m/s), the lack of orientation dependence for maximum pressure difference over the entire velocity range, and good pressure signal amplification (139% of a standard pitot reading).

17.5   CONCLUDING REMARKS

The CSC offers unique potential for providing ultra-low NO_x combustion and flame speed control. The small-diameter flame within the CSC in combination with the vigorous mixing of the exhaust jet allows ultra-low NO_x production at equivalence ratios within the thermal NO_x regime. Operation within the thermal NO_x temperature regime provides turn-down ratio benefits by extending the flame blow-off limit and allowing greater mass consumption of fuel. To assess the CSC potential, an experimental facility was constructed with the capability of independent control of geometric and operational parameters and was outfitted with emission diagnostic equipment. Earlier work [1] provided support for the ultra-low NO_x potential of the CSC, as well as indirect evidence of the vigorous mixing produced by the exhaust jet. The emission characterization study yielded typical NO_x concentrations in the range of 10 ppm at 3% O_2.

Countercurrent Swirl Combustor flame speed control relies on the existence of a countercurrent shear layer in the near field of the flame. The countercurrent shear layer provides a mechanism for producing high volumetric heat releases due to the enhanced spatial amplification of turbulent structure growth rates. Controlling the vorticity within the shear layer also provides a technique for supplying a reactant stream to the flame with various degrees of turbulence, thus providing a variable flame speed. Used in combination with the suppressive effects of swirl, the flame speed exhibits potential for control. The present study focused on the issue of flame speed control. To address the issue, an experimental technique was devised to determine a chamber averaged flame speed. The experimental facility was modified to incorporate a novel flame speed measurement apparatus. Preliminary qualitative and quantitative results suggest that the swirl and shear layer vorticity are integral components of the primary governing physics. Local flame structure modifications were observed with varying degrees of countercurrent shear, and quantitative results revealed the importance of swirl. Flame speeds were observed between laminar and about 3.5 times laminar values.

A heuristic model of the CSC internal mechanics has been proposed based on extensive observations. The model provides explanations for qualitative and

quantitative observations, as well as a technique for predicting future operation. The focus of the present study was to gain an understanding about the governing physics involved in the CSC combustion process, not necessarily flame speed maximization. Further increases in turbulent flame speed are anticipated in future studies. This will be accomplished by developing a leading order set of dimensionless control parameters which can be used to assess the competing tendencies of turbulence generation caused by countercurrent shear and the turbulence suppression effects of global swirl. Further advances in the burner design will require a more careful examination of the flow field — measurements of the time averaged and turbulence quantities within the burner are planned using LDV and PIV — to determine local flame speed coupling to shear-layer turbulence, and the extent to which local stoichiometry control may be needed to increase volumetric heat release while avoiding burner stability boundaries. The detailed flow measurements will be used to design a second generation burner capable of higher volumetric heat release rates, while maintaining the low-emission characteristics that the CSC has consistently demonstrated.

ACKNOWLEDGMENTS

REFERENCES

1. Lonnes, S., D. Hofeld, and P. Strykowski. 1996. Dynamic containment combustor operation and experimental emission results. *Technical Meeting of the Central States Section of the Combustion Institute Proceedings*. St. Louis, Missouri. 170–75.
2. Syred, N., A. C. Styles, and A. Sahatimehr. 1980. Emission control by cyclone combustor technology. *J. Inst. Energy* 54(128):125.
3. Najim, S. E., A. C. Styles, and N. Syred. 1981. Flame movement mechanisms and characteristics of gas fired cyclone combustors. *18th Symposium (International) on Combustion Proceedings*. Pittsburgh, PA: The Combustion Institute. 1949–57.
4. Mirzaie, H., and N. Syred. 1989. The use of multi inlet cyclone combustor to minimize NO_x formations. *3rd Symposium (International) of Gas–Solid Flows — 1989 Proceedings*. San Diego, CA (presented at *the 3rd Joint ASCE/ASME Mechanics Conference*).
5. Strykowski, P. J., and R. K. Wilcoxon. 1993. Mixing enhancement due to global oscillations in jet with annular counterflow. *AIAA J.* 31:3.

6. Strykowski, P. J., A. Krothapalli, and S. Jendoubi. 1996. The effect of counterflow on the development of compressible shear layers. *J. Fluid Mechanics* 308:63–96.

7. Beer, J. M., N. A. Chigier, T. W. Davies, and K. Bassindale. 1971. Laminarization of turbulent flames in rotating environments. *Combustion Flame* 16:39–45.

8. Toqan, M. A., J. M. Beer, P. Jansohn, N. Sun, A. Testa, A. Shihadeh, and J. D. Teare. 1992. Low NO_x emission from radially stratified natural gas–air turbulent diffusion flames. *24th Symposium (International) on Combustion Proceedings.* Pittsburgh, PA: The Combustion Institute. 1391–97.

Chapter 18

COUNTERCURRENT SHEAR LAYER CONTROL OF PREMIXED FLAMES

E. Koc-Alkislar, L. Lourenco, and A. Krothapalli

Using a novel shear layer control technique, the blow-out limit for a rich premixed propane–air jet flame issuing from an axisymmetric nozzle is increased by an order of magnitude. This technique is based on the self-excitation of a countercurrent shear layer that is established by the introduction of a reverse flow around the perimeter of an axisymmetric jet through the gap between nozzle and surrounding suction collar. An experimental study is carried out to observe the effect of suction collar and countercurrent flow to the blow-out velocity of an anchored flame. A maximum blow-out velocity of 30 m/s is achieved, given a specific collar geometry, and velocity ratio $-U_2/U_1 = 0.022$. The velocity ratio $-U_2/U_1$ is defined as the ratio of suction velocity to the jet exit velocity. To document the effects of geometry other tests are conducted with different suction collar dimensions while keeping the countercurrent volumetric flow rate constant. The instantaneous and time-averaged strain rate fields, provided by the Particle Imaging Velocimetry technique, are used to investigate the mechanism responsible for this remarkable increase of the blow-out limit.

18.1 INTRODUCTION

One of the problems in combustors that utilize premixed flames is the attainment of stable performance over an extended range of operation (turndown ratio). The condition, at which the combustion wave is driven back causing the flame to be extinguished when the flow velocity exceeds the burning velocity everywhere in the flow field, is of particular interest to this study. The physical mechanisms responsible for the blow-out limits and flame stabilization of jet flames is still a topic of extensive research [1, 2]. The flame stabilization technique discussed in this paper is aimed to control the velocity gradient in the region close to

the nozzle exit at very high-flow rates. The technique is based on a simplified approach to this complex phenomenon, which can be summarized as follows. The burning velocity depends upon a number of variables such as the mixture strength, the flame temperature, and thermal and molecular diffusivities of the mixture [3]. In practical systems, the nozzle exit velocity profile has spatial variation that greatly influences the flame stability. Typically, the flame is stabilized within the shear layer region where the velocities are lower. When the flow rate is very high, the velocity in the flame exceeds the burning velocity everywhere and the flame blows out. It is generally accepted that the limiting speed that can be achieved while keeping the flame anchored to the nozzle exit is determined by the maximum sustainable strain rate measured at the nozzle exit. By the introduction of a small countercurrent flow, the strain field in the nozzle exit region is effectively altered to achieve conditions for flame anchoring and stabilization.

Typically, the premixed propane flame blow-out occurs at a jet exit velocity on the order of 2 m/s at stoichiometric conditions. Several attempts have been made in the past to increase the blow-out limit by introducing a bluff body, which reduces the gas velocity at the nozzle exit, so that a flame can be anchored at the rim. Such a manipulation of the flow near the nozzle, with the addition of rings, produces a modest extension (< 30–50% increase) of this blow-out limit. Our objective is to develop new strategies, which can extend the limiting velocity by one order of magnitude. We believe that an active shear layer control technique, which has produced significant mixing enhancement in cold and heated jets [4, 5], is worthy of investigation. This hypothesis was confirmed by an early study [6] that reported an increase by threefold of the blow-out velocity. The data in the present paper show that this limit can be further increased. Having established that the mechanism responsible for this increase is hydrodynamic in nature, a Particle Imaging Velocimetry (PIV) system is used to characterize the velocity field, in both the cold reactant flow and the hot post-flame regions, of the premixed jet flame issuing from the modified round nozzle burner.

## 18.2 EXPERIMENTAL APPARATUS AND PROCEDURES

The burner in the test facility, shown in Fig. 18.1, is an axisymmetric nozzle, which is concentrically placed into the circular suction collar. To achieve a top-hat velocity profile with laminar boundary layer at the nozzle exit, a fourth order polynomial with a large contraction ratio of $31.6 : 1$ and an exit diameter of $D = 10.16$ mm is used in the design. The suction collar assembly is connected to a vacuum pump through a series of solenoid valves so that a counterflow, which is in the opposite direction of the fuel–air mixture flow, can be established
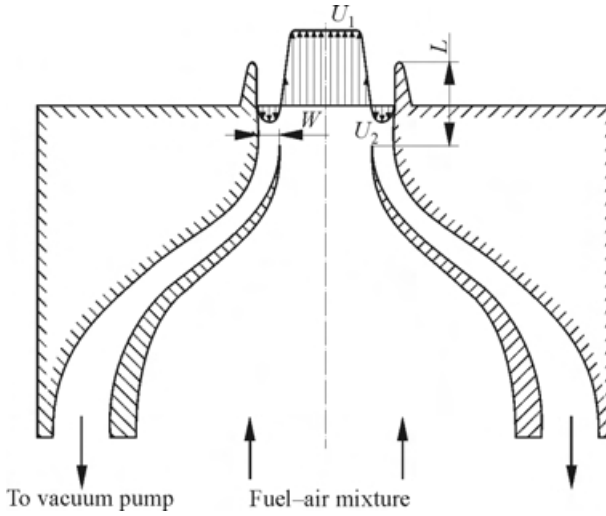
Figure 18.1 Burner configuration with suction collar

uniformly through the gap. The local countercurrent shear layer is thus created in the near field of the jet. The choice of the collar dimensions and shape was based on previous experiments conducted in nonreacting flows by Strykowski and Niccum [7]. The premixed flame is produced using the arrangement shown in Fig. 18.2. Prior to mixing and propane, fuel flow rates are metered and monitored throughout the experiment by means of electronic mass flow meters. Seeding of the flow is achieved with solid particles introduced into the air stream through a settling chamber by means of an aerosol generator. The particle seeder consists of a fluidized bed connected to a cyclone for the efficient removal of large particles or particle agglomerates. The seeded air and the fuel are thoroughly premixed and supplied to the nozzle burner through a mixing chamber. In this facility, the solid seeding for both the primary jet and the environment air is aluminum oxide particles with a nominal diameter of 0.3 μm.

In the experiment parameters such as the equivalence ratio (Φ) of the mixture and the velocity ratio, $r = -U_2/U_1$, between the mixture flow (U_1) and counterflow (U_2) are varied. For most of the experiments, the extension length (L) of the collar above the burner exit and the gap width (W) between the nozzle exit and the collar were kept constant as $L/D = 1.0$ and $W/D = 0.23$, respectively. However, these parameters can be easily varied, and their influence on the total performance of the system is also evaluated. Experimental results show that the nozzle exit velocity varies from 3.9 to 30 m/s corresponding to the Reynolds number of $2.6 \cdot 10^3$ to $2 \cdot 10^4$, based on the nozzle diameter and the exit velocity.
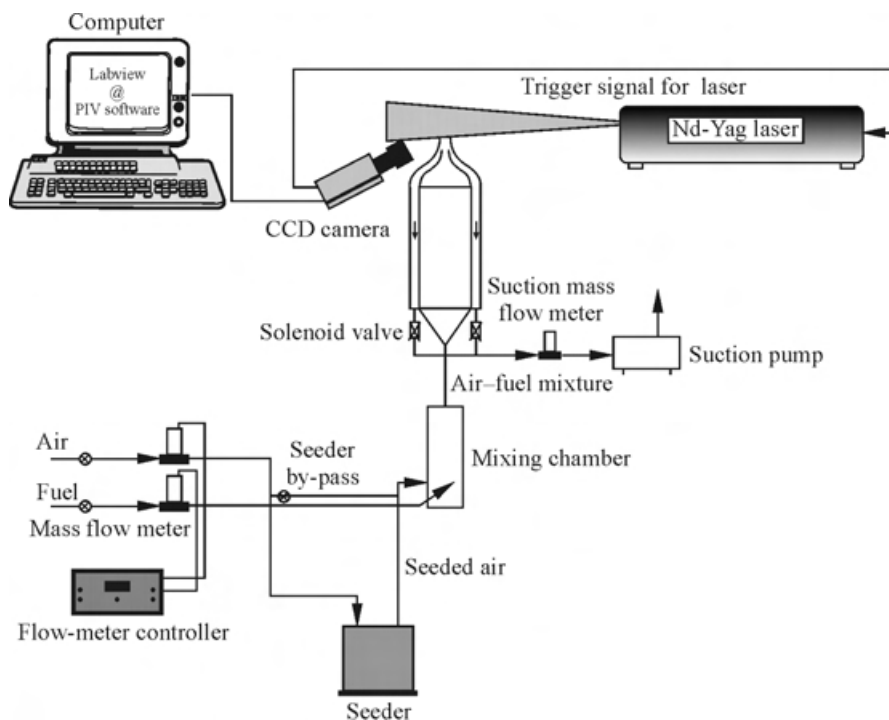
Figure 18.2 Experimental facility

Measurement Techniques and Instrumentation

The main feature of the Particle Image Velocimeter used in this experiment is its capability to record two images in quick succession, from which the velocity field is derived by a cross-correlation algorithm. This is possible by integrating the PIV system's two main components: the *Kodak* ES1.0 digital video camera and the *Lumonics* Nd–Yag laser illumination system, with adjustable repetition rate from 10–20 Hz. By proper control of the Pockells cell timing and applied voltage, the laser produces two illumination pulses with varied interval from 0.1–200 μs. The heart of the camera is the CCD interline transfer sensor, KAI-1001, with a resolution of $1008(H) \times 1018(V)$ pixels. Each square pixel measures 9 μm on the side with 60% fill ratio with microlens, and a center to center spacing of 9 μm. The camera is also equipped with a fast electronic shutter and outputs 8-bit digital images, via a progressive scan readout system, at a rate of 30 frames per second.

The unique feature of the *Kodak* ES1.0 camera, implemented by *Kodak* in collaboration with the FMRL, is its ability to be operated in the "triggered

dual-exposure mode." Operation in this mode is possible due to the CCD sensor architecture, which incorporates both a light sensitive photodiode array and a masked register array. During the exposure cycle, light is converted to charge in the photodiode area of the array; after exposure, the charge on the photodiode is transferred to the masked area of the array. The maximum time for complete transfer of the charge is 5 μs, but using a programming feature of the camera to control electronics, this time setting can be made as small as 1 μs. However, image quality may not be preserved, as the times less than 5 μs may be too short to ensure that all charge is transferred, especially in the case of very high-intensity images. The image acquisition in the "triggered dual-exposure mode" is initiated by an external trigger signal. The first image is illuminated by the first laser pulse, which is triggered in advance, to account for the usual delay between flash lamp trigger and Pockells cell trigger, i.e. by 160–240 μs. Once the first image is transferred to the read-out section of the sensor, the charge is depleted from the photodiode, and a second laser pulse re-illuminates the sensor. To achieve total separation between the two images, the second trigger pulse to the Pockells cell of the laser is delayed with respect to the first pulse by an amount that exceeds 5 μs.

With the above-described arrangement it is possible to acquire up to 15 image pairs per second. This instrument is well suited for use in flows with velocity reversals and wide dynamic range from very low speed (millimeters per second) up to very high speed (hundreds of meters per second). This is because the image pairs are recorded in separate frames, with variable separation from 1 μs up to several hundreds of microseconds. The image data acquisition is done using an *Imaging Technologies* ICPCI board, which resides on a single slot of the PCI bus of a personal computer. The computer's CPU is an *Intel* 150 MHz Pentium with 64 Mbytes of RAM, running under the NT operating system.

To produce the displacement field the digital image pairs are processed with a matching technique. In this approach a cost function, C, is maximized or minimized. The cost function is set up to model the match between two corresponding regions of the images. Typically, if I_1 and I_2 are the image intensity distributions of the first and the second image, one can write:

$$C\left(\vec{s}\right) = C\left\{I_1\left(\vec{x}\right), I_2\left(\vec{x}\right)\right\}$$

Herein it is assumed that the second image is an exact translated copy of the first image, therefore

$$I_2\left(\vec{x}\right) = I_1\left(\vec{x} - \Delta\vec{s}\right)$$

or

$$I_2\left(\vec{x}\right) = I_1\left(\vec{x}\right) \cdot \delta\left(\vec{x} + \Delta\vec{s}\right)$$

The average image translation is represented by $\Delta\vec{s}$ and the function I_2 usually represents a small block (interrogation window) in a larger image, I_1.

The match is obtained for the value $\Delta\vec{s}$ that maximizes (or minimizes) C. The cost function chosen to maximize is the cross-correlation, G, defined as:

$$G(\vec{x}) = I_1(\vec{x}) \cdot I_2(\vec{x}) = \int\limits_{-\infty}^{\infty} I_1(\vec{x}) I_2(\vec{x} - \vec{u}) \, d\vec{u}$$

The cross-correlation is effectively computed using Fourier transforms. Consider the Fourier transform of the first exposure image:

$$\Im\{I_1(\vec{x})\} = \int\limits_{-\infty}^{\infty} I_1(\vec{x}) \cdot e^{-2\pi j(\vec{x}\cdot\vec{\omega})} d\vec{x} = \widetilde{I}_1(\vec{\omega})$$

where $\Im$ is the Fourier transform operator, $j = \sqrt{-1}$, and $\vec{\omega}$ is the spatial frequency coordinate. Similarly, the Fourier transform of the second exposure image is:

$$\Im\{I_2(\vec{x})\} = \int\limits_{-\infty}^{\infty} I_1(\vec{x}) \cdot \delta(\vec{x} + \Delta\vec{s}) \cdot e^{-2\pi j(\vec{x}\cdot\vec{\omega})} d\vec{x} = \widetilde{I}_1(\vec{\omega}) \cdot e^{-2\pi j(\Delta\vec{s}\cdot\vec{\omega})}$$

The cross-correlation function, G, is obtained computing the inverse Fourier transform, $\Im^{-1}$, of the product of the multiplication of the transform of the first image by the complex conjugate of the transform of the second image,

$$G(\vec{x}) = \Im^{-1}\left\{\widetilde{I}_1^{\,2}(\vec{\omega}) \cdot e^{-2\pi j(\Delta\vec{s}\cdot\vec{\omega})}\right\} = \Im^{-1}\left\{\widetilde{I}_1^{\,2}(\vec{\omega})\right\} \cdot \delta(\vec{x} + \Delta\vec{s})$$

The cross-correlation function G is thus the transformed image intensity pattern displaced with respect to the origin by the average displacement coordinates. The peak position is found with sub-pixel resolution by means of a Gaussian interpolator as described by Lourenco and Krothapalli [8].

One of the main shortcomings of the conventional processing scheme presented in the previous paragraph is the inherited spatial resolution. This limitation is due to the averaging caused by the typical correlation window size, of the order of 16–32 pixel. Since the measurement represents an average over the correlation window, it can be weighted towards the areas of the window with higher seeding density and/or reduced velocity. This is especially restricting when the technique is applied to the study of flows with large velocity and/or seeding density gradients, e.g., reacting flows.

To achieve velocity data with high spatial resolution the processing algorithm is further developed. With the new processing approach the particle images themselves comprise the interrogation region, which has sizes ranging from 3 to 4 pixel square. Such a scheme will allow not only accurate representation of the gradient fields, but measurements in the proximity of a solid surface, as well.

The displacement between image pairs is found in the usual manner by means of a cross-correlation, and a velocity (displacement) vector is assigned at the mid-distance between image pairs. Therefore, each particle pair contributes to a second-order approximation of the velocity. However, these velocities are evaluated in an unstructured grid. The flow field is described at any point by an analytical function using a least squares fitting algorithm. The function that is used is a second-order polynomial,

$$\vec{u} = \vec{a} \cdot x^2 + \vec{b} \cdot x + \vec{c} \cdot y^2 + \vec{d} \cdot y + \vec{e} \cdot x \cdot y + \vec{f}$$

The marked advantage of this approach is that the field is described at any point with accuracy of second order, including the derivatives that are found by differentiating the previous equation:

$$\frac{\partial}{\partial x} \vec{u} = 2\vec{a} \cdot x + \vec{b} + \vec{e} \cdot y$$

$$\frac{\partial}{\partial y} \vec{u} = 2\vec{c} \cdot y + \vec{d} + \vec{e} \cdot x$$

For the purposes of presentation, the velocity field is usually presented at regular intervals. This new scheme is very efficient and incorporates a vector validation procedure, making it independent of operator intervention. The time it takes to compute a vector field depends on the computer hardware and it ranges from 350 mesh points per second on a PC 150 MHz Pentium to 1400 mesh points per second on a 200-megahertz dual Pro.

18.3 RESULTS AND DISCUSSION

18.3.1 Global Observation

It is well known that in a jet flame blow-out occurs if the air–fuel mixture flow rate is increased beyond a certain limit. Figure 18.3 shows the relationship between the blow-out velocity and the equivalence ratio for a premixed flame. The variation of blow-out velocity is observed for three different cases. First, the suction collar surrounding the burner is removed and the burner baseline performance obtained. Next, the effect of a suction collar itself without suction flow is documented. These experiments show that for the nozzle geometry studied, the free jet flame (without the presence of the collar) blows out at relatively low exit velocities, e.g., 2.15 m/s at $\Phi = 1.46$, whereas for $\Phi > 2$ flame lift-off occurs. When the collar is present without the counterflow, the flame is anchored to the collar rim and blows out with the velocity of 8.5 m/s at $\Phi = 4$. Figure 18.4a shows the photograph of the premixed flame anchored to the collar rim. The collar appears to have an effect similar to a bluff-body flame stabilizer. The third
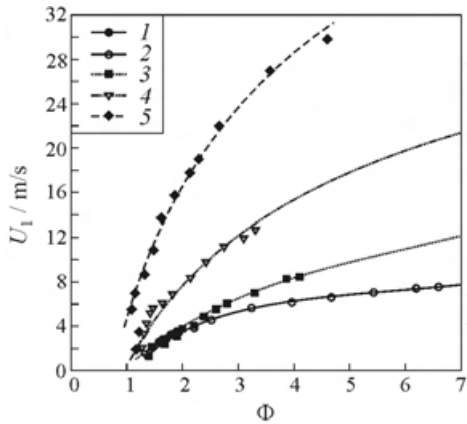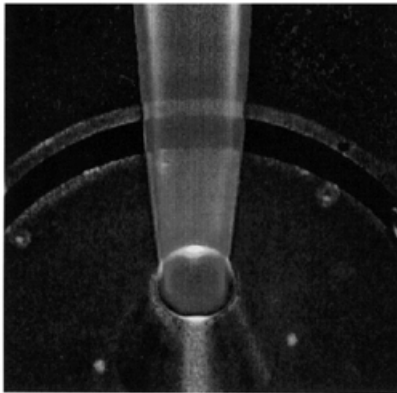
Figure 18.3 Variation of blow-out velocity with equivalence ratio. Suction collar $L/D = 1.0$, $W/D = 0.23$: 1 — free jet blow-off; 2 — free jet lift-off; 3 — $U_2 = 0$ m/s; 4 — 0.18; and 5 — 0.60 m/s

group of experiments was performed when the suction flow is activated. In this case a dramatic increase in blow-out velocity is observed as shown in Fig. 18.3. For example, with the counterflow velocity of 0.6 m/s, the blow-out velocity is extended to 30 m/s at $\Phi = 4$. Under these conditions, the flame anchors to the nozzle rim as shown in Fig. 18.4b. When using a Bunsen burner flame, the counterflow was found to be effective even for lean mixtures ($\Phi = 0.59$) [6]. Hence, counterflow shear layer control is quite effective in extending the blow-out limit of premixed flames by an order of magnitude for a range of equivalence ratios.

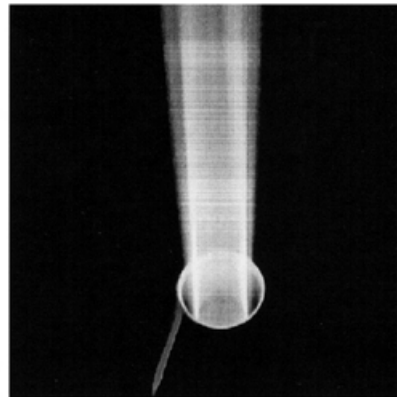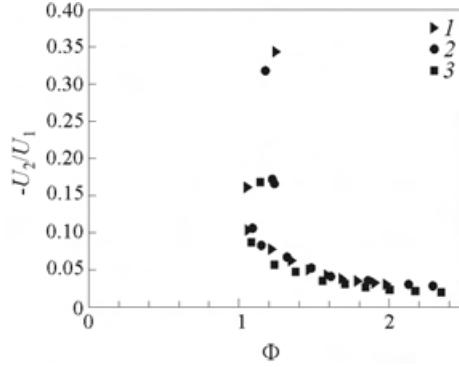The effect of suction velocity on the flame stabilization can be observed in Fig. 18.5, where the suction mass flow rate is kept constant while varying Φ. For a given Φ there is a limiting velocity ratio $(-U_2/U_1)$ below which the flame will blow out. For example, at $\Phi = 1$, the limiting velocity ratio is about 0.1. At higher values of Φ, this ratio decreases as shown in the figure.

Figure 18.4 Propane–air premixed flame attached to suction collar rim for $-U_2/U_1 = 0.0$ (a), and to nozzle exit for $-U_2/U_1 = 0.022$ (b)

Also, the data for different gap widths are included in the figure. The gap width seems to have an insignificant effect on the limiting velocity ratio.

18.3.2 Detailed Observations

A detailed investigation of the flow, using PIV, with and without control is carried out. The instantaneous velocity field is obtained by the method described in section 18.2, with interrogation regions of 6×6 pixels corresponding to a physical dimension of 0.36×0.36 mm. Typical mean and instantaneous velocity fields of the near region of a flame without suction at $U_1 = 3.9$ m/s and $\Phi = 2.0$ are shown in Figs. 18.6a and 18.6b, respectively.

Figure 18.5 Variation of velocity ratio with equivalence ratio for different collar dimensions with $Q_2 = 5.5 \cdot 10^{-5}$ m^3/s: 1 — $W/D = 0.21$ ($U = 0.71$ m/s); 2 — 0.23 ($U = 0.60$ m/s); and 3 — 0.31 ($U = 0.41$ m/s)
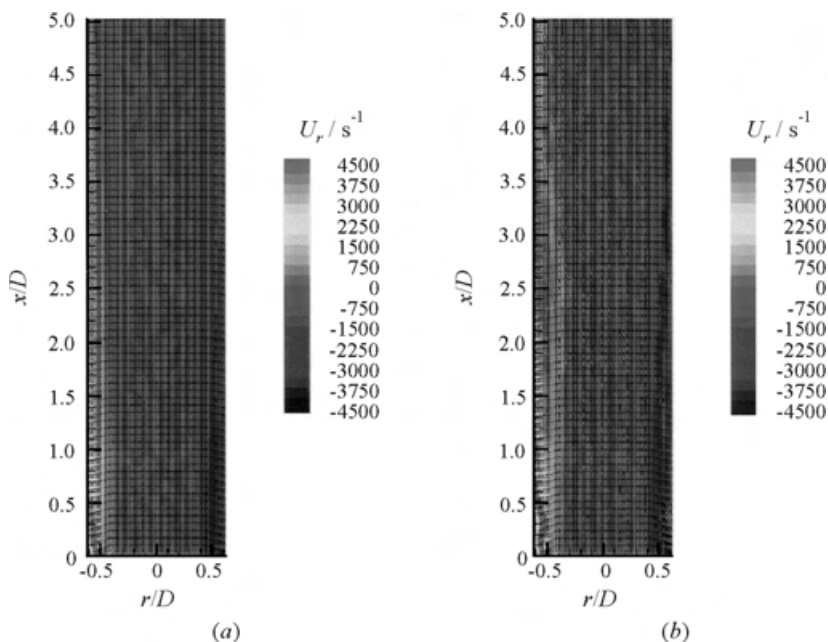
The mean velocity field is obtained by averaging 60 instantaneous velocity fields. For these conditions the flame is anchored to the collar lip. Superimposed on
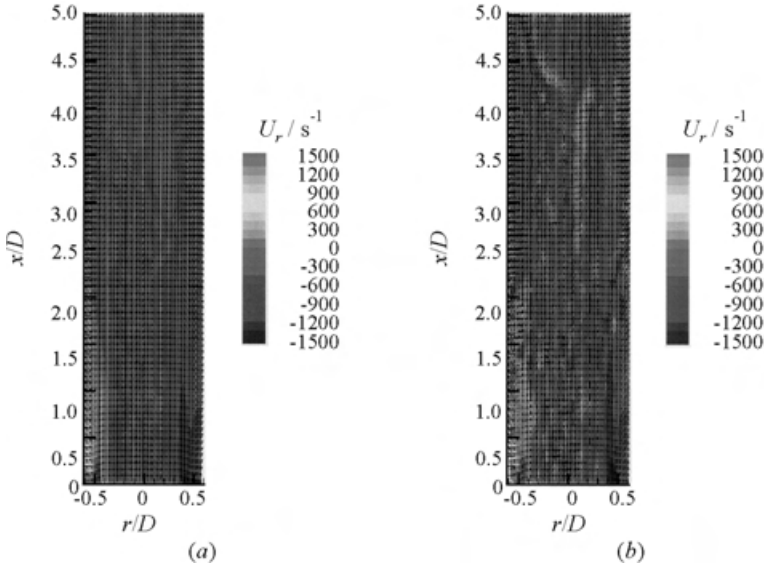

Figure 18.6 Time-averaged strain U_r and velocity field (a) and instantaneous strain and velocity field (b) of the premixed flame for $-U_2/U_1 = 0.0$. The scale of the velocity vector length is 3.6 m/s per 1 mm
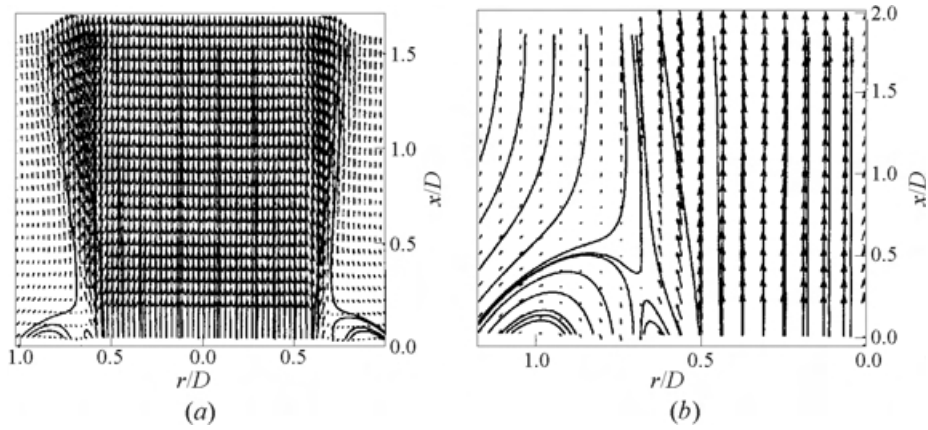
Figure 18.7 Time-averaged strain U_r and velocity field (*a*) and instantaneous strain and velocity field (*b*) of the premixed flame for $-U_2/U_1 = 0.022$. The scale of the velocity vector length is 7.2 m/s per 1 mm
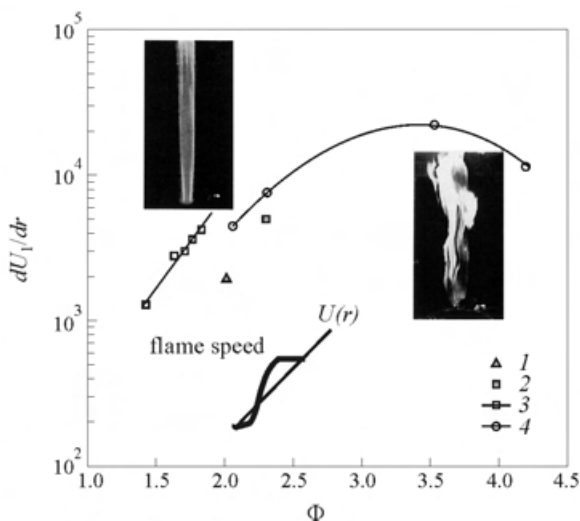
Figure 18.8 Variation of strain rate with equivalence ratio for a free jet flame: *1* — $U_r = 0.0$, *2* — $U_r = 0.17$ m/s, *3* — blow-out, and *4* — lift-out

Figure 18.9 Velocity and streamline pattern (*a*) and near-exit region flow details (*b*)

the velocity field is the magnitude of the velocity gradient dU_1/dr shown in gray color contours. The maximum velocity gradient observed at the base of the flame is about 2000 s^{-1}. However, when the suction is applied, the magnitude of the velocity gradient has increased to about 5000 s^{-1} as shown in Fig. 18.7. The conditions of the flame are: $U_1 = 7.8$ m/s; $\Phi = 2.3$; and $U_2 = -0.022U_1$. The magnitude of the velocity gradient sustained under these conditions is considerably larger than what is normally observed in a premixed laminar flame [9]. For a premixed jet flame with an exit top-hat velocity profile with laminar boundary layers (without the collar), the measured velocity gradient for blow-out and lift-off is shown in Fig. 18.8 for different equivalence ratios. The data corresponding to the two cases shown in Figs. 18.6 and 18.7 are also included in Fig. 18.8. It is clearly observed that the values of the velocity gradient do not exceed the free jet values.

In order to ensure that most of the counterflow is entrained from the ambient medium, PIV pictures are taken of the near field as shown in Fig. 18.9. These figures clearly show that the flow in the vicinity of the nozzle exit is significantly altered by the presence of the suction flow. The velocity field and the associated streamline pattern show a region of reversed flow clearly suggesting the presence of a countercurrent shear layer. It is also clear that most of the reverse flow is the entrained ambient air.

18.4   CONCLUDING REMARKS

The instantaneous velocity field measurements indicate that a secondary stream, travelling in the direction opposite to the primary flow, is established within the collar to create the countercurrent shear layer. The dynamics of the countercurrent shear layer is conducive to the stabilization of the premixed jet flame up to

an exit velocity of 30 m/s. The countercurrent velocity required to accomplish this control is $U_2 = -0.02U_1$.

The results presented above clearly demonstrate the merits of the countercurrent shear layer control as a flame stabilization technique. With the use of the high-resolution PIV, the near flame structure is measured with sufficient detail to obtain the velocity gradients with accuracy. From these measurements, it is observed that the transverse velocity gradient dU_1/dr assumes large values at the nozzle exit as compared to that of laminar premixed Bunsen burner flames.

The physical mechanism responsible for this control is currently being investigated. The attractiveness of this technique is its capability to extend the range of operation over an order of magnitude.

ACKNOWLEDGMENTS

REFERENCES

1. Peters, N., and F. A. Williams. 1983. Lift-off characteristics of turbulent jet diffusion flames. *AIAA J.* 21:423–29.
2. Broadwell, J. E., W. J. A. Dham, and M. G. Mungal. 1985. Blow-out of turbulent diffusion flames. *20th Symposium (International) on Combustion Proceedings*. Pittsburgh, PA: The Combustion Institute. 303–10.
3. Lewis, B., and G. von Elbe. 1961. *Combustion, flames and explosions of gases*. New York: Academic Press.
4. Strykowski, P. J., A. Krothapalli, and D. Wishart. 1993. Enhancement of mixing in high-speed heated jets using a counterflowing nozzle. *AAIA J.* 31:2033–38.
5. Strykowski, P. J., A. Krothapalli, and S. Jendoubi. 1996. The effect of counterflow on the development of compressible shear layers. *J. Fluid Mechanics* 308:63–96.
6. Shen, H., A. Krothapalli, L. Lourenco, S. Lonnes, D. L. Hofeldt, and P. J. Strykowski. 1995. The application of countercurrent shear layer control to combustion processes. *8th ONR Propulsion Meeting Proceedings*. Eds. G. D. Roy and F. A. Williams. La Jolla, CA: University of California at San Diego. 287–95.
7. Strykowski, P. J., and D. L. Niccum. 1991. The stability of countercurrent mixing layers in circular jets. *J. Fluid Mechanics* 227:309–43.
8. Lourenco, L., and A. Krothapalli. 1995. On the accuracy of velocity and vorticity measurements with PIV. *Experiments Fluids* 18:421–28.
9. Mungal, M. G., L. Lourenco, and A. Krothapalli. 1995. Instantaneous velocity measurements in laminar and turbulent premixed flames using on-line PIV. *Combustion Science Technology* 106:239–65.

Chapter 19

CONTROL OF OSCILLATIONS IN PREMIXED GAS TURBINE COMBUSTORS

R. Bhidayasiri, S. Sivasegaram, and J. H. Whitelaw

Pressure oscillations with RMS value up to 10 kPa in two models of lean-burn gas turbine combustors, with heat release around 100 kW, have been actively controlled by the oscillation of fuel flow. The flames were stabilized behind an annular ring and a step in one arrangement, and downstream of an expansion and aided by swirl in the other. Control was sensitive to the location of addition of oscillated fuel. Oscillations in the annular flow were attenuated by 12 dB for an overall equivalence ratio of 0.7 by the oscillation of fuel in the core flow and comprising 10% of the total fuel flow, but negligibly for equivalence ratios greater than 0.75. Oscillation of less than 4% of the total fuel in the annulus flow led to attenuation by 6 dB for all values of equivalence ratio considered. In the swirling flow, control was more effective with oscillations imposed on the flow of fuel in a central axial jet than in the main flow, and oscillations were ameliorated by 10 dB for equivalence ratio up to 0.75, above which the flame moved downstream so that the effectiveness of the actuator declined. The amelioration of pressure oscillations resulted in an increase in NO_x emissions by between 5% and 15%.

19.1 INTRODUCTION

Environmental concerns have led to the development of combustors which burn lean mixtures with consequently low NO_x emissions. One limitation in ducted flows stems from naturally occurring oscillations which can have amplitudes sufficient to do physical damage, and these may stem from acoustic coupling in a range of equivalence ratios from 0.75 to 1.2 and from poor stabilization close to the lean flammability limit. Longitudinal frequency modes dominated the flows with frequencies of the order of 100 Hz [1–4] and generally gave rise to amplitudes larger than those for transverse modes with frequency of the order of

1 kHz, which were, in any case, more readily ameliorated by modifications to the combustor duct [5]. Ducts with exit nozzles sometimes gave rise to bulk mode (Helmholz) frequencies which were associated with poor flame stabilization [6, 7]. These investigations were characterized by comparatively simple geometric configurations and by heat release rates far below those of practical combustors.

Effective methods for the passive suppression of combustion oscillations associated with longitudinal and bulk mode frequencies have been developed. But, as pointed out in [8], implied modifications to the flow arrangement were unacceptable in engine practice. Consequently, active control methods have been successfully developed to suppress combustion oscillations by imposing oscillations on the flow in a way that counteracts the naturally occurring oscillations by oscillation of the pressure field [9, 10], the bulk flow rate [11], the flow of gaseous fuel [8, 12, 13], a liquid-fuel spray [14], the ignition of a mixture of gaseous fuel and air [15], and a spray of water [16]. Comparison of the performance of the various control methods [14] suggested that control by the oscillation of the flow of fuel is the most appropriate for practical combustors. However, the conclusions were based on experiments with simple configurations and modest heat release rates.

The experiments reported here allow evaluation of active control of naturally occurring oscillations in the two ducted-flow arrangements shown in Figs. 19.1 and 19.2 with a main flow of a lean fuel–air mixture and a secondary flow of a richer mixture. The geometrical configurations are models of two land-based industrial gas turbine combustors developed for use with turbines for power generation [17]. In the first model, the flame was stabilized on a combination of an annular ring and a backward-facing step, and in the second behind an expansion and assisted by swirl. Preliminary investigations [18–20] identified the importance of geometric parameters in the first flow arrangement. For example, the amplitude of oscillations was smallest when the two flame holders were co-planar. The second-flow arrangement combined stabilization by a sudden expansion and swirl, with unpremixedness as an additional variable. Results from the previous investigations to quantify the influence of swirl on ducted premixed flames [21] and on open quarl stabilized flames [22, 23] have been utilized.

Both practical combustors had pilot streams carrying a fuel–air mixture richer than that of the main flow. These could also serve as a convenient location for the addition of oscillations to the fuel flow to control naturally occurring oscillations. Oscillation of fuel in the main flow will be more effective if it is applied close to the entry to the burner. Hence the present study examined the possibility of control by oscillation of fuel at locations corresponding to both portions of the combustor in-flow.

The experiments with the first flow arrangement involved nominal heat release rates of the order of 100 kW, with up to 10% of the total mass flow in the pilot stream and associated with up to 15% of the total heat release. In the second-flow arrangement, the pilot stream of the practical combustor was re-
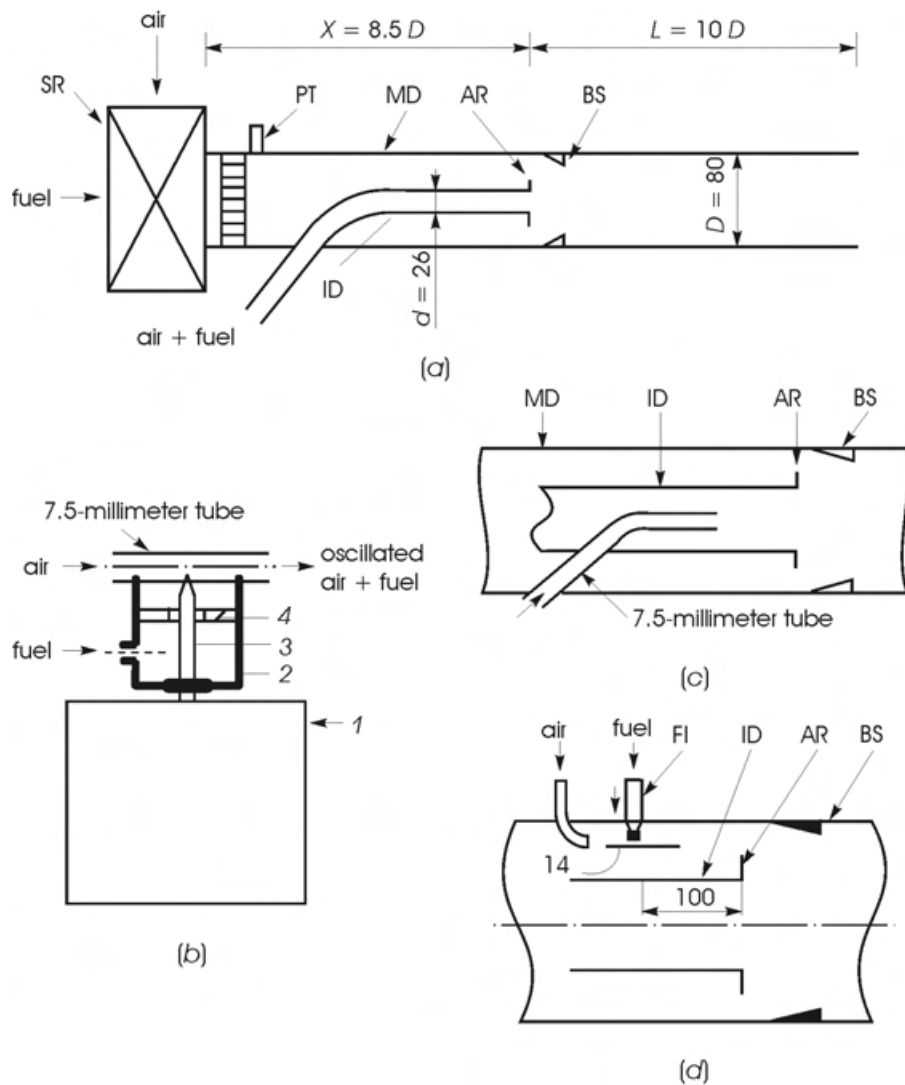
Figure 19.1 Annular flow arrangement and devices to oscillate fuel flow; AR — annular ring; BS — backward-facing step; FI — fuel injector; ID — inner duct; MD — main duct; PT — pressure transducer; SR — swirl register (all dimensions are in mm). (*a*) annular flow arrangement; (*b*) needle valve arrangement to oscillate fuel flow: *1* — vibrator, *2* — receiver, *3* — needle, *4* — spider; (*c*) arrangement to deliver oscillated fuel to inner duct; and (*d*) arrangement to oscillate fuel flow with three circumferentially equispaced injectors
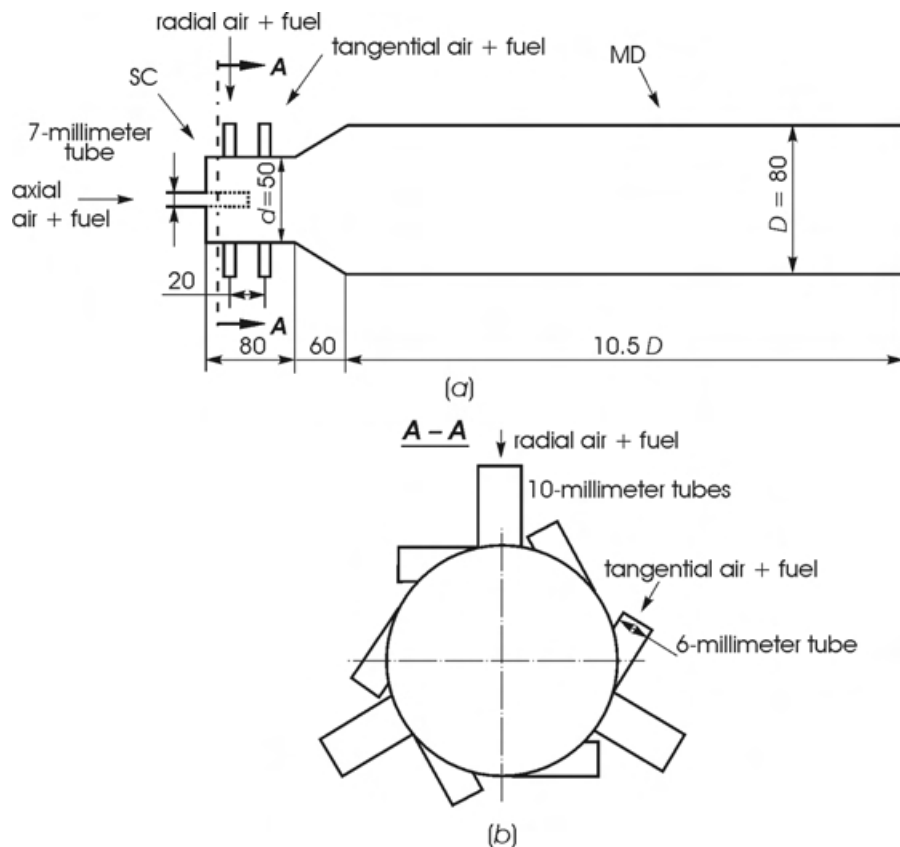
Figure 19.2 Flow arrangement with swirl (*a*): MD — main duct; SC — swirler (all dimensions are in mm); and swirler arrangement (section *A*–*A*) (*b*)

placed by an axial jet which carried up to 6% of the total air flow and up to 12% of the total fuel flow. The flammability and stability limits, and the amplitude and frequency of oscillations, were quantified in both arrangements as a function of flow rates of fuel and air. The duct lengths upstream and downstream of the annular ring were additional variables in the first flow arrangement, and the swirl number and the degree of unpremixedness in the second.

Active control was implemented by imposing the oscillations at the dominant frequency but with a difference in phase, and the control strategy was similar to that of [8] and only essential details are provided here. The actuators used to impose oscillations on the flow of fuel have been characterized in [14], and the details given here are limited to those most relevant to the present experiments.

The flow arrangements and the experimental procedure are described in the following section. The results are presented in section 19.3, and their implications are discussed in section 19.4. Section 19.5 summarizes the important conclusions.

19.2   FLOW ARRANGEMENTS
AND EXPERIMENTAL PROCEDURE

The principal dimensions of the burners are shown in Figs. 19.1 and 19.2. Figure 19.1 also shows the arrangements for oscillating the fuel flow. The flow arrangement shown in Fig. 19.1 comprised two coaxial ducts with the annular space between them carrying the main premixed flow, and the inner duct carrying the richer pilot stream. All flows entered the combustor through flexible pipes connected to pressurized supplies of air and fuel. The main air and fuel were mixed in a swirl register and flowed past a honeycomb flow straightener before burning downstream of the annular flow section, and the richer flow in the inner duct was premixed upstream of the point of entry to the combustor. The flame stabilized behind the annular ring of area blockage ratio 0.29 located at the exit of the inner duct, and a backward-facing step of area blockage ratio 0.35 located downstream of the ring.

In the flow arrangement shown in Fig. 19.2, the main air and fuel were premixed upstream of their entry through the swirler with its six tangential and three radial inlets. The equivalence ratios of the fuel–air mixtures entering in the tangential and radial directions were independently varied by varying the proportion of mixture, and the swirl number was varied between zero and approximately 3.75. An axial inlet at the upstream end of the swirler introduced an oscillated mixture of fuel and air. In both flow arrangements, experiments were carried out with duct lengths that ensured complete combustion and favored the occurrence of naturally occurring acoustic oscillations of large amplitude.

Two devices were used to oscillate the flow of part of the fuel. In one, a needle valve was mounted on a vibrator (*Ling*, 403) and was driven by a power amplifier (*Derritron*, TA120) to provide a sinusoidally oscillating fuel flow which was injected radially into a tube of diameter 7.5 mm carrying a steady flow of air that delivered the oscillated fuel flow to the combustor. In the annular flow arrangement, the oscillated fuel flow comprised a part of the fuel flow through the inner duct and entered the duct as an axial jet at the centre as shown in the figure. The same device was used in the swirling flow arrangement, to provide the entire fuel flow through the axial inlet to the swirler and, alternatively, through one of the six tangential inlets, in experiments to control pressure oscillations by the oscillation of fuel in the main flow. The mean fuel flow rate was manually

controlled and the frequency and amplitude of oscillation were controlled by software. Fluid dynamic damping limited the RMS value of the oscillated input from the needle valve to a maximum of 0.35 of the mean fuel flow rate through the device [14]. With up to 12% of the total fuel subject to oscillation by the needle valve, the RMS oscillation of heat release was around 4.2 kW compared with a total heat release rate of around 100 kW.

The second device comprised a set of three circumferentially located pintle-type injectors (*Keihin*, 10450-PG7-0031) to inject fuel radially into the main duct of the first flow arrangement as near-rectangular pulses. The frequency and duration of fuel injection were software controlled, and the fuel flow from each injector was delivered close to the outer edge of the annular ring flame holder by a cross-jet of air (1.2×5 mm), directed along the duct axis with exit velocity up to 100 m/s. The amplitude of the oscillated input was limited by the volume injection rate of the injectors. Propane, rather than methane, provided up to 3.5 kW of the total heat release of around 100 kW. With fluid dynamic damping, the RMS of the oscillated fuel flow corresponded to a heat release of around 1.8 kW.

Transition to combustion with discrete-frequency oscillations was associated with a 0.01 change in overall equivalence ratio and an increase of between 5 and 10 dB in free-field sound level (*Brüel & Kjaer* 4234, meter type 2218) measured at a distance of 1.5 m from the combustor axis in its exit plane. These oscillations were actively controlled using a feedback control circuit that modified the phase and amplitude of the feedback signal from a pressure transducer (*Kistler* 6121, charge amplifier 5007) located close to the upstream end of the duct, and the pressure antinode of oscillations in both flow arrangements, to provide the input signal to the controlling actuator (the device to oscillate fuel flow). The phase difference was predetermined, and the amplitude of input was either incremented or decremented in even steps according to whether the amplitude of feedback pressure signal increased or decreased during the preceding cycle [8]. The phase of the input signal was variable in increments of around $1.4°$ while control was in progress. The amplitude of the pressure oscillations and their attenuation were quantified using a spectrum analyzer (*Spectral Dynamics*, 340) that processed the pressure signal to provide the value of the discrete frequency to within 1.25 Hz and the RMS pressure fluctuation to within 0.01 kPa.

The mass flow rates of air and fuel were measured with a set of float-type flow meters to a precision of 1%, and the overall equivalence ratio was determined with an uncertainty of less than 2%. The swirl number of the second-flow arrangement was defined at the exit of the swirler as

$$\mathrm{Sw} = \frac{\int\limits_0^{d/2} 2\pi r^2 \rho u w \, dr}{(d/2)\int\limits_0^{d/2} 2\pi r \rho u^2 \, dr}$$

where u and w are the local mean velocity components in the axial and tangential directions, respectively, ρ is the density, and d is the diameter of the swirler. They were based on velocity measurements in isothermal flow, obtained with a five-hole probe of overall diameter 3 mm for values of swirl number less than unity. Larger swirl numbers were evaluated by extrapolation on the basis of increase as the square of the ratio of the tangential to overall air flow rates. It was varied between 0.6 and 3.75 to quantify the effect of swirl number on combustion oscillations.

A water-cooled sampling probe of internal diameter 1 mm and external diameter 5 mm with a 3-meter long heated line was used to measure concentrations of unburned hydrocarbon (flame ionization detector, *Analysis Automation*, 520) and NO_x (chemiluminescence analyzer, *Thermal Environment Instruments*, 42) at the combustor exit on a wet basis. The former, measured to a precision of the order of 1 ppm, was used to ensure complete consumption of fuel within the duct, and the latter with a precision of around 0.2 ppm was used to quantify the effect of oscillations on NO_x emissions.

19.3   RESULTS

The results will be presented in two sub-sections, corresponding to the two flow arrangements. The emphasis is on the control of naturally occurring oscillations, but consideration is also given to the implications of oscillations for stabilization and NO_x emissions, particularly in relation to lean-burn combustors. Concentrations of unburned hydrocarbon at the combustor exit confirmed that a downstream duct length of around 10 duct diameters (D) was sufficient to ensure complete consumption in both flow arrangements, and this length was used in all the results reported here. Since oscillations of large amplitude could not be sustained at values of overall equivalence ratio around 0.6 as in practical combustors, experiments in active control were carried out with values of equivalence ratio up to 0.9 that ensured large amplitudes.

19.3.1   Annular Flow Arrangement

Measurements were obtained with a ratio of flow rates (flow rate in the annulus/flow rate in the inner duct) of 9, so that the bulk mean velocities upstream of the annular ring were nearly equal to those in practical combustors. Deviations from this ratio were allowed where they provided insight into the nature of the oscillations. Results relating to the influence of the geometric and flow parameters on flame stabilization and combustion oscillations are presented first,
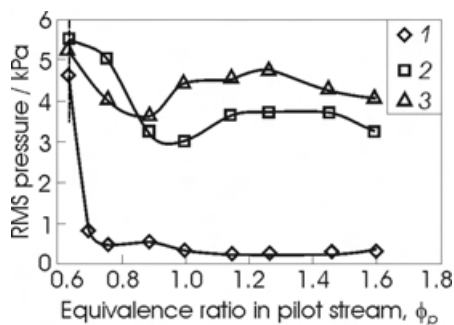
Figure 19.3 Influence of equivalence ratio on antinodal RMS pressure fluctuation; annular flow arrangement, bulk mean velocity in main flow, $U_m = 7.5$ m/s; bulk mean velocity in pilot stream, $U_p = 8$ m/s; $Re_m = U_m D/\nu = 40{,}000$, axial separation between annular ring and step, $\Delta = 0.5D$. $1 - \phi_m = 0.62$; $2 - 0.70$; $3 - 0.76$; dashed line corresponds to flame detachment
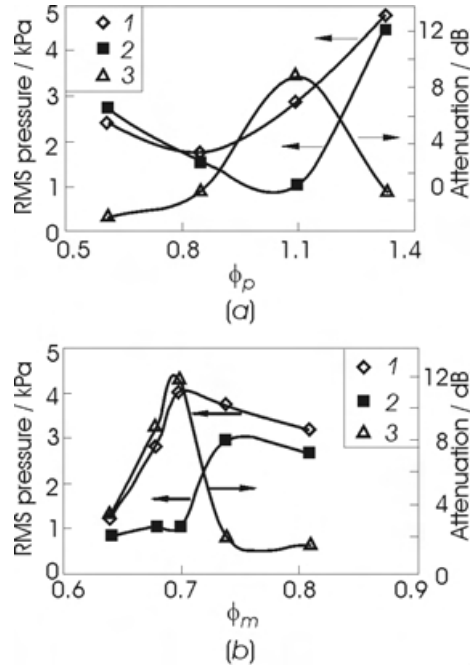
followed by those relating to the active control of naturally occurring oscillations.

Equivalence ratios greater than around 0.6 in the pilot stream and in the main flow ensured that the flame stabilized behind the step and the annular ring as in a practical combustor, whereas equivalence ratios of 0.7 or more in the main flow led to rough combustion. Tests with upstream duct lengths between $5.5D$ and $12D$ showed that, with flame stabilization behind the annular ring as well as the step as intended, oscillations were dominated by the quarter-wave frequency of the duct length upstream of the flame holder. The influence of the equivalence ratio of the pilot stream on the amplitude of oscillations was small, except for values around 0.62 at which the amplitude increased as the lean limit was approached (Fig. 19.3), causing the flame to detach from the annular ring and stabilize on the step. This increase in amplitude close to the lean limit was associated with poor stabilization at the inner edge of the ring, as with the bulk-mode oscillations observed close to the extinction limit in premixed flames in ducts with an exit nozzle [6]. Combustion oscillations also caused the flame to detach from the annular ring for equivalence ratio around 0.9 and stabilize on the step alone to give rise to antinodal RMS pressure fluctuations of around 2 kPa, compared with more than 5 kPa with the flame attached to the annular ring.

An oscillated fuel flow was provided in the form of a central jet within the duct carrying the pilot stream. The dimensions of the tube carrying the oscillated flow implied that the mean velocity and equivalence ratio of the jet had to be larger than that of the pilot stream to enable the oscillation of at least 5% of the total fuel flow. An examination of the influence of the bulk mean velocities of the pilot stream and the central jet on the amplitude of oscillations in this flow arrangement showed that, for the present range of flow conditions, values of the bulk mean velocity of the pilot stream less than that of the annular flow had no effect on the amplitude of oscillations, although larger values led to a decrease in amplitude [20]. The amplitude was also insensitive to the bulk mean velocity of the oscillated jet for values up to 3.5 times
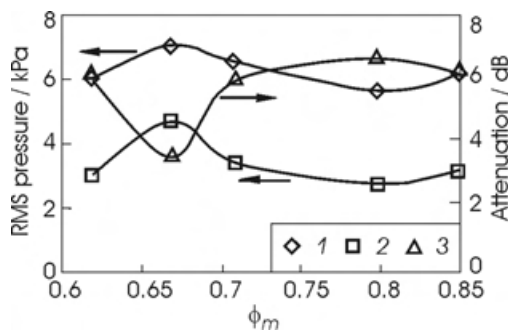
that of the annular flow, partly due to the decay of the jet within the inner duct. Thus active control was implemented with a bulk mean velocity in the pilot stream equal to that in the main flow and that of the oscillated jet less than 3.5 times this value.

Preliminary experiments showed that it was necessary to oscillate 7% of the total fuel flow to achieve useful attenuation and that the result was insensitive to phase within 30° of the optimum. Control performance was sensitive to the mean equivalence ratio in the pilot stream. Figure 19.4a shows that the attenuation was maximum when the equivalence ratio in the pilot stream was close to unity. Figure 19.4b shows that the attenuation increased to around 12 dB as the equivalence ratio was increased from the lean stability limit of around 0.65 in the annular duct to 0.7. The attenuation declined, however, with further increase in overall equivalence ratio and was negligible for values

Figure 19.4 Active control by oscillation of fuel in pilot stream; annular flow arrangement; $U_m = 7.5$ m/s; $U_p = 8$ m/s; $\mathrm{Re}_m = 40{,}000$; bulk mean velocity of oscillated fuel jet, $U_j = 20$ m/s; mean equivalence ratio ϕ_j of oscillated fuel jet $= 2.5$; (a) $\phi_m = 0.68$; (b) $\phi_p = 1.1$; 1 — without control; 2 — with control; and 3 — attenuation

greater than 0.75. The figure also shows that attenuation was poor at an equivalence ratio of around 0.65 and, in general, it appears that attenuation of small amplitudes of oscillation requires a more sensitive control system. The difficulty in controlling oscillations at equivalence ratios greater than 0.75 was due to the oscillated fuel not being available at the location where it was most effective.

Active control has been found to be sensitive to the location of addition of oscillated fuel in disk-stabilized flames. The injection of fuel close to the outer edge of the flame-holding disk led to the largest reduction in RMS pressure fluctuation [14], and the importance of the location of addition of oscillated fuel in a sudden expansion flow has been confirmed recently [24]. Pressure oscil-
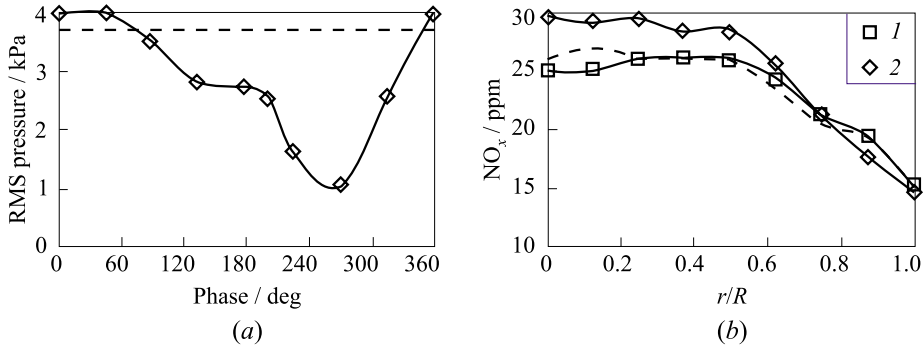
Figure 19.5 Active control by oscillation of fuel in main flow; annular flow arrangement; $U_m = U_p = 7.5$ m/s; $Re_m = 40,000$; 1 — without control; 2 — with control; and 3 — attenuation

lations in the annular flow arrangement with a frequency of around 125 Hz were associated with the annular ring, and their amplitude was more sensitive to fuel concentration in the annular flow than at the centre, mainly because the most intense part of the heat release was in the part of the flame developing from the outer edge of the annular ring. Thus imposed oscillations on the heat release in this part of the flame were likely to be effective. The injectors were preferred to the needle valve arrangement despite their smaller oscillated input, because the latter implied flow asymmetry with a single tube delivering oscillated fuel to the main flow. Active control was implemented by the oscillation of fuel in the annular flow with the three injectors and using the cross-jets of air to deliver the oscillated fuel close to the outer edge of the annular ring. The oscillated injection of approximately 3.5% of total fuel into the main flow led to the amelioration of pressure fluctuations by around 6 dB (Fig. 19.5) for the range of equivalence ratios examined, compared with the oscillation of up to 10% in the pilot stream and ineffective control with equivalence ratio greater than 0.75.

It has been shown recently [25] that concentrations of NO_x tend to reduce with increase in the amplitude of discrete-frequency oscillations. The mechanisms remain uncertain, but may be associated with the imposition of a near-sine wave on a skewed Gaussian distribution with consequent reduction in the residence time at the adiabatic flame temperature. Profiles of NO_x concentrations in the exit plane of the burner are shown in Fig. 19.6 as a function of the amplitude of oscillations with active control used to regulate the amplitude of pressure oscillations. At an overall equivalence ratio of 0.7, the reduction in the antinodal RMS pressure fluctuation by 12 dB, from around 4 kPa to 1 kPa by the oscillation of fuel in the pilot stream, led to an increase of around 5% in the spatial mean value of NO_x compared with a difference of the order of 20% with control by the oscillation of the pressure field in the experiments of [25]. The smaller net increase in NO_x emissions in the present flow may be attributed to an increase in NO_x due to the reduction in pressure fluctuations that is partly offset by a decrease in NO_x due to the oscillation of fuel on either side of stoichiometry at the centre of the duct.

Figure 19.6 Influence of control by oscillation of fuel in inner duct on NO_x emissions; annular flow arrangement; $U_m = U_p = 7.5$ m/s; $Re_m = 40{,}000$; $\phi_m = 0.7$; $\phi_p = 1.1$; $\phi_j = 2.5$; (a) effect of phase on amplitude of oscillation; (b) exit profiles of NO_x for three conditions of control: *1* — RMS pressure 4.0 kPa, *2* — 1.0 kPa, dashed line corresponds to the case without control

19.3.2 Flow Arrangement with Swirl
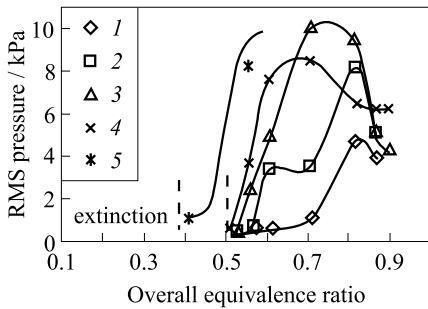
Figure 19.7 Influence of swirl on antinodal RMS pressure fluctuation; flow arrangement with swirl; bulk mean axial velocity of main flow in swirler, $U_m = 17$ m/s, Reynolds number in swirler (for isothermal conditions), $Re_s = U_m D/\nu = 56{,}000$; *1* — Sw = 0.6; *2* — 1.35; *3* — 1.8; *4* — 2.4; and *5* — 3.75

The flammability and stability limits of Fig. 19.7 were obtained using fuel–air mixtures with the same equivalence ratio in the radial and tangential inlets, and without an axial jet. The lean flammability limit decreased from 0.57 to 0.4 as the swirl number was increased from 0.6 to 3.75, and the region of high-heat release moved closer to the swirler which represented an acoustic pressure antinode for the naturally occurring oscillations associated with a quarter wave in the entire duct, with frequency close to 200 Hz. Thus, swirl led to an increase in the amplitude of oscillations and to an earlier transition from smooth to rough combustion with antinodal RMS pressures up to 10 kPa, and initiated at an equivalence ratio of 0.5 for a swirl number of 3.75

compared with 5 kPa and 0.75 for a swirl number of 0.6. The flame tended to attach to a location within the swirler due to the large region of flow reversal. Detailed experiments were limited to swirl numbers between 0.6 and 1.35 to prevent thermal damage to the pressure transducer.

Figure 19.7 also shows that the amplitude of oscillations decreased with equivalence ratios greater than around 0.8 for swirl numbers up to 1.35, and at smaller values of equivalence ratio for larger swirl numbers. This is in contrast with results for ducted flames behind steps and bluff bodies, where the amplitude is nearly always a maximum near stoichiometry. This appears to be due to a shift in the location of flame stabilization by up to 50 mm, from close to the exit of the swirler to the end of the expansion section, since the amplitude of oscillations depends strongly on the intensity of heat release near the acoustic pressure antinode. This shift in flame location may have been related to the movement of the flame attachment with pressure oscillations.
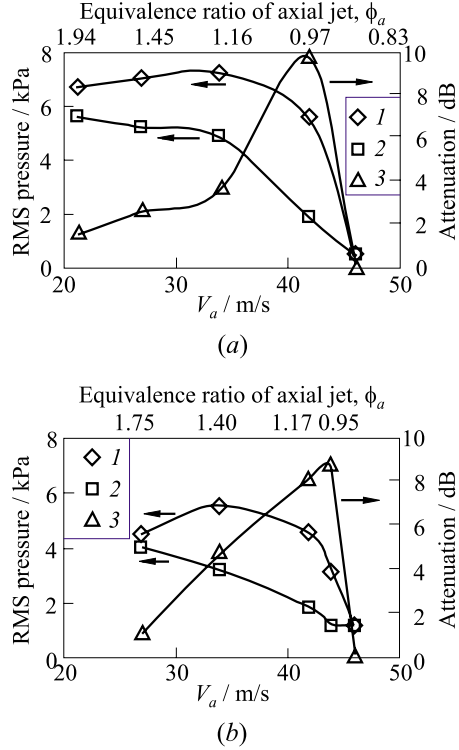
The needle valve oscillated up to 12% of the total fuel, and flow rates larger than around 3% of the total implied that the bulk mean velocity in the axial jet was greater than the bulk flow in the swirler and the mean equivalence ratio was greater than unity. It was found that the amplitude of oscillations was unaffected by values of bulk mean velocity of the axial jet greater than 2.5 times that in the swirler for a main flow swirl number of 1.35, and 4 times that value for a swirl number of 0.6. Larger values of axial jet velocity led to a decrease in amplitude due to the penetration of the swirl-induced recirculation region by the jet and the consequences for the distribution of heat release.

A difference between the equivalence ratios of the axial jet and the main flow, and the radial and tangential flows entering the swirler, implied unpremixedness, and the resulting effect on combustion oscillations and their control was quantified. A higher equivalence ratio in the axial jet than in the main flow, and in the radial rather than in the tangential flow, led to larger amplitudes of pressure oscillations than in uniformly mixed flows, whereas larger equivalence ratio of the tangential than the radial flow led to smaller amplitudes. The increased amplitude resulted from increase in fuel concentration close to the central region of the duct where the flame was stabilized, and this is supported by isothermal-flow results [26]. These also suggest greater nonuniformity of fuel concentration from the axial jet than from a difference in the equivalence ratios of the radial and tangential inlets, and that the degree of unpremixedness declines with swirl number greater than around unity.
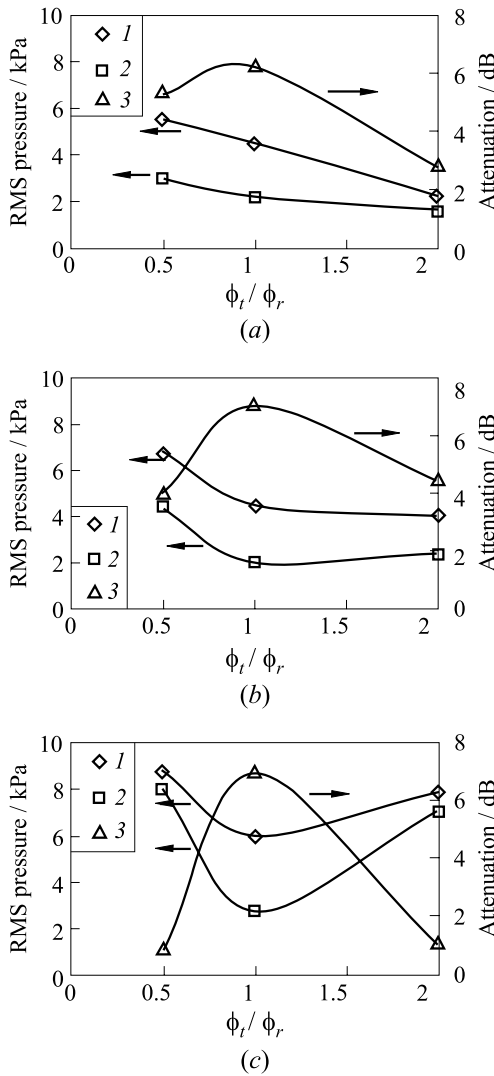
Control was implemented by the oscillation of fuel in the axial jet. Tests with a wide range of flow conditions showed that the oscillation of more than around 6% of the total fuel flow did not result in improved attenuation of the oscillations, except for small overall equivalence ratios around 0.65 for which the larger flow rates of fuel in the axial jet led to an increase in amplitude of oscillations and the oscillation of that flow resulted in an increase in attenuation.

The effect of the mean velocity of the axial jet was also examined without varying the proportion of fuel oscillated. The increase in total air flow rate due to the increase in the bulk mean velocity of the axial jet from 21 to 47 m/s was of order 1% of the total air flow rate so that its effect on the overall equivalence ratio and oscillations was small. The results of Fig. 19.8 for a swirl number of 1.35 show that the attenuation increased to 10 dB with the velocity of the axial jet up to 42 m/s, and further increase to 47 m/s caused the amplitude to fall from around 6 kPa to less than 1.5 kPa and the attenuation to decrease from 10 dB to almost zero. Similar results were observed with the swirl number of 0.6; the attenuation improved with axial jet velocity up to 60 m/s, after which the amplitude and attenuation decreased. The decline in the amplitude of oscillation and its attenuation by active control was due to the interaction between the axial jet with a large velocity and the central recirculation zone, which caused the flame to move further down-

Figure 19.8 Influence of velocity of oscillated jet, V_a, on control effectiveness; flow arrangement with swirl; Sw = 1.35; U_m = 17 m/s; Re_s = 56,000; average velocity of axial jet, U_a = 42 m/s; 5% of total fuel oscillated; (a) $\phi_0 = 0.63$; (b) $\phi_0 = 0.76$; 1 — without control; 2 — with control; and 3 — attenuation

stream of the swirler and heat release to occur further from the pressure antinode. The consequent increase in the distance between the point of entry of the oscillated fuel and the active burning zone reduced the effectiveness of the oscillated input due to increased fluid dynamic damping and development of a large difference in phase between different parts of the oscillated flow, especially with swirl surrounding the oscillated axial jet.

Unpremixedness was introduced and Fig. 19.9 shows that the amplitude of pressure oscillations generally decreased with the proportion of fuel added tangentially due to a decrease in the fuel concentration near the centre of the duct. Control was most effective when there was no unpremixedness in the main

Figure 19.9 Influence of unpremixedness on control; flow arrangement with swirl; $Sw = 0.60$; $U_m = 17$ m/s; $U_a = 60$ m/s; $Re_s = 56,000$; $\phi_0 = 0.73$; (*a*) 5% of total fuel oscillated, mean equivalence ratio of axial jet, $\phi_a = 0.73$; (*b*) 7%, $\phi_a = 1.1$; (*c*) 11%, $\phi_a = 1.73$; *1* — without control; *2* — with control; and *3* — attenuation

flow, indicating that the spatial variation in fuel concentration adversely affected the effectiveness of the temporal variation in fuel concentration imposed on the flow.

Figure 19.10*a* quantifies control performance with the oscillation of 5% of the total fuel in the axial jet for a swirl number of 1.35. It was increasingly effective with values of overall equivalence ratio less than 0.8 and the decline in amplitude with equivalence ratio greater than around 0.7. As explained earlier in connection with the results of Fig. 19.7, this was due to the downstream movement of the flame and the decline in effectiveness of the oscillated input. It should be noted that control was also hampered by the effect of the pressure oscillations at the pressure antinode on the coherence of the oscillated input.

With flow rates of fuel and air larger by a factor of two, Fig. 19.10*b* shows that the amplitude of pressure oscillations increased by around 40% so that the power associated with the pressure oscillations increased by a factor of two, the factor by which the heat release and the oscillated input were increased. The attenuation of pressure oscillations, although around 2 dB less than in the flows of Fig. 19.10*a*, is important and, again, control was not effective for overall equivalence ratio greater than 0.78. The

results suggest that the heat release rate and the change in flame location with equivalence ratio are important to the effectiveness of control.

The possibility of improving control was examined by allowing the fuel flow in one of the six tangential inlets to pass through the needle-valve arrangement before entering the swirler, while ensuring that the bulk flow rates in the six tangential jets remained the same. Figure 19.11 shows that, for an overall equivalence ratio of 0.73 and a swirl number of 0.6, the amplitude of oscillation increased with the proportion of oscillated fuel due to the unpremixedness caused by the higher value of mean fuel concentration in the oscillated flow. The attenuation also increased with the fuel flow to around 5.5 dB with oscillation of around 10% of the fuel, compared with around 7 dB by the oscillation of 7% of the fuel in the axial jet and the same overall equivalence ratio and swirl number. As expected, control was less effective with higher swirl numbers due to the greater dissipation of the oscillated input.

The effect of oscillations on NO_x emissions was quantified by using control to vary the amplitude, and an attenuation of 6 dB, a factor of two, increased the averaged emissions by up to 15%.
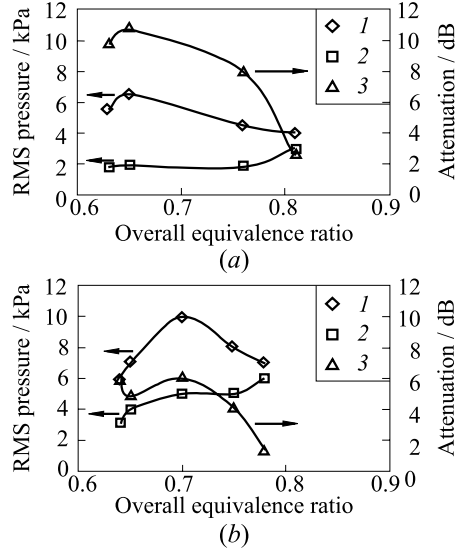
Figure 19.10 Influence of heat release on control effectiveness; flow arrangement with swirl; Sw = 1.35; 5% of total fuel oscillated (a) Re_m = 35,000, U_m = 17 m/s, U_a = 42 m/s; (b) Re_s = 70,000, U_m = 34 m/s, U_a = 84 m/s; 1 — without control; 2 — with control; and 3 — attenuation
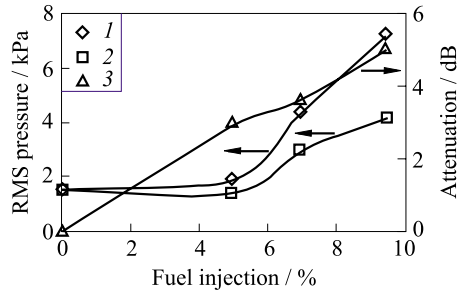
Figure 19.11 Control of oscillations by oscillation of fuel in the main flow; flow arrangement with swirl; Sw = 0.60; U_m = 17 m/s; Re_s = 56,000; U_a = 60 m/s; $\phi_t = \phi_r = \phi_p$ = 0.73; 1 — without control; 2 — with control; and 3 — attenuation

19.4 DISCUSSION

Active control of naturally occurring oscillations in the two flow arrangements resulted in levels of attenuation which were generally less than those achieved in premixed flames stabilized behind simple bluff bodies. Difficulties were experienced in controlling pressure oscillations over certain ranges of equivalence ratio for different reasons and the experiments confirmed the importance of the location of fuel addition.

In both arrangements, the position of the flame changed with flow conditions with serious implications for the amplitude of pressure oscillations and their attenuation. In the annular flow, an increase in the flow rate in the pilot stream caused the recirculation behind the annular ring to become smaller and deflect towards the wall, as shown by flow visualization studies in isothermal flow [26]. This resulted in deflection of the flame towards the duct wall and a decrease in the RMS pressure oscillations. In flows with swirl, the position of flame stabilization moved upstream with increasing swirl, causing increase in the amplitude of oscillations. Pressure oscillations of large amplitude caused a change in the position of the flame in both flow arrangements, with serious implications for control. In the annular flow, the flame detached from the main annular ring to stabilize downstream behind the step and, in the flow with swirl, the position of flame attachment shifted from the beginning of the expansion section to its end. This implied a decrease in the amplitude of pressure oscillations, but less effective control with actuators designed to introduce the oscillated fuel close to the normal position of flame stabilization.

The tendency of premixed flames to detach from the flame holder to stabilize further downstream has also been reported close to the flammability limit in a two-dimensional sudden expansion flow [27]. The change in flame position in the present annular flow arrangement was a consequence of flow oscillations associated with rough combustion, and the flame can be particularly susceptible to detachment and possible extinction, especially at values of equivalence ratio close to the lean flammability limit. Measurements of extinction in opposed jet flames subject to pressure oscillations [28] show that a number of cycles of local flame extinction and relight were required before the flame finally blew off. The number of cycles over which the extinction process occurred depended on the frequency and amplitude of the oscillated input and the equivalence ratios in the opposed jets. Thus the onset of large amplitudes of oscillations in the lean combustor is not likely to lead to instantaneous blow-off, and the availability of a control mechanism to respond to the naturally occurring oscillations at their onset can slow down the progress towards total extinction and restore a stable flame.

Extrapolation of the results from the present laboratory models to practical combustors should take into account the difference in the heat release rates, and

for comparable flow conditions the oscillated input may need to be increased almost in proportion to the heat release. It should, on the other hand, be noted that the large amplitudes of oscillation in the present study, especially those which posed problems of control, were associated with values of equivalence ratio greater than 0.75 in the main flow compared with values around 0.6 or less in their practical counterparts. The RMS pressure oscillations in the present flows were of the order of 10% of the combustion chamber pressure compared with around 2% for the pressurized combustion chamber of practical combustors, so that control may be achieved in the latter by the oscillation of a smaller proportion of fuel than in the laboratory models. The present findings have, nevertheless, drawn attention to a potential problem which requires the control system to track the dominant frequency, to provide a controlling input with the correct phase and amplitude, and to provide it at a location which may change.

19.5   CONCLUDING REMARKS

Acoustic quarter-waves with an antinode at the upstream end of the combustor and RMS pressures up to 10 kPa have been shown to dominate the flows in the two combustors tested. The quarter-wave occupied the duct length upstream of the annular ring in the first arrangement and the entire duct length in the swirling flow.

Pressure oscillations in the first arrangement depended on the equivalence ratio of the flow in the annulus and decreased with velocities in the pilot stream greater than that in the main flow due to decrease in size of the recirculation zone behind the annular ring and its deflection towards the wall. Increase in swirl number of the second arrangement caused the lean flammability limit to decrease, and the pressure oscillations to increase at smaller values of equivalence ratio. Unpremixedness associated with large fuel concentrations at the centre of the duct increased the pressure oscillations. Pressure oscillations caused the position of flame attachment to move downstream in both flows with a decrease in amplitude of oscillations.

Active control in the first arrangement was examined for values of overall equivalence ratio up to 0.9 and with the pulsation of the fuel in the core flow (with the oscillated fuel comprising up to 10% of the total fuel flow). This led to an increase in attenuation from 4 to 12 dB as the equivalence ratio was increased from the lean stability limit of around 0.65 to 0.7. The small attenuation at the equivalence ratio around 0.65 was due to the small amplitude and the need for a feedback signal of significant amplitude. Control became less effective for larger equivalence ratios and insignificant for values greater than 0.75 due to the oscillated fuel not being available at the location where it was most effective.

Although the oscillation of fuel in the annulus was limited by the actuator to 4% of the total fuel flow, the addition of the oscillated fuel close to the outer edge of the annular ring flame holder resulted in attenuations around 6 dB for the range of equivalence ratios considered.

Control was more effective with the oscillation of fuel through a central jet than in the main flow of the swirl-stabilized arrangement with attenuations between 8 and 10 dB for equivalence ratios up to 0.75. With equivalence ratios greater than 0.78, the position of the flame moved from the upstream to the downstream end of the expansion. The attenuation was limited by the decay of the effectiveness of the oscillated input with distance from the point of injection, and the effect of the pressure oscillations at the pressure antinode on the coherence of the oscillated input.

The limitations of control may require more sophisticated combinations of sensor and actuator, with the former capable of identifying the region of active burning and the latter able to oscillate fuel at the correct location.

Measured NO_x concentration at the exits of the two combustors increased up to 15% with amelioration of pressure oscillations.

ACKNOWLEDGMENTS

REFERENCES

1. Kilham, J. K., E. G. Jackson, and T. B. Smith. 1965. Oscillatory combustion in tunnel burners. *10th Symposium (International) on Combustion Proceedings*. Pittsburgh, PA: The Combustion Institute. 1231–40.
2. Heitor, M., A. M. K. P. Taylor, and J. H. Whitelaw. 1984. Influence of confinement on combustion instabilities of premixed flames stabilized on axisymmetric baffles. *Combustion Flame* 57:109–21.
3. Crump, J. E., K. C. Schadow, V. Yang, and F. E. C. Culick. 1986. Longitudinal combustion instabilities in ramjet engines: Identification of acoustic modes. *J. Propulsion Power* 2:105–9.
4. Sivasegaram, S., and J. H. Whitelaw. 1987. Oscillations in confined disk stabilised flames. *Combustion Flame* 68:121–29.
5. Culick, F. E. C. 1989. Combustion instabilities in liquid fuelled propulsion systems: An overview. AGARD CP 450. Paper No. 1.

6. Sivasegaram, S., and J. H. Whitelaw. 1987. Combustion oscillations in dump combustors with a constricted exit. *Institute of Mechanical Engineers Proceedings* 202(C3):205–10.

7. Macquisten, M. A., and A. P. Dowling. 1993. Low frequency combustion oscillations in a model afterburner. *Combustion Flame* 94:253–64.

8. Hendricks, E. W., S. Sivasegaram, and J. H. Whitelaw. 1992. Control of oscillations in ducted premixed flames. In: *Aerothermodynamics in combustors*. Boston, MA: Kluwer. 215–30.

9. McManus, K. R., T. Poinsot, and S. Candel. 1993. A review of active control of combustion instabilities. *Progress Energy Combustion Science* 1:1–29.

10. Paschereit, C. O., E. Gutmark, and W. Weisenstein. 1998. Control of thermoacoustic instabilities and emissions in an industrial type gas turbine combustor. *27th Symposium (International) on Combustion Proceedings*. Pittsburgh, PA: The Combustion Institute.

11. Bloxsidge, G. J., A. P. Dowling, N. Hooper, and P. J. Langhorne. 1988. Active control of reheat buzz. *AIAA J.* 26:783–90.

12. Langhorne, P. J., A. P. Dowling, and N. Hooper. 1990. Practical active control system for combustion oscillations. *J. Propulsion Power* 6:324–30.

13. Neumeir, Y., and B. T. Zinn. 1996. Experimental demonstration of active control of combustion instabilities using real time modes observation and secondary fuel injection. *26th Symposium (International) on Combustion Proceedings*. Pittsburgh, PA: The Combustion Institute. 2811–18.

14. Sivasegaram, S., R-F. Tsai, and J. H. Whitelaw. 1995. Control of combustion oscillations by forced oscillation of part of the fuel. *Combustion Science Technology* 105:67–83.

15. Wilson, K. J., E. Gutmark, and K. C. Schadow. 1992. Flame kernel pulse actuator for active combustion control. In: *Active control of noise and vibration*. ASME DSC-38:75–81.

16. Sivasegaram, S., R-F. Tsai, and J. H. Whitelaw. 1995. Control of oscillations and NO_x concentrations in ducted premixed flames by spray injection of water. *ASME, HTD Proceedings* 317-2:169–74.

17. Norster, E. R., and S. M. De Pietro. 1996. Dry low emissions combustion system for EGT small gas turbines. *Transactions Institute of Diesels and Gas Turbine Engineers* 495:1–9.

18. Grün, M. 1994. The influence of geometry on oscillations for premixed flames with complex flow arrangement. Diploma Thesis. Rheinisch-Westfälische Technische Hochschule. Aachen, Germany.

19. Bhidayasiri, R., S. Sivasegaram, and J. H. Whitelaw. 1997. Control of combustion and NO_x emissions in open and ducted flames. *4th International Conference on Technologies and Combustion for a Clean Environment Proceedings*. 2. Paper No. 29.1.

20. Bhidayasiri, R., S. Sivasegaram, and J. H. Whitelaw. 1997. Control of combustion oscillations in a gas turbine combustor. *7th Asian Congress of Fluid Mechanics Proceedings*. 107–9.

21. Sivasegaram, S., and J. H. Whitelaw. 1991. The influence of swirl on oscillations in ducted premixed flames. *Combustion Science Technology* 85:195–205.

22. Feikema, D., R-H. Chen, and J. F. Driscoll. 1991. Blow-out of nonpremixed flames: Maximum coaxial velocities achievable with and without swirl. *Combustion Flame* 86:347–58.

23. Bhidayasiri, R., S. Sivasegaram, and J. H. Whitelaw. 1997. The effect of flow boundary conditions on the stability of quarl stabilized flames. *Combustion Science Technology* 123:185–205.

24. Lee, J. G., and D. A. Santavicca. 1998. Application of flame evolution imaging to the optimization of an active control system for suppressing combustion instability. *27th Symposium (International) on Combustion Proceedings*. Pittsburgh, PA: The Combustion Institute.

25. Poppe, C., S. Sivasegaram, and J. H. Whitelaw. 1998. Control of NO_x emissions in confined flames by oscillations. *Combustion Flame* 113:13–26.

26. Bhidayasiri, R. 1998. Control of combustion. Ph.D. Thesis. Imperial College, University of London.

27. De Zilwa, S. R. N., L. Khezzar, and J. H. Whitelaw. 1998. Plane sudden expansion flows. Thermofluids Section Report TF/98/05. Imperial College, Department of Mechanical Engineering.

28. Sardi, E., A. M. K. P. Taylor, and J. H. Whitelaw. 1999. Extinction of turbulent counterflow flames under periodic strain. *Combustion Flame* 120(3):265–84.

Chapter 20

OPEN-LOOP CONTROL
OF SWIRL-STABILIZED SPRAY FLAMES

S. Acharya, E. J. Gutmark, J. Stephens, and J. Li

Open-loop control of a swirl-stabilized diffusion flame was experimentally studied for three different swirl-stabilized combustor configurations, each with a different swirl number range. Control was achieved by forcing the air stream and/or the fuel stream. The effect of the forcing amplitude and the phase difference between the forcing signals was studied for selected configurations. The burners in the first and second configurations tested both represent a coaxial flow configuration with a conventional air-blast atomizing nozzle. The maximum swirl numbers that could be achieved with these combustors were 0.3 and 1, respectively. The third nozzle is a conical high-swirl preburner with swirl-air injected tangentially along the length of the preburner. Swirl numbers as high as 3 could be achieved with this burner. Forcing the air stream alone led to increases in the radial entrainment of air and higher temperatures associated with improved mixing and enhanced heat release. This was noted to be true even at the highest swirl number studied.

20.1 INTRODUCTION

There is a considerable amount of work in the area of active combustion control of gaseous combustion (see [1, 2] for recent reviews on this topic). The majority of these studies have dealt with a bluff-body-stabilized combustor or a dump combustor where the recirculation induced by a bluff body or by a sudden expansion is used to stabilize the flame. Active control strategies have been used to primarily suppress thermo-acoustic instabilities resulting from a coupling between the heat release and the acoustic modes in the combustor. These control strategies have generally relied on modulating and phase shifting the fuel so as to

decouple the pressure and heat release with respect to each other. Control strategies have also looked at improving fuel efficiency and reducing pollutants [3], and in extending flammability limits [4].

Large-scale structures play an important role in the mixing between fuel and air. The dynamical nature of these structures consequently control the combustion and heat release process. The thermo-acoustic instability is therefore strongly dependent on the dynamics of the large-scale structures. The temporal and spatial evolution of these structures is reasonably well understood for simple flows such as mixing layers [5], shear layers [6], and jets [7], but in more complex, multiphase flows (such as sprays) this behavior is not well understood. To complicate matters, in the swirling flows considered in the present study, the influence of swirl on the dynamical instabilities is also not understood. What is known is that swirl effects the combustion instability in a complex way; for premixed gaseous flame, Sivasegaram and Whitelaw [8] show that swirl reduces instability for disk-stabilized combustion, but increases the instability for flames stabilized behind sudden expansions and annuli with a small clearance at the wall. Unlike the large body of literature dealing with control of nonswirling gaseous flames, there is very little work reported on control of swirl-stabilized spray combustion.

The present paper deals with the control of swirl-stabilized spray combustion, and while many studies have reported detailed measurements of velocity, temperature, and species concentrations in such systems (see, for example, [9–11]), there is virtually no work done in understanding the dynamical instabilities in a swirl-stabilized spray combustor, and in developing suitable control strategies. Swirl modifies the longitudinal mode instabilities (or spanwise vortices), and azimuthal instabilities may be quite significant in swirling flows. As noted earlier, large-scale structures play an important role in longitudinal mode instabilities in a nonswirling gaseous flame, and it is not clear how swirl modifies the spatial and temporal characteristics of these large-scale structures, and how this influences the associated instabilities in the flame. The rather complex behavior of the swirl induced/modified instabilities is reflected in the contrary effects swirl produces in premixed gaseous flames: a stabilizing effect of swirl in disk-stabilized premixed flames and a destabilizing effect of swirl on flames stabilized past sudden expansions [8].

To control swirl induced/modified instability, and to enhance the combustion performance, controlling or manipulating the large-scale structures and the interaction of the fuel with these structures is of critical importance. In non-swirling flows, as noted earlier, several studies ameliorated combustion instability by lagging the fuel injection when instability was observed. In several recent studies, enhancements in fuel efficiency and reduction of emissions have been observed by controlling the relative phase between the fuel injection and the air vortex cycle [12]. Greater mixing is observed when injecting fuel at the initial line of vortex formation (zero phase difference). Injecting the fuel out of

phase when the vortices are developed leads to undesirable pockets of fuel-rich or air-rich regions. Injecting fuel several times during the vortex evolution can have the same effect as fuel staging. However, this has only been demonstrated for nonswirling flows, where the large-scale instabilities are well understood, and the coherence of the organized structures in the near-field can be established by low-level forcing of the air stream. The primary objective of the present paper is to explore the feasibility and benefits of active forcing in swirling flames. Preliminary efforts of the co-authors, Stephens *et al.* [13–15], confirm the potential of controlling coherent structures in swirling flows.

In the present work, three swirling flow configurations are considered. The first represents a low-swirl conventional geometry with an air-assist atomizing nozzle and a coaxial swirling flow field. The maximum swirl number obtained in this configuration is around 0.3. The second configuration is similar to the first except that moderate swirl numbers (as high as 1) could be achieved, and a *Parker–Hannifan Simplex* Atomizing Nozzle is used. In the third configuration, high-swirl numbers are obtained (as high as 3) using a split-cone preburner similar to the *ABB* EV burner (Sattelmayer *et al.*, [16]). The burner consists of four split leaves of a cone that are offset relative to each other. Air is introduced through these offsets generating a vortex core. A pressure-atomizer located at the base of the conical preburner injects fuel into the vortex core.

20.2   EXPERIMENTAL ARRANGEMENT

In the first configuration (low-swirl), the tests were performed using a small-scale model of a swirl-stabilized combustor (Fig. 20.1) operating at nearly 30 kW heat release. The combustor had a single air stream which could be acoustically modulated and swirled. The swirl was applied aerodynamically by tangential jets. The swirl number was varied by changing the momentum ratio between the axial flow and the tangential jets. At the center of the air jet, liquid fuel (ethanol) was injected through an atomizer-fogger in a conical pattern either continuously or pulsating. Measurements described in this paper were performed without confining the flame to allow easy access for measurements.

Axial and swirling air streams in the combustor issued from a circular chamber through a conical nozzle. The chamber was utilized both as an acoustic resonator and a settling chamber. It contained a honeycomb to straighten the flow and two acoustic drivers to apply acoustic excitation to the jet. The nozzle exit diameter was 3.8 cm and the maximum Reynolds number based on this diameter and the exit velocity with and without air forcing was 4800 and 1400, respectively. The tests were performed with total air flow rate of 85 l/min, and fuel flow rate of 0.063 l/min. The swirl was applied with tangential air injection and the maximum swirl number tested was $N_S = 0.30$.
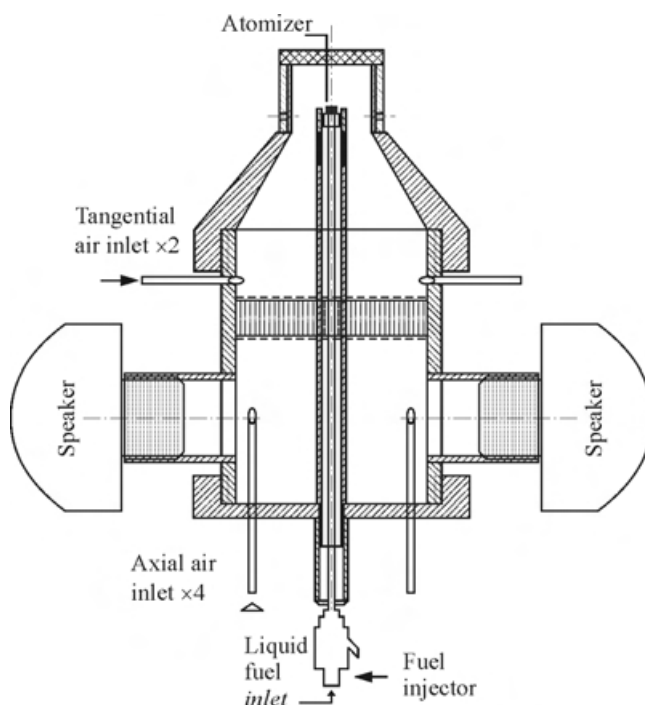
Figure 20.1 Schematic drawing of the model combustor (configuration 1)

Fuel was injected through a tube mounted in the center of the air nozzle. A pressure fed fogger, which was mounted upstream of the nozzle exit, was used to atomize the ethanol fuel. The atomized liquid fuel was pulsed using an automotive fuel injector. The fuel could be pulsed up to 700 Hz. The frequency of the fuel pulsations used in the present experiments was governed by the resonant frequency of the combustor settling chamber. Measurements of maximum pressure and velocity fluctuations found the resonant Helmholtz frequency to be 200 Hz. Temperature measurements over a wide range of frequencies showed a maximum heat release when operating at the resonant Helmholtz frequency due to high-velocity fluctuations at the exit plane [13–15]. The response of the fuel injection system was verified using a high-speed video recording and triggered strobe lamps.

The fuel and air were pulsed independently at a frequency of 200 Hz and the phase between them could be varied in a full range of 360°. The air flow was modulated at the resonating frequency to generate coherent air vortices at the nozzle exit.
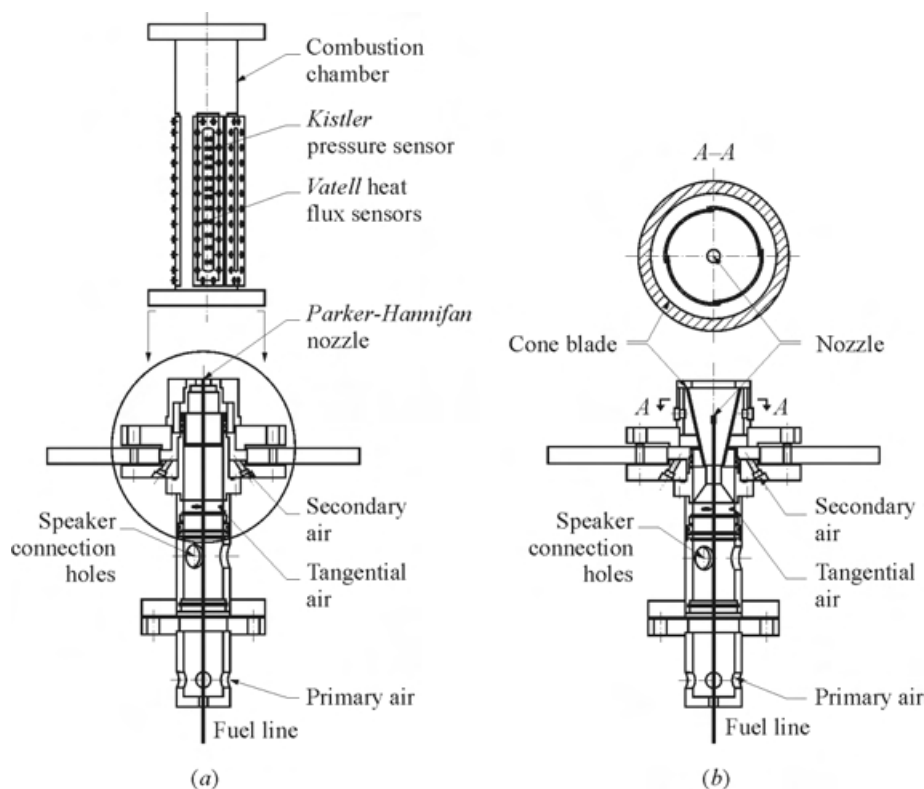
Figure 20.2 Schematic drawing of (*a*) the large-scale combustor with a moderate swirl (configuration 2) and (*b*) conical preburner with high swirl (configuration 3)

In the second configuration (moderate swirl) tested (see Fig. 20.2*a*), only the air stream was forced and no liquid-fuel pulsations were imposed. The experiments were performed with a *Parker–Hannifan* Research Simplex Atomizer. The atomizing nozzle consisted of a primary liquid ethanol feed with a coaxial primary air stream. The air stream passed through a set honeycomb, flow-straightener, and swirl vanes to provide the necessary level of swirl. Three loudspeakers were used to excite the primary air.

The air flow rate was set at 0.3 g/s, and the fuel flow rate was set at 0.9 g/s (above the rich flammability limit). The forcing frequency was chosen to be 592 Hz. This frequency was chosen to coincide with the natural frequency of the air chamber since the resonance would amplify the forcing signal. The amplitude of the forcing is 20% of the mean exit velocity at the nozzle.

In the third configuration shown in Fig. 20.2*b* (high swirl), the experiments are performed in a conical preburner. The combustor has provisions for three air-stream feeds: primary, secondary, and tangential air streams. In this study, only the primary and secondary air streams are used. The conical preburner consists of four-offset leaves of a 25° split-cone. The gaps between the blades at the inlet are about 2 mm. The primary inlet is located at the bottom with a radius of about 7.5 mm. The outlet of the burner has a radius R_0 of 41.3 mm. There is a small lip at the exit of the preburner. The secondary air enters tangentially through the offset gaps leading to a swirling vortex core.

For all three configurations, ethanol is used as the liquid fuel. It is pressurized to 90 psi in a fuel tank by high-pressure nitrogen, metered, and sent to the nozzle through a tube mounted in the center of the air chamber.

For configuration 1, hot wire anemometry was used for the velocity measurements. Average velocity, turbulent intensity, and spreading rate were estimated from velocity data taken with a *Dantec* 55P01 hot wire probe. The swirl numbers were estimated by measurements taken with a *Dantec* 55P61 *x*-wire probe. For configurations 2 and 3, velocity and droplet size were measured, under non-reacting conditions, using a two-component Laser Doppler Velocimeter (LDV) and Phase-Doppler Particle Analyzer (PDPA) system operating in the forward-scatter mode for droplet measurements and in the backward-scatter mode for the gas-phase measurements. For the droplet velocity and size measurements, water is used instead of fuel. For the gas phase, a smoke generator is used to inject smoke into the air flow and served the role of seed particles. The velocities of the measured smoke particles represent the air velocity.

The flame temperature was measured using a type B thermocouple which was mounted inside a ceramic tube. The thermocouple voltage was digitized and analyzed using a digitizing board. Voltage data was then processed through a FORTRAN program which was developed to convert voltage to temperature, correct for radiation losses to the surrounding environment, and average and plot the temperature values.

20.3   RESULTS AND DISCUSSION

20.3.1   Configuration 1: Small-Scale Coaxial Combustor (Low Swirl)
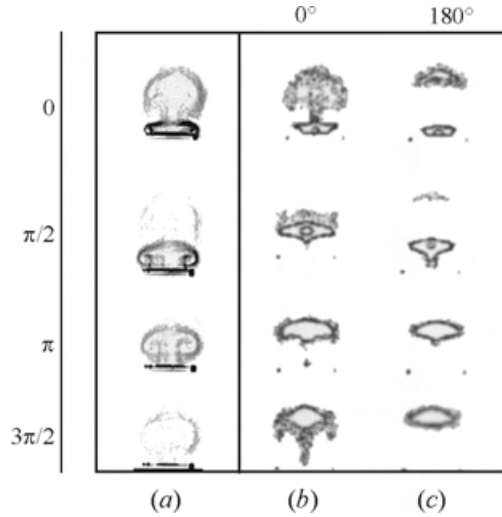
Cold Flow Visualization

The cold flow visualization shows the effects of active air forcing and liquid-fuel pulsations. Higher air flow rates, three times higher than those used in the combustion studies, were used for flow visualization. At the higher flow rates, the structures would be imaged more distinctly. The images captured show the

effects of air forcing, liquid-fuel pulsation, and the relative phase angle between the forcing signals.

The air flow was visualized by injecting smoke into the combustor settling chamber. Without air forcing, the naturally existing axial and helical vortices are weak and disorganized. Images of these natural vortical structures could not be clearly captured during this experiment. With forcing, the air vortices are reinforced. In Fig. 20.3a, one can see the growth of an air vortex at four instances of time. At time 0, the vortex begins to form at the nozzle exit. At times $\pi/2$, π, and $3\pi/2$, the air vortex continues its roll-up until it is fully developed. At times 0 and $\pi/2$ one can see secondary vortices from the previous forcing cycle.

Figure 20.3 Flow visualization at four time instances of a forcing cycle: air vortices (a); fuel/air vortices (b) and (c)

The effects of liquid fuel pulsation without air forcing were visualized at four instances of time (images not included). At time 0, a high concentration of fuel became visible at the nozzle exit. At time $\pi/2$, the fuel droplets became evenly dispersed through the quarter cycle. Times π and $3\pi/2$ showed similar droplet distributions, homogeneous throughout the flow.

Figures 20.3b and 20.3c provide a representation of air vortex interaction with liquid-fuel spray. These images have been averaged over time and contoured to show fuel droplet distribution relative to the air vortex. Fuel injection at two relative phase angles are shown at four instances of time during a forcing cycle. Figure 20.3b shows the most desirable case (0° phase angle) for fuel–air mixing. Liquid fuel is injected at time 0 into the air vortex. At times $\pi/2$ and π, the fuel droplets are concentrated at the leading edge of the air vortex during its early stages of its formation. At $3\pi/2$, the entrained fuel droplets wrap around the vortical structure leading to a homogeneous dispersion of fuel which is desirable for efficient combustion. Figure 20.3c shows a 180° relative phase change from the previous case. The liquid-fuel droplets do not become fully entrained into the air vortex. High concentrations of fuel droplets were observed at the leading edge of the vortex throughout the forcing cycle.

Flame Structure

The differences between the flame structure corresponding to four different test conditions, i.e., unforced and forced cases with 0 and 0.3 swirl numbers, were assessed by their visual appearances using a CCD camera. Figures 20.4*a* and 20.4*b* show the unforced flame both with and without swirl, respectively. Figures 20.4*c* and 20.4*d* show the corresponding photographs with air forcing. The baseline flame, without forcing or swirl, was partially lifted. The flame was predominantly yellow due to rich sooty combustion. Slight reattachment was obtained with swirl resulting in a shorter, wider flame and improved heat release at the flame holder. Full reattachment was obtained with air forcing. Forced flames were shorter, more intense, and predominantly blue indicating a significant reduction in soot formation. Swirl has little effect on the structure of a highly forced flame.
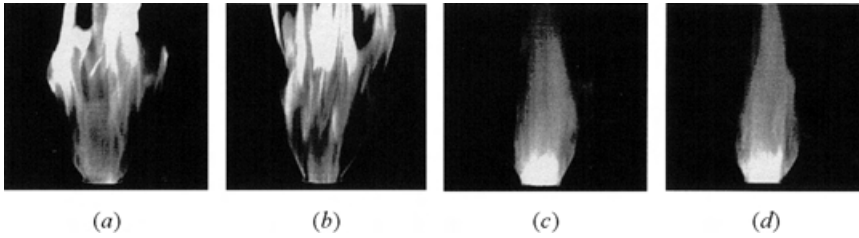

Figure 20.4 Flame structure. No forcing: (*a*) $N_S = 0.3$; (*b*) $N_S = 0$. High forcing: (*c*) $N_S = 0.3$; (*d*) $N_S = 0$

Flow Field Measurements

Mean and turbulent axial velocity was measured in the entire flow field at the same conditions for which the flame tests were conducted. These tests were aimed to elucidate the mixing process at the different forcing conditions. Four cases were compared: no forcing and no swirl, no forcing with swirl ($N_S = 0.3$), forcing (forcing level $\approx 60\%$) without swirl, and forcing with swirl.

The mean velocity variation along the jet axis for the four cases is shown in Fig. 20.5. Without forcing, swirl accelerated the decay of the mean velocity along the axis. The potential core, which was nearly 3 diameters long, vanished. This observation corresponds to an enhanced spreading rate of the swirling jet. The initial exit velocity of the forced jet was much higher than that of the unforced jet due to "acoustic streaming." The mean velocity increased from 1.2 m/s in the unforced case to 6.1 m/s in the forced jet. The increased mean flow was a result of strong induced velocity and entrainment caused by the coherent vortices which
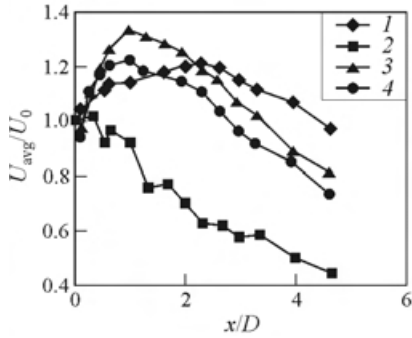
Figure 20.5 Average centerline velocity vs. axial distance for configuration 1. No forcing: *1* — no swirl; *2* — high swirl. High forcing: *3* — no swirl; and *4* — high swirl
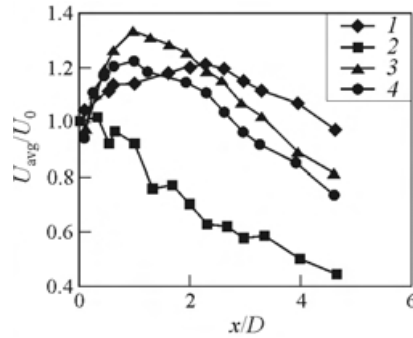
Figure 20.6 Centerline temperature vs. axial distance: high forcing – pulser off for configuration 1 (T_{bl} represents the corresponding centerline temperature for the unforced case). *1* — No swirl; *2* — low swirl; and *3* — high swirl

were generated due to flow excitation. The mean flow of the forced jet exhibited an acceleration of nearly 30% in the first diameter, followed by a faster decay than the unforced jet. The effect of swirl on the forced jet was, however, minimal.

Effect of Primary-Air Forcing

The centerline temperature distributions are presented in Fig. 20.6 for the case where the primary air is forced alone (no fuel pulsations). Close to the nozzle-base, significant enhancements in the centerline temperature (relative to the baseline unforced case) are observed with forcing, with temperature ratios as high as 2.4 for the no-swirl case. The higher temperatures are a direct consequence of higher flow entrainment and turbulence levels associated with forcing (see section on velocity distributions). Furthermore, with forcing, the coherence of the near-field vortical structures is enhanced, permitting droplets entrained into these structures greater residence times for vaporization and combustion. With swirl, the enhancement levels decrease, but are still of the order of 2 near the centerline. *This implies that the basic mechanism of enhanced mixing through increased entrainment into the near-field vortical structures also applies to swirling flows.* This observation is further supported by the radial profiles (not shown) which indicate a weak influence of swirl on the radial profiles. The lower enhancement levels associated with swirl are presumably associated with a decreased coherence of the vortical structures with swirl which make them less receptive to forcing.

For all cases, the enhancement levels decrease in the axial direction, and are again associated with a loss of coherence and breakdown of the vortical structures.

Effect of Fuel Pulsations
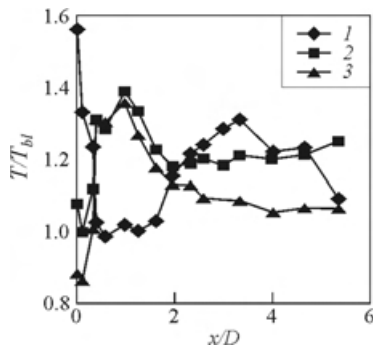
Figure 20.7 Centerline temperature vs. axial distance: no air forcing, with fuel pulsation, configuration 1: *1* — no swirl; *2* — low swirl; and *3* — high swirl

The effect of fuel pulsations alone (no air forcing) is shown in the centerline temperature ratio distributions of Fig. 20.7. Fuel pulsations produce a spray pattern with a fanning (open and close) motion. The fuel pulsations themselves serve as a forcing signal to the primary air stream (through interchange of mass, momentum, and energy from the droplet phase to the gas phase), and can reinforce the natural instabilities in the primary air stream. In the present case, the fuel pulsations are introduced at 200 Hz, and it is presumed that they excite the primary air stream in a manner similar to that of acoustic forcing. Fuel pulsations alone and the associated effect on the air stream therefore lead to enhancements in

the temperature ratio distributions shown in Fig. 20.7. For the no-swirl case, the highest temperature enhancements occur very close to the base of the flame. In the presence of swirl, they are displaced downstream in the axial direction, and maximum enhancement levels are noted around $x/D = 1$. In fact, close to the flame base a decrease in temperature is noted with fuel pulsations. This may be due to the velocity defect expected with swirl near the centerline in the absence of the fuel spray. This defect increases with swirl number, and at sufficiently high swirl numbers a central recirculation region is formed. With a continuous fuel spray injecting fuel radially and vertically outwards, this velocity defect is presumably reduced or eliminated. Fuel pulsations, associated with periodic injection of fuel, can lead to periodic resurgence of the velocity-defect region, with an accompanying decrease in temperature.

**Combined Air Forcing and Fuel Pulsations**

The effect of forcing both the primary air stream and the fuel stream is next examined to explore the effect of the phase angle between the two forcing signals.

Recall from earlier visualization plots, the differences in the droplet–air interaction for a phase angle of 0° and 180°. For a phase angle of 0°, the droplets are injected into the flowfield during the incipient stages of vortex formation. As the vortex develops, the droplets entrained remain in the vortex and enjoy long residence times for vaporization and combustion. Higher temperatures are therefore expected for the 0° phase angle. At 180°, the droplets are injected into the fully formed vortex, and vortex breakdown or loss of coherence occurs shortly after the fuel injection. Therefore relative residence times in the near-field vortical structures is smaller, and the droplet vaporization and combustion are adversely affected. Lower temperatures are therefore expected for 180° phase difference. At 90° and 270° phase differences, the performance is expected to be between the 0° and 180° cases.

These expectations are borne out in the temperature vs. phase angle plots shown in Figs. 20.8 and 20.9. Figures 20.8a and 20.8b show the temperatures for the nonswirling case at two radial locations ($r/R = 0$ and 0.67) and three axial locations ($x/D = 0.16$, 0.34, and 0.67). Figures 20.9a and 20.9b show similar temperature profiles for the swirling flow case. For both swirling and nonswirling flows, the centerline profiles clearly indicate that maximum temperatures are obtained when the fuel is injected in-phase with the beginning of a vortex formation cycle (phase angle of 0° and 360°). Temperature ratios as high as 2.3 and 1.75 are obtained for the nonswirling and swirling flow cases, respectively. Expectedly these values decrease in the downstream direction. Figures 20.8b and 20.9b indicate that the temperature ratios also decrease in the radial direction. This is consistent with the earlier results shown for primary air forcing alone where the highest temperature ratios were always obtained along the centerline. This is
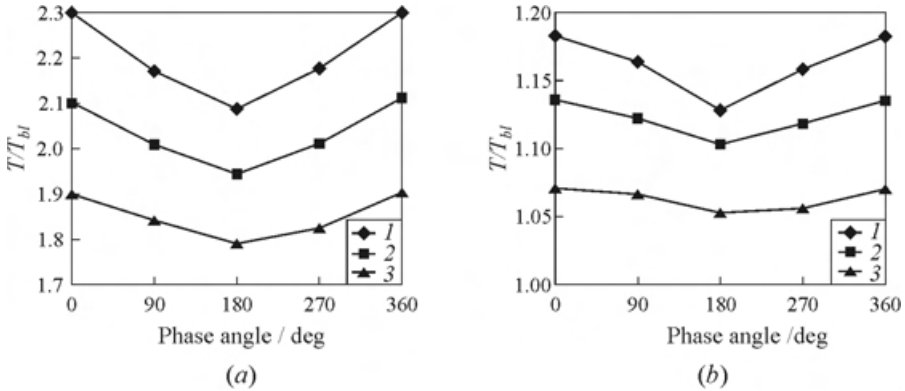
Figure 20.8 Centerline temperature vs. phase angle, $N_S = 0$ (configuration 1): (a) $r/R = 0$; (b) 0.67. 1 — $x/D = 0.16$; 2 — 0.34; and 3 — 0.67
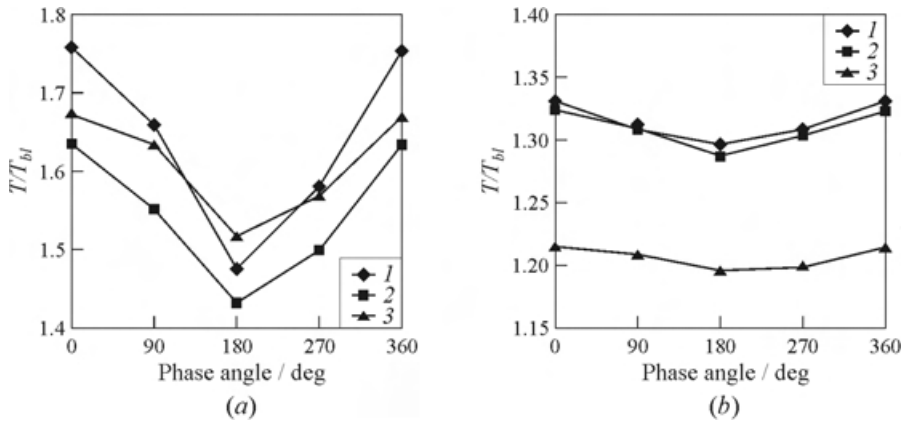
Figure 20.9 Centerline temperature vs. phase angle, $N_S = 0.3$ (configuration 1): (*a*) $r/R = 0$; (*b*) 0.67. *1* — $x/D = 0.16$; *2* — 0.34; and *3* — 0.67

because the region near the flame base close to the centerline is associated with flame vaporization and mixing, and is most benefited by higher entrainments, velocities, and turbulence levels that accompany forcing.

20.3.2 Configuration 2: Large-Scale Coaxial Combustor with *Parker–Hannifan* RSA Nozzle (Moderate Swirl)

Since both configurations 1 and 2 are similar, with differences primarily in flow conditions and geometrical scale, results presented for configuration 2 will be limited to the gas-phase and droplet-phase velocities, with and without forcing. As noted earlier, configuration 2 represents a higher swirl case (swirl number of 0.85) than configuration 1. The preferred mode frequency for the air jet in this configuration is 592 Hz, and therefore this was used as the forcing frequency. Figures 20.10*a* and 20.10*b* show the velocities of the droplet phase with and without forcing, while Figs. 20.11*a* and 20.11*b* show the corresponding gas-phase velocities. For the unforced case, a recovering wake-type velocity profile with a velocity defect along the centerline is noted. The defect persists up to nearly 6 diameters downstream of the nozzle exit. The velocity defect is produced by the swirl, and at sufficiently high swirl values the defect becomes large to produce a central recirculation. The droplet velocities are noted to be somewhat higher than the gas-phase velocity, but, in general, follow the trends of the gas-phase velocity quite well. Forcing appears to have a twofold effect. First, the velocity defect profile is eliminated. Second, the velocities are higher with
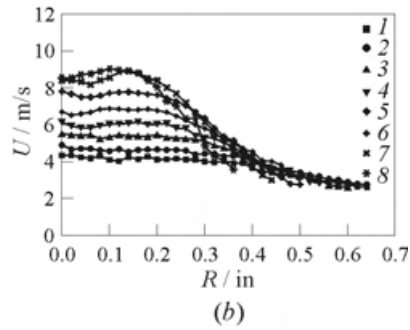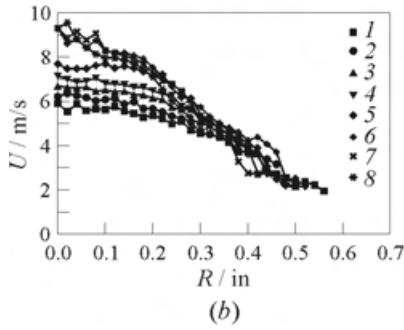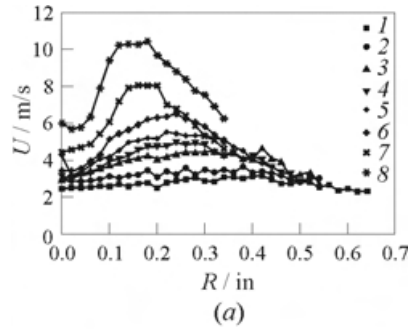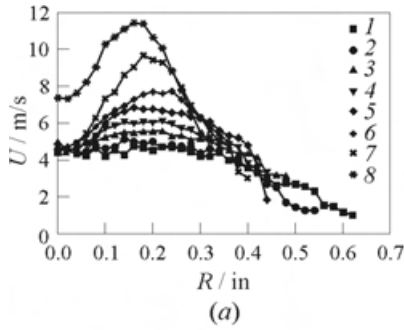
Figure 20.10 Axial velocity measurements of droplet phase for configuration 2 without (*a*) and with (*b*) forcing: *1* — $z = 1.5$ in.; *2* — 1.25; *3* — 1.0; *4* — 0.875; *5* — 0.75; *6* — 0.625; *7* — 0.5; and *8* — 0.375 in.
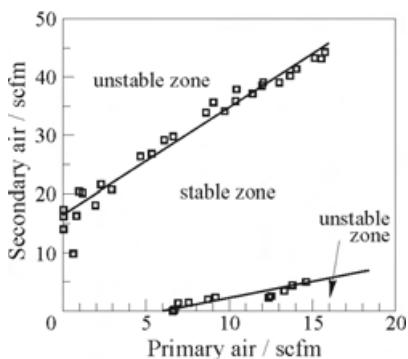
Figure 20.11 Axial velocity measurements of gas phase for configuration 2 without (*a*) and with (*b*) forcing: *1* — $z = 1.5$ in.; *2* — 1.25; *3* — 1.0; *4* — 0.875; *5* — 0.75; *6* — 0.625; *7* — 0.5; and *8* — 0.375 in.

forcing, particularly in the centerline region. Thus in the velocity defect region of the unforced case, there is a substantial difference in the velocity between the unforced and forced cases, with the forced centerline velocity being nearly twice as high as the unforced velocity at axial distances spanning 2.5–3.5 nozzle diameters from the nozzle. These higher velocities are associated with increased entrainment induced by forcing. The entrained air has strong radial component along the jet edges, and is turned axially upwards along the symmetry plane.

20.3.3 Configuration 3: High-Swirl Conical Preburner (High Swirl)

As noted earlier, in this configuration extremely high swirl numbers (greater than 3) can be generated. In presenting the temperature and velocity data for

this combustor, the length scales are nondimensionalized by R_0 (the exit radius of the conical preburner) and velocity is nondimensionalized by U_0 (the average velocity at the conical preburner exit). The origin of both the radial (R) and the axial (Z) directions are located at the center of the conical preburner exit plane. The study was conducted with the atomizing nozzle located at $Z/R_0 = -1.5$. This location was found to be the most suitable primarily from the perspective of keeping the conical-blade surfaces cool. Lower locations led to occasional impingement of the fuel droplets on the blade surfaces.

Figure 20.12 Flame stability regime for configuration 3

Figure 20.12 shows a stability map of the conical preburner system investigated. In developing the stability map, the fuel flow rate is maintained constant at 0.36 g/s while the primary and secondary air flow rates are varied systematically. The flame is considered to be stable if it could be sustained for a long period of time. As shown in Fig. 20.12, unstable regimes can be noted both for low and high secondary air flow rates.

Figure 20.13 shows the temperature contours for the three different cases 1, 2, and 3 indicated in the figure. The cases correspond to three stable flow conditions of the secondary flow rate Q, entering through the offset gaps and primary air flow rate Q_p entering from the base at the bottom: (1) $Q_S = 8.8$ scfm, $Q_p = 0.0$ scfm; (2) $Q_S = 5.0$ scfm, $Q_p = 3.8$ scfm; and (3) $Q_S = 8.8$ scfm; $Q_p = 3.8$ sfcm.
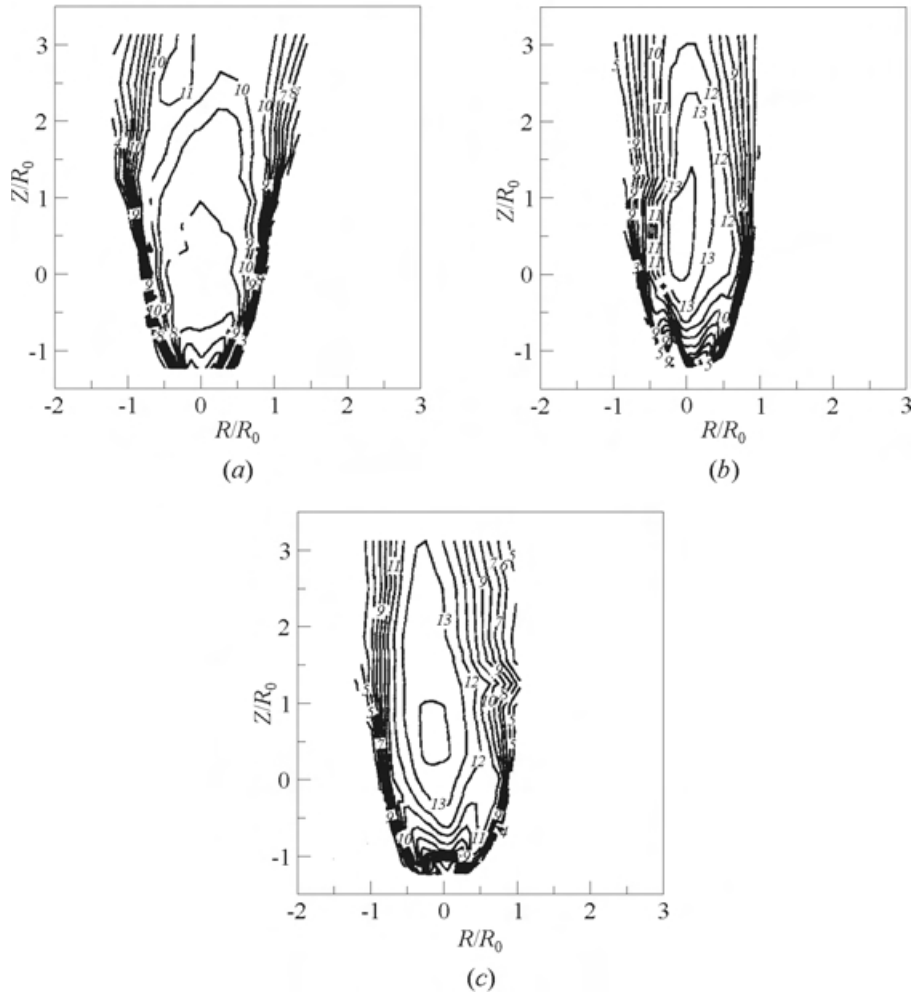
For case 1, with no primary air, the temperature in the inner recirculation zone is low, and the peak temperatures occur in the high-speed shear layer regions. The inner recirculation zone is fuel rich, and droplet heat up and vaporization occur primarily in this region.

In the shear layer region, sufficient air is available for complete combustion, and this region is associated with the highest temperatures. In case 2, the total air is kept the same (at 8.8 scfm) as in case 1, but now primary air is introduced at the expense of the secondary air. Except for the region in the near vicinity of the nozzle, the highest temperatures are now obtained in the middle of the conical preburner. This is presumably associated with the greater availability of air in the midregions in this case.

In case 3, the total air is greater than in cases 1 and 2, and therefore this condition is more fuel lean than the other two cases. The temperature levels are noted to be lower than case 2 but higher than case 1. In comparing the evolution

Figure 20.13 Temperature contours for different flow conditions (configuration 3): (a) $Q_s = 8.8$ scfm; $Q_p = 0.0$ scfm; (b) $Q_s = 5.0$ scfm; $Q_p = 3.8$ scfm; and (c) $Q_s = 8.8$ scfm; $Q_p = 3.8$ scfm. 1 — $0\,°C$; 2 — 100; 3 — 200; 4 — 300; 5 — 400; 6 — 500; 7 — 600; 8 — 700; 9 — 800; 10 — 900; 11 — 1000; 12 — 1100; 13 — 1200; 14 — 1300; and 15 — $1400\,°C$
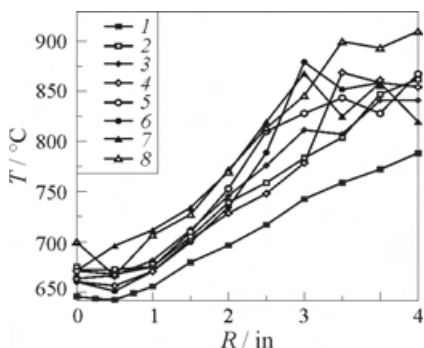
Figure 20.14 Centerline temperature for configuration 3: *1* — unmodulated; *2* — $f = 180$ Hz; *3* — 200; *4* — 220; *5* — 240; *6* — 260; *7* — 270; and *8* — 280 Hz

of the temperature profiles in the three cases, it is noted that the most uniform profiles are obtained for case 3. However, case 3 exhibits the widest flame and associated temperature distribution of the three cases.

Figure 20.14 shows the centerline temperature distribution in the conical preburner forced at different frequencies. It is apparent that even for highly swirling flames, forcing can be used to increase mixing and flame temperatures. Highest temperature levels were obtained for forcing in the neighborhood of 260–280 Hz.

20.4 CONCLUDING REMARKS

Active control of a swirl-stabilized spray flame was experimentally studied. Three combustor configurations representing low swirl, moderate swirl, and high swirl were studied. The following main conclusions were noted.

1. Air vortices were excited and controlled by acoustic excitation in both nonswirling and swirling flows.

2. In a forced flow, when fuel is injected in-phase with air vortices, the spray becomes entrained in the vortical structure leading to a homogeneous distribution of fuel throughout the flow and highest temperatures. Injecting fuel at a time when the vortex is fully formed leads to dense pockets of liquid fuel at the structure's leading edge which is undesirable for efficient combustion.

3. Air forcing had a significant effect on the flame structure. At the baseline conditions, the flame was lifted and sooty. With air forcing, the flame became fully reattached to the flame holder. Swirl had little effect on the structure of a highly forced flame.

4. Velocity measurements showed an increase in mean flow with forcing implying a strong radial air entrainment caused by the coherent structures.

Swirl had a significant effect on increasing the spreading rate in an unforced flow, but virtually no effect in a forced flow. Swirl had little effect on increasing turbulent intensity in a forced flow.

5. Primary air forcing had a significant effect on temperature in both nonswirling and swirling flows for all three configurations studied. Throughout the flame, significant effects of centerline temperature were observed. This implies that the mechanism of mixing enhancement due to entrainment in the near-field vortical structure applies to swirling flows.

6. Liquid-fuel pulsations proved to be most effective in a forced flame. Injecting fuel in-phase with air vortices provided the highest temperatures. In both nonswirling and swirling flames, injecting fuel out of phase with air vortices proved to be least efficient.

The present study is now focusing attention on feedback loop control where forcing will be used to reduce instabilities and minimize pollutants in swirling flames.

ACKNOWLEDGMENTS

REFERENCES

1. McManus, K. R., T. Poinsot, and S. Candel. 1993. A review of active control of combustion instabilities. *Progress Energy Combustion Science* 19:1–29.

2. Annaswamy, A. M., and A. F. Ghoneim. 1995. Active control in combustion systems. *IEEE Control Systems*. 49–63.

3. Gutmark, E., T. P. Parr, D. M. Hanson-Parr, and K. C. Schadow. 1990. Use of chemiluminescence and neural networks in active combustion control. *23rd Symposium (International) on Combustion Proceedings*. Pittsburgh, PA: The Combustion Institute. 1101–6.

4. Schadow, K. C., E. Gutmark, and K. J. Wilson. 1992. Active combustion control in a coaxial dump combustor. *Combustion Science Technology* 81:285–300.

5. Ho, C. M., and L. S. Huang. 1982. Subharmonics and vortex merging in mixing layers. *J. Fluid Mechanics* 119:443–73.

6. Ho, C. M., and P. Huerre. 1985. Perturbed shear layers. *Annual Reviews Fluid Mechanics* 16:365–424.

7. Hussain, A. K. M. F. 1983. Coherent structures — reality and myth. *J. Physics Fluids* 26:2816.

8. Sivasegaram, S., and J. H. Whitelaw. 1991. The influence of swirl on oscillations in ducted premixed flames. *Combustion Science Technology* 85:195–205.

9. Presser, C., A. K. Gupta, and H. G. Semerjian. 1993. Aerodynamic characteristics of swirl spray flames: Pressure-jet atomizer. *Combustion Flame* 92:25–44.

10. Ghaffarpour, M., and B. Chehroudi. 1993. Experiments on spray combustion in gas turbine model combustor. *Combustion Flame* 92:173–200.

11. Lee, K., and B. Chehroudi. 1994. Structure of a swirl-stabilized spray-flame relevant to gas turbines and furnaces. *25th Symposium (International) on Combustion Proceedings*. Pittsburgh, PA: The Combustion Institute.

12. Gutmark, E., T. P. Parr, K. J. Wilson, K. Yu, R. A. H. Smith, D. M. Hanson-Parr, and K. C. Schadow. 1996. Compact waste incinerator based on vortex combustion. *Combustion Science Technology* 121:333–49.

13. Stephens, J. R., S. Acharya, and E. J. Gutmark. 1997. Controlled swirl-stabilized spray combustor. AIAA Paper No. 97-0464.

14. Stephens, J. R., S. Acharya, and E. J. Gutmark. 1997. Swirl-stabilized spray combustion with periodic heat addition. AIAA Paper No. 97-0464.

15. Stephens, J. R., S. Acharya, E. J. Gutmark, and D. C. Allgood. 1997. Active forcing of air and fuel feed in swirl stabilized spray combustion. *ISOABE Proceedings*. Chattanooga, TN.

16. Sattelmayer, T., M. P. Felchlin, J. Hauman, J. Hellat, and D. Styner. 1992. Second-generation low-emission combustor for *ABB* gas turbines: Burner development and tests at atmospheric power. *J. Engineering Gas Turbines Power* 114:118–25.

Chapter 21

LIQUID-FUELED ACTIVE CONTROL FOR RAMJET COMBUSTORS

K. H. Yu, K. J. Wilson, T. P. Parr, and K. C. Schadow

An experimental study on active combustion control (ACC) was performed to better understand physical mechanisms associated with liquid-fueled control processes and to explore a practical ACC design based on pulsed liquid-fuel injection that may be suitable for future propulsion devices. The novel features of the present study include direct liquid-fuel injection into the combustion zone and controlled dispersion of fuel droplets using vortex–droplet interaction. Active instability suppression was demonstrated in a partially premixed dump combustor with additional pulsed liquid-fuel injection for control. Fuel distribution and combustion characteristics were investigated in terms of pulsed injection timing. In the present case, pressure oscillations were suppressed when the pulsing was in phase with the inlet vortex shedding. When the same control system was applied in higher output combustors, the relative amount of pulsed fuel appeared to play a critical role. The study not only sheds new light on the importance of dynamic interaction between flow structures and pulsed sprays in controlling spatial distribution of fuel droplets, but it also identifies important parameters for scale-up. Such results and understanding could be used to design a practical ACC system for future ramjets.

21.1 INTRODUCTION

As the requirements for future military combustors become increasingly demanding, an advanced combustion control system that can effectively shorten the combustor development time and improve the combustor performance will be an important technological asset to our military. Active combustion control (ACC) is an attractive idea because it relies on proper timing of fuel injection rather than spatial changes of flow field as required in passive approaches. Since timing adjustment is simpler than potential geometry modifications associated

with passive control, ACC provides flexibility in performance and eliminates costly design changes.

21.1.1 Background

In the past, studies on ACC have been motivated by undesirable combustor behaviors that include combustion instabilities [1–10], poor burning efficiency [8–13], limited operational range [8–10, 14], and excessive production of pollutants [8, 12, 13, 15–17]. These studies have contributed greatly to the present understanding of fast-response ACC, but several technological challenges still remain before the ACC technique can be implemented to practical propulsion systems. One such challenge is the use of liquid fuel for control, and maximization of control efficiency via direct injection into the combustion chamber. Such a control has been difficult to obtain and the physical processes were not well understood.

Liquid fuel was seldom utilized in the previous ACC studies because it was not only difficult to actuate liquid-fuel injection at high frequencies, but the combustion delays associated with liquid-fuel atomization, droplet heating, vaporization, and burning processes made such a control extremely slow for fast-response *in situ* type controllers. As a result, the use of liquid fuel was confined to either steady injection process [13] or upstream addition of prevaporized fuel [4, 7] which limited the ACC flexibility associated with temporal responsiveness. The goal of this project is to make ACC more practical for propulsion systems by studying direct liquid-fueled ACC in a closed-loop controller setting.

21.1.2 Rayleigh's Criterion

Extensive reviews of active instability suppression techniques are found in McManus *et al.* [18] and Candel [19]. Also, Zinn and Neumeier [20] provide an overview of research and developmental needs for practical applications. Most of the previous studies have used actuators impractical in liquid-fueled systems, such as loudspeakers that impose acoustic perturbations on gaseous flow. The major emphasis in the present study was to establish active instability suppression using liquid-fuel injection. According to Rayleigh's criterion [21, 22], combustion–acoustics interaction can be used to damp the undesirable oscillations provided that pressure fluctuations p' and heat release fluctuations q' satisfy the proper phase relation such that

$$\iint_{V} \int_{T} \frac{p'q'}{\overline{p}} \, dt \, d\vartheta < 0$$

where the double integral is taken over an instability period T and over the combustor volume V. One simple way to achieve heat release oscillations with controllable phase is to pulse the fuel injection.

Recent advances in active control and liquid-fuel-actuator technology have provided an ideal background for extending ACC to liquid-fueled combustors. Because heat release oscillations are affected by an instantaneous population of various-size fuel droplets in the local area, the dispersion of the fuel droplets inside the combustor must be controlled, as well as the global fuel flux into the combustor. Pulsating liquid fuel directly into the combustor effectively controls the global temporal fuel flux. Then, the interaction between fuel droplets and large-scale flow features was utilized as a means to control fuel spatial dispersion. The fuel-droplet size in this case needs to be sufficiently small for fast combustion response. Moreover, the droplets with the Stokes number less than unity are more strongly affected by interaction with flow structures [23–28]. Because the severity of the interaction was sensitive to the initial slip velocity, the injection timing became an important control parameter.

21.2   SYSTEM COMPONENTS AND INTEGRATION

21.2.1   Liquid-Fuel Actuator

The most important component in ACC is the actuator that can affect instantaneous combustion heat release. After evaluating several types of high-frequency fuel injectors, an automotive injector (*Bosch Jetronics*) that provided high-frequency response as well as high-volume flow rate has been chosen. A square wave with adjustable duty cycle was used for the injector electronic control unit (ECU) signal, which extended the frequency response. Figure 21.1 shows a series of pulsating ethanol sprays from the injector driven at different frequencies with customized square waves. The images were obtained by illuminating the droplets with a pulsed laser sheet (20 ns pulse width) that traversed along the center axis of the pulsating jet. They show clearly the fuel modulation at high frequencies and the extent of spatial modulation that could be obtained downstream.

The injector, when used directly, was not suitable for ACC at high frequencies as it produced very large droplets. To reduce droplet size, a swirl-based atomizer with 300 μm exit diameter [29] was fitted at the fuel jet exit. In this close-coupled configuration, the automotive fuel injector was used as a high-frequency solenoid valve for the fuel line. This new combination actuator improved the overall atomization characteristics while maintaining good frequency
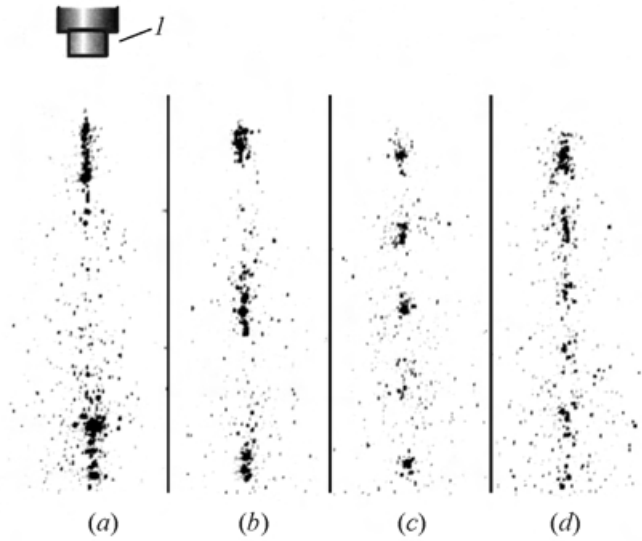
Figure 21.1 Planar Mie-scattering images of pulsed fuel injection with $\Delta p = 275$ kPa and the duty cycle equal to 50%: (*a*) $f = 240$, (*b*) $f = 480$, (*c*) $f = 960$, and (*d*) $f = 1140$ Hz. *1* — pulsed fuel injector
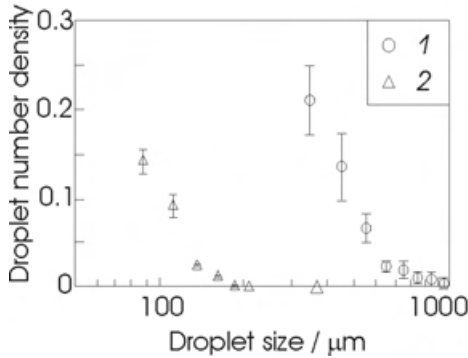

Figure 21.2 Average droplet size distribution with and without the atomizer: *1* — automotive injector, *2* — atomizer/ injector combination

response up to 1 kHz. Figure 21.2 shows the average droplet sizes measured from high-speed photographs [30] of sprays. About fourfold reduction in droplet size was obtained by close-coupling the atomizer with the fuel injector.

21.2.2 Simple Phase-Delay Controller

For active instability suppression, the approach taken in the present study is to pulse the liquid fuel at the instability frequency and adjust the timing using a simple closed-loop circuit. Because the empha-
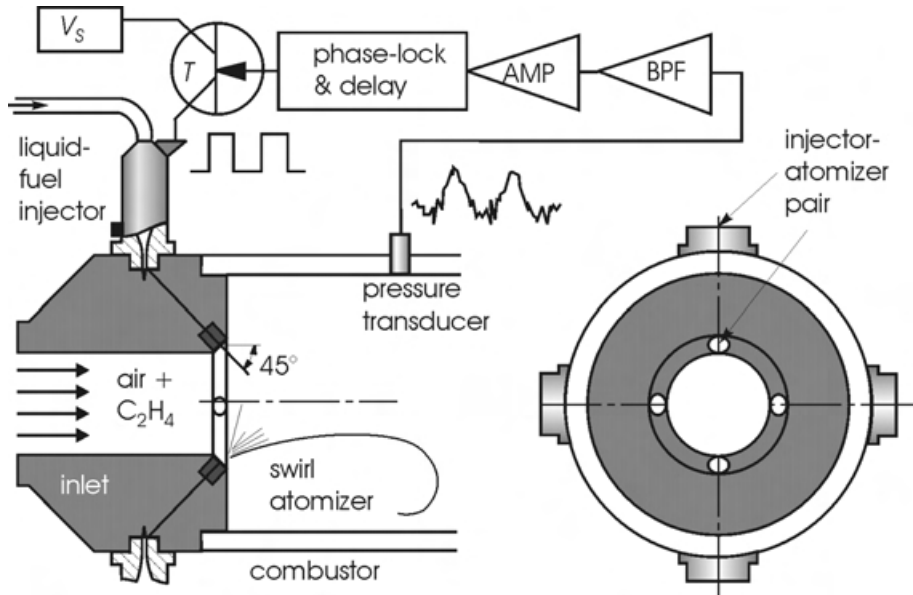
Figure 21.3 Injector set-up

sis was on extending active control to liquid-fueled combustors, a simple phase-delay circuit was utilized instead of a more sophisticated controller based on an adaptive technique [31] or model-based design approaches [32–34]. Figure 21.3 shows the ACC system that was used to control the fuel injection scheduling in the dump combustor. A *Kistler*[TM] pressure transducer, mounted at one inlet diameter downstream of the dump plane, was used to detect the oscillations in combustor pressure. Then, with the combustor pressure signal as reference, the phase shift for the injection cycle was digitally controlled using a *Wavetek*[TM] Variable Phase Synthesizer. The liquid fuel was injected through the four fuel actuators that were spaced 90° apart along the circumference of the inlet at the dump plane. The initial injection angle was fixed at 45° with respect to the air flow direction.

## 21.3   PHYSICAL MECHANISMS AND INTERACTIONS

To better understand how periodic fuel injection affected the turbulent mixing processes, cold flow simulation experiments were performed and the physical

mechanisms were compared between gaseous fuel and liquid-fuel injections. The inlet air flow was forced using a $Ling^{\text{TM}}$ electro-pneumatic transducer (94A-M1) to simulate unstable flow conditions. This resulted in an oscillating inlet flow with large amplitude of RMS fluctuations, which was about 60% of the centerline velocity, and periodic roll-up of large-scale vortices in the dump combustor shear layer.

21.3.1 Vortex Dynamics

In gaseous fuel injection, acoustic forcing of the fuel feed line not only creates periodic fuel flux, but it also sheds a pair of counter-rotating fuel vortices and affects shear layer vortex dynamics. Thus, turbulent mixing can be easily manipulated by the timing of pulsed fuel injection. In a gaseous-fueled experiment, fuel flow was forced with compression drivers at the same frequency as the simulated instability frequency but at different timings. Planar Mie-scattering images were taken as a function of fuel injection timing and air vortex development phase.

Figure 21.4 presents a sequence of phase-averaged images showing the turbulent mixing between smoke-seeded gaseous fuel flow and central air [35]. Each
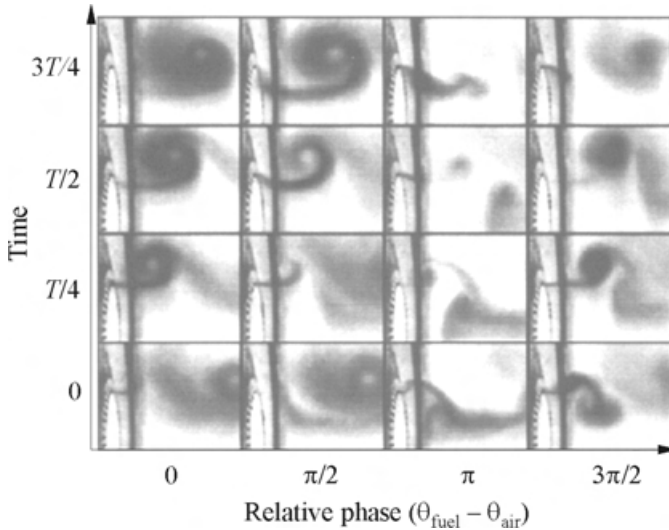

Figure 21.4 Vortex dynamics manipulation by actively controlling relative phase of fuel injection with respect to air vortex shedding

row corresponds to a particular stage of air vortex development while each column represents a fixed timing of fuel injection with respect to the air vortex shedding. Ten instantaneous images that were obtained at an identical phase of the oscillations and correspond to the same injection timing were averaged in an effort to filter out random features associated with flow turbulence. Fuel–air mixing was drastically altered by the relative timing of the pulsed fuel injection, which affected vortex dynamics. For instance, an in-phase fuel injection caused fuel streams to be stretched between surrounding air flows while an out-of-phase fuel injection resulted in pockets of concentrated fuel lumps that did not disperse very well. Such discrepancies in fuel–air mixing would certainly affect combustion performance.

21.3.2 Controlling the Spatial Distribution of Fuel Droplets

With liquid-fuel injection, the initial mixing takes place between two different phases. Because of the density difference, liquid-fuel flow is less affected by pressure waves in the combustor. Also, since the fuel droplets are much smaller than the dominant flow features in the combustor, the effect of fuel droplets on the shear-flow vortex dynamics is negligible. Furthermore, the droplets from any practical fuel injectors are distributed over a wide range of size, resulting in nonuniform time scales for combustion. Therefore, modulating the global fuel flux may or may not result in controlled oscillations of local turbulent mixing and heat release. Consequently, ACC using pulsed liquid-fuel injection is much more difficult than corresponding gaseous fuel injection.

In the present experiment, a new approach was utilized which relied upon timing-dependent droplet dispersion behavior. As a result of pulsed sprays interacting with periodic flow structures, the fuel droplet dispersion behavior was sensitive to the timing of fuel injection that determined the initial slip velocity between fuel and air flow. Figure 21.5 shows the liquid-fuel droplet dispersion as a function of the injection timing and vortex development phase [23]. Ethanol was injected periodically into the oscillating inlet flow, and the two-phase flow was visualized again in a phase-locked fashion. The sequences of images representing phase-averaged data on fuel droplet dispersion with respect to the underlying vortex structures were put together as illustrated. Again the images were phase-averaged to filter out random motion associated with turbulence. On one hand, when fuel was injected after the vortex shedding ($t = 0 \sim \pi/2$), the droplets clustered in the core of the jet flow. On the other hand, fuel droplets injected ahead of the vortex shedding ($t = \pi \sim 3\pi/2$) were subjected to the accelerating flow associated with the vortices, causing rapid dispersion into the recirculation zone. This concept, which utilizes the difference in slip velocity between fuel droplets and the surrounding air flow, provides some control over spatial distribution of fuel droplets.
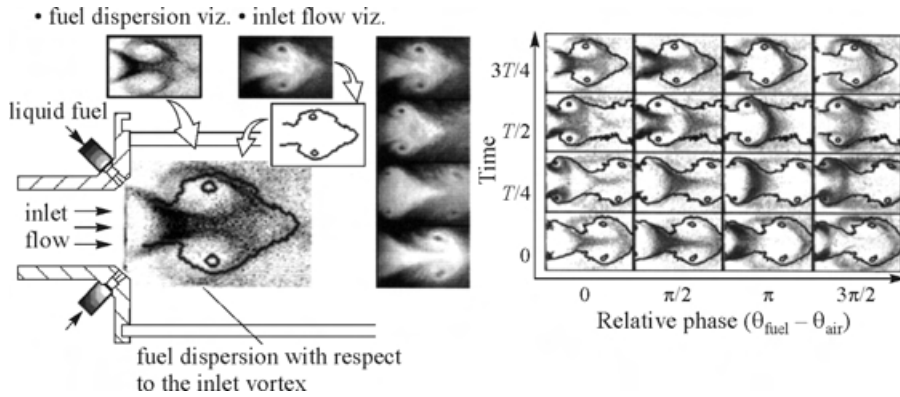
Figure 21.5 Phase-averaged fuel-droplet dispersion as a function of fuel injection timing with respect to the inlet flow vortex

21.4   DEMONSTRATION AND SCALE-UP

To demonstrate liquid-fueled active combustion control, instability suppression experiments were performed under several conditions. Figure 21.6 shows the dump combustor set-up used in the demonstration experiments. Three configurations in which naturally unstable oscillations were observed are shown. Table 21.1 lists the specific flow conditions where instabilities occurred. The case number in the table corresponds to the combustor configuration used.

21.4.1   Detailed Case Study

The first case with relatively low-combustor output was investigated in detail to better understand the physical processes involved. Figure 21.7 shows the pressure oscillation amplitude at the peak frequency that was measured as a function of overall equivalence ratio (ϕ) and the secondary fuel injection frequency. Strong pressure oscillations at 35 Hz were observed in the vicinity of the lean-mixture flammability limit. The oscillation amplitude was particularly strong when the injection frequency was between 32 and 38 Hz. The oscillation frequency often shifted toward the injection frequency, but it was not always identical to the injection frequency.

To determine the origin of the instability frequency, acoustic analysis was performed which revealed that both the quarter-wave mode of the inlet and the Helmholtz mode of the combustor–inlet system occurred at 35 Hz. The phase
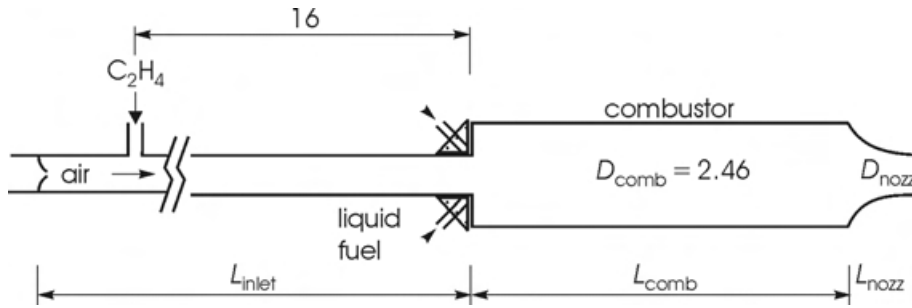
| Config.	Liquid fuel	L_{inlet}	L_{comb}	D_{nozz}	L_{nozz}
1	Ethanol	58.5	10.2	1.29	1.85
2	Heptane	25.8	11.8	0.615	1.85
3	Heptane	25.8	12.9	0.862	1.32

All dimensions are in terms of D_{inlet}

Figure 21.6 Model ramjet dump combustor with direct liquid-fuel injection for control

Table 21.1 Average flow conditions during naturally unstable operations[*]

Case	Flow rate (g/s)				ϕ	Unstable conditions		
	Air	Ethylene	Ethanol	Heptane		$\dfrac{\overline{P}_{comb}}{P_{exit}}$	f (Hz)	$\dfrac{P'_{rms}}{\overline{P}_{comb}}$
1A	45	1.0	0.75	—	0.47	1.02	34	0.008
1B	45	1.3	0.75	—	0.58	N/A	35	0.005
2	115 ± 2	3.3	—	0.62	0.51	2.20 ± 0.03	87	0.042
3A	146 ± 2	5.1	—	0.73	0.59	1.59	98	0.092
3B	198 ± 2	7.0	—	0.65	0.57	2.06	96	0.089

[*]Uncertainties in the measured quantities are the same as the last digit except as noted.

and amplitude of 35 Hz oscillations were measured at different axial locations, and the results are presented in Fig. 21.8. Toward the upstream, the amplitude of pressure oscillations increased slightly and the phase of 35 Hz oscillations trailed that near the dump plane. While this trend is somewhat similar to that observed in a duct with longitudinal waves, the result is not consistent with pure quarter-wave mode nor does it match that of the Helmholtz mode oscillations. This indicates that the present instability is the result of more complex interaction between the two acoustic modes interacting with combustion heat release.
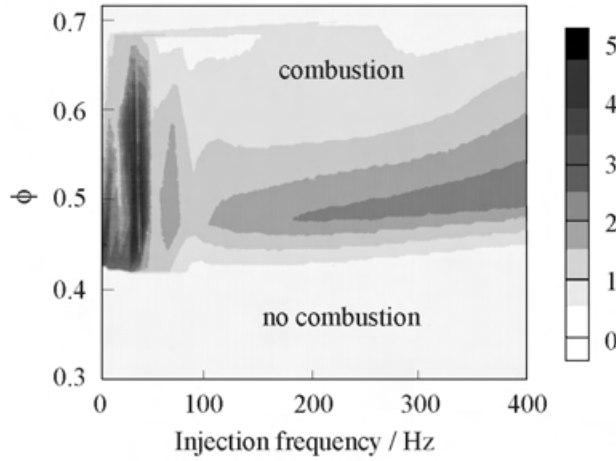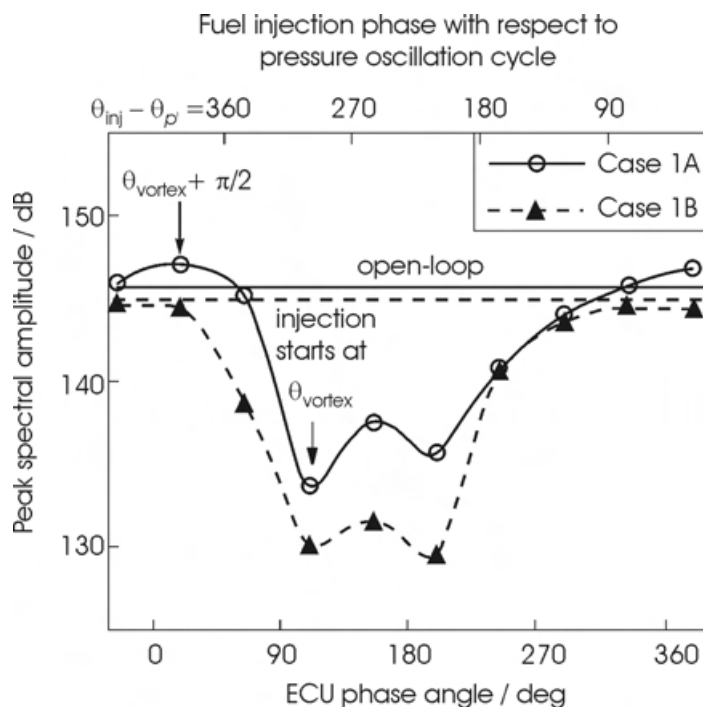
Figure 21.7 RMS amplitude of combustor pressure oscillations at the peak instability frequency (10^{-2} psi)
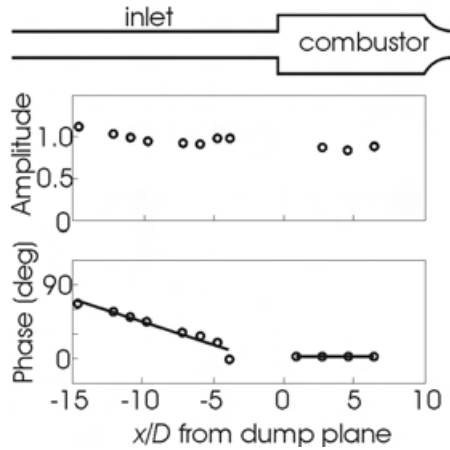
Figure 21.8 Instability mode shape for Case 1A

The closed-loop controller of Fig. 21.3 was applied to suppress the oscillations. Figure 21.9 shows the average RMS amplitude of pressure oscillations as a function of the phase delay assigned to the ECU. To assist the phase-lock, the pressure signal was filtered between 25 and 40 Hz using a *Butterworth* band-pass filter. The actual phase delay with respect to the pressure signal is also shown in the top abscissa. With the closed-loop control, the oscillation amplitude was sensitive to the injection timing. The amplitude reached maximum when the pulsed injection started at phase $\pi/2$ after the vortex shedding, and it was minimum when the start of the injection was synchronized with the vortex shedding. The maximum amplitude in this case was very close to the natural oscillation amplitude without the control. For the two conditions shown at $\phi = 0.47$ and 0.58, the sound pressure level was reduced by 12 and 15 dB, respectively. The phase relation was not affected by small changes in operating conditions.

Fuel injection phase with respect to
pressure oscillation cycle

$\theta_{inj} - \theta_{p'} = 360$ 270   180   90

Peak spectral amplitude / dB

$\theta_{vortex} + \pi/2$

150

Case 1A
Case 1B

open-loop

injection
starts at

140

θ_{vortex}

130

0   90   180   270   360

ECU phase angle / deg

Figure 21.9 Pressure oscillation spectral amplitude as a function of injection timing. The two straight lines show the amplitude levels for uncontrolled cases

Figure 21.10 shows the transient behavior of the combustor pressure as the proper phase-delay was applied at time $t = 0$ and the comparison of the pressure spectra. The high-amplitude oscillations were quickly brought under control and all of the harmonics, as well as the fundamental, were effectively suppressed in this case. The RMS pressure amplitude under active control was maintained well below 0.5% of the combustor pressure. It should also be noted, however, that oscillations at a very small level are still needed to maintain the phase-lock and vortex-synchronized fuel injection.

21.4.2 Higher Output Combustors

With the success of active instability suppression at the 70 to 80 kW level, scale-up experiments were conducted by increasing the amount of premixed inlet
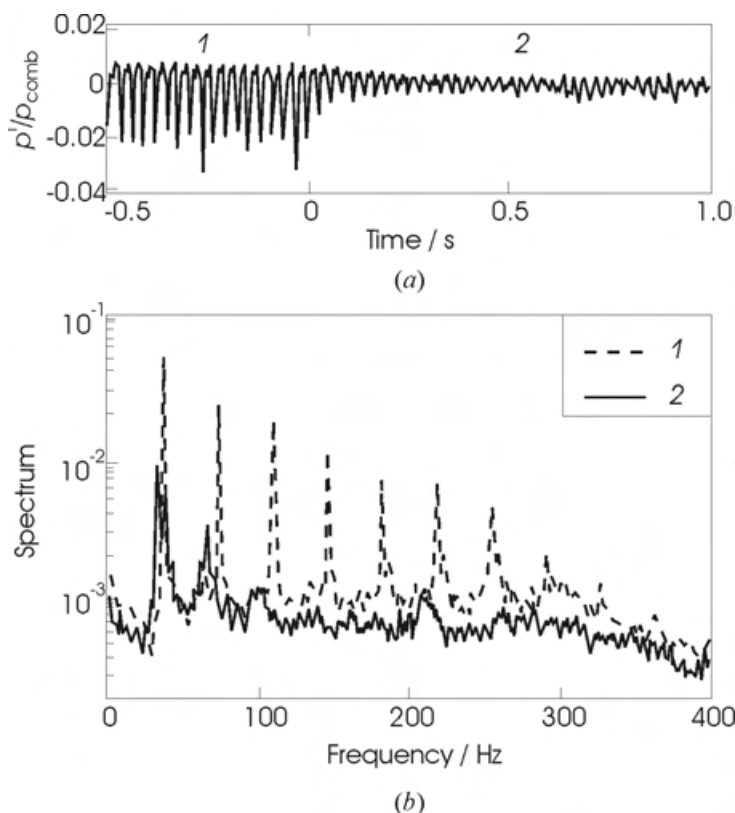
Figure 21.10 Active instability suppression in Case 1A: (*a*) onset of active control, *1* — without control, *2* — with closed-loop control; (*b*) comparison of pressure spectra. *1* — uncontrolled, *2* — controlled

flow up to a factor of four. Since the combustor in configuration 1 was rather stable at higher flow rates, the combustor and inlet lengths and the exhaust nozzle size were systematically modified. Self-sustaining combustion instabilities were observed at configurations 2 and 3 with the unstable conditions listed in Table 21.1. Because the actuator characteristics for the liquid-fuel injection are critical for active control and those used in configuration 1 were well proven, they were not changed in the scale-up experiments. The controller fuel was, however, changed from ethanol to heptane in an effort to increase the amount of periodic heat release potential, since the enthalpy of combustion for heptane is about 66% higher than that of ethanol. The atomization characteristics of the fuel droplets were affected very little by this change.
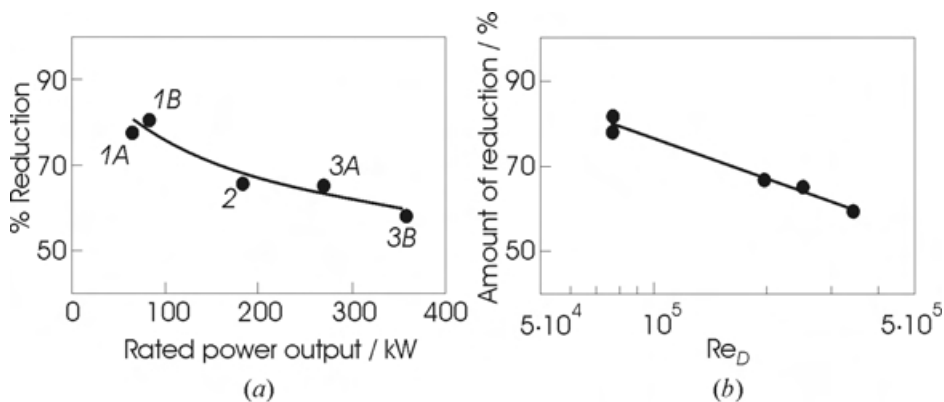
Figure 21.11 Relative amount of instability suppression as a function of (*a*) rated power output, and (*b*) the inlet flow Reynolds number

By applying the closed-loop control to the unstable combustors, it was again possible to reduce pressure oscillation amplitude significantly at the peak frequency even with the higher power level. Initial observations, however, revealed that the amount of reduction was related to the nominal combustor power output. The relative effectiveness of the controller was quantified in terms of the oscillation amplitude reduction achieved with the control at various scales. Figure 21.11 shows the general trend associated with flow scale, which appears to indicate that the control effectiveness diminishes with the increasing Reynolds number. Later, it will be shown that this trend was more likely the result of the reduction in the relative amount of fuel being pulsated.

21.4.3 Parameters Important to Scale-Up

To elucidate the possible causes of the decrease in suppression potential, the effects of flow residence time and relative pulsating fuel amount were examined. One possible explanation for the above trend is the reduction in flow residence time as the flow rate was increased. At these conditions some of the larger fuel droplets that persisted in the downstream may not have had enough time to react completely if the residence time became very short. When the residence time was estimated by the reference time scale which is the combustor length divided by inlet velocity (Fig. 21.12), the general trend appears to be consistent with the expectation. The scatter in the plot reflects the crudeness of the estimation; larger droplets do not follow the carrier flow very well.

The relative contribution of heat release from the pulsed fuel injection provides another explanation. Because the same actuator system was utilized in all
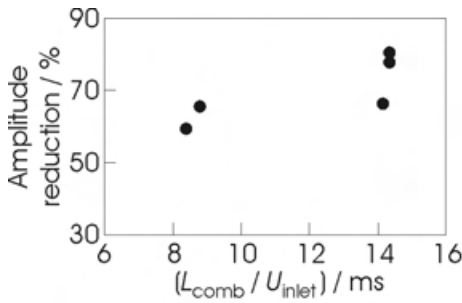
Figure 21.12 Effect of flow residence time on control effectiveness

of the experiments, this ratio was subject to change as the primary steady fuel flux was modified or the type of fuel was changed in the system. Figure 21.13a shows the dependence on the ratio of the power output from controlled fuel injection to the total power output. The resulting relationship between the control effectiveness and the power ratio was quite similar to the dependency on the Reynolds number. Figure 21.13b shows another measure of the control effectiveness in terms of the total number of oscillation cycles required to bring the amplitude to the controlled level. As the relative power ratio was lowered to about 0.1, the control became only marginally effective requiring many cycles to bring down the oscillation amplitude. Again, the result correlated well with the ratio suggesting a critical amount of pulsed fuel injection required for effective control. The results indicate that the relative contribution of heat release from pulsed fuel injection is an important parameter affecting the control effectiveness and will play an important role during scale-up.
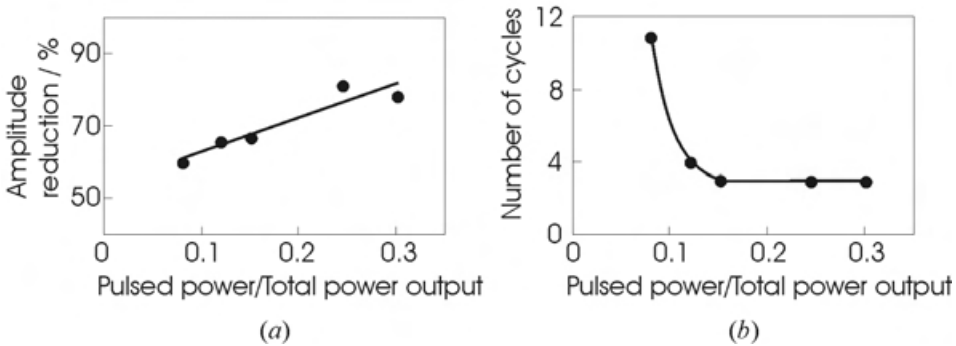
Figure 21.13 Dependence of active control effectiveness on pulsed power fraction

21.4.4 Limitation of Simple Phase-Shift Controller

Intermittent loss of control was observed in the high output cases with only marginally effective pulsed fuel injection. Figure 21.14 shows the pressure history
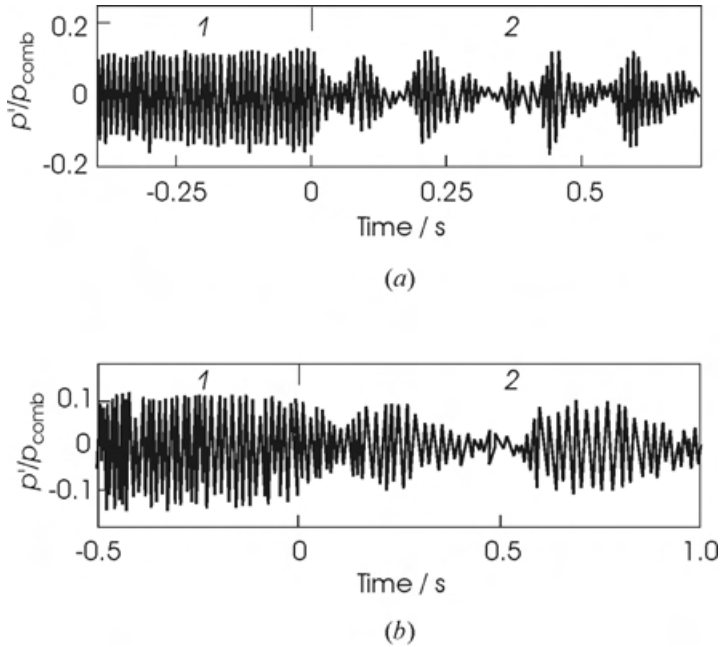
Figure 21.14 Periodic loss of control in (*a*) Case 3A; (*b*) Case 3B: *1* — without control, *2* — with closed-loop control

for the two cases in which the oscillation amplitude was first reduced then grew back in a repeated fashion. This behavior was apparently caused by the inability of the fixed-phase controller to simultaneously suppress oscillations over a broad band of frequencies. In the simple controller, *Butterworth* band-pass filter was used to obtain the phase lock on the pressure signal. Since the filter introduces an electronic phase shift which changes with the signal frequency, the pre-assigned phase shift may not stay uniform unless the oscillation frequency remains the same.

Figure 21.15 shows the transient response of the measured pressure shortly before and after the onset of the control. In Fig. 21.15*b*, the apparent frequency of the oscillations was deduced as a function of time by measuring the zero crossing. Two sets of data are plotted since every other zero crossing corresponds roughly to one period of oscillation. The curve fit coincides with the average of the two. Figure 21.15*c* shows the resulting phase shift associated with the frequency change in Fig. 21.15*b*. At about 40 ms after the control was turned
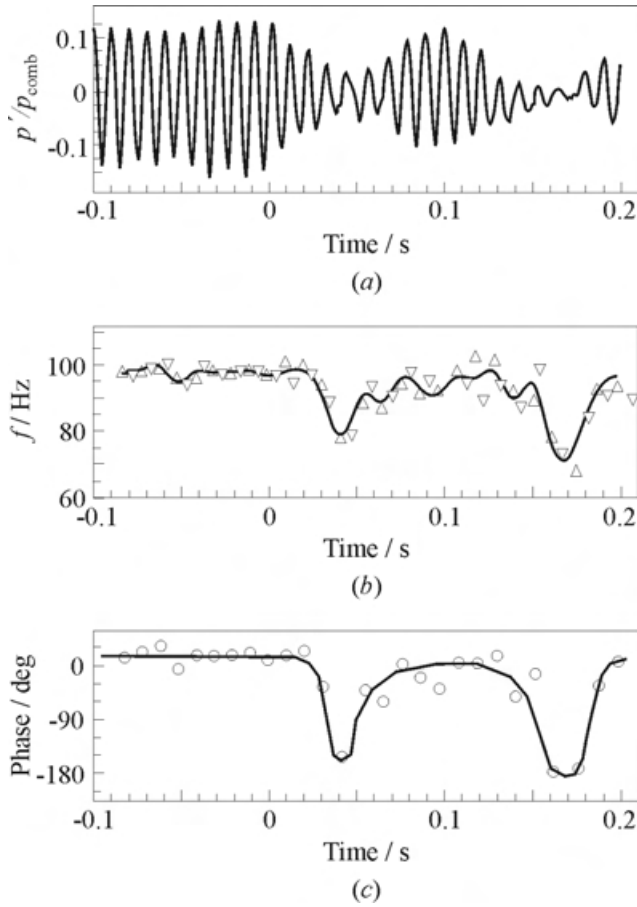
Figure 21.15 Transient system response to onset of control at time $t = 0$ in Case 3A: (*a*) measured amplitude, (*b*) apparent frequency of pressure oscillations, and (*c*) fuel injection phase based on the controller frequency response

on, the oscillation amplitude reached the minimum value. At the same time, the apparent frequency of the oscillation was lowered by almost 20 Hz, about a half of the band-pass filter width. As a result, the overall phase shift was changed by 180°, making the new phase delay more suitable for pressure amplification than suppression. As the amplitude grew, the oscillation frequency returned to the original level and once again the phase setting shifted into the suppression mode. This result clearly shows a limitation of the simple fixed-phase-type controller in suppressing complex modes of instabilities.

21.5   CONCLUDING REMARKS

There are opportunities to advance propulsion technologies by incorporating our understanding of vortex dynamics in turbulent shear layers with fast active combustion control, which will replace current controls that are based on passive strategies. In most propulsion devices, combustion control still relies on passive techniques which require individually customized modifications in geometry and/or materials. Unlike passive control, which utilizes certain spatial arrangements for desired outcome, active control is based on precise scheduling of temporal events. This switch in emphasis from spatial to temporal precision will allow more flexibility into the combustor design, and may revolutionize combustion control in the long run.

The present study was conducted in an effort to better understand ACC mechanisms and to design practical ACC based on pulsed liquid-fuel injection suitable for propulsion devices. The controller utilized a simple fixed phase-delay approach that has been studied previously, but the direct liquid-fuel injection and the novel use of vortex–droplet interaction made the present study unique. The demonstration experiment in a 102-millimeter dump combustor showed that combustion instabilities can be successfully suppressed using properly designed pulsed liquid-fuel injection.

The study shed new light on the importance of dynamic interaction between flow structures and pulsed sprays in liquid-fueled ACC. The results provided valuable information on the fuel injection timing for desired outcome. In the present case, the fuel injection timing that was synchronized with the air vortex shedding led to the suppression of pressure oscillations. When the fuel injection timing was delayed a quarter cycle after the vortex shedding, combustor pressure oscillations reached the highest amplitude. The scale-up test revealed a critical role of the relative amount of modulated heat release from pulsed fuel injection.

Because the initial emphasis of this study was on extending ACC to liquid-fueled combustors, a simple closed-loop controller, which had been well tested in the previous studies involving gaseous fuel, was utilized. Such a controller, however, may not be effective in a combustor where the oscillation frequencies drift significantly with the control. The main problem was the frequency-dependent phase shift associated with the frequency filter. For such a case, it would be more useful to employ an adaptive controller that can rapidly modify the phase setting depending on the shift in the dominant oscillation frequencies.

Future studies should explore the use of more sophisticated controller logic and other system related components including better actuators and sensors. For proper application of ACC, however, basic understanding of the physical mechanisms and related combustion processes is the key element, as indicated by the present study.

ACKNOWLEDGMENTS

REFERENCES

1. Lang, W., T. Poinsot, and S. Candel. 1987. Active control of combustion instability. *Combustion Flame* 70:281–89.

2. Bloxsidge, G. J., A. P. Dowling, N. Hooper, and P. J. Langhorne. 1988. Active control of reheat buzz. *AIAA J.* 26:783.

3. Poinsot, T., F. Bourienne, S. Candel, and E. Esposito. 1989. Suppression of combustion instabilities by active control. *J. Propulsion Power* 5:14–20.

4. Langhorne, P. J., A. P. Dowling, and N. Hooper. 1990. A practical active control system for combustion oscillations. *J. Propulsion Power* 6:324–33.

5. Schadow, K. C., E. Gutmark, and K. J. Wilson. 1992. Active combustion control in a coaxial dump combustor. *Combustion Science Technology* 81:285–300.

6. Gulati, A., and R. Mani. 1992. Active control of unsteady combustion-induced oscillations. *J. Propulsion Power* 8(5):1109–15.

7. Sivasegaram, S., R-F. Tsai, and J. H. Whitelaw. 1995. Control of combustion oscillations by forced oscillation of part of the fuel supply. *Combustion Science Technology* 105:67.

8. McManus, K. R., U. Vandsburger, and C. T. Bowman. 1990. Combustor performance enhancement through direct shear layer excitation. *Combustion Flame* 82:75–92.

9. Wilson, K. J., E. Gutmark, K. C. Schadow, and R. A. Smith. 1991. Active control of a dump combustor with fuel modulation. AIAA Paper No. 91-0368.

10. Gutmark, E., T. P. Parr, D. M. Hanson-Parr, and K. C. Schadow. 1989. Stabilization of combustion by controlling the turbulent shear flow structure. *7th Symposium on Turbulent Shear Flows Proceedings*. Paper No. 23-1.

11. Yu, K., A. Trouve, and S. Candel. 1991. Combustion enhancement of a premixed flame by acoustic forcing with emphasis on role of large-scale structures. AIAA Paper No. 91-0367.

12. Gutmark, E., T. P. Parr, D. M. Hanson-Parr, and K. C. Schadow. 1990. Use of chemiluminescence and neural networks in active combustion control. *23rd Symposium (International) on Combustion Proceedings*. Pittsburgh, PA: The Combustion Institute. 1101–6.

13. Brouwer, J., B. A. Ault, J. E. Bobrow, and G. S. Samuelsen. 1990. Active control for gas turbine combustors. *23rd Symposium (International) on Combustion Proceedings*. Pittsburgh, PA: The Combustion Institute. 1087–92.

14. Gutmark, E., T. P. Parr, D. M. Hanson-Parr, and K. C. Schadow. 1991. Closed-loop amplitude modulation control of reacting premixed turbulent jet. *AIAA J.* 29(12):2155–62.

15. Parr, T. P., E. J. Gutmark, K. J. Wilson, K. Yu, R. A. Smith, D. M. Hanson-Parr, and K. C. Schadow. 1996. Compact incinerator afterburner concept based on vortex combustion. *26th Symposium (International) on Combustion Proceedings*. Pittsburgh, PA: The Combustion Institute. 2033–55.

16. Keller, J. O., and I. Hongo. 1990. Pulse combustion: The mechanism of NO_x production. *Combustion Flame* 80:219–37.

17. Sivasegaram, S., and J. H. Whitelaw. 1996. Control of flame and emissions by oscillation. *9th ONR Propulsion Meeting Proceedings*. Eds. G. D. Roy and K. Kailasanath. Washington, DC: Naval Research Laboratory. 272–85.

18. McManus, K. R., T. Poinsot, and S. Candel. 1993. A review of active control of combustion instabilities. *Progress Energy Combustion Science* 19:1–29.

19. Candel, S. M. 1992. Combustion instabilities coupled by pressure waves and their active control. *24th Symposium (International) on Combustion Proceedings*. Pittsburgh, PA: The Combustion Institute. 1277–96.

20. Zinn, B. T., and Y. Neumeier. 1997. Active control of combustion instabilities. AIAA Paper No. 97-0461.

21. Lord Rayleigh. 1945. *The theory of sound*. Dover. 227.

22. Putnam, A. 1971. *Combustion driven oscillations in industry*. New York: Elsevier.

23. Yu, K. H., T. P. Parr, K. J. Wilson, K. C. Schadow, and E. J. Gutmark. 1996. Active control of liquid-fueled combustion using periodic vortex–droplet interaction. *26th Symposium (International) on Combustion Proceedings*. Pittsburgh, PA: The Combustion Institute.

24. Lazaro, B. J., and J. C. Lasheras. 1989. Particle dispersion in a turbulent, plane, free shear layer. *J. Physics Fluids A* 1:1035–44.

25. Longmire, E. K., and J. K. Baton. 1992. Structure of a particle-laden round jet. *J. Fluid Mechanics* 236:217–57.

26. Glawe, D. D., and M. Samimy. 1993. Dispersion of solid particles in compressible mixing layers. *J. Propulsion Power* 9(1):83–89.

27. Chung, J. N., and T. R. Troutt. 1988. Simulation of particle dispersion in an axisymmetric jet. *J. Fluid Mechanics* 186:199–222.

28. Chang, E., and K. Kailasanath. 1996. Simulation of particle dynamics in a confined shear flow. *AIAA J.* 34(6):1160–66.

29. Parr, T. P., E. J. Gutmark, D. M. Hanson-Parr, and K. Yu. 1995. Control of sooty high-energy-density fuel combustion. *8th ONR Propulsion Meeting Proceedings*. Eds. G. D. Roy and F. Williams. La Jolla, CA: University of California at San Diego. 215–24.

30. Lefebvre, A. H. 1989. *Atomization and sprays*. Bristol, PA: Taylor & Francis. 380.

31. Billoud, G., M. A. Galland, C. Huynh Huu, and S. Candel. 1992. Adaptive active control of combustion instabilities. *Combustion Science Technology* 81:257–83.

32. Yang, V., A. Sinha, and Y-T. Fung. 1992. State-feedback control of longitudinal combustion instabilities. *J. Propulsion Power* 8(1):66–73.

33. Fung, Y-T., and V. Yang. 1992. Active control of nonlinear pressure oscillations in combustion chambers. *J. Propulsion Power* 8(6):1282–89.

34. Annaswamy, A. M., M. Fleifil, J. W. Rumsey, J. P. Hathout, and A. F. Ghoniem. 1997. An input–output model of thermoacoustic instability and active control design. MIT Report No. 9705. Cambridge, MA.

35. Yu, K., K. J. Wilson, T. P. Parr, and K. C. Schadow. 1996. Active combustion control using multiple vortex shedding. AIAA Paper No. 96-2760.

Chapter 22

ROBUST FEEDBACK CONTROL OF COMBUSTION INSTABILITIES WITH MODEL UNCERTAINTY

V. Yang, B. S. Hong, and A. Ray

This paper deals with the development of a robust feedback controller for suppressing combustion instabilities in propulsion systems with distributed actuators. Emphasis is placed on the treatment of model and parameter uncertainties in both time and frequency domains. The control synthesis is based on an improved H_∞ algorithm which guarantees the stability of all perturbed dynamics within a given uncertainty bound. The scheme is capable of rejecting exogenous disturbances arising from sensor and plant noises, while optimizing the system performance. Implementation of the controller in a generic dump combustor with longitudinal pressure oscillations has been successfully achieved.

22.1 INTRODUCTION

The use of feedback-control techniques to modulate combustion processes in propulsion systems has recently received extensive attention [1–3]. Most of the previous studies involved direct implementation of existing control methods designed for mechanical devices, with very limited effort devoted to the treatment of model and parametric uncertainties commonly associated with practical combustion problems. It is well established that the intrinsic coupling between flow oscillations and transient combustion responses prohibits detailed and precise modeling of the various phenomena in a combustion chamber, and, as such, the model may not accommodate all the essential processes involved due to the physical assumptions and mathematical approximations employed. The present effort attempts to develop a robust feedback controller for suppressing combustion instabilities in propulsion systems. Special attention is given to the treatment of model uncertainties. Various issues related to plant

disturbance, sensor noise, and performance specification are also discussed in detail.

A variety of feedback-control techniques have been used in suppressing combustion instabilities, as summarized in Table 22.1. The most primitive type is the proportional (P)-controller in a single-input and single-output (SISO) setting, in which the stability and performance are achieved only by an operation amplifier between the sensor and actuator. The P-controller can be extended to form a proportional-integral-derivative (PID) control system, in which the I-control is for zero steady error since it integrates the error in time and the D-control is for transient response since it regulates the tendency of motion [4]. Conceptually, there are only three control parameters in a PID system, and, as such, the controller design is greatly simplified. However, when the plant dynamics is of high order, such a low-order controller may not fulfill various performance requirements. For linear systems, a PID controller can be extended to accommodate a filter with phase compensation in the frequency domain, or to form an integral state-feedback controller in the time domain. If all the states cannot be measured, an observer is usually needed [11, 12]. It is straightforward to design an observer for a linear time-invariant system, but not for a time-varying or nonlinear system.

In the frequency domain, the open-loop dynamics can be easily represented by the Bode plot through either theoretical modeling or system identification [5, 6, 1, 7–10]. The representation of system dynamics in the frequency domain simplifies the filter design and the stability analysis based on the Nyquist criterion. The robustness of a controller is traditionally predicted in terms of phase and gain margins. However, when uncertainties in both phase and gain simultaneously take place, the issue of robustness should be judged by the magnitude of the μ or H_∞ norm of the closed-loop system [21].

In the time domain, a state-feedback controller processes all state information to determine the system stability and performance. Among the various designs, the linear quadratic regular (LQR) controller appears to be the most robust, with its gain margin in the range of $[1/2, \infty)$ and the phase margin of at least $60°$ [22]. However, the LQR controller is useful only if all the states of a combustion system can be determined. An observer is often needed to meet this requirement, and the resulting system becomes a linear quadratic Guassian (LQG) controller [13]. The scheme may be further extended for nonlinear problems using an energy method in terms of the Lyapunov function [19]. The major deficiency of LQG regulators lies in their failure to guarantee gain and phase margins [23]. An H_∞-based structure singular value (μ) may be required to judge robust stability and performance [21].

Nonmodel-based controllers, such as the least mean square (LMS) and artificial neural network back-propagation adaptive controllers, employ iterative approaches to update control parameters in real time [14–17]. However, those methods may encounter difficulties of numerical divergence and local optimiza-

Table 22.1 Survey of active combustion control techniques

Control technique	Application	Remarks
PID design	Nonlinear generic combustion instability [4]	1. Easy to adjust control parameters 2. May not fulfill various performance requirements
Bode–Nyquist frequency domain design and Root locus	Generic combustion instability [5] Low-frequency combustion instability [6] Low-frequency combustion instability [1] Thermoacoustic instability in premixed laminar combustor [7] Coaxial dump combustor [8] Longitudinal combustion instability in premixed combustor [9] Liquid-fueled combustion systems [10]	1. Easy to identify systems and design controller in frequency domain 2. Fail in time-varying and nonlinear systems 3. Only for SISO, can be more general in H_∞ and μ control 4. Controllability and observability can not be predicted 5. Easy for filter design 6. Can sense as the basis of phase-lead and phase-lag compensator design
Observer-based design: Adaptive observer and Model-based observer	Thermoacoustic instability in rocket motor [11] Longitudinal combustion instability [12]	1. Nominal model-based observer can be extended to optimal LQG regulator 2. Adaptive observer has no guarantee of convergence; its algorithm is one branch of the gradient iterative rules
LQR and LQG control	Thermoacoustic instability in premixed laminar combustor [13]	1. LQR control has optimal and robust properties of gain and phase margins, but requires measurements of all states 2. LQG control has no robust property and is used only for rejection of intensity-known noise

Table 22.1 Survey of active combustion control techniques (Continued)

Control technique	Application	Remarks
LMS adaptive and Neural Network back propagation	Large-scale solid rocket motor [14] Generic combustion instability [15] Dump combustor [16] Boiler combustion systems [17]	1. Sensitive to initial conditions and gradient dynamic parameters 2. Has similar algorithm in System ID 3. May be replaced by off-line ID plus Bode–Nyquist or observer-based controller
Fuzzy logic control	Longitudinal combustion instability [18]	1. Only effective when many states can be sensored 2. Need experience to set up logic rules and scales 3. Not used alone
Lyapunov-based design	Generic combustion instability [19]	1. Need more generalized control algorithms 2. Nonlinear H_∞ control is based on Lyapunov design, but with general algorithms
H_∞ and μ control	Generic combustion instability [20]	1. Observer-based controller with robust property; valid for intensity-unknown disturbance 2. Can regulate frequency domain property 3. Accommodate model uncertainty

tion, and consequently can not guarantee stability and performance. In addition, most adaptive algorithms do not accommodate any physical model of plant dynamics. It is formidable to establish general rules for system improvement and to conduct problem diagnostics. Rules-based controllers such as fuzzy logic controller is effective only if almost complete states can be measured [18]. To set up logic rules and scales requires extensive physical understanding and operation experience, which usually are not available for complex systems.

While the control schemes summarized in Table 22.1 have been employed in various combustion problems with some success, direct implementation of these

techniques on practical propulsion systems may not be feasible due to concerns with robustness, reliability, and operationability. Compared with mechanical devices, a combustion chamber with feedback-control fuel burning exhibits several distinct features [1]:

– distributed actuation arising from the burning of injected fuel;

– time lag associated with the complex chain of fuel injection–atomization–ignition–combustion processes;

– intensive noise due to intricate fluid dynamics and combustion unsteadiness;

– time variation due to transient operation; and

– model uncertainties due to physical assumptions and mathematical approximations employed.

In view of this, a robust scheme based on the H_∞ control theory [24] is developed in the present work. The algorithm guarantees both stability and performance for a family of perturbed plants with model uncertainties and exogenous inputs (i.e., chamber disturbances and sensor noises) over a wide range of operating conditions, an advantage especially desired for combustion dynamics problems.

The outline of this paper is as follows. First, a theoretical model of unsteady motions in a combustion chamber with feedback control is constructed. The formulation is based on a generalized wave equation which accommodates all influences of acoustic wave motions and combustion responses. Control actions are achieved by injecting secondary fuel into the chamber, with its instantaneous mass flow rate determined by a robust controller. Physically, the reaction of the injected fuel with the primary combustion flow produces a modulated distribution of external forcing to the oscillatory flowfield, and it can be modeled conveniently by an assembly of point actuators. After a procedure equivalent to the Galerkin method, the governing wave equation reduces to a system of ordinary differential equations with time-delayed inputs for the amplitude of each acoustic mode, serving as the basis for the controller design.

The second part of the work involves implementing a robust controller. The key issue in the controller design is the treatment of system dynamics uncertainties and rejection of exogenous disturbances, while optimizing the flow responses and control inputs. Parameter uncertainties in the wave equation and time delays associated with the distributed control process are formally included. Finally, a series of numerical simulations of the entire system are carried out to examine the performance of the proposed controller design. The relationships among the uncertainty bound of system dynamics, the response of flow oscillation, and controller performance are investigated systematically.

22.2 FORMULATION OF COMBUSTION DYNAMICS

The combustion system considered in the present work is shown in Fig. 22.1, representing a generic model for several types of air-breathing combustors such as ramjet and gas turbine engines. Fuel and oxidizer are delivered to the chamber, in which large excursions of unsteady motions take place due to the internal coupling between flow oscillations and transient combustion response. To control combustion instabilities, the strategy described in [1] is followed with several steps involved in a closed loop. First, the instantaneous chamber conditions are monitored by sensors at rates sufficient to resolve the characteristics of unsteady motions. The measured signals are then processed through a controller to modulate the mass flow rate of a secondary supply of fuel. Finally, the injected fuel reacts with combustor flow as it travels downstream, exerting a distribution of external influences on the oscillatory flowfield for instability control.
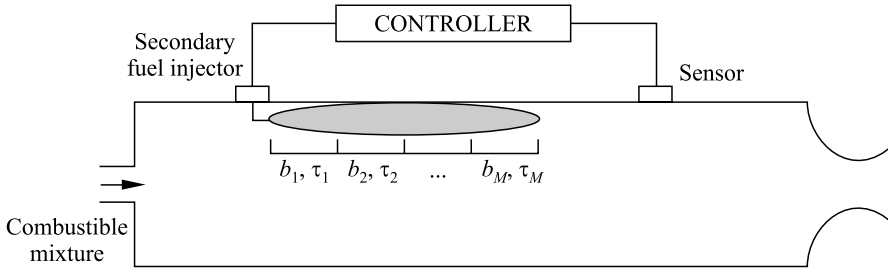
Figure 22.1 Schematic of feedback control system with distributed actuators

The formulation of combustion dynamics can be constructed using the same approach as that employed in the previous work for state-feedback control with distributed actuators [1, 4]. In brief, the medium in the chamber is treated as a two-phase mixture. The gas phase contains inert species, reactants, and combustion products. The liquid phase is comprised of fuel and/or oxidizer droplets, and its unsteady behavior can be correctly modeled as a distribution of time-varying mass, momentum, and energy perturbations to the gas-phase flowfield. If the droplets are taken to be dispersed, the conservation equations for a two-phase mixture can be written in the following form, involving the mass-averaged properties of the flow:

$$mass \qquad\qquad \frac{\partial \rho}{\partial t} + \mathbf{v}_g \cdot \nabla \rho = \mathsf{W} \qquad\qquad (22.1)$$

$$\textit{momentum} \qquad \rho\frac{\partial \mathbf{v}_g}{\partial t} + \rho\mathbf{v}_g\cdot\nabla\mathbf{v}_g = -\nabla p + \mathsf{F} \tag{22.2}$$

$$\textit{energy} \qquad \frac{\partial p}{\partial t} + \overline{\gamma}p\nabla\cdot\mathbf{v}_g = -\mathbf{v}_g\cdot\nabla p + \mathsf{P} \tag{22.3}$$

where

$$\mathsf{W} = -\rho\nabla\cdot\mathbf{v}_g - \nabla\cdot(\rho_l\delta\mathbf{v}_g) \tag{22.4}$$

$$\mathsf{F} = \nabla\cdot\tau_v + \delta\mathbf{F}_l + \delta\mathbf{v}_l\omega_l \tag{22.5}$$

$$\mathsf{P} = \frac{\overline{R}}{\overline{C}_V}\left[Q + \delta Q_l + \nabla\cdot\mathbf{q} + \delta\mathbf{v}_l\cdot\mathbf{F}_l \right.$$

$$\left. + \left\{(h_l - e_g) + \frac{1}{2}(\delta\mathbf{v}_l)^2\right\}\omega_l - \overline{C}_V T_g\nabla\cdot(\rho_l\delta\mathbf{v}_l)\right] \tag{22.6}$$

and $\delta\mathbf{v}_l = \mathbf{v}_l - \mathbf{v}_g$, $\delta h_l = h_l - C_l T$. The subscripts g and l stand for the mass-averaged quantities for gas and liquid phases, respectively, and ρ is the density of the mixture; the viscous stress tensor and conductive heat flux vector are represented respectively by τ_v and $\mathbf{q}$; Q is the energy released by homogeneous reactions in the gas phase; and the force of interaction and energy transfer between gas and liquid are $\delta\mathbf{F}_l$ and δQ_l, respectively.

Whatever physical means are devised, control inputs must be theoretically treated as sources in the above conservation equations. Therefore, Eqs. (22.1)–(22.3) are modified by adding control inputs W_c, F_c, and P_c, on the right-hand side. The subscript c represents the effects arising from the control inputs. If one considers only the influence associated with heat released from the injected fuel, P_c takes the form

$$\mathsf{P}_c = \frac{\overline{R}}{\overline{C}_V}Q_c = \frac{\overline{R}}{\overline{C}_V}\dot{w}_c\Delta H_c \tag{22.7}$$

where Q_c stands for the rate of energy release in the gas phase, $\dot{w}_c$ for the burning rate of the control fuel [mass/(time·volume)], and ΔH_c for the heat of combustion per unit fuel mass.

A wave equation governing the unsteady motions is then derived by decomposition of all dependent variables as sums of the mean and fluctuation parts. Thus

$$\rho = \overline{\rho} + \rho'(\mathbf{r}, t)\,; \quad \mathbf{v}_g = \overline{\mathbf{v}}_g(\mathbf{r}) + \mathbf{v}_g'(\mathbf{r}, t)\,; \quad p = \overline{p} + p'(\mathbf{r}, t) \tag{22.8}$$

Now substitute Eq. (22.8) into Eqs. (22.1)–(22.3), collect coefficients of like powers, and rearrange the results to obtain the following wave equation in terms of pressure fluctuation:

$$\nabla^2 p' - \frac{1}{\overline{a}^2}\frac{\partial^2 p'}{\partial t} = h + h_c \tag{22.9}$$

where h contains all physical processes of acoustic motions, mean flow, and combustion under conditions with no external forcing. Its explicit expression is given in [25].

The control source h_c arising from combustion of the injected fuel can be treated as a distributed actuator, with its spatial distribution approximated by an array of M discrete sources [1]. If a generalized time-lag theory of Crocco and Cheng is used to model the process of the control fuel from injection to complete combustion, then h_c can be written as

$$h_c = -\frac{\overline{R}\Delta H_c}{\overline{a}^2 \overline{C}_V} \sum_{k=1}^{M} \frac{\partial \dot{m}_{\text{in}}(t - \tau_k)}{\partial t} b_k \delta(\mathbf{r} - \mathbf{r}_k) \qquad (22.10)$$

where $\dot{m}_{\text{in}}$ stands for the mass flow rate of the injected fuel. The time delay, τ_k, is the time at which an element of fuel burns at the kth combustion source, measured from the moment of its injection. The spatial distribution parameter, b_k, measures the fraction of the control fuel currently burning within the volume represented by the kth combustion source, located at $\mathbf{r}_k$. Conservation of mass requires that $\sum_{k=1}^{M} b_k = 1$.

Since the source terms in Eq. (22.9) and its associated boundary conditions are treated as small perturbations to the acoustic field, within second-order accuracy, the solution can be legitimately approximated by a synthesis of the normal modes of the chamber with time-varying amplitudes $\eta_n(t)$.

$$p'(\mathbf{r}, t) = \overline{p} \sum_{n=1}^{\alpha} \eta_n(t)\varphi_n(\mathbf{r}) \qquad (22.11)$$

where φ_n is the normal mode function. After substituting Eq. (22.11) into Eq. (22.9), and applying a spatial-averaging technique equivalent to the Galerkin method, the following system of equations is obtained for the temporal evolution of each mode.

$$\ddot{\eta}_n + \omega^2_n \eta_n + \sum_{i=1}^{N} [D_{ni}\dot{\eta}_i + E_{ni}\eta_i] + F^{NL}_n(\eta_1, \eta_2 \cdots \dot{\eta}_1, \dot{\eta}_2 \cdots)$$
$$= U_n(t) + d_n(t), \ n = 1, 2, \cdots N \quad (22.12)$$

where $d_n(t)$ denotes plant disturbances. The coefficients D_{ni} and E_{ni} represent all linear processes. The function F^{NL}_n accommodates all nonlinear effects of gasdynamic coupling and combustion response. The control input to the nth mode takes the form

$$U_n(t) = \frac{\overline{R}\Delta H_c}{\overline{C}_V \overline{p} V} \sum_{k=1}^{M} b_k \varphi_n(\mathbf{r}_k) \frac{\partial \dot{m}_{\text{in}}(t - \tau_k)}{\partial t} \qquad (22.13)$$

The state of the acoustic field must be determined to complete the formulation. In the present study, the instantaneous pressure oscillation is monitored by a finite number of point sensors, located at positions $\mathbf{r}_{si}$. The output signal of each sensor becomes

$$y_i(t) = \overline{p} \sum_{n=1}^{N} \eta_n(t) \varphi_n(\mathbf{r}_{si}) + \theta_i \tag{22.14}$$

where θ_i is the measurement noise with respect to the ith sensor.

The formulation described above provides a useful framework for treating feedback control of combustion instability. However, direct application of the model to practical problems must be exercised with caution due to uncertainties associated with system parameters such as D_{ni} and E_{ni} in Eq. (22.12), and time delays τ_k and spatial distribution parameters b_k in Eq. (22.13). The intrinsic complexities in combustor flows prohibit precise estimates of those parameters without considerable errors, except for some simple well-defined configurations. Furthermore, the model may not accommodate all the essential processes involved because of the physical assumptions and mathematical approximations employed. These model and parameter uncertainties must be carefully treated in the development of a robust controller. To this end, the system dynamics equations, Eqs. (22.12)–(22.14), are extended to include uncertainties, and can be represented with the following state-space model:

$$\begin{aligned} \dot{x}_p &= (A_p + \Delta)x_p + G\nu + Ld \\ y &= Cx_p + \theta \end{aligned} \tag{22.15}$$

where $x_p = (\varsigma \ \dot{\varsigma})^T$ with $\dot{\varsigma} = \eta$, and $\eta \equiv [\eta_1, \eta_2, \cdots, \eta_N]^T$. The nominal linear system matrices are:

$$A_p \equiv \begin{bmatrix} 0 & I \\ (-\Omega - E) & -D \end{bmatrix} \quad \text{with} \quad \Omega \equiv \text{diag}\,({\omega_1}^2, {\omega_2}^2, \cdots, {\omega_N}^2)$$

The input vector $\nu(t)$ is related to the mass injection rate of the secondary fuel, $\dot{m}_{\text{in}}$, as

$$\nu(t) = \begin{bmatrix} (b_1 + \delta b_1)\,\dot{m}_{\text{in}}\,(t - \tau_1 - \delta\tau_1) \\ (b_2 + \delta b_2)\,\dot{m}_{\text{in}}\,(t - \tau_2 - \delta\tau_2) \\ \vdots \\ (b_M + \delta b_M)\,\dot{m}_{\text{in}}\,(t - \tau_M - \delta\tau_M) \end{bmatrix} \tag{22.16}$$

The model and parametric uncertainties are represented by a differential operator Δ and can be properly treated as a disturbance to the plant, $w_s = \Delta(x_p)$, which physically represents the energy amplification from input to output. Its global behavior is characterized by the L_2 gain as follows:

$$\|\Delta\|_\infty < \frac{1}{\gamma}$$

i.e.,

$$\int\limits_0^T \|w_s(t)\|^2 \, dt \leq \frac{1}{\gamma^2} \int\limits_0^T \|x_p(t)\|^2 \, dt \,, \qquad \forall T \in [0, \infty) \qquad (22.17)$$

22.3   ROBUST CONTROL

22.3.1   Generalized Plant

With an appropriate specification of the system performance weighting and objective function, a generalized plant dynamics is established, as shown in Fig. 22.2. The feedback controller processes the measured signal y to determine the injection rate of the control fuel $\dot{m}_{\text{in}}$ based on a regulated relationship between variables w and z, where w is associated with disturbance and uncertainty, and z with the objectives of system performance and stability.

The system dynamics uncertainty $\Delta(s)$ contains parametric and model uncertainties, and its L_2 gain bounded as $\|\Delta(s)\|_\infty < 1/\gamma$. Based on the L_2-gain control theory, the first task of a robust controller for stabilizing perturbed plants is to endow the closed-loop system with the following property:

$$\int\limits_0^T \|z_s\|^2 \, dt \leq \int\limits_0^T \|w_s\|^2 \, dt \,, \qquad \forall T > 0, \quad \forall w_1 \in L_2(0, T) \qquad (22.18)$$

for the zero-state initial condition, with z_s being x_p/γ.

Another source of uncertainty arises from actuators, mainly due to the time delay and spatial distribution from injection to complete combustion of the secondary fuel. A nonrational transfer function of time delay $e^{-\delta\tau s}$ is used to treat the multiplicative uncertainty by embedding it in the family

$$\{1 + \Delta_\tau (j\omega) \, W_\tau (j\omega)\} : \|\Delta_\tau (j\omega)\| \leq 1 \qquad (22.19)$$

where $\Delta_\tau(j\omega)$ accounts for the phase uncertainty and acts as a scaling factor for the magnitude of the perturbation specified by the weighting function $W_\tau(j\omega)$. It is chosen in such a manner that the normalized perturbation satisfies

$$\left| e^{-\delta\tau j\omega} - 1 \right| \leq |W_\tau(j\omega)| \,, \quad \forall \omega \qquad (22.20)$$

where $\delta\tau = \max_k |\tau_k|$. For robust stability, a closed-loop system must fulfill the requirement

$$\int\limits_0^T \|z_\tau\|^2 \, dt \leq \int\limits_0^T \|w_\tau\|^2 \, dt \,, \quad \forall T > 0, \quad \forall w_\tau \in L_2(0, T) \qquad (22.21)$$

where w_τ and z_τ are shown in Fig. 22.2.
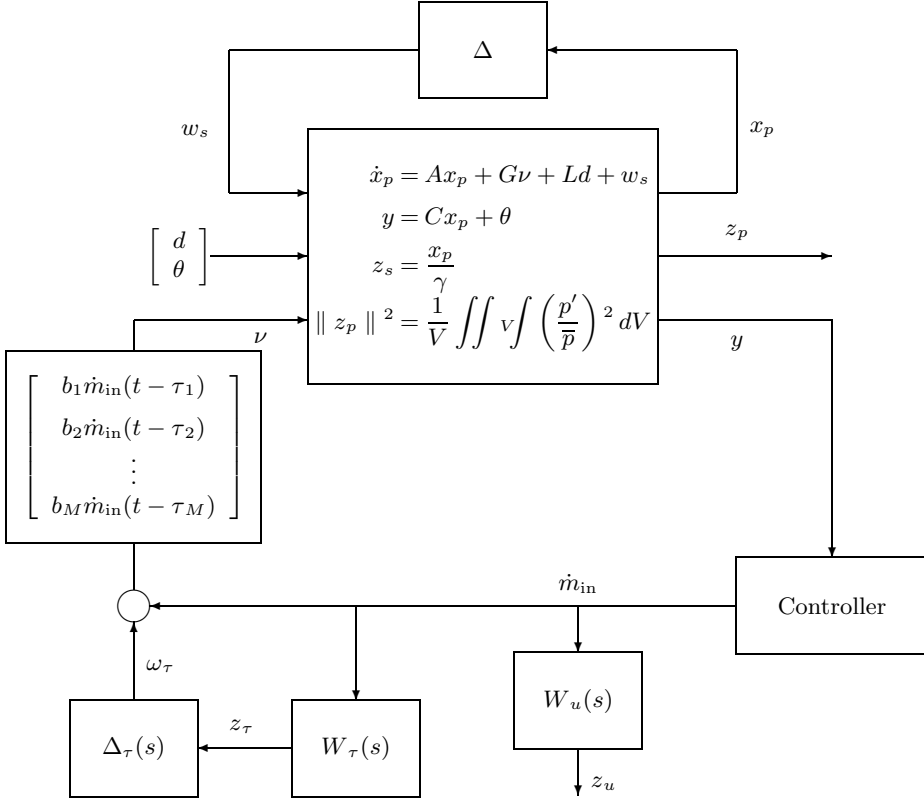
Figure 22.2 Generalized plant dynamics

In addition, the control system must feature a desired performance in terms of its ability to suppress flow oscillations, measured by a positive quadratic energy-like function as follows:

$$\|z_p\|^2 = \frac{1}{V} \iiint\limits_{V} \left(\frac{p'(\mathbf{r}, t)}{\overline{p}} \right)^2 dV \qquad (22.22)$$

The system is free of oscillations when z_p approaches zero. Since the acoustic mode satisfies the orthonormal property, Eq. (22.22) can be simplified as

$$\|z_p\|^2 = \frac{1}{V} \left\langle \sum \varphi_n \eta_n, \sum \varphi_m \eta_m \right\rangle = \sum {\eta_n}^2 = \|\eta\|^2 \qquad (22.23)$$

In order to regulate the dynamics of the secondary fuel injector according to prescribed system performance and stability requirements, the controller needs

to modulate the frequency response of the control fuel injection rate, instead of $\dot{m}_{in}(t)$ directly. A performance variable $z_u(t)$ is thus defined by incorporating a performance weighting $W_u(s)$ into control action as

$$\widehat{z}_u(s) = W_u(s)u(s) \tag{22.24}$$

where $u(s)$ and $\widehat{z}_u(s)$ are the Laplace transforms of $\dot{m}_{in}(t)$ and $z_u(t)$, respectively. The performance weighting W_u can be properly chosen by considering the bandwidth of the control system and the steady operation of the injector.

Based on the above performance concerns, Eqs. (22.22) and (22.24), an L_2-gain robust controller is designed such that the plant disturbance d and sensor noise θ have minimum effect on the plant dynamics and control actions. In an energy sense, this can be specified by

$$\int_0^T \left(\|qz_p\|^2 + \|rz_u\|^2 \right) \, dt$$

$$\leq \int_0^T \left[(\alpha d)^2 + (\beta\theta)^2 \right] \, dt, \qquad \forall T > 0, \quad \forall d, \theta \in L_2(0, T) \tag{22.25}$$

where r, q, α, and β are positive scalars, representing the weightings of plant dynamics, control action, plant disturbance, and sensor noise, respectively. Increasing q (or r), or decreasing α (or β), implies better performance is desired. When α (or β) is set smaller, a more stringent requirement of rejecting plant disturbance (or sensor noise) is specified. When q (or r) is set larger, the response of acoustic motions (or control action) is emphasized. If exogenous inputs (i.e., plant disturbance and sensor noise) are absent, the L_2-gain control optimizes the performance objective function

$$J = \int_0^\infty \left(\frac{q}{V} \iiint_V \left(\frac{p'(\mathbf{r}, t)}{\overline{p}} \right)^2 dV + \|rz_u\|^2 \right) dt \tag{22.26}$$

Based on Eqs. (22.18), (22.21), and (22.25), a sufficient condition for the existence of a robust controller which stabilizes all perturbed plants with desired performance, subject to some uncertainty bound, can be obtained as follows:

$$\int_0^T \left(\|z_s\|^2 + \|qz_p\|^2 + \|rz_u\|^2 + \|z_\tau\|^2 \right) \, dt$$

$$\leq \int_0^T \left(\|w_s\|^2 + \|\alpha d\|^2 + \|\beta\theta\|^2 + \|w_\tau\|^2 \right) \, dt, \quad \forall T > 0, \quad \forall w \in L_2(0, T) \tag{22.27}$$

or succinctly,

$$\int_0^T \|z\|^2 dt \le \int_0^T \|w\|^2 dt, \qquad \forall T > 0, \quad \forall w \in L_2(0, T) \tag{22.28}$$

with

$$z = \begin{bmatrix} z_s \\ qz_p \\ rz_u \\ z_\tau \end{bmatrix}, \qquad w = \begin{bmatrix} w_s \\ \alpha d \\ \beta \theta \\ w_\tau \end{bmatrix}$$

The generalized plant shown in Fig. 22.2 can be expressed as a state space realization as

$$\begin{aligned} \dot{x} &= Ax + B_1 w + B_2 u \\ z &= C_1 x + D_{12} u \\ y &= C_2 x + D_{21} w \end{aligned} \tag{22.29}$$

where the state of the generalized plant x contains the plant state x_p and states induced from actuator dynamics and stability and performance weighting.

22.3.2 Robust Control Design

The robust controller consists of two main components: the first is an observer, which estimates the states of the generalized plant described by Eq. (22.29), and consequently the dynamics in the combustion chamber. It is capable of treating exogenous inputs and uncertainty-induced disturbances. The second is a state-feedback control gain, which determines the control action based on the estimated states $\widehat{x}$. The final configuration of the controller is plotted in Fig. 22.3.

The remaining task lies in the determination of the control matrix X and observer matrix Z such that the sufficient condition for robust performance, Eq. (22.28), holds. A Lyapunov-based approach is employed to obtain these two matrices. After some lengthy and complicated manipulations of Eq. (22.29) and the control structure shown in Fig. 22.3, the following two Riccati equations are derived, whose positive-definite solutions correspond to the control and observer matrices, X and Z.

$$A^T X + XA + C^T{}_1 C_1 - XB_2 B_2{}^T X + XB_1 B_1{}^T X = 0 \tag{22.30}$$

$$Z^{-1}(A + B_1 F_1) + (A + B_1 F_1)^T Z^{-1} - C_2{}^T C_2$$
$$+ F_2{}^T F_2 + Z^{-1} B_1 B_1{}^T Z^{-1} = 0 \tag{22.31}$$
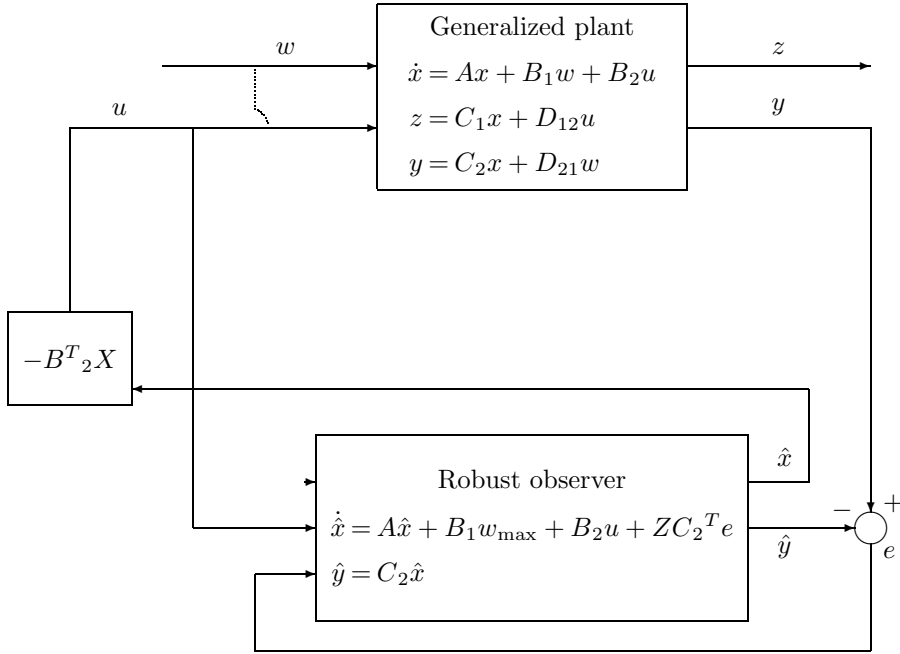
Figure 22.3 Synthesis of robust controller

where $F_1 = B_1{}^T X$, $F_2 = -B_2{}^T X$, and $w_{\max} = F_1 \widehat{x}$. An optimization procedure based on the D–K iteration scheme may be employed to further improve the controller design by relaxing its conservativeness [26].

22.4 PARAMETRIC STUDY

As a specific example to study the characteristics of the controller, the problem involving four modes of longitudinal oscillations is considered herein. The natural radian frequency of the fundamental mode, normalized with respect to $\pi \overline{a}/L$, is taken to be unity. The nominal linear parameters D_{ni} and E_{ni} in Eq. (22.12) are taken from [1], representing a typical situation encountered in several practical combustion chambers. An integrated research project comprising laser-based experimental diagnostics and comprehensive numerical simulation is currently conducted to provide direct insight into the combustion dynamics in a laboratory dump combustor [27]. Included as part of the results are the system and actuator parameters under feedback actions, which can
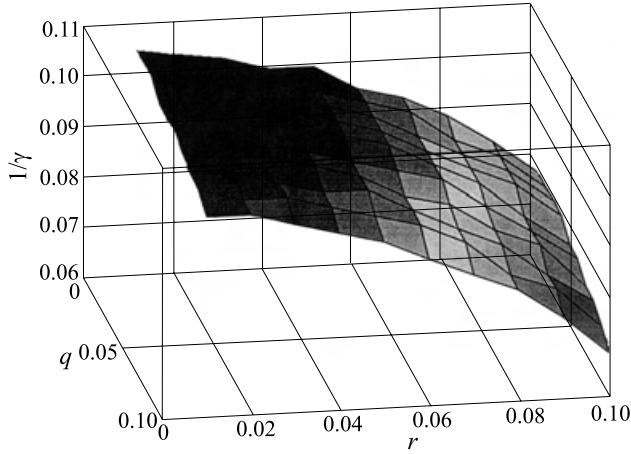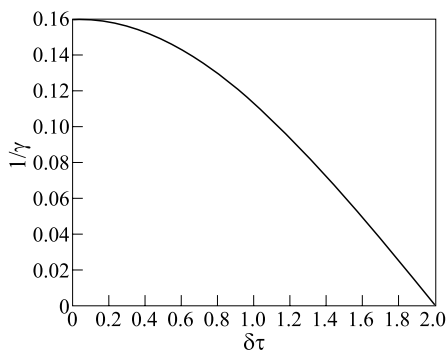
Figure 22.4 Trade-off between plant uncertainty and performance

be directly incorporated into the controller design established in the present work.

An extensive series of studies is conducted to investigate the effects of various weighting factors associated with the mechanical energy of the oscillatory field (q), actuation energy (r), plant disturbance (α), and sensor noise (β) on the robustness and performance of the controller. Also included in the parametric investigation are the affordable bound of system dynamics uncertainty ($1/\gamma$) and the maximum time delay of the distributed combustion of control fuel ($\delta\tau$). Results indicate that

(1) The trade-off between oscillation energy and control fuel is similar to that based on the LQR control;

(2) The ability of rejecting exogenous inputs depends strongly on the values of α and β;

(3) A significant trade-off exists between performance requirements (q, r) and allowable disturbances (α, β);

(4) The affordable uncertainty bound $1/\gamma$ is insensitive to the disturbance weightings α and β;

(5) The affordable uncertainty bound $1/\gamma$ is sensitive to q and r; Fig. 22.4 shows the relationship between affordable uncertainty bound $1/\gamma$ and (q, r);

Figure 22.5 Affordable plant uncertainty vs. time delay uncertainty

(6) There is a trade-off between the affordable model uncertainty bound $1/\gamma$ and the maximum time delay $\delta\tau$; Fig. 22.5 shows this relationship.
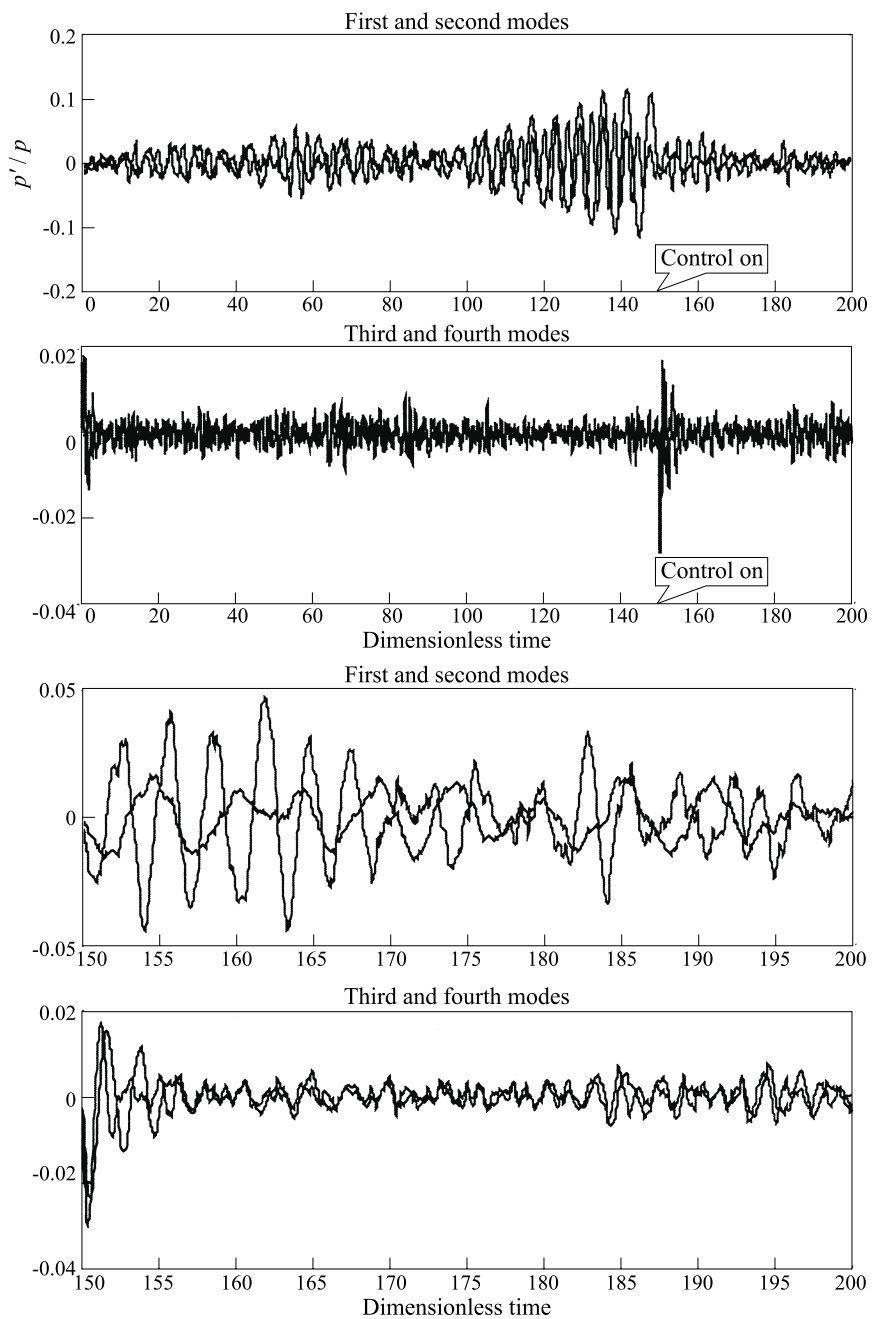
The time responses of pressure oscillation and control fuel injection rate are simulated for two cases: one for the nominal system and the other for a perturbed system with 50% parameter uncertainties from the nominal values. The following data are used in both cases.

|	
Maximum perturbed value of time delays	$\delta\tau = 0.8$
Weighting parameters	$(\gamma, q, r, \alpha, \beta) = (20, 0.1, 0.1, 10, 0.2)$
White plant disturbance intensity	10^{-3}
White sensor noise intensity	10^{-5}
Initial conditions	an impulse of intensity $0.01/\text{s}$

Figures 22.6 and 22.7 present the results. The control scheme developed in the present work indeed guarantees robust performance for a wide variety of perturbed systems with significant model uncertainties.

22.5   CONCLUDING REMARKS

A comprehensive framework of robust feedback control of combustion instabilities in propulsion systems has been established. The model appears to be the most complete of its kind to date, and accommodates various unique phenomena commonly observed in practical combustion devices. Several important aspects of distributed control process (including time delay, plant disturbance, sensor noise, model uncertainty, and performance specification) are treated systematically, with emphasis placed on the optimization of control robustness and system performance. In addition, a robust observer is established to estimate the instantaneous plant dynamics and consequently to determine control gains. Implementation of the controller in a generic dump combustor has been successfully demonstrated.

Figure 22.6 Time history of pressure oscillation in nominal case
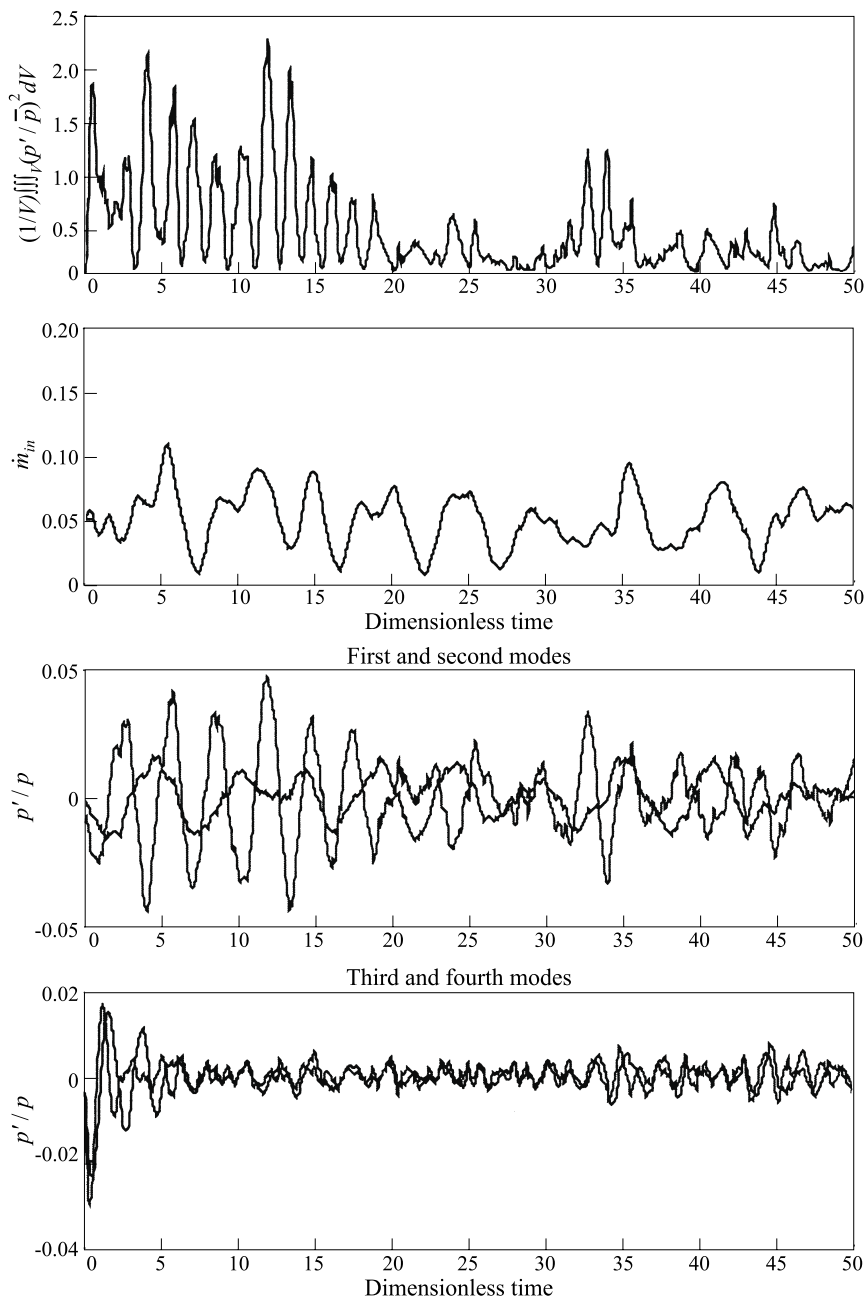
Figure 22.7 Time response of perturbed system with 50% model uncertainty

ACKNOWLEDGMENTS

REFERENCES

1. Fung, Y. T., V. Yang, and A. Sinha. 1991. Active control of combustion instabilities with distributed actuators. *Combustion Science Technology* 78:217–45.
2. McManus, K. R., T. Poinsot, and S. M. Candel. 1993. A review of active control of combustion instabilities. *Progress Energy Combustion Sciences* 19:1–29.
3. Schadow, K. C., V. Yang, F. E. C. Culick, T. J. Rosfjord, G. J. Sturgess, and B. T. Zinn. 1997. Active combustion control for propulsion systems. AGARD-R-820. Advisory Group for Aerospace Research and Development, North Atlantic Treaty Organization.
4. Fung, Y. T., and V. Yang. 1992. Active control of nonlinear pressure oscillations in combustion chambers. *J. Propulsion Power* 8:1282–89.
5. Bloxsidge, G. J., A. P. Dowling, N. Hooper, and P. J. Langhorne. 1987. Active control of an acoustically driven combustion instability. *J. Theoretical Applied Mechanics*. Special issue, supplement to vol. 6.
6. Langhorne, P. J., A. P. Dowling, and N. Hopper. 1990. Practical active control system for combustion oscillations. *J. Propulsion Power* 6:324–33.
7. Schadow, K. C., E. Gutoiark, and K. J. Wilson. 1992. Active combustion control in a coaxial dump combustor. *Combustion Science Technology* 81:285–300.
8. Gulati, A., and R. Mani. 1992. Active control of unsteady combustion-induced oscillations. *J. Propulsion Power* 8.
9. Annaswamy, A. M., and A. F. Ghoniem. 1995. Active control in combustion systems. *IEEE Control Systems Magazine* 15:49–63.
10. Hantschk, C., J. Hermann, and D. Vortmeyer. 1996. Actively instability control with direct-drive servo valves in liquid-fueled combustion systems. *26th Symposium (International) on Combustion Proceedings*. Pittsburgh, PA: The Combustion Institute. 2835–41.
11. Yang, V., A. Sinha, and Y. T. Fung. 1992. State feedback control of longitudinal combustion instabilities. *J. Propulsion Power* 8:66–73.
12. Neumeier, Y., and Ben. T. Zinn. 1996. Experimental demonstration of active control of combustion instabilities using time modes observation and secondary fuel injection. *26th Symposium (International) on Combustion Proceedings*. Pittsburgh, PA: The Combustion Institute. 2811–88.
13. Annaswamy, A. M., J. P. Hathout, M. Fleifil, and A. F. Ghoniem. 1998. Model-based active control design for thermoacoustic instability. *Combustion Science Technology* 132:99–138.
14. Billoud, G., M. A. Galland, C. Huynh Huu, and S. Candel. 1992. Adaptive active control of combustion instabilities. *Combustion Science Technology* 81:257–83.

15. Allen, M. G., C. T. Butler, S. A. Johnson, E. Y. Lo, and F. Russo. 1993. An imaging neural network combustion control system for utility boiler applications. *Combustion Flame* 94:205–14.

16. Kemal, A., and C. T. Bowman. 1996. Real-time adaptive feedback control of combustion instability. *26th Symposium (International) on Combustion Proceedings.* Pittsburgh, PA: The Combustion Institute. 2803–9.

17. Koshigoe, S., T. Komatsuzaki, and V. Yang. 1999. Active control of combustion instability with on-line system identification. *J. Propulsion Power* 15:383–89.

18. Menon, S., and Y. Sun. 1996. Fuzzy control of reheat buzz. AIAA Paper No. 96-2759.

19. Krstic, M., A. Knipadanam, and C. Jacobson. 1999. Self-tuning control of a nonlinear model of combustion instabilities. *IEEE Trans. on Control Systems Technology* 7:424–36.

20. Hong, B. S., A. Ray, and V. Yang. 1998. Robust feedback control of combustion instability. American Control Conference.

21. Packard, A., and J. C. Doyle. 1993. The complex structured singular value. *Automatica* 29:71–109.

22. Safonov, M. G., and M. Athans. 1997. Gain and phase margin for multiloop LQG regulators. *IEEE Transaction on Control.* 22.

23. Doyle, J. C. 1978. Guaranteed margins in LQG regulators. *IEEE Trans. on Automatic Control* 23:756–57.

24. Doyle, J. C., K. Glover, P. Pramod, and B. A. Francis. 1988. State-space solutions to standard H_2 and H_∞ control problems. *IEEE Trans. on Automatic Control* 34:831–47.

25. Fung, Y. T. 1991. Active control of linear and nonlinear pressure oscillations in combustion chambers. PhD Thesis. The Pennsylvania State University.

26. Zhou, K., J. C. Doyle, and K. Glover. 1996. *Robust and optimal control.* New Jersey: Prentice-Hall.

27. Yang, V., D. A. Santavicca, and A. Ray. 1997. Intelligent control of gas turbine combustion dynamics for performance and emission improvement. *10th ONR Propulsion Meeting Proceedings.* Eds. G. D. Roy and D. Netzer. Monterey, CA. Naval Postgraduate School. 32–37.

28. Adams, R. J., J. M. Buffergton, A. G. Sparks, and S. S. Banda. 1994. *Robust multivariable control, advances in industrial control.* London: Springer-Verlag.

29. Crump, J. E., K. C. Schadow, V. Yang, and F. E. C. Culick. 1986. Longitudinal combustion instabilities in ramjet engines: Identification of acoustic modes. *J. Propulsion Power* 2(2):105.

30. Culick, F. E. C. 1971. Nonlinear growth and limiting amplitude of acoustic oscillations in combustion chamber. *Combustion Science Technology* 3:1–16.

Chapter 23

ENHANCEMENT OF LIQUID HYDROCARBON SUPERSONIC COMBUSTION USING EFFERVESCENT SPRAYS AND INJECTORS WITH NONCIRCULAR NOZZLES

V. A. Sabel'nikov, Yu. Ph. Korontsvit, K. C. Schadow, V. V. Ivanov, and S. A. Zosimov

The results from a ducted combustion test program on supersonic mixing and combustion enhancement are presented. The test was conducted in a scramjet combustor using aerated (by air or hydrogen) liquid kerosene (effervescent) jets injected through elliptic nozzles from tube-micropylons and fin-pylons. Kerosene jets were injected into a two-dimensional diverging-area supersonic combustor in two ways: (1) through nozzles drilled in tube-micropylons at an angle of 45° relative to the main-stream air flow direction and (2) through nozzles drilled at the base of fin-pylons. In the latter case a co-flow injection was used. Tests were conducted at an entrance Mach number of M = 2.5 and a total temperature in the range $T_t = 1650$–1800 K. The tests results for elliptic nozzles were compared to baseline results obtained with circular nozzles. The axial static pressure distributions on the combustor walls as well as the calculated pressure–area integrals showed that when injected from tube-micropylons the effervescent kerosene sprays performed better for elliptic nozzles than for round nozzles. Injection from fin-pylons did not show noticeable difference in combustion efficiency for elliptic and round nozzles.

23.1 INTRODUCTION

Supersonic combustion depends considerably (along with the kinetics) on the intensity of turbulent mixing. The significant factors in supersonic mixing enhancement are: (1) the decrease in mixing intensity in supersonic flows, and

(2) the short residence time due to shorter length of the combustor and increased flow speed. A few enhancement techniques seen in the literature are [1–4]: (1) the interaction between fuel jets, shock, and expansion waves; (2) the use of injectors with geometry that favors the generation of intense longitudinal vortices (e.g., NASA swept wedges); and (3) the use of a noncircular nozzle geometry (e.g., elliptic nozzles) for fuel supply.

So far, the above listed techniques of mixing intensification were used to accelerate the gaseous fuel jet mixing. The main mechanism of mixing intensification in gaseous jets is vortex induced and is related to the excitation of large-scale modes of instability. Application of such a mechanism is apparently limited for jets of liquid fuel (e.g., kerosene, the fuel of promise for small-dimension hypersonic vehicles). Hence, the idea of aeration (hereinafter referred to as barbotage) of liquid fuel jets by a gas (effervescent sprays) is appealing. Investigations conducted at the Moscow Aviation Institute (MAI) [5] and at Central Aerohydrodynamic Institute (TsAGI) showed that effervescent sprays, by their expansion angle, behave similarly to gaseous jets.

The main objective of the present investigation was to study the potential possibilities of supersonic mixing combustion enhancement by using gas aerated (hydrogen or air) liquid kerosene with noncircular nozzles. Fuel was injected through elliptic nozzles from injectors of two geometries: (1) tube-micropylons and (2) fin-pylons. Tests were conducted under scramjet combustor conditions. Flow parameters at the combustor entrance were M = 2.5 and T_t = 1650–1800 K. This paper presents ignition delay characteristics, axial pressure distributions, combustion efficiencies, and pressure–area integrals for elliptic and round nozzles.

23.2 EXPERIMENTAL FACILITY AND TEST METHODOLOGY

Tests were conducted using a scramjet combustor and the hypersonic facility of MAI equipped with kerosene-fueled preheater (vitiated air). Oxygen mass fraction $Y^0{}_{O_2}$ in the vitiated air was slightly lower than in the atmospheric air. $Y^0{}_{O_2}$ values for each test run can be found in Table 23.1. With an oxygen mass fraction in atmospheric air of 0.232, the kerosene equivalence ratio (ER) in vitiated air is determined by the following relation:

$$ER = \frac{0.232}{Y^0{}_{O_2}} L_0 \frac{G_{ker}}{G_1}, \qquad (23.1)$$

where L_0 = 14.7 is the stoichiometric coefficient for kerosene combustion in atmospheric air, and G_{ker} and G_1 are mass rates of kerosene and vitiated air,
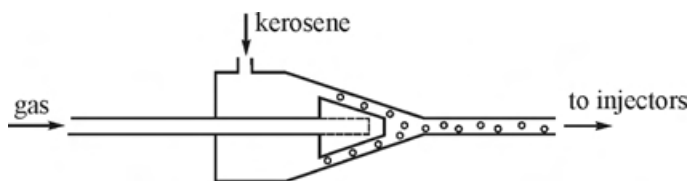
Table 23.1 Tests parameters

RUN No.	Nozzles	P_t MPa	T_t K	P_m MPa	G_{air} kg/s	G_{O_2} kg/s	$G_{h,ker}$ kg/s	G_{ker} kg/s	$\dfrac{G_{bg}}{G_{ker}}$	$Y^0{}_{O_2}$	ER
Tube-micropylons injectors, barbotage by hydrogen											
1	Round	1.44	1690	*	2.125	0.522	0.103	0.132	*	0.16	0
1	Round	1.44	1650	1.5	2.125	0.522	0.103	0.132	~ 0.015	0.16	1.06
2	Elliptic	1.46	1790	*	2.185	0.257	0.101	0.08	*	0.1548	0
2	Elliptic	1.45	1780	2.18	2.185	0.257	0.101	0.08	~ 0.01	0.1548	0.69
3	Elliptic	1.41	1780	*	2.097	0.257	0.106	0.07	*	0.1539	0
3	Elliptic	1.42	1750	1.6	2.097	0.257	0.106	0.07	~ 0.01	0.1547	0.62
Tube-micropylons injectors, barbotage by air											
9	Elliptic	1.46	1754	*	2.175	0.257	0.1189	0	*	0.1354	0
9	Elliptic	1.45	1793	2.29	2.125	0.2514	0.1182	0.094	0.16	0.1347	0.945
9	Elliptic	1.44	1756	1.96	2.115	0.2514	0.1187	0.075	0.18	0.1335	0.763
9	Elliptic	1.44	1756	1.86	2.116	0.2514	0.1184	0.07	0.19	0.1341	0.709
10	Round	1.43	1771	*	2.08	0.257	0.1254	0	*	0.1224	0
10	Round	1.45	1736	2.39	2.155	0.2514	0.1220	0.094	0.16	0.1304	0.962
10	Round	1.46	1775	2.16	2.137	0.2514	0.1212	0.075	0.18	0.1308	0.771
10	Round	1.44	1727	2.15	2.144	0.2514	0.1217	0.07	0.19	0.1304	0.720
Fin-pylons injectors, barbotage by air											
11	Round	1.43	1765	*	2.109	0.257	0.1226	0	*	0.1278	0
11	Round	1.45	1745	2.45	2.045	0.2514	0.1231	0.1011	0.16	0.1272	1.1
11	Round	1.42	1788	2.08	2.064	0.2514	0.1226	0.078	0.18	0.1259	0.87
11	Round	1.43	1807	2.05	2.064	0.2514	0.1223	0.0782	0.19	0.1263	0.86
12	Elliptic	1.41	1732	*	2.077	0.257	0.1216	0	*	0.1286	0
12	Elliptic	1.42	1755	2.19	2.087	0.2536	0.1218	0.098	0.16	0.1288	1.05
12	Elliptic	1.42	1764	1.95	2.082	0.2536	0.1216	0.081	0.18	0.1288	0.87
12	Elliptic	1.42	1762	1.91	2.080	0.2536	0.1217	0.079	0.19	0.1286	0.85

Remarks: * denotes air supply for cooling of injectors, no fuel supply; G_{air} is the air mass rate through preheater, kg/s; G_{O_2} is the oxygen mass rate through preheater, kg/s; $G_{h,ker}$ is the kerosene mass rate through preheater, kg/s; G_{ker} is the kerosene mass rate through combustor model, kg/s; P_m is the total pressure of mixture in injectors; G_{bg}/G_{ker} is the ratio of barbotage gas mass rate to kerosene mass rate.

respectively. Total flow parameters and other parameters characterizing the facility and combustor operation regimes are given in Table 23.1.

Figure 23.1a depicts the schematic view of the combustor. The combustor has four sections: (1) a 150-millimeter long section with a constant cross-sectional area of 52×104 mm (height $h = 52$ mm and width $w = 2h$); (2) a 150-millimeter long section with a divergence angle of $6.85°$ along the upper wall leading to an exit cross-sectional area of 70×104 mm; (3) a 300-millimeter long section with

Figure 23.1 Schematic of test configuration (all dimensions in mm): (*a*) combustor and injectors location; (*b*) geometry of tube-micropylons, and (*c*) geometry of fin-pylons

Figure 23.2 Schematic of the mixing (barbotage) device

divergence angle of 1.9° along the upper wall leading to an exit cross-sectional area of 80 × 104 mm; (4) a 570-millimeter long section with a constant cross-sectional area. Thus, the total length of the combustor is 1050 mm with an area-expansion ratio of 1.7. Flow from the combustor was exhausted into still atmosphere. Axial pressure distributions were measured from taps placed on the upper and lower combustor walls.

Kerosene jets were aerated (barbotated) with hydrogen or air. Barbotage device scheme is shown in Fig. 23.2. The mass fraction of the gas was small enough: while the kerosene mass rate was 60–130 g/s, hydrogen mass rate was about 1 g/s and the air mass rate was about 10 g/s. Mixture pressure in the barbotage device was in the range 1.5–2.5 MPa. The volume fractions of kerosene and gas at the nozzle exit of the injectors were of the same order of magnitude. Injection of effervescent kerosene sprays into the flow with a much lower pressure level causes the explosion of the jet that promotes the vaporization and mixing of liquid kerosene [5]. Fuel was injected into the combustor in two ways: (1) at an angle of 45° relative to the main-stream air flow direction throughout tube-micropylons; (2) in the co-flow direction with main-stream flow throughout the fin-pylons. The injectors were mounted in rows of four on the top and bottom combustor walls. The distance between the combustor entrance and the injectors location was 105 mm. Fuel injection for both injector types was performed through either round nozzles of diameter 1.2 mm or elliptic nozzles with principal axis dimensions 0.6 and 1.9 mm. The scheme of injector placement is given in Fig. 23.1a, and injector geometries are given in Fig. 23.1b (tube-micropylons) and Fig. 23.1c (fin-pylons).

Three test runs (No.1 to No.3) were done with hydrogen-barbotated kerosene at fixed fuel equivalence ratios. Four other test runs (No. 9 to No. 12), where kerosene was barbotated with air, were done in the following way: after the desired combustor entrance conditions were reached the fuel was injected during 20–30 s. During this time interval the magnitude of ER (see Eq. (23.1)) was gradually decreased and changed from values nearly stoichiometric to values at which combustion blow-off took place. To ignite the combustor, high-pressure

Table 23.2 Flow parameters at $x = 900$ mm from the combustor entrance

RUN No.	Nozzles	ER	M	η	σ
Tube-micropylons injectors, barbotage by hydrogen					
1	Round	1.06	0.98	1	0.368
2	Elliptic	0.69	1.02	1	0.354
3	Elliptic	0.62	1.08	1	0.345
Tube-micropylons injectors, barbotage by air					
9	Elliptic	0.945	1.06	1	0.344
9	Elliptic	0.763	1.05	1	0.334
9	Elliptic	0.709	1.5	0.7	0.352
10	Round	0.962	1.1	0.98	0.338
10	Round	0.771	1.33	0.8	0.342
10	Round	0.720	1.9	0.4	0.322
Fin-pylons injectors, barbotage by air					
11	Round	1.1	1.1	1	0.336
11	Round	0.87	1.1	0.93	0.33
11	Round	0.86	1.2	0.79	0.34
12	Elliptic	1.05	1.1	1	0.337
12	Elliptic	0.87	1.1	0.95	0.333
12	Elliptic	0.85	1.2	0.89	0.331

η is the combustion efficiency; σ is the total pressure recovery coefficient

throttling air jets were injected during 0.5–1.0 s in the section located at a distance of 780 mm from the combustor entrance. After ignition, the air throttling jets were switched off.

During the tests, the axial pressure distributions on the upper and lower walls of combustor were measured. In test run No. 2 (see Table 23.1), the total pressure field was measured in the combustor exit plane. Measurements were carried out by a 10-point transversing rake. In the other test runs, the total and static pressures were measured at a single point in the combustor exit plane.

Experimental data were analyzed using a one-dimensional (1D) method based on the solution of the conservation equations of the energy, mass, and momentum at known (from experiment) axial pressure distributions on the walls of the combustor (pressure being assumed constant over cross-sections of the combustor). The results from the 1D calculation for the section at a distance of 900 mm from combustor entrance are given in Table 23.2.

23.3 TESTS RESULTS

Figure 23.3 shows axial normalized static pressure P/P_t (where P is the static pressure and P_t is the pressure in the preheater) distributions on the combustor walls for the test runs No. 9 (elliptic nozzles) and No. 10 (round nozzles). In this test, kerosene was barbotated with air and fuel was injected at an angle of 45° relative to the main-stream air flow direction throughout tube-micropylons. The flow in the combustor remained supersonic in test runs No. 9 and No. 10 over the range of ER given in Table 23.2.

It can be seen from Fig. 23.3 that the values of the pressure along the length of the combustor are higher almost everywhere in the case of the elliptic nozzles, i.e., enhancement of supersonic combustion took place when kerosene was injected through elliptic nozzles. Figure 23.3 shows that at the aft of the combustor, a flow separation occurred for the case ER = 0 (due to overexpansion of the flow). It is also seen from Fig. 23.3 that after some induction and delay
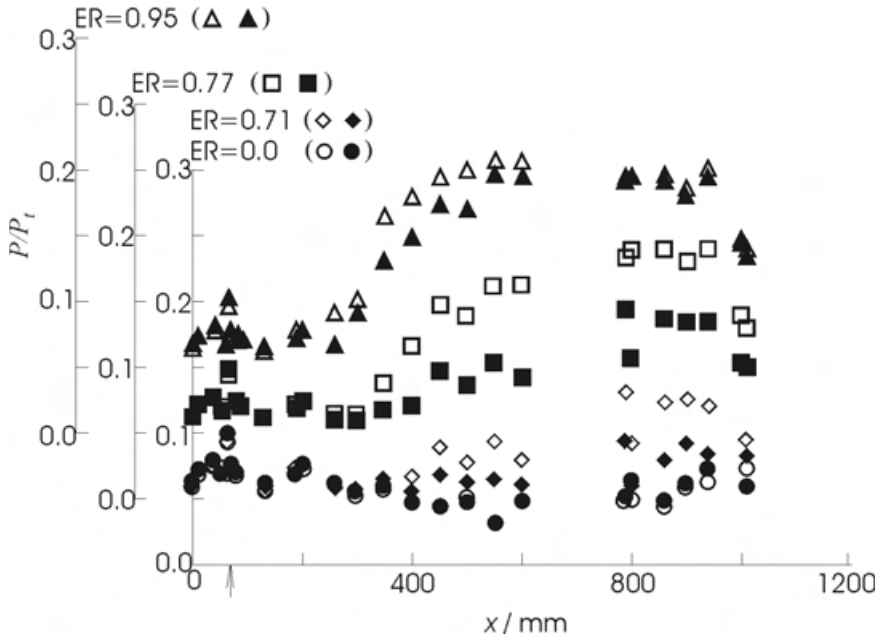
Figure 23.3 Axial static pressure distributions on combustor wall for tube-micropylons. *1* — ER = 0.95, *2* — 0.77, *3* — 0.71, and *4* — 0.0. Open symbols — elliptic nozzles; filled symbols — round nozzles
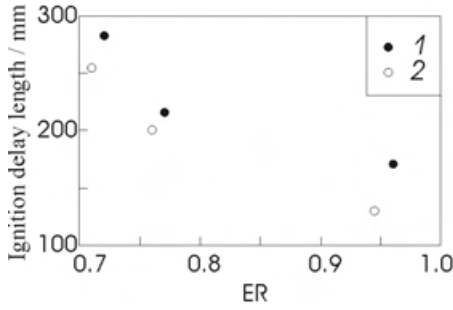
Figure 23.4 Ignition delay lengths for tube-micropylons. *1* — elliptic and *2* — round nozzles
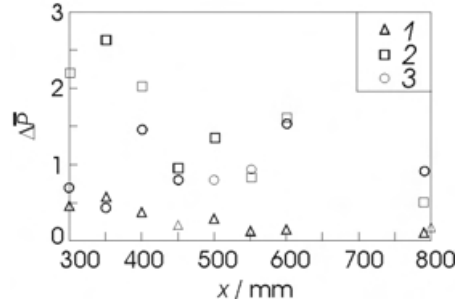
Figure 23.5 Normalized difference of combustion-induced pressure rises for elliptic and round nozzles drilled at tube-micropylons. *1* — ER = 0.95, *2* — 0.76, and *3* — 0.71

length (for the combustion cases) pressure increased monotonously along the combustor (with the exception of the aft of the combustor). Figure 23.4 shows the dependence of ignition delay length on ER. It can be concluded that ignition delay length was shorter for elliptic nozzles.

Supersonic combustion enhancement can be analyzed using the local characteristics — normalized difference of pressure rise due to combustion for elliptic and round nozzles, i.e.,

$$\Delta \overline{P} = \frac{P_{\text{ell}} - P_{\text{round}}}{P_{\text{round}} - P_{\text{no combustion}}} \tag{23.2}$$

The results of calculation of $\Delta \overline{P}$ are presented in Fig. 23.5. It can be seen from $\Delta \overline{P}$ along the length of the combustor, the elliptic nozzles provide better combustion performance than round nozzles. A better indicator of enhancement of supersonic mixing and combustion is obtained from the analysis of the impact of the fuel supply mode on the characteristic pressure–area integral for the diverging-area supersonic combustor [6, 7]. The combustion-induced pressure–area integrals for the 2D combustor (Fig. 23.1*a*) were calculated from the measured axial wall pressure distributions from the following relationship [7]

$$\Delta F = w \int (P_{\text{combustion}} - P_{\text{no combustion}}) \tan \Theta \, dx \tag{23.3}$$

where Θ is the local wall angle with respect to flow and x is the axial coordinate. Figure 23.6 shows a normalized combustion-induced pressure–area integral
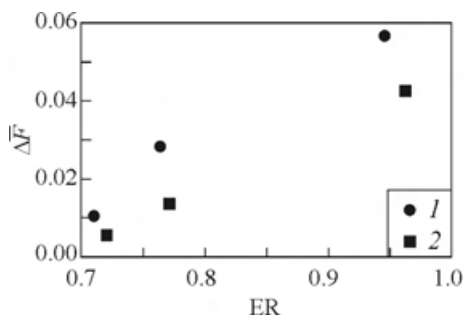
Figure 23.6 Comparison of normalized combustion-induced pressure–area integrals for tube-micropylons with elliptic (*1*) and round (*2*) nozzles
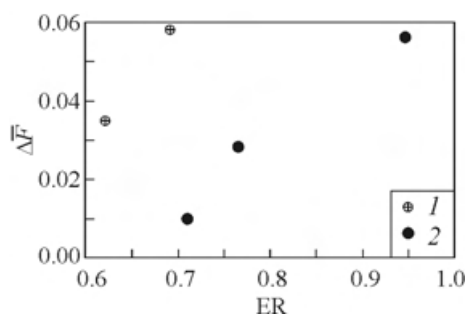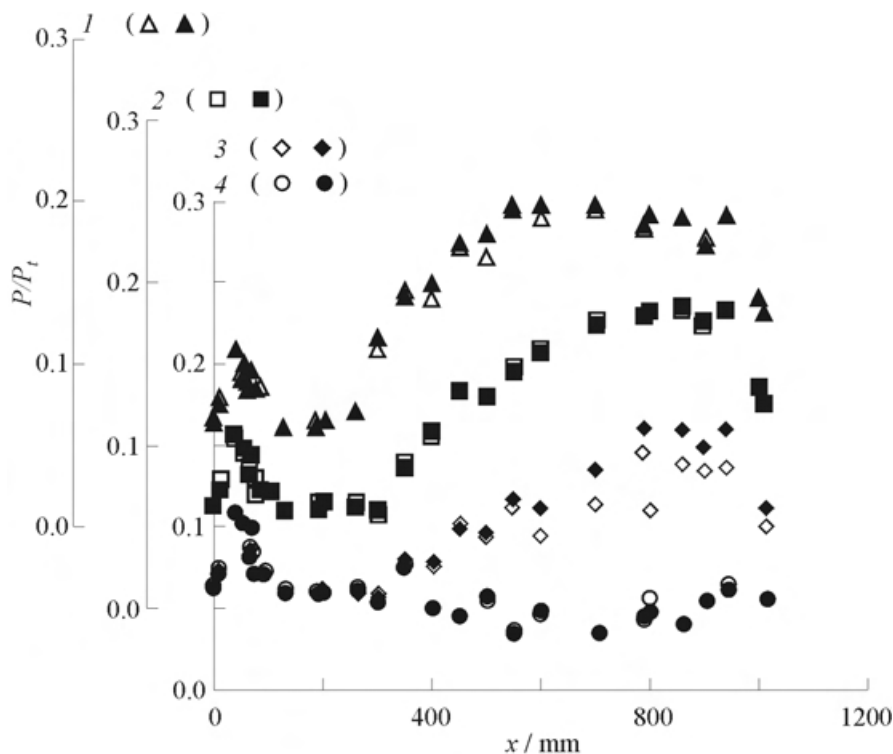
Figure 23.7 Impact of type of gas for kerosene aeration on normalized combustion-induced pressure–area integral for tube-micropylons with elliptic nozzles: *1* — hydrogen and *2* — air

$\Delta\overline{F} = \Delta F/I_1$, where $I_1 = (P + \rho u^2)_1 hw$ is the axial impulse function at the combustor entrance. It is seen that the magnitude of $\Delta\overline{F}$ increases with increasing values of ER and is clearly higher for elliptic nozzles than for round nozzles.

Hydrogen was used for the aeration of kerosene in test runs No. 1 to No. 3 (see Table 23.1). The influence of the type of gas used for aeration on the magnitude of $\Delta\overline{F}$ is illustrated in Fig. 23.7. One can conclude that barbotage of kerosene with hydrogen provided higher mixing and combustion enhancement than barbotage with air. The possible reasons of higher hydrogen barbotage efficiency are the following: (1) greater specific work capacity of hydrogen during expansion compared to that of air, and (2) favorable influence of hydrogen on combustion kinetics of kerosene. The last factor is hardly possible since hydrogen fraction in the mixture is quite low (about 1%).

Figure 23.8 presents axial pressure distributions for two tests for which air-barbotated kerosene was injected through round (test run No. 11) and elliptic nozzles (test run No. 12) located at the base of fin-pylons in the co-flow direction of the main-stream flow. One can conclude from Fig. 23.8 that the combustion-induced pressure rises for elliptic and round nozzles are nearly the same, i.e., mixing and combustion efficiencies practically remain the same for both types of nozzles.

This conclusion is confirmed by the calculation of the combustion-induced pressure–area integrals for both types of nozzles (Fig. 23.9). It follows from comparison of Figs. 23.6 and 23.9 that tube-micropylons with injection at an angle of 45° relative to the main-stream air flow direction provide better performance than fin-pylons with co-flow injection.

Figure 23.8 Axial static pressure distributions on combustor wall for fin-pylons. *1* — ER = 1.05, *2* — 0.87, *3* — 0.85, and *4* — 0.0. Open symbols — elliptic nozzles; filled symbols — round nozzles
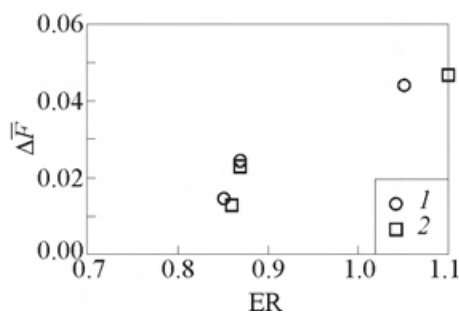
Figure 23.9 Comparison of normalized combustion induced pressure–area integral for fin-pylons with elliptic (*1*) and round (*2*) nozzles

23.4 CONCLUDING REMARKS

An experimental study was carried out to study the supersonic mixing and combustion enhancement in scramjet combustors using aerated (by gas) liquid kerosene jets (effervescent sprays) injected through elliptic nozzles from tube-micropylons and fin-pylons. The following results were obtained:

1. Elliptic nozzles provided greater mixing and combustion efficiencies in comparison with round nozzles for the cases when barbotated kerosene was injected from tube-micropylons at an angle of 45° relative to the main-stream air flow direction.

2. Barbotage of kerosene with hydrogen provided higher mixing and combustion enhancement compared to barbotage with air at injection from tube-micropylons.

3. Test results obtained for fin-pylons with co-flow injection of barbotated kerosene did not show a noticeable difference in mixing and combustion efficiencies with round and elliptic nozzles.

4. Injection from tube-micropylons at an angle of 45° relative to the main-stream air flow direction provided greater mixing and combustion efficiencies in comparison to co-flow injection from fin-pylons.

The investigation showed efficient supersonic combustion of a liquid hydrocarbon fuel when using effervescent sprays and elliptic nozzles for the injection of the fuel. In the future, it would be interesting to study the possibilities of supersonic combustion enhancement using the elliptic nozzles drilled at the base of NASA swept wedges.

ACKNOWLEDGMENTS

REFERENCES

1. Gutmark, E. J., K. S. Schadow, and K. H. Yu. 1995. Mixing enhancement in supersonic free shear flows. *Annual Reviews Fluid Mechanics* 27:375–417.
2. Haimovitch, Y., E. Gartenberg, and A. S. Roberts, Jr. 1994. Investigation of rump injector for supersonic mixing enhancement. NASA-CR-4634.
3. Haimovitch, Y., E. Gartenberg, A. S. Roberts, Jr., and G. B. Northam. 1997. Effects of internal nozzle geometry on compression-ramp mixing in supersonic flow. *AIAA J.* 35(4):663–70.

4. Kopchenov, V. I., and K. Lomkov. 1992. The enhancement of the mixing and combustion processes applied to scramjet-engine. AIAA Paper No. 92-3428.

5. Avrashkov, V. N., S. I. Baranovsky, and D. M. Davidenko. 1990. Penetration height of a liquid jet saturated by gas bubbles. *Izvestiya Vuzov, Aviatsionnaya Tekhnika* 4:96–98.

6. Kay, I. W., W. T. Peschke, and R. N. Guile. 1990. Hydrocarbon-fuelled scramjet combustor investigation. AIAA Paper No. 90-2337.

7. Stouffer, S. D., U. Vandsburger, and G. B. Northam. 1994. Comparison of wall mixing concepts for scramjet combustors. AIAA Paper No. 94-0587.

Chapter 24

DIODE LASER SENSORS FOR COMBUSTION MEASUREMENTS AND CONTROL

D. S. Baer and R. K. Hanson

Recent developments for measurements in high-temperature and high-speed flows are discussed including diode-laser sensors for *in situ* combustion measurements and control in forced combustion systems; for emission measurements of CO, CO_2, and unburned hydrocarbons in an industrial-model combustor using an extractive probe and fast-flow gas-sampling techniques; and for measurements of gas temperature, H_2O concentration, and velocity in hypervelocity flows generated in a high-enthalpy shock tunnel for aerodynamic ground-test applications.

24.1 INTRODUCTION

Diode-laser sensors, based on absorption spectroscopy, offer new capabilities for fast and accurate measurements of a variety of important parameters. These include gas temperature, velocity, species concentrations, mass flux, and thrust in combustion systems. The sensors utilize tunable, narrow-linewidth, semiconductor diode-lasers as light sources. These lasers, which are presently available in the wavelength range from 600 to 2000 nm, are robust, reasonably economical, and are readily compatible with optical fibers to facilitate measurements in remote locations. Moreover, the semiconductor lasers have inherently high bandwidths and thus may be rapidly tuned in wavelength over absorption features by simply modulating the laser injection current, typically yielding complete measurements in less than 1 ms. In addition, the outputs of multiple lasers can be easily combined into a single fiber (multiplexing) using off-the-shelf fiber-optic components to enable simultaneous absorption measurements at multiple wavelengths along a common path.

For the last decade, semiconductor diode-laser sensors have been developed at Stanford University for measurements of important parameters in laboratory- and industrial-scale gaseous flowfields. For example, a mass flux sensor was developed based on rapid measurements of O_2 absorption near 760 nm in supersonic flowfields [1]; and a multiplexed sensor was developed for the simultaneous measurement of various pollutants representing unburned hydrocarbons (CH_4, CH_3Cl) near 1.65 μm [2].

An application for multiplexed diode-laser sensors with a potentially large impact is for measurements of important parameters at several locations in a gas turbine combustion system. In this example, illustrated schematically in Fig. 24.1, the multiplexed diode lasers are applied for simultaneous absorption measurements in the inlet, combustion, afterburner, and exhaust regions. For example, measurements of O_2 mass flux at the inlet may be determined at the inlet from Doppler-shifted O_2 absorption lineshapes near 760 nm. Measurements of gas temperature and H_2O concentrations in the combustion and afterburner regions may be determined from H_2O lineshape measurements near 1.4 μm. Finally, measurements of velocity, temperature, and species concentrations (e.g., CO, CO_2, unburned hydrocarbons) may be recorded in the exhaust for the determination of momentum flux (component of thrust) and combustor emissions.
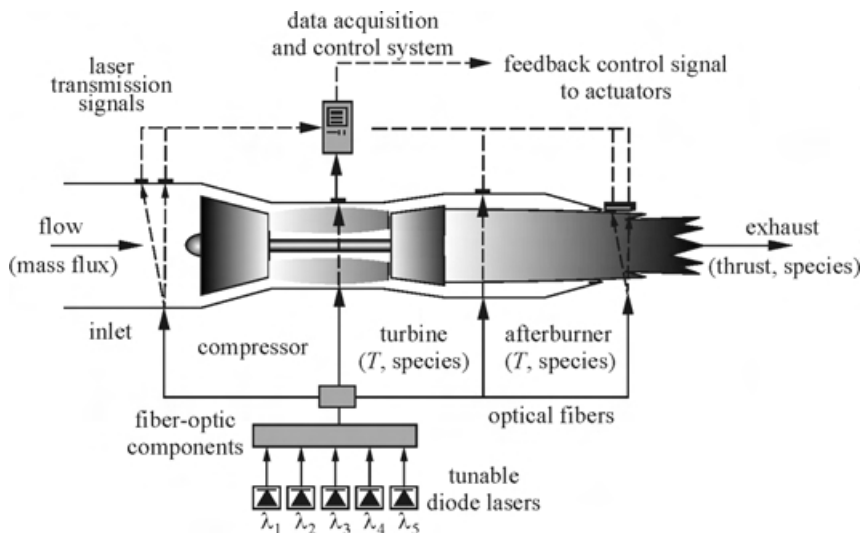
Figure 24.1 Schematic diagram for a potential application of multiplexed diode-laser sensors for measurements of gas temperature, species concentrations, velocity, mass flux, and thrust at several locations in military- and industrial-scale gas turbines (e.g., aeropropulsion, incineration, power generation applications)

24.2 *IN SITU* COMBUSTION MEASUREMENTS AND CONTROL

A multiplexed diode-laser sensor system has recently been applied for measurements in and control of a 5-kilowatt forced combustor which serves as a model of an afterburner in a naval waste incineration system under development at the Naval Air Warfare Center (NAWC) at China Lake. In brief, the multistage incineration system converts solid waste to gaseous waste using a starved-air pyrolysis chamber and then removes the hazardous components using a secondary oxidation chamber or afterburner which utilizes the concepts of forced vortex combustion for a compact and efficient design. Details of the afterburner, including the design, the application of advanced diagnostics, and the determination of the destruction and removal efficiency (DRE), for both small- and large-scale systems have been published previously [3–5].

The general arrangement of the multiplexed diode-laser sensors for measurements in the forced combustor at Stanford University is shown in Fig. 24.2. The primary air flow (65 l/min) through the central jet ($d = 2.1$ cm) was acoustically forced (up to 30% RMS of the flow rate) to create coherent vortices at
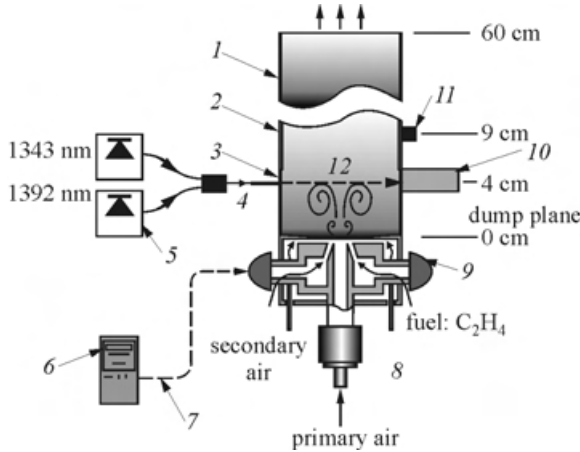
Figure 24.2 Schematic diagram of the setup used to measure and control H_2O concentration and gas temperature in the combustion region (*in situ*) of a forced 5-kilowatt combustor at Stanford University: *1* — steel duct; *2* — quartz duct; *3* — Al duct; *4* — multiplexed beam; *5* — tunable diode lasers; *6* — data acquisition and control computer; *7* — control signals; *8* — primary air driver: $A_{air} \sin(2\pi f_0 t)$; *9* — fuel drivers: $A_{fuel} \sin(2\pi f_0 t + \theta_{fuel})$; *10* — demultiplexing box; *11* — Si detector (ND filter); and *12* — laser beam

the preferred mode of the jet. Secondary airflow (15 l/min) was circumferentially injected (without modulation) normal to the primary airflow. The fuel flow (4.5 l/min C_2H_4) was acoustically modulated (near 100% RMS of the flow rate) and injected circumferentially at a 15° angle relative to the primary air. A water-cooled aluminum duct ($D = 9.9$ cm, 6-centimeter length) was sealed to the injection nozzle. This duct was fitted with three optical ports and a pressure transducer located at $x/d = 2$ (4.2 cm from dump plane). A 15-centimeter quartz extension duct was attached to allow visual inspection of the combustor, and an additional silicon photodiode, located at $x/d = 4$, was used to measure soot luminosity. A steel extension was added to bring the total duct height to 60 cm.

Details of the laser system and the operating conditions employed to control the lasers have been described previously [6]. The system includes two independently operated distributed feedback (DFB) InGaAsP diode lasers tuned over the desired transitions near 1.34 μm and 1.39 μm ($2\nu_1$, $\nu_1 + \nu_3$ bands) by ramp-modulating the individual injection currents at 10 kHz rates to yield single-sweep (100 μs) spectrally resolved absorption records. The individual laser outputs were combined into a single path using appropriate single-mode fiber splitters and couplers. An optical fiber delivered the multiwavelength beam to the combustor and a GRIN lens (0.25 pitch, 3-millimeter) collimated the light through the flowfield. The transmitted multiwavelength light was de-multiplexed (spectrally separated) into the constituent laser wavelengths by directing the beam at a nonnormal incidence angle onto a diffraction grating (1200 g/mm, $\lambda_b = 1.0$ μm). The beams were diffracted at angles specific to each wavelength and were subsequently monitored with InGaAs photodiodes (500-kilohertz
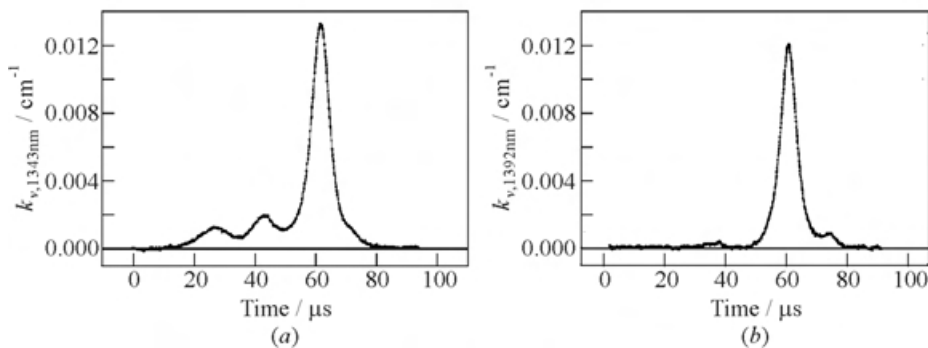
Figure 24.3 Typical single-sweep measurements of spectral absorption coefficients (k_ν, cm^{-1}) obtained by simultaneously tuning two independent diode lasers at 10-kilohertz rates across H_2O transitions near 1343 nm (a) and 1392 nm (b). The measurements were made over a 5-centimeter path through the combustion region of a 5-kilowatt forced combustor operating on C_2H_4–air

bandwidth, 2-millimeter diameter). The detector voltages were digitized by a 12-bit A/D card installed in a personal computer. The measurement cycles were repeated at a 3-kilohertz rate (each cycle required 200 μs for data transfer and 100 μs for the simultaneous operation of signal acquisition and gas-temperature/control-signal computation). The relatively short delay between the measurement and the subsequent control signal output (0.4 ms) was approximately 30 times shorter than the effective response time of the actuator ($\tau_{act} = 14$ ms), which was limited by the gas flow time to the probed region.

Figure 24.3 shows typical single-sweep (raw data) measurements of spectral absorption coefficients obtained simultaneously by tuning two diode lasers independently at 10-kilohertz rates across H_2O transitions near 1343 and 1392 nm over a 5-centimeter path through the combustion region ($x/d = 2$) of the forced combustor (jet diameter $d = 2.1$ cm, $\phi = 0.75$). The product of the spectral absorption coefficient at frequency ν (k_ν, cm^{-1}) and path length (L, cm) is given by $k_\nu L = \ln(I_0/I)_\nu$, where I and I_0 are the transmitted and
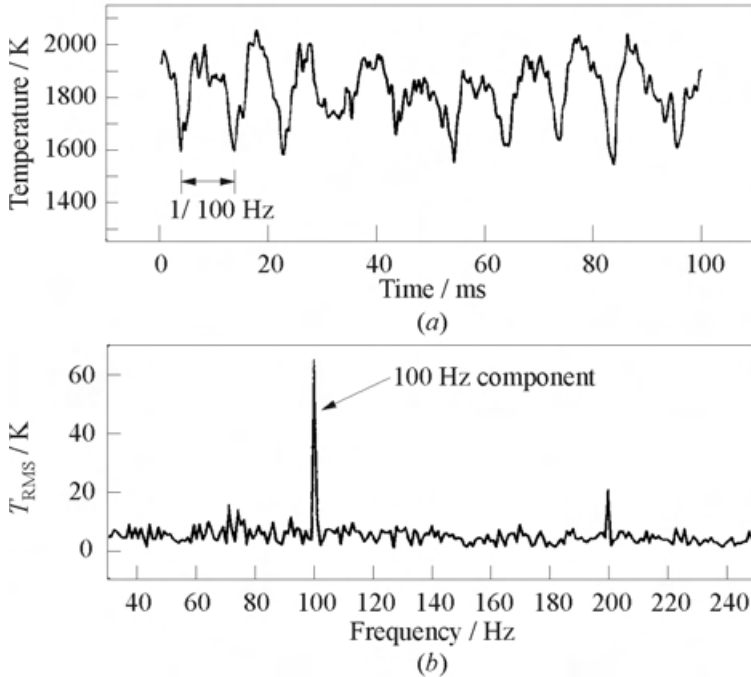
Figure 24.4 Measurements of gas temperature recorded at 3-kilohertz rate at $x/d = 2$ in the 5-kilowatt combustor (a) and the power spectral density (1-hertz resolution) of a 1-second history of the temperature measurements (b). Steady parameters: $\phi = 0.75$, $f_0 = 100$ Hz, $A_{air} = 25$ W, and $\theta_{fuel} = 200°$

unattenuated laser intensities (power), respectively. The gas temperature was determined from the ratio of the peak absorption coefficients.

A time history of temperature measurements recorded at $x/d = 2$ (4.2 cm from the dump plane) is illustrated in Fig. 24.4a. The large periodic oscillations at the forcing frequency ($f_0 = 100$ Hz) are suggestive of strong, coherent vortices and a proper relative phase ($\theta_{\text{fuel}} = 200°$) between the primary air and fuel forcing. The power spectral density of the measured temperature during a 1-second interval (Fig. 24.4b) confirms that the temperature oscillations are a result of the applied forcing. For the case of optimized forcing, the RMS temperature component at the forcing frequency, T_{RMS}, is 60 K.
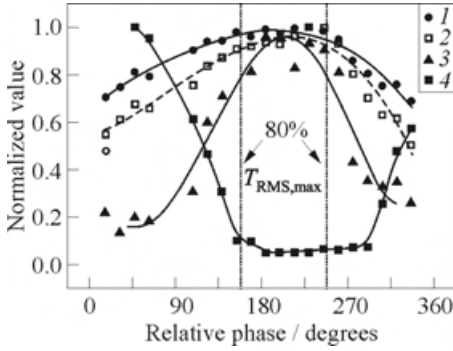
Figure 24.5 Variation in mean temperature T_{mean} (1), mean mole fraction $X_{\text{H}_2\text{O}}$ (2), RMS temperature at the driving frequency f_0 T_{RMS} (3), and luminosity L (4), with relative phase of fuel and air, θ_{fuel} in the forced 5-kilowatt combustor. Normalization values: $T_{\text{mean}} = 1740$, $X_{\text{H}_2\text{O}} = 0.105$, and $T_{\text{RMS}} = 60$ K. Steady parameters: $\phi = 0.75$, $f_0 = 100$ Hz, $A_{\text{air}} = 25$ W, and $A_{\text{fuel}} = 1.1$ W. Vertical dotted lines correspond to relative phase values which yield T_{RMS} values greater than 80% of $T_{\text{RMS, max}}$

Figure 24.5 shows the normalized variation in the measured parameters: (temporally averaged) temperature, T_{mean}, water mole fraction (temporal mean), $X_{\text{H}_2\text{O}}$, the magnitude of oscillations at the forcing frequency, T_{RMS}, and the corresponding changes in luminosity (L, primarily due to emission from soot), as the relative phase between the primary air and fuel forcing was adjusted. The magnitude of L varies inversely with T_{mean}, $X_{\text{H}_2\text{O}}$ and T_{RMS} indicating that optimization of (any one of) these parameters may correspond to an increase in combustion efficiency. The vertical dotted lines bound the phase values where T_{RMS} is greater than 80% of $T_{\text{RMS, max}}$ and indicate a measure of performance (open-loop operational boundaries) for the closed-loop control strategies. The variations in the measured parameters follow similar trends, although T_{RMS} was the most phase-sensitive (T_{RMS} varied by a factor of 5, T_{mean} varied by a factor of 1.3, $X_{\text{H}_2\text{O}}$ varied by a factor of 2).

The outputs of the sensors were used in two closed-loop control strategies developed for combustor performance optimization [7]. The objective of the first strategy, based on an adaptive least-mean squares (LMS) algorithm, was to maximize the magnitude and coherence of temperature oscillations at the forcing frequency f_0 in the measured region. The LMS algorithm was used to determine

Figure 24.6 Time response of control strategy based on a combination of hill-climbing and LMS algorithms which simultaneously varied phase (bottom frame, right axis) and amplitude (bottom frame, left axis) to (primarily) maximize X_{H_2O} and (secondarily) maximize T_{RMS}. The horizontal dotted lines denote phase values that correspond to T_{RMS} greater than 80% of $T_{RMS, max}$ in the open-loop experiments

the RMS temperature value at the driving frequency (T_{RMS}) from the measured temperature time history. The measured T_{RMS} value was compared with a desired T_{RMS} value ($T_{RMS, desired}$) to generate an error signal (Fig. 24.6). The phase (θ_{fuel}) and amplitude (A_{fuel}) of the fuel forcing were adjusted adaptively (using the LMS algorithm) to minimize the error signal and augment oscillations present when the air was forced. Thus this strategy yielded a control output after each measurement.

The goal of the second strategy, which was based on an adaptive hill-climbing algorithm, was to maximize the water-vapor mole fraction (X_{H_2O}) in the measured region. This strategy was derivative based and adjusted the phase between the fuel and air acoustic drivers in fixed-step increments to increase the value of X_{H_2O}. The time response of this strategy was based on the period used to determine the current (mean) X_{H_2O} value, and the size of the incremental step in phase (10° in this case). Large phase steps led to correspondingly large changes in X_{H_2O}, and thus accurate derivatives. Unfortunately, large steps also resulted in poor steady-state performance as the controller necessarily perturbed

the optimum solution by this large phase step. As the step size decreased, the resulting changes in $X_{\mathrm{H_2O}}$ became so small that the averaging period had to be increased in order to limit derivative noise. However, since values of $X_{\mathrm{H_2O}}$ changed for reasons other than phase adjustment (e.g., a time-varying fuel flow due to rotameter instabilities), long averaging periods led to control decisions that were not correlated with the phase step. Since most $X_{\mathrm{H_2O}}$ fluctuations were at frequencies larger than 10 Hz, and $10°$ of phase shift did not dramatically affect performance, the applied control settings represented a good balance between response time, stability, and long-term steady-state performance.

The LMS control strategy was able to maintain an entirely blue flame although values of mean temperature (T_{mean}) and $X_{\mathrm{H_2O}}$ often decreased below the open-loop results due to excessive fuel forcing amplitudes (A_{fuel} values). Furthermore, measured values of T_{mean}, T_{RMS}, and $X_{\mathrm{H_2O}}$ reached their respective maxima at, and then decreased above, particular A_{fuel} values. A possible explanation for this effect is that when fuel forcing exceeds a particular level, the different streams of fuel and air remain somewhat unmixed and, as a result, combustion may be incomplete at the measurement location. Thus, in subsequent measurements the hill-climbing algorithm strategy was employed in addition to, but independent from, the LMS algorithm to regulate A_{fuel} in order to maximize $X_{\mathrm{H_2O}}$ and ensure that the combustion process is near completion at the measurement location [7].

## 24.3 FAST EXTRACTIVE-SAMPLING MEASUREMENTS OF COMBUSTOR EMISSION

Extractive sampling techniques offer the potential for high-measurement sensitivity for cases where *in situ* techniques are unnecessary or difficult due to lack of optical access. Accurate determinations of species concentrations from measured absorption spectra, however, rely on reliable values of spectroscopic parameters (i.e., line strengths, positions, broadening parameters) for the target species for the conditions measured. Moreover, the appropriate probe wavelengths must be selected to avoid spectroscopic interference from neighboring absorption features of other constituent species in the sampled gas. Thus, prior to the implementation of a spectroscopy-based measurement technique, the database which consists of calculated spectroscopic parameters should, in general, be verified experimentally.

For example, a diode-laser sensor was applied to measure CO and CO_2 concentrations in combustion gases using fast extraction-sampling techniques [8]. The sensor was based on an external cavity diode laser (ECDL) operating over the spectral region 6321–6680 cm^{-1} which includes the R-branch of the CO 3ν band, the R-branch of the $2\nu_1 + 2\nu_2 + \nu_3$ CO_2 band, and selected lines of the

$\nu_1 + 2\nu_2$ and $2\nu_2 + \nu_3$ bands of H_2O. Survey spectra were obtained by using the internal wavelength ramp of the diode-laser controller. Absorption measurements of individual rotational transitions were recorded through external modulation of the laser at a repetition rate of 120 Hz with a sawtooth-injection voltage of 6 V (peak-to-peak).

The ECDL output was passed through an optical isolator to prevent reflections into the laser cavity and split into two beams using a single-mode 1×2 fiber splitter. One output was directed through a solid étalon with a free spectral range of 2.01 GHz to monitor the wavelength tuning of the laser. The other output was directed into a multipass absorption cell and focused at the exit into an InGaAs detector (200-kilohertz bandwidth). The cell had a 0.3-liter volume and consisted of two astigmatic mirrors with a 20-centimeter separation and a nominal absorption pathlength of 36 m. The astigmatic mirror combination made effective use of the small mirror area and allowed a high-absorption path to volume ratio, ideal for fast-flow experiments.

Figure 24.7 compares the measured and calculated absorption of the R-branch of the CO 3ν band. The measured spectra, obtained at 296 K, 338-torr
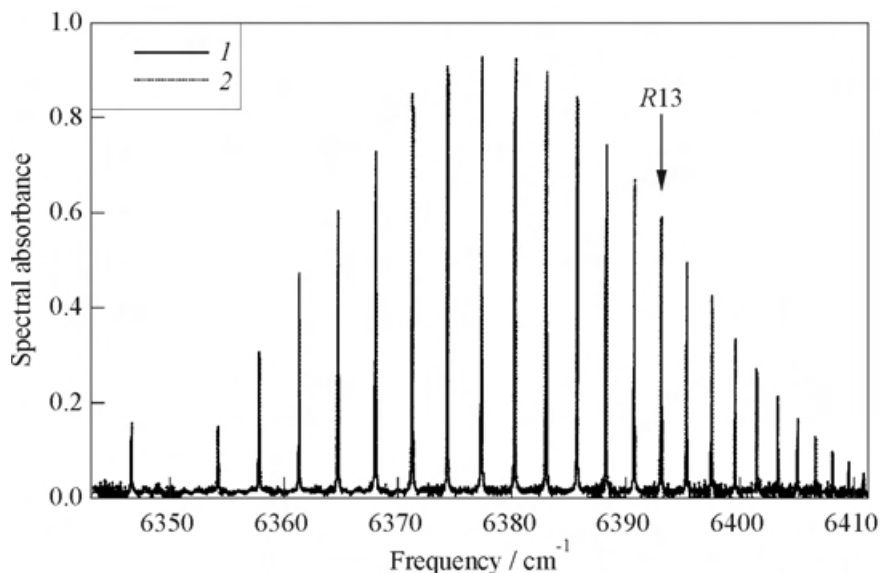
Figure 24.7 Comparison of the measured (*1*) and calculated (*2*, using the HITRAN 92 database) spectral absorbance of the R-branch of the CO 3ν band. The data were obtained at 296 K, 338 Torr, $X_{CO} = 9.91\%$, $X_{Ar} = 9.79\%$ in air, over an absorption pathlength of 3227 cm. Spectral absorbance is defined by $k_\nu L = \ln(I_0/I)$

total pressure, 3227-centimeter absorption path, and a mixture of 9.91% CO and 9.79% argon in air, are in good agreement with calculations, indicating that spectroscopic parameters of CO are accurate to within the experimental uncertainty of 3%. Similar survey spectra measurements of the R-branch of the CO_2 $2\nu_1 + 2\nu_2 + \nu_3$ band were recorded and compared with calculations. Lines with low rotational levels up to $J'' = 10$ were found to be in good agreement with HITRAN calculations. The line strengths of transitions with high rotational quantum numbers were overpredicted [9].

Closely spaced absorption lines allowing measurements of CO and CO_2 in a 1-cm^{-1} scan are available in the spectral range of the ECDL but require the ratio of CO to CO_2 mole fractions to be within one or two orders of magnitude due to limitations in measurement dynamic range. Since equivalence ratio variations from $\phi = 0.67$ to $\phi = 1.47$ change the calculated equilibrium CO-to-CO_2 mole-fraction ratio more than a factor of 10^5, the appropriate line pair for species detection depends on the value of ϕ. For maximum detectivity and minimum CO_2 interference, the CO $R13$ line was chosen to determine CO partial pressures for gas-sampling measurements in the burned-gas region above a CH_4–air flame. The line strength of this transition corresponds to 58% of the maximum line strength at 296 K within the CO 3ν R-branch. CO_2 partial pressures were obtained by measuring the absorption of the CO_2 $R16$ line, the strongest CO_2 line at 296 K.

The experimental setup for diode-laser sensing of combustion gases using extractive sampling techniques is shown in Fig. 24.8. The measurements were performed in the post-flame region of laminar methane–air flames at atmospheric conditions. A premixed, water-cooled, ducted flat-flame burner with a 6-centimeter diameter served as the combustion test-bed. Methane and air flows were metered with calibrated rotameters, premixed, and injected into the burner. The stoichiometry was varied between equivalence ratios of $\phi = 0.67$ to $\phi = 1.47$.

Post-flame gas temperatures were measured with uncoated type-S thermocouples (3 mm wire diameter), corrected for radiation losses. The measurement location was 2 cm above the burner, and 1.5 cm from the sampling probe where no probe-induced cooling of the combustion gases was observable. The estimated uncertainty in the measured temperatures (± 20 K) was primarily due to uncertainty in bead size.

A water-cooled stainless-steel probe (4.1-millimeter internal diameter) with four inlet holes (0.50-millimeter diameter) was used to continuously sample combustion products 2 cm above the burner. The samples were drawn through an ice-bath-cooled water trap, a drying column, and a 5-micron filter to reduce the water mole-fraction and to remove particles. Temperature and static pressure in the absorption cell were monitored using a type-S thermocouple and a pressure gauge. The flow entered the cell on the same end as the optical beam and exited on the opposite end through 0.5-inch windows before
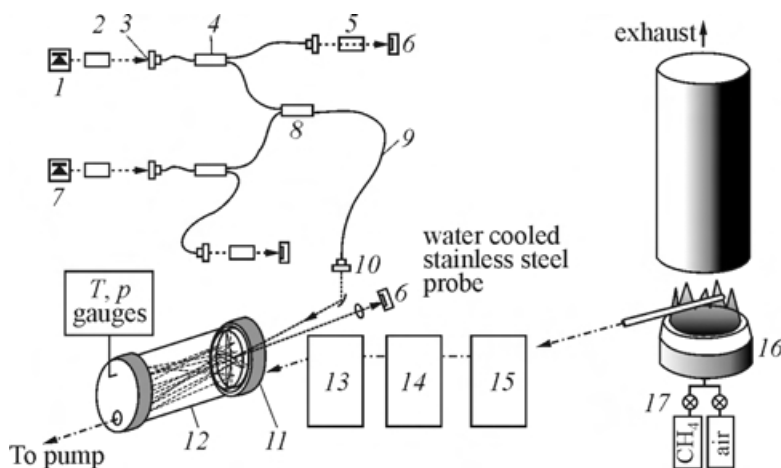
Figure 24.8 Experimental schematic of the multiplexed diode-laser sensor system used to measure CO, CO_2, CH_4, and H_2O absorption by sampling hot combustion gases: *1* — ECDL 1.49–1.58 μm; *2* — optical isolator; *3* — fiber coupler; *4* — 1 $\times$ 2 fiber splitter; *5* — étalon; *6* — InGaAs detector; *7* — DFB 1.65 μm; *8* — 2 $\times$ 1 fiber combiner; *9* — optical fiber; *10* — fiber pitch; *11* — concave mirror; *12* — multipass flowcell; *13* — particle filter; *14* — drying column; *15* — cold trap; *16* — premixed flat-flame burner; and *17* — rotameters

it was drawn through a two-stage rotary pump and vented into the exhaust stack. For typical measurement conditions (cell pressure of 195 Torr, temperature of 296 K), the total measurement time was less than 1 s (rise and fall times of 325 ms, gas transport time of 260 ms). The minimum cell response time achieved was 42 ms using a pumping rate of 5.6 l/s and with a cell pressure of 70 Torr [8, 9].

Figure 24.9*a* shows a plot of measured total carbon (CO plus CO_2, mole percent) versus equivalence ratio. The solid line was calculated assuming chemical equilibrium at the measured temperatures. The data points represent the measured CO and CO_2 mole fractions (dry basis) using the fast extractive-sampling system. Horizontal bars represent the uncertainty in ϕ due to reading and calibration errors; vertical bars represent the uncertainty in the CO and CO_2 mole-fraction sum due to line strength and absorption measurement uncertainty. The data are consistent to within 4% of the equilibrium predictions at all values of ϕ, indicating reliable operation of the system.

Figure 24.9*b* illustrates measured CO and CO_2 mole fractions as a function of equivalence ratio. The solid lines represent chemical equilibrium calculations of CO and CO_2 mole fractions at measured temperatures. The vertical bars represent the uncertainty in measured CO and CO_2 mole fractions due to line
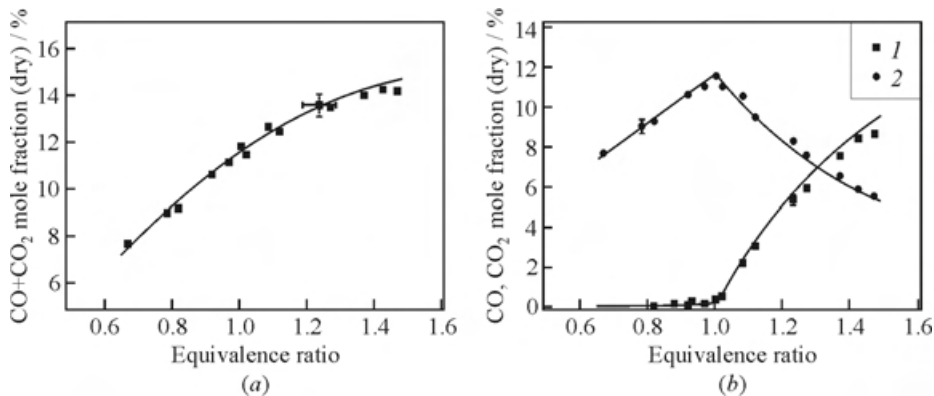
Figure 24.9 (*a*) Comparison of measured sum mole fractions of CO and CO_2 (symbols) to calculated (curve) equilibrium values (dry basis) and (*b*) comparison of measured mole fractions of CO (*1*) and CO_2 (*2*) to calculated (curves) equilibrium values (dry basis)

strength and absorption measurement uncertainty. The CO_2 data agree to within 3% with calculated equilibrium values in the fuel-lean region. For $\phi > 1$ the measured CO_2 mole fractions are slightly higher and the CO mole fractions slightly lower than the calculated equilibrium values, suggesting some conversion of CO to CO_2 in the sampling probe. The effects of sampling probe conversion of CO to CO_2 had been previously measured and published for various probes and system parameters [10].

24.4 CLOSED-LOOP CONTROL OF AN INDUSTRIAL-SCALE FORCED-VORTEX COMBUSTOR

Multiplexed diode-laser sensors were applied for measurement and control of gas temperature and species concentrations in a large-scale (50-kilowatt) forced-vortex combustor at NAWC to prove the viability of the techniques and the robustness of the equipment for realistic combustion and process-control applications [11]. The scheme employed was similar to that for measurements and control in the forced combustor and for fast extractive sampling of exhaust gases above a flat-flame burner at Stanford University (described previously).

The general arrangement of the diode-laser sensor system for measurements in the 50-kilowatt incinerator (afterburner) facility at China Lake is illustrated
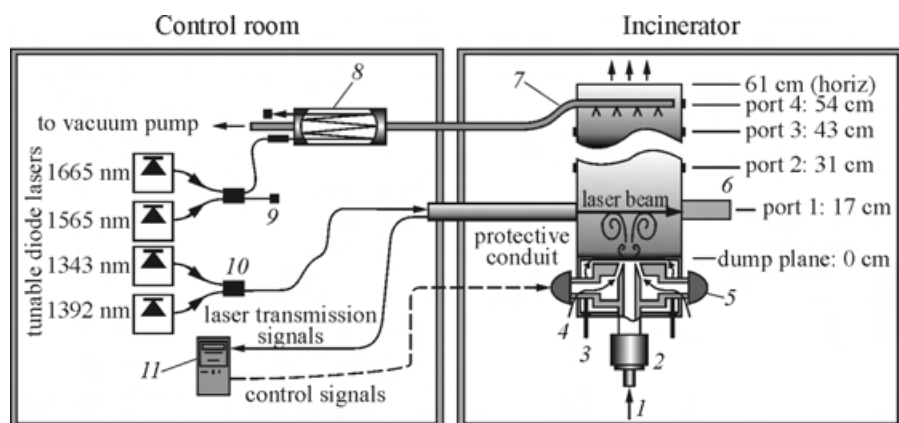
Figure 24.10 Schematic diagram of the combustion-control experiment at China Lake: *1* — primary air; *2* — primary air driver $\sin(2\pi f_0 t)$; *3* — pyrolysis gases: $N_2 + C_2H_4$; *4* — secondary air; *5* — secondary air drivers $\sin(2\pi f_0 t + \theta)$; *6* — demultiplexing box; *7* — sampling probe; *8* — multipass fast-sample cell (36-meter path); *9* — InGaAs detector; *10* — multiplexed beam; and *11* — data acquisition and control computer

in Fig. 24.10. The primary air flow (974 l/min) through the central jet (3.84-centimeter diameter) was acoustically forced (up to 30% RMS) to create coherent vortices at the preferred mode of the jet. Secondary air flow (100 l/min) was acoustically modulated (near 100% RMS) and injected circumferentially at a 15° angle relative to the primary air. The pyrolysis surrogate (45 l/min N_2 and 43 l/min C_2H_4) was circumferentially injected normal to the primary air flow. A water-cooled aluminum duct (18-centimeter diameter, 61-centimeter length) was sealed to the injection nozzle. Four ports along the length of the duct allowed for optical access or the insertion of sampling probes. Without forcing, the long, sooty flamelets can extend beyond the end of the duct. However, with proper forcing (at the appropriate phase angle) the flame becomes compact, intense, entirely blue, and resembles a lifted, premixed flame.

Details of the laser systems and the operating conditions employed to control the lasers were described above. The multiwavelength beam was brought to the incinerator via an optical fiber encased in a protective conduit and directed through the flowfield using a GRIN lens (0.25 pitch, 3-millimeter diameter). For extractive sampling, the water-cooled, stainless-steel probe was used to continuously direct combustion products into the multipass cell. The extracted gas was cooled, dried, and filtered to preserve the integrity of the silver-coated mirrors.

Differential absorption spectroscopy techniques were used to determine absolute species concentrations (C_2H_4, CO, and CO_2) by tuning the wavelength of the lasers across transitions near 1646 nm ($\nu_1 + \nu_9$, $\nu_5 + \nu_9$ bands of C_2H_4), the $R13$ transition of CO (3ν band) near 1564 nm, and the $R16$ transition of CO_2 near 1572 nm ($2\nu_1 + 2\nu_2 + \nu_3$ band). The absorption measurements were recorded in the multipass cell.

Figure 24.11 compares values of T_{RMS} measured at port 1 using the *in situ* measurement technique with values of CO concentrations measured at port 4 using the fast extractive-sampling technique. The minimum in CO concentration corresponds to the maximum in T_{RMS}, as expected. Since the presence of CO in the exhaust serves as an indicator of combustor performance, the correlation between measured T_{RMS} and CO concentration validates the use of rapid, nonintrusive T_{RMS} measurements for active combustion control [11].
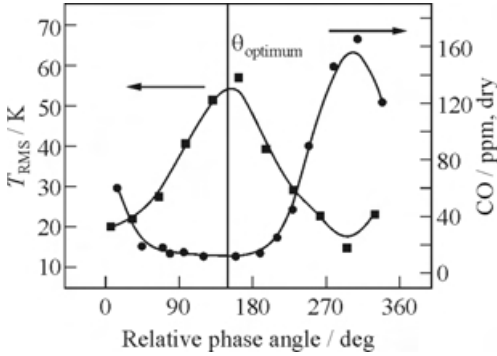

Figure 24.11 Variation of T_{RMS} (left axis) values measured at port 1 ($x/d = 4$) and CO concentration (right axis) of gases sampled from port 4 ($x/d = 14$) with relative phase angle between primary and secondary air driving in the 50-kilowatt forced combustor at China Lake

The amplitude of temperature fluctuations was controlled in a feedback loop by adjusting the relative phase between the primary and secondary forced air flows. A demonstration of the closed-loop performance is illustrated in Fig. 24.12. The controller converged on the optimum phase with a $1/e$ rise time of approximately 30 control steps (Fig. 24.12a). Figure 24.12b illustrates the difference between the power spectra with control off (i.e., neither primary nor secondary drivers) and control optimized. The response time necessary to reach the optimum phase was slowed by the large variations in the measured coherence (examples shown in Fig. 24.12a) which are attributed to the complex interactions between the inlet mode, the combustor modes, and the preferred mode of the jet.

In this initial demonstration in the China Lake combustor, each control step required approximately 10 s, primarily due to the slow data transfer rate and computation of the (1-hertz resolution) power spectrum. Significantly faster response times may be obtained by using other algorithms to compute the magnitude of temperature fluctuations (e.g., a 3-kilohertz control response rate has been obtained at Stanford University [7]). Improved response
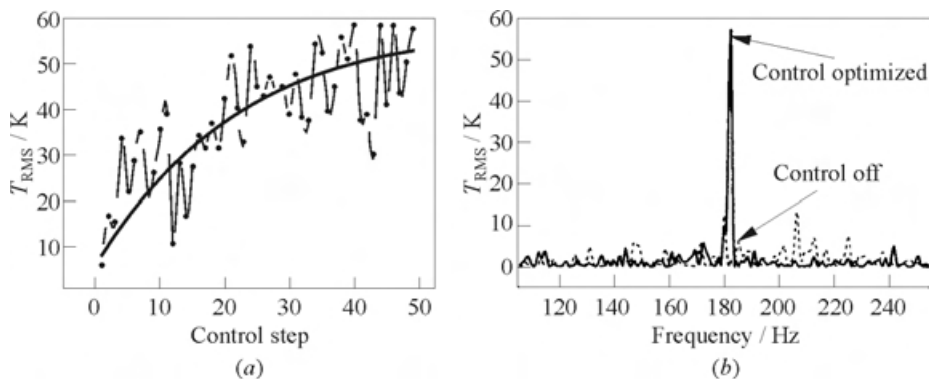
Figure 24.12 Measured T_{RMS} values (*a*) for successive feedback control steps during closed-loop control of the 50-kilowatt forced combustor at China Lake, feedback was based on a simplex hill-climbing algorithm which is adjusting the phase between the primary and secondary air drivers to maximize T_{RMS} values; (*b*) illustrates representative power spectra with and without control

times would allow nearly continuous phase (and thus coherence) optimization and, as a result, significantly minimize the mismatch between the various acoustic modes of the system.

To check for the presence of C_2H_4 (unburned fuel) in the exhaust, a DFB laser beam was directed through the multipass cell filled with gases sampled from port 3 and current-tuned across C_2H_4 transitions near 1646 nm ($\nu_1 + \nu_9$, $\nu_5 + \nu_9$ bands). The C_2H_4 and CO concentrations were measured at four representative flow conditions: no forcing, primary air forcing only, secondary air forcing at a nonoptimized phase angle, and with the optimized phase angle. As shown in Fig. 24.13, the concentrations of C_2H_4 and CO decreased considerably as the forcing was optimized. The detection limits for the present system (20-hertz bandwidth), indicated by the dashed lines, were 10 ppm for CO, 3 ppm for CO_2, and 3 ppm for C_2H_4.

These results are consistent with previous measurements which showed that CO concentration was lowest at the combustor operating conditions that most efficiently reduced the overall emission of toxic gases. Thus a measurement of CO concentration can serve as an effective indicator of combustor performance. The results demonstrate the applicability of multiplexed diode laser sensors for rapid, continuous measurements and control of multiple flowfield parameters, including trace species concentrations, in high-temperature combustion environments.
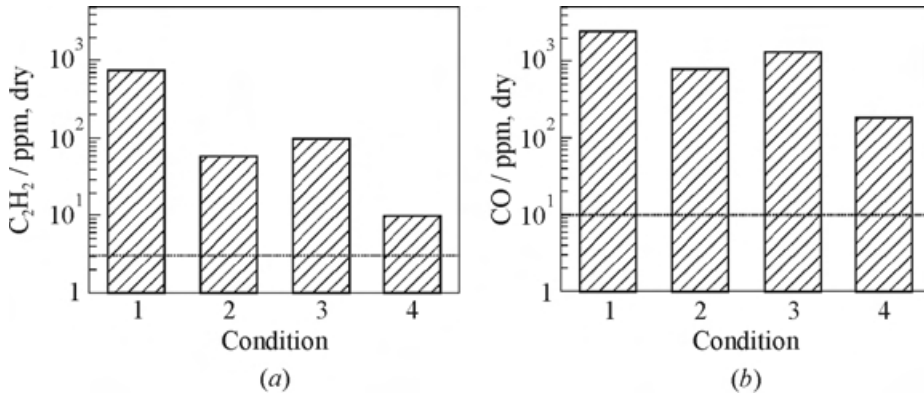
Figure 24.13 Measured C_2H_4 (*a*) and CO (*b*) concentrations in exhaust of the 50-kilowatt combustor at China Lake using extractive sampling of gases from port 3 at four representative flow conditions: 1 — no forcing; 2 — primary air forcing; 3 — poor phase angle; and 4 — optimum phase angle. Detection limits indicated by horizontal dashed lines

24.5 HYPERVELOCITY FLOWFIELD MEASUREMENTS

Multiplexed diode laser sensors have also been applied for measurements of gas temperature, velocity, and H_2O partial pressures in hypervelocity air flows at the Calspan University of Buffalo Research Center's (CUBRC) Large Energy National Shock Tunnel (LENS Tunnel) in Buffalo, New York [12]. The sensors were developed to provide quantitative characterization of the facility operation and, in particular, the freestream flow properties as a function of time. The measurements were recorded using a hardened probe, which contained critical optical components and photodetectors, that was installed directly into the hypersonic shock-tunnel near the nozzle exit to minimize complications due to boundary layers and facility vibration.

Figure 24.14 illustrates schematically the setup of the electronics and optical components within the probe and the remote laser-control systems. The distance between the two arms of the probe was 18 cm and the overall length was 40 cm. The nozzle exit diameter was 121 cm. The beam was directed from one arm of the probe to the other through wedged ($3°$) windows to eliminate interference effects. The 1400-nanometer beam (λ_1) was directed at a $54°$ angle with respect to the bulk gas velocity. The 1396-nm beam (λ_2) was directed through the test gas in a multipass arrangement (5 passes) using a pair of high-reflectivity gold-coated mirrors to increase the absorption path length
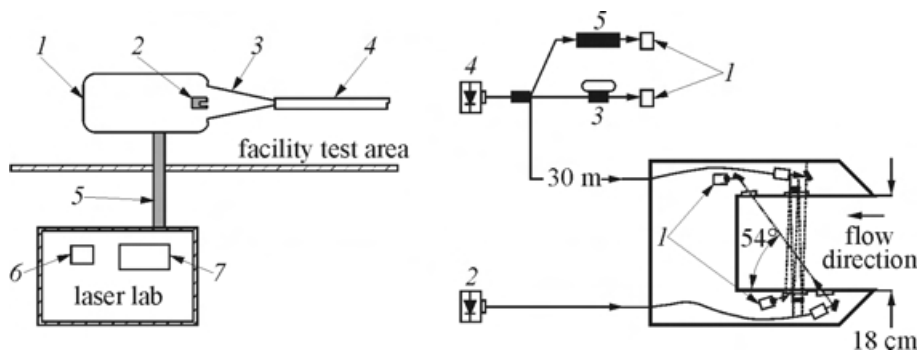
Figure 24.14 The left panel is a plan of the testing area near the LENS (reflected shock) tunnel: *1* — 8′ test section; *2* — TDL probe; *3* — 4′ nozzle M = 8–16; *4* — 8″ reflected shock tube; *5* — fiber optic and signal line conduit; *6* — data acquisition; and *7* — TDL system optical table. The right panel is a schematic diagram of the setup used to record water-vapor absorption in high-enthalpy flows: *1* — InGaAs detectors; *2* — tunable diode laser $\lambda_1 = 1400.74$ nm; *3* — ring interferometer; *4* — tunable diode laser $\lambda_2 = 1395.69$ nm; and *5* — H_2O reference cell

and signal-to-noise ratio. The laser transmission intensities were monitored with InGaAs photodetectors (2.6-megahertz bandwidths) mounted inside the probe. The fiber-coupled beams were divided into three paths using a 1×3 splitter and directed through the flowfield to measure absorption in the moving gas, through an interferometer to monitor the laser wavelength changes, and through a low-pressure static cell filled with water vapor to monitor the unshifted (reference) absorption.

The wavelengths of the distributed feedback diode lasers were independently current-tuned at an 8-kilohertz rate across the H_2O transitions to yield high-resolution absorption lineshape measurements every 125 μs. Figure 24.15 contains sample (raw data) traces from a high (10 MJ/kg) enthalpy shock-tunnel run. Figure 24.15*a* shows the absorbance as a function of laser frequency near 1400 nm. Figure 24.15*b* shows the absorption trace near 1396 nm recorded simultaneously. Both of the signals can be used to infer the translational temperature and partial pressure of water, while only one is Doppler-shifted and hence sensitive to the local flow velocity. The small absorption peak to the right in Fig. 24.15*a* is due to the static sample of water present in the open portion of the beam near the laser; this provides a convenient means of simultaneously monitoring both the unshifted and shifted line positions. Excellent agreement was found between the measurements of translational ($T_{\text{tran}} = 561$ K) and rotational ($T_{\text{rot}} = 560$ K) temperatures and the corresponding values of water-vapor partial
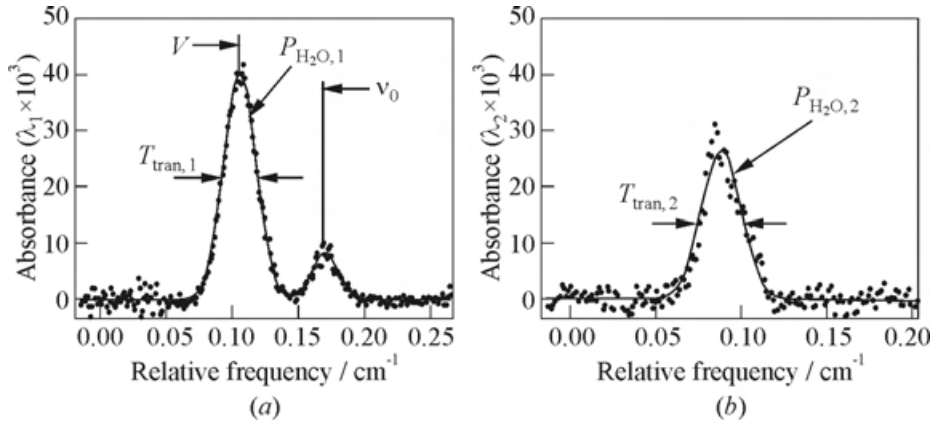
Figure 24.15 Single-sweep data traces of H_2O absorption recorded in a hypersonic flow with an enthalpy of 10 MJ/kg. The panels shows the absorbance (as a function of laser frequency, cm^{-1}) near 1.400 μm (*a*) and 1.395 μm (*b*) recorded simultaneously. $V = 4630\pm50$ m/s; $T_{tran,1} = 561\pm15$ K; $P_{H_2O,1} = 0.43\pm0.03$ Torr; $T_{tran,2} = 544\pm35$ K; and $P_{H_2O,2} = 0.45 \pm 0.06$ Torr

pressures. The measured velocity ($V = 4630$ m/s) is in good agreement with the flowfield calculations based on the reflected shock conditions and the expansion produced by the hypersonic nozzle.

The results obtained demonstrate the applicability of diode-laser absorption diagnostics for direct multiparameter gas measurements in hypervelocity flowfields for improved characterization of high-enthalpy facilities.

24.6   CONCLUDING REMARKS

Tunable diode-laser sensors offer considerable promise for combustion research and development and also for process sensing and control applications. These devices are rugged and relatively easy to operate and they have been demonstrated to yield simple and quantitative measurements of species, temperature, and velocity, where line-of-sight measurements are useful or preferred. These techniques will grow in use as costs of laser sources and fiber-optic components decrease and access to more wavelength regions improves.

Future applications are likely to involve real-time measurements and control of various combustion systems including gas turbines, waste incinerators, and aeropropulsion systems.

ACKNOWLEDGMENTS

REFERENCES

1. Philippe, L. C., and R. K. Hanson. 1992. Laser absorption mass flux sensor for high-speed air flows. *Optics Letters* 16:2002–4.

2. Chou, S. I., D. S. Baer, and R. K. Hanson. 1997. Diode-laser absorption measurements of CH_3Cl and CH_4 near 1.65 μm. *Applied Optics* 6:3288-93.

3. Parr, T. P., E. J. Gutmark, K. J. Wilson, K. Yu, R. A. Smith, D. M. Hanson-Parr, and K. C. Schadow. 1996. Compact incinerator afterburner concept based on vortex combustion. *26th Symposium (International) on Combustion Proceedings*. Pittsburgh, PA: The Combustion Institute. 2033–55.

4. Parr, T. P., K. J. Wilson, K. Yu, R. A. Smith, and K. C. Schadow. 1996. Paper 97S-043. *15th International Conference on Incineration and Thermal Treatment Technologies Proceedings*. Savannah, GA.

5. Cole, J. A., D. W. Hansell, N. C. Widmer, and W. R. Seeker. 1997. Paper 97S-043. *Spring Meeting of the Western States Section of the Combustion Institute Proceedings*. Livermore, CA.

6. Baer, D. S., M. E. Newfield, N. Gopaul, and R. K. Hanson. 1994. Multiplexed diode-laser sensor system for simultaneous H_2O, O_2 and temperature measurements. *Optics Letters* 19(22):1900–2.

7. Furlong, E. R., D. S. Baer, and R. K. Hanson. 1998. Real-time adaptive combustion control using diode-laser absorption sensors. *27th Symposium (International) on Combustion Proceedings*. Boulder, CO.

8. Mihalcea, R. M., D. S. Baer, and R. K. Hanson. 1997. Diode-laser absorption sensor system for combustion monitoring and control applications. *33rd Joint Propulsion Conference Proceedings*. NY: AIAA. AIAA Paper No. 97-3356.

9. Mihalcea, R. M., D. S. Baer, and R. K. Hanson. 1997. Diode-laser sensor for measurements of CO, CO_2, and CH_4 in combustion flows. *Applied Optics* 6: 8745–52.

10. Schoenung, S. M., and R. K. Hanson. 1981. CO and temperature measurements in a flat flame by laser absorption spectroscopy and probe techniques. *Combustion Science Technology* 24:227–37.

11. Furlong, E. R., R. M. Mihalcea, M. E. Webber, D. S. Baer, and R. K. Hanson. 1997. Diode-laser sensor system for closed-loop control of a 50-kW incinerator. *33rd Joint Propulsion Conference Proceedings*. NY: AIAA. AIAA Paper No. 97-2833.

12. Wehe, S. D., D. S. Baer, and R. K. Hanson. 1997. Tunable diode-laser absorption measurements of temperature, velocity, and H_2O in hypervelocity flows. *33rd Joint Propulsion Conference Proceedings*. NY: AIAA. AIAA Paper No. 97-3267.

SECTION FOUR

EMISSIONS
AND PLUMES

Chapter 25

ASYMPTOTIC ANALYSIS OF FLAME STRUCTURE PREDICTING CONTAMINANT PRODUCTION

F. A. Williams and J. C. Hewson

Many propulsion problems require knowledge of trace species in combustion processes. These species are produced by finite-rate chemical-kinetic mechanisms that involve large numbers of elementary steps. Reduced chemistry and improved mathematical simplifications are needed to describe production of species such as contaminants with sufficient efficiency and accuracy for propulsion applications. The research reported here selects the production of oxides of nitrogen in methane–air diffusion flames as an example problem for developing the methods necessary for addressing these difficult tasks. Production rates are calculated with thermal, prompt, and nitrous oxide mechanisms taken into account, as well as consumption processes collectively termed reburn. For this purpose, it is necessary to extend the well-known four-step methane–air flame-chemistry description to six steps, with acetylene taken out of steady state and one-step production of nitric oxide included. Emission indices are calculated as functions of the rate of scalar dissipation at the stoichiometric mixture fraction for near-atmospheric pressures and shown to be in reasonable agreement with results obtained from numerical integrations. It is shown that the mechanisms are strongly dependent on the flame temperature and on superequilibrium concentrations of radicals, both fuel-derived and from hydrogen–oxygen chemistry. For flames in near-normal ambient atmospheres, it is found that the prompt mechanism usually is most important. For longer residence times, and especially for ambient pressures and temperatures above standard, the thermal mechanism increases in importance, but this increase is offset almost entirely by consumption through reburn reactions. Accuracies of emission indices are within a factor of two. The results demonstrate methods for calculating contaminant production with reasonable generality and simplicity.

25.1 INTRODUCTION

Interest in production of contaminants in flames ranges from concern about pollutant emissions, such as smoke and oxides of nitrogen, to the desire to know ion

and electron concentrations in connection with communications and detectability problems. Engine signatures depend strongly on trace contaminants. It is often easier to predict principal flame characteristics than to predict contaminant levels because the contaminants depend on fine details of the chemical kinetics of combustion. The work reported here is directed towards obtaining improved useful methods for calculating concentrations of these species in combustion processes.

The research to be described here lies in the realm of combustion theory. Combustion is an applied science in the sense that advances in combustion contribute comparatively directly to engineering improvements [1]. The present research is aimed at increasing understanding of combustion processes that occur in gas turbines, internal combustion engines, rockets, industrial furnaces, open fires, and gaseous detonations. Like most if not all sciences, combustion now can be divided into three equally important parts, namely, computation, experiment, and theory [2]. Traditionally, theory suggests and explains experiments, and experiments test and motivate theory. The newer third component, computation, interacts similarly. For example, nowadays sometimes theory explains computational results, computations test theory, experiments test computational results, etc. All three components are now essential to progress of the science. Although the present work falls in the category of theory, it makes use of experiments and especially computations. Computations are made for real chemistry, with complete descriptions at the level of elementary chemical kinetics. The validity of the reduced chemistry employed here is checked against computations with detailed chemistry. Background in combustion theory for the present work appears in textbooks [3–5].

Kinetic data for real flames are improving continually. For some time now there has been a large body of research in progress employing numerical methods to incorporate this kinetic information in predictions of the structure and dynamics of real flames (e.g., [6–23]). The numerical approach, correctly pursued, provides accurate predictions of flame structure and of flame speeds. However, the procedure is somewhat laborious and is seldom carried to a point at which simple formulas for flame properties as functions of pressure, temperature, or composition can be obtained. In addition, numerical computations with full chemistry are not well suited to address questions of multidimensional flows and instabilities or turbulence because the computational resources required for that are too extensive. In contrast, the analytical research pursued here can be used in addressing these more complex problems. The work often provides formulas for flame properties, stability boundaries, and amplification or damping rates, with realistic chemistry. These formulas are readily used over wide ranges of conditions and contribute to improved understanding of combustion processes.

The general approach followed below is now fairly well developed [24–43]. Beginning with the full, detailed chemistry, systematic reduction to a small num-

ber of overall chemical steps is effected. This reduction is based on identifying large or small values of nondimensional ratios of reaction-rate parameters. Ratios of reaction rates to flow rates or diffusion rates (Damköhler numbers) also are involved. The systematic reduction enables the rates of the overall steps in the reduced chemistry to be related rigorously to the rate parameters of the key elementary steps. The resulting analytical description of the chemistry is then simple enough for application of asymptotic methods to prediction of flame structure and stability. These asymptotic methods sometimes can be based on the now well-known activation-energy asymptotics (AEA), in which a nondimensional activation energy for the overall chemical step is treated as a large parameter. More often nowadays, however, use is made of rate-ratio asymptotics instead, in which ratios of certain reaction rates are treated formally as large or small parameters. Rate-ratio asymptotics (RRA) is being found to offer greater richness and flexibility in describing combustion processes, including diffusion flames and combustion waves, such as deflagrations and detonations. Within the context of these asymptotic methods, then, various techniques of applied mathematics, such as stability theory, bifurcation analysis, or WKB-type methods, are applied, depending on what is appropriate for the problem. Techniques of matched asymptotic expansions, with imposition of necessary uniformity, are central to the analysis. The results thus predict the flame structure and dynamics as related to the underlying chemistry.
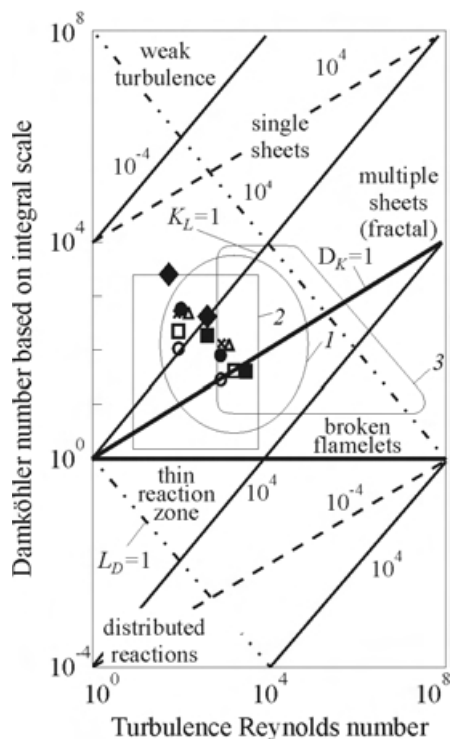
Figure 25.1 Regimes of turbulent combustion: *1* — offshore flares, *2* — spark-ignition engines, *3* — supersonic combustion, K_L — turbulent kinetic energy referred to laminar ratio of kinematic viscosity to chemical time, D_K — Damköhler number based on Kolmogorov scale, L_D — integral scale referred to thickness of laminar deflagration

The problem to which these methods are applied here is one of turbulent combustion in the reaction-sheet regime. It is known that turbulent reacting flows exhibit different regimes of turbulent combustion, as illustrated in Fig. 25.1. The diagram shown applies to both premixed flames
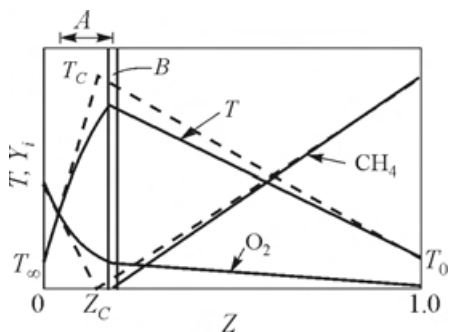
Figure 25.2 Illustration of the structure of the methane–air diffusion flame according to RRA: A — oxygen-consumption zone thickness $O(\epsilon)$, B — fuel-consumption zone thickness $O(\delta)$

and diffusion flames, although a number of the zones indicated pertain only to premixed flames. The upper part of the diagram, mainly above the horizontal line at unity, is the reaction-sheet regime, also called the flamelet regime. It is seen from this diagram that most practical applications fall within this regime. In this regime, the contaminant production occurs in an ensemble of laminar flamelets in the turbulent flow. The research described here therefore addresses the structure and production rates in the laminar flamelets.

Methane–air diffusion flames are selected for the example to be studied here. The temperature T and species mass fractions Y_i (for species i) in such flames are functions of the mixture fraction Z, which varies from zero in air to unity in fuel and measures the fraction of the material present that came from the fuel. Figure 25.2 is a schematic illustration of major profiles in the methane–air diffusion flame as functions of Z, obtained by the rate-ratio asymptotics described above. The work to be reported here adds to this picture the chemistry relevant to the production of oxides of nitrogen.

This work is of interest not only because of the desire to reduce pollutant production in furnaces and engines fueled by natural gas, the major component of which is methane, but also because methane is the simplest model hydrocarbon fuel, whose combustion characteristics provide information relevant to the burning of all hydrocarbon fuels. For these reasons, there has been extensive experimental, computational, and theoretical study of the detailed flame structure and chemistry of methane–air diffusion flames. The laminar counterflow configuration, which constitutes a convenient and often-used flamelet model, is selected here, although the analysis is carried out in a mixture-fraction variable to render the results independent of the laminar-flow configuration to the maximum extent possible. In an effort to advance understanding of emissions mechanisms and to provide formulas that can be helpful for estimating emissions, theoretical work is completed, directed towards providing analytical expressions for properties of flame structures and for species concentrations in diffusion flames, relevant to emissions of oxides of nitrogen.

The theoretical results are evaluated through comparison with results of numerical integrations for the counterflow configuration with potential-flow boundary conditions.

25.2 THEORETICAL ANALYSIS

The emission index in general is defined as the mass of pollutant emitted per unit mass of fuel consumed. In quasi-steady diffusion flames, this is the ratio of the mass flux of pollutant out of the flame to the mass rate of consumption of fuel per unit flame area. Depending on the application, it may be more desirable to consider only the flux of pollutant to the air or the sum of the pollutant flux to both air and fuel. The latter definition is selected here, and a pollutant balance for the flame then enables the emission index to be expressed as the ratio of the mass rate of production of pollutant per unit area to the mass rate of consumption of fuel per unit area. In terms of the mass rate of production of species i per unit volume $\widehat{\omega}_i$, the mixture fraction, and the magnitude of its gradient $|\nabla Z|$, the mass rate of production of species i per unit area is

$$\widetilde{\omega}_i = \int_0^1 \frac{\widehat{\omega}_i}{|\nabla Z|}\, dZ \tag{25.1}$$

Following existing convention, oxides of nitrogen (NO_x) are considered here to consist of NO and NO_2 since N_2O generally is treated separately, and in addition, N_2O emissions are small compared with those of NO and NO_2. The NO_x emission index for methane–air flames then is defined here as

$$E_{NO_x} = 1000 \frac{(W_{NO_2}/W_{NO})\widetilde{\omega}_{NO} + \widetilde{\omega}_{NO_2}}{-\widetilde{\omega}_{CH_4}} \tag{25.2}$$

where W_i denotes the molecular weight of species i. This definition reflects the convention that all NO_x is converted to NO_2 in evaluating the emission index and results in the traditional units of g pollutant per kg fuel.

To obtain the $\widetilde{\omega}_i$ of Eq. (25.2), it is necessary to know the $\widetilde{\omega}_i$ of Eq. (25.1), which depend on the elementary reaction steps for NO and NO_2 production and the rates of these steps throughout the flame. Those rates, in turn, depend on the temperature profiles and the profiles of concentrations of the reactants in the elementary steps. A considerable amount of information concerning the flame structure therefore is needed to evaluate E_{NO_x} accurately. Analytical approximations for this necessary information are sought in the present work.

The starting point for any study of this kind is a set of elementary reactions and their associated reaction-rate parameters. Although literally hundreds of elementary steps are potentially relevant, calculations with full detailed mechanisms show that most of them are unimportant. A starting chemical-kinetic mechanism needs to be selected that includes all of the important elementary steps. Since the nitrogen chemistry is a small perturbation on the chemistry of the main flame, it is convenient to separate the flame chemistry from the nitrogen chemistry in the starting mechanism. The starting chemistry, which

involves 102 elementary steps, is too extensive to be given here but may be found elsewhere [44]. It makes use of detailed numerical studies with full chemistry and associated evaluations of elementary rate parameters available in the literature [45–48].

The earliest analytical studies of diffusion-flame structure were based on one-step AEA. This type of description is insufficient for the present investigation because it neither provides needed profiles of intermediate species nor relates results to elementary rate parameters. Many RRA flame-structure analyses have now been completed, using a well-known four-step reduced-chemistry description [33], in which the intermediates CO and H_2, as well as the radical H, are treated as species that do not necessarily obey chemical-kinetic steady-state approximations. There is not just one RRA analysis of nonpremixed methane–air flames with four-step reduced chemistry but rather a variety of them; a number of small parameters occur, and different analyses leading to different internal structures arise from different relative ordering of these small parameters. Theories for nearly the entire combination of possible orderings have now been published, the most recent and most general of these being the work of Bai and Seshadri [49]. In the present work, it is necessary to select a particular RRA approach that provides the most reasonable trade-off between simplicity and fidelity in achieving the goal of maximizing the accuracy of predictions of E_{NO_x}. This selection involves not only orderings but also determination of appropriate "truncations," judicious neglect of terms in specific formulas to simplify algebra.

In considering previous four-step methane–air diffusion-flame RRA analyses, it was determined that the investigation of Yang and Seshadri [50] is the most relevant. Contrary to Bai and Seshadri [49], that work [50] treats oxygen leakage as being small rather than order unity (this last selection being best for describing inhibition by halogen-containing species [51] but not providing good O_2 profiles for the present study), considers near-equilibrium conditions for the water-gas shift (much better here than the opposite limit of slow CO oxidation), and addresses two limits, one in which the layer of radical nonequilibrium is thin compared with the fuel-consumption layer and the other in which the fuel-consumption layer is thin compared with the radical-nonequilibrium layer. It has been found that the first of these two limits poorly describes the structure and radical profiles in the fuel-consumption zone and thus predicts prompt-NO production rates that are an order of magnitude too low; therefore the present analysis takes the fuel-consumption layer to be thin compared with the radical-nonequilibrium layer on the fuel side of the flame, as illustrated in Fig. 25.3. To include all of the important NO_x chemistry, especially the prompt mechanism, it is necessary to augment the set of elementary steps in the fuel chemistry. In particular, C_2 species are important contributors to the concentrations of the CH radical that carries the prompt path, and the fuel chemistry considered here therefore contains more elementary steps than previous RRA
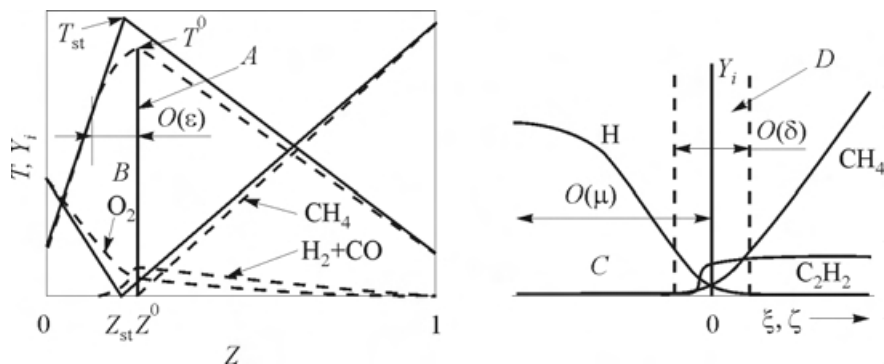
Figure 25.3 The reaction zone configuration used in the present analysis. On the left side solid lines for T, Y_{O_2}, and Y_{CH_4} represent the outer solution, and the dashed lines show profiles resulting from finite reaction rates in the oxygen-consumption layer. The right side corresponds to an expanded view of the regions around Z^0 in the left sketch, represented by a single line there, showing the structure of the radical-equilibrium and fuel-consumption layers: A — location of fuel and radical layers, B — oxidation layer, C — radical-equilibration layer, and D — fuel-consumption layer

analyses, these being combined into five overall steps, rather than the traditional four, so that nonsteady-state C_2 species can be permitted. A new RRA analysis of the main flame structure thus is modified from that of Yang and Seshadri [50].
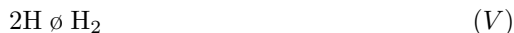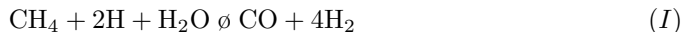
Analytical approximations appropriate for the nitrogen chemistry have been addressed previously mainly in relatively rudimentary fashion. For example, it has long been known that the effective activation energy for the thermal mechanism is high enough to render AEA accurate [5], and that approximation is used here for the thermal process with the improved description of the underlying flame structure. It is also found here that AEA is appropriate for the nitrous oxide mechanism and plays a role in the reverse-Zel'dovich reburn, but it is inapplicable for the prompt mechanism and for other reburn steps. Methods of RRA are developed here for these latter processes, in place of the rough, order-of-magnitude estimates employed in previous work [52] for the prompt mechanism. A brief review of these earlier efforts is available [42]. Since steady-state approximations are accurate for most intermediate nitrogen-containing species, a one-step overall description of the NO_x chemistry is employed, incorporating the influences of all of these elementary steps. This one-step description has been previously derived and tested numerically and was found to provide reasonable results [47]. The main contribution here is to work this one-step description into an appropriate RRA analysis, a task that has not been attempted previously.

25.3 REDUCED CHEMISTRY

The limitations encountered when obtaining an analytical solution to the conservation equations, as in the present work, differ from those encountered applying direct computational methods. For example, the cost of numerical computations is dependent on the grid and, especially, on the number of species for which conservation equations must be solved; additional reactions do not add significantly to the computational effort. With RRA techniques, further limitations arise on the number of different reaction paths that can conveniently be included in the analysis. The analysis typically follows a sequence of reactions that make up the main path of oxidation, the most important reactions, while parallel sequences are treated as perturbations to the main solution and often are sufficiently unimportant to be neglected. The first step thus identifies a skeletal mechanism of 63 elementary steps by omitting the least important steps of the detailed mechanism [44].

Some steps that have been included in previous RRA studies are not incorporated into the present analysis because they are not important, while others that have previously been neglected are found to be important and are retained.

Steady-state approximations are introduced into the skeletal mechanism to obtain the following six-step reduced mechanism:

$$CH_4 + 2H + H_2O \rightleftharpoons CO + 4H_2 \qquad\qquad (I)$$

$$2CO + H_2 \rightleftharpoons C_2H_2 + O_2 \qquad\qquad (II)$$

$$CO + H_2O \rightleftharpoons CO_2 + H_2 \qquad\qquad (III)$$

$$3H_2 + O_2 \rightleftharpoons 2H + 2H_2O \qquad\qquad (IV)$$

$$2H \rightleftharpoons H_2 \qquad\qquad (V)$$

$$N_2 + O_2 \rightleftharpoons 2NO \qquad\qquad (VI)$$

While most of the steady states leading to this mechanism are quite well justified, some of them, particularly those for some stable molecules such as HCN, are not, and these will lead to some inaccuracies in the predictions, although not in the hot reaction zone where the contaminants are produced. In numerical calculations accuracies giving errors within a few percent are achievable, but the additional assumptions required for an RRA analysis lead to errors on the order of 20%.

In this reduced scheme, step I is the fuel-consumption step, which is seen also to consume radicals. Step II is the step for production of C_2 species not in steady state, important for obtaining correct CH profiles. Step III is the water-gas shift that burns CO. The oxygen is consumed by step IV, which is the source of radical production through the hydrogen–oxygen branched chain.

Step V describes the three-body radical recombination. Finally, step VI includes the three mechanisms of NO production, as well as reburn.

Derivation of the reduced mechanism involved introduction of steady-state approximations for the species OH, O, HO_2, HCO, CH_2O, CH_2OH, CH_3, C_2H_6, C_2H_5, C_2H_4, C_2H_3, HCCO, CH_2 (the triplet), CH_2^* (the singlet), CH, HCN, HNCO, NCO, NH_2, NH, N, N_2O, and N_2H. These approximations result in a set of coupled nonlinear algebraic relations among the concentrations of the steady-state species, containing rate constants and concentrations of other species. These relations are readily written down from the skeletal mechanism. While the full steady states can be employed in numerical computations with reduced chemistry, approximations to the algebraic equations are needed to proceed with analytical solutions by RRA. The resulting truncated steady states employed in the present work are given elsewhere [44]. Many of them follow from earlier studies, while some, particularly for the C_2 and nitrogen chemistry, are new. They all have been tested through numerical flame-structure computations employing the full steady states. Steady-state expressions for concentrations of some species are not needed in the analysis; especially for stable species, these often give poor concentration profiles.

## 25.4 FORMULATION AND SOLUTION OF THE DIFFUSION-FLAME PROBLEM

In both AEA and RRA, there are inert convective-diffusive regions on the fuel and oxidizer sides of the main reaction regions of the diffusion flame. Conservation equations are written for each of the outer inert regions, and their solutions are employed as matching conditions for the solutions in the inner reaction regions. The inner structure for RRA is more complicated than that for AEA because the chemistry is more complex [53]. The inner solutions nevertheless can be developed, and matching can be achieved. The outer solutions will be summarized first, then the reaction region will be discussed.

In the present analysis, the outer convective-diffusive zones flanking the reaction zone are treated in the Burke–Schumann limit with Lewis numbers unity. Lewis numbers different from unity are taken into account where reactions occur. These Lewis-number approximations are especially accurate for methane–air flames and would be appreciably poorer if hydrogen or higher hydrocarbons are the fuels. To achieve a formulation that is independent of the flame configuration, the mixture fraction is employed as the independent variable. The connection to physical coordinates is made through the so-called scalar dissipation rate,

$$\chi = 2 \mid \nabla Z \mid^2 \frac{\lambda}{\rho c_p} \qquad (25.3)$$
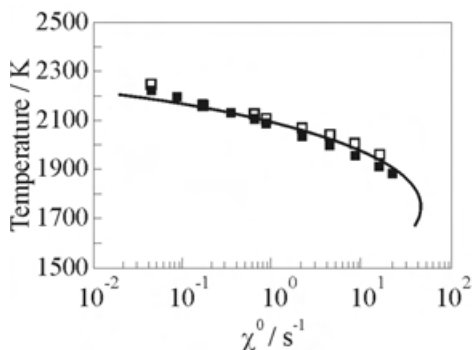
Figure 25.4 Comparison between RRA predicted T^0 (curves) and peak temperatures from full numerical calculations. Hollow symbols show results with the detailed mechanism, while the solid symbols provide results using only the skeletal mechanism. Calculations for methane–air diffusion flames at $p = 1$ bar and fuel and oxidizer stream temperatures of $T_F = T_O = 300$ K
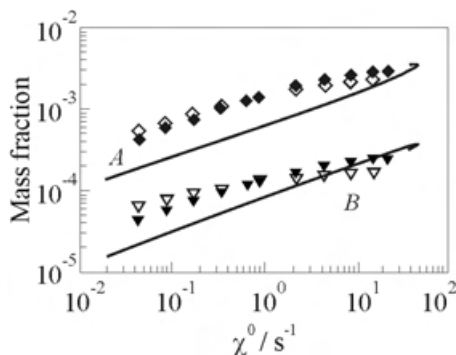
Figure 25.5 Comparison between steady-state radical levels predicted at Z^0 and peak radical mass fractions from full numerical calculations. Hollow symbols show results with the detailed mechanism, while the solid symbols provide results using only the skeletal mechanism. Calculations for methane–air diffusion flames at $p = 1$ bar and fuel and oxidizer stream temperatures of $T_F = T_O = 300$ K. $A = Y_O$, $B = Y_H$

where λ denotes the thermal conductivity, ρ the density, and c_p the specific heat at constant pressure for the mixture. Attention is restricted to ideal-gas mixtures, for which $\rho = p\overline{W}/(\overline{R}T)$ with $\overline{W}$ denoting the average molecular weight. For a given pressure and boundary temperatures, the flame structure depends on one parameter, which generally is taken to be χ_{st}, the stoichiometric scalar dissipation, that is, χ evaluated from outer-zone solutions at $Z = Z_{st}$, the stoichiometric value of the mixture fraction.

In the reaction region the chemical source terms appear. The structure of this region is illustrated in Fig. 25.3, where it is seen that the limit $\delta < \mu < \varepsilon$ is the one considered here. All three of these small parameters are related to appropriate Damköhler numbers [44]. The RRA analysis [44] results in predictions of peak temperature as a function of strain rate, shown in Fig. 25.4. The excellent agreement here is important for being able to calculate contaminant production with good accuracy. Figure 25.5 shows the sufficient agreement obtained for important radicals as well.

The C_2 chemistry and NO_x are introduced as perturbations on the above structure [44]. Important results from the C_2 chemistry concern predictions of CH and CH_2 profiles. These predictions are important for determining the

production by the prompt mechanism. The integrals that appear in calculating the prompt prediction are shown in Fig. 25.6. The resulting comparisons are seen there to be excellent. Separate predictions are made of contributions from the thermal, prompt, nitrous oxide, and reburn mechanisms [44]. Those results are then combined to obtain the complete prediction. With X_i denoting the mole fraction of species i and the subscripts T, P, N, and R identifying the thermal, prompt, nitrous oxide, and reburn mechanisms, respectively, the result

$$-\int_0^1 \frac{\rho\chi}{2}\frac{d^2 Y_{\mathrm{NO}}}{dZ^2}\frac{dZ}{|\nabla Z|} = \frac{\lambda_{st}\,|\,\nabla Z\,|\,_{st} W_{\mathrm{NO}}}{\overline{W} c_{p\,st}}\left(\frac{X_{\mathrm{NO}}^0}{1-Z_{st}} + \frac{X_{\mathrm{NO}}^0}{Z_{st}}\right)$$

$$= \widetilde{\omega}_T + \widetilde{\omega}_P + \widetilde{\omega}_N - \widetilde{\omega}_{R1} X_{\mathrm{NO}}^0 - \widetilde{\omega}_{R2} X_{\mathrm{NO}}^0 - \widetilde{\omega}_{R3}(X_{\mathrm{NO}}^0)^2 - \widetilde{\omega}_{R4}(X_{\mathrm{NO}}^0)^2 \quad (25.4)$$

is obtained. Here the subscripts 1, 2, 3, and 4 for R refer to contributions from reverse thermal (the N atom), reverse prompt (the CH radical), the imidogen radical, and the amidogen radical, respectively. Peak contaminant concentrations and emission indices are calculated from these RRA predictions.
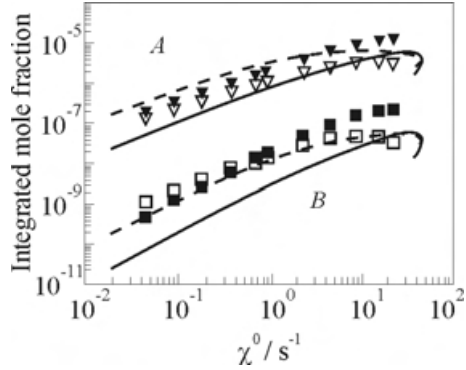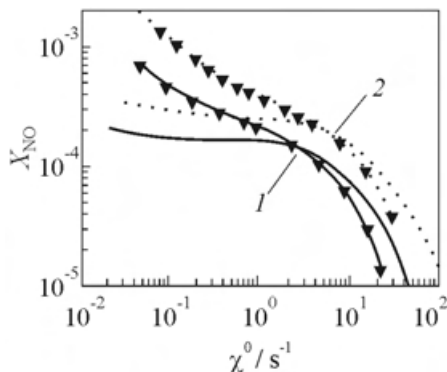

25.5   RESULTS

Figure 25.7 shows the predicted peak mole fraction of NO. It is seen that the peak NO concentrations range from values on the order of 10 ppm at high-scalar dissipation rates to values reaching 1000 ppm at high-ambient temperatures and low scalar dissipation; the latter values are reduced greatly when radiant energy loss is included. In reburn contributions it is found that $R2$ dominates at high-scalar dissipation and $R3$ at low [44]. Predictions for reburn are in good agreement with numerical results.

Figure   25.6   Comparison between integrated mole fractions of CH ($A = \int X_{\mathrm{CH}_2}\,dZ$) and CH$_2$ ($B = \int X_{\mathrm{CH}}\,dZ$) from asymptotics and full numerical calculations. The calculations are for methane–air diffusion flames at $p = 1$ bar and oxidizer and fuel stream temperatures of $T_F = T_O = 300$ K. Hollow symbols represent results from numerical computations using the starting mechanism while filled symbols are results using only the skeletal mechanism: the solid curves are the original RRA results and the dashed curves improvements [44]

The contributions of the three production mechanisms and that of the sum of the reburn reactions to the NO$_x$ emission index are plotted in Figs. 25.8 and 25.9, along with the net emission index, as functions of χ^0 for ambient

Figure 25.7 Calculated peak values of X_{NO} for $p = 1$ bar. Curves with symbols represent numerical computations; curves without symbols represent the RRA analysis: $1 — T_O = T_F = 300$ K, $2 — 500$ K

conditions. It is evident that for most values of χ^0 the prompt mechanism is the primary production mechanism, and the nitrous oxide mechanism is negligible. For longer residence times, higher flame temperatures and lower superequilibrium radical mole fractions lead to a decrease in the importance of the prompt mechanism along with an increase in the importance of the thermal mechanism. At the same time the importance of reburn increases to offset the thermal production; reburn increases because of an increase in the ratio of NO to radical mole fractions.
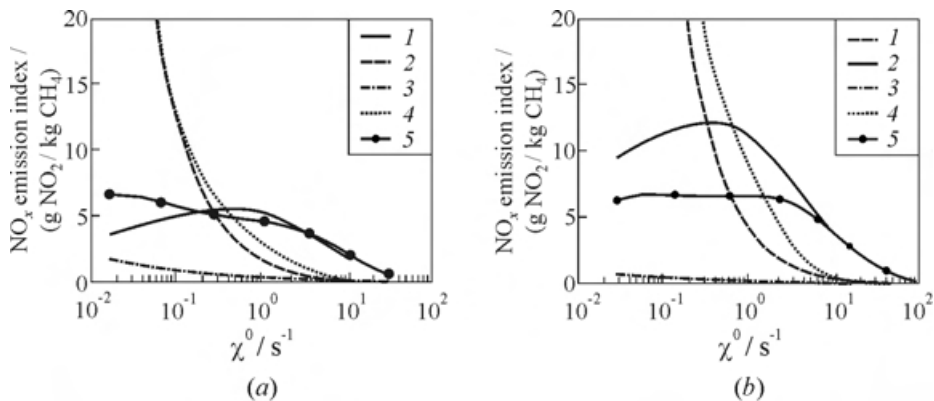
The contributions of the different mechanisms at elevated pressures ($p = 2$ bar) are shown in , and
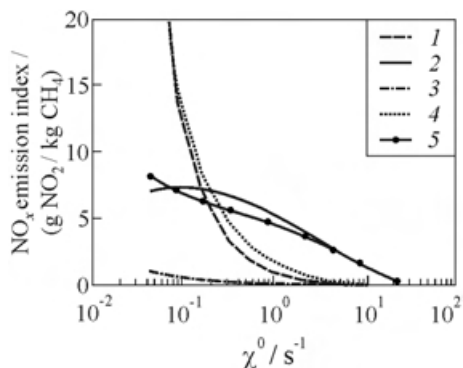

Figure 25.8 The relative contributions of the thermal E_T (*1*), prompt E_P (*2*), and nitrous oxide E_N (*3*) mechanisms as well as reburn E_R (*4*) to the emission index and the net emission index found from Eq. (25.2) (symbols *5* — E_{NO_x}) as predicted by numerical computations using the starting mechanism for flames at $p = 1$ bar and oxidizer and fuel stream temperatures of $T_F = T_O = 300$ K
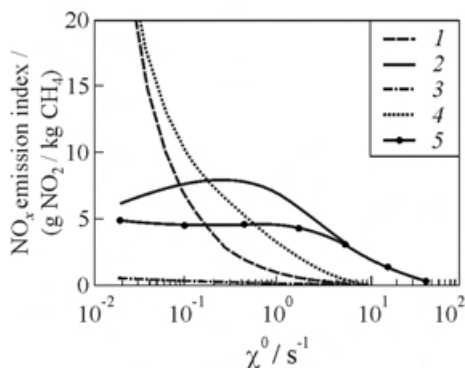
Figure 25.9 The relative contributions of the thermal E_T (*1*), prompt E_P (*2*), and nitrous oxide E_N (*3*) mechanisms as well as reburn E_R (*4*) to the emission index and the net emission index found from Eq. (25.2) (symbols *5* — E_{NO_x}) as predicted by RRA analysis for methane–air diffusion flames at $p = 1$ bar and oxidizer and fuel stream temperatures of $T_F = T_O = 300$ K

Figure 25.10 The relative contributions of the thermal E_T (1), prompt E_P (2), and nitrous oxide E_N (3) mechanisms as well as reburn E_R (4) to the emission index and the net emission index found from Eq. (25.2) (symbols 5 — E_{NO_x}) as predicted by RRA analysis for methane–air diffusion flames at (a) $p = 2$ bar and oxidizer and fuel stream temperatures of $T_F = T_O = 300$ K and (b) $p = 1$ bar and oxidizer and fuel stream temperatures of $T_F = T_O = 500$ K
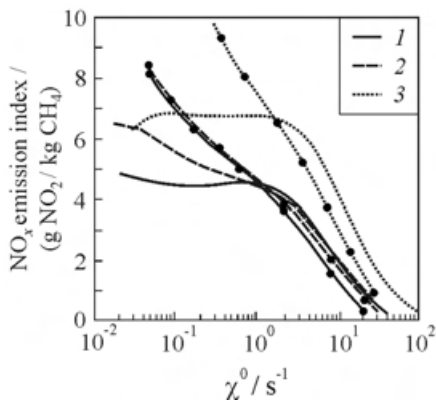
Figure 25.11 Comparison between the predicted net emission index (including all mechanisms) using RRA and numerical calculations for atmospheres: 1 — 1.0 bar, 300 K; 2 — 2.0 bar, 300 K; and 3 — 1.0 bar, 500 K. Curves with symbols represent numerical computations with the starting mechanism; curves without symbols represent the RRA analysis

those with higher boundary temperatures ($T_F = T_O = 500$ K) are shown in Fig. 25.10b. In all cases the relative importance of each mechanism is similar. Thermal production and reburn experience the greatest relative increases in each case, though these effects largely offset each other for both the detailed and RRA results, and the prompt mechanism is still most important at moderate to high-scalar dissipation rates. Higher temperatures in the fuel and oxidizer streams increase the rates of all mechanisms; since reburn still largely offsets the increase in the thermal mechanism, the increase in the rate of the prompt production with temperature can account for much of the change in net emissions in Fig. 25.10b.

Figure 25.11 compares the resulting net emissions indices for different at-

mospheres. The total NO_x emission index is found from the sum of all terms, $\widetilde{\omega}_{NO} = \widetilde{\omega}_T + \widetilde{\omega}_P + \widetilde{\omega}_N - \widetilde{\omega}_{R1}X^0{}_{NO} - \widetilde{\omega}_{R2}X^0{}_{NO} - \widetilde{\omega}_{R3}(X^0{}_{NO})^2 - \widetilde{\omega}_{R4}(X^0{}_{NO})^2$, in Eq. (25.2). To find the emission index using numerical calculations, the rates from step VI are integrated for constructing Fig. 25.11. This corresponds to the emission index that is found for the one-step reduced description of the nitrogen chemistry, but it differs from that found if all of the elementary rates in the starting mechanism contributing to NO production are integrated. Nonnegligible quantities of HCN and NH_3 are produced in the flame. The reduced mechanism effectively converts these to NO, so that the resulting emission index includes NO_x, HCN, and NH_3 emissions. The detailed chemistry gives a lower NO_x emission index than the reduced chemistry or RRA (by 15%–30%) when based only on NO and NO_2 but agrees if presumed conversion of HCN and NH_3 is added. Emissions of HCN and NH_3 occur only to the fuel side, and if these species pass through the flame again, they are converted almost completely to NO. It therefore is reasonable to include them in counting NO_x emissions by calculations from detailed chemistry. A single-step description of the nitrogen chemistry accomplishes this automatically.

Agreement between the numerical and asymptotic results in Fig. 25.11 is good except for small values of χ^0 where small relative errors in the thermal and reburn terms (both large numbers) result in sizable errors for their difference. Emissions in general decrease by at least an order of magnitude as the scalar dissipation rate is increased from small to large values. The shape of each curve also helps to show the regimes in which each mechanism is important; each curve has a "hump" near $\chi^0 = 1$ s^{-1} which is near the peak of prompt emissions. For $\chi^0 > 1$ s^{-1} the prompt mechanism is of primary importance, while for $\chi^0 < 1$ s^{-1} the thermal and reburn processes gain in importance, leading eventually to a steep increase in emissions for $\chi^0 \ll 1$ s^{-1}, an increase that would be lessened substantially by inclusion of influences of radiant energy loss.

25.6   CONCLUDING REMARKS

A number of conclusions can be drawn from this first detailed analysis of NO production in methane–air diffusion flames by techniques of RRA. It is found that all production mechanisms have rates dependent on the peak flame temperature T^0. The production rates for the thermal and nitrous oxide mechanisms increase sufficiently rapidly with T^0 that they are calculated by AEA after the peak flame temperature, and superequilibrium radical mole fractions are obtained from the RRA analysis of the primary flame structure. The flame temperature depends on the temperature of the fuel and oxidizer streams and

is also strongly affected by finite-rate kinetics, specifically slow three-body radical recombination reactions. The RRA analysis provided an exceptionally good prediction of the flame temperature, which decreases as the scalar dissipation rate, χ^0, increases, or increases for a fixed χ^0 when the pressure increases. The various mechanisms also depend strongly on superequilibrium radical mole fractions; these arise from slow recombination reactions, and radicals' levels vary in a manner opposite to the flame temperature. The effect of the flame temperature on the thermal and nitrous oxide mechanisms is much more important, and these contributions to emissions increase with increasing pressure or decreasing χ^0.

The rate of prompt production and several contributions to reburn are determined by mole fractions of fuel-derived radicals, especially CH and CH_2. These also exist in superequilibrium concentrations; as χ^0 increases, so does the fuel-consumption rate and the production rate for these radicals, while their consumption rates are roughly fixed. Despite the many simplifications that were made to predict CH and CH_2 mole fractions, good predictions of these quantities are obtained, allowing good predictions of prompt and reburn. Like radicals of the hydrogen–oxygen system, CH and CH_2 mole fractions are greater for large scalar dissipation rates. Therefore, the prompt production rate increases with increasing χ^0, unlike those of the thermal and nitrous oxide mechanisms. When the production rate is normalized by the fuel-consumption rate, which is proportional to χ^0, to give the emission index, the prompt contribution to the emission index has little dependence on χ^0, peaking at intermediate values and decreasing for small and large values.

For flames with near-normal ambient atmospheres, the prompt mechanism is important for most conditions. Since both the thermal mechanism and reburn become the fastest as χ^0 decreases, they mostly counterbalance each other. When the pressure or temperature of the fuel and oxidizer streams increases, the rates of thermal production and reburn increase faster than the prompt rate (though prompt production does increase with temperature); so these former two mechanisms increase in relative importance. It follows that the prompt contribution will be less important in engine applications than for open burning.

From the present study, it may be observed, in general, that analytical methods employing RRA can help to contribute to understanding of mechanisms of NO_x production in diffusion flames and can provide predictions of emission indices that are within about a factor of two of the true values. In achieving this degree of accuracy, it is necessary to study carefully each individual chemical-kinetic process and to introduce approximations designed to retain sufficient accuracy while providing convenient simplification. Studies of trace species like NO_x typically do not introduce any new zones into RRA flame-structure analyses but do add additional chemical-kinetic processes that need to be analyzed in the various known reaction zones. Significant extents of additional flame-structure

analyses thereby are required. Techniques similar to the methods employed in the present work should be able to be developed for addressing emissions of other pollutants from diffusion flames, such as carbon monoxide, polycyclic aromatics, and soot.

The present study is only the first step in employing these RRA methods for problems of interest in propulsion. Methane has been considered to be the fuel because it is the simplest hydrocarbon example. Future work should now use the approach developed here to address other hydrocarbon fuels of greater practical interest for propulsion. The knowledge developed in the present study enables this extension to be performed. The RRA methods, in general, appear to hold great promise for future calculations of contaminant production in combustion processes.

ACKNOWLEDGMENTS

REFERENCES

1. Linan, A., and F. A. Williams. 1993. *Fundamental aspects of combustion*. New York: Oxford University Press.
2. Williams, F. A. 1992. The role of theory in combustion science. *24th Symposium (International) on Combustion Proceedings*. Pittsburgh, PA: The Combustion Institute. 1–17.
3. Zel'dovich, Ya. B., G. I. Barenblatt, V. B. Librovich, and G. M. Makhviladze. 1980. *The mathematical theory of combustion and explosion*. Moscow: Nauka.
4. Buckmaster, J. D., and G. S. S. Ludford. 1982. *Theory of laminar flames*. Cambridge, UK: Cambridge University Press.
5. Williams, F. A. 1985. *Combustion theory*. 2nd ed. Menlo Park, CA: Benjamin/Cummings Publ. Co.
6. Dixon-Lewis, G. 1967. Computation of structures of premixed flames. *Proc. Royal Society (London)* 298A:495–507.
7. Day, M. J., D. V. Stamp, K. Thompson, and G. Dixon-Lewis. 1971. Inhibition of hydrogen–air and hydrogen–nitrous oxide flames by halogen compounds. *13th Symposium (International) on Combustion Proceedings*. Pittsburgh, PA: The Combustion Institute. 705–21.
8. Dixon-Lewis, G., and R. J. Simpson. 1977. Aspects of flame inhibition by halogen compounds. *16th Symposium (International) on Combustion Proceedings*. Pittsburgh, PA: The Combustion Institute. 1111–19.

9. Warnatz, J. 1978. Calculation of the structure of laminar flat flames. *Berichte Bunsenges Physicalische Chemie* 82:193–200, 643–50, 834–40.

10. Westbrook, C. K. 1980. Inhibition of laminar methane–air and methanol–air flames by hydrogen bromide. *Combustion Science Technology* 23:191–202.

11. Heimerl, J. M., and T. P. Coffee. 1980. The detailed modeling of premixed, laminar steady-state flames. 1. Ozone. *Combustion Flame* 39:301–15.

12. Coffee, T. P., and J. M. Heimerl. 1981. Transport algorithms for premixed, laminar steady-state flames. *Combustion Flame* 43:273–89.

13. Warnatz, J. 1981. Concentration-, pressure-, and temperature-dependence of the flame velocity in hydrogen–oxygen–nitrogen mixtures. *Combustion Science Technology* 26:203–14.

14. Warnatz, J. 1981. The structure of laminar alkane-, alkene-, and acetylene flames. *18th Symposium (International) on Combustion Proceedings*. Pittsburgh, PA: The Combustion Institute. 369–84.

15. Cherian, M. A., P. Rhodes, R. J. Simpson, and G. Dixon-Lewis. 1981. Kinetic modelling of the oxidation of carbon monoxide in flames. *18th Symposium (International) on Combustion Proceedings*. Pittsburgh, PA: The Combustion Institute. 385–96.

16. Westbrook, C. K., and F. L. Dryer. 1981. Chemical kinetics and modeling of combustion processes. *18th Symposium (International) on Combustion Proceedings*. Pittsburgh, PA: The Combustion Institute. 749–67.

17. Oran, E. S., and J. P. Boris. 1987. *Numerical simulation of reacting flows*. New York: Elsevier.

18. Frenklach, M., H. Wang, and J. J. Rabinowitz. 1992. Optimization and analysis of large chemical kinetic mechanisms using the solution mapping method — combustion of methane. *Progress Energy Combustion Science* 18:47–73.

19. Grotheer, H. H., S. Klem, H. S. T. Driver, R. J. Hutcheon, R. D. Lockett, and G. N. Robertson. 1992. Elementary reactions in the methanol oxidation system. *Berichte Bunsenges Physicalische Chemie* 96:1360–75.

20. Baulch, D. L., C. J. Cobos, R. A. Cox, C. Esser, P. Frank, Th. Just, J. A. Kerr, M. J. Pilling, J. Troe, R. W. Walker, and J. Warnatz. 1992. Evaluated kinetic data for combustion modeling. *J. Physical Chemical Reference Data* 21:411–734.

21. Baulch, D. L., C. J. Cobos, R. A. Cox, P. Frank, G. Hayman, Th. Just, J. A. Kerr, T. Murrells, M. J. Pilling, J. Troe, R. W. Walker, and J. Warnatz. 1994. Summary table of evaluated kinetic data for combustion modeling: Supplement 1. *Combustion Flame* 98:59–79.

22. Leung, K. M., and R. P. Linstedt. 1995. Detailed kinetic modeling of C_1–C_3 alkane diffusion flames. *Combustion Flame* 102:129–60.

23. Linstedt, R. P., and L. Q. Maurice. 1995. Detailed kinetic modelling of *n*-heptane combustion. *Combustion Science Technology* 107:317–53.

24. Rogg, B., A. Linan, and F. A. Williams. 1986. Deflagration regimes of laminar flames modeled after the ozone decomposition flame. *Combustion Flame* 65: 79–101.

25. Peters, N., and F. A. Williams. 1987. The asymptotic structure of stoichiometric methane–air flames. *Combustion Flame* 68:185–207.

26. Williams, F. A. 1988. Asymptotic methods for flames with detailed chemistry. In: *Mathematical modeling in combustion science*. Eds. J. D. Buckmaster and T. Takeno. New York: Springer-Verlag. 44–51.

27. Trevino, C., and F. A. Williams. 1988. Asymptotic analysis of the structure and extinction of methane–air diffusion flames. In: *Dynamics of reactive systems. Part I: Flames*. Eds. A. L. Kuhl, J. R. Bowen, J.-C. Leyer, and A. A. Borisov. AIAA progress in astronautics and aeronautics ser. Washington, DC: American Institute of Aeronautics and Astronautics 113:129–65.

28. Rogg, B., and F. A. Williams. 1988. Structures of wet CO flames with full and reduced kinetic mechanisms. *22nd Symposium (International) on Combustion Proceedings*. Pittsburgh, PA: The Combustion Institute. 1441–51.

29. Bui, M., K. Seshadri, and F. A. Williams. 1989. Structure of heptane–air counterflow diffusion flames. *4th Conference (International) on Supercomputing Proceedings*. Eds. L. P. Kartashev and S. I. Kartashev. St. Petersburg, FL: International Supercomputing Institute II:490–95.

30. Chelliah, H. K., and F. A. Williams. 1990. Aspects of the structure and extinction of diffusion flames in methane–oxygen–nitrogen systems. *Combustion Flame* 80: 17–48.

31. Chung, S. H., and F. A. Williams. 1990. Asymptotic structure and extinction of CO/H_2 diffusion flames with reduced kinetic mechanisms. *Combustion Flame* 82:389–410.

32. Gutheil, E., and F. A. Williams. 1991. A numerical and asymptotic investigation of structures of hydrogen–air diffusion flames at pressures and temperatures of high-speed combustion. *23rd Symposium (International) on Combustion Proceedings*. Pittsburgh, PA: The Combustion Institute. 513–21.

33. Smooke, M. D. 1991. *Reduced kinetic mechanisms and asymptotic approximations for methane–air flames*. New York: Springer-Verlag.

34. Bui-Pham, M., K. Seshadri, and F. A. Williams. 1992. The asymptotic structure of premixed methane–air flames with slow CO oxidation. *Combustion Flame* 89: 343–62.

35. Card, J. M., and F. A. Williams. 1992. Asymptotic analysis of the structure and extinction of spherically symmetrical n-heptane diffusion flames. *Combustion Science Technology* 84:91–119.

36. Card, J. M., and F. A. Williams. 1992. Asymptotic analysis with reduced chemistry for the burning of n-heptane droplets. *Combustion Flame* 91:187–99.

37. Linteris, G. T., and F. A. Williams. 1992. Asymptotic and numerical predictions of carbon monoxide–nitrous oxide flame structure. *24th Symposium (Interna-*

tional) on Combustion Proceedings. Pittsburgh, PA: The Combustion Institute. 803–11.

38. Peters, N., and B. Rogg. 1993. *Reduced kinetic mechanisms for applications in combustion systems*. New York: Springer-Verlag.

39. Seshadri, K., N. Peters, and F. A. Williams. 1994. Asymptotic analyses of stoichiometric and lean hydrogen–air flames. *Combustion Flame* 96:407–27.

40. Sanchez, A. L., A. Linan, and F. A. Williams. 1992. A bifurcation analysis of high-temperature ignition of H_2–O_2 diffusion flames. *24th Symposium (International) on Combustion Proceedings*. Pittsburgh, PA: The Combustion Institute. 1529–37.

41. Zhang, B. L., J. M. Card, and F. A. Williams. 1996. Application of rate-ratio asymptotics to the prediction of extinction for methanol droplet combustion. *Combustion Flame* 105:267–90.

42. Williams, F. A. 1996. Use of asymptotic methods for predicting pollutant production in turbulent combustion. In: *Dynamics of exothermicity in honor of Antoni Kazimierz Oppenheim*. Ed. J. R. Bowen. Combustion science and technology ser. Amsterdam: Gordon and Breach 2:75–95.

43. Williams, F. A. 1997. Reduced kinetic schemes in combustion. In: *Propulsion combustion: Fuels to emissions*. Ed. G. D. Roy. Washington, DC: Taylor & Francis. 93–128.

44. Hewson, J. C., and F. A. Williams. 1998. Rate-ratio asymptotic analysis of methane–air diffusion-flame structure for predicting production of oxides of nitrogen. *Combustion Flame* 117:441–76.

45. Hewson, J. C. 1997. Pollutant emissions from nonpremixed hydrocarbon flames. Ph.D. Thesis. University of California at San Diego, La Jolla, CA.

46. Bollig, M., H. Pitsch, J. C. Hewson, and K. Seshadri. 1996. Reduced *n*-heptane mechanism for nonpremixed combustion with emphasis on pollutant relevant intermediate species. *26th Symposium (International) on Combustion Proceedings*. Pittsburgh, PA: The Combustion Institute. 729–37.

47. Hewson, J. C., and M. Bollig. 1996. Reduced mechanisms for NO_x emissions from hydrocarbon diffusion flames. *26th Symposium (International) on Combustion Proceedings*. Pittsburgh, PA: The Combustion Institute. 2171–79.

48. Rightley, M. L., and F. A. Williams. 1997. Structures of CO diffusion flames near extinction. *Combustion Science Technology* 125:181–200.

49. Bai, X. S., and K. Seshadri. 1997. Rate-ratio asymptotic analysis of nonpremixed methane flames. *Combustion Theory Modeling* 3:51–75.

50. Yang, B., and K. Seshadri. 1992. Asymptotic analysis of the structure of nonpremixed methane–air flames using reduced chemistry. *Combustion Science Technology* 88:115–32.

51. Seshadri, K., and N. Ilincic. 1995. The asymptotic structure of nonpremixed methane–air flames with oxidizer leakage of order unity. *Combustion Flame* 101: 69–80.

52. Røkke, N. A., J. E. Hustad, O. K. Sønju, and F. A. Williams. 1992. Scaling of nitric oxide emissions from buoyancy-dominated hydrocarbon turbulent-jet diffusion flames. *24th Symposium (International) on Combustion Proceedings.* Pittsburgh, PA: The Combustion Institute. 385–93.

53. Seshadri, K., and N. Peters. 1988. Asymptotic structure and extinction of methane–air diffusion flames. *Combustion Flame* 73:23–44.

Chapter 26

THE ROLE OF FLAME–WALL THERMAL INTERACTIONS IN FLAME STABILITY AND POLLUTANT EMISSIONS

P. Aghalayam, P. A. Bui, and D. G. Vlachos

Thermal-transport interactions between a flame and a wall are examined using detailed simulations for premixed hydrogen–air mixtures in a stagnation reactor. Numerical bifurcation theory is employed to efficiently obtain multiple solutions and perform parametric studies. Local stability analysis is applied to determine the onset of oscillatory instabilities in distributed flames. At relatively lower temperatures, it is found that oscillations emerge at the edges of flammability limits. While oscillations have a kinetic origin, flame–wall thermal interactions are a prerequisite for self-sustained oscillations at atmospheric pressure. It is also shown that oscillations may exist even at elevated pressures of technological interest to gas turbines. Both regimes for avoiding and methods for suppressing oscillatory instabilities for propulsion systems are discussed. In addition to flame instabilities, a new microcombustor/heat exchanger concept is examined as a possible new combustion method for NO_x reduction. For laminar flows, the thermal coupling with the wall may be weak to extinguish a flame and reduce NO_x in the bulk of the flame. It is shown that straining the flame can increase the heat flux at the wall, prior to extinction, with a concomitant reduction in NO_x. This idea is verified by simulating a high-intensity turbulent combustor.

26.1 INTRODUCTION

Flames interact with the walls of a combustor through various mechanisms, which affects flame stability and pollutant emissions. For example, thermal quenching by cold walls in internal combustion engines can cause an increase of unburned hydrocarbon emissions [1–3], as has been shown by impinging a

combusted mixture on a cold wall. Alternatively, if extinction can be avoided, energy exchange at the wall can decrease flame temperatures resulting in low NO_x emissions. This concept may lead, for some applications, to an alternative homogeneous combustion process (surface assisted) for NO_x reduction at the source. Now the role of surface-stabilized flame–wall thermal interactions, in both reduction of NO_x and flame stability, is not well understood.

Aside from thermal interactions, chemical interactions between flames and surfaces are also important. Chemical interactions are typically manifested either by radical recombination on cold (relatively inert) walls [4, 5] or by heterogeneous combustion on chemically active surfaces (catalysts). Among the available technologies, catalysts have the best potential for NO_x reduction. A review on recent advances in catalytic combustion is given elsewhere [6]. The focus here is on combustion near inert surfaces.

In this paper, the authors present a novel way of studying flame–wall interactions by considering an unreactive mixture impinging on a flat wall (a stagnation microreactor). By changing the hydrodynamic strain rate and/or the composition, one can control the location of the laminar flame with respect to the surface, and, thus, modify the degree of flame–wall thermal interactions. By extracting energy at the back of the surface, one can use an integrated microcombustor/heat exchanger to control surface temperature, flame stability, and pollutant emissions. Results from the stagnation microreactor are compared with a perfectly stirred reactor (PSR) of high turbulent intensity to elucidate the role of transport in emissions.

26.2   MODEL

Two combustor configurations are used. The first is a stagnation laminar flow impinging on a flat wall and the second is a PSR. The governing equations and solution methods have been summarized in previous publications (e.g., [7, 8]). Continuation algorithms are employed to compute multiple solutions and critical points, such as ignitions and extinctions. A new methodology for local stability analysis of premixed and diffusion flames has been recently developed [7], for the first time, and applied to premixed H_2–air mixtures at 1 atm. New results at various pressures will be discussed below. This methodology provides a unique framework, within the numerical bifurcation theory, to map out regions of instabilities of distributed flames. Furthermore, it gives insight into methodologies for suppressing the instabilities. The thermodynamic and transport properties are computed using the CHEMKIN databases [9, 10]. The chemistry used here is the H_2–O_2 subset of the Miller–Bowman mechanism [11], for the first part of the paper on flame stability, and the subset of the GRI 2.11 mechanism, for the second part of the paper on emissions. No substantial difference in results between the two mechanisms was found.

26.3 THE ROLE OF FLAME–WALL THERMAL INTERACTIONS IN OSCILLATORY INSTABILITIES

Stationary Simulations and Local Dynamics
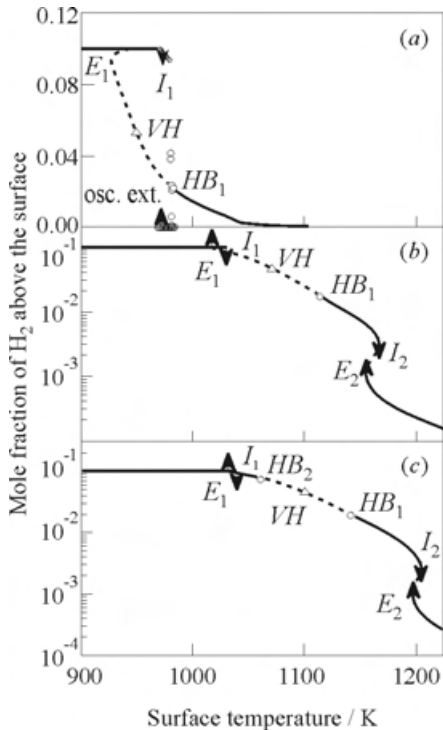
Figure 26.1 The mole fraction of H_2 just above the surface as a function of the surface temperature for 1 (*a*), 3 (*b*), and 4 atm (*c*), respectively. Gas-phase ignitions and extinctions are represented by arrows. The HB and VH points are indicated with circles and triangles, respectively. Stable and unstable branches are represented by solid and dashed curves, respectively. The mixture is 10% H_2–air and the strain rate is 200 s^{-1}

Figure 26.1 shows the mole fraction of H_2 just above the surface vs. the surface temperature for a mixture of 10% H_2 in air at various pressures. At atmospheric pressure (Fig. 26.1*a*), the mole fraction of H_2 is almost insensitive to surface temperature until a turning point, called an ignition (I_1), is reached, where the system jumps from an unreactive state to a reactive one. As the surface temperature decreases from high values, the H_2 mole fraction increases, and a Hopf bifurcation (HB) point is first found at ~ 980 K, outside the multiplicity regime. The solution branch between the HB_1 and the extinction E_1 is locally unstable (dashed curve).

Even though the bifurcation behavior exhibits a *Z*-shaped curve, it is more complicated due to the existence of the HB. For example, upon ignition, the system is expected to oscillate because no locally stable stationary solutions are found (an oscillatory ignition). Time-dependent simulations confirm the existence of self-sustained oscillations [7, 12]. The envelope of the oscillations (amplitude of H_2 mole fraction) is shown in circles (a so-called continuation in periodic orbits).

As the surface temperature decreases slightly below the HB temperature, self-sustained harmonic oscillations of small amplitude appear. The oscillations increase sharply in amplitude, as the surface temperature decreases (see

Fig. 26.1a). At first, multistage ignitions and extinctions occur followed by a relaxation (long period) mode [7]. Oscillations die a few degrees below the ignition temperature at a saddle-loop infinite-period homoclinic orbit bifurcation point. This is an example where both ignition and extinction are oscillatory.

An important outcome of these simulations is the location of HB points (largely ignored in previous work), which is important for the development of extinction theory. In particular, the turning point E_1 lies on a locally unstable stationary solution branch and does not coincide with the actual extinction, as previously thought. The actual extinction point is the termination point of oscillations. Thus, local stability analysis is essential to properly analyze flame stability and develop extinction theory.

The conditions where the temperature gradient at the surface is zero are determined by van't Hoff (VH) points, denoted by triangles in Fig. 26.1. If surface radiation is neglected, VH points correspond to adiabatic operation, i.e., conditions for self-sustained combustion. For each pressure, a second VH point occurs at a higher temperature (not shown for figure clarity).

At a higher pressure of 3 atm (see Fig. 26.1b), the bifurcation behavior is more complex, showing a double Z-shaped curve. The HB point has now shifted to an even higher surface temperature. A new feature at higher pressures is a second set of turning points (I_2 and E_2) that appears at high temperatures. The branch $E_1 I_2$, with concentrations of radicals in intermediate values, is hereafter called a partially ignited branch. The branch at high temperatures, referred to as fully ignited (upon I_2-ignition), is the most vigorous combustion branch. It has been shown that unlike the first ignition and extinction, which are radical-induced [13], the second ignition and extinction are thermally controlled by reaction exothermicity.

The local stability in the neighborhood of the second set of turning points is simply deduced because no new HB point is found: the intermediate branch is locally unstable, whereas the partially ignited branch and fully ignited branch are locally stable. The temperature range for self-sustained oscillations is larger at this higher pressure.

As the pressure increases further, a second HB point (HB_2) appears at the extinction point E_1 and shifts toward the other HB (HB_1) point. An example is shown for 4 atm in Fig. 26.1c. Ignition I_1 is no longer oscillatory, because the stationary partially ignited branch becomes locally stable in the vicinity of I_1. Time-dependent simulations indicate that the two HB points are supercritical, i.e., self-sustained oscillations die and emerge at these points with zero amplitude. In this case, the first extinction E_1 defines again the actual extinction of the system.

To investigate the effect of composition at high pressures, two-parameter bifurcation diagrams are constructed. An example is shown in Fig. 26.2. Cuts at fixed compositions are shown in Fig. 26.1. A nonextinction regime is found on each side of the stoichiometric point, within which the flame cannot be
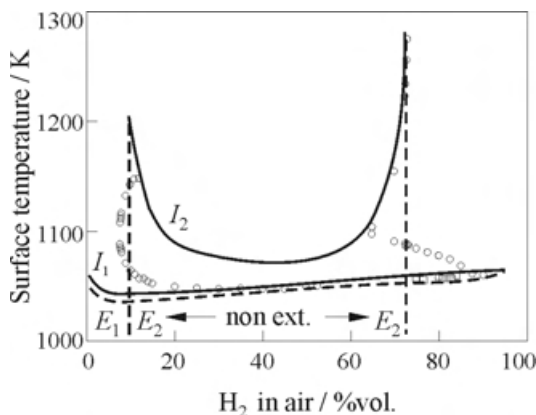
extinguished solely by thermal quenching. In this regime, the fully ignited branch is disconnected from the rest of the solutions (lack of E_2). This unexpected behavior, first predicted a few years ago [14], is caused by the kernel of gas-phase reactions being away from the surface (by a few millimeters), resulting in a weak flame–wall thermal interaction. Besides the advantage of flame robustness, it turns out that this bifurcation feature also has a strong influence on NO_x emissions and energy production.

As the inlet composition changes, HB points emerge from the first extinction E_1 (a so-called Tokens–Bogdanov point) at $\sim 50\%$ and $\sim 90\%$ H_2 in air.

Figure 26.2 Ignitions (solid curves), extinctions (dashed curves), HB (open circles), and HB temperatures with the heat of all reactions set to zero (open squares) as functions of inlet H_2 concentration in air at 4 atm. The strain rate is 200 s^{-1}

They then shift away from the multiplicity regime and turn back to themselves giving rise to two HBs for some compositions, as shown in Fig. 26.2. HBs finally die at the second ignition I_2 near the edges of the nonextinction regime. It is clear from this diagram that self-sustained oscillations exist for fuel-lean and fuel-rich mixtures when the HB points are outside the multiplicity regime (near $\sim 10\%$ and $\sim 80\%$ H_2 in air). It appears that the emergence of the second ignition I_2 leads to a nonextinction regime, due to high-reaction exothermicity, and destroys oscillatory instabilities.

Several mechanisms have been previously proposed for oscillations. Due to the fact that oscillations exist for Lewis numbers both less and greater than 1, it seems that the thermodiffusive mechanism alone cannot explain these oscillations. To study the role of the heat of reaction, a numerical experiment is performed by switching off the heat of the gas-phase reactions (squares in Fig. 26.2). HBs are found between $\sim 75\%$ and $\sim 85\%$ H_2 in air, but the HBs lie within the multiplicity regime $I_1 E_1$ in Fig. 26.2 and oscillations are not stable.

To explain the role of transport, simulations have been also performed in an isothermal PSR. Oscillatory instabilities were again found [8]. These facts indicate that oscillations are radical induced. However, without the heat of reactions, no self-sustained oscillations are found for these conditions. The heat of reactions is a prerequisite at these conditions to pull the HB point outside the multiplic-
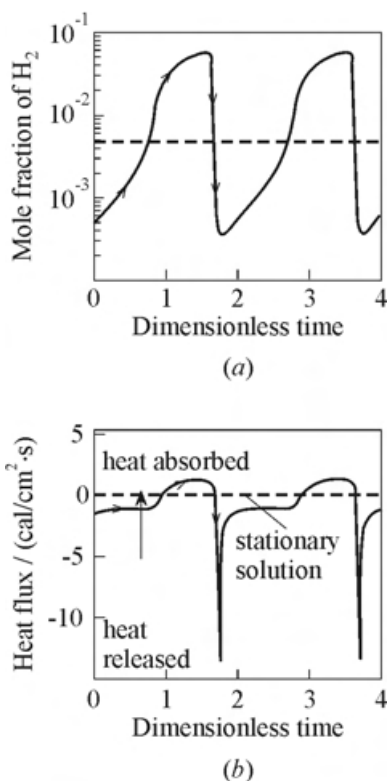
Figure 26.3 The mole fraction of H_2 just above the surface (a) and the wall heat flux (b) as functions of the dimensionless time, $2\alpha t$, for 10% H_2–air mixture at a surface temperature of 1100 K. Self-sustained oscillations and stationary solutions are represented by solid and dashed curves, respectively. The pressure is 4 atm and the strain is $\alpha = 200$ s^{-1}

ity regime and induce self-sustained oscillations (a thermoradical mechanism). For highly exothermic flames, i.e., in the nonextinction regime, the flame–wall thermal interaction is weak, and no oscillations occur. Similar behavior was observed at 1 atm as well [7]. The nonextinction regime defines then, for every pressure, a regime within which oscillations can be avoided.

Time-Dependent Simulations and Global Dynamics

The above simulations were performed at stationary conditions. However, it is important to examine time-dependent situations to characterize global dynamics far from stationary attractors.

As an example of self-sustained oscillations, a 10% H_2–air mixture at a surface temperature of 1100 K is chosen at 4 atm. This surface temperature is lower than the VH point and lies in between the two HB points shown in Fig. 26.1c. Oscillations occur across the entire flame, as shown in computer outputs and animations. Due to paper limitations, here the time-dependent behavior just above the surface is only shown. In particular, Fig. 26.3 shows the mole fraction of H_2 just above the surface (Fig. 26.3a) and the wall heat flux (Fig. 26.3b) vs. the dimensionless time. The self-sustained oscillations are periodic and surround the unstable stationary solution (dashed line). Even though the stationary solution requires power input (albeit a small one), during a period of self-sustained oscillations, a high-power output occurs upon ignition. It is interesting to notice that although energy can be gained, on the average, during a cycle of self-sustained oscillations, a process is not possible for the corresponding stationary solution. This is an example

where periodic operation is superior over the stationary one, regarding flame sustainability.

During the time interval in which the system requires power the maximum temperature is at the wall, and radicals are built up. The system ignites, due to chemical autocatalysis (I_1-ignition), when the concentrations of radicals are sufficiently high. The heat liberated during ignition rapidly pushes the flame away from the surface due to thermal expansion. Conductive heat loss at the wall forces the flame slowly to drift back toward the surface where it finally extinguishes. This cycle is continuously repeated in every period of oscillations. When the composition is within the nonextinction regime, the heat released upon I_1-ignition is so high that it pushes the flame a few millimeters away from the wall. As a result, the flame–wall thermal interaction is weak (a low-heat transfer coefficient) and not sufficient to cause either flame extinction or pulsation.

26.4   THE ROLE OF FLAME–WALL THERMAL INTERACTIONS IN NO$_x$

After the bifurcation behavior is examined, the role of flame–wall thermal interactions in NO$_x$ is studied. First, adiabatic operation is considered. Next, the roles of wall quenching and heat exchange in emissions are discussed. Two parameters are studied: the inlet fuel composition and the hydrodynamic strain rate. Results for the stagnation microreactor are contrasted with the PSR to understand the difference between laminar and turbulent flows.

Emissions at Adiabatic Operation

The adiabatic surface temperature (for stagnation flow) and the adiabatic PSR temperature are shown in Fig. 26.4a as a function of the inlet fuel composition. The residence time in the PSR is simply taken as the inverse of the hydrodynamic strain rate. In both cases, the adiabatic temperature exhibits a maximum near the stoichiometric composition. The limits of the adiabatic operation are $\sim 8\%$ and $\sim 70\%$ inlet H$_2$ in air for the stagnation reactor. For a PSR, the corresponding limits are $\sim 12\%$ and $\sim 77\%$ inlet H$_2$ in air. Beyond these compositions, the heat generated from the chemical reactions is not sufficient to sustain combustion.

Figure 26.4a also shows the mole fraction of the fuel just above the stagnation surface and in the PSR vs. the inlet mole fraction of fuel. On the fuel-lean side, there is a minimum in the fuel mole fraction for both reactors considered. As the
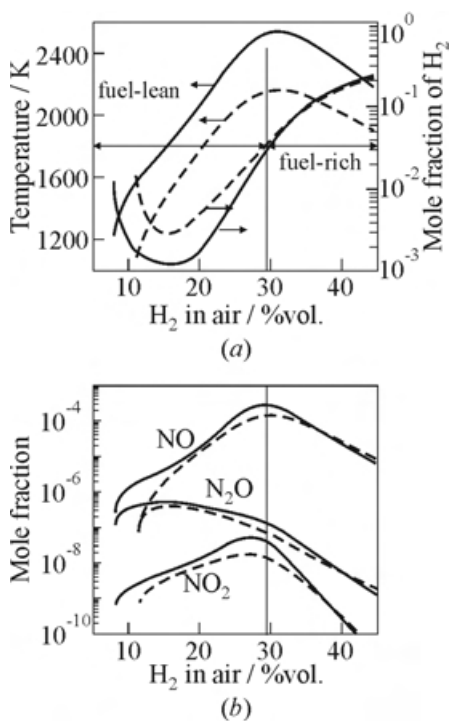
Figure 26.4 Surface temperature and surface fuel mole fraction (*a*), and NO$_x$ (*b*) as functions of inlet composition, along the adiabatic curve, for the stagnation reactor (solid curves) and the PSR (dashed curves). The fuel-lean and fuel-rich regions are indicated. The conditions are pressure of 1 atm, inlet temperature of 25 °C, a strain rate of 1000 s^{-1} (stagnation reactor), and a residence time of 1 ms (PSR)

inlet composition decreases, less fuel is fed. On the other hand, the adiabatic temperature decreases resulting in a drop of reactivity. At sufficiently fuel-lean conditions, the reactivity effect dominates and fuel emissions increase. The qualitatively similar behavior between the two reactors indicates that chemistry, rather than details of the transport, determines the shape of fuel emissions as a function of inlet composition.

Figure 26.4*b* shows the corresponding NO$_x$ species vs. the inlet fuel concentration. As the inlet fuel concentration increases, the NO and NO$_2$ emissions increase up to the stoichiometric point. Reaction path analysis shows that the activated reactions of the thermal NO$_x$ mechanism dominate the formation of NO, and NO$_2$ is produced from NO.

Based on conventional thinking, lower temperatures should result in a decrease of thermally produced NO$_x$. However, despite the substantially lower temperatures in the PSR, as shown in Fig. 26.4*a*, the NO$_x$ mole fractions do not significantly differ between the two reactors, except for very fuel-lean mixtures, near extinction of self-sustained flames. Similar behavior was recently observed when radiation from the surface was included [15]. A significant reduction in surface temperature was then observed, whereas NO$_x$ remained relatively unaffected. This unexpected behavior is discussed below.

The Role of Thermal Quenching in Emissions

The temperature of the surface can be systematically lowered by continuation techniques at a fixed composition (vertical cuts in Fig. 26.4). Experimentally,

the surface temperature can be controlled by using the back of the stagnation surface as a heat exchanger. Reduction in surface temperature can result in low thermal NO_x (surface-assisted homogeneous combustion). However, extinction (if one exists) sets a lower temperature of operation. A significant difference between the two reactors is that the stagnation microreactor can exhibit a nonextinction regime, as shown in Fig. 26.2. In contrast, since the temperature in a PSR is uniform, mixtures of all compositions extinguish at sufficiently low temperatures [8]. This difference in bifurcation behavior, caused by turbulence, has a strong influence on the role of thermal quenching in NO_x emissions.

Figure 26.5a shows an example of the fuel and NO_x mole fractions as a function of the surface (stagnation) or PSR temperature, for 28% inlet H_2 in air (a nonextinguishable mixture in the stagnation reactor for these conditions). The maximum temperature displayed in Fig. 26.5 indicates adiabatic operation shown in Fig. 26.4. As the temperature decreases, the fuel and NO_x mole fractions are relatively unaffected in the stagnation reactor. In contrast, in a PSR, there is a gradual drop in all NO_x species with decreasing temperature, especially around 950 K, where the system extinguishes. Furthermore, there is a significant increase in NO_2 mole fraction at surface temperatures below 500 K in the stagnation reactor. Reaction path analysis [15] indicates that the increase in NO_2 at low temperatures is caused by the enhanced levels of HO_2, which preferentially reacts with NO according to $NO + HO_2 = NO_2 + OH$. Strongly exothermic mixtures, such as the 28% H_2 in air, which lie within the nonextinction regime, burn a few millimeters away from the surface. As a result, the thermal coupling between the gas-phase and the surface is weak. Consequently, thermal quenching at the wall (due to radiation or heat exchange) does not have a significant influence on NO emissions in distributed flames, when the bulk of the chemistry (reaction zone) occurs away from the surface. In other words, the boundary layer near the surface serves as a postcombustion zone for such flames.

The PSR is a lumped parameter system, where the temperature is uniform over the entire reactor. As a result, the fuel and NO_x emissions are strongly temperature dependent. As extinction is approached in the PSR, the radical mole fractions decrease sharply, and so do the NO_x species. Thus, turbulent mixing in a PSR is responsible for the high sensitivity of NO_x to temperature.

Figure 26.5b is the corresponding plot for 12% inlet H_2 in air. In this case, there is an extinction at about 1000 K for both reactors. The qualitative features are similar to that of the PSR discussed above for 28% H_2 in air. For such fuel-lean mixtures, the flame is attached to the surface. As a result, the thermal coupling between the surface and the gas phase is strong, and reduction in surface temperature affects the entire thermal boundary layer resulting in significant reduction of NO_x. These results indicate that the bifurcation behavior, in terms of extinction, determines the role of flame–wall thermal interactions in emissions.
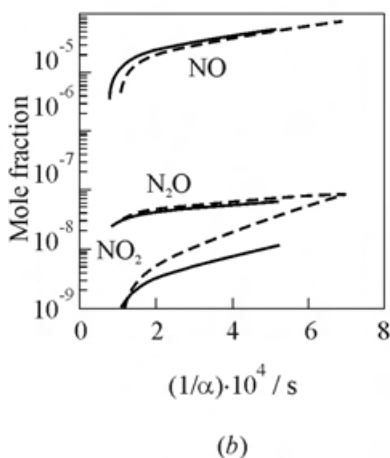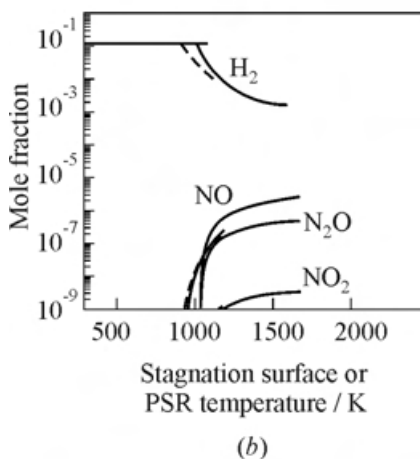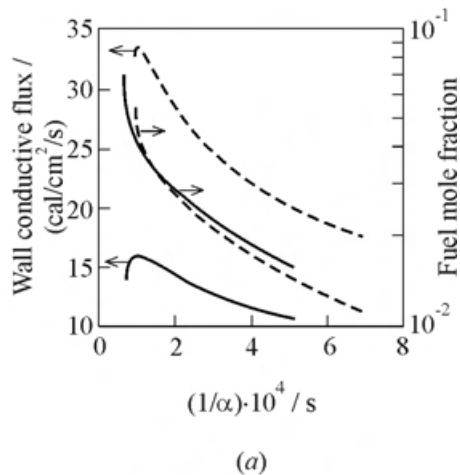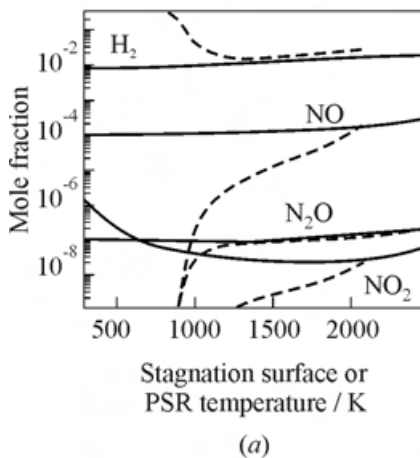
Figure 26.5 Surface mole fractions of fuel and NO$_x$ as functions of stagnation surface (solid curves) and PSR temperature (dashed curves), for 28% inlet H$_2$ in air (*a*) and 12% inlet H$_2$ in air (*b*). The maximum temperature indicates adiabatic operation. The conditions are the same as in Fig. 26.4

Figure 26.6 Wall conductive flux and surface fuel mole fraction (*a*) and NO$_x$ near the surface (*b*) vs. the inverse of the strain rate for a stagnation reactor with the surface at temperatures of 500 K (dashed curves) and 1000 K (solid curves). The conditions of pressure and inlet temperature are the same as in Fig. 26.4

It is expected that as one increases the heat transfer coefficient in a stagnation reactor for nonextinguishable mixtures through straining, one could approach the PSR behavior regarding the role of thermal quenching in NO_x emissions.

The Role of Strain Rate in Emissions and Wall Heat Flux

It is expected that as the strain rate increases, the overall coupling between the surface and the gas-phase increases, since the flame is pushed toward the surface. Figure 26.6a shows the wall heat flux that can be extracted from the system, and the fuel mole fraction near the surface vs. the inverse of the strain rate for 28% inlet H_2 in air, at two surface temperatures. The end points of the curves in Fig. 26.6, at high-strain rates, are the extinction points. The conductive heat flux exhibits a maximum as the strain rate increases from low values, which is at first counterintuitive. In addition, with increasing strain rate the fuel mole fraction increases monotonically, while the mole fractions of NO_x decrease, as seen in Fig. 26.6b. The species mole fractions show sharper changes with strain rate near extinction, as the mole fractions of radicals decrease sharply near extinction.

Figure 26.6 shows that the extractable heat is higher at lower surface temperatures. While the mole fraction of NO is lower at lower surface temperatures, the NO_2 and N_2O mole fractions are higher. The increased levels of NO_2 at low temperatures are due to an increase in HO_2 as mentioned above. Overall, the concentrations of NO_2 and N_2O are significantly lower than that of NO.

Figure 26.7 shows profiles of temperature and fuel mole fraction at three strain rates, at two surface temperatures, for 28% inlet H_2 in air. Figure 26.8 shows the corresponding NO_x mole fraction profiles. At low-strain rates, the maximum temperature in the flame is approximately the same at both surface temperatures, indicating that, for these nonextinguishable mixtures, the reduction in surface temperature does not significantly affect overall reactivity and NO_x emissions. The reactor can be thought of as partitioned into three sections: a preheating zone, a combustion zone where fast chemistry happens, and a postcombustion zone with minimal influence on flame stability and emissions.

As the strain rate increases, the flame approaches the surface, the thermal boundary layer shrinks, and the maximum temperature decreases. Consequently, larger gradients develop near the surface resulting in a higher wall heat flux. Upon further straining, the reactivity decreases due to a low residence time, leading eventually to extinction as shown in Fig. 26.6. At high-strain rates, the flame–wall thermal coupling is stronger, and reduction in surface temperature propagates throughout the entire length of the reactor. As a result, thermal quenching significantly reduces NO_x emissions. It appears then that turbulence
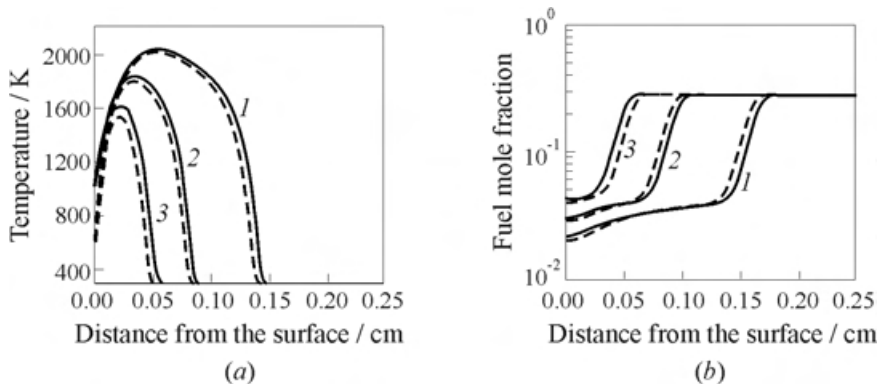
Figure 26.7 Profiles of temperature (a) and fuel (b) for surface temperatures of 500 K (dashed curves) and 1000 K (solid curves) for a 28% inlet H_2–air mixture. The conditions of pressure and inlet temperature are the same as in Fig. 26.4. 1 — $\alpha = 3000 \text{ s}^{-1}$; 2 — 5000; and 3 — 8000 s^{-1}
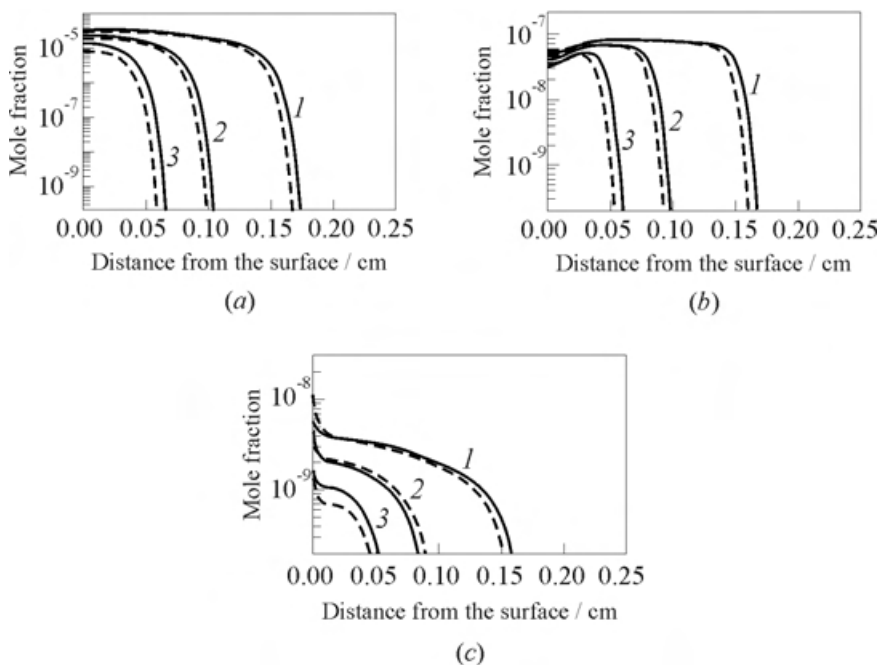
Figure 26.8 Profiles of NO (a), N_2O (b), and NO_2 (c), corresponding to Fig. 26.7: 1 — $\alpha = 3000 \text{ s}^{-1}$; 2 — 5000; and 3 — 8000 s^{-1}

can be used to control the surface temperature and NO_x emissions in surface-stabilized flames.

26.5   CONCLUDING REMARKS

The interactions between premixed hydrogen–air flames and a wall have been studied using numerical bifurcation techniques. Oscillatory instabilities have been found for the first time. Even though oscillations have a kinetic origin, the thermal coupling with the wall is important in making oscillatory instabilities stable at atmospheric pressure. It was also found that such instabilities persist up to high pressures of interest to gas turbines. However, one can avoid oscillations by systematically controlling either the mixture composition or the wall heat losses. In addition, it has been shown that the flame–wall thermal coupling becomes stronger at higher strain rates. As a result, more heat can be extracted at higher stain rates (prior to but not very near extinction) with a concomitant reduction in flame temperatures and NO_x emissions. It appears then that turbulence is desirable to increase the heat transfer coefficient between a solid (e.g., walls, particles, etc.) and a flame in integrated microreactor/heat exchangers, in order to reduce NO_x at the source. Extension of these studies to catalytic surfaces, as another means of controlling NO_x emissions at the source, is highly desirable.

ACKNOWLEDGMENTS

REFERENCES

1. Daniel, W. A. 1956. Flame quenching at the walls of an internal combustion engine. *6th Symposium (International) on Combustion Proceedings*. Pittsburgh, PA: The Combustion Institute. 886–94.
2. Westbrook, C. K., A. A. Adamczyk, and G. A. Lavoie. 1981. A numerical study of laminar flame wall quenching. *Combustion Flame* 40:81–99.
3. Poinsot, T. J., D. C. Haworth, and G. Bruneaux. 1993. Direct simulation and modeling of flame–wall interaction for premixed turbulent combustion. *Combustion Flame* 95:118–32.

4. Aghalayam, P., P.-A. Bui, and D. G. Vlachos. 1998. The role of radical wall quenching in flame stability and wall heat flux: Hydrogen/air mixtures. *Combustion Theory Modeling* 2:515–30.

5. Aghalayam, P., and D. G. Vlachos. 1998. The roles of thermal and chemical quenching in NO_x and fuel emissions: Combustion of surface-stabilized hydrogen/air mixtures. *AIChE J.* 44(9):2025–34.

6. Vlachos, D. G., and Y. K. Park. 2001 (in press). Recent advances in catalytic combustion over transition metals. *Catalysis Reviews — Science Engineering*.

7. Bui, P.-A., D. G. Vlachos, and P. R. Westmoreland. 1999. On the local stability of multiple solutions and oscillatory dynamics of spatially distributed flames. *Combustion Flame* 117:307–22.

8. Kalamatianos, S., and D. G. Vlachos. 1995. Bifurcation behavior of premixed hydrogen/air mixtures in a continuous stirred tank reactor. *Combustion Science Technology* 109(1–6):347–71.

9. Kee, R. J., P. M. Rupley, and J. A. Miller. 1991. The CHEMKIN thermodynamic data base. Sandia National Laboratories Report, SAND87-8215B.

10. Kee, R. J., P. M. Rupley, and J. A. Miller. 1991. Chemkin-II: A FORTRAN chemical kinetics package for the analysis of gas-phase chemical kinetics. Livermore, CA: Sandia National Laboratories Report, SAND89-8009.

11. Miller, J. A., and C. T. Bowman. 1989. Mechanism and modeling of nitrogen chemistry in combustion. *Progress Energy Combustion Science* 15:287–338.

12. Bui, P.-A., D. G. Vlachos, and P. R. Westmoreland. 1997. Self-sustained oscillations in distributed flames modeled with detailed chemistry. *Eastern States Section, Chemical and Physical Processes in Combustion Proceedings*. Pittsburgh, PA: The Combustion Institute. 337–40.

13. Vlachos, D. G. 1995. The interplay of transport, kinetics, and thermal interactions in the stability of premixed hydrogen/air flames near surfaces. *Combustion Flame* 103(1–2):59–75.

14. Vlachos, D. G., L. D. Schmidt, and R. Aris. 1993. Ignition and extinction of flames near surfaces: Combustion of H_2 in air. *Combustion Flame* 95:313–35.

15. Aghalayam, P., and D. G. Vlachos. 1998. NO_x and fuel emissions in combustion of hydrogen/air mixtures near inert surfaces. *27th Symposium (International) on Combustion Proceedings*. Pittsburgh, PA: The Combustion Institute.

STRUCTURE AND NO$_x$ EMISSION PROPERTIES OF PARTIALLY PREMIXED FLAMES

J. P. Gore

Injecting a fuel-rich mixture into an oxidizer stream forms partially premixed flames. Experimental studies of laminar and turbulent partially premixed flames have shown that minimum levels of NO emission indices are obtained at an optimum level of partial premixing. Experimental and computational studies of moderate stretch rate, opposed-flow, partially premixed flames have been conducted to improve our understanding of the observed NO behavior. Measurements of major gas species and NO concentrations are used first to gain confidence in the mechanism. Then the computations are used to delineate the NO chemistry. Predictions of NO emission indices and integrated rates of N$_2$ fixing reactions for a range of partial premixing are used to delineate the reasons for the NO behavior. The results show that the minimum NO emissions at an optimum level of partial premixing result from a decrease in the prompt initiation reaction resulting from decrease in CH radical concentrations. Near the optimum equivalence ratio, the increase in thermal NO caused by the increases in oxygen concentrations and temperatures is not sufficient to offset the decrease in the prompt contribution.

27.1   INTRODUCTION

Partially premixed flames are formed when a rich mixture of fuel and oxidizer is injected into an oxidizer stream. Below a certain value of the equivalence ratio of the rich mixture, a flame structure involving a premixed flame in the vicinity of a diffusion flame exists. Several experimental studies of NO emission properties of partially premixed laminar [1–4] and turbulent [5–10] flames have been reported in the literature. The results from the most recent studies indicate that using an optimum level of partial premixing can reduce NO emissions.

Computational studies of partially premixed flames have also been reported [11–16]. Authors have tried to explain the variation of NO emission indices with the level of partial premixing using one or more of the following: residence time, flame stretch, radiation heat loss, and chemical mechanism-based arguments. However, a complete explanation of the NO emission has not been offered in the literature.

In the following, the previous work is reviewed. Then the present experiments and computations are discussed. The data are compared with the predictions next. This is followed by a discussion of the computational results for NO and the mechanism of minimization of NO emissions with partial premixing. The paper ends by mentioning the benefits of partial premixing for elimination of smoke, which require further work.

27.2   BACKGROUND

Gore [1] reported, for the first time, that an optimum level of partial premixing results in minimum NO emissions for laminar methane–air flames. This discovery was based on measurements of NO emission indices for seven (7) flames with burner tube equivalence ratios (Φ_B) ranging from 1.6 to infinity. Subsequently, Gore and Zhan [2] confirmed this result based on measurements for seventeen (17) flames. The minimum in NO emission index was observed for $\Phi_B = 2$. Kim et al. [3] found that NO emission index reached a minimum for $\Phi_B = 2.2$ for ethane–air flames. It increased to a maximum at $\Phi_B = 1.3$ and decreased again with decreasing Φ_B. Gore and Zhan [2] attributed the increase in NO at higher values of Φ_B to the increase in prompt-NO production and the increase in NO at lower values of Φ_B to the increase in thermal NO. Kim et al. [3] stated that the maximum at $\Phi_B = 1.3$ resulted from the peak in prompt reaction rate for this equivalence ratio and concluded that the minimum at $\Phi_B = 2.2$ resulted from a competition between the prompt and the thermal mechanisms.

Driscoll et al. [5] studied NO emission properties of turbulent partially premixed hydrogen–air and methane–air flames. The emission results for hydrogen–air flames showed that the emission index decreased monotonically with increasing levels of partial premixing because of the reduction in residence time caused by increasing jet velocity. The results for the methane–air flames were more complicated.

Turns et al. [6] studied turbulent partially premixed flames burning methane, propane, and ethylene with air. The NO emission indices for methane and propane flames first increased and then decreased with increased levels of partial premixing. The NO emission indices for ethylene flames continuously increased at least in the limited range of partial premixing considered in the experiments. The results were qualitatively explained by the opposing effects of flame radiation and residence time on NO emissions.

Røkke *et al.* [7] studied turbulent partially premixed propane–air flames for a variety of jet exit diameters and velocities. The NO emission indices increased continuously with increase in partial premixing. The authors explained this result by stating that increased levels of partial premixing broaden the fuel consumption zone causing an increase in the prompt-NO production.

Gore *et al.* [8] reported, for the first time, the existence of an optimum level of partial premixing for minimum NO emissions from turbulent jet flames. The optimum equivalence ratio (Φ_B) for a minimum emission index was found to be 1.5, which is less than that found for the laminar flames discussed above. Lyle *et al.* [15] confirmed the existence of an optimum level of partial premixing for both confined and unconfined turbulent flames. Lyle *et al.* [15] established that changes in thermal NO production do not control the emission behavior of partially premixed turbulent flames. More recently, Kemal *et al.* [10] have shown that a minimum in NO emissions can also be obtained for sudden dump-stabilized turbulent partially premixed flames.

Because of multiple complexities, experimental efforts to gain insight into the NO behavior with partial premixing are very challenging. Detailed numerical simulations can help to find the basic reasons for the NO emission behavior. Williams and coworkers [11, 12] predicted a nonmonotonic behavior of emission index as a function of fuel stream equivalence ratio, qualitatively in agreement with earlier experimental observations. However, quantitatively the two chemical mechanisms used in [11] and [12] yielded significantly different values of emission indices. Takeno and coworkers [13] have studied the details of NO chemistry for diffusion, partially premixed, and premixed flames. These authors discovered the "reverse prompt" mechanism that was considered to be a possible reason for the NO emission behavior reported by Gore and Zhan [2]. Takeno and coworkers [13] have not discussed the existence of an optimum level of partial premixing for minimum NO emissions based on their simulations.

Blevins and Gore [14, 15] found that low-stretch-rate partially premixed flames involve multiple peaks in the profiles of intermediate hydrocarbon species. In particular, the CH species existing between the premixed and the diffusion flame part of the partially premixed flames were observed to react with NO and create an intermediate NO consumption zone. DuPont *et al.* [16] for low-stretch-rate flames also found the double peaks of intermediate hydrocarbon species and the NO consumption zone. However, Tanoff *et al.* [17] used the CH peak to characterize the location of the rich premixed flame and the OH peak to characterize the location of the diffusion flame. The NO concentration profiles showed that the peak NO mole fractions first increased and then decreased with increasing levels of partial premixing. However, the emission index of NO was not reported.

Blevins and Gore [9] found that, for the low-stretch-rate flames, the NO emission index increased from the diffusion flame value up to $\Phi_B = 2.5$ in contrast to the experimental data. However, the NO emission index decreased at lower Φ_B and reached a minimum at $\Phi_B = 1.6$. Based on this background, the

objects of the present work were to obtain measurements of major species and NO concentrations in one-dimensional diffusion and partially premixed flames in order to evaluate the predictions of a popular chemical kinetics package. The computations are then used to gain further insight into the NO emission behavior with various degrees of partial premixing. Numerical experiments for additional flames help in this process.

27.3 EXPERIMENTAL METHODS

The geometry of the present opposed-flow burner is identical to the one designed by Puri and coworkers (see [18] for example). The burner consists of two opposing ducts with 20-millimeter diameter separated by 15 mm. The exhaust is extracted by a vacuum pump though a water-cooled annulus mounted around the bottom duct and a guard co-flow of nitrogen is issued from an annulus around the top duct. Experiments were performed with methane (99% purity) and premixed air introduced from the bottom duct and air admitted from the top duct. The flow rates were monitored using choked orifice meters.

The operating conditions for the three flames studied experimentally are shown in Table 27.1. All three flames appeared blue for the present operating conditions. The fuel velocity was maintained at 70 cm/s and the air velocity was varied. The changes in air velocity were used to generate a temperature profile for the three flames that had a width between 90% temperature drop on either side of the peak to be identical. This procedure matches the overall gradient in temperature on two sides of the peak. The present conclusions are not affected by this choice. Measurements of stable species mole fractions were obtained using sampling and gas chromatography. The sampling technique involved a quartz microprobe with a 500-micron outer diameter conical tip and an 80-micron orifice for the major species concentration measurements and a 110-micron orifice for the NO concentration measurements. The conical tip expanded to a 2.97-millimeter outer diameter tube over a 10 mm distance. An evacuated bulb was connected to the sampling probe and samples were collected and analyzed

Table 27.1 A summary of operating conditions

Flame	Air velocity cm/s	Fuel velocity cm/s	Fuel temperature K	Air temperature K
Diffusion	70	70	320	560
$\Phi_B = 2.20$	60	70	320	560
$\Phi_B = 1.42$	50	70	320	560

using a gas chromatograph and a calibrated thermal conductivity detector. The sampling probe is choked during the collection of the sample in this method. The details of this procedure are given in [19].

The NO concentration measurements were made using a chemiluminescence analyzer calibrated with 89 ppm standard mixture of NO in N_2. A choked flow orifice controls the sample flow rate through the analyzer and therefore the probe is not choked during sampling for NO measurements. The pressure drop across the analyzer is approximately 80 kPa and the exit of the analyzer is operated at 10 kPa absolute pressure.

Problems with sampling measurements of NO have been discussed extensively in the literature. However, recent measurements by Nguyen *et al.* [20] show that measurements of NO using quartz probes are in agreement with laser-induced fluorescence data.

27.4 COMPUTATIONAL METHODS AND NUMERICAL EXPERIMENTS

A detailed derivation of the conservation equations is given by Kee *et al.* [21]. The OPPDIF code described by Lutz *et al.* [22] was used to obtain solutions of these. Variable specific heat, thermal conductivity, and mass diffusion velocities for the different species were considered using the CHEMKIN library [23]. The source terms in species and energy equations were calculated using GRIMECH 2.11 [24], which includes 49 gas-phase species up to C_2 hydrocarbons and species involved in NO chemistry. The convergence and tolerance criteria, which ultimately control the grid spacing and the number of iterations, for the numerical solutions were set to the default values in [22] and to two times as strict as the default values and the answers were found to be within 5%.

The predictions for the three flames considered in the experiments were compared with measurements. In addition, a series of flames were considered in numerical experiments designed to delineate the reasons for the unique NO emission behavior.

27.5 RESULTS AND DISCUSSION

27.5.1 Comparison with Experimental Data

Figure 27.1 shows measurements and predictions of major species mole fractions for the three flames. The agreement between the experimental data and the
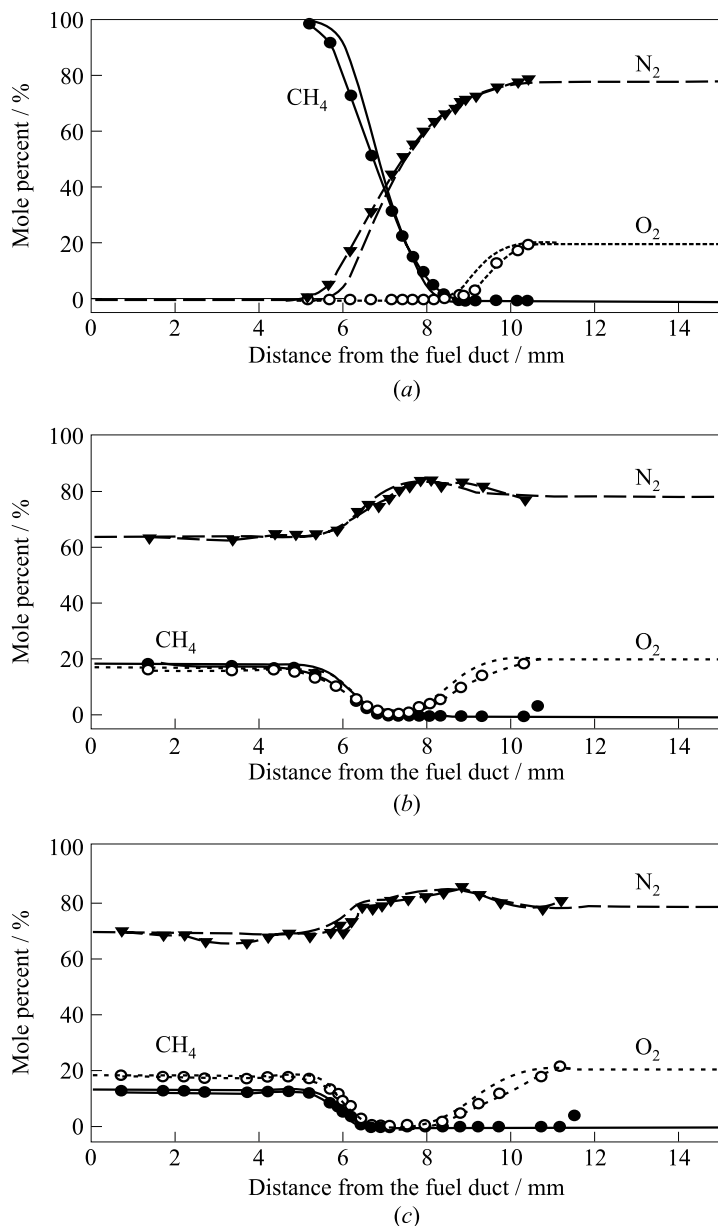
Figure 27.1 Measurements and predictions of mole fractions of CH_4, O_2, and N_2 as a function of distance from the fuel duct for diffusion (a) and partially premixed opposed flow flames with $\Phi_B = 2.2$ (b) and 1.42 (c), $T_{air} = 560$ K and $T_{fuel} = 321$ K, $V_{air} = 70$, 60, and 50 cm/s, $V_{fuel} = 70$ cm/s, distance between ducts 1.5 cm

predictions is excellent. For the two partially premixed flames, the mole fraction of O_2 in the fuel stream is equal to or greater than that of CH_4. The broad valley in the O_2 profiles for the partially premixed flames is indicative of the flame structure. The model captures the nonmonotonic variation of N_2 extremely well.

Figure 27.2 shows measurements and predictions of CO_2 and CO mole fractions. The sharp peaks in the mole fraction profiles of these species cause gradient-broadening errors near the flame sheet. The measurements also show the effects of broadening of the profiles caused by finite spatial resolution of the probe. However, overall the comparison between measurements and predictions is as good as any reported in the literature or better.

Figure 27.3 shows a comparison of measurements and predictions of NO mole fractions. As seen in Fig. 27.3a, the mole fractions of NO on the fuel-rich side of diffusion flame are underestimated by the analysis. Closer examination suggests that a serious overestimate of the rates of the NO recycle route in GRIMECH 2.11 causes these errors. As the level of partial premixing is increased, the recycle reactions become less important and the measurements and predictions of NO agree extremely well. The measured and computed peak values of NO decrease from over 100 ppm to approximately 60 ppm with increasing partial premixing. However, the width of the NO profile becomes broader and the fuel consumption rate changes with increasing level of partial premixing as well. Therefore, NO emission index behavior must be considered with the help of the numerical experiment.

27.5.2 Numerical Experiments

One diffusion flame and fifteen partially premixed flames were considered in the numerical experiment. Each flame had equal fuel and air stream velocities of 70 cm/s. Figure 27.4 shows the predicted emission index of NO plotted as a function of equivalence ratio. The experimentally observed minimum in NO emissions for an optimum level of partial premixing is seen. Between $\Phi_B = 2$ and $\Phi = 100$, the emission index of NO (EINO) increases slightly. Part of this increase is caused by the decrease in the fuel consumption rate with a broadening of the reaction zone caused by partial premixing. The changes in the CH_4 consumption rate are illustrated in the bottom panel. The wider NO production profiles also contribute to the higher integrated production rate. The observed optimum equivalence ratio is around 1.4, which is much lower than the experimental data. Part of the discrepancies is caused by the overestimate of the recycling route particularly for the diffusion flames. However, with this caveat, the fact that the model has captured the qualitative effect of partial premixing is remarkable.
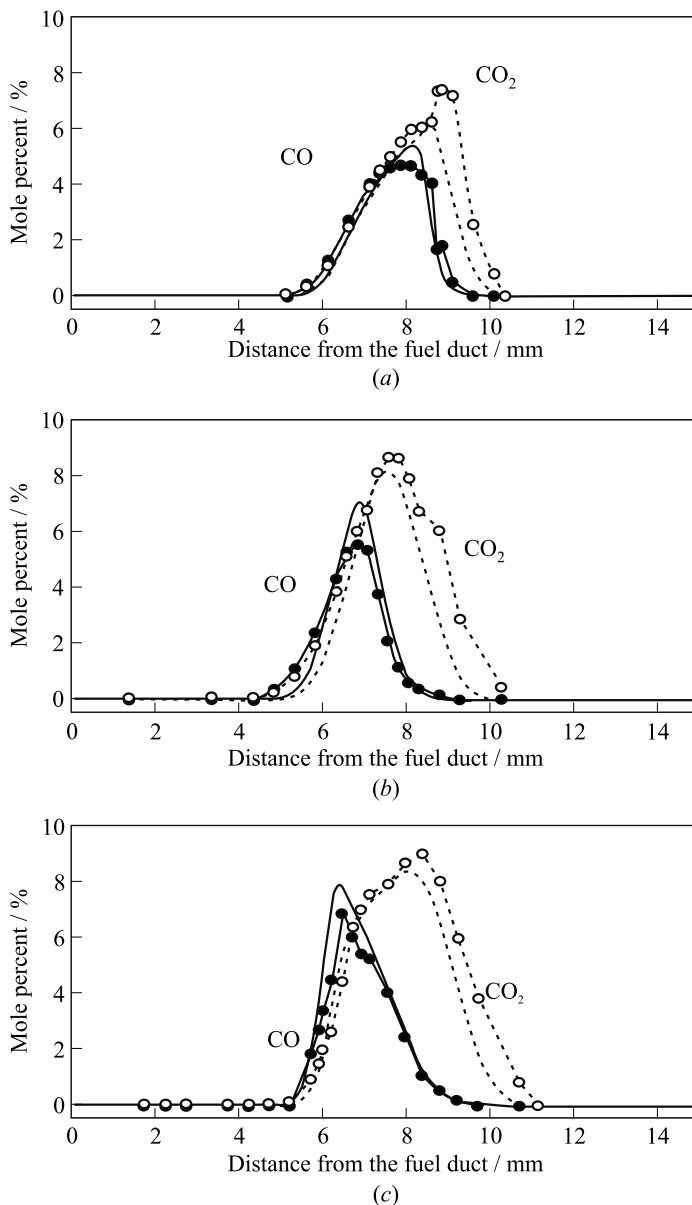
Figure 27.2 Measurements and predictions of mole fractions of CO_2 and CO as a function of distance from the fuel duct for diffusion (a) and partially premixed opposed flow flames with $\Phi_B = 2.2$ (b) and 1.42 (c), $T_{air} = 560$ K and $T_{fuel} = 321$ K, $V_{air} = 70$, 60, and 50 cm/s, $V_{fuel} = 70$ cm/s, distance between ducts = 1.5 cm
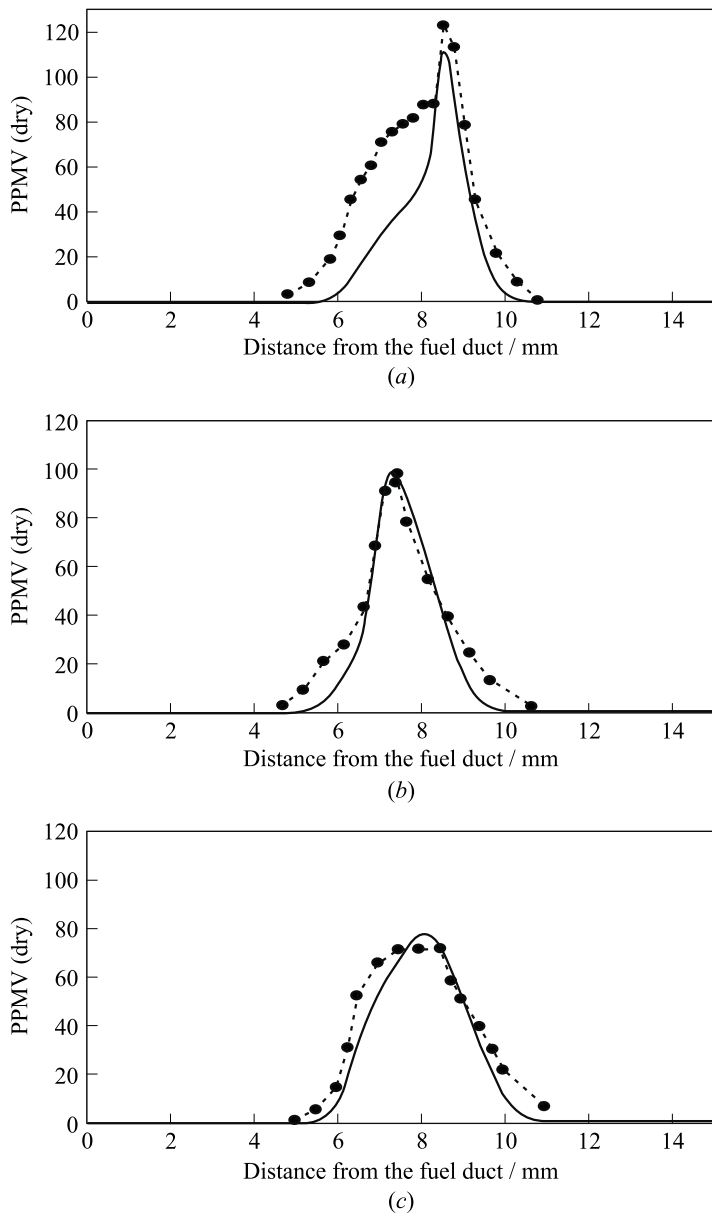
Figure 27.3 Measurements and predictions of mole fractions of NO as a function of distance from the fuel duct for diffusion (*a*) and partially premixed opposed flow flames with $\Phi_B = 2.2$ (*b*) and 1.42 (*c*), $T_{air} = 560$ K and $T_{fuel} = 321$ K, $V_{air} = 70$, 60, and 50 cm/s, $V_{fuel} = 70$ cm/s, distance between ducts 1.5 cm
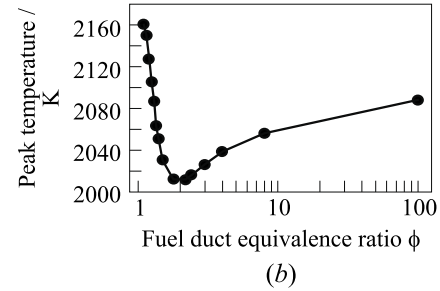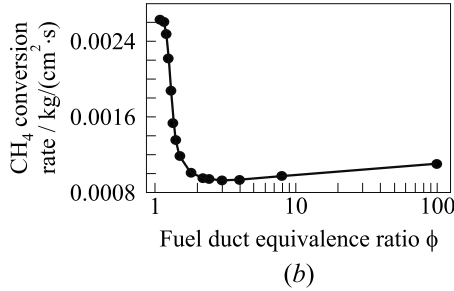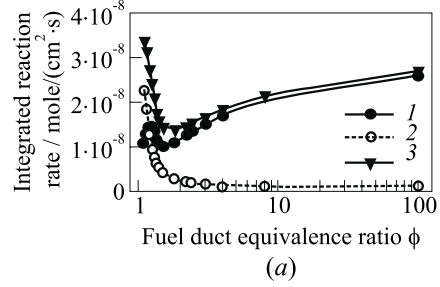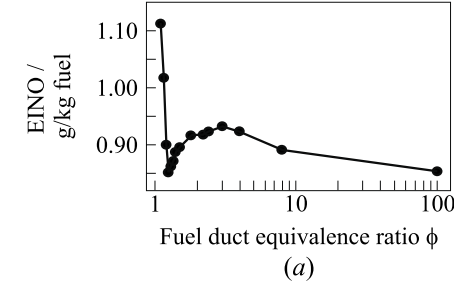
Figure 27.4 Predictions of EINO (a) and CH_4 consumption rate (b) as a function of fuel duct equivalence ratio Φ_B for opposed flow flames with $T_{\text{air}} = 560$ K and $T_{\text{fuel}} = 300$ K; $V_{\text{air}} = 70$ cm/s, $V_{\text{fuel}} = 70$ cm/s, distance between ducts 1.5 cm

Figure 27.5 Integrated reaction rate of prompt and thermal NO initiation reactions (a) and peak temperature (b) as a function of fuel duct equivalence ratio Φ_B for opposed flow flames with $T_{\text{air}} = 560$ K and $T_{\text{fuel}} = 300$ K; $V_{\text{air}} = 70$ cm/s, $V_{\text{fuel}} = 70$ cm/s, distance between ducts 1.5 cm. 1 — $CH + N_2 \rightarrow N + HCN$ (240); 2 — $N_2 + O \rightarrow NO + N$ (-178); and 3 — total

Figure 27.5a shows the rates of the N_2 fixing reactions. Reaction #240: ($CH + N_2 \rightarrow HCN + N$) is the initiation step for the prompt NO route and the reaction #-178: ($N_2 + O \rightarrow NO + N$) is the initiation step for the thermal route. Figure 27.5 shows that the prompt NO totally dominates the thermal contribution until around $\Phi_B = 2.0$. Below this equivalence ratio, the thermal NO begins to increase but does not equal the prompt NO until an equivalence ratio of 1.2 is reached. The prompt NO decreases with increasing levels of partial premixing up to $\Phi_B = 1.6$. This decrease is mainly caused by the reduction in the mole fractions of CH radical.

Eventually, the temperature increase compensates for this decrease and the prompt contribution reaches a local maximum at $\Phi_B = 1.3$. This local maximum has been observed experimentally in [3]. The overall N_2 fixing rate follows the

qualitative prompt NO behavior until $\Phi_B = 1.6$ and, below this value, begins to follow the thermal NO behavior. The net result is the observed emission index profile. Thus the minimum in NO emissions at an optimum level of partial premixing results from a reduction in prompt NO contributions and a lack of increase in the thermal NO contribution. The reasons for a lack of rapid increase in thermal NO were considered next.

The peak temperature decreases by up to 80 K between $\Phi_B = 100$ and 2 with increasing levels of partial premixing as shown in Fig. 27.5b. Therefore, the peak thermal contribution decreases and the integrated thermal contribution, as shown in Fig. 27.5a, does not increase rapidly. Beyond equivalence ratio of 2, the peak temperature increases rapidly and the thermal contribution follows. However, before the thermal contribution increases significantly and at Φ_B where the prompt contribution has decreased significantly, an optimum equivalence ratio for minimum NO is found.

The decrease in temperature predicted by the analysis is relatively small and has not been observed experimentally. Experiments with higher precision and accuracy are warranted for checking if this is an artifact of the present chemistry that does not include the effects of higher hydrocarbon formation and radiative heat loss. The peak temperature was found to decrease because of a decrease in the peak volumetric heat release rate caused by a broadening of the reaction zone.

27.6 CONCLUDING REMARKS

The following conclusions can be drawn from the present study:

1. The OPPDIF code combined with the CHEMKIN database and GRIMECH 2.11 provides excellent predictions of major species concentrations and very good predictions of the intermediate and final product species for all three flames studied herein.

2. This methodology results in excellent predictions of NO mole fractions for partially premixed flames. The discrepancies for diffusion flame are on the fuel-rich side and therefore related to reactions that occur in the absence of O_2.

3. An optimum equivalence ratio for the minimum NO emission is observed in qualitative agreement with jet flame experimental data. The reasons for the quantitative differences are unknown.

4. A study of the N_2 fixing reactions shows that the minimum NO emissions at the optimum equivalence ratio occur because of a reduction in the prompt NO formation rates caused by a decrement in the CH radical

concentrations. The increase in thermal NO contribution overwhelms the reductions in prompt contributions only at leaner conditions.

The following recommendations are made.

The present study shows that partial premixing has a firm scientific basis as a NO pollutant reduction strategy. Further work is needed to establish if the current NO reduction strategies in gas turbine engines, such as higher primary swirl, inadvertently utilize the benefits of partial premixing. Even more importantly, work is needed to establish the design rules for optimizing such strategies.

Photographs of diffusion and partially premixed flames in the present study and many of the references cited here have shown that this strategy can be applied to soot reduction and possibly smoke elimination. Further work is needed to establish the window of opportunity to utilize partial premixing for smoke elimination, without affecting stability, ignition, and re-light capabilities.

ACKNOWLEDGMENTS

REFERENCES

1. Gore, J. P. 1994. NO_x reduction using lean direct injection in naval engines. *7th ONR Propulsion Meeting Proceedings*. Eds. G. Roy and P. Givi. Buffalo, NY: State University of New York at Buffalo. 28–33.

2. Gore, J. P., and N. J. Zhan. 1996. NO_x emission and major species concentrations in partially premixed laminar methane/air co-flow jet flames. *Combustion Flame* 105:414–27.

3. Kim, T. K., B. J. Alder, N. M. Laurendeau, and J. P. Gore. 1995. Exhaust and *in situ* measurements of nitric oxides for laminar partially premixed C_2H_6–air flames: Effect of premixing level at constant fuel flow rate. *Combustion Science Technology* 110–111:361–78.

4. Heberle, N. H., G. P. Smith, D. R. Crosley, J. B. Jeffries, J. A. Muss, and R. W. Dibble. 1995. Laser induced fluorescence measurements in atmospheric pressure partially premixed methane/air flames. *Joint Technical Meeting of the Western States, Central States, Mexican Sections of the Combustion Institute and American Flame Research Committee Proceedings*. 134–38.

5. Driscoll, J. F., R. H. Chen, and Y. Yoon. 1992. Nitric oxide levels of turbulent jet diffusion flames: Effects of residence time and Damköhler number. *Combustion Flame* 88:37–49.

6. Turns, S. R., F. H. Myhr, R. V. Bamdaru, and E. R. Maund. 1993. Oxide of nitrogen emission from turbulent jet flames: Part II — Fuel dilution and partial premixing effects. *Combustion Flame* 93:255–69.

7. Røkke, N. A., J. E. Hustad, and O. K. Sønju. 1994. A study of partially premixed unconfined propane flames. *Combustion Flame* 97:88–106.

8. Gore, J. P., N. M. Laurendeau, and S. H. Frankel. 1995. NO_x reduction using lean direct injection in naval engines. *8th Propulsion Meeting Proceedings*. Eds. G. D. Roy and F. A. Williams. La Jolla, CA: University of California at San Diego. 1–9.

9. Blevins, L. G., and J. P. Gore. 1999. The computed structure of low-strain rate partially premixed CH_4/air flames: Implications for NO formation. *Combustion Flame* 116:546–66.

10. Kemal, A., J. Dorn, and C. T. Bowman. 1997. Control of nitrogen oxide emissions from air-breathing combustors using partial premixing of fuel and air. Western States Section of the Combustion Institute. Paper No. 97F-136.

11. Li, S. C., and N. Ilincic. 1995. Influences of sprays on strained partially premixed flames. AIAA Paper No. 95-2555.

12. Li, S. C., and F. A. Williams. 1996. Experimental and numerical studies of NO_x formation in two-stage methane–air flames. ASME Paper No. 96-GT-545.

13. Nishioka, M., Y. Kondoh, and T. Takeno. 1996. Behavior of key reactions of NO formation in methane–air flames. *26th Symposium (International) on Combustion Proceedings*. Pittsburgh, PA: The Combustion Institute. 2139–45.

14. Blevins, L. G., and J. P. Gore. 1997. NO_x reduction using lean direct injection in naval engines. *10th ONR Propulsion Meeting Proceedings*. Eds. G. D. Roy and D. Netzer. Monterey, CA: Naval Postgraduate School. 150–54.

15. Lyle, K. H., L. K. Tseng, J. P. Gore, and N. M. Laurendeau. 1999. A study of pollutant emission characteristics of partially premixed turbulent jet flames. *Combustion Flame* 116:627–39.

16. DuPont, V., M. Pourkashanian, A. P. Richardson, A. Williams, and M. J. Scott. 1996. The importance of prompt-NO formation and of NO reconversion in strained laminar binary rich partially premixed flames. In: *Transport phenomena in combustion*. Washington, DC: Taylor & Francis 1:263–74.

17. Tanoff, M. A., M. D. Smooke, R. J. Osborne, T. M. Brown, and R. W. Pitz. 1996. The sensitive structure of partially premixed methane–air vs. air counterflow flames. *26th Symposium (International) on Combustion Proceedings*. Pittsburgh, PA: The Combustion Institute. 1121–28.

18. Tseng, L. K., J. P. Gore, I. K. Puri, and T. Takeno. 1996. Acetylene and ethylene mole fractions in methane/air partially premixed flames. *26th Symposium (Inter-

national) on Combustion Proceedings. Pittsburgh, PA: The Combustion Institute. 993–99.

19. Gore, J. P., and S. M. Skinner. 1991. Mixing rules for state relationships of methane and acetylene/air diffusion flames. *Combustion Flame* 87:357–64.

20. Nguyen, Q. V., R. W. Dibble, C. D. Carter, G. J. Fiechtner, and R. S. Barlow. 1996. Raman–LIF measurements of temperature, major species, OH and NO in methane–air bunsen flames. *Combustion Flame* 105:499–510.

21. Kee, R. J., J. A. Miller, G. H. Evans, and G. Dixon-Lewis. 1988. A computational model for the structure and extinction of strained, opposed flow, premixed methane–air flames. *22nd Symposium (International) on Combustion Proceedings.* Pittsburgh, PA: The Combustion Institute. 1479–95.

22. Lutz, A. E., R. J. Kee, J. F. Grcar, and F. M. Rupley. 1997. OPPDIF: A Fortran program for computing opposed-flow diffusion flames. Sandia Report SAND96-8243.

23. Kee, R. J., F. M. Ruply, and J. A. Miller. 1987. The Chemkin thermodynamic database. Sandia Report SAND987-8215 (Reprinted April 1994).

24. Bowman, C. T., R. K. Hanson, D. F. Davidson, W. C. Gardiner, Jr., V. Lissianski, G. P. Smith, D. M. Golden, M. Frenklach, and M. Goldenberg. 1995. http://www.me.berkeley.edu/gri_mech/.

Chapter 28

AN INNOVATIVE METHOD FOR REDUCING GASEOUS EMISSIONS FROM POWER TURBINE COMBUSTORS

S. Singh and R. E. Peck

An experimental study of spray combustion with porous inserts was performed using a laboratory combustor consisting of an on-axis fuel nozzle/air swirler in a concentric pipe with high-bypass air flow. The fuel used in all tests was Jet-A. Combustor performance was evaluated by measuring exhaust emissions and flame temperatures for different operating conditions with and without ceramic foam inserts of various properties. Experimental results indicated that the enhanced heat transfer in the flame zone could reduce nitrogen oxides (NO_x) and unburned hydrocarbon (UHC) emissions by up to 60%, while carbon monoxide concentrations depended on sustaining rapid burnout downstream of the porous layer. NO_x concentrations were found to be a function of the location, thickness, and pore size of the insert. Placing a second porous layer downstream could yield further reductions in NO_x/UHC emissions. Test results for different firing rates and equivalence ratios revealed the residence time in the porous layer is an important factor regulating combustor performance.

28.1 INTRODUCTION

Due to strict environmental regulations, turbine engine manufacturers and users are facing great challenges in reducing NO_x, SO_x, CO, and hydrocarbons to meet the compliance limits. To date, several innovative methods have been developed and introduced into the market to combat these problems. However, often, while reducing NO_x or other pollutants, new problems arise. These problems are lower turn-down ratio, poor thermal efficiency, flame instability, uneven temperature distribution in the combustor, and noise. These problems are even more pronounced in a liquid fuel fired turbine combustor. Therefore, the present research

is aimed at reducing gaseous emissions, mitigating combustion instabilities, and increasing thermal efficiency. Specific objectives are outlined as follows:

1. To reduce emissions for a wide range of firing rates at different equivalence ratios.

2. To increase the turn-down ratio while producing low levels of emissions.

3. To improve heat release rates and thermal performance.

28.2   TECHNICAL APPROACH

To investigate these research objectives, the contemporary concept of utilizing the superior radiation, thermal, and physical properties of porous media, which have gained acceptance in reducing emissions and improving thermal efficiency, has been used. As a feasibility study, a preliminary investigation was conducted. It was found that when a porous matrix is inserted in a circular duct, the flow velocity oscillation, for example, is suppressed, and NO_x and other gaseous emissions are reduced [1]. Therefore, a combined experimental and theoretical research approach is undertaken to bring the concept to a technical and commercial success.

The experimental research was conducted by inserting porous media in a laboratory combustor simulating the actual engine component to determine their effectiveness in reducing emissions while extending the range of firing rates and equivalence ratios. The complementary combustion and heat transfer modeling work are aimed at optimizing the porous matrix geometry and properties using the data obtained to help reduce the number of tests needed to finalize the combustor design.

28.3   EXPERIMENTAL FACILITIES

Experiments are conducted in a continuous-flow combustion test facility consisting of three modular sections including an inlet, combustor and exhaust. These components are constructed of 12.7-centimeter (5-inch) I.D. schedule–40, 316 stainless-steel pipe and can withstand operating conditions of 1.4 MPa (200 psig) maximum pressure and a 530 K (500 °F) wall temperature. The inlet section contains the fuel supply line and mounting brackets for the fuel injector and interchangeable air swirlers. The exhaust section contains various access ports for sampling probes and cooling water injection. The primary combustor section, shown in Fig. 28.1, is 30.5 cm (12 in.) long and contains an ignitor and
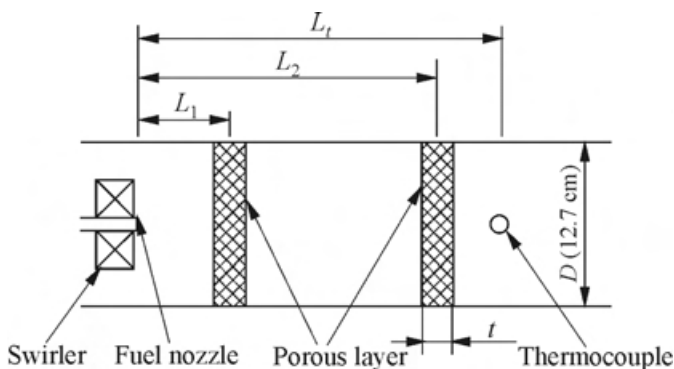
Figure 28.1 Combustor test section

two $15 \times 4 \times 1.3$ cm ($6 \times 1.5 \times 0.5$ in.) flat quartz glass windows for optical access. The modular arrangement enables altering the overall length of the combustor, repositioning optical access, and/or installing a specially designed combustion chamber.

Combustion air is normally supplied by three centrifugal compressors, each rated for 0.08 kg/s (0.15 lb/s) of air at 0.8 MPa (120 psig) pressure giving an overall mass flow rate of 0.23 kg/s (0.45 lb/s). The inlet flow rates are measured either with an *Annubar*^{TM} model ANR–73 device or with calibrated orifice plates. An electrically driven 10-centimeter (4-inch) butterfly valve is installed in the exhaust line to regulate the combustor back pressure. An electric heating system is being installed to preheat the inlet air up to 200 °C (400 °F). Liquid fuel is normally supplied from a 114-liter (30-gallon) N_2 pressurized tank. Higher flow rates can be delivered by a high-pressure electric fuel pump from a 950-liter (250-gallon) reservoir. Fuel flow rates are generally measured with calibrated rotameters.

Exhaust gas temperature measurements are made with a fine-wire R-type thermocouple connected to an *Omega*^{TM} model 660 digital readout. Gas samples are extracted using a 6.4-millimeter (0.25-inch) O.D. water-cooled stainless-steel suction probe and then filtered, dried, and analyzed for CO, CO_2, O_2, UHC, and NO_x. Instrumentation includes a *Beckman* model 864 NDIR CO_2 analyzer, *Beckman* model 867 NDIR CO analyzer, *Siemens* OXYMAT 5E paramagnetic O_2 analyzer, *Siemens* FIDAMAT 5E–E FID total hydrocarbon analyzer, and a *Beckman* model 955 Chemiluminescent NO/NO_x analyzer. Certified span gases are used for instrument calibration. PC-based data acquisition is available during experimentation. All of the emissions data reported here were obtained approximately 24 pipe diameters downstream of the fuel injector and represent average exhaust concentrations.

Typical combustor operating conditions are 0.07–2.0 kg/s of air at 1 atm pressure. Using Jet-A fuel at overall equivalence of 0.1–0.5 yields a firing rate of 50–100 kW. Based on a combustor volume of 0.002 m^3 the highest combustion intensity is 25,000–50,000 kW/m^3. This value can be increased by operating at higher fuel flow rates. For the tests reported here the fuel was injected using a *Delavan*™ model 30609 air atomizing nozzle. The nozzles produce hollow-cone sprays having a SMD of about 25 μm. Larger SMDs are found for decreased assist-air flow or increased fuel flow. In practice, stable flames could be obtained and soot generation was reduced at atomizing air flow rates a little above the nominal values of 0.0003 kg/s. To stabilize the flames, a 70-millimeter ID, 45-degree blade-angle swirler was attached to the nozzle assembly. The Swirl number of the swirler was 0.73 and about 60% of the mainstream combustion air was estimated to bypass the swirler through the annular passage between the swirler and the pipe wall.

One or more 12.7-centimeter (5-inch) OD porous layers can be installed in the rig at any axial location in the three sections. Each layer could be positioned using one custom-made retaining ring behind. In all of the tests reported here the porous material was a SiC ceramic foam supplied by *Hi–Tech Ceramics* of Alfred, New York. All the ceramic foams were 12.7 cm (5 in.) in diameter with varying thickness from 1.3 cm (0.5 in.) to 2.5 cm (1 in.). Two different pore sizes were tested, including 8 ppcm (20 ppi) and 18 ppcm (45 ppi). According to the manufacturer the porosity of the ceramic foams was about 80%.

28.4   RESULTS AND DISCUSSION

Experiments were designed to study the effects of porous media on spray combustion and resulting emissions. A number of factors could affect combustion performance with the presence of porous inserts, including the location, thickness, and pore size of the porous insert and operating conditions such as firing rate and fuel–air ratio. For different operating conditions, the baseline tests without porous inserts were completed. After the baseline tests, the same operating conditions were repeated with porous layers installed at various locations. More tests were then completed with different porous material properties.

28.4.1   Tests at 13.2 kW Firing Rate

The combustor was first tested with one SiC porous ceramic layer installed at a firing rate of 13.2 kW. Nine cases with varying insert location, thickness, or pore size were tested. For some of the experiments the equivalence ratio (ϕ)

was varied by changing the main air flow. The geometric parameters L, t, and p denote the distance between the midplane of the porous layer and the nozzle exit, the thickness, and the pore size of the insert, respectively. The baseline case without a porous insert is represented as $t = 0$ or $L/D = \infty$.

Temperature profiles were measured at several axial locations to locate the peak temperatures in the combustor. The axial distance between the nozzle and the temperature-measurement cross-section is denoted by L_t. With one insert in place, the peak gas temperature immediately downstream of the insert was lowered but the high-temperature region was extended radially, i.e., the pattern factor was improved, as shown in Fig. 28.2. The peak temperatures at each axial location are shown as a function of the distance from the nozzle, or L_t/D, in Fig. 28.3. For the baseline case the highest temperature of 1418 K was found at 1.8 pipe diameters downstream of the nozzle. With one porous layer present, the peak gas temperature was about 200 K lower at $L_t/D = 1.8 \sim 2.2$ but increased by up to 120 K and 200 K at 0.5 and 3.2 pipe diameters downstream of the nozzle, respectively. The highest flame temperature was lowered but the high-temperature region was extended to upstream and downstream.

The placement of a porous solid in the combustion chamber has a significant impact on the internal heat transfer processes. Gas enthalpy could be transferred to the solid insert by convection. Radial and axial conduction and radiation
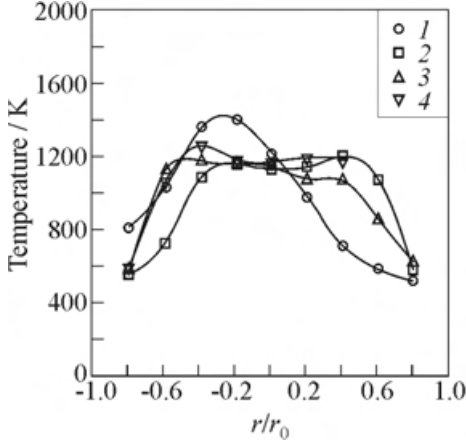
Figure 28.2 Gas temperature profiles at 2.2 pipe diameters downstream of the nozzle ($Q_{in} = 13.2$ kW, $\phi = 0.237$, $t = 25.4$ mm, $p = 8$ ppcm): $1 — L/D = \infty$; $2 — 1.5$; $3 — 1.1$; and $4 — 0.7$
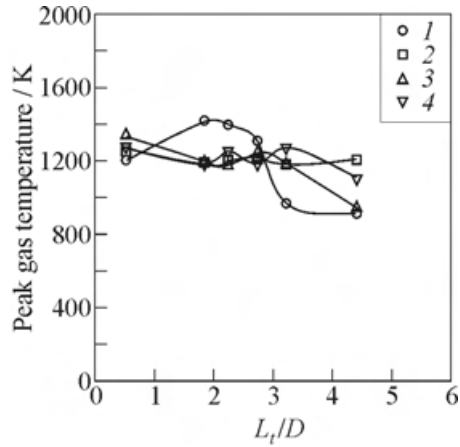
Figure 28.3 Peak gas temperature as a function of axial distance from the nozzle, L_t/D ($Q_{in} = 13.2$ kW, $\phi = 0.237$, $t = 25.4$ mm, $p = 8$ ppcm): $1 — L/D = \infty$; $2 — 1.5$; $3 — 1.1$; and $4 — 0.7$

within the solid matrix could dissipate the enthalpy from the center hot region, resulting in the improved pattern factor. Since the emissivity of the solid is much higher than that of the gaseous phase, the insert could enhance the radiation from the flame to the upstream fresh mixture and downstream combustion products. While the radiation feedback from the insert could enhance droplet vaporization, the increased radiant heat loss from the flame also resulted in the temperature decrease at $L_t/D = 1.8 \sim 2.2$ because the energy propagated downstream with more in the form of radiation and less in the form of gas enthalpy. The reactions downstream of the insert could be suppressed by the decreased temperature, resulting in an extended reaction zone.

Another process involves the fluid mechanics. The large-scale mixing due to swirl-induced recirculation and smaller scale turbulence mixing could be reduced by the inserts. And, it has been reported that the magnitudes of the turbulence intensities are lower in the small-pore ceramic foam [2]. Chemical reactions of the exit flows could be suppressed due to the reduced turbulence mixing strength. This effect could be another cause for the lower temperatures at $1.8 \sim 2.2$ pipe diameters downstream of the nozzle.

The following sections describe the influence of the porous layer on exhaust concentrations of nitrogen oxides, carbon monoxide, and unburned hydrocarbons. Additional experiments using two porous layers were conducted and the second layer was found to affect pollutant emissions. Results for different operating conditions are also included.

28.4.2 Effect of Insert Location

Nitrogen oxides emissions were sensitive to the location of the porous layer, as shown in Fig. 28.4. The lowest NO_x concentrations were found at $L/D = 1.0 \sim 1.5$. Porous inserts reduce NO_x emissions by eliminating hot spots downstream. Therefore, the reduction of NO_x was ineffective when the insert was installed at $L/D = 3.6$, downstream of the highest temperature region for the baseline case ($L/D = 1.8$). When the insert was placed at $L/D = 1.0$ or 1.5, upstream near the high-temperature or rapid reaction region, reactions in that region were probably slower than for $L/D = 0.7$ and the peak temperatures at 2.2 pipe diameters downstream of the nozzle were slightly lower (Fig. 28.5). As a result, prompt NO formation was probably reduced due to the slower reactions and thermal NO formation decreased because of the reduced gas temperatures, yielding the lower NO_x emissions. When the insert was close to the nozzle ($L/D = 0.7$), the spray was heated effectively by the radiation feedback and unburned droplets were vaporized by convection and radiation within the convolute path of the hot solid matrix. As a result, the CO and UHC emissions were the lowest at $L/D = 0.7$ (about 60% lower than the baseline case for UHC and 30% lower for
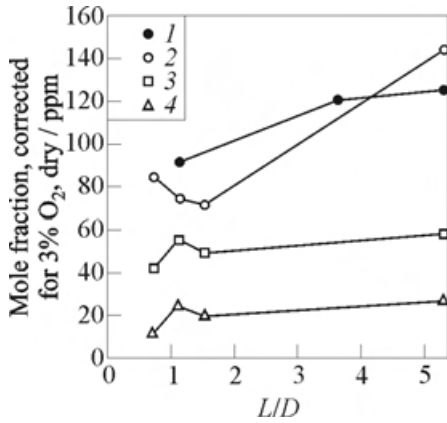
Figure 28.4 Exhaust species concentrations as a function of the insert location, L/D ($p = 8$ ppcm, $Q_{\text{in}} = 13.2$ kW): 1 — NO_x, $t = 1.3$ cm, $\phi = 0.196$; 2 — NO_x, $t = 2.5$ cm, $\phi = 0.237$; 3 — CO $\times 10^{-1}$, $t = 2.5$ cm, $\phi = 0.237$; and 4 — UHC as $C_2 \times 10^{-1}$, $t = 2.5$ cm, $\phi = 0.237$
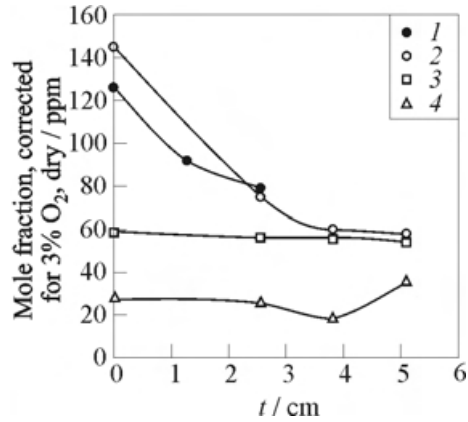
Figure 28.5 Exhaust species concentrations as a function of the insert thickness, t ($L/D = 1.1$, $p = 8$ ppcm, $Q_{\text{in}} = 13.2$ kW): 1 — NO_x, $\phi = 0.196$; 2 — NO_x, $\phi = 0.237$; 3 — CO $\times 10^{-1}$, $\phi = 0.237$; and 4 — UHC as $C_2 \times 10^{-1}$, $\phi = 0.237$

CO). As the insert was moved further downstream, the prevaporizing effect was reduced and CO and UHC emissions could increase because reactions in the hot region were suppressed by the insert. Hence, less improvement was observed in CO and UHC emissions when the insert was installed at $L/D = 1.0 \sim 1.5$ than at $L/D = 0.7$.

28.4.3 Effect of Insert Thickness

Figure 28.5 shows the exhaust gas emissions as a function of the insert thickness when $L/D = 1.1$. NO_x concentration was found to decrease by about 60% with increasing thickness, although the thickness effect on NO_x is less evident when the insert was thicker than 25.4 mm. Heat loss from the flame increased with increased thickness. And, reactions could be less active within and downstream of the thicker inserts because the turbulence mixing strength probably decreased with increased thickness. Hence, the NO_x emission was lower for the thicker layers. When $t > 2.5$ cm, however, no significant change was observed in gas temperatures. As a result, the thickness effect on the NO_x emission was small when $t > 2.5$ cm. Little change in CO concentration occurred when the inserts

were placed at 1.1 diameters downstream of the nozzle. For the same insert position, the inserts were found to reduce UHC emissions when $t = 38.1$ mm. However, the UHC concentration was higher for the 50.8-millimeter thick insert than for the baseline case. When t was smaller than 3.8 cm, the optical thickness (k) of the flame decreased and the radiation feedback probably decreased, yielding the higher UHC concentrations. When $t = 5.1$ cm, the optical thickness was larger than that at $t = 3.8$ cm. But when k is very large, radiation energy does not increase significantly with increasing k because radiation output is proportional to $(1 - \exp(-k))$. When $t = 5.1$ cm, the radiation feedback was probably even smaller because the porous layer was so thick that part of it was placed in a relative cold region of the flame. Furthermore, as discussed earlier, the reaction rates were probably lower for the thicker insert. These influences combined and caused the highest UHC concentration at $t = 5.1$ cm.

28.4.4 Effect of Pore Size

For the smaller pore size heat loss from the flame was larger because the solid surface increased and convection between the porous layer and the flame was enhanced. Furthermore, as discussed earlier, the turbulence strength of the exit flows decreased for the smaller pore size, as did the reaction rates. As a result, it was found that the gas temperatures immediately downstream of the insert were lower for the smaller pore size, yielding lower NO_x concentration, as shown in Fig. 28.6. The extinction coefficient was larger for the smaller pore diameters [3] and radiation feedback was probably enhanced for the smaller pore size. However, this effect could be offset by the suppressed mixing for the smaller pore size. Therefore, no obvious change in CO emission was found although the UHC emission decreased slightly with decreased pore size.

28.4.5 Effect of the Second Layer

Additional experiments were conducted using two porous inserts. Subscripts 1 and 2 are introduced to denote the first layer and the second layer, respectively. Hence, a one-layer test corresponds to the case where $L_2/D = \infty$ and $t_2 = 0$. The baseline case is indicated as $L_1/D = L_2/D = \infty$ and $t_1 = t_2 = 0$. The NO_x concentration was reduced when the second layer was placed at $L/D = 3.6$ and the first layer was installed at $L_1/D = 1.1$ or 0.7, as shown in Fig. 28.7. For the other cases no significant change in NO_x concentration was observed with the second layer installed. In most cases, the CO and UHC concentrations were higher with the second insert in place than for $L_2/D = \infty$, especially for the smaller pore size. Generally, it was found that the gas temperatures
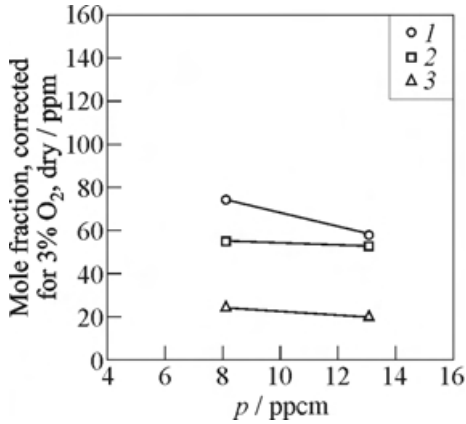
Figure 28.6 Exhaust species concentrations as a function of the pore size, p ($L/D = 1.1$, $t = 2.5$ cm, $Q_{in} = 13.2$ kW, $\phi = 0.237$): 1 — NO_x; 2 — CO $\times 10^{-1}$; and 3 — UHC as $C_2 \times 10^{-1}$
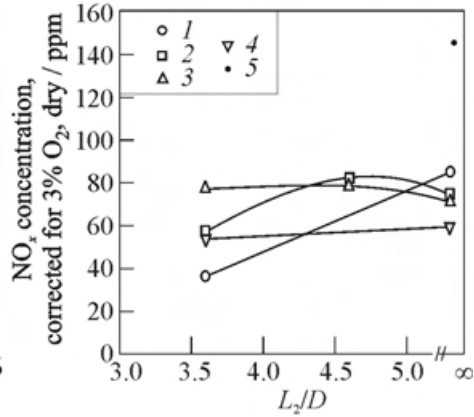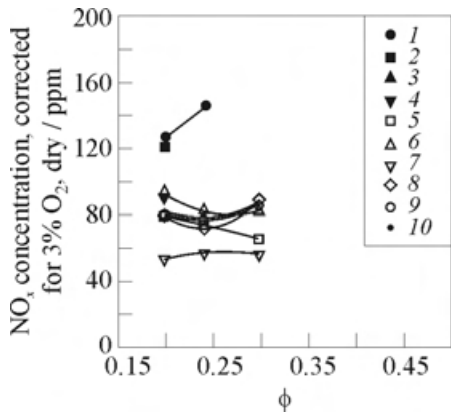
Figure 28.7 NO_x concentrations as a function of L_2/D ($p_1 = p_2 = 8$ ppcm, $Q_{in} = 13.2$ kW, $\phi = 0.237$): 1 — $L_1/D = 0.7$, $t_1 = t_2 = 2.5$ cm; 2 — $L_1/D = 1.1$, $t_1 = t_2 = 2.5$ cm; 3 — $L_1/D = 1.5$, $t_1 = t_2 = 2.5$ cm; 4 — $L_1/D = 1.1$, $t_1 = 3.8$ cm, $t_2 = 2.5$ cm; and 5 — $L_1/D = L_2/D = \infty$

between two inserts and close to the second layer were increased with the second layer installed. The energy release rates were probably increased between two inserts due to the radiation feedback from the second layer. The UHC and CO emission did not decrease with the enhanced reactions because radiation heat loss was increased and/or turbulence mixing was suppressed. Similar emission trends have been observed for nonpremixed gas flames having submerged porous media [4].

28.4.6 Effect of Equivalence Ratio

Species concentrations are shown as a function of equivalence ratio in Fig. 28.8 for different insert configurations. The data were obtained by fixing the firing rate and varying the main air flow. For the baseline case without any inserts, the NO_x concentration was 15% higher at the higher fuel–air ratio ($\phi = 0.237$) because the combustion temperatures are generally higher. With one or two porous layers in the combustor, the increase in NO_x emission was small ($< 7\%$) when the equivalence ratio was increased from 0.196 to 0.237. At the lower equiva-

Figure 28.8 NO_x concentrations as a function of equivalence ratio, ϕ ($p_1 = p_2 =$ 8 ppcm, $Q_{in} = 13.2$ kW): $1 — L_1/D = \infty$, $L_2/D = \infty$; $2 — L_1/D = 3.6$, $L_2/D = \infty$, $t_1 = 1.3$ cm; $3 — L_1/D = 1.1$, $L_2/D = \infty$, $t_1 = 1.3$ cm; $4 — L_1/D = 1.1$, $L_2/D = 3.6$, $t_1 = t_2 = 1.3$ cm; $5 — L_1/D = 1.1$, $L_2/D = \infty$, $t_1 = 2.5$ cm; $6 — L_1/D = 1.1$, $L_2/D = 3.0$, $t_1 = 2.5$ cm; $7 — L_1/D = 1.1$, $L_2/D = 3.6$, $t_1 = t_2 = 2.5$ cm; $8 — L_1/D = 1.5$, $L_2/D = \infty$, $t_1 = 2.5$ cm; $9 — L_1/D = 1.5$, $L_2/D = 3.6$, $t_1 = t_2 = 2.5$ cm; and $10 — L_1/D = 1.5$, $L_2/D = 4.6$, $t_1 = t_2 = 2.5$ cm

lence ratio ($\phi = 0.197$), yellow flames were observed to exit from the center of the porous layers when $L_1/D < 1.5$. The presence of soot indicates that many fuel-rich pockets existed in the flame and the fuel was not evaporated sufficiently upstream of the insert because the residence times were too short. Also, the combustion was not homogeneous and the NO_x concentration did not decrease even though the fuel–air ratio was low. At the higher fuel–air ratios, the flame shape changed from a relatively slender jet to a distributed reaction zone and the exit yellow flame disappeared. The flame volume and residence time increased, resulting in complete fuel vaporization upstream of the porous insert. As a result, combustion was more homogeneous and the NO_x emission did not increase at the higher fuel–air ratio.

The CO and UHC concentrations were found to decrease with increased equivalence ratio. For a gas turbine combustor, low CO levels can be achieved only in a fairly narrow range of equivalence ratios, from about 0.7 to 0.9 [5]. This range is quite likely shifted by the presence of a porous media in the reaction. At very lean equivalence ratio, burning rates are slow due to low temperatures and the CO levels are high; at equivalence ratios close to stoichiometric, the CO levels are high because there are insufficient oxidizing species. For the results reported here, the equivalence ratios were below 0.30. For this condition, the burning rates were slower at the lower fuel–air ratio and the residence times were reduced by increased air flow, yielding the higher CO and UHC emissions.

Other issues of importance to combustor performance include soot production, pressure loss, and mechanical lifetime of the material. Too much soot in the exhaust could indicate poor combustion efficiency and unwanted particulate (smoke) emissions. For the baseline case without any inserts in the combustor, a slightly sooting flame was found. When one or two porous layers were inserted into the flame, no soot residue was found in the porous foams. It was thought

that at the operating conditions the solid temperatures were high enough to burn the soot attached to the surface of the porous layer and soot formation was not increased.
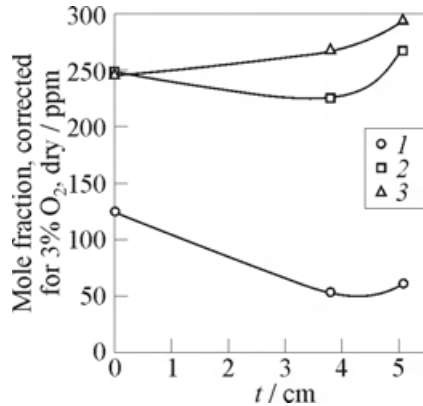
High-pressure loss in a gas turbine combustor would result in excess specific fuel consumption and thus should be avoided. When $\phi = 0.237$ and $p = 8$ ppcm, the porous layers created an additional pressure drop of about 150 Pa for one 2.5-centimeter-thick porous layer and about 300 Pa for a 5.1-centimeter-thick foam. The loss of efficiency due to the pressure drop is estimated as 0.086% for 2.50-centimeter-thick insert and 0.17% for 5.1-centimeter-thick insert.

Thermal cracking was observed for the SiC ceramic foam. The cracking problem was less severe when the insert was placed at $L/D = 0.7$ and 1.1 than at $L/D = 1.5$. When $L/D = 1.5$, the spatial temperature gradients within the porous layer could be large because the insert was placed near the highest temperature region for the baseline case, i.e., $L_t/D = 1.8$. Generally, small cracks had developed within the foam after several start-up and shut-down cycles. Thicker or smaller pore size inserts were found to have better resistance to thermal cracking.

28.4.7 Tests at 19.1 kW Firing Rate

Combustor performance was also evaluated at a higher firing rate of 19.1 kW (1508 kW/m²). One porous layer with different thickness was installed in various locations of the combustion chamber. Emissions data are plotted in Fig. 28.9.

A sooting flame with high CO and UHC emissions was observed for the baseline case without a porous insert in the combustor. With the inserts in place, NO_x emission was reduced, but little change was found for CO and UHC emissions. During the experiments with one porous layer placed at $L/D = 1.1$ the pressure drop through the insert increased slowly to about 800 Pa; gas temperatures decreased by up to 600 K downstream of the inserts. The porous foams were found to be

Figure 28.9 Exhaust concentrations as a function of insert thickness, t ($L/D = 1.1$, $p = 8$ ppcm, $Q_{in} = 19.1$ kW): 1 — NO_x, $\phi = 0.237$; 2 — CO $\times 10^{-1}$, $\phi = 0.237$; and 3 — UHC as $C_2 \times 10^{-1}$, $\phi = 0.237$

soot-clogged. Generally, soot is formed only in fuel-rich regions of the flame. However, even when the overall equivalence ratio in the primary zone is very

low, imperfect fuel–air mixing can create local regions in which pockets of fuel-rich mixture are enveloped in oxygen-deficient gases at high temperature, leading to high rates of soot formation.

For the tests at the higher firing rate (19.1 kW), the main air flow rate was increased proportional to the increased fuel flow in order to maintain the same fuel–air ratio ($\phi = 0.237$) as that used in the tests at the 13.2 kW firing rate. As discussed earlier, about 60% of the combustion air bypassed the swirler. This portion of air was probably not well mixed with the spray and shortened the residence time, resulting in incomplete fuel vaporization upstream of the porous layer. Hence, liquid-fuel burning in a colder solid surface produced large amounts of soot and high CO and UHC emissions. When the porous layer was soot-clogged, the actual pore size became smaller and the turbulence mixing of the exit flows was suppressed, causing the lower temperatures downstream. Similar observations were reported in [6].

When the insert was moved downstream to $L/D = 1.5$, the soot-deposit problem was alleviated. When $L/D = 1.5$, the UHC concentration was lower than for $L/D = 1.1$. Longer residence time and better mixing were obtained upstream of the porous layer when the insert was moved downstream to $L/D = 1.5$, improving the combustion efficiency.

In summary, whether or not the porous insert was installed, combustion was incomplete but NO_x emissions did not increase when the firing rate increased from 13.2 to 19.1 kW. The reason is that the residence time was shorter for the higher firing rate because increasing the main air flow was the only way to maintain the same fuel–air ratio for the combustor configuration. For the same reason large amounts of soot particles were generated at the higher firing rate and soot deposited in the porous matrix. The soot-deposit problem could be prevented by moving the insert further downstream. Further experiments have shown that the problem could be solved by reducing the main air flows or by using radial air injection upstream of the insert to enhance mixing.

28.5 CONCLUDING REMARKS

A laboratory combustor containing porous media and burning atomized Jet-A fuel was tested for exhaust emissions and flame temperatures. The major findings of this study are as follows:

1. With the porous layers installed, flame radiation increased, lowering the peak flame temperatures and extending the reaction zone. The combustor pattern factor improved due to the radial conduction and radiation within the solid matrix.

2. Because hot spots were eliminated by the porous inserts, the NO_x emissions were reduced by 30%–60%.

3. The thickness (t), location (L/D), and pore size (p) of the porous media were all shown to affect NO_x emissions. The NO_x emissions decreased with increasing thickness up to $t \approx 2.5$ cm and with smaller pore sizes. The lowest NO_x emissions were found when $L/D = 1.1$–1.5.

4. The porous inserts hastened fuel vaporization by radiation feedback and convection yielding lower UHC emissions. When the insert was close to the nozzle $(L/D = 0.7)$, 60% reduction in UHC emissions was obtained. The optimum insert thickness for low UHC emissions was found to be 2.5–3.8 cm.

5. In spite of rapid fuel vaporization, generally, CO emission was not reduced by porous layers because turbulence mixing was suppressed and/or flame temperatures were lowered.

6. The addition of a second porous layer could further reduce NO_x emissions. Improved mixing is necessary to promote CO and UHC burnout.

7. The emissions were greatly influenced by the primary zone equivalence ratios. The residence times at the high-temperature region decreased with decreased fuel–air ratio, resulting in a drastic increase in CO and UHC emissions. CO and UHC emissions also increased for very lean mixtures because of lower combustion temperatures. For the baseline cases NO_x emissions were found to increase with increased fuel–air ratio; whereas, with porous inserts installed, varying fuel–air ratio generally had little influence on the NO_x concentrations.

8. When the firing rate was increased, the flames generated more soot particles, and had higher CO and UHC emissions both with and without porous inserts present. Using porous inserts would generate soot-deposit problems at very low fuel–air ratios $(\phi < 0.3)$.

9. The combustion stability was increased by porous inserts. The porous layers had enough heat capacity to ignite the spray in the event of flame blow-out due to short interruptions in fuel or air supplies.

10. For the conditions studied, the pressure drop through the porous inserts caused a negligible decrease in thermal efficiency.

11. Thermal cracking in the porous materials was observed. The material durability was higher for thicker or smaller pore-size foams.

In summary, porous inserts could benefit combustor performance. More materials and combustion research is needed to develop the technology for practical applications.

ACKNOWLEDGMENTS

REFERENCES

1. Singh, S. 1992. Industrial burner with low NO$_x$ and CO emissions. U.S. Patent No. 5,174,744.
2. Hall, M. J., and J. P. Hiatt. 1994. *J. Physics Fluids* 6:469.
3. Howell, J. R., M. J. Hall, and J. L. Ellzey. 1996. *Progress Energy Combustion Science* 22:121.
4. Meng, W. H., C. McCordic, J. P. Gore, and K. E. Herold. 1991. *ASME/JSME Thermal Energ. Proc.* 5:181.
5. Lefebvre, A. H. 1983. *Gas turbine combustion.* New York: Hemisphere.
6. Kaplan, M., and M. J. Hall. 1995. *J. Experimental Thermal Fluid Science* 11:13.

Chapter 29

AFTERBURNING CHARACTERISTICS OF PASSIVELY EXCITED SUPERSONIC PLUMES

K. H. Yu and K. C. Schadow

Supersonic afterburning plumes that respond to passive excitation were experimentally studied to explore the role of initial mixing control in the modification of the afterburning flame characteristics. The plume flow field was simulated with pressured-matched supersonic jets that were discharged from a Mach 2 nozzle into air. To create passive excitation in the plume–air shear flow, an open cavity with adjustable geometry was fitted at the nozzle exit setting up flow-induced cavity resonance. Depending on the excitation frequency, turbulent compressible mixing characteristics were substantially modified in the excited shear flow. Planar Mie-scattering images and jet pressure measurements revealed the importance of large coherent structures, which appeared to modify turbulence energy cascade characteristics in the initial shear layer. To quantify the effects of excitation on supersonic mixing and afterburning characteristics, the changes in the initial shear layer growth and the afterburning flame luminosity were measured as a function of the excitation frequency. While substantial increase in the shear layer growth rate was observed with the excitation at or near the jet preferred mode, the afterburning intensity was either increased or decreased depending on the excitation frequency. In general, high-frequency excitation caused an increase in the visible light emission while low-frequency excitation effectively lowered the flame luminosity.

29.1   INTRODUCTION

Exhaust products and by-products that are discharged from a propulsion device form a moving cluster of gases and particles, called plume. High-temperature plumes emit electromagnetic waves over a wide spectrum of wavelengths. Since many propulsion devices operate fuel-rich in order to maximize the specific impulse, the plumes often contain some incompletely burned fuel species that may

start an exothermic reaction process with entrained air causing afterburning. Afterburning is a concern because it amplifies the plume emissions in certain wavelengths that can cause interference with the guidance or tracking systems. Furthermore, intense emissions from the plumes can be used for detection and targeting purposes.

Therefore, the ability to modify afterburning characteristics in fuel-rich plumes is desirable. To modify afterburning characteristics, chemical additives such as potassium compounds have often been utilized in double-base propellants [1]. In a diffusion flame experiment, it was shown that potassium vapors inhibited the hydrogen reaction over a wide range of additive concentration [2]. Such additives work by consuming free radicals in the flow before they become available in the chain branching reactions of hydrogen–oxygen combustion. However, since the additives add extra weight to the propellants, they may degrade the overall propulsion performance and add to the radar cross-section. In addition, they do not work in certain situations, particularly those involving the presence of chlorine species [1].

Controlling the mixing between plume and air is another possible way to affect afterburning characteristics. In the past, research on mixing control for fuel-rich plume combustion has been conducted to increase performance of ducted rockets. For instance, in ducted rockets, afterburning characteristics were affected by nonstandard geometry nozzles that altered exit momentum thickness and redistributed vorticity in the initial shear layer [3]. Recently, a novel technique, based on flow-induced resonance of jets discharging over open cavities, was developed for passively exciting supersonic jets. Such a technique allows systematic control of turbulent compressible mixing in high-speed shear flows [4].

In the present study, the cavity technique was used to better understand the physical basis of mixing control approach for plume afterburning modification. Simulated plumes were created and the passive excitation was systematically applied to the initial shear layer of the plumes. The authors' interest was not only in evaluating the afterburning characteristics of excited plumes, but also in studying the physical mechanisms that cause the excitation as well as the basic excitation response of turbulent compressible shear layers. Such issues are of interest when one considers a mixing control approach because afterburning initiation behavior must be sensitive to the state of the plume–air mixing in the initial shear layer.

29.2 DYNAMICS OF PLUME–AIR SHEAR FLOWS

In general, the plume flow field is divided into the near-field, transition, and far-field regions [5]. The near-field region which is shown in Fig. 29.1 consists of a nearly inviscid jet core dominated by strong wave structures and a thin
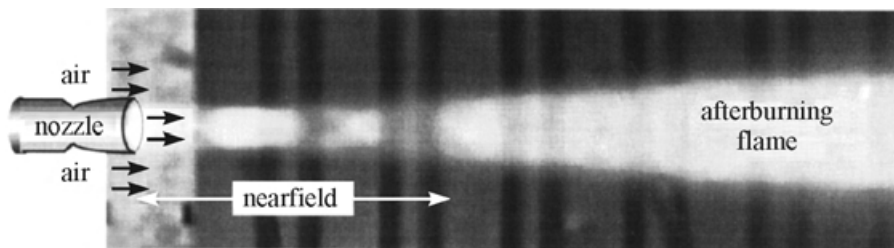
Figure 29.1 Near field of supersonic afterburning plume

developing shear layer at the plume boundary in which turbulent mixing with ambient air flow takes place. In the transition region the potential core of the jet disappears as the shear layer merges at the jet center axis, and, eventually, the velocity profile becomes self-similar at the far-field region. Upon ignition in the near field, the afterburning flame typically extends through the transition zone. In the present study, the dynamics of the initial shear layer is only considered, since the afterburning ignition process must be highly sensitive to the mixing in the near-field flow.

In the initial mixing process that precedes afterburning initiation, it is important to consider large and fine scales of flow turbulence. Large-scale structures in a shear layer develop from flow instabilities, and are responsible for bulk mixing of the plume products and surrounding air. Fine-scale structures arise as a result of large-scale structure breakdown, and are responsible for afterburning initiation through molecular-level mixing of fuel and air. For afterburning suppression, it is generally desired to enhance the development of large-scale vortices to increase the rate of cooling by bulk mixing, while minimizing fine-scale mixing and thus the rate of heat release [6].

Mixing characteristics in the shear layers are affected not only by the jet and flight Mach numbers but also by the nozzle and base region design, altitude, and the motor pressure ratio that determines the nozzle exit temperature and pressure. The occurrence of afterburning appears to be dependent on these factors, which therefore provide control parameters to alter the afterburning process. Figure 29.2 shows some of the large coherent structures that develop in the initial shear layer between the primary Mach 2 jet that simulated the plume flow and the surrounding air flow at Mach 1.3. It can be seen from these images that the coherent structure characteristics such as vortex size and shape will depend sensitively on the nozzle base region design.

As the relative velocity difference is increased, however, coherent structure development is suppressed by compressibility effect [7, 8] and thus the effect on mixing by coherent structures diminishes. The compressibility effect can be quantified in terms of the convective Mach number, which is defined as the
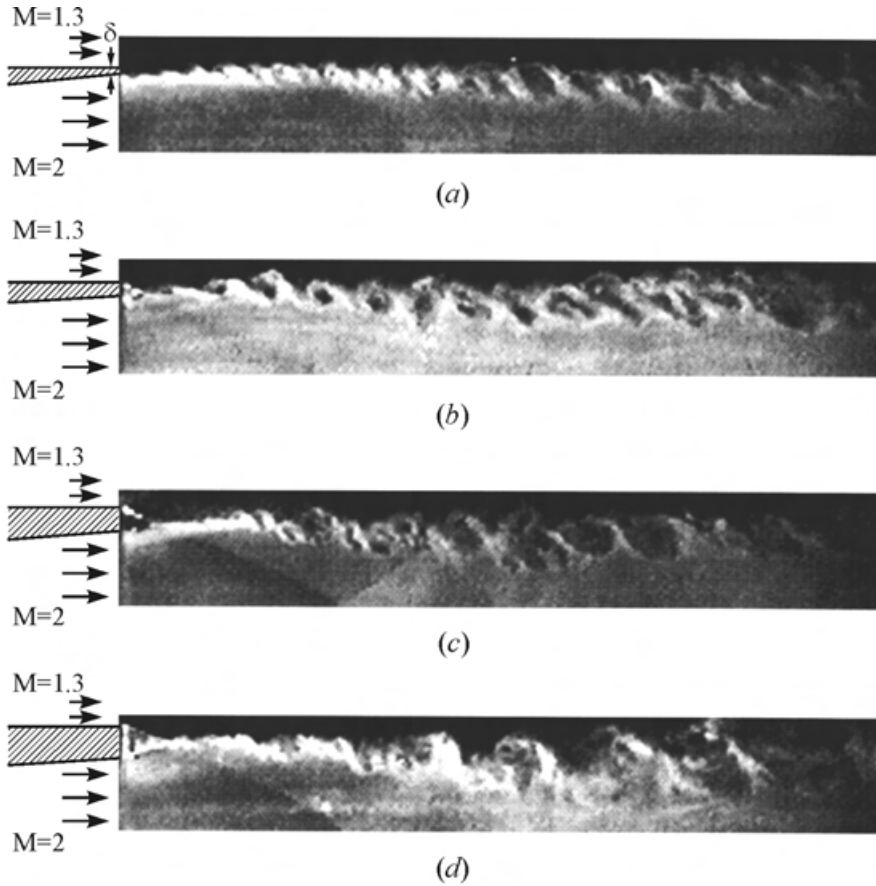
Figure 29.2 Large-scale structure in the initial shear layer as a function of nozzle lip thickness, δ: $\delta = 1.3$ (*a*), 2.2 (*b*), 4.1 (*c*), and 5.4 mm (*d*)

relative Mach number of each stream in a Galilean frame of reference that moves with the large-scale structure. For instance, $M_{C1} = (U_1 - U_c)/a_1$ and $M_{C2} = (U_c - U_2)/a_2$, where U_1 and U_2 are the free stream velocities in a stationary frame and U_c is the convective velocity of the large-scale structure. It is well known that the normalized shear layer growth decreases sharply beyond M_{C1} greater than 0.3 and reaches about 20% of the incompressible value at sufficiently high M_{C1} [9].

Since plume–air mixing typically occurs at high convective Mach numbers, a special technique was needed to apply mixing control over the stabilizing influence of the compressibility effect. Thus, flow-induced cavity resonance was uti-

lized to organize and control large-scale structures in the plume–air shear flow. In the next three sections, the physical mechanisms of cavity resonance as well as the effects on turbulent mixing and afterburning reaction will be examined in detail.

29.3 FLOW EXCITATION USING CAVITY RESONANCE

The effects of plume excitation on turbulent mixing and afterburning combustion were investigated using supersonic free jets that simulated plumes at Mach 2 exit condition. Figure 29.3 shows the experimental setup and instrumentation used in the present study. In the cold flow case, air from a high-pressure supply was utilized. For hot flows, a gas generator was used to establish supersonic free jets of various composition gases at different exit temperatures. Hot gases were generated as the products of primary reaction in the plenum chamber involving ethylene flow and oxygen-enriched air flow. Table 29.1 summarizes the flow conditions for the four selected cases. The jets were discharged through a circular converging-diverging nozzle with a conical expansion. During a typical run, the average stagnation pressure was held constant by regulating the reactant flow rates within $\pm 0.4\%$ of the desired value. The nozzles were operated at the design value, which ranged between 1.95 and 2.00 for the selected cases.

To excite a supersonic jet using cavity acoustics, an acoustically open cavity was placed along the direction of the jet at the nozzle exit close to the shear layer. An acoustically open cavity is characterized by a cavity length-to-depth
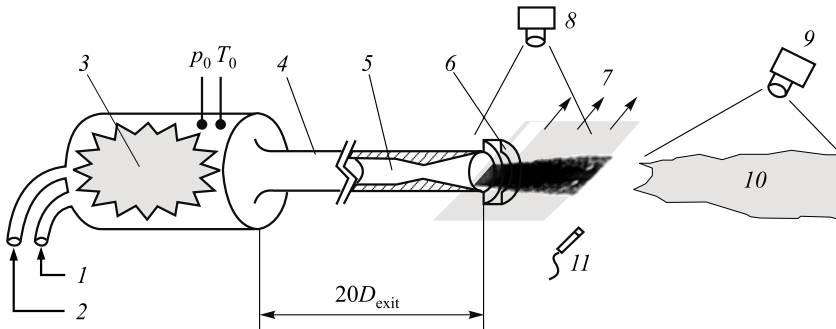
Figure 29.3 Experimental setup and instrumentation: *1* — fuel; *2* — oxidizer, N_2, seed-particles; *3* — plenum chamber; *4* — flow straightener; *5* — c/d nozzle ($D_{\text{throat}} = 19.0$ mm, $D_{\text{exit}} = 24.7$ mm); *6* — cavity; *7* — laser sheet; *8* — Mie-scattering collection device; *9* — CCD; *10* — afterburning flame; and *11* — microphone

**Table 29.1** Experimental flow conditions based on average parameters

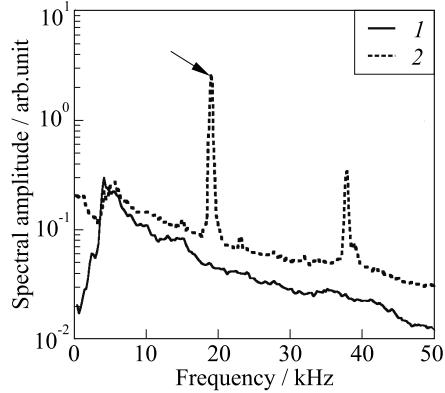|	Case 1	Case 2	Case 3	Case 4
Mach number	2.0	2.0	2.0	2.0
Exit velocity, m/s	500 ± 10	1380 ± 20	1620 ± 20	1660 ± 20
Exit temperature, K	155 ± 8	1300 ± 30	1470 ± 30	1550 ± 30
Reynolds number, UD/ν	$2.2 \cdot 10^6$	$1.7 \cdot 10^5$	$1.3 \cdot 10^5$	$1.2 \cdot 10^5$
Gas	air	Products of $C_2H_4 + O_2 + N_2$ reactions with		
		$\phi = 0.7$	$\phi = 2.0$	$\phi = 2.0$
Ambient temperature, K	293 ± 10	298 ± 10	298 ± 10	298 ± 10
Ambient pressure, kPa	94	94	94	94
M_{C1}	0.84	1.33	1.39	1.41
M_{C2}	0.84	1.28	1.34	1.36

(a)

(b)
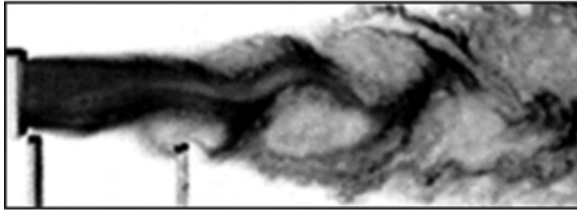
(c)

Figure 29.4 Instantaneous planar Mie-scattering images of fully expanded Mach 2 jets: (a) natural unexcited jets; (b) and (c) excited jets using flow-induced cavity resonance

ratio sufficiently small not to allow shear-layer reattachment on the cavity floor. Figure 29.4 illustrates this technique and shows three planar Mie-scattering images of the jets, obtained with 20 ns laser pulses. The images of forced jets clearly show the large coherent structures in the initial shear layer. Also, it can be seen from the images that excited shear layers often spread at a much higher rate than the corresponding natural shear layer. A circular jet discharging over a rectangular cavity was affected only at the localized region tangent to the cavity, and the effect was sensitive to the resonance tuning of the cavity acoustics [10]. Thus, annular cavities were used in the subsequent tests.

To understand the physical mechanisms of cavity resonance, a series of cold flow experiments was conducted with various size cavities and the resulting frequencies were analyzed. The results will be presented in the following paragraphs, while the effect on mixing will be discussed in the next section.

To determine the dominant frequency of excitation, the near-field acoustic spectrum was obtained using a microphone. Typical near-field acoustic spectra for an excited jet and a natural jet are shown and compared in Fig. 29.5. When multiple peaks were observed in the spectrum, the peak with the highest spectral amplitude was denoted as the excitation frequency. By systematically varying the dimensions of the cavity, flow excitation occurred over a wide range of frequencies (4–40 kHz). Table 29.2 summarizes the normalized data. Initial tests were performed with semi-annular cavities to eliminate possible

Figure 29.5 Typical spectra of near-field acoustics. *1* — natural, *2* — excited. Arrow shows f_{exc}

pressure mismatching associated with flow ejection effect in fully annular cavities. The semi-annular cavities in this case were flush mounted at the nozzle exit ($x = L$) to simplify the acoustic analysis.

In characterizing the physical mechanisms, attempts were made to fit existing theoretical results to the data. Assuming a two-dimensional cavity with relatively small radiation loss through the open end, the allowed frequencies can be quantified to fit the boundary conditions. It is straightforward to use separation of variables to show that the allowed modes are given by

$$\frac{f_{mn}L}{U} = \frac{c}{2U}\sqrt{(m-1)^2 + \left(n - \frac{1}{2}\right)^2 \left(\frac{L}{d}\right)^2} \qquad (29.1)$$

Table 29.2 Semi-annular cavity dimensions and excitation frequency using cold Mach 2 jet (Case 1)

Length (L/D)	Depth (d/D)	Frequency (fD/U)
0.267	0.457	1.6
0.308	0.208	0.201
0.308	0.269	1.92
0.308	0.521	1.41
0.308	0.601	1.29
0.308	0.685	1.19
0.308	0.773	1.49
0.308	0.773	0.744
0.308	0.849	0.693
0.308	0.898	0.667
0.409	0.457	1.84
0.539	0.903	0.841
0.565	0.478	1.16
0.628	0.919	1.33
0.719	0.914	1.28
0.775	0.939	1.21
0.808	0.909	1.24
1.05	0.262	2.20
1.05	0.513	1.07
1.05	0.771	1.11
1.05	0.898	0.901
1.34	0.524	1.16
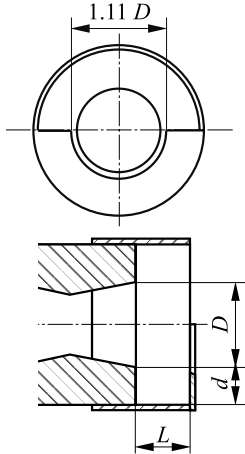
where c is the speed of sound in the cavity and the ordered integers (m, n) denote the longitudinal (L) and the transverse (d) mode numbers, respectively. Some of these modes are shown together with the data in Fig. 29.6. Although some agreement was found for $n = 2$ and $n = 4$, most of the data deviated significantly from calculations. In reality, the radiation loss through the open end is very significant unless $L/d \ll 1$ [11]. The net effect of using a more appropriate radiation boundary condition is to change the effective depth of the cavity resulting in a shift of the curves.

Another approach to explain the excitation frequency was based on the acoustic feedback of vortex-generated disturbances [12]. For instance, flow over a cavity produces pressure fluctuations in the cavity, which disturb initial shear flow at the nozzle lip. The disturbance propagates downstream, and the interaction between the oscillating shear layer and the trailing edge of the cavity produces sound waves which propagate upstream through the cavity starting a new disturbance cycle.

In this scenario, the fundamental period T is the sum of the disturbance convection time in the shear layer and the acoustic feedback time. Thus,

$$T = \tau_{\text{conv}} + \tau_{\text{acoustic}} =$$
$$\frac{L}{\kappa U} + \frac{L}{c} \quad (29.2)$$

where κU is the convection velocity of the large-scale structures (i.e., $U_c = \kappa U$). From this expression, the Strouhal number fL/U can be derived:
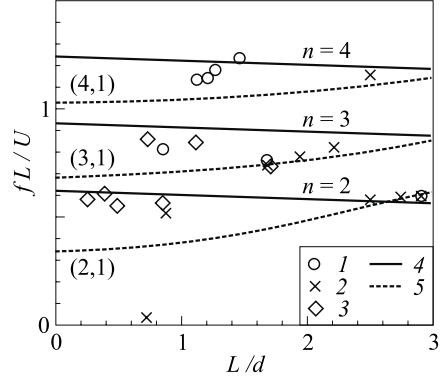
$$\frac{f_n L}{U} = \frac{n}{U/c + 1/\kappa} \qquad (29.3)$$

If one further generalizes the equation by assuming that there are certain phase lags in the leading and trailing edge processes, then Eq. (29.3) can be written in the following form

$$\frac{f_n L}{U} = \frac{n - \gamma}{U/c + 1/\kappa} \qquad (29.4)$$

where γ denotes the phase lag effect and is a weak function of L/d. Equation (29.4) is identical to Rossiter's semiempirical equation [13]. In Fig. 29.6, better agreement was obtained using Rossiter's formula and the constants extrapolated from the Rossiter's data. Some discrepancies and data scatter

Figure 29.6 Normalized frequency of cavity-induced oscillations as a function of cavity geometry. $1 - L = 23$ mm, $2 - d = 7.6$ mm, $3 -$ others, $4 - $ [13], and $5 -$ acoustic eigenmode, f_{mn}

could be attributed to neglecting other potentially important parameters such as finite shear layer thickness [12] and the cavity transverse acoustics associated with the cavity depth.

29.4 EFFECTS ON TURBULENT MIXING OF NONREACTING JETS (CASES 1 & 2)

As discussed in the previous section, excited shear layers dispersed at a higher rate than the natural shear layer growth rate. The amount of increase depended on the excitation frequency and amplitude. It was difficult to assess the effect of amplitude due to the passive nature of the excitation technique, but the frequency effect was investigated by comparing the results obtained with various cavities [14]. The results will be discussed in this section along with two other issues. One deals with the compressibility effect such as extending the results to a higher convective Mach number and the other concerned with possible thrust penalty associated with the passive excitation method.

First, the shear layer thickness at various axial locations in the near field was quantified using time-averaged Mie-scattering images. The shear layer thickness was defined as the radial distance over which the average Mie-scattering intensity dropped from 90% to 10% of the core value. Figure 29.7 shows the results
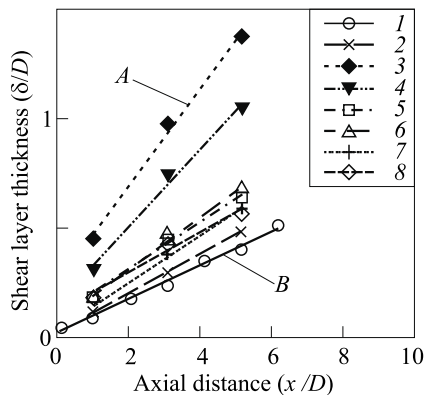
Figure 29.7 Spatial growth of excited shear layer thickness for several different frequencies. *1* — natural, *2* — 4.1 kHz, *3* — 13.5, *4* — 14.0, *5* — 24.1, *6* — 26.0, *7* — 28.6, and *8* — 38.9 kHz; A — $\partial\delta/\partial x = 0.227$ and B — 0.078
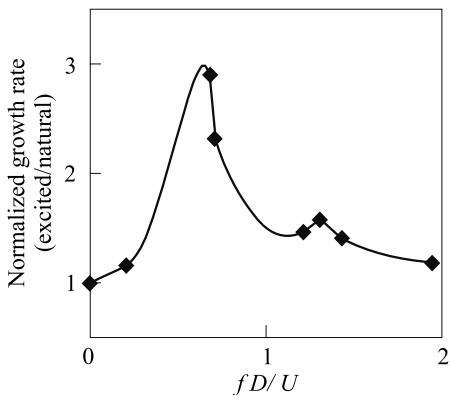
Figure 29.8 Excited shear layer growth rate as a function of excitation frequency (Case 1)

for several different excitation frequencies, which indicated the existence of the preferred mode frequency for maximum shear layer growth. The growth rate was measured using a linear regression fit and was plotted in Fig. 29.8 as a function of normalized excitation frequency. The maximum increase was observed at the Strouhal number of about a half. This suggests that the frequency dependence is related to the jet instability mode. Since the subsonic jet preferred mode occurs at the Strouhal number ranging between 0.24 and 0.64 [15], it implies that the preferred mode of supersonic jets occurs within a similar Strouhal number range as that of subsonic jets.

The measured growth rate for the natural case compared well with the reported values for visual thickness growth in fully developed planar compressible shear layers [9]. This finding is consistent with the results from other studies in which fully expanded supersonic jets were used [16, 17]. Both the natural shear layer growth rate and the excited shear layer growth rate were compared against the data from other facilities [8, 9, 18–20] in a normalized growth rate plot (Fig. 29.9). The present data for natural shear layer growth compare well with other data which include both planar and axisymmetric cases. There was a substantial increase in the growth rate with excitation even at a much higher convective Mach number, which was obtained with a high-temperature non-reacting jet.
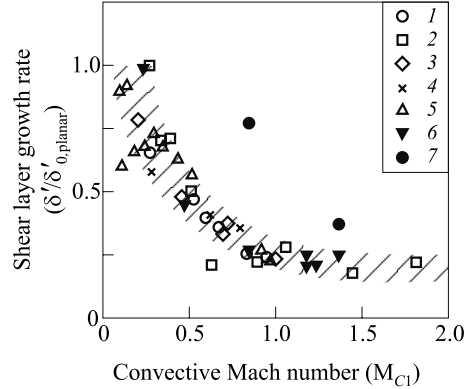
The high-temperature jet (Case 2) was tested as an intermediate step between exciting a cold nonreacting jet and a hot afterburning plume. The flow

condition was selected such that the gas composition and shear layer compressibility were similar to those in the afterburning plumes. Although the convective Mach number for this case ($M_C = 1.3$) was much higher than that for the cold jet case ($M_C = 0.84$), the jet was successfully excited and large coherent structures were generated in the shear layer. Figure 29.10 shows planar Mie-scattering images of hot jets excited using a semi-annular cavity and the corresponding acoustic spectra. The increase in the initial shear layer growth was not as drastic as in the cold jet, suggesting the stabilizing influence of high compressibility. Nevertheless, there was a substantial increase in the shear layer growth and the images clearly indicated formation of large-scale organized structures in the initial shear layer. Again, the excitation frequency was identifiable as a sharp peak in the microphone spectrum.

Figure 29.9 Normalized growth rate vs. convective Mach number for natural and excited shear layers: 1 — [8]; 2 — [9]; 3 — [19]; 4 — [18]; 5 — [20]; 6 — present facility (natural); and 7 — excited with cavity acoustics
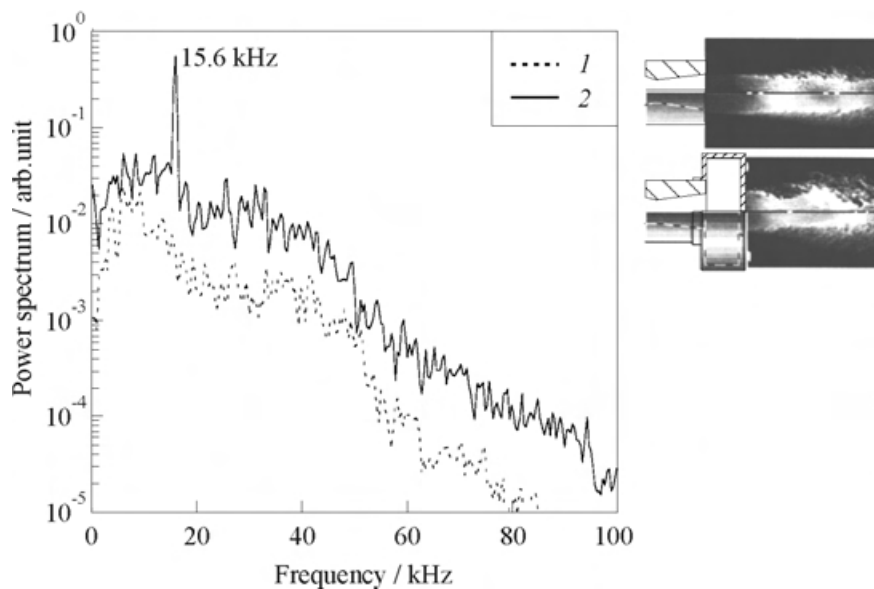
Also, in the cold jet case, pressure profiles were measured to assess possible thrust penalty associated with the flow-induced resonance. Near-field pressure profiles, which are plotted in Fig. 29.11 for typical forced and natural cases, again show the faster growth associated with the excitation. In the far field, the static pressure became identical to the ambient pressure. To obtain the thrust force, far-field total pressure profiles were integrated over the jet cross-sectional area. The measurement at 18 exit diameters downstream for the excited case showed that there was a force deficit of about 8% compared to the natural case. This appears to be the maximum amount of thrust penalty caused by periodic impingement of shear flow on the cavity trailing edge.

## 29.5 PLUME AFTERBURNING CONTROL (CASES 3 & 4)

In this section, the effect of plume excitation on afterburning will be presented. For the excitation of simulated afterburning plumes, cavity dimensions were further modified to include the variation of the dimension x, which is the distance between the nozzle lip and the cavity trailing edge ($x \leq L$). In this case,

Figure 29.10 Acoustic power spectra and images of natural (*1*) and excited (*2*) jets for Case 2
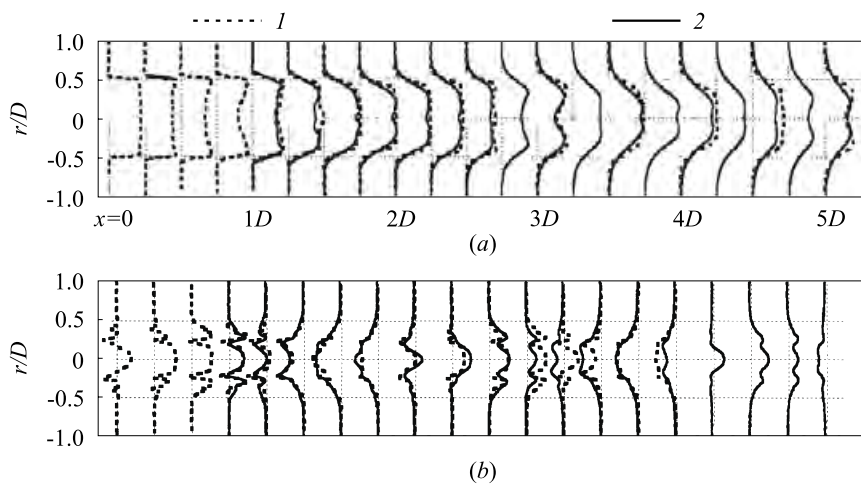
Figure 29.11 Comparison of pressure measurements in the near field of the natural (*1*) and excited (*2*) jets. Case 1: (*a*) total pressure profiles, and (*b*) static pressure profiles

fully annular cavities were used to produce symmetric excitation and maximize the effect. Also, the nozzle exit protruded into the cavity ($x < L$), creating a Helmholtz-resonator shape which was susceptible to both the Helmholtz mode oscillations and the coupled convective-acoustic mode oscillations discussed in the previous section.

Table 29.3 lists the new cavity dimensions that resulted in well-organized oscillations. The fundamental resonance frequencies for these cavities ranged between 20 and 40 kHz for the coupled convective-acoustic mode and 6 and 9 kHz for the Helmholtz mode. As before, the dominant frequencies included not only the fundamental mode frequencies, but also many higher harmonics and overtones.

Figure 29.12 shows the planar Mie-scattering images of the initial shear layer of an afterburning jet and the corresponding acoustic spectrum. Again, shear layer excitation resulted in formation of large-scale periodic structures and increased the growth rate. While it is clear that the increased growth rate and the changes in the shear layer structure dynamics will affect the turbulent mixing

Table 29.3 Cavity dimensions and the resulting oscillation frequencies

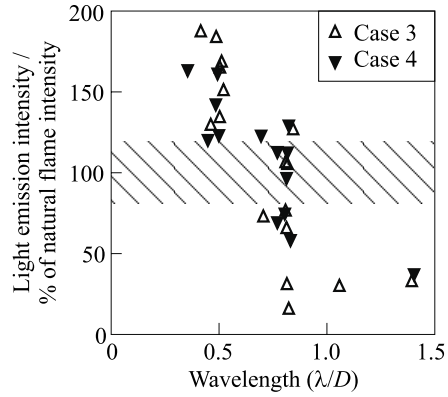| x/D	L/D	d/D	fD/U (Case 3)	fD/U (Case 4)
0.411*	1.412	1.143	0.270	—
0.411	1.412	1.143	—	0.797
0.513	0.909	0.898	0.405	0.406
0.513	0.909	1.143	0.351	0.364
0.513	0.898	1.143	0.355	0.349
0.513	1.412	1.143	0.691	—
0.565	1.412	1.143	0.355	0.346
0.616*	1.412	1.143	0.205	0.199
0.616	1.412	1.163	0.347	0.338
0.616	1.412	1.143	0.340	0.346
0.616	0.909	1.143	0.351	0.342
0.616	0.898	1.143	—	0.364
0.616	0.898	1.143	0.351	0.346
0.616	0.909	0.898	0.622	0.628
0.667	0.898	1.143	0.591	0.582
0.667	0.909	1.143	0.572	—
0.719	0.898	1.143	0.564	0.564
0.719	1.412	1.143	0.552	—
0.719	0.909	1.143	—	0.571
0.821	0.899	1.143	0.571	—

*Semi-annular cavities.
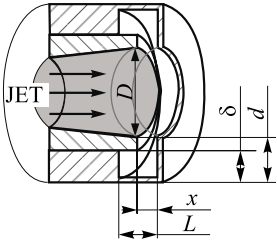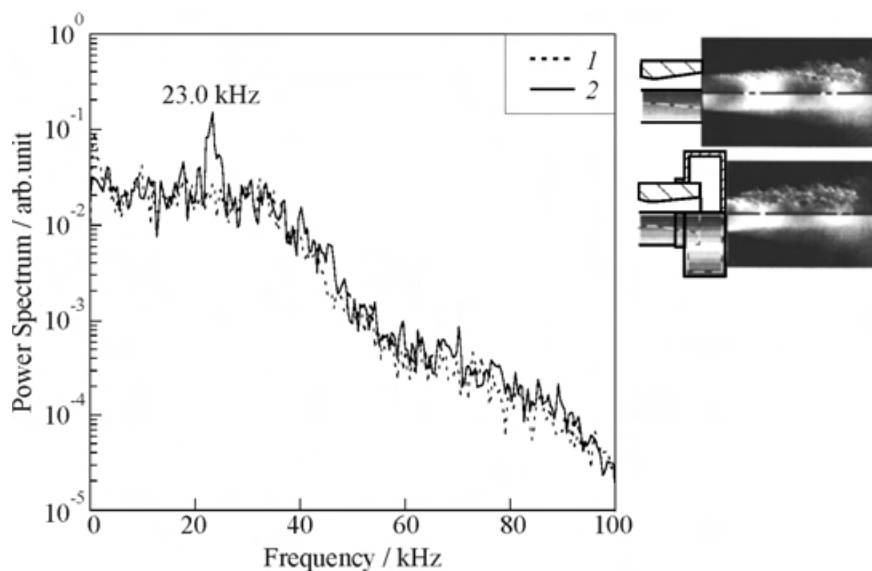
Figure 29.12 Acoustic power spectra and images of natural (*1*) and excited (*2*) jets for Case 4

processes in the initial shear layer, how these changes will influence afterburning flames is not readily obvious. For instance, on one hand, the afterburning flames could be adversely affected by the increased amount of cold surrounding flow entrainment and the increased strain rate due to large-scale structures. On the other hand, increased supply of fresh oxidizer into the fuel-rich products may help promote early afterburning reaction in the initial mixing layer, and could enhance the combustion intensity via increased molecular-level mixing. Ultimately, the balance between these two opposing influences would determine the net outcome on the afterburning flames.

Figure 29.13 shows the time-averaged visible light emission from excited afterburning flames plotted against the wavelength of the excited structures. The wavelength was deduced from measured frequency and calculated convective velocity U_c. The amount of global emission was measured over a one-second time period and was normalized by the amount of emission from the natural flames. The effect was investigated in the frequency range covering the jet preferred mode, where the shear layer growth was most drastically affected. Within this range, afterburning intensity was reduced by low-frequency excitation, which produced relatively long wavelength large-scale structures. Equivalently, high-frequency excitation that produced relatively short wavelength large-scale structures increased the amount of emission.

The above trend appears to be related to the change in average ignition distance. In Fig. 29.14a, the average flame lift-off height was plotted as a function of the excitation frequency. The flame lift-off height, which is related to the ignition distance, was inversely affected by the excitation frequency. Since the flow time scale decreased with increasing frequency, the data were plotted as a function of the Damköhler number in Fig. 29.14b, where the characteristic flow time scale was estimated by large-eddy turnover time as $1/U$ and the characteristic chemical reaction time was computed using an ignition delay model [21] for ethylene jet. While the results did not show any evidence of critical Damköhler number, the range

Figure 29.13 Time-averaged visible light emission from excited afterburning jets. The shaded area shows the fluctuation in the natural flame intensity

of the Damköhler number was of the order one. This indicates that the present competition between afterburning enhancement and reduction mechanism was the result of the two time scales being similar.
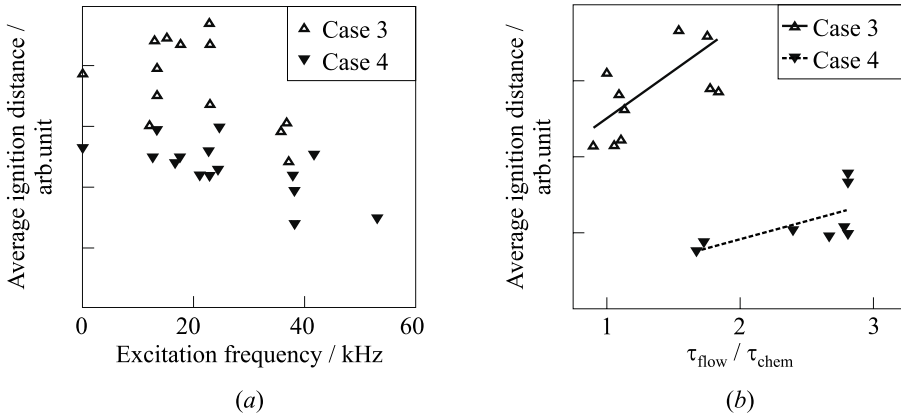
Figure 29.14 Change in flame lift-off height as a function of (a) excitation frequency and (b) Damköhler number

Lastly, it is interesting to note that the transition wavelength, at which the effect of excitation on global emission changes the direction from reduction to enhancement and *vice versa*, coincided with the preferred mode wavelength [22]. Assuming that the increase in visible light emission was due to enhanced afterburning, it appears that large-scale structures with the wavelength shorter than the preferred mode promoted faster energy transfer into fine-scale structures causing better molecular mixing between high-temperature plume and surrounding air. On the other hand, those with wavelength longer than the preferred mode adversely affected plume afterburning by entraining cold air into the plume with a high rate of strain. Then, the fact that the plume afterburning characteristics were most significantly affected by excitation at frequencies close to the jet preferred mode may be explained by the turbulent energy cascade phenomenon which was sensitive to the initial size of energy containing eddies in relation to the preferred mode wavelength.

29.6   CONCLUDING REMARKS

Past ONR sponsored research related to rocket plumes has explored the possibility of passive mixing control for afterburning modification. While many mixing control techniques tended to generate large-scale structures that could be used to quench afterburning, they could also enhance afterburning as the breakdown of large-scale structures intensified fine-scale mixing. As a result, the net effect of large-scale structures on plume afterburning was poorly understood, and it was difficult to assess the effectiveness of a mixing control approach. In this study, a novel technique, which is based on flow-induced cavity resonance, was used to control large-scale structure frequencies, thus making it possible to perform controlled experiments for enhanced understanding of the physical processes.

A systematic investigation on the effect of plume excitation revealed that plume afterburning intensity can be significantly altered depending on the characteristics of large coherent structures. In particular, the excitation frequency played an important role in changing the plume afterburning intensity either in positive or negative directions. The direction of the change was related to the turbulence cascade characteristics of large-scale structures with wavelength similar to that of the preferred mode. The results indicate that the properly designed mixing control approach could effectively alter the plume afterburning characteristics.

The present study has provided much insight into the dynamics of turbulent mixing in the initial plume–air shear layer, particularly that of the large-scale periodic structures which can affect the plume afterburning characteristics. While there is a need for better understanding on plume–air mixing control, such insight will undoubtedly provide a tool for designing an effective afterburning control

system. Also, in the present study, only passive techniques have been employed. Future studies should consider active techniques as well, especially in light of the fast developing actuator technology and the drastic effect periodic structures can have on afterburning intensity.

ACKNOWLEDGMENTS

REFERENCES

1. Terminology and assessment methods of solid propellant rocket exhaust signatures. 1993. AGARD Propulsion and Energetics Panel Working Group 21. Advisory Report AGARD-AR-287.
2. Miller, E., and S. Mitson. 1985. The suppression of afterburning in solid rocket plumes by potassium salts. AIAA Paper No. 85-1253.
3. Yu, K. H., K. C. Schadow, K. J. Kraeutle, and E. J. Gutmark. 1995. Supersonic flow mixing and combustion using ramp nozzle. *J. Propulsion Power* 11(6):1147–53.
4. Yu, K. C., and K. C. Schadow. 1994. Cavity-actuated supersonic mixing and combustion control. *Combustion Flame* 99:295–301.
5. Dash, S. M. 1986. Analysis of exhaust plumes and their interaction with missile airframes. In: *Tactical missile aerodynamics*. Eds. M. J. Hemsch and J. N. Nielsen. Progress in astronautics and aeronautics ser. Washington, D.C.: AIAA 104:778–851.
6. Schadow, K. C., K. H. Yu, and D. W. Netzer. 1998. Exhaust plume characterization and control. In: *Propulsion combustion: Fuels to emissions*. Ed. G. D. Roy. Washington, DC: Taylor & Francis. 329–58.
7. Bogdanoff, D. W. 1983. Compressibility effects in turbulent shear layers. *AIAA J.* 21(6):926–27.
8. Chinzei, N., G. Masuya, T. Komuro, A. Murakami, and K. Kudou. 1986. Spreading of two-stream supersonic turbulent mixing layers. *J. Physics Fluids* 29(5):1345–7.
9. Papamoschou, D., and A. Roshko. 1988. The compressible turbulent shear layer: an experimental study. *J. Fluid Mechanics* 197:453–77.
10. Yu, K. H., E. Gutmark, and K. C. Schadow. 1993. Passive control of coherent vortices in compressible mixing layers. AIAA Paper No. 93-3262.
11. Tam, C. K. W. 1976. The acoustic modes of a two-dimensional rectangular cavity. *J. Sound Vibration* 49(3):353–64.
12. Tam, C. K. W., and P. J. W. Block. 1978. On the tones and pressure oscillations induced by flow over rectangular cavities. *J. Fluid Mechanics* 89:373–99.

13. Rossiter, J. E. 1966. Wind-tunnel experiments on the flow over rectangular cavities at subsonic and transonic speeds. Aeronautical Research Council Reports and Memo No. 3438.

14. Yu, K. H., R. A. Smith, K. J. Wilson, and K. C. Schadow. 1996. Effect of excitation on supersonic jet afterburning. *Combustion Science Technology* 113–114:597–612.

15. Gutmark, E., and C.-M. Ho. 1983. Preferred modes and the spreading rates of jets. *J. Physics Fluids* 6(10):2932–38.

16. Strykowski, P. J., and A. Krothapalli. 1993. The countercurrent mixing layer: Strategies for shear-layer control. AIAA Paper No. 93-3260.

17. Wishart, D. P. 1995. The structure of a heated supersonic jet operating at design and off-design conditions. Ph.D. Thesis. Tallahassee, FL: Department of Mechanical Engineering, Florida State University.

18. Clemens, N. T., and M. G. Mungal. 1992. Two- and three-dimensional effects in the supersonic mixing layer. *AIAA J.* 30(4):973–81.

19. Goebel, S. G., and J. C. Dutton. 1990. Velocity measurements of compressible, turbulent mixing layers. AIAA Paper No. 90-0709.

20. Hall, J. L., P. E. Dimotakis, and H. Rosemann. 1993. Experiments in nonreacting compressible shear layers. *AIAA J.* 31(12):2247–54.

21. Beach, H. L., Jr. 1992. Supersonic combustion status and issues. In: *Major research topics in combustion.* Eds. M. Y. Hussaini, A. Kumar, and R. G. Voigt. New York: Springer-Verlag. 1–15.

22. Yu, K. H., and K. C. Schadow. 1997. Role of large coherent structures in turbulent compressible mixing. *J. Experimental Thermal Fluid Science* 14:75–84.

CONCLUSION

Chapter 30

CHEMICAL PROPULSION: WHAT IS IN THE HORIZON?

G. D. Roy

30.1 INTRODUCTION

Propulsion research has progressed steadily and well along focussed avenues during the past several decades. The outstanding contributions by talented researchers in the combustion discipline have led to the unprecedented fuel economy, reliability, and safety of the propulsion engines of today. Whereas fundamental problems in combustion related to propulsion are being solved at laboratories (in universities and industry), innovative systems are made commercially available. Laboratory experiments and numerical simulations lead to design optimizations that would otherwise involve heavy capital investment and long development times. Advances in Computational Fluid Dynamics (CFD) and in computational hardware led to a new frontier in numerical simulation and prediction of combustion phenomena through Computational Combustion Dynamics (CCD). The advent of microelectromechanical systems (MEMS) technology, diode lasers, miniature sensors, controls, and diagnostics makes it possible to control combustion starting at the fuel tank all the way to the exhaust pipe. Today's combustion researcher, developer, and designer have extremely powerful tools at hand.

To develop a totally new engine concept and to find commercial or military applications is a major challenge. When piston engines were the norm, the introduction of gas turbine engines was criticized as an exercise in futility. Research and perseverance have shown otherwise, and gas turbine engines are the engines of choice for most propulsion applications today. The time is right to focus on developing a new engine, to provide an alternate choice, perhaps a better choice, for certain applications.

30.2   LIMITATIONS OF PRESENT SYSTEMS

What are the choices for chemical propulsion in this century — an engine operating on a totally different fuel, one operating on a different thermodynamic cycle, or a combination of both? Of course, the choice depends upon the application. It is worthwhile to develop a new concept of engines, ensure there are no show stoppers, identify the issues, select appropriate approaches to solve the issues, and establish the fundamental understanding needed to develop the concept into a practical engine.

Before venturing into an alternate engine concept, it is prudent to briefly examine the limits and operational characteristics of existing or already tried engines. Most of the U.S. tactical missiles employ solid rocket motors due to their simplicity, small volume, and high-speed capability, but have a limited range, especially powered range. For missiles requiring longer range and carrying heavier payloads, turbojets/turbofans are employed because of their increased specific impulse. However, they become prohibitively expensive for higher Mach number operation, and are used for subsonic flight. Ramjets and ducted rockets have been developed for providing long powered range at higher Mach number (M = 2–4). However, they typically require solid propellant boosters to accelerate them to ramjet takeover speeds (M = 1.8–2.5), which increases cost and complexity. They, also, do not have the capability to loiter at subsonic speeds. Combined cycle engines — such as air turbo rockets, turbo ramjets, etc. — offer the potential for missions that require wide range in operating speed, but they are too complex and expensive [1].

30.3   HIGH-ENERGY-DENSITY FUELS

Increased range, speed, stealth, reliability, reduced size, and the capability to operate over a wide range of operational conditions without penalty in performance are desired of modern propulsion systems. Further, these should be achieved with less fuel consumption using an engine that costs less. An attractive way to increase the range of a given propulsion system is to increase the energy per unit volume of its fuel. For liquid hydrocarbon-fueled ramjets and cruise missiles, a new class of "high-density strained-hydrocarbon fuels" have been synthesized and its combustion characteristics were evaluated [2]. Research efforts in the development and characterization of these fuels are given in Section 1 of this book. The utilization of these fuels has not been demonstrated in actual engines, though the major issues in combusting these fuels are solved, and synthesis techniques for larger scale productions are in place [3].

The advantages of these fuels are often underestimated, considering the probable higher cost of the fuel compared with conventional fuels like JP-10 or diesel

oil. However, the system advantages are to be evaluated very carefully. For example, a 20% range increase in a cruise missile means staying away from the hostile war zone or target, by this extra distance. If the platform is manned (aircraft or ship), this results in reductions in risk to life, as well. A systems study incorporating this factor will show that the range advantages obtained by using these fuels will outweigh the cost of making them. With appropriate high-energy strained-hydrocarbon fuels, range increases over 40% can potentially be achieved in volume-limited systems. These fuels will have an impact in commercial transport as well — by providing longer nonstop flights. However, cost will be of primary importance since fuel cost/passenger mile is a deciding factor.

Research and development (R&D) in this decade should focus on manufacturing/refining these fuels through more economical synthetic routes and from cheaper starting materials. If sufficient quantities are made available, demonstration of the utilization of these fuels in real systems will be possible. Computational tools are in place to perform numerical experimentation [4]. The next step should be making large quantities of these fuels, and evaluating these fuels so as to transfer this science to technology applications.

30.4   CONTROL OF COMBUSTION PROCESSES

Though control of combustion dates back to almost a century, when centrifugal governors were introduced to control the speed of steam engines, as the engines become more complex, complex control systems are needed to maintain desired and optimal performance. As a result of the extensive research performed on atomization, vaporization, and mixing of fuel and oxidizer it has been possible to design engines with substantial improvement in specific fuel consumption, and consequently reduction in operational costs. However, mixing enhancement is largely confined to passive or active influence around the fuel injection area. Future engines should be controlled before combustion, during combustion, and after combustion, to ensure maximum utilization of energy, optimum and stable performance, and environmental compliance.

A focussed multidisciplinary, multiuniversity research program is sponsored by ONR to investigate such a scenario of obtaining all the above through the controlofcombustionprocessesoccurringinapropulsionengine[5–8].Figure**30.1** shows the roadmap of this effort. The control of mixing all through the combustion process will play the most important role. This becomes more demanding and difficult as the flow velocities increase and the combustor length (and volume) decreases. Further advances in this area are needed and accelerated R&D is in order. Joint industry–university and industry–government R&D efforts are also underway to implement the control strategies developed by university researchers in industry applications. These joint endeavors substantially reduce
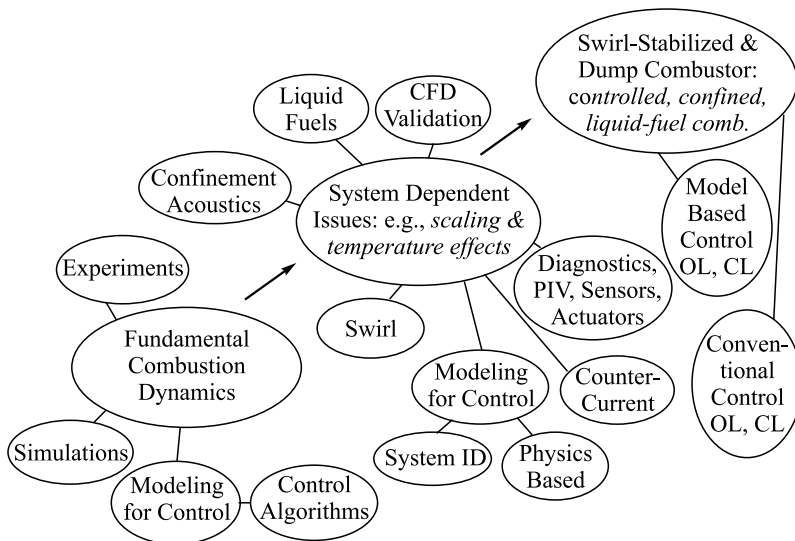
Figure 30.1 Control of combustion processes roadmap

the time it takes and the cost to realize technology applications. It is hoped that future engines will perform equally well in off-design conditions, with improved reliability and easier maintenance.

30.5   PULSE DETONATION ENGINES

An engine concept that utilizes a more efficient thermodynamic cycle that consumes less fuel, and is simple and capable of operation at both subsonic as well as supersonic speeds, would be an attractive alternative for future propulsion systems. Pulse detonation engines (PDE), in principle, can provide higher efficiency [9], and better performance over a wide range of operating conditions, with fewer moving parts.

Over several decades, extensive research has been undertaken on the fundamental theory and the mechanisms involved in detonation. Extensive information on this research is in the literature [10]. But of the three fundamental combustion phenomena — deflagration, explosion, and detonation — only detonation has not found exploitation in practical civilian or military applications to the extent that this phenomenon warrants. This is partly due to the fact that the science and technology involved is very complex due to the intense and fast energy release rates and their interaction with the confinement prescribed by the
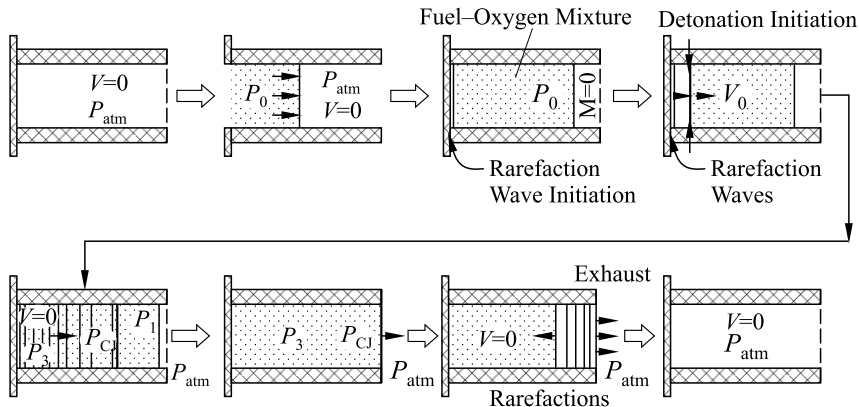
Figure 30.2 Schematic of PDE operation [9]

application. The lack of decisive customer demand for devices based on detonation phenomena is another factor that has prevented the transition of detonation science to technology.

The climate has changed in both of these areas. Measurements with very high spatial and temporal resolution, recently made possible, will help to understand and control detonation wave propagation in confined geometry. The evolution of MEMS enables advanced control strategies. Further, current advances in CCD and the capability of modern computers make it possible to perform meaningful computations, parametric studies, and scale-up of the transient process. With the increasing emphasis in costs and economic fuel usage, simple and thermodynamically more efficient engines are receiving added attention. PDE has this potential, with a wider operational envelope and fewer moving parts. In a PDE, detonation is initiated in a tube that serves as the combustor. The tube can be of constant area, axisymmetric, variable area, or nonaxisymmetric. The detonation wave rapidly traverses the chamber resulting in a nearly constant-volume heat addition process that produces a high pressure in the combustor and provides the thrust. The operation of multitube configurations at high frequencies (100 Hz and more) can produce a near-constant thrust. A schematic of PDE operation is shown in Fig. 30.2 [9].

In Fig. 30.3, the thermodynamic efficiencies of a constant-pressure Brayton cycle, a constant-volume Humphery cycle (which approximates a PDE cycle), and a true detonation Chapman–Jouguet (CJ) cycle for a typical hydrocarbon fuel are compared [11]. Though the constant-volume cycle shows substantial efficiency advantage, this zeroth order comparison cannot be taken as the correct quantitative comparison, since PDE operates in a pulsed transient mode. How-
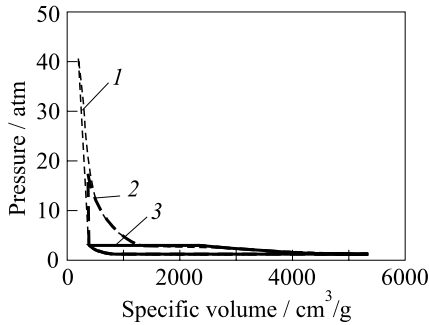
Figure 30.3 Comparison of thermo-dynamic efficiency of various cycles. *1* — CJ cycle; *2* — Humphery cycle; and *3* — Brayton cycle [11]
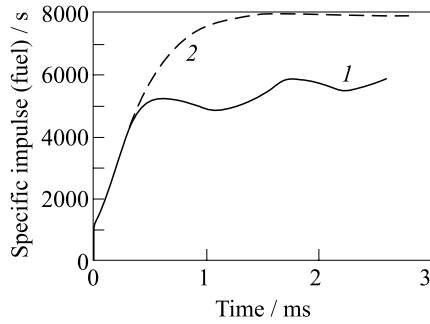
Figure 30.4 Variations of I_{sp} with tube exit relaxation modes. *1* — very fast relaxation; *2* — very slow relaxation [11]

ever, this gives the confidence that one begins with a much more efficient cycle to develop PDE.
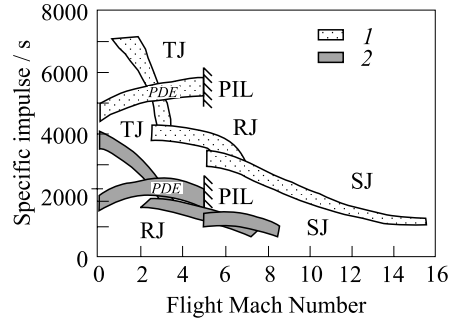
30.5.1 Scientific and Engineering Challenges

During the past several years, universities and industry have studied PDEs, detonation physics as applied to PDE, and the performance and operational envelope of PDE, as well as have demonstrated single and multicycle detonations. Calculation of the theoretical cycle efficiency requires prediction of detonation wave structure, and the resulting head-end pressure–time history, which is dependent upon the PDE geometry. The geometry influences the evacuation and refilling times as well as the pressure history, while the detonation wave traverses the tube. This could result in considerable differences in the calculation of PDE cycle efficiency. Various assumptions made and the boundary conditions used in the formulation will predict varying performance advantages. Figure 30.4 shows the variation in the specific impulse, depending upon how the exit boundary conditions of the detonation tubes are prescribed [11]. As can be seen, substantial difference can occur when the gases are relaxed instantaneously to the ambient as opposed to gradual relaxation. The performance of PDE varies with the altitude at which it flies and the type of fuel it uses. Hence, the development of PDE performance criteria and the tools to predict accurately the performance are vital not only for design, but also for comparison with other competing technologies. Performance and operational envelope of various engines provided by Adroit Systems, Inc. are shown in Fig. 30.5 [12].

A PDE, using hydrogen or hydrocarbon fuels, has a performance advantage and exhibits nearly constant specific impulse over the flight regime. It also provides the capability of propulsion from subsonic to supersonic speeds without a booster. The simplicity in design and easy scalability could result in reduced development time and cost of PDE-based air-breathing propulsion systems.

Several investigations on detonation for propulsion applications have been reported [13, 14]; however, research during the past decades focussed mainly on the fundamental physics of detonations. Due to the difficulties involved in initiating, sustaining, and controlling detonations in prescribed configurations, a PDE-based practical propulsion system has not yet emerged. There has been a renewed interest due to the recent advances in combustion diagnostics and CCD, and the search for propulsion system applicable to both subsonic and supersonic flight. In order to utilize PDE, high-frequency ($>$ 100 Hz), multitube operation will be required. Multicycle PDE operation has been demonstrated by industry using gaseous fuels, and a demonstration using liquid fuels is underway [15]. In addition to the engineering issues regarding valves, thermal management, packaging, etc., several scientific issues need to be further addressed. Future research should focus on the following challenges:


Figure 30.5 Comparison of specific impulse and flight Mach number for hydrogen (1) and hydrocarbons (2). PDE performance estimated using ASI Performance deck; turbojet, ramjet, and scramjet performance levels reflect well-designed systems for man-rated thrust classes. TJ — turbojets; RJ — ramjets; SJ — scramjets; PDE — pulse detonation engines; PIL — preignition limit [12]

1. Understanding the complex physical, chemical, and thermodynamic phenomena associated with liquid-phase injection, mixing and ignition, those which influence rapid development of detonation waves, and the role of transverse waves in the detonation process.

2. Investigating efficient fuel injection and ignition.

3. Exploring methods of efficiently integrating PDE with mixed compression supersonic inlets, and high-performance exhaust nozzles.

4. Understanding the dynamic coupling between multitube detonation chambers.

5. Developing complex diagnostics including semiconductor surface sensors and optical sensors, based on tunable laser diodes for sensing both gaseous and liquid characteristics.

6. Investigating adaptive, active control to ensure optimal performance while maintaining margin of stability.

7. Performing mathematical analysis, advanced computational simulation, and modeling of detonation of multicomponent mixtures using real chemistry and molecular mixing.

These issues should be addressed simultaneously and cross-fertilized in order to make timely progress in PDE development.

Though the fundamental issues in developing PDE are the same, depending on the operational modes such as a Pulse Detonation Rocket Engine (PDRE) or a Pulse Detonation Air-Breathing Engine (PDABE), or the fuel (gas or liquid) and oxidant (oxygen or air), the challenges can vary. It is easier to detonate a gaseous fuel than a liquid fuel, and is easier to detonate with oxygen rather than air. The Navy is interested in liquid fuel and air as the oxidant, which is the most difficult scenario. In order to sustain detonation a minimum number of transverse waves is shown to be required in a given cross-section. The fundamental difficulty in detonating a fuel in air is illustrated in Fig. 30.6 [16]. In Fig. 30.6*a*, for a given channel width, the detonation structure is shown for ethylene–oxygen mixture. For the same channel width, the detonation structure is shown for ethylene–air (Fig. 30.6*b*). The number of transverse waves has decreased with air mixture, having a damping effect on
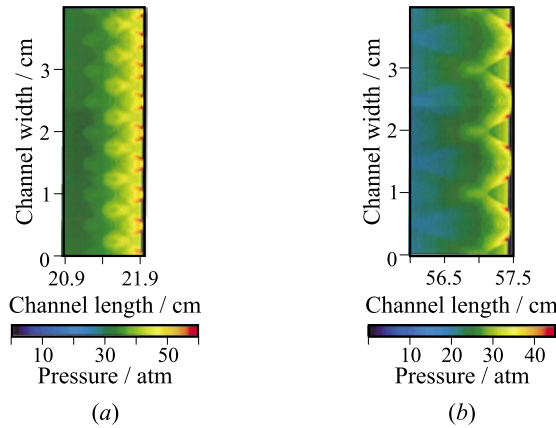
Figure 30.6 Comparison of detonation structures with ethylene–oxygen (*a*) and ethylene–air (*b*) [16]
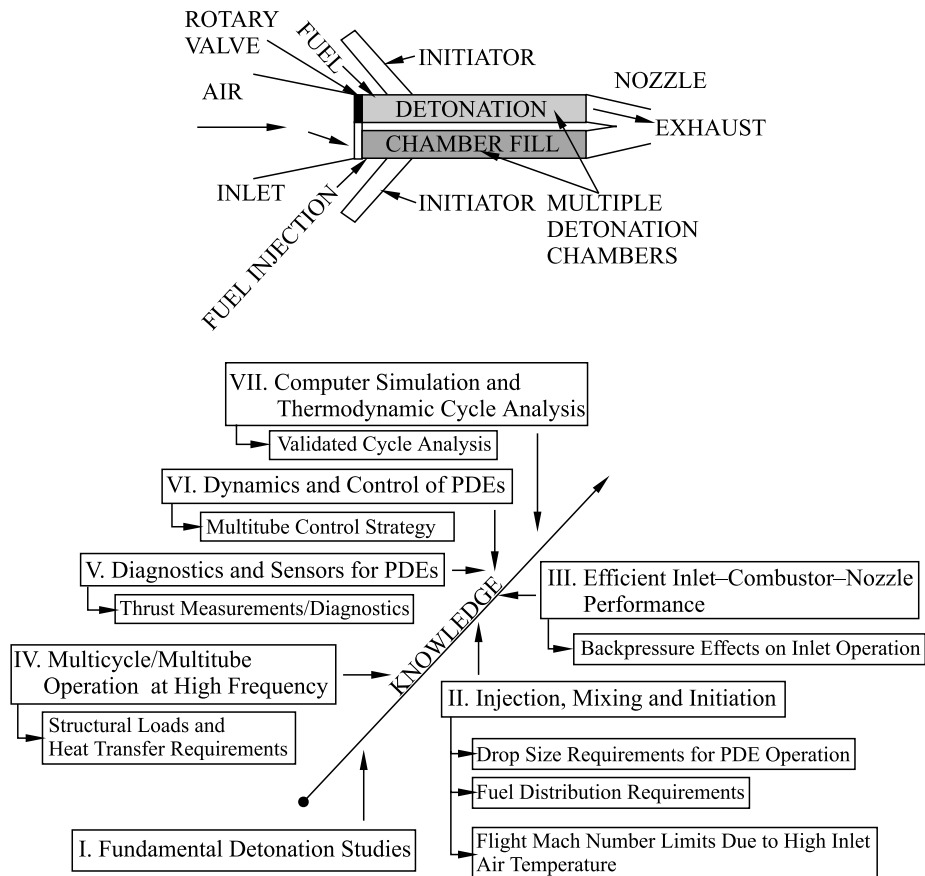
Figure 30.7 Expected knowledge from ONR PDE research

the detonation propagation. Since weight taken by an oxygen tank on board a missile is a penalty, direct detonation of liquid fuel in air is a challenge to be addressed.

The scientific issues indicated earlier are presently addressed in a five-year focussed research program sponsored by ONR. A research roadmap has been formulated with the participation of several U.S. universities, industry, and international research organizations. The scientific research areas addressed and the knowledge (transition elements to technology) expected from this program to help the development community in their PDE efforts are shown in Fig. 30.7.

30.5.2 Opportunities in PDE Research and Development

In today's climate any evolving or innovative technology should meet two criteria: (*a*) operational reliability, efficiency, etc., and (*b*) be able to compete with existing technology with sufficient margin. Small incremental advantages do not warrant substantial investment when R&D funds are getting scarce. Several R&D opportunities arise from the challenges pointed out earlier. First of all, there is a need for reliable performance prediction. This opportunity comprises not only direct numerical simulation of the PDE process in a realistic control volume, but also the reduced chemical reactions formulation, and appropriate user-friendly model development. Inter-agency sponsorship is needed to develop a "mutually agreed upon and verifiable" performance prediction strategy.

There is opportunity in the future not only to perform CCD simulations to understand and develop parametrics of components, but also to elucidate inlet, combustor, nozzle interactions, and optimization. Further a validated system code is needed from the system performance prediction, comparison, optimization, and design points of view. The study should be extended to various fuel–oxidizer combinations.

Development of benchmark experiments that can accurately measure performance of simple PDE configurations, which can be used for CCD code validations, is required. This will also provide fuel droplet size and distribution, species concentration, and soot and thrust measurements.

The fuels area offers significant future opportunities for the synthetic chemists and combustion scientists. A tailored fuel may be in order since fuels that exhibit rapid initiation and rapid development of chemical reactions can significantly influence the detonation process.

There is also an opportunity to use the concept of controlled in-chamber blending of two fuels exhibiting different detonability characteristics [17].

Simple axisymmetric detonation tubes of constant cross-sections have been used in most of the laboratory scale and development experiments. Such a cross-section offers ease of fabrication and stacking; however, to minimize the length of the detonation chamber and to sustain efficient detonation propagation and scale-up, a noncircular varying geometry cross-section may be more appropriate. There are opportunities to explore this aspect both from the basic detonation initiation and propagation points of view, and from the engineering design and packaging points of view.

Tailored fuel injection, multicycle operation, and multichannel configurations provide a challenging opportunity for control of detonation-based propulsion systems. By sequencing the firing order and controlling the number of cycles, fluidic thrust vectoring without external fins and actuators may be feasible. This will further the competitive edge of PDE due to the associated reduction in drag, and improved acceleration, deceleration, and maneuverability.

30.6 CONCLUDING REMARKS

The past several decades have seen substantial advances in chemical propulsion. A number of scientific accomplishments such as sequential fuel injection and active feed-back control with diode-laser sensors have been transitioned to technology applications. In the 21st century, the demands on engines used in chemical propulsion systems are increasing, whereas the development time and costs — both capital and operational — are to be reduced. This leads research to a multidisciplinary, multiorganizational structure and to a close and constant interaction among scientific/technology/industry/customer communities. The old paradigm of a scientific research leading to technology development and product changed to a new paradigm of integration, shown in Fig. 30.8.
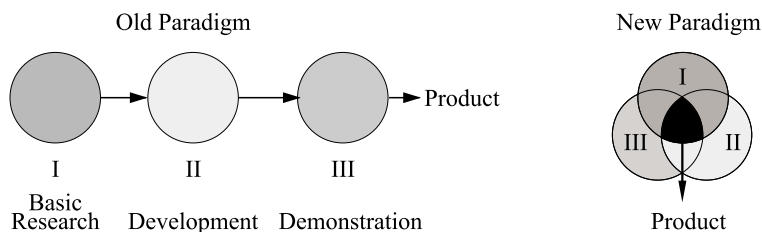
Figure 30.8 A comparison of the new and old paradigms

Research in this decade should focus on new energetic and tailored fuels with faster energy release rates. The combustion process should be controlled at all steps to obtain optimal performance from the chemical propulsion system at all conditions of operation. Detonation processes should be investigated with reference to propulsion applications such as a multitube multicycle PDE. Investigations of new and novel combustion concepts are in order. With the unprecedented tools on hand — ultrafast computing capability, *in situ* diagnostics with high temporal and spatial resolution, and faster data processing algorithms — maybe quantum leaps can become reality in chemical propulsion in the near future.

REFERENCES

1. Jenson, G. E., and D. W. Netzer, eds. 1996. *Tactical missile propulsion*. AIAA progress in astronautics and aeronautics ser. Washington, DC: American Institute of Aeronautics and Astronautics 170.
2. Roy, G. D. 2000. Utilization of high-density strained-hydrocarbon fuels for propulsion. *J. Propulsion Power* 16(4):546–51.

3. Moriarty, R. M., L. A. Enache, D. Pavlovic, D. Huang, and M. Rao. 1996. Synthesis of high-energy compounds. *9th ONR Propulsion Meeting Proceedings*. Eds. G. D. Roy and K. Kailasanath. Washington, DC: Naval Research Laboratory. 123–9.

4. Chang, E. J., and K. Kailasanath. 1998. Dynamics and microexplosion of high-energy fuels injected into a combustor. *Combustion Science Technology* 137: 217–36.

5. Krstic, M. 1999. Nonlinear control of combustion instabilities. *12th ONR Propulsion Meeting Proceedings*. Eds. G. D. Roy and S. L. Anderson. Salt Lake City, UT. 39–46.

6. Mashayek, F. 1999. Simulation and modeling of two-phase turbulent flows for prediction and control of combustion systems. *12th ONR Propulsion Meeting Proceedings*. Eds. G. D. Roy and S. L. Anderson. Salt Lake City, UT. 88–95.

7. Vaudrey, M. A., W. R. Saunders, and B. Eisenhower. 2000. A test-based methodology for *a priori* selection of gain/phase relationships in proportional phase shifting control of combustion instabilities. ASME Paper No. 2000-GT-0530.

8. Annaswamy, A. M., M. Fleifil, J. W. Rumsey, R. Prasanth, J. P. Hathout, and A. F. Ghoniem. 2000. Thermoacoustic instability: Model based optimal control designs and experimental validation. *IEEE Transactions on Control Systems Technology* 8(6).

9. Bussing, T., and G. Pappas. 1994. An introduction to pulse detonation engines. AIAA Paper No. 94-0263.

10. Roy, G. D., S. M. Frolov, K. Kailasanath, and N. Smirnov, eds. 1999. *Gaseous and heterogeneous detonations: Science to applications*. Moscow: ENAS Publ.

11. Kailasanath, K. 1999. A review of research on pulse detonation engines. *17th Colloquium (International) on the Dynamics of Explosions and Reactive Systems Proceedings*. Heidelberg, Germany.

12. Christofferson, E. 1999. Private communications.

13. Nichols, J. A., H. R. Wilkinson, and R. B. Morrison. 1957. Intermittent detonation as thrust-producing mechanism. *Jet Propulsion* 27:534–41.

14. Dabora, E. K., and J. C. Broda. 1993. Standing normal detonations and oblique detonations for propulsion. AIAA Paper No. 93-2325.

15. Bussing, T. R. A., T. E. Bratkovitch, and J. E. Hinky, Jr. 1997. Practical implementation of pulsed detonation engines. AIAA Paper No. 97-2748.

16. Li, C., and K. Kailasanath. 2000. Detonation diffraction in pulse detonation engines. AIAA Paper No. 2000-3470.

17. Frolov, S. M., V. Ya. Basevich, A. A. Belyaev, and M. G. Neuhaus. 1999. Application of fuel blends for controlling detonability in pulsed detonation engines. In: *Gaseous and heterogeneous detonations: Science to applications*. Eds. G. D. Roy, S. M. Frolov, K. Kailasanath, and N. N. Smirnov. Moscow: ENAS Publ. 313–30.